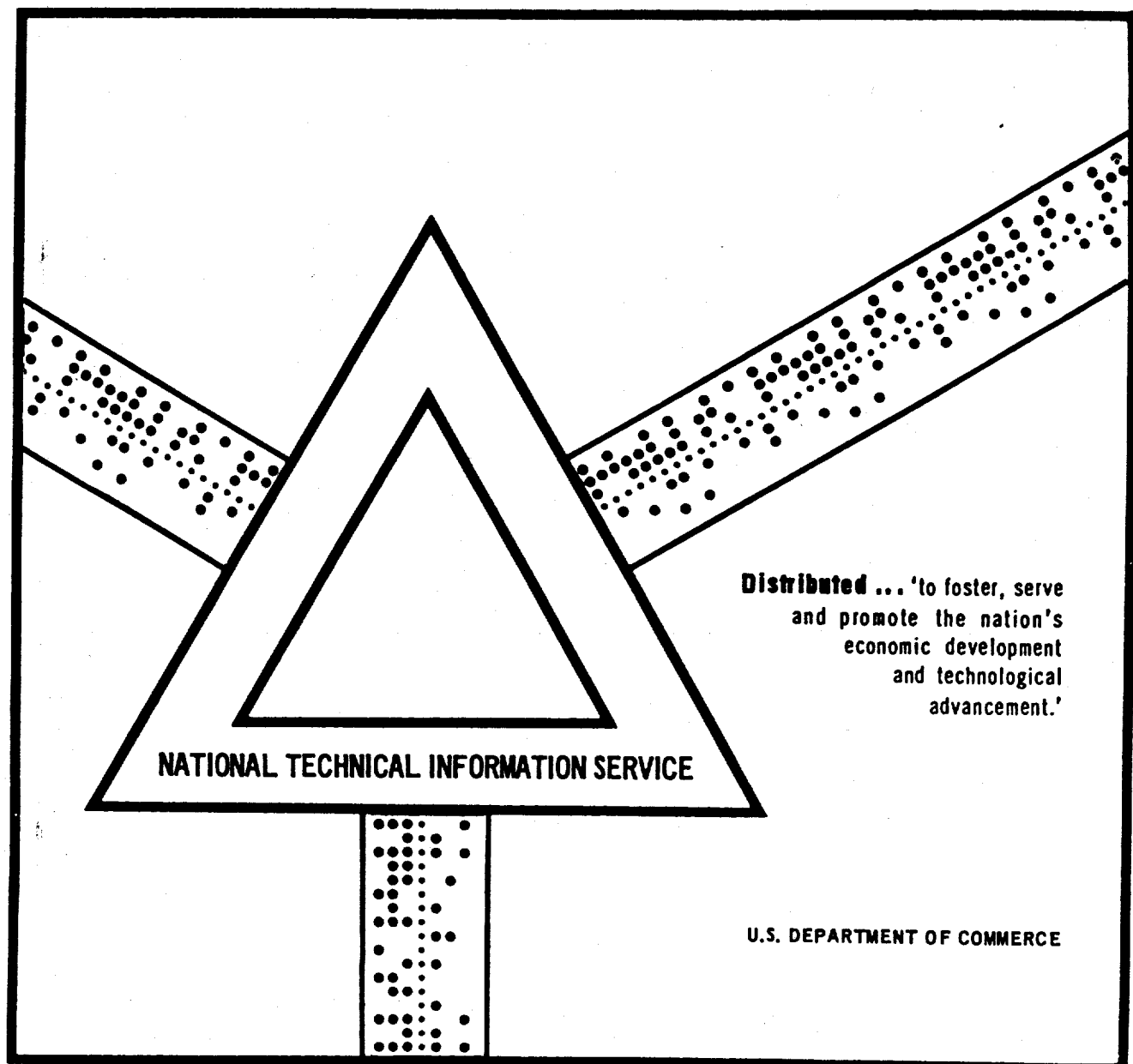


PROCEEDINGS OF THE SYMPOSIUM ON SPACECRAFT  
ATTITUDE DETERMINATION, SEPTEMBER 30, OCTO-  
BER 1-2, 1969. VOLUME I. UNCLASSIFIED PAPERS

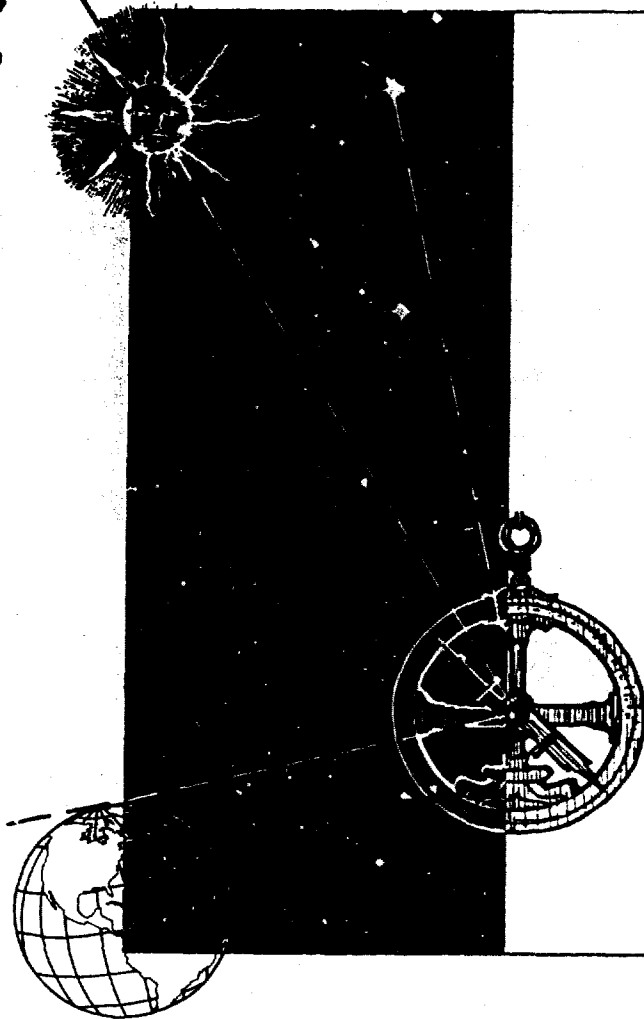
L. J. Henrikson, et al

Aerospace Corporation  
El Segundo, California

31 October 1969



AD704600



*PROCEEDINGS  
OF THE  
SYMPOSIUM ON  
SPACECRAFT  
ATTITUDE  
DETERMINATION*

*September 30,  
October 1-2, 1969*

VOLUME I  
UNCLASSIFIED PAPERS

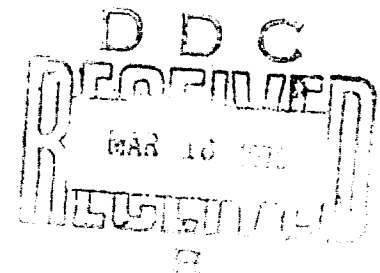
Cosponsored by AIR FORCE SYSTEMS COMMAND  
Space and Missile Systems Organization  
and THE AEROSPACE CORPORATION

Held at The Aerospace Corporation  
2350 El Segundo Boulevard  
El Segundo, California

69 OCT 31

Reproduced by  
NATIONAL TECHNICAL  
INFORMATION SERVICE  
Springfield, Va 22151

THIS DOCUMENT HAS BEEN APPROVED FOR PUBLIC  
RELEASE AND SALE; ITS DISTRIBUTION IS UNLIMITED



484

Air Force Report No.  
SAMSO-TR-69-417, Vol I

Aerospace Report No.  
TR-0066(5306)-12, Vol I

PROCEEDINGS OF THE SYMPOSIUM ON  
SPACECRAFT ATTITUDE DETERMINATION,  
SEPTEMBER 30, OCTOBER 1-2, 1969

Volume I: Unclassified Papers

Cosponsored by  
AIR FORCE SYSTEMS COMMAND  
Space and Missile Systems Organization  
and THE AEROSPACE CORPORATION

Held at  
THE AEROSPACE CORPORATION  
2350 El Segundo Boulevard  
El Segundo, California

69 OCT 31

This document has been approved for public  
release and sale; its distribution is unlimited

PAGES \_\_\_\_\_  
ARE  
MISSING  
IN  
ORIGINAL  
DOCUMENT



## FOREWORD

---

These proceedings are published by The Aerospace Corporation, El Segundo, California, under Air Force Contract No. F04701-69-C-0066. Any other applicable contract number or company sponsorship is cited in a footnote on the first page of the individual paper.

This document was submitted on 4 December 1969, for review and approval, to Captain D. Evans, SAMSO (SMTAE).



L. J. Henriksen  
The Aerospace Corporation  
Cochairman




D. Evans, Captain, USAF  
SAMSO  
Cochairman



J. E. Lesinski  
The Aerospace Corporation  
Cochairman

The views expressed in each paper are those of the author. Publication of this report does not constitute Air Force or Aerospace approval of the report's findings or conclusions. It is published only for the exchange and stimulation of ideas.



A. J. Schiewe  
Director, Control and Sensor  
Systems Subdivision  
Electronics Division  
Engineering Science Operations  
The Aerospace Corporation



D. Evans, Captain, USAF  
Project Officer

## PREFACE

---

The Symposium on Spacecraft Attitude Determination was held at The Aerospace Corporation, El Segundo, California, on September 30 and October 1-2, 1969. It was cosponsored by the Air Force Systems Command, Space and Missile Systems Organization, and The Aerospace Corporation.

The symposium brought together 306 representatives from 44 industrial, governmental, and educational organizations concerned with spacecraft attitude determination.

The purpose of the symposium was in general to present a broad coverage of the spacecraft attitude determination problem and in particular to review the advances in sensing and data processing techniques related to spacecraft attitude determination, to assess current capabilities, and to provide an exchange of ideas among people who have an active interest in the field. The sponsors hope that the symposium has stimulated new ideas and will lead to the advancement of spacecraft attitude determination potentials.

Symposium cochairmen were D. Evans, Captain, USAF, L. J. Henrikson, and J. E. Lesinski.

## ABSTRACT

---

These proceedings contain reproductions of the unclassified papers presented at the Symposium on Spacecraft Attitude Determination, held at The Aerospace Corporation on September 30 and October 1-2, 1969. Classified papers appear in Volume II.

The symposium consisted of six sessions. A brief summary of the material in each of these sessions follows.

Session I (Unclassified), Attitude Estimation Concepts, is devoted to papers surveying the general theory, modeling, and estimation algorithm concepts of use in estimating spacecraft attitude.

Session II (Unclassified), Attitude Sensors and Sensing Techniques, presents papers examining the current state of the art and future potential of some of the sensing techniques used in attitude determination.

Session III (Unclassified), Attitude Determination Systems I, comprises papers regarding attitude determination operational and design experience for several different satellite systems.

Session IV (Secret), SPARS, contains papers that discuss the hardware, algorithms, and system test results.

Session V (Secret), Attitude Determination Systems II, concerns papers on United States attitude determination requirements and classified applications.

Session VI (Secret) is the Panel Discussion. An edited transcription of the panel discussion and audience participation appears in Volume II of these proceedings.

Also included in the present volume are biographical sketches of the chairmen and speakers, and a list of the symposium attendees.

## CONTENTS

---

FOREWORD	ii
PREFACE	iii
ABSTRACT	v
Opening Session: KEYNOTE ADDRESS	1 1
Session I: ATTITUDE ESTIMATION CONCEPTS	5
Session II: ATTITUDE SENSORS AND SENSING TECHNIQUES	113
Session III: ATTITUDE DETERMINATION SYSTEMS I	187
Session IV: SPARS	279
Session V: ATTITUDE DETERMINATION SYSTEMS II	385
Session VI: PANEL DISCUSSION	415
BIOGRAPHIES	419
SYMPOSIUM ATTENDEES	427

OPENING SESSION

KEYNOTE ADDRESS

Dr. Ivan A. Getting  
President  
The Aerospace Corporation  
El Segundo, California

---

## KEYNOTE ADDRESS

Dr. Ivan A. Getting  
President  
The Aerospace Corporation  
El Segundo, California

It is my pleasure to welcome you to this Spacecraft Attitude Determination Symposium on behalf of both the Space and Missile Systems Organization of the Air Force, and The Aerospace Corporation. We are pleased to be hosts to a symposium on a very timely subject, a symposium which, we anticipate, will yield a useful exchange of ideas.

Let me define the topic of this symposium. A general definition of spacecraft attitude determination is:

The estimation of the angular orientation of a meaningful spacecraft-defined coordinate system.

In earlier days, attitude determination was often an implicit part of the attitude control system. As control system specifications became more precise, the attitude determination requirements became tighter, and the estimation of satellite attitude itself came to be recognized as a difficult and important task. At the same time, experiments on board spacecraft began to require highly accurate knowledge of sensor pointing directions. In the case of wide-field-of-view sensors the requirements, in addition to or even instead of pointing, emphasized high-accuracy knowledge of the line-of-sight direction. This then has led to the need for precision attitude determination. Some examples of early attitude determination include many of the gravity-gradient-stabilized satellites with such measurement devices as sun sensors and magnetometers. Also in this category are several of the early Air Force's OV1 series and such NASA satellites as the RAE. Examples of satellites with high-accuracy attitude determination requirements are, for NASA, the OAO and, for the Air Force, the TACSAT, the synchronous communications satellite--both of which will be discussed in this symposium.

Perhaps I ought to try to define what is meant by high accuracy. And if I may, I would like to fall back on a comment made in my introduction, regarding my involvement in high-accuracy radar. Indeed, during World War II, when we went to industry to obtain high-accuracy gear trains for driving antenna mounts, I found to my amazement that although it was easy to get a gear train with an accuracy of one angular mil (about four minutes of arc), it was almost impossible to improve this by a factor 10. In fact, you could not specify shaft concentricity, bearing concentricity, or diameters of gear trains, and have them produced if you wanted a factor of four or five improvement in an accuracy of one mil. Yet in the business of attitude specification of satellites we consider one mil as a useful definition of where high accuracy begins. As a matter of reference, 10 seconds of arc or a twentieth of a mil from synchronous altitude corresponds to about one mile on the earth at the nadir.

This is roughly the way in which attitude determination requirements have evolved. It is also important to note that this evolution has occurred very rapidly, and the requirements for more and higher-precision attitude determination are mushrooming. Because the need is mushrooming whereas the field is still relatively young, it seems very timely to bring together people from NASA, the Air Force, industry, and the universities who are interested in this area. It is felt that this is particularly appropriate because industry has expended considerable effort in studying the problem of satellite attitude determination, much of which is not as yet available in the open literature.

Attitude determination as considered in this symposium is of primary interest in the area of unmanned satellites. This can be readily

seen by noting the papers being presented, as well as the fact that this subject is of equal importance to both NASA and to the Air Force. It is of course reasonable that "automatic" attitude determination is most important for unmanned satellites carrying experiments with sensors for which pointing directions need to be held and known with accuracy. Because of the importance to both NASA and the Air Force, it is hoped that this symposium will help to stimulate a rewarding and continuing cooperation between these two agencies, associated contractors, and academic professionals.

In attitude determination systems the attitude sensors may be any of a large variety: sun sensors, magnetometers, horizon sensors, star trackers, star scanners, gyro packages, combinations of these, and others. The estimation techniques applied to the outputs of these sensors may vary from use of the outputs as direct measurements, to simple attitude deduction methods, to highly sophisticated estimation and data processing procedures. The data processing may be entirely "on board," or may be done partially

or wholly in ground-based data-processing centers. In all cases the end result is an estimate of the angular orientation of some frame associated with the spacecraft.

In view of these considerations the first part of the symposium attempts to survey the state of the art of estimation, data processing, and sensing concepts and techniques. These tools combined with the results of the design, analysis, and hardware experience of many contemplated and flying systems presented in the next few sessions should help to define the state of the art of attitude determination capabilities. From such a dissemination of existing experience and knowledge in this collection of related fields, it is hoped that the panel and audience discussion at the end of the five sessions will not only be able to define the current status of attitude determination, but also determine its potential and discern the direction which it should go from here.

Again, let me welcome you to the symposium.

SESSION I

ATTITUDE ESTIMATION CONCEPTS

Chairman:  
Prof. Harold Sorenson  
University of California at San Diego  
La Jolla, California

---

Foundations of the Problem of Attitude Determination from a Spinning Gyrostat	7
A Limited Memory Attitude Determination System Using Simplified Equations of Motion	15
Modeling of Environmental Torques of a Spin-Stabilized Spacecraft in a Near- Earth Orbit	29
A Least-Squares Attitude Determination Algorithm Utilizing Star mapper and Sun Sensor Time Pulses	53
Filtering Quantized Observations	71
Applications of Nonlinear Estimation Theory to Spacecraft Attitude Determination Systems	89



(U) FOUNDATIONS OF THE PROBLEM OF ATTITUDE DETERMINATION  
FROM A SPINNING GYROSTAT

Robert E. Roberson  
Consultant, Fullerton, California  
and  
Professor of Aerospace Engineering  
University of California, San Diego  
La Jolla, California

ABSTRACT

(U) The foundation problem of attitude determination from a spinning gyrost is to establish a relationship between a certain body frame and a certain external reference frame. This work shows how the sensor frame and various celestial frames appear in a natural way as intermediaries and distinguish between the relationships that can be considered known and those that must be obtained by observation. Modifications introduced by attitude control considerations also are included. The role of vehicle dynamics is described, and the nature of external and body frames likely to lead to simple predictive dynamic models are described for the case of the gyrost.

INTRODUCTION

(U) Consider two dextral orthonormal vector bases that are in some way associated with a spinning body: an "operational frame"  $O = \{O_i\}$  and a "sensor frame"  $S = \{S_i\}$ . Further, let  $G = \{G_i\}$  be an "orientation reference frame" whose own characteristics are in some sense known. In this work we examine the problem of determining the orientation of  $O$  with respect to  $G$  using observations made in  $S$ . We shall not leave matters at this level of generality, of course, and will quickly focus on a more concrete situation. We shall find, however, that many of the ingredients of the specific problem are brought out most clearly by considering it in its more general framework.

(U) In the case of spinning spacecraft, a well-known method for determining the orientation of the body is based on the detection of the times at which the images of celestial bodies cross one or more body-mounted slits.

(U) As usually applied, the purpose of this kind of attitude determination is to establish the inertial direction of the "spin axis" of the body. The body normally is considered to be rigid, except

perhaps for the inclusion of a dissipative precession damper. The dynamical behavior of the latter is such that the axis of maximum moment of inertia, as well as the instantaneous angular velocity vector, is kept almost coincident with the body's angular momentum vector as the latter slowly drifts under the action of the small natural external torque. Under these conditions there is no ambiguity about the meaning of "spin axis": it is simultaneously the principal axis, the angular velocity vector, and the angular momentum vector. These vectors become temporarily misaligned during the application of any control torques, but after some transient period they again resume their alignment.

(U) Because the traditional accuracy requirements in astronomical engineering for this class of attitude determination problems have not been extreme, it has not been customary or needful to refine the dynamical model further. All factors considered, past problems of attitude determination from quasi-rigid spinning bodies have had relatively straightforward -- though this is not to imply trivial -- solutions.

(U) The situation becomes somewhat different when these requirements are changed as follows:

1. The goal is to determine not just the orientation of a "spin axis" in the body, but of a prescribed body-associated vector basis having no special dynamical characteristics of its own;
2. The spinning body is not rigid, but is a quasi-rigid body containing sources of angular momentum -- a quasi-rigid gyrostati;
3. The requirement for accuracy in attitude determination is extreme.

With these changes the problem of attitude determination from a spinning body is more involved. It is difficult and perhaps misleading -- even dangerous -- to extrapolate directly the concepts, the experience and engineering judgment, the very terminology from the original to the modified problem.

(U) There often is a temptation in engineering practice to regard a problem that is new to us as a new problem. A moment's reflection, however, tells us that the present problem -- as I have stated it in general terms -- is scarcely new. For it is exactly the problem of the observational astronomer, who makes his observations: 1) from the surface of a quasi-rigid spinning body that almost certainly is nearly a classical gyrostati; 2) at an extremely high level of precision; 3) for purposes that include the ability to establish the orientation of other earth-fixed frames with respect to an external (real or virtual) orientation reference frame. To be sure, he may have found it more convenient to measure an angle than to measure slit crossing times; he may have found it more convenient to use methods of data reduction that are amenable to handling by desk calculator; he may have found that the motions undergone by his base are both slower and more regular than those undergone by a spinning spacecraft. But, in principle, many of the foundations of his problem are exactly those of ours, and we should explicitly recognize the fact. I shall not pursue the analogy further -- I am not an astronomer -- but I believe it would be interesting, and perhaps profitable, to do so.

(U) The purpose of this note is to discuss some of the foundations of this kind of attitude determination problem, foundations that are initially independent of the specific application and the details of how we may choose to implement an attitude determination scheme. In this way we

shall be able to see how our implementation path can bifurcate at various points and to get a clear perspective on the choices we face in finding our way along it. Special emphasis is on the role of the kinematics and dynamics of the gyrostatic observational base. If I accomplish nothing else in this work, I hope I will be able to demonstrate that a variety of "valid routes exist which all lead to the same place. One places the burden of implementation here, another places it there, but which is "best" is a pointless quibble until each has been explored and perfected to a level where quantitative comparisons can be made among their results.

### THE GRAPH

(U) Stripped to its fundamentals, the interrelationships of our problem can be visualized best by introducing a system graph. The frames mentioned previously are represented by vertices, and the relative orientations between them (as expressed by direction cosine matrices, for example) by edges of the graph. The present work specifically concerns attitude determination from slit crossing of star images, so it is convenient to introduce a celestial frame  $X$  with respect to which star lines of sight are definitively known. (As one example, this might be a frame established by the mean equator and mean equinox of 1950.0, since star catalogs are available in that frame. For definiteness in the discussion, this "standard frame"  $X_S$  is assumed in the sequel.) Now refer to Fig. 1 in which the four frames -- the standard celestial  $X_S$ , the body-associated  $S$  and  $O$ , and the external reference  $G$  -- are represented by points.

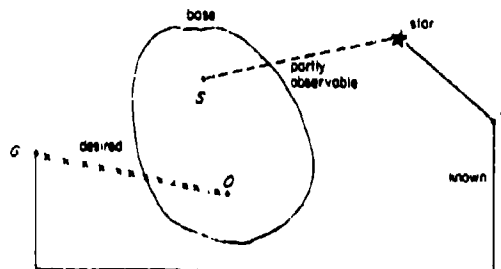


Fig. 1. Elementary System Graph

A typical star is shown, joined to the  $X_S$ -frame by a solid line to show that the relationship is known through the star catalog. The connection between the  $S$ -frame and the star is dashed to designate that the relationship has partial observability. The relationship between  $G$  and  $X_S$

can be presumed known in principle, once these frames have been explicitly defined, for the G-frame has been postulated as a reference frame external to the body. As illustration, it might be a frame fixed in the rotating Earth (to the degree a frame can be fixed in a non-rigid blob) or some celestial frame different from  $X_G$ . In any case, other aspects of the  $G X_G$  relationship are discussed later.

(U) The relationship denoted by the line of crosses is the one desired. Presumably it is not amenable to direct observation, or we would have no problem to discuss. It follows that to go from O to G it must be through the chain O, S, star,  $X_G$ , G. (Naturally, there always are possibilities of multiple sensors of the same or different types, with the corresponding possibilities of combining their outputs to make the inference. I assume here, however, that the rationale is to be developed for the single sensor.)

(U) The one link obviously missing in Fig. 1 is that between O and S. How that gap is bridged depends on the details of the application, but basically there seems to be two ways. First, a direct observation might be possible under some conditions; for example, using autocollimators in the case of nearby stations on a sufficiently rigid base when the frames can be defined adequately by accessible optical flats, or by some similar precision optical or mechanical link. This option usually is not available in unmanned spacecraft. Second, simultaneous or intermittent observations on an external phenomenon from both stations. In particular, the common external observable may be the star field itself, though it might conceivably be something else. We assume the former for the purpose of discussion. It might be asked, if direct observations can be made to relate O to a celestial frame -- if not  $X_G$  itself, at least one calculable from  $X_G$  -- why the frame S ever enters the picture at all. The answer is that S might not enter if the sensing capabilities from O were fully equal to those from S. In practical cases, however, it can happen that observations are possible from O only occasionally and only on some subset of stars, whereas it can be made frequently on a large star family from S. The astronomical analog might be a situation in which O is a relatively cloudy site in a polar latitude equipped only with a zenith transit (I paint the picture black!) whereas S is a well-equipped desert observatory. The key is that the relationship between S and O does not change rapidly, so the occasional observations from O will, after some time, amass enough data to fix the relationship over a useful time period. On the other hand, the relationship between O and G may change rapidly and not very predictably.

(U) In any case, the establishment of the OS relationship is what an instrument engineer might call "boresighting." We assume here that it can be done and is done -- that the missing link between O and S is filled in -- and turn our attention primarily to the chain of links between S and G via  $X_G$ .

(U) The situation at this point can be neatly summarized by a paraphrase of Leopold KRONECKER's famous epigram about the real integers. The frames thus far introduced are the work of God; all else is the work of man.

## SECONDARY REQUIREMENTS AND AUXILIARY FRAMES

(U) We first dispose of the path  $X_G G$  for a particular choice of G. One can imagine various definitions of G that might arise in practical problems. The case where G is embedded in the Earth (modeled as a rigid body) is interesting for illustrative purposes and does represent a situation of general interest. I shall not cite all of the details that enter the  $X_G G$  relationship, but just enough to show that its complete specification might not be trivial in practice.

(U) An Earth-fixed frame could be either geodetic or astronomical in nature, and these do not necessarily coincide. The astronomer's pole is the "conventional pole" formalized by a 1967 IAU resolution as the "CIO" or "Conventional Origin." It is implicitly defined by defining the latitudes of five stations near  $38^\circ N$  as their average latitudes observed during the period 1900-1905. The "true pole," in the sense of the angular velocity vector departs somewhat from the conventional pole; the observed relationship, if required, can be found from the reports of the Bureau International de l'Heure. The prime meridian of this system is defined from the conventional pole through the Greenwich zero of latitude. (This used to be the mounting base of the Airy transit instrument, but I have not troubled to verify whether this is still the case. I cite it merely to show that the choice is quite definite and explicit.)

(U) Geodetic frames, however, are based on best ellipsoidal fits to surface geodetic data. Although the conventional pole probably will be imposed as a constraint in the future, it has not been in the past. The only conventional constraint on the various geodetic ellipsoids has been that in each case there exists some axis of rotational symmetry. Note also that there is no assurance that the center of mass of the Earth lies either on this axis or in the plane of the equator of a geodetic ellipsoid.

(U) To develop a rationale to establish a relationship between  $X_S$  and  $G_A$ , we must recognize that the observations from  $S$  are going to give, in effect, a body orientation with respect to  $X_S$ ; but if the star lines of sight had been treated as known with respect to some other celestial frame  $X_C$ , then the observations from  $S$  would determine the body orientation with respect to that frame instead. We can, in general, interpose between  $G_A$  and  $X_S$  a frame  $X_C$  such that; first, star lines of sight are converted periodically from the catalog frame  $X_S$  to the chosen  $X_C$ ; second,  $G_A$  is related to  $X_C$  by a known, preferably simple, transformation. The exact choice is open --  $X_C$  can range anywhere from  $X_S$  itself to  $G_A$  itself -- and is primarily a software consideration.

(U) To make the idea more definite, consider the following example. Suppose that  $X_C$  is chosen as the celestial frame based on the true equator and true equinox at the beginning of the day under consideration. The star lines of sight have to be updated just once a day; typically from  $X_C$  to a frame  $X_1$  based on the mean equator and mean equinox at the beginning of the current Besselian year (applying corrections for precession and proper motion), and then from  $X_1$  to  $X_G$  by means of the so-called independent day numbers which correct for precession, nutation, annual aberration and further proper motion. On the other side,  $G_A$  is related to  $X_C$  directly by Greenwich apparent sidereal time obtained using the so-called "equation of the equinoxes."

(U) Other choices than this example are possible, of course, but the point has been made that intermediary frames between  $X_S$  and  $G$  generally arise. The system graph now has the general character shown in Fig. 2.

an attitude reference frame -- we denote it  $R$  -- with respect to which the body will be forced to satisfy a certain approximate kinematical relationship. More specifically, a frame  $B$  embedded in the body will be so constrained. For example, the frame  $B$  might be held by an attitude control system to an approximate alignment with  $R$ , the case of "three-axis control," or one axis of  $B$  might be held approximately fixed with respect to  $R$ , as in the case of a spinning body. (The latter is of primary consideration in the present work.)

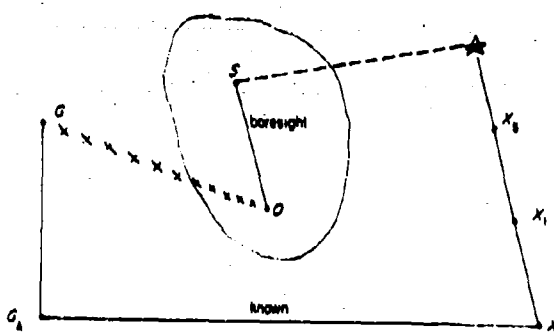


**Fig. 2. First Modified Graph**

(U) The reference frame must be presumed given by the system, typically in terms of some celestial frame or an earth frame. This is not to say it is fixed with respect to either of these, merely that it is known with respect thereto. For example, a very common attitude reference frame for spacecraft is that in which one axis is the geocentric vertical through the satellite. The other two axes could be aligned in and normal to the orbit plane; the detail is not important here. In either case the R-frame is determined solely by the satellite ephemeris. Any other definition of R will have the same qualitative property, namely that the frame can be assumed known with respect to an Earth-fixed frame (say  $G_A$ ) or a celestial frame (say  $X_2$ ) that can be tied to the system graph at some indefinite point which itself is known with respect to the other celestial frames. For definiteness, we tie it to  $X_0$  without loss in generality.

(U) The body B-frame may be known with respect to the other body frames S and O in the nominal sense. It could be established by plan axes, by the attitude control system, or in some other way. Two facts are important, though. First, it does not necessarily have any preferred dynamical characteristics of its own (as principal axes might have, for example):

second, its true relationship to  $O$  or  $S$  would have to be estimated as a part of the attitude determination process if there is any reason to establish it more precisely than could be done from a priori nominal considerations.

(U) Figure 3 shows the system graph modified to take account of the control relationship. The two possible definitions of  $R$  are depicted by "a-dashed" and "b-dashed" lines. It is evident that as a matter of logic it does not matter which way  $R$  is defined, for given one definition it is easy enough (in principle) to define the alternative relationship using the known  $X, G, A$  link. It does make a difference in practice, however, depending on how  $R$  eventually finds its way into the attitude determination. It has not yet done so, at the stage of Fig. 3, but if it does the definition should be used which reduces the burden of computation. For example, if  $R$  were determined by the satellite ephemeris and if it were established that the "b-dashed" relationship were the more natural to use as a part of the attitude determination process, it would just be good sense to ask for an ephemeris with respect to  $G$ , rather than  $X$ , and conversely, if the "a-dashed" relationship were the one directly needed.

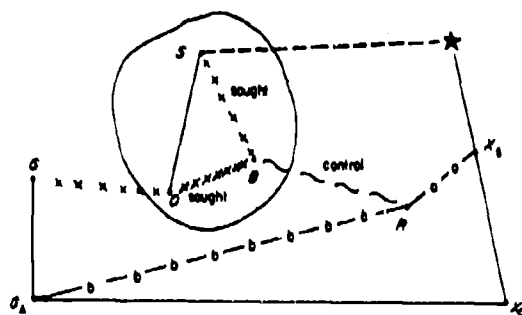


Fig. 3. Modification for Control

#### ROLE OF ROTATIONAL DYNAMICS

(U) I shall not go into detail about the observables of our problem, but a few general statements are needed as a basis for discussing the role of the satellite's rotational dynamics.

(U) Consider a star sensor in which the  $S$ -frame is rigidly embedded. For definiteness, visualize the  $S_2$  axis as the optical axis of the sensor and the  $S_1, S_3$ -plane as its focal plane. Denote by  $\lambda^S$  the direction cosine matrix of the line of sight to a particular star resolved in the  $X$ -frame. (This may be any of the  $X$ -frames introduced previously, without changing the

discussion that follows.) Let  $A^{SX}$  be the direction cosine matrix relating the  $S$  and  $X$  frames according to  $S = A^{SX}X$ . The star line of sight then resolves in the  $S$ -frame as  $\lambda^S = A^{SX}\lambda^X$  and the coordinates of that star image in the  $S_1, S_3$ -plane are closely

$$s_i = c\lambda_i^S / \lambda_2^S \quad (i = 1, 3) \quad (1)$$

where  $c$  is the focal length of the sensor optical system.

(U) A star image is detected by the sensor when the coordinates in the focal plane satisfy the equation of a slit in that plane. In normal engineering practice, such slits are linear; say one has the equation  $ax + by = 1$ , where  $x$  and  $y$  are rectangular cartesian coordinates in the  $S_1, S_3$ -plane. When  $s_1$  and  $s_3$  given by Eq. (1) satisfy this equation, i. e. when

$$a(-c\lambda_1^S) + b(-c\lambda_3^S) = 1(\lambda_2^S), \quad (2a)$$

an event is detected. We can write this in matrix form by introducing the row matrix

$$\sigma = [ca \quad cb \quad 1],$$

in which case, we can say that the matrix equation characterizing a star sighting is

$$\sigma\lambda^S = \sigma A^{SX}\lambda^X = 0. \quad (2b)$$

(If one takes account of such effects as slit deviations from nominal location and shape, focal plane tilt, and optical distortion, the right hand side may be a small nonlinear term in  $\lambda^S$ . The conceptual basis can be described just as well, however, if we set these deviation terms equal to zero.)

(U) Recognize that Eq. (2) is satisfied at a single sighting of a specific star in a specific slit. As the satellite rotates, many stars are sighted sequentially, generally in more than one slit, and a different value of the time is attached to each event. The total data stream from the sensor can be regarded as a collection of "satisfied equations" having the same general structure, but different  $\sigma$ -matrices (perhaps selected from two possibilities) and different  $\lambda^X$ -matrices (selected from a star population that depends on the sensor sensitivity, field of view, satellite motion). Most important for our present discussion, the data stream contains

matrices  $A^{SX}$  sampled at different instants. The matrix  $A^{SX}$  is one possible characterization of satellite attitude, and it changes with time as the satellite rotates.

(U) Attitude determination is the use of the data stream to infer  $A^{SX}$  at some desired time.

(U) But suppose the star line of sight is known in the R-frame instead. Equation (2b) becomes

$$O A^{SR} \lambda^R = 0 \quad (3a)$$

and the same attitude determination process determines  $A^{SR}$  instead. If the line of sight were known in the G-frame, we would have

$$O A^{SG} \lambda^G = 0 \quad (3b)$$

instead, and the attitude would be determined as a relationship between the S-frame and the G-frame. Figure 3 makes it clear that any of these alternatives are equally acceptable as a way-station to the ultimate determination of the desired relationship between G and O. The point is that the data stream has the same structure in all of these cases, so the same type of attitude determination algorithm will automatically provide the relationship between the S-frame and the frame in which the star locations are given. There is no special reason to regard an X-frame as preferential in this regard except that the  $\lambda^X$  change much slower in it, and less frequent updating is required.

(U) In this discussion, I will focus only on a sequential estimation process, though this is not the only way one might approach a determination of the A-type matrix from the conditions of slit crossing.

(U) Although the event on which the observation is based is a slit crossing, the actual observable is related to time. It might be the slit crossing time itself, or the deviation of that time from a predicted value. In the former case, the only way to tie all of the observed times together and to the instant at which the attitude is to be evaluated is by a knowledge of the satellite rotation; more specifically, by a knowledge of how the rotation depends on the pertinent parameters of the vehicle. In the latter case, exactly the same kind of knowledge is required in order to predict a time of slit crossing.

(U) In short, the true role of the dynamics and kinematics of satellite rotation is to establish a time scale for the way the observed events ought to occur if the satellite parameters and rotational initial conditions have the values that we think they have. The observations, of whatever detailed character, are a measure of the difference between the vehicle's actual behavior and the way its "predictive model" or "dynamic model" behaves. The deviations occur from four sources:

1. errors in the physical measurement.
2. imperfections in Eq. (2)
3. errors in our estimate of vehicle parameters and initial state
4. imperfections in the dynamic model

The deviations actually are used to revise our estimate of vehicle parameters and initial state. Obviously, if the revision is to be a valid one, the errors and imperfections in Items 1, 2 and 4 must be reduced as far as possible to avoid contaminating the estimation.

(U) The characteristics we would like in the dynamic model are: firstly, that deviations in the observables be linearly related to deviations in the parameter family, for only in this linear case is the underlying body of estimation theory as broad as we would like; secondly, that the model be complete enough to avoid getting substantial deviations simply from effects ignored in the model. The linearization requirement implies, in effect, that a description of the rotation can be found which is in some sense "simple," and it is this subject that I wish to address in the remainder of the work.

(U) The rotational behavior of any spinning body is essentially nonlinear, and this is no less true for the spinning gyrost that this work views as the spacecraft. To linearize, one must expand about some state of motion -- preferably, about some state of steady motion if the resulting linear equations are to have constant coefficients. The problem of completeness is one that has to be examined separately for each satellite system design, but for many cases it is enough to consider the "natural" motion of an otherwise rigid, torque-free gyrost as a basic guide in the sense discussed below, and to assure completeness of the model by introducing other pertinent effects as perturbations.

(U) The basic question we face in our formulation of the dynamic model is "What motion is it natural to linearize with respect to?" Suppose we find that there is a set of "modeling axes"  $M$  in the body whose motion with respect to a set of "kinematic reference axes"  $K$  is a simple motion, in the sense that it can be represented as a small deviation from a state of steady rotation. Then it is natural to decompose the direction cosine matrix in the middle of Eq. (2b) so that equation becomes

$$(\sigma A^{SM}) A^{MK} (A^{KX} \lambda X) = 0 \quad (4)$$

The quantity  $\lambda K = A^{KX} \lambda X$  is calculable, of course, because the motion of  $K$  is known. The quantity  $\sigma A^{SM}$  is subject to estimation in the same way as  $\sigma$  itself, or the matrices  $A^{SB}$ ,  $A^{OB}$  which Fig. 3 suggests might be desired. The middle matrix,  $A^{MK}$ , is the one whose behavior is linearly predictive.

#### REMARKS ON GYROSTAT BEHAVIOR

(U) I shall conclude by remarking briefly on the major candidates for frames  $M$  and  $K$ , based on what is known of the unperturbed motion of free gyrostats.

(U) First, how does a spinning gyrostat look to a space-fixed observer. It looks much like any other spinning body. We picture its motion with respect to inertial space by introducing the usual Euler angles (Fig. 4) relating the body frame  $M$  to some inertial frame  $X$ . Under certain conditions, we find that the gyrostat spins with almost constant rate  $\dot{\psi}$  about the body axis ("spin axis")  $M_3$ , while that axis precesses about  $X_3$  at an almost constant angle  $\theta$  at an almost constant rate  $\dot{\phi}$ . These conditions, basically, are that the body be not too asymmetric about  $M_3$  and that  $X_3$  be normal to the invariable plane; that is, it is aligned with the total angular momentum of the satellite. It seems reasonable, therefore, to consider a kinematic reference ( $K$ ) frame which is inclined to  $X_3$  at a certain angle  $\theta_0$  and which precesses about  $X_3$  at a certain constant rate  $\dot{\phi}_0$ . (It turns out the equations can be linearized whenever  $\dot{\phi}_0$  is used, but the  $M_3$  body axis does not then closely follow the corresponding  $K_3$ -axis.) This  $K$ -frame is not precisely any of the frames depicted in Fig. 3.

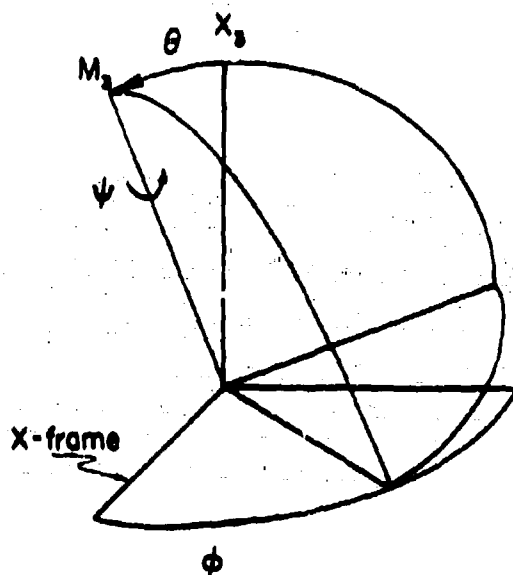


Fig. 4. Euler Angles for the Spinning Gyrostat

(U) However, the function of the attitude control system is to keep a body, say  $B_3$  (close to  $M_3$ , presumably), in approximate alignment with a corresponding axis  $R_3$  of the  $R$ -frame. To the extent it does this successfully and efficiently, it gradually moves the angular momentum vector around in space until the natural precessional motion tends to keep  $B_3$  close to  $R_3$ . Under these circumstances, the  $R$ -frame could serve as a kinematic reference frame with respect to which the dynamical description could be linearized. But if the  $R$ -frame itself were in a state of steady rotation about  $R_3$  with respect to an  $X$ -frame or the  $G$ -frame, that  $X$ -frame or  $G$ -frame would serve equally well as the  $K$ -frame.

(U) In conclusion, the kinematic reference frame should be based on the system angular momentum, but in cases of practical interest one might be able to select the  $R$ -frame,  $G$ -frame or  $X$ -frame of Fig. 3 as equally valid approximate realizations of that "most natural" choice.

(U) As regards the body frame, a natural choice exists if the gyrostat is not a gyrostat but a simple rigid body, namely the choice of the  $M$ -frame as principal axes of inertia. These are the axes about which the angular motion undergoes purely periodic excursions in the body, so their choice effectively removes any secular part of the motion that would tend to make large angles develop between  $K$  and  $M$ . For the true gyrostat there is a somewhat analogous set of eigenvalue-like body axes, but unfortunately

their use does not result in an angular velocity vector which, except for the component on  $M_3$ , has purely periodic components. It follows that the M-frame inevitably drifts secularly with respect to the K-frame, and linearization might be invalidated if the drift is great enough. It is possible to choose a body frame with respect to which there is purely periodic motion (no secular drift) on axes  $M_1$  and  $M_2$ . However, the frame is not an inherent property of the body, being initial-condition dependent. Most investigators have a distaste for working with this kind of body frame.

(U) Thus, we have seen there are certain "natural" choices for the M and K frames to use in the dynamic model, and that there are certain approximations to them which we would have reason to believe might be acceptable. Perhaps most important, we have seen that a variety of paths to our problem would seem a priori to be equally acceptable. To decide rationally which is "best" cannot be done without pursuing each to the point where all relevant software considerations are clearly understood.



A LIMITED MEMORY ATTITUDE  
DETERMINATION SYSTEM USING SIMPLIFIED  
EQUATIONS OF MOTION\*

by Edwin G. Foudriat  
Marquette University  
Milwaukee, Wisconsin

ABSTRACT

A sequential limited memory attitude determination system is developed for a spinning spacecraft. The limited memory estimation system is derived from the least-square procedure and employs past measurements, both to delete the old data from the covariance matrix in order to maintain filter sensitivity and to augment the measurement error term. The extrapolation of the spacecraft states across the memory interval is made practical by a set of simplified spacecraft equations for which long computation time intervals are permitted.

The report develops the simplified equations which employ time averaging of the first order perturbations and demonstrates their accuracy in the arc second range over a time interval as long as 1000 sec. The concept of limited memory and the computational method for incorporating it into a Kalman filter computer program is derived. Results indicate that the limited memory system is superior to the nonlinear Kalman filter both in speed of convergence and accuracy and that arc second accuracy for a spacecraft optical axis is feasible with the limited memory filter. The data indicates that a substantial portion of the system capability is due to the augmentation of the measurement error.

INTRODUCTION

It is well known that the nonlinear Kalman filter becomes insensitive to state and parameter errors if the state disturbance noise is negligible. [1][2] This condition exists for the accurate determination of attitude for a spinning satellite in an earth's field environment; in most cases the spacecraft motion is disturbed by magnetic, gravity gradient, aerodynamic, solar, and micrometeoroid torques. Usually in a well-designed satellite in a near earth environment the aerodynamic, solar, and micrometeoroid torques are negligible, while the magnetic and gravity gradient torques should be modeled if accuracies in the arc second range are desired. (Note that only the micrometeoroid torques can be considered random.)

Concepts for alleviating the insensitivity problem for the Kalman filter, proposed by Schmidt,[1] and Jazwinski,[3] and Lee,[4] have been classed as limited memory filters. Of these, Schmidt's procedure, which augments the Kalman filter with an additional gain term, is the only technique which does not add considerable computational complexity to the filter. The maximum likelihood technique of Jazwinski requires the batch processing of two Kalman filters even for the simple linear system.

The technique of Lee, based upon the weighted least-squares, has been extended to the nonlinear problem by the author.[5] The nonlinear version requires the extrapolation of the state and state transition matrix across the memory length at each measurement point. In general, this calculation increases considerably the computer solution time and complexity and the subsequent filter considered impractical. However, a set of equations of motion for the spinning body in an earth torqued environment have been developed [6] whereby exceptionally long integration time intervals can be used. This sub-

---

\* This work on this report is sponsored in part by NASA grant NGR-50-001-009 and in part by a consultant agreement with Honeywell, Inc.

stantially reduces the computation time for the extrapolation. Hence the nonlinear weighted least-squares technique is a feasible filter for the attitude determination problem.

This paper will outline the approach used to develop the simplified equations of motion and demonstrate their accuracy for the torqued spinning body. The nonlinear least squares limited memory technique will be outlined, and the equations for the implementation of the filter presented. Results of a simulation study demonstrating convergence and accuracy capabilities of this limited memory scheme will be presented.

#### EQUATIONS OF MOTION FOR A SPINNING SATELLITE

The most common method of determination of the spacecraft orientation is the solution of Euler's equations, including those torque effects which may be significant. If one requires solutions over a long period of time or needs the equation solutions as only one step in an analysis (for example, the attitude determination problem), then it is of interest to determine in what manner the equations of motion may be computed accurately yet rapidly by elimination of unnecessary terms and by increase in the computational speed.

One of the most interesting methods for analysis of spin stabilized satellites, developed primarily by V. V. Beletskii,[7] uses the concepts of time-averaging of the torques in order to determine the longer term motions in the satellite orientation. The method is similar to the nonlinear analysis concept of slowly varying phase and amplitude discussed by McLachlin[8]. Using these techniques, Beletskii has been able to predict the effects of aerodynamic, gravity, and magnetic field torques on the stability and orientation of a satellite over daily and monthly time intervals.

The concept employed by Beletskii is equally applicable to deriving the differential equation form for calculating the satellite motion. Using two sets of transformations, first, from inertial to angular momentum axes, and second, from angular momentum to principal body axes the resultant differential equations [6] become

$$\dot{\tau} = \frac{T_x}{r}$$

$$\dot{\xi} = \frac{T_y}{r \sin \tau}$$

$$\dot{\phi} = \frac{T_z}{r}$$

$$\begin{aligned} \dot{\theta} = & r \cos \psi \sin \psi \left( \frac{1}{L_x} - \frac{1}{L_y} \right) \\ & + \frac{T_x \sin \phi - T_y \cos \phi}{r} \end{aligned} \quad (1)$$

$$\begin{aligned} \dot{\psi} = & r \left( \frac{\sin^2 \psi}{L_x} + \frac{\cos^2 \psi}{L_y} \right) + \frac{T_y \cot \tau}{r} \\ & + \frac{(T_y \sin \phi + T_x \cos \phi) \cot \theta}{r} \end{aligned}$$

$$\begin{aligned} \dot{\psi} = & r \cos \theta \left( \frac{1}{L_z} - \frac{\sin^2 \psi}{L_x} - \frac{\cos^2 \psi}{L_y} \right) \\ & - \frac{(T_y \sin \phi + T_x \cos \phi)}{r \sin \theta} \end{aligned}$$

where

$r$  = angular momentum magnitude

$T_x, T_y, T_z$  = torques applied to the spacecraft along the angular momentum axes  $x, y,$  and  $z$

$L_x, L_y, L_z$  = spacecraft principal inertia

and where the angles  $\tau, \xi, \phi, \theta,$  and  $\psi$  are defined in Figure 1.

In order to have a consistent set of equations it is necessary to develop the torque equations in terms of the state variables and the earth's fields experienced during the orbit. The three torques considered are the interaction between the spacecraft and the earth's magnetic field, the eddy current torque resulting from currents induced on the spacecraft by the earth's magnetic field, and the gravity gradient torque resulting from interaction between the mass distribution and the gravitational field. Experience has shown that these are the major torque contributions for a high density spacecraft. However, the analytical procedures used are not limited to these specific torques and are equally applicable to solar, aerodynamic, and others resulting from spacecraft motion or orientation.

The magnetic field interaction torque in the angular momentum coordinate frame is

$$\underline{T}_M = \underline{E}^{-1} \underline{M} \times \underline{B} \quad (2)$$

where  $\underline{B}$  = earth's magnetic field vector

$\underline{M}$  = body-axis residual magnetic dipole

$E$  = Euler angle transformation of Figure 1 b, momentum to body axis

Carrying the cross product, equation (2) becomes

$$\begin{aligned} \underline{T}_M = & \begin{pmatrix} (E_1^T \underline{M}) B_z - (E_3^T \underline{M}) B_y \\ (E_2^T \underline{M}) B_x - (E_1^T \underline{M}) B_z \\ (E_1^T \underline{M}) B_y - (E_2^T \underline{M}) B_x \end{pmatrix} \quad (3) \end{aligned}$$

where  $E_i$  is the  $i$ th column vector of  $E$ .

The magnetic eddy current torques can be written as

$$\underline{T}_E = K((E^{-1} \underline{\omega} \times \underline{B}) \times \underline{B}) \quad (4)$$

where  $K$  = magnetic eddy current loss constant

$\underline{\omega}$  = total angular velocity

Assuming the angular velocity of the angular momentum axes is negligible in comparison with the angular velocity of the body axes, the eddy current torques become

$$\underline{T}_E = K(\underline{B}(\underline{g}^T \underline{A}^T \underline{B}) - A_g(\underline{B}^T \underline{B})) \quad (5)$$

where  $A$  = matrix relating angular velocity of body axes to the angular momentum frame

$$\underline{g}^T = (\dot{\theta}, \dot{\phi}, \dot{\psi})$$

The gravity gradient torques, available in many references (e.g., 9) are given by

$$\underline{T}_G = \frac{3\mu}{R^3} (\underline{r}^1 \times (L \underline{r}^1)) \quad (6)$$

where  $\mu$  = earth's gravitational constant

$R$  = satellite radius from center of earth

$\underline{r}^1$  = local vertical unit vector

$L$  = inertia diagonal matrix

The local vertical unit vector is obtained in angular momentum coordinates by

$$\underline{r}^1 = T F^{-1} (1, 0, 0)^T$$

where  $F^{-1}$  and  $T$  are the transforms from local vertical to inertial frame and inertial to angular momentum frame, respectively. The former frame involves the spacecraft orbital elements while the latter involves  $\tau$  and  $\xi$ . The term  $L \underline{r}^1$  can be written in angular momentum coordinates as  $E^{-1} L E \underline{r}^1$  so that equation (5) becomes

$$\underline{T}_G = \frac{3\mu}{R^3} \underline{r}^1 \times (E^{-1} L E) \underline{r}^1 \quad (7)$$

Equations (3), (5), and (7) describe the three torques in terms of the state variables and their rates, and the orbital elements  $R$ ,  $\Omega$ ,  $i$ , and  $U$ .

A set of approximate differential equations can be developed which are greatly simplified over the state equations (1) when the torques in equations (3), (5), and (7) are used. In order to derive the simplified set, time averaging of the first order perturbation torque is used; that is, the first order torques are obtained as functions of time and then averaged to eliminate those terms which are cyclic and result in no net change over a period. This is identical to the method used by Beletskii [7]. In contrast to his development, averaging here is carried out for the differential equations instead of on the generalized work function because the torques which influence all state motions are required.

The derivation procedure is illustrated for a symmetric body,  $L_x = L_y \neq L_z$ . Assuming the torques are first order small equations (1) become

$$\begin{aligned} \dot{r}_0 &= \dot{\xi}_0 = \dot{\theta}_0 = \dot{\phi}_0 = \dot{\psi}_0 = 0 \\ \dot{\phi} &= \frac{r_0}{L_x} \\ \dot{\psi} &= \frac{b r_0 \cos \theta_0}{L_x} \end{aligned} \quad (8)$$

Equation (3) can be used to develop the first order torques by substitution into equations (3), (5), and (7). Since the torques become functions of time only, a set of first order perturbation equations can be written. The resultant equations are still very complex. Since many of the terms are periodic with periods

$$T_1 = \frac{2\pi L_x}{r_0} \quad T_2 = \frac{2\pi L_x}{U r_0 \cos \theta_0}$$

the method of slowly varying amplitude and phase (8) can be employed. For example, the

torque term  $T_x$  becomes

$$T_x = \lim_{T \rightarrow \infty} \frac{1}{T} \int_0^T T_x(\tau, \epsilon, r, \theta, \psi) d\tau \quad (9)$$

The use of equation (9) eliminates from the right-hand side of equation (1) all those terms which have net average of zero over the periods  $T_1$  or  $T_2$ .

Reference 6 develops the components for the magnetic, eddy current, and gravity gradient torques of equations (3), (5), and (7) in terms of the state variables. Using these results, equations (1) become

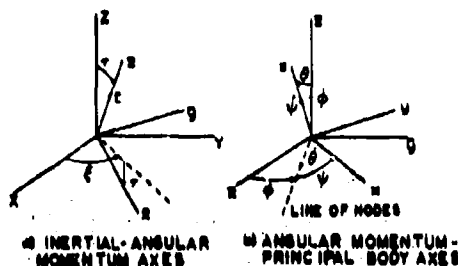


Figure 1 Axis Systems for Spin-Stabilized Satellite

$$\dot{\tau} = \frac{KB_x B_y (1 + b \cos^2 \theta)}{L_x} - \frac{B_y M_z \cos \theta}{r} + \frac{3 \mu L_x (1 - a)(2 - 3 \sin^2 \theta) r_2 r_3}{2R^3 r}$$

$$\dot{\epsilon} = \frac{KB_y B_z (1 + b \cos^2 \theta)}{L_x \sin \tau} + \frac{B_x M_z \cos \theta}{r \sin \tau} + \frac{3 \mu L_x (1 - a)(2 - 3 \sin^2 \theta) r_1 r_3}{2R^3 r \sin \tau}$$

$$\dot{r} = \frac{rK(B_z^2 - B^2)(1 + b \cos^2 \theta)}{L_x}$$

$$\dot{\theta} = - \frac{bK \sin 2\theta (B^2 + B_z^2)}{L_x}$$

(10)

$$\begin{aligned} \dot{\psi} = & \frac{r}{L_x} + \frac{KB_y B_z (1 + b \cos^2 \theta) \cot \tau}{L_x} + \frac{B_x M_z \cos \theta \cot \tau}{r} - \frac{B_z M_z \cos \theta}{r} \\ & + \frac{3 \mu L_x (1 - a) \cot \tau (2 - 3 \sin^2 \theta) r_1 r_3}{2R^3 r} \\ & + \frac{3 \mu L_x (1 - a) \cos^2 \theta (r_1^2 + r_2^2 - 2r_3^2)}{4R^3 r} \end{aligned}$$

$$\dot{\psi} = \frac{br}{L_x} - \frac{br \sin \theta (\theta - \theta_0)}{L_x} + \frac{B_z M_z}{r} - \frac{3 \mu L_x (1 - a) \cos \theta (r_1^2 + r_2^2 - 2r_3^2)}{2R^3 r}$$

where  $B^2 = B_T^2$

$$e = \frac{L_z}{L_x}$$

and  $r_1, r_2$ , and  $r_3$  are components of equation (6).

It is possible to develop a similar procedure for the nonsymmetric inertia body. However, the initial solutions are in the form of elliptic functions so that a closed form solution for all terms of the differential equation similar to equation (10) is not available. It is, however, possible to evaluate the nonsymmetric body equations without a great deal of increase in complexity and hence possible to employ the same filter procedures to be presented for either symmetric or nonsymmetric body.

#### ACCURACY ANALYSIS FOR THE TIME AVERAGED PERTURBATION EQUATIONS OF MOTION

In the preceding section a set of time-averaged perturbation equations were developed which describe the motion of a spin-stabilized spacecraft in an earth orbital environment. This set affords a marked simplification over the exact equations and since the torques are time-averaged it should be feasible to employ large integration step sizes for their solution. Since these equations possess distinct advantages when employed in the computer modeling of the motion of a spinning satellite, an accuracy comparison between the time-averaged set and the exact equations is important.

The true magnetic field experienced by a satellite is rather complex. However, an approximate field can be generated by assuming that the earth's field results from a dipole aligned with its spin axis and the satellite is in a circular orbit.

The spacecraft used in the comparison simulation was the conceptual mechanization of a horizon definition experiment by Honeywell, Inc. for the NASA Langley Research Center [9]. The nominal spacecraft uses a 300 km, sun synchronous orbit with the following parameters and initial conditions:

$$L_x = L_y = 56.68 \text{ slug-ft}^2$$

$$L_z = 65.62 \text{ slug-ft}^2$$

$$M_x = M_y = M_z = 0.51052 \times 10^{-3} \text{ ft-lb/Gauss}$$

$$K = 0.141739 \times 10^{-4} \text{ ft-lb-sec/Gauss}^2$$

$$i = \text{inclination} = 97.38^\circ$$

$$u = \text{arg. of latitude} = 97.3^\circ$$

$$\Omega = \text{long. of ascending node} = 0^\circ$$

$$\omega_0 = \text{orbital rate} = .0634^\circ/\text{sec}$$

$$\omega_x = 0$$

$$\left. \begin{aligned} \omega_y &= 0.00365471 \text{ rad/sec} \\ \omega_z &= 0.31415926 \text{ rad/sec} \end{aligned} \right\} \text{ body axis angular rates}$$

$$\psi = \phi = 0^\circ$$

$$\theta = .5757^\circ$$

$$r = 20.61617134 \text{ ft-sec}$$

$$\tau = 99.9995^\circ$$

$$\xi = 314.4154^\circ$$

For this comparison, both sets were programmed for digital computer solution using IBM 7040. This section presents the comparative results. Since the computer used was limited in storage and computational speed was reduced because a large portion of the program was run in double precision, it was decided to program the symmetric body and include only the magnetic field effects.

Using the above conditions, the true equations (1) and approximate equations (10) were solved using a 4th order Runge-Kutta integration routine with a fixed interval size of 0.1 sec. Figures 2-5 compare the solutions. Figure 2 shows the motions for the angles  $\tau$  and  $\xi$  over a 40 sec time period. This short time is used to illustrate the effect of averaging, that is, the exact solution has oscillations not present in the averaged solution. The averaged solution, however, duplicates precisely the long term motions of the exact set. Solutions over periods of 800 sec indicate differences in magnitude to be of the order of  $0.0001^\circ$ .

Figure 3 compares the cone angle,  $\theta$ , for the exact and approximate solutions over a 600 sec interval. In this case, the exact solution has approximately a 20 sec period, which makes the exact motion difficult to represent; hence the envelope has been indicated. Again the angular difference is of the order of  $0.0001^\circ$ .

Figure 4 compares the angular momentum for the exact and approximate solutions. Again the approximate solution (which closely approximates the mean of the exact solution) represents the average change but does not have the oscillations.

The error in the body angular spin position is represented by the term

$$\delta = \phi_s + \psi - \psi_s$$

This term is a more realistic representation of the spin than the individual Euler angles. For example, at the conditions  $\theta = 0$ , the torque terms in equation (1) are infinite although no singularity exists in the equations (10). Similarly, Grosch [10] shows, for small cone angle,  $\theta$ , the sum and difference of the spin and precession angle are more useful for system representation. Figure 5 shows the spin position error over a time interval of 800 sec to be less

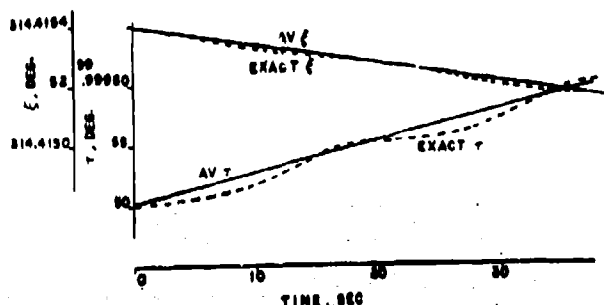


Figure 2 Comparison of Exact and Averaged Momentum Solutions

then 0.0002°. As shown in reference 6, further reduction of this error should be possible by more accurate selection of the initial angular momentum for the approximate equations.

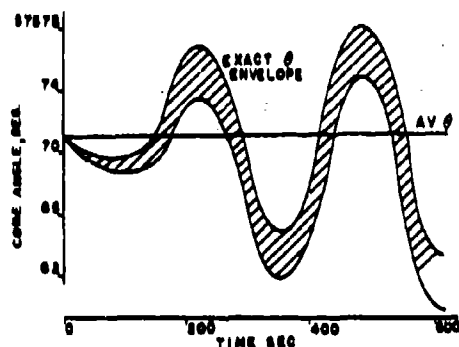


Figure 3 Exact and Averaged Cone Angle Comparison

The computer solution comparison indicates that the approximate equations of motion are capable of representing a spinning satellite in an earth's field environment to within one sec over long time intervals and hence should be adequate for precision attitude determination.

#### LEAST SQUARES LIMITED MEMORY FILTER

The general model for a dynamic system and its measurement equations are

$$\begin{aligned}\dot{\underline{x}} &= \underline{f}(\underline{x}, t) + \underline{w} \\ \underline{y}(k) &= \underline{H}(\underline{x}(k), k) + \underline{v}(k) \\ k &= 1, \dots, p\end{aligned}\quad (11)$$

where  $\underline{x}$  = augmented state vector model of system including any unknown parameters

$\underline{y}(k)$  = measurement equation

$\underline{H}(\underline{x})$  = measurement model

$\underline{w}$  = system noise

$\underline{v}(k)$  = measurement noise

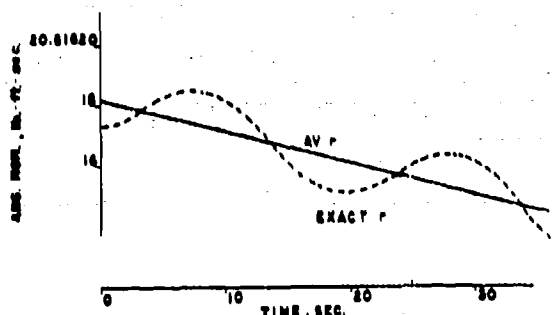


Figure 4 Exact and Averaged Angular Momentum Solutions

It is assumed that the noise is white, gaussian with

$$E[\underline{w}] = E[\underline{v}] = 0$$

$$E[\underline{v}\underline{v}^T] = R(k) \delta(t - k) \quad (12)$$

$$E[\underline{w}\underline{w}^T] = Q(t) \delta(t - \tau)$$

In the attitude determination problem considered the neglected torques should not be represented as gaussian white noise. Hence  $\underline{w}$  is zero.

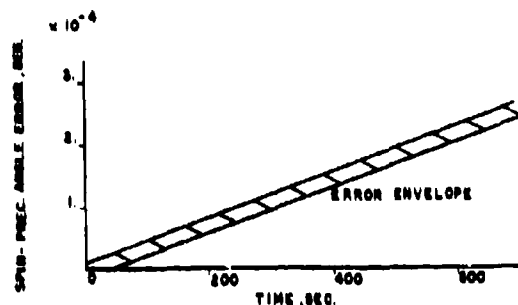


Figure 5 Spin-Precession Angular Error Comparison

The weighted least-squares solution for an improved estimate for  $\hat{x}(p)$ , given an initial estimate  $\hat{x}_0(p)$ , is

$$\hat{\underline{x}}(p) = \hat{\underline{x}}_0(p) + \left( \sum_{k=q}^p \hat{Q}(k) \hat{Q}^T(k) \right)^{-1} \cdot \left( \sum_{k=q}^p \hat{Q}(k) R^{-1/2}(k) (\underline{y}(k) - H(\hat{\underline{x}}_0, k)) \right) \quad (13)$$

where

$$\hat{V}(k) = \nabla_{\underline{x}(p)} H(\underline{x}(k), k) R^{-1/2}(k) \Big|_{\underline{x}_0} \quad (14)$$

Equation (13) assumes that only the measurements  $k \in I[q, p]$  are employed, and hence can be classified as a limited memory system.

To obtain a sequential limited memory filter algorithm it is necessary to formulate a method for adding new data and eliminating old data as the new measurements are taken. The most common method uses the standard inversion lemma to handle the matrix inversion in equation (13). Adding a new  $(p+1)$  term, this equation can be written as

$$\begin{aligned}
 P_{p+1,q} &= \left( \sum_{k=q}^{p+1} \hat{V}(k) \hat{V}^T(k) \right)^{-1} \\
 &= \left( \sum_{k=q}^p \hat{V}(k) \hat{V}^T(k) + \hat{V}(p+1) \hat{V}^T(p+1) \right)^{-1} \quad (15) \\
 &= P_{p,q} - P_{p,q} \hat{V}(I + \hat{V}^T P_{p,q} \hat{V})^{-1} \hat{V}^T P_{p,q}
 \end{aligned}$$

Subtracting the  $q$ th term gives

$$P_{p+1, q+1} = P_{p+1, q} + P_{p+1, q} \hat{V} (I - \hat{V}^T P_{p+1, q} \hat{V})^{-1} \hat{V}^T P_{p+1}$$

The filter algorithm requires a method for extrapolating the estimate and the covariance matrix to the new measurement point, that is calculating  $\hat{z}_0(p+1)$  and  $P_{p,q}(p+1)$  given  $\hat{z}_0(p)$  and  $P_{p,q}(p+1)$ . For the nonlinear case (again an approximation from the linear case) the equations developed by Cox [8] and others should be adequate. They are

$$\begin{aligned} \hat{g}_n(p) &= g(\hat{x}(p), p) \\ p_{p,q}(p+1) &= \Phi(p+1, p) p_{p,q}(p) \Phi^T(p+1, p) \\ &\quad + O(p) \end{aligned} \quad (17)$$

In addition to the update, the state transition matrix,  $\Phi(t, p)$ , is needed to evaluate the terms  $\hat{Y}(k)$  of equation (14); that is,

$$\nabla_{\underline{x}(p)} H(\underline{x}(k), k) = \begin{bmatrix} \frac{\partial H}{\partial x_1(k)} & \frac{\partial x_1(k)}{\partial x_1(p)} \\ \vdots & \vdots \\ \frac{\partial H}{\partial x_n(k)} & \frac{\partial x_1(k)}{\partial x_n(p)} \end{bmatrix} \quad (18)$$

Note that in evaluating equation (1<sup>a</sup>) at  $k=g$  it is necessary to integrate both state and state transition backwards from  $k = p+1$ . In this process it becomes feasible to evaluate measurement error portion, that is, the second term in equation (13)

$$\sum_{k=q+1}^{p+1} \hat{Q}(k) R^{-1/2}(k) (\underline{y}(k) - \underline{H}(\hat{\underline{x}}_0, k))$$

at all points within the interval at which time corresponds to a measurement point. These terms can be used to reinforce the error and hence conceivably obtain the improved convergence and accuracy.

The advantage of the simplified equations developed in the previous sections becomes apparent. With them it is possible without a prohibitive increase in computer time to evaluate the filter equation at  $k = q$  because extremely long integration intervals ( $\Delta t = 500$  sec) are feasible. Hence in a few cycles through the Runge-Kutta integration routine the value of state and state transition can be obtained at  $k = q$  and the limited memory filter implemented.

## ATTITUDE DETERMINATION MEASUREMENT SYSTEM:

The previous sections have developed a least-squares limited memory filter and a set of simplified equations which are computationally compatible. The remaining feature of any attitude determination system, the measurement, will be discussed in this section.

The measurement is based on star transit across a body mounted telescope as employed originally for Project Scanner. The measurement is taken when the slit plane of the telescope and the star are coincident. The time of occurrence of this event is recorded and it is this

time which is employed to determine the precise vehicle attitude.

The geometric condition satisfied is

$$H(\underline{x}(t), t) = \underline{a}_r^T E \underline{T}_s = 0 \quad (19)$$

where  $\underline{a}_r$  = rth slit normal vector

$\underline{s}_l$  = lth star vector

Besides the measurement equation, the measurement gradient,  $\nabla_{\underline{x}}(k) H(\underline{x}, k)$ , is required in equation (18). This is

$$\frac{\partial H(k)}{\partial \underline{x}_1(k)} = \underline{a}_r^T \frac{\partial E}{\partial \underline{x}_1} \underline{T}_s$$

$$\frac{\partial H(k)}{\partial \underline{x}_2(k)} = \underline{a}_r^T \frac{\partial E}{\partial \underline{x}_2} \underline{T}_s$$

$$\frac{\partial H(k)}{\partial \underline{x}_3(k)} = \underline{a}_r^T \frac{\partial E}{\partial \underline{x}_3} \underline{T}_s$$

$$\frac{\partial H(k)}{\partial \underline{x}_4(k)} = \underline{a}_r^T E \frac{\partial \underline{T}}{\partial \underline{x}_4} \underline{s}_l \quad (20)$$

$$\frac{\partial H(k)}{\partial \underline{x}_5(k)} = \underline{a}_r^T E \frac{\partial \underline{T}}{\partial \underline{x}_5} \underline{s}_l$$

$$\frac{\partial H(k)}{\partial \underline{x}_l(k)} = 0 \quad l = 6, \dots, n$$

In addition to the gradient, the covariance of the additive noise in the measurement equation is required. The actual measurement equation (19) does not contain time explicitly but time is the quantity recorded at each measurement event. While this fact does not affect the measurement equation, it creates a problem since the additive noise term in the measurement equation is not readily available. An approximation to the additive noise can be made by considering

$$H(\underline{x}(t_+)) \approx H(\underline{x}(k)) + \frac{dH}{dt} \bigg|_k n \quad (21)$$

where  $k$  = measured time

$t_+$  = true time

$n$  = random time error

Noting that  $\frac{\partial H}{\partial t} = 0$  so that

$$\frac{dH}{dt} = \nabla_{\underline{x}}^T \frac{d\underline{x}}{dt}$$

the additive noise term is  $\nabla_{\underline{x}}^T H \frac{d\underline{x}}{dt} \bigg|_k n$

Assuming  $E[n] = 0$  and uncorrelated with  $\underline{x}$ , then the measurement noise covariance  $R(k)$  is given by

$$R(k) = E \left[ \left( \nabla_{\underline{x}}^T H \frac{d\underline{x}}{dt} \bigg|_k n \right)^2 \right] \quad (22)$$

Assuming  $\dot{\theta}$ ,  $\dot{\phi}$ ,  $\dot{\psi}$ , and  $\dot{\gamma}$  are negligible in comparison to  $\dot{\alpha}$  and  $\dot{\delta}$  and that the first terms in equation (10) predominate, then

$$R(k) = E \left[ \left( \underline{a}_r^T \frac{\partial E}{\partial \underline{x}} \underline{T}_s + \underline{a}_r^T \frac{\partial E}{\partial \underline{x}} \underline{T}_s \right. \right. \\ \left. \left. b \cos^2 \theta \right)^2 \frac{r^2}{L_x^2} \bigg|_k n^2 \right] \quad (23)$$

If one further assumes that the random variables  $\underline{x}(k)$  can be replaced by their present estimates and the covariances are negligible in comparison to the means, then

$$R(k) = \left[ \left( \underline{a}_r^T \frac{\partial E}{\partial \underline{x}} \underline{T}_s + \underline{a}_r^T \frac{\partial E}{\partial \underline{x}} \underline{T}_s \right. \right. \\ \left. \left. b \cos^2 \theta \right)^2 \frac{r^2}{L_x^2} \right] \sigma_n^2(k) \quad (24)$$

While it is true that the measurement noise in above form is correlated, the use of  $R(k)$  as the weighting matrix is more desirable than attempting to process an alternate form of the measurement equation.

The value used for  $\sigma_n$  is determined from the work of Ostro<sup>14</sup> and Romanczyk Ref. 12, who show both analytically and experimentally that the standard deviation,  $\sigma$ , for estimating the center of the star, corresponds to the equation

$$\sigma_n = \sigma_0 \left( \frac{r - m}{5.82} \right) \quad (25)$$

Assuming a +1 magnitude star had angular errors with a 10 sec standard deviation, equation (25) is used to generate the standard deviation used in equation (24).

## COMPUTER SIMULATION

A computer simulation using the above formulation of the attitude determination problem has been developed for an IBM 7040 in order to study the effectiveness of the limited memory procedures. The simulation consists of two programs, the first to generate star sighting and the second to employ the nonlinear least squares limited memory estimation concept in determining



the attitude of typical spacecraft. Only the second of these programs is discussed in this report.

The computer flow diagram for the limited memory estimation system is shown in Figure 6. This program is relatively straight-forward in that it follows a fairly standard pattern for sequential filtering with a few exceptions. The

first is the method for storing star data in the memory and the method by which new data is added and old deleted. Due to the fact that the IBM 7040 was limited to 16,000 words of storage, it was decided to read a segment of stars into the memory from tape and process these stars. When the sequential filter needed a new star not in the memory then those stars no longer needed in the filter are eliminated, the set of stars in

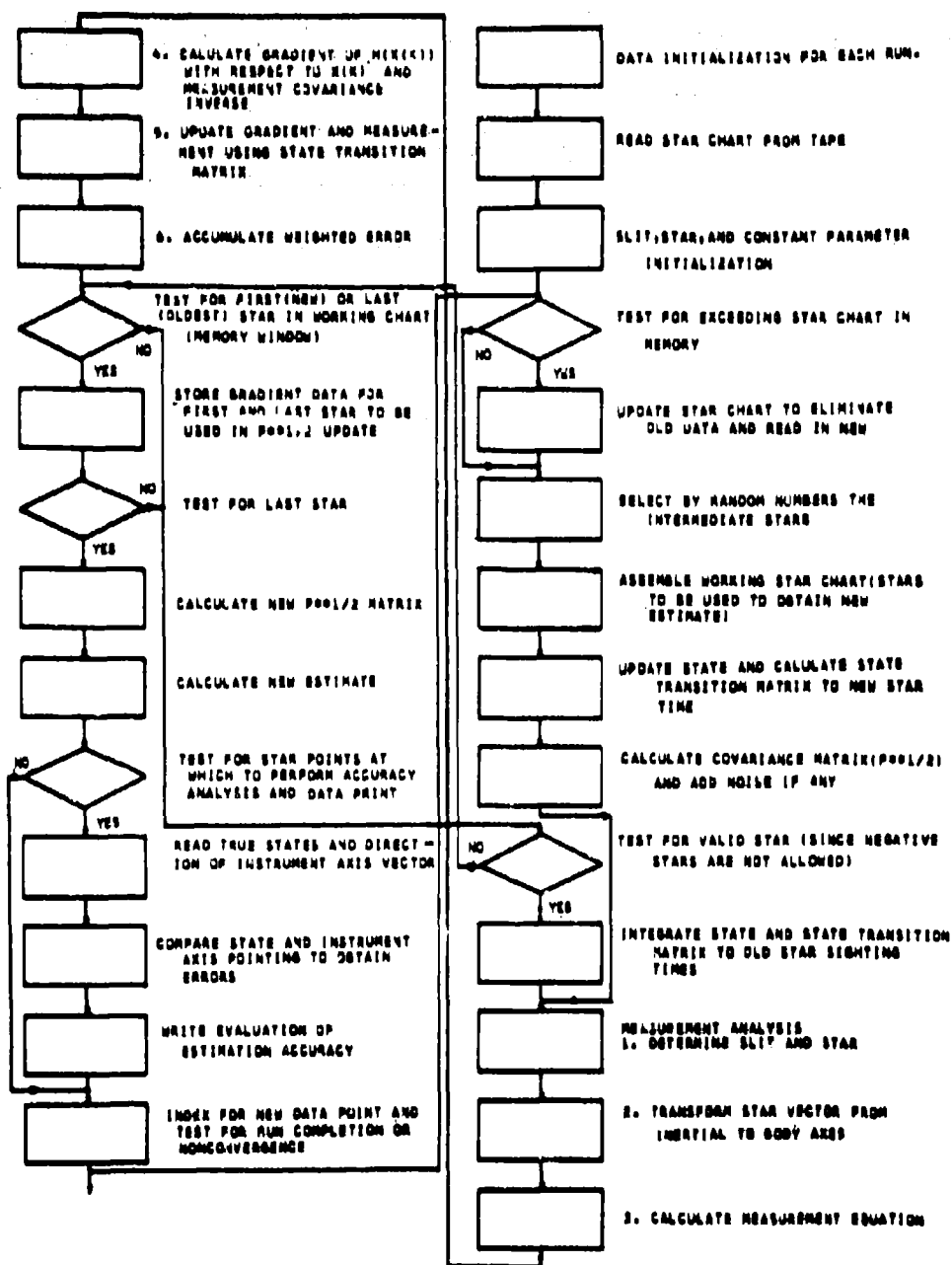


Figure 6 Limited Memory Computer Flow Diagram

the memory but still required by the filter are shifted, and new stars read in. The tape is then reindexed back to the proper point.

The second is the method by which stars can be selected for processing within the next data cycle for the least squares limited memory system. Two alternatives using random selection of stars are available. The first uses an ordered sequence, and the second selects a fixed step size and then selects a particular star with a band of 5-10 stars about that fixed point. This latter technique leads to a somewhat more uniform selection of stars across filter memory length.

The integration of the state and the solution of the state transition matrix use a fourth order Runge-Kutta routine. The state transition matrix is used to extrapolate the covariance matrix but not exactly as indicated in equation (17). Instead the  $Pl/2$  concept as reported in reference 13 is used. This latter procedure eliminates the need for double precision in the calculation of  $P$  while at the same time assuring a positive definite covariance matrix.

The processing of star data for a particular measurement update is straight-forward. The newest star is processed first as in the Kalman filter and then if the least-squares limited memory procedure is being used any additional previously measured stars are processed until all selected stars within the memory window have been included.

Once all star points within the window have been processed the new covariance matrix is calculated. Due to the fact that this solution may cause difficulties because of large subtractive changes in  $P$ , the computer augments  $P$  in two steps, first adding the new data and then subtracting the old data. Before the subtraction to  $P$  is accomplished, its effect is tested by the equation

$$\hat{Q}^T P_{p,q} \hat{Q} < \epsilon \quad (26)$$

If this condition is not satisfied,  $n/2$  is not augmented by deletion of the old data.

Using the new  $P$  matrix, the new estimate is obtained and, at specific points, the accuracy of the estimate is compared to that of the exact solution.

### SIMULATION RESULTS

The simulation results employed a spacecraft model similar to that used for the study of the perturbation equation accuracy. Only the eddy current torque was used in order to simplify modeling. This parameter was assumed to be unknown, and hence augmented to the state vector. In addition, changes in initial conditions were made.

The placement of the stars shown in Table I would be similar to those in a typical low altitude orbit where earth blockage might eliminate stars within a  $140^\circ$  portion of a revolution for a vehicle with its nominal spin axis normal to its orbital plane.

TABLE I

Star	Mag.	Az.	Elevation
1	+1.5	$10^\circ$	$0^\circ$
2	+2.5	$-5^\circ$	$70^\circ$
3	+1.0	$10^\circ$	$165^\circ$
4	+3.0	$0^\circ$	$225^\circ$

The star magnitudes were used to weigh the accuracy of the sighting data according to equation (25) with a +1.0 nominal magnitude star assumed to have a  $\sigma = 10$  sec magnitude. The filter assumed all stars were +1.0 magnitude.

The capability of least squares limited memory filter considering various factors such as memory length and number of stars processed at each estimation point is compared with the Kalman filter in Figures 7-11.

As noted previously, it is feasible to incorporate within the filter additional measurements since the augmentation of the covariance matrix requires the integration of the state backwards to the  $q$ th measurement time. Equation (13) considers the summation from the time  $q+1$  to  $p+1$  but the program incorporates the  $q$ th measurement error (instead of  $q+1$ ) as this does not seem to be a serious alteration of the least-squares procedure. (It should be noted that the  $q$ th measurement error is always available but the  $q+1$  may not.) This positive weighting of the  $q$ th measurement is different from the limited memory scheme of Lee [4] who proposed that this measurement error should be subtracted.\*

With these considerations in mind, Figures 7-11 present the estimation errors in the x-z inertial plane orientation, angular momentum,  $\tau$ ,  $\theta$ , and  $K$ , respectively. (Note that the inertial plane orientation and spin angle are nearly identical. The former is useful in assessing the accuracy for a horizon definition experiment.) Considered are estimates with a memory length of 100 and 200 stars and an inclusion of either 5 or 8 stars within the memory band. These results are compared to the nonlinear Kalman filter. In most cases the results are substantially improved

\* Actually this study has not investigated the methods used to weight the terms of equation (13). When the model and system are identical equation (13) is correct but when model and true system differ, the method of weighting and for that matter the method for error comparison (i.e., what is meant by best fit) are no longer straightforward.

both in terms of more rapid convergence as well as better accuracy. For example, the system with memory length of 200 stars and 5 stars/sighting maintains an x-z inertial plane orientation accuracy of 10 sec after 75 star sightings and an angular momentum accuracy of .00002 #-ft-sec after 114 star sightings. This latter is a considerable improvement over the Kalman filter which barely reaches .00002 #-ft-sec at 399 sightings. These results are displayed consistently over the whole group of limited memory conditions with the possible exception of cone angle. In addition the estimation errors tend to be more randomly distributed and not subject to the bias error caused by insensitivity which occurs in the Kalman system.

The system with 5 stars and 200 star memory length appears to give the best results. However, since a random selection of stars within the memory window was used, the results may differ depending upon the exact stars used. To show the true effects of differences in the number of stars and memory length a Monte Carlo simulation and a statistical analysis of the results would be required.

It is possible to show separately the effectiveness of processing additional stars at each measurement point in reducing the state error. This may be shown by considering the condition with measurement noise but with no data elimination for the covariance matrix. Essentially the system uses the Kalman weighting gain but uses more than the last measurements at each point.

Figure 12 shows the effect of using one and five measurement stars across a 100 star length band on the precession angle error,  $\psi$ . Figure 13 shows estimation errors for the angular momentum direction angle for the same conditions as above except that two different measurement noise sequences have been included. In all these cases it can be seen that the convergence and accuracy considering additional measurements is greatly improved over the single measurement condition. This result would indicate that the considerable improvement of the least squares limited memory filter over the Kalman filter is due to the inclusion of additional measurements.

#### CONCLUDING REMARKS

The results of the study have shown that the limited memory nonlinear filter system when used in combination with the time averaged spinning satellite equations results in an excellent practical attitude determination algorithm. The second of arc accuracy of the equations permits precision to be maintained while the insensitivity to time intervals used for computation simplifies the integration subroutine and still permits extrapolations of the state and state transition matrix across the memory length.

The least-squares limited memory filter simulation results indicated improved speed of convergence and accuracy over the nonlinear Kalman filter for all state variables. For the



Figure 7 Spin Angle Estimation Error

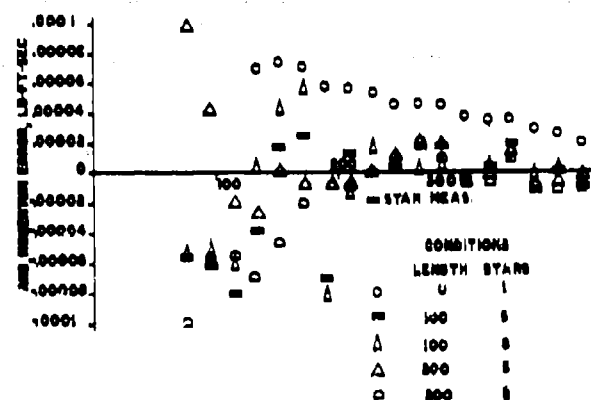


Figure 8 Angular Momentum Estimation Error

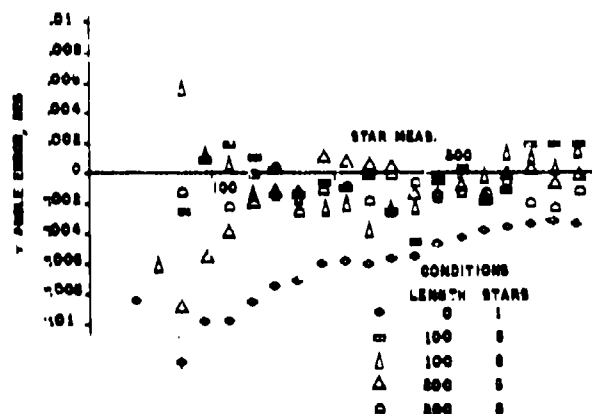


Figure 9 Angle Estimation Error

results presented the limited memory filter does not appear to be sensitive to either the memory length or the number of stars included within the memory. The results do indicate that the addition of past data does contribute significantly to the convergence and accuracy.

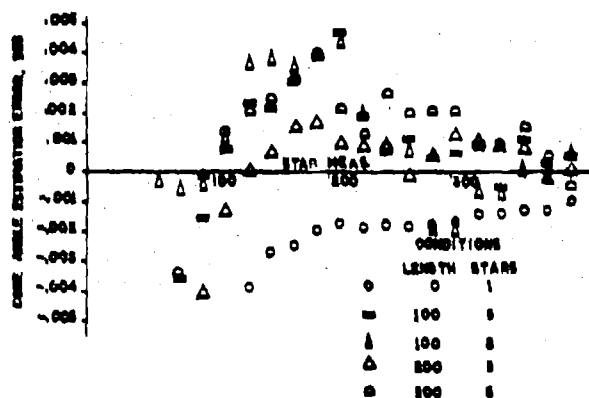


Figure 10 Cone Angle Estimation Error

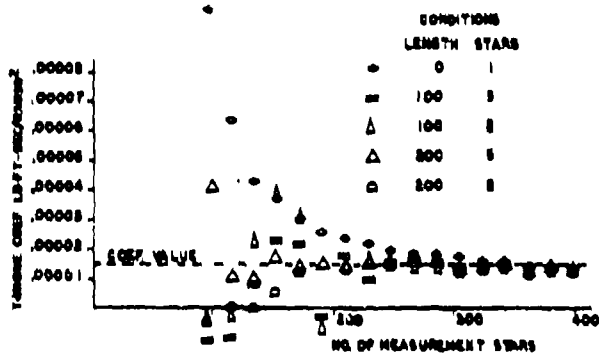


Figure 11 Torque Coefficient Estimate

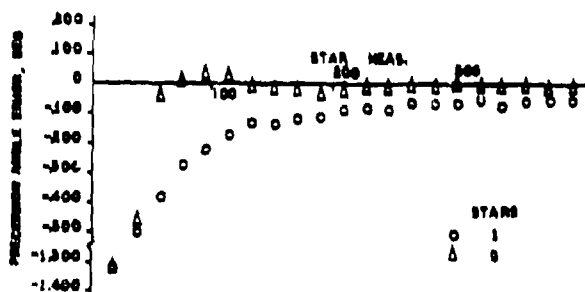


Figure 12 Effect of Added Measurements on  $\psi$  Error

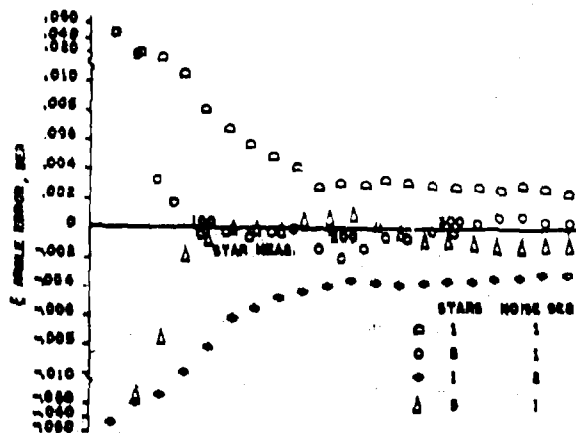


Figure 13 Effect of Added Measurements on  $E$  Error

#### REFERENCES

1. Schmidt, S. F., "Compensation for Modeling Errors in Orbit Determination Problems," Analytical Mechanics Assoc., Inc. Interim Rpt. No. 67-16 Contract NAS3-11048, Nov. 1967.
2. Schlee, F. H., Standish, C. J., and Toda, N. F., "Divergence in the Kalman Filter," AIAA Journal Vol. 5, No. 6, June 1967, pp. 114-1120.
3. Jazwinski, A. H., "Limited Memory Optimal Filtering," 1968 JACC Proc. pp. 383-389.
4. Lee, R. C. K., "The 'Moving Windows' Approach to the Problems of Estimation and Identification," Aerospace Rpt. No. TR-1001 (2307)-23, June 1967.
5. Foudriat, E. G. and Nayak, P. R., "Development of a Limited Memory Filter System for Precision Attitude Determination of a Spinning Spacecraft," Semiannual Prog. Rpt., NASA NGR-50-001-009, Nov. 1968.
6. Foudriat, E. G., "Simplified Equations of Motion for a Torqued Spin Stabilized Satellite," (to be published as portion of contractor rpts. on NASA Contract NAS1-8801, Attitude Referenced Radiometer Study, Honeywell, Inc.)
7. Beletskii, V. V., "Motion of an Artificial Satellite About its Center of Mass," NASA Tech. Trans., NASA TT F-429, 1965.
8. McLachlin, R. W., Ordinary Nonlinear Differential Equations in Engineering and Physical Science, Oxford Press, London, 2nd ed., 1958, Ch. 5.

9. Tidwell, N. W., et al, "Conceptual Mechanization Studies for a Horizon Definition Spacecraft-Attitude Control Subsystem," NASA CR-66382, Contract NAS1-6010, Honeywell, Inc., May 1967.
10. Grosch, C. B., "Orientation of a Rigid Torque Free Body by Use of Star Transits," J. of Spacecraft, Vol. 4, No. 5, May 1967, pp. 562-566.
11. Cox, H., "On the Estimation of State Variances and Parameters for Noisy Dynamic Systems," IEEE Trans. on A.C., Vol. A.C.-9, No. 1, Jan. 1964, pp. 5-12.
12. Ostroff, A. J. & Romanczyk, K. C., "Design of an Electronically Scanned Star Sensor with Digital Output," NASA TN D-5281, June 1969.
13. Bellantoni, J. F., & Dodge, K. W., "A Square Root Formulation of the Kalman-Schmidt Filter," AIAA Jour., Vol. 5, No. 7, July 1967, pp. 1309-1314.

# MODELING OF ENVIRONMENTAL TORQUES OF A SPIN-STABILIZED SPACECRAFT IN A NEAR-EARTH ORBIT<sup>1</sup>

N. W. Tidwell  
Honeywell Inc.  
Minneapolis, Minnesota

## ABSTRACT

Passive stellar mapping attitude determination systems require, in lieu of a rate gyro package, an accurate vehicle model to meet continuous 14-arc-second attitude accuracy requirements. Such a vehicle model is used in the attitude determination data reduction algorithm for propagation of vehicle state from one observation to the next within the 14-arc-second accuracy. The accuracy requirement is met by identifying, modeling, and evaluating environmental disturbances that perturb vehicle motion, and thereby establishing the torques to be included in the vehicle model. This paper is concerned with modeling disturbance torques experienced by spin-stabilized spacecraft. Several sources of torques are presented, and all but five eliminated due to constraints and mission requirements. The five torques discussed are caused by induced eddy currents, aerodynamic pressure, solar pressure, residual magnetic moment, and gravity gradient. A computer program developed to simulate the particular mission was used to evaluate the behavior of the torques, and a simulation was performed to determine the attitude effect of each torque relative to the untorqued vehicle. The results of the simulation are summarized in this paper, and the relative importance of each torque is noted. Attitude prediction time for 14-arc-second accuracy is shown for various combinations of torques used in the vehicle model. Of the five torques, the magnetic interaction torques were the most significant in terms of spin decay. Torques caused by solar pressure and gravity gradient were the next most significant, while the aerodynamic torque was the least significant. The solar pressure and gravity gradient torques had the greatest effect on precession ( $\Delta\theta$  and  $\Delta\psi$ ). State propagation within 14 arc seconds was possible for five minutes using only the residual magnetic moment and the eddy current torques in the vehicle model.

## INTRODUCTION

The need for infrared measurement research and detection techniques is critical to the success of U. S. space programs devoted to earth resources detection, military surveillance, and meteorology research. An essential part of infrared measurement experimentation and detection techniques is the determination of the experiment axes attitude and, in turn, the experiment's line of sight at the time of the experiment measurement. In the evolution of infrared research and implementation, the growing complexity of the missions has demanded greater precision attitude determination. Many missions are presently demanding a continuous time history of the experiment pointing direction of 1 to 30 arc seconds for periods of one year or more. To meet these requirements, long life attitude measurement instrumentation and sophisticated and effi-

cient data reduction techniques are being developed.

Figure 1 is a schematic of an attitude determination system designed to have a lifetime of

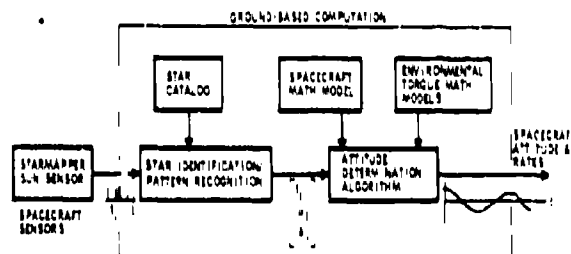


Fig. 1. Schematic of Attitude Determination System

<sup>1</sup>This work was performed under NASA contract NAS1-8801.

one year and an attitude accuracy of 14 arc seconds. This concept is the result of an Attitude-Referenced Radiometer Study<sup>2</sup>, conducted by NASA Langley Research Center. The requirement is for continuous attitude estimation for 14-arc-second accuracy in an inertial frame. The concept consists of a passive scanned star-mapper and sun mapper on a spin-stabilized vehicle. The output of the attitude determination sensor is transit times of a celestial body. A ground data reduction program uses the transit times to estimate the spacecraft attitude. In lieu of a gyro rate package, a vehicle model including significant environmental torque models is used.

In developing a vehicle model for long-life mission, two requirements that must be met are:

- (1) The model must propagate the vehicle state within 14 arc seconds from celestial observation to observation. This is important during daylight operation because stray light reduces the star-mapper capability to detect stars, and, consequently, times between observations are lengthened.
- (2) The speed of data reduction must be sufficient to prevent any backlogging of data collected throughout the one-year period. This requires simplification of the model and, at the same time, 14-arc-second propagation accuracy. One example of simplification is minimization of the number of parameters required to be estimated because the number of differential equations in the estimator increases according to  $n(n+1)/2$  where  $n$  is the order of the state.

These two requirements led to an investigation of the environmental disturbances for the ARRS mission requirements given in Table 1. In the investigation, several sources of torques were identified, and the torques due to eddy currents, residual magnetic moments, solar pressure, aerodynamic pressure and gravity gradient were modeled.

The purpose of this paper is to present the five sources of torque and to discuss the various torque models that were used. Computer simulations performed during the investigation determined the attitude deviation resulting from each torque relative to an untorqued vehicle. Also, the validity of comparing each torque to the untorqued case rather than to the five torque case was determined through the use of a torque linearity simulation. Simplifications of the models were made where possible, and suggestions for simplification were also noted. Pre-

diction time for various combinations of torque used in the model is given in this paper.

Table 1. ARRS Mission Requirements

<b>Orbital Parameters</b>	
- Altitude - 500 km	
- Eccentricity - zero (circular orbit)	
- Inclination - 97.38° (near-polar sun synchronous) = 1	
- Phasing - 3:00 a.m. or 3:00 p.m. used $\Omega = 45^\circ$ longitude of the ascending node	
<b>Spacecraft Configuration</b>	
- Shape - see Fig. 2	
- Inertia characteristics: $I_y = 65 \text{ slug-ft}^2$	
$I_x = I_z$	
$I_y/I_x = 1.2$	
- Magnetic characteristics: $M_x = M_y = M_z$	
Moment coefficients: $M_x = M_y = M_z$	
$M_x = 0 (\pm 5 \times 10^{-6}) \text{ ft-lb/Gauss}$ due to pre-flight compensation uncertainties	
$\Delta M_x$ due to differences in sunlight and dark conditions = 5% of $M_x$	
Eddy current coefficients:	
$1.4 \times 10^{-5} \text{ ft-lbs-sec}$ $Q$	
- Experiment optical axis: lies in spin plane	
<b>Operational Characteristics</b>	
- Spin rate: 3 revolutions per minute	
- Attitude: spin axis nominally perpendicular to orbit plane within $\pm 5^\circ$ . No control applied during instrument measurement period.	

The results of the investigation show that the residual magnetic moment and eddy currents produce significant short-term spin decay and should be included in the vehicle model. The model for the eddy current torque has three coefficients; however, simulations showed that a single coefficient model is a good substitute for the three coefficient model.

The prediction time without attitude update was shown to be approximately five minutes when eddy current and residual magnetic moments torque are included in the vehicle model. Simulations also showed that cyclic torque terms may be deleted, thus improving the numerical evaluation speed of the vehicle model.

<sup>2</sup>The Attitude-Referenced Radiometer Study (ARRS) was conducted by Honeywell Inc. for NASA Langley Research Center under NAS1-8801 contract. The purpose of the study was to advance the technique for the design and fabrication of radiometric experiments for orbital application.

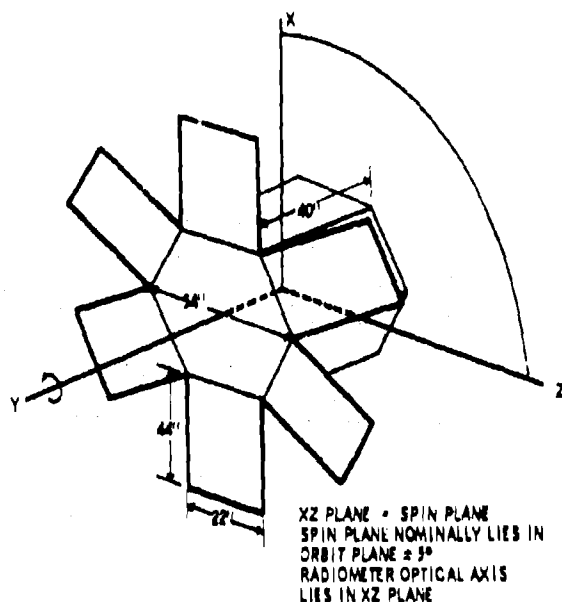


Fig. 2. Spacecraft Configuration

### TORQUE MODELS

Several sources that cause perturbation on the spacecraft are:

- Active attitude control torques
- Electromagnetic radiation from the spacecraft
- Internal moving parts
- Meteorites
- Vehicle outgassing
- Eddy currents
- Residual magnetic moment
- Solar pressure
- Aerodynamic pressure
- Gravity gradient

The mission plan requires that the attitude control torque be suspended during measurements. The attitude is maintained by the spin stability of the spacecraft, and only periodic attitude corrections are required, thus eliminating the need for an active attitude control torque model.

The electromagnetic radiation from the spacecraft is due to a planned 0.5k-watt transmitter, which causes at most  $4 \times 10^{-8}$  ft-lbs when the

energy is in one direction. The effect of this torque is negligible and is no longer considered.

Internal moving parts can be a large contributor to vehicle motion, but the present mission does not require moving parts such as tape recorders, gimbals, dithering mirrors, etc.; therefore, no model is required.

Torques due to meteorites are extremely small which Beletskii (Ref. 1) shows to be negligible. Based on Beletskii's work, meteorite effects are not considered further.

Vehicle outgassing, (Ref. 2), due to trapped air pockets has an exponential decay and is insignificant after several orbits. The effect of this torque will not enter the attitude determination problem.

The five remaining sources of torque are investigated and analyzed in the following pages. The constraints given in Table 1 are used in the derivation of the torques due to the sources. A computer program was devised to simulate the mission and compute the effects of the torques on attitude. The vehicle model and equations used in that simulation are given in Appendix A, while the coordinate frames used in the program are given in Appendix B.

The computer program computed the attitude for an untorqued vehicle and the attitude and torque for the torqued vehicle. It then computed the differences in the attitude and torque for output. In all the simulation runs, the orbit parameters were identical. The true anomaly,  $\psi$ , longitude of the ascending node,  $\Omega$ , and the inclination,  $i$ , are 187 degrees, 45 degrees, and 97.83 degrees, respectively. The attitude angles,  $\psi$ ,  $\Omega$ , and  $\theta$  are defined in Appendix A.

### Residual Magnetic Moments

Torque Equation -- A torque will exist due to the interaction of current flow in the spacecraft electrical circuits and induced moments with the earth's magnetic field. The magnitude of the moment is expected to vary due to changes in spacecraft control modes and power usage. While the design of the spacecraft can reduce the magnitude of the moment, a residual magnetic moment will remain.

The general equation for the torque due to the residual magnetic moment is

$$\vec{T} = \vec{M} \times \vec{B} \quad (1)$$

and in body axis

$$\begin{aligned} T_x &= M_y B_z - B_y M_z \\ T_y &= M_z B_x - B_z M_x \\ T_z &= M_x B_y - B_x M_y \end{aligned} \quad (2)$$



where

$M_x, M_y, M_z$  = body axis residual magnetic moments, ft-lbs/Gauss, and

$B_x, B_y, B_z$  = body axis components of the earth's magnetic field, Gauss

**Computer Simulation** -- The residual magnetic moment torque model was programmed and a one-orbit simulation was made using the following values of the moments:

$$M_x = M_y = M_z = 5.170856 \times 10^{-6} \text{ ft-lb/G}$$

This value of the moment is representative of moment values experienced on the early Tiros spacecrafts. Initial conditions were chosen such that a cone angle of 0.51 deg was obtained and the principal y-axis of the body was misaligned to the orbit normal by approximately 7.5 deg. The orbit parameters were chosen with the true anomaly at the equator and a south heading. The right ascension of 45 deg represents a 3 a.m. or 3 p.m. launch condition, and the inclination gives the sun synchronous retrograde orbit. Figure 3 shows the value of the  $T_x, T_y$ , and  $|T|$  as a function of time.

The peaks of the envelope in all three of the torque plots represent the south and north pole of the earth, respectively. At these points, the magnetic field components are greatest in the

orbit plane and thus give the largest cyclic variations. The y-component of torque is cyclic with a period of 20 seconds and mean value of zero. This component of torque is a function of  $B_x, M_z, M_y$  and  $B_z$ , where  $M_x$  and  $M_z$  are constants and  $B_x$  and  $B_z$  are cyclic in body axes with a 20-second period due to the spacecraft spin. The x-component is also cyclic, with a period of 20 seconds (3 rpm spin rate) and with the mean varying with position in orbit. The mean of the x-component of torque is nonzero because of the  $(M_z B_y)$  term. The cyclic portion is due to the  $M_y B_z$  term.

The cyclic nature of the torque does not create a cyclic variation in the attitude difference,  $\Delta\theta$ . The deviation in  $\theta$  at 5700 seconds is -75 arc seconds. Although  $\Delta\phi$  and  $\Delta\psi$  have spin rate cyclic variation, the extent of the variation is insignificant over the full orbit, approximately 1 arc sec variation of  $\Delta\phi$  at 5702.4 seconds. These results suggest that short-term variation of torque with a period of 20 seconds and mean of zero may be deleted from the torque model. The difference,  $\Delta\psi$ , has orbital variation on a mean drift of 40 arc seconds per orbit. The  $\Delta\psi$  has orbital variation about the mean drift of  $\pm 10$  arc seconds.

#### Eddy Currents

**Torque Equation** -- Eddy currents are induced in the spacecraft due to the spin motion of the spacecraft. Vinti (Ref. 3), showed that the interaction of the generated eddy currents and earth's magnetic field produced a torque

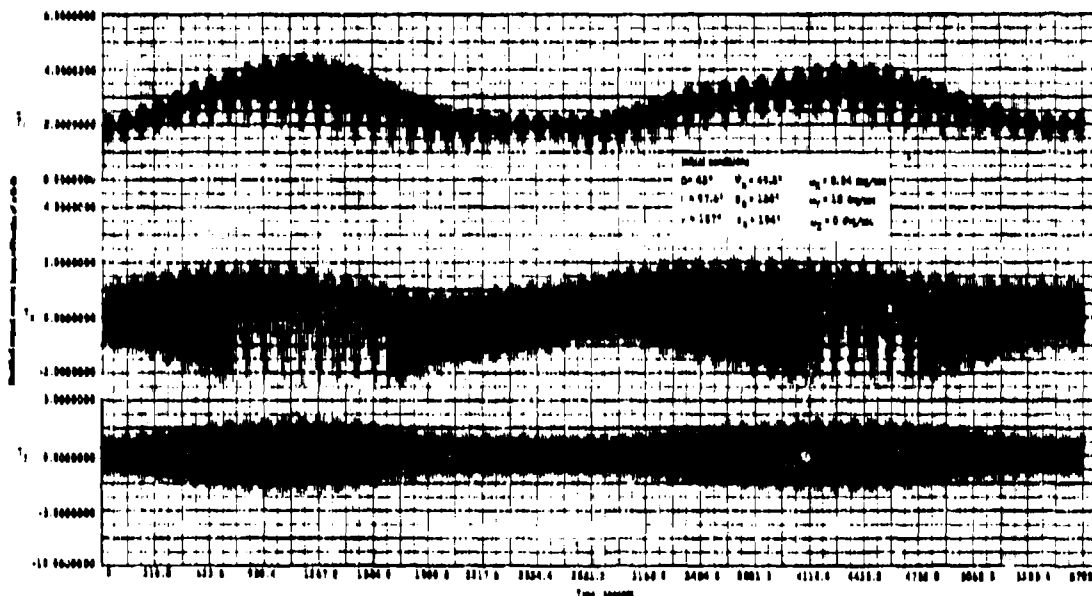


Fig. 3. Torque on Spacecraft Due to Residual Magnetic Moments

that precessed the spin axis of a spherical spacecraft in addition to causing spin decay. The work of Vinti resulted in the following equation for the torque on a spherical-conducting spacecraft:

$$\vec{T} = K (\vec{\omega} \times \vec{B}) \times \vec{B} \quad (3)$$

where

$\vec{\omega}$  = spacecraft spin vector

$\vec{B}$  = earth's magnetic field

$K$  = a coefficient based on the spacecraft dimensions and conductivity

The appealing feature of this model is the single coefficient. In using this model the attitude determination estimation program need estimate only one coefficient. The subject spacecraft configuration, however, is not a sphere and a new model was derived to determine if more coefficients are necessary to describe the eddy current effects.

The general expression in Gaussian units for the torque on a spacecraft due to eddy current interaction is

$$\vec{T} = \frac{1}{c} \iiint \vec{r} \times (\vec{J} \times \vec{H}) dV \quad (4)$$

where

$\vec{J}$  = volume eddy current density

$\vec{r}$  = direction from the center of mass to the element of volume

$c$  = speed of light in vacuum

$\vec{H}$  = earth's magnetic field strength =  $\frac{B}{\mu}$

$\mu$  = permeability = 1 for aluminum

The volume current density (Ref. 4) in closed form is given by

$$\vec{J} = \frac{1}{2} \sigma^{-1} (\vec{\omega} \times \vec{H}) \times \vec{r} + \nabla \phi$$

where

$\sigma$  = static electrical conductivity

$\phi$  = potential that is required to satisfy the boundary condition and Laplace equation,  $\nabla^2 \phi = 0$

For a sphere, the potential,  $\phi$ , is a constant, and  $\nabla \phi = 0$ . The solution is now easily obtained for the sphere by integrations over the volume.

For the "Hat" configuration, the eddy current density was derived for the skin of the spacecraft, assuming that each solar panel and cylinder sides are electrically isolated, and the skin was chosen to be thin, thus reducing the eddy current volume density to a two-dimensional problem. First, the eddy current density in the rectangular panel must be computed in closed form. This eddy current density is known once  $\phi$  is known. The

potential,  $\phi$ , is determined by the boundary conditions, i.e., currents normal to the boundary are zero, and Laplace's equation. This boundary value problem is the Neumann-type for which very few closed-form solutions are known (Ref. 5). However, for the two-dimensional case with simply connected regions and the boundary conditions satisfying Gauss's theorem

$$\oint \frac{\partial \phi}{\partial n} ds = 0 \quad (\text{integral on the boundary condition around the boundary})$$

where

$\frac{\partial \phi}{\partial n}$  = gradient at the surfaces

$ds$  = differential element along the boundary

The Neumann problem can be reduced to the Dirichlet problem by using the Cauchy-Riemann conditions. The Cauchy-Riemann conditions transform  $\phi$  into a stream function,  $\psi$ . Following this procedure, solutions for the stream functions are obtained. The torque integral is rephrased in terms of the stream function before integration. The torque expression is obtained by integration over the volume of each panel relative to a common body axis frame and adding all torque due to each panel. Carrying out the integration, the closed-form torque equation for the "Hat" configuration is:

$$\begin{aligned} L_x &= -p_1 (\omega_x H_y^2 - \omega_y H_x H_y) \\ &\quad - p_2 (\omega_x H_z^2 - \omega_z H_x H_z) \\ L_y &= p_3 [\omega_y (H_x^2 + H_z^2) - \omega_x H_x H_y \\ &\quad - \omega_z H_y H_z] \\ L_z &= -p_1 (\omega_z H_y^2 - \omega_y H_y H_z) \\ &\quad - p_2 (\omega_z H_x^2 - \omega_x H_x H_z) \end{aligned} \quad (5)$$

where the  $p$ 's are constants evaluated using the dimensions and conductivity of the cylinder panels and solar panels.

The equations for the  $p$ 's are.

$$\begin{aligned} p_1 &= \left\{ \frac{1}{4} \sigma c^{-2} \cdot \omega L^2 - \frac{1}{4} \sigma c^{-2} \cdot \omega L^2 \cdot \frac{1}{4} \sigma c^{-2} \cdot \omega L^2 \cdot \frac{1}{4} \sigma c^{-2} \cdot \omega L^2 \cdot \left( \frac{1}{4} \sigma c^{-2} \cdot \omega L^2 \right) \right. \\ &\quad \left. + \frac{1}{4} \sigma c^{-2} \cdot \omega L^2 \cdot \left( \frac{1}{4} \sigma c^{-2} \cdot \omega L^2 \right) \sum_{m=1}^{\infty} \left( \frac{1}{m^2} \right)^2 \left[ \frac{m^2 L^2}{\omega L^2} \cdot \frac{1}{\omega L^2} \right] \sinh \frac{m^2 L^2}{\omega L^2} \right\} \\ &\quad + \frac{1}{4} \sigma c^{-2} \cdot \omega L^2 \cdot \sum_{m=1}^{\infty} \left( \frac{1}{m^2} \right)^2 \left[ \frac{m^2 L^2}{\omega L^2} \cdot \frac{1}{\omega L^2} \right] \sinh \frac{m^2 L^2}{\omega L^2} \left\{ \right\} \end{aligned}$$

$$P_2 = \left\{ \frac{1}{4} \sigma \tau^2 \epsilon \omega^2 \left( \frac{h}{d} \right)^2 \sum_{m=1}^{\infty} \left( \frac{1}{m^2} \right)^2 \left[ \left( \frac{h}{d} \right)^2 \left( \frac{m^2 \pi^2}{4d} \right) + \left( \frac{h}{d} \right)^4 \left( \frac{m^2 \pi^2}{4d} \right) \right] \right. \\ \left. + \frac{1}{4} \sigma \tau^2 \epsilon \omega^2 \left( \frac{h}{d} \right)^2 \sum_{m=1}^{\infty} \left( \frac{1}{m^2} \right)^2 \left[ \left( \frac{h}{d} \right)^2 \left( \frac{m^2 \pi^2}{4d} \right) + \left( \frac{h}{d} \right)^4 \left( \frac{m^2 \pi^2}{4d} \right) \right] \right\} \quad (6)$$

$$P_3 = \left\{ \frac{1}{4} \sigma \tau^2 \epsilon \omega^2 \left( \frac{h}{d} \right)^2 \sum_{m=1}^{\infty} \left( \frac{1}{m^2} \right)^2 \left[ \left( \frac{h}{d} \right)^2 \left( \frac{m^2 \pi^2}{4d} \right) + \left( \frac{h}{d} \right)^4 \left( \frac{m^2 \pi^2}{4d} \right) \right] \right. \\ \left. + \frac{1}{4} \sigma \tau^2 \epsilon \omega^2 \left( \frac{h}{d} \right)^2 \sum_{m=1}^{\infty} \left( \frac{1}{m^2} \right)^2 \left[ \left( \frac{h}{d} \right)^2 \left( \frac{m^2 \pi^2}{4d} \right) + \left( \frac{h}{d} \right)^4 \left( \frac{m^2 \pi^2}{4d} \right) \right] \right\}$$

where

$\sigma$  = static electrical conductivity

$\tau$  = thickness of cylinder panels

$\epsilon$  = thickness of solar panels

$W$  = width of cylinder panels

$L$  = length of cylinder panels

$h$  = length of solar panels

$d$  = width of solar panels

$m = 2n-1$ , where  $n = 1, 2, 3, \dots$

$a = \frac{\sqrt{3}}{2} W$

$L_1 = L - L_2$  = distance from center of mass to end of cylinder opposite solar panel end

The torque expression has three coefficients for the "Hat" configuration spacecraft as compared to the single coefficient for the spherical configuration. The three coefficients were evaluated using the baseline dimensions of the vehicle and a static conductivity of aluminum at 20°C (Ref. 3). The values used in the evaluation of the coefficient are:

$\gamma = 0.0254$  cm

$\epsilon = 0.0254$  cm

$W = 55.9$  cm

$L = 101.1$  cm

$h = 111.8$  cm

$d = 55.9$  cm

$L_2 = 43.1$  cm

$\sigma = 2.83 \times 10^{-11} \frac{\text{sec}^2}{\text{ohm-cm}}$

The coefficient values are:

$$P_1 = 2.075 \times 10^{-6} \frac{\text{ft-lb-sec}}{G^2}$$

$$P_2 = 7.20 \times 10^{-5} \frac{\text{ft-lb-sec}}{G^2}$$

$$P_3 = 6.226 \times 10^{-6} \frac{\text{ft-lb-sec}}{G^2}$$

**Computer Simulation Results** -- The "Hat" configuration model was programmed and evaluated relative to an untorqued vehicle using the computed coefficient. A second simulation was conducted to compare the spherical model and the "Hat" model. In order to compare, the coefficient  $P_3$  was chosen to be the same as the spherical model coefficient,  $K$ , and  $P_1$  and  $P_2$  ratio kept the same as the ratio of the above computed values. Figure 4 is a plot of the "Hat" configuration torque using the computed coefficients for a one-half orbit simulation. The y-component of the torque varies only as a function of orbit position. However, the x-component of torque exhibits variation at the spin frequency and the spin vector precession frequency (motion of  $\omega$  in the body). The peak points of the torque occur at the poles because of the greater magnitude of the field at the poles.

The attitude deviation,  $\Delta\theta$ , does not possess a cyclic variation, but  $\Delta\psi$  and  $\Delta\phi$  possess a spin rate cyclic variation. The deviation in  $\Delta\theta$  at 2700 seconds is 3500 arc sec, and  $\Delta\phi$  and  $\Delta\psi$  have a peak-to-peak variation of 37.5 arc sec. The results suggest, for accurate propagation of spacecraft attitude, that the torques due to eddy currents be included in the model.

It is of interest to reduce the number of parameters required to be estimated by the algorithm. Thus, comparison of the two eddy current modes was made using the following coefficients:

$$K = 0.25 \times 10^{-5} \frac{\text{ft-lb-sec}}{G^2}$$

$$P_1 = 0.46 \times 10^{-6} \frac{\text{ft-lb-sec}}{G^2}$$

$$P_2 = 0.3 \times 10^{-4} \frac{\text{ft-lb-sec}}{G^2}$$

$$P_3 = -0.25 \times 10^{-5} \frac{\text{ft-lb-sec}}{G^2}$$

A computer simulation was conducted computing the difference in attitude generated by the two models. The differences of the two models are for  $(\Delta\theta)$  at 2700 seconds 1.4 arc second, and  $\Delta\psi$  are 0.4 arc second peak to peak about a zero mean at 2700 seconds. For the

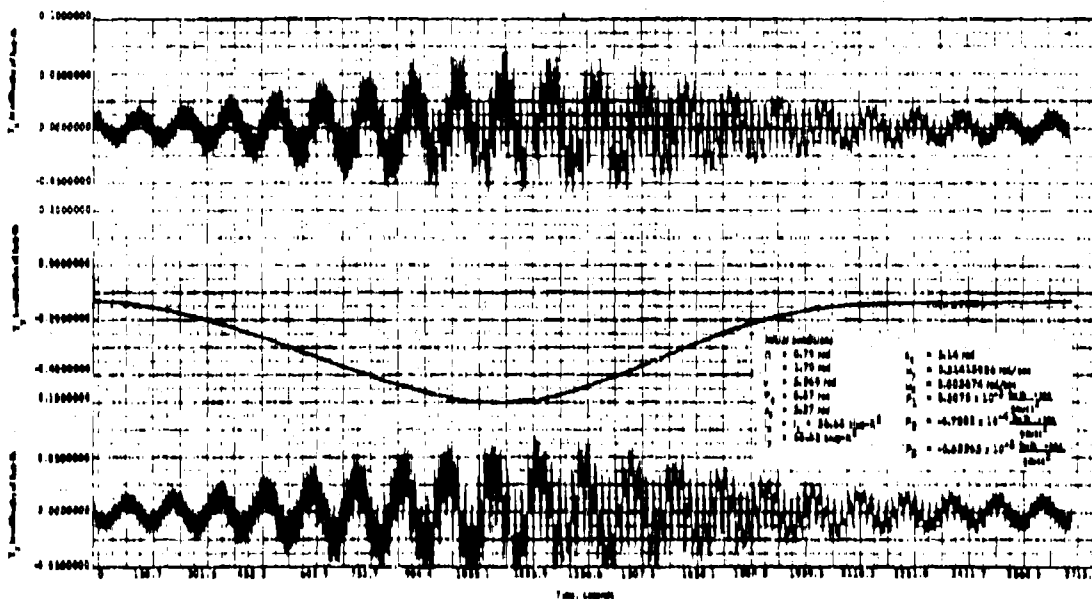


**Fig. 4. ARRS Eddy Current Torque on Half Orbit.**

stated values of the coefficients, the differences say that the spherical model is adequate for the attitude determination algorithm.

## Solar Radiation

Interplanetary radiation originates primarily from the solar system. Galactic radiation, compared to solar radiation, contributes little to the total radiation pressure exerted on a unit area of a spacecraft. Solar radiation is further divided into electromagnetic radiation and particle radiation. Electromagnetic radiation consists of photons which propagate in wave forms having wavelengths in the continuous spectrum. Photons have zero rest mass, no electrical charge, and no magnetic moment, but they do possess energy resulting in a force producing a pressure termed "light pressure." Particle radiation consists of electrons, protons, neutrons, alpha and beta particle plasma and many other subparticles. These particles, which have a rest mass, are expelled from the sun at velocities of from 400 to 1500 km per second. This particle radiation which sweeps throughout interplanetary space is termed "solar wind."

Electromagnetic Radiation -- The intensity of electromagnetic radiation is inversely proportional to the square of the distance from the sun. About 99 percent of this solar energy lies in the narrow band from 3000 to 4000 angstroms, (Ref. 6), with the remaining 1 percent distributed in the ultraviolet, infrared and radio frequencies. The incident electromagnetic radiation power density (the solar constant) received outside the

earth's atmosphere at a distance of one astronomical unit from the sun is  $1398 \pm 1$  percent watts/meter<sup>2</sup>. This power density which produces "light pressure" is virtually unchanged with high solar activity. The radiation pressure  $P_r$  acting on a nonreflective surface normal to the incoming radiation is given by

$$P = \frac{E}{C}$$

where

$P_e$  = pressure due to electromagnetic radiation

$E_0$  = solar constant ( $1396 \text{ w/m}^2$ )

C = velocity of light ( $2.998 \times 10^8$  m/s)

hence

$$P_o = 4.658 \times 10^{-8} \text{ newton/meter}^2$$
$$= 0.971 \times 10^{-8} \text{ lb/ft}^2$$

Particle Radiation -- The solar atmosphere is composed primarily of ionized particles that flow continuously outward from the sun. This flow, which represents an expansion of the solar corona, is called the "solar wind." The corona is composed primarily of hydrogen; hence, the solar wind consists primarily of highly ionized hydrogen particles (electrons and protons). Since the mass of the proton is 1837 times the mass of the electron, the energy of the solar wind can be determined from the particle energy

of the proton alone, which is about one Kev during quiet sun periods. During quiet sun periods, the velocity of solar wind particles at one astronomical is about 400 km per second with a density of about 10-100 particles per cubic centimeter (Ref. 6). The pressure, which equals the energy density on a surface normal to the particle velocity, is given by

$$P_p = m N V^2$$

where

$P_p$  = pressure due to solar particles

$m$  = proton particle mass ( $1.67 \times 10^{-24}$  gm)

$N$  = particle density (10-100/cm<sup>3</sup>)

$V$  = particle velocity (400 km/sec)

Thus, the pressure on a surface normal to solar particle radiation during quiet sun period is

$$P_p = 5.8 \times 10^{-11} \text{ to } 5.8 \times 10^{-10} \text{ lb/ft}^2$$

During active sun periods, however, the solar pressure due to particle radiation is greatly magnified. Solar flares cause a rapid expansion of the corona, producing an increase in the velocity and density of the solar plasma.

Solar flares vary in magnitude and brightness and are classified according to their area (percent of solar disk involved). Observations have shown that the frequency and duration of solar flares vary as a function of their class. Small flares (class 1) occur every few hours and have durations of about 10 to 40 minutes.

Conversely, the large flares (classes 3 and 3+) occur more rarely but have longer durations. As many as six or seven class 3+ flares with mean durations of about three hours may be expected in one year during the active portion of the 11-year solar cycle.

As a result of a class 3+ flare, the solar plasma velocity may increase to about 1500 km per second with particle density increasing to as high as 100 particles per cubic centimeter (Ref. 6 and 8). During this brief period, the solar particle radiation pressure is

$$P_p = 7.8 \times 10^{-9} \text{ lb/ft}^2$$

Based on the foregoing estimates, the particle radiation pressure is at least an order of magnitude less than the electromagnetic radiation pressure and may be neglected.

In developing the solar pressure disturbance torque model, a constant pressure

$$P = 1 \times 10^{-7} \text{ lb/ft}^2$$

is used for a surface normal to the sun line with no variation due to solar activity.

Equations (Ref. 9) -- The torque on a body due to solar pressure is computed from the following three formulas taken from Beletskii (Ref. 1):

$$\vec{m}^+ = \int_{S_1} \hat{n} \times \vec{r}_s (\hat{n} \cdot \hat{r}) ds \quad (7)$$

$$\vec{m}^- = 2 \int_{S_2} \hat{n} \times \vec{r}_s (\hat{n} \cdot \hat{r})^2 ds \quad (8)$$

$$\vec{T} = P [(1 - \epsilon_0) \vec{m}^+ + \epsilon_0 \vec{m}^-] \quad (9)$$

where

$S$  = region of body in sunlight;  $ds$  is an area differential

$\vec{r}_s$  = vector from body's C.M. to  $ds$

$\hat{r}$  = unit vector directed from sun

$\hat{n}$  = unit outer normal to  $ds$

$P$  = pressure exerted locally by sunlight

$\epsilon_0$  = body's reflection coefficient

The integrations described in Eqs. (7) and (8) are performed over two distinct surfaces -- the solar panels and end of the spacecraft (Fig. 5) and the sides of the spacecraft (Fig. 5). To simplify the model, three assumptions are made:

- 1) That the sun never shines on the end of the spacecraft opposite the solar panels
- 2) That the shadow of an outside end of a solar panel never strikes any part of the spacecraft
- 3) That the sides of the spacecraft (i.e., not the solar panels) constitute a circular cylinder rather than a hexagonal one.

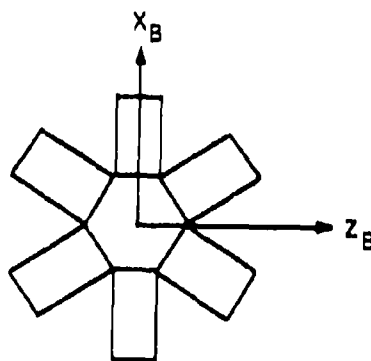


Fig. 5. Relation of Solar Panels and End of Spacecraft to the Body Axes

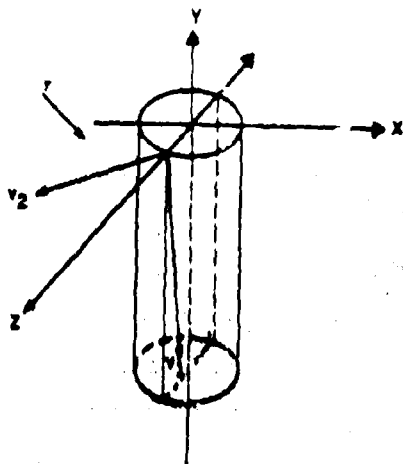


Fig. 8. Spacecraft in Unprimed Coordinate System

The integrations of Eqs. (7) and (8) over the end solar panels are quite simple; the integrations over the sides are considerably more complicated.

Sunlight passing between two solar panels may strike the spacecraft. If so, the integration of Eqs. (7) and (8) must be performed over the sunlit region. The limits of integration, i.e., the lines bounding the sunlit region, are described by Eqs. (10), (14), (15), and (16).

Since this end of the spacecraft is always fully illuminated, integration of Eqs. (7) and (8) is performed to obtain a closed form for:

$$\bar{M}^+ = \begin{bmatrix} -C_0 b_0 L_2 S \\ 0 \\ a_0 b_0 L_2 S \end{bmatrix}$$

$$\bar{M}^- = \begin{bmatrix} 0 \\ 0 \\ 0 \end{bmatrix}$$

where

$$\hat{r}_B = \begin{bmatrix} a_0 \\ b_0 \\ c_0 \end{bmatrix} = \text{direction cosines of sun vector in the body frame}$$

$L_2$  = length from center mass of vehicle to the solar panel end

$S$  = area exposed to the sun

This torque is zero because sunlight does not fall on this surface for this mission.

All computations in this section are done in the unprimed coordinate system of the cylindrical coordinate system. The body of the spacecraft is approximated by a circular cylinder of length  $L$ . Figure 8 shows the configuration in the unprimed coordinate system (this system is described in Appendix B).

Figure 8 also shows the unit vectors  $\hat{v}_1$ ,  $\hat{v}_2$ , and  $\hat{r}$ . The unit vector,  $\hat{r}$ , is directed from the sun. It has the same components as  $\hat{r}_B$  in body coordinates

$$\hat{r} = \begin{bmatrix} a_0 \\ b_0 \\ c_0 \end{bmatrix}$$

We define  $\hat{v}_1$  and  $\hat{v}_2$  to be unit vectors along two adjacent solar panel edges. The sunlight by these two edges will strike the cylinder.

The problem, then, will be to find the region of integration, i.e., the region on the cylinder where the sunlight falls. This area will be bounded by some combination of the following lines:

- The circles forming the top and bottom of the cylinder
- The shadows formed by the adjacent edges of two solar panels
- The lines which border the sunlit and dark sides of the cylinder.

The lines under (c) are most easily described in the cylindrical coordinate system (described in Appendix B). They are described by  $\hat{r} \cdot \hat{n} = 0$ , or

$$\theta = -\tan^{-1}(c_0/a_0) \quad (10)$$

$$\theta = \pi - \tan^{-1}(c_0/a_0)$$

To achieve the description of the lines under (b), we must consider the projection of  $\hat{v}_1$  and  $\hat{v}_2$  onto the cylinder. In the unprimed system,

$$\hat{v}_1 = \hat{i} \sin 30^\circ + \hat{k} \cos 30^\circ$$

The projection of  $\hat{v}_1$  onto the cylinder lies in the plane which is common to  $\hat{v}_1$  and  $\hat{r}$ . Call this plane  $P_1$ .  $P_1$  has a non-zero normal:

$$\begin{aligned} \bar{N} &= \hat{v}_1 \times \hat{r} \\ &= -\hat{i} b_0 \cos 30^\circ + \hat{j} (a_0 \cos 30^\circ - c_0 \sin 30^\circ) \\ &\quad + \hat{k} b_0 \sin 30^\circ \end{aligned}$$

A point known to be on the plane is  $(0, 0, r_3)$  where  $r_3$  is the radius of the cylinder. Knowing the normal to  $P_1$  and a point on  $P_1$  is enough to determine the plane uniquely. The equation for  $P_1$  is found to be

$$-\frac{\sqrt{3}}{2} b_0 x + \frac{1}{2} (\sqrt{3} a_0 - c_0) y + \frac{b_0}{2} z = r_3 \frac{b_0}{2} \quad (11)$$

In a similar manner,  $P_2$ , the plane which is the sun's projection of  $v_2$ , has equation

$$-\frac{\sqrt{3}}{2} b_0 x + \frac{1}{2} (\sqrt{3} a_0 + c_0) y - \frac{b_0}{2} z = -r_3 \frac{b_0}{2} \quad (12)$$

The cylinder has the equation

$$x^2 + z^2 = r_3^2 \quad (13)$$

If Eqs. (10) and (13) are solved simultaneously, the result is a line which describes the projection of  $v_1$  on the cylinder (at least on the sunny side of the cylinder). A similar explanation holds for the simultaneous solution of Eqs. (7) and (13). These results are expressed in Eqs. (14) and (15) in the cylindrical coordinate system.

For  $\hat{v}_1$

$$y = r_3 b_0 / (\sqrt{3} a_0 - c_0) (\sqrt{3} \sin \theta - \cos \theta + 1) \quad (14)$$

and for  $\hat{v}_2$

$$y = r_3 b_0 / (\sqrt{3} a_0 + c_0) (\sqrt{3} \sin \theta + \cos \theta - 1) \quad (15)$$

The lines under (a) are described by

$$\begin{aligned} [y = 0] \\ [y = -L] \end{aligned} \quad (16)$$

Equations (10), (14), (15) and (16) describe the lines on the surface of the cylinder which are candidates for the integration limits in Eqs. (7) and (8). Depending on the direction from which the sun is shining, different integration limits exist. They fall into six distinct categories which are shown in Figs. 7 through 12.

Case 1 is shown in Fig. 9. Both shadows run off the left edge of the sunlit part of the cylinder before they strike the lower end of the cylinder. If  $f(y, \theta)$  is allowed to represent either integrand in Eqs. (7) or (8), then

$$\int_{\theta_1}^{\theta_2} \int_{y_1}^{\theta_2} f(y, \theta) dy d\theta = r_3 \int_{\theta_1}^{\theta_2} \int_{K_1}^{K_2} \frac{G(\theta)}{F(\theta)} f(y, \theta) dy d\theta \quad (17)$$

where

$$K_1 = r_3 b_0 / (\sqrt{3} a_0 - c_0)$$

$$K_2 = r_3 b_0 / (\sqrt{3} a_0 + c_0)$$

$$F(\theta) = \sqrt{3} \sin \theta - \cos \theta + 1$$

and

$$G(\theta) = \sqrt{3} \sin \theta + \cos \theta - 1$$

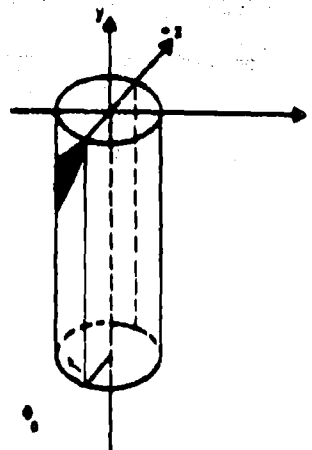
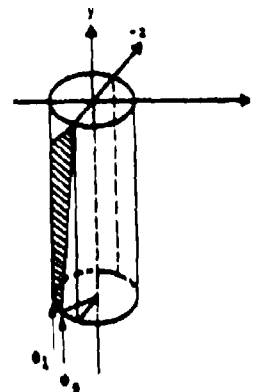


Fig. 7. Both Shadows Intersecting Left Edge of Sunlit Area



$$\int_{\theta_1}^{\theta_2} \int_{y_1}^{\theta_2} f(y, \theta) dy d\theta = r_3 \int_{\theta_1}^{\theta_2} \int_{K_1}^{K_2} \frac{G(\theta)}{F(\theta)} f(y, \theta) dy d\theta$$

Fig. 8. Shadows Intersecting Edge of Sunlit Area and End of Spacecraft

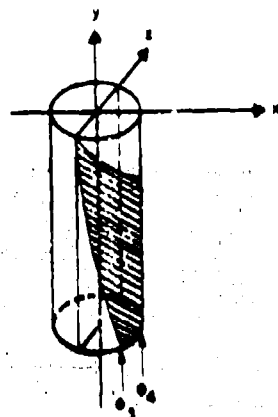


Fig. 9. Shadows Intersecting Right Edge of Sunlit Region and End of Spacecraft

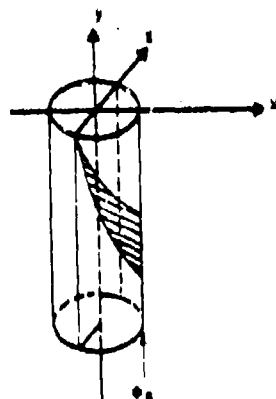


Fig. 10. Both Shadows Intersecting Right Edge of Sunlit Region

The other five cases are shown in Figs. 8 through 12. It is assumed that the reader is viewing along the line of  $\tau$ , so that the  $n \cdot \tau = 0$  lines are the right and left visible edges of the cylinder.

Equations corresponding to Eq. (17) have been calculated for each case. In six cases, the possibility that the shadow due to the end of the solar panel may strike the spacecraft has been ignored.

This seems a reasonable assumption. If the solar panels are never shorter than the length of the cylinder, the angle between the y-axis and  $r$  would have to exceed 45 degrees for this to occur. This sort of thing is not expected.

In order to find some of the preceding integration limits, it is necessary to invert Eqs. (14) and (15). Their inversions are Eqs. (16) and (19), respectively.

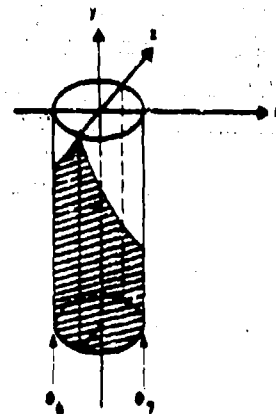


Fig. 11. Each Shadow Intersecting Nearest Edge of Sunlit Region

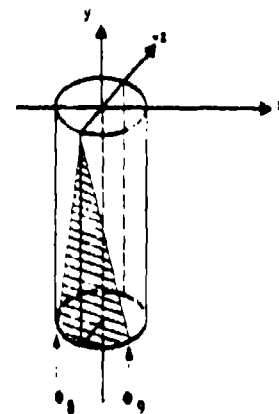


Fig. 12. Both Shadows Intersecting End of Spacecraft



$$\theta_1 = \sin^{-1} \left[ \frac{1}{3} (y/K_1 - 1) / 4 \right. \\ \left. + \sqrt{(3-y/K_1) (1+y/K_1) / 4} \right] \quad (18)$$

$$\theta_2 = \sin^{-1} \left[ \frac{1}{3} (y/K_2 + 1) / 4 \right. \\ \left. - \sqrt{(3+y/K_2) (1-y/K_2) / 4} \right] \quad (19)$$

It is important to check carefully to see that  $\theta$  as yielded by Eqs. (18) or (19) lies on the sunny half of the spacecraft as defined by the two  $n \cdot \hat{r} = 0$  lines. If not, the correct value will be  $\theta_1 = \pi - \theta_2$ .

Any integral expressed as a solution to one of the six cases can be written as a linear combination of some integrals of the following general form:

$$r_3 \int_{-L}^L \int_{-L}^L \frac{KH(\theta)}{r^3} \hat{r}(y, \theta) dy d\theta = I \quad (20)$$

where

$$H(\theta) = d \sin \theta - \cos \theta + 1,$$

and  $d$  can take on the value of  $\pm 1$

and

$$K = \begin{bmatrix} K_1 & \text{if } d = 1 \\ -K_2 & \text{if } d = -1 \end{bmatrix}$$

The general evaluation of  $I/r_3$  [Eq. (20)] has been performed for both functions which  $\hat{r}(y, \theta)$  represents. The result for

$$\vec{m}^+ = \int_{-L}^L \frac{KH(\theta)}{r^3} (\hat{n} \cdot \hat{r}) dy d\theta$$

is:

For the  $\hat{i}$ -component:

$$K \left\{ \frac{1}{3} \sin^3 \theta + \cos \theta + \frac{1}{3} \cos \theta (\sin^3 \theta + 3) \right\} \\ + \frac{1}{3} (K+L) \left\{ \frac{1}{3} \sin^3 \theta + \cos \theta + \frac{1}{3} \cos \theta (\sin^3 \theta + 3) \right\}$$

For the  $\hat{j}$ -component:

$$K \left\{ \frac{1}{3} \sin^3 \theta + \cos \theta + \frac{1}{3} \cos \theta (\sin^3 \theta + 3) \right\} \\ + \frac{1}{3} (K+L) \left\{ \frac{1}{3} \sin^3 \theta + \cos \theta + \frac{1}{3} \cos \theta (\sin^3 \theta + 3) \right\}$$

For the  $\hat{k}$ -component:

$$K \left\{ \frac{1}{3} \sin^3 \theta + \cos \theta + \frac{1}{3} \cos \theta (\sin^3 \theta + 3) \right\}$$

$$+ \frac{1}{3} (K+L) \left\{ \frac{1}{3} \sin^3 \theta + \cos \theta + \frac{1}{3} \cos \theta (\sin^3 \theta + 3) \right\}$$

$$\vec{m}^+ = \int_{-L}^L \frac{KH(\theta)}{r^3} (\hat{n} \cdot \hat{r}) dy d\theta$$

For the  $\hat{i}$ -component:

$$K \left\{ \frac{1}{3} \sin^3 \theta + \cos \theta + \frac{1}{3} \cos \theta (\sin^3 \theta + 3) \right\}$$

$$+ \frac{1}{3} (K+L) \left\{ \frac{1}{3} \sin^3 \theta + \cos \theta + \frac{1}{3} \cos \theta (\sin^3 \theta + 3) \right\}$$

$$+ \frac{1}{3} (K+L) \left\{ \frac{1}{3} \sin^3 \theta + \cos \theta + \frac{1}{3} \cos \theta (\sin^3 \theta + 3) \right\}$$

$$+ \frac{1}{3} (K+L) \left\{ \frac{1}{3} \sin^3 \theta + \cos \theta + \frac{1}{3} \cos \theta (\sin^3 \theta + 3) \right\}$$

$$+ \frac{1}{3} (K+L) \left\{ \frac{1}{3} \sin^3 \theta + \cos \theta + \frac{1}{3} \cos \theta (\sin^3 \theta + 3) \right\}$$

$$+ \frac{1}{3} (K+L) \left\{ \frac{1}{3} \sin^3 \theta + \cos \theta + \frac{1}{3} \cos \theta (\sin^3 \theta + 3) \right\}$$

$\hat{j}$ -component = 0.

For the  $\hat{k}$ -component:

$$K \left\{ \frac{1}{3} \sin^3 \theta + \cos \theta + \frac{1}{3} \cos \theta (\sin^3 \theta + 3) \right\}$$

$$+ \frac{1}{3} (K+L) \left\{ \frac{1}{3} \sin^3 \theta + \cos \theta + \frac{1}{3} \cos \theta (\sin^3 \theta + 3) \right\}$$

$$+ \frac{1}{3} (K+L) \left\{ \frac{1}{3} \sin^3 \theta + \cos \theta + \frac{1}{3} \cos \theta (\sin^3 \theta + 3) \right\}$$

$$+ \frac{1}{3} (K+L) \left\{ \frac{1}{3} \sin^3 \theta + \cos \theta + \frac{1}{3} \cos \theta (\sin^3 \theta + 3) \right\}$$

$$+ \frac{1}{3} (K+L) \left\{ \frac{1}{3} \sin^3 \theta + \cos \theta + \frac{1}{3} \cos \theta (\sin^3 \theta + 3) \right\}$$

$$+ \frac{1}{3} (K+L) \left\{ \frac{1}{3} \sin^3 \theta + \cos \theta + \frac{1}{3} \cos \theta (\sin^3 \theta + 3) \right\}$$

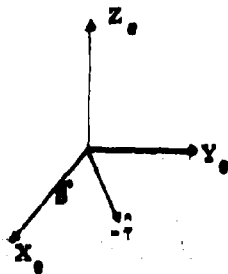
This solves the problem in the unprimed system. To solve it for the other five V-shaped areas, we must transform  $\hat{r}$  into the primed coordinate system

$$\begin{bmatrix} \hat{r}_1 \\ \hat{r}_2 \\ \hat{r}_3 \end{bmatrix} = M^T(t) \begin{bmatrix} \hat{r}_1' \\ \hat{r}_2' \\ \hat{r}_3' \end{bmatrix} \quad i = 1, 2, 3, 4, 5, 6$$

After finding  $\vec{T}'$ , the torque in the primed system, we transform it back to body coordinates

$$\vec{T}_B = M(t) \vec{T}'$$

The only remaining problem is to devise a means for determining  $\vec{T}_B$  as a function of time and body orientation. The negative of  $\hat{r}_1$ ,  $-\hat{r}_1$ , lies in the ecliptic at an angle,  $S$ , from the  $X_0$  axis



$S$  is a measure of the time of year.  $S = 0$  on the first day of spring. In the ecliptic frame,

$$\hat{r}_s = \begin{bmatrix} -\cos S \\ -\sin S \\ 0 \end{bmatrix}$$

Hence, in body coordinates,

$$\hat{r}_B = \begin{bmatrix} a_0 \\ b_0 \\ c_0 \end{bmatrix} = E(\psi, \theta, \phi) G^T(s) \hat{r}_s$$

In the computer simulations of flights, real time seldom exceeds two or three hours, and it will be assumed that  $S$  is a constant.

A computer subprogram was written to calculate solar pressure torque. The computer

program is called at each time step of the numerical integration of the equations of motion of the space craft, and the torque at that time and place is computed. It should be emphasized that the integrations of Eqs. (7) and (8) are not performed numerically but are evaluated analytically at each time step.

**Computer Simulation Results --** A simulation of one-half orbit was performed. A plot of the torque is shown in Fig. 13. The x- and y-components both exhibit cyclic variations. However the y-component is 20 times smaller than the x-component. The envelope of the x-component torque is essentially constant over the simulation time, indicating very little dependency on orbit position. The peak to peak of the x-component is symmetric about zero, but Fig. 13 does not show this due to sampling points being 4.8 seconds apart. Fig. 14 shows the cyclic variation clearly. The magnitude of the torque is essentially constant over the simulation period at  $2.75 \times 10^{-5}$  ft-lb.

The deviations in attitude relative to the untorqued vehicle exhibit only slight variation at the spin frequency. Again, this suggests that terms in the torque expression that are cyclic may be deleted from the model. The torque causes a spinup of the vehicle which results in a deviation,  $\Delta\theta$ , of 100 arc seconds at 2700 seconds. The angles  $\theta$  and  $\psi$  deviate positively from the untorqued case and are +65 and +10 arc seconds, respectively, at 2700 seconds. These deviations appear linearly as a function with time, except for  $\Delta\theta$  which is increasing nonlinearly.



Fig. 13. Torque on Spacecraft Due to Solar Pressure

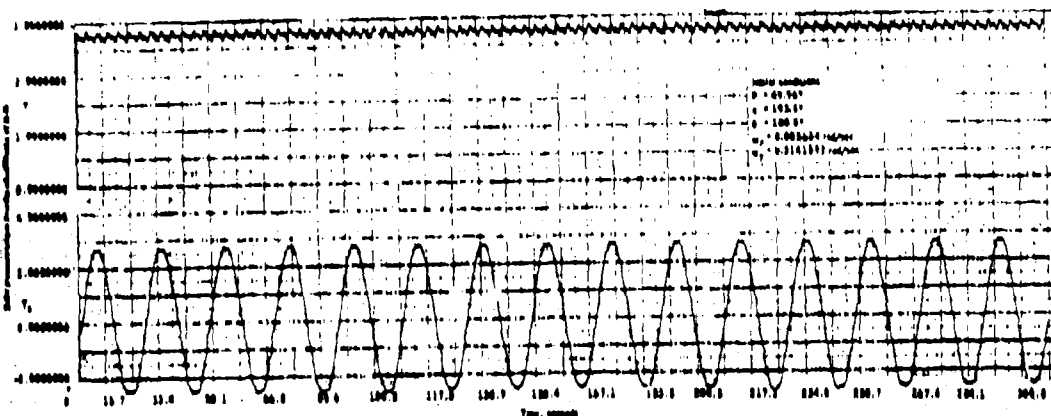


Fig. 14. Torque Resulting from Solar Pressure Effect on Spacecraft

The computer program of the solar pressure torque was found to be very slow in execution. This slowness of execution is due to evaluation over the spacecraft cylinder to account for the shadowing, and is required at each integration step. Three approaches to remedy the execution time were considered: (1) remove the effect of cylinder torque and consider only torque due to solar pressure; (2) compute and store torque due to spacecraft shadowing for one or two spin periods; and (3) compute torque due to solar panels normally and add cylinder torque based on the store of torque data for all subsequent scans.

Approach 1 was tried unsuccessfully; Approach 2 was successful.

Comparing the results, the attitude difference for the modified solar pressure torque at 2700 seconds is

$$\begin{aligned}\Delta\theta &= +87.2 \text{ arc sec} \\ \Delta\phi &= +74.0 \text{ arc sec} \\ \Delta\psi &= +10.0 \text{ arc sec with a 1.25 arc sec} \\ &\quad \text{variation}\end{aligned}$$

and the correct model gives

$$\begin{aligned}\Delta\theta &= +100 \text{ seconds of arc} \\ \Delta\phi &= +87.5 \text{ arc sec} \\ \Delta\psi &= +9.0 \text{ arc sec with a 1.25 arc sec} \\ &\quad \text{variation at the spin frequency}\end{aligned}$$

Based on these results, the modified solar pressure is sufficiently accurate for simulation periods of 1/2 orbit, and was used in subsequent analysis.

#### Gravity Gradient

Equations. -- The equations for the gravity gradient are expressed in a body-fixed axis

system (principal body axes).

The torque on a rigid body due to the gravity gradient is

$$\bar{T}_G = \frac{3\mu}{R^3} \hat{r} \times \hat{I} \cdot \hat{r} \quad (21)$$

assuming that the earth is spherical.

Further,

- $\mu$  = Earth's gravitational constant  
=  $1.4082 \times 10^{16} \text{ ft}^3/\text{sec}^2$
- $\hat{r}$  = Unit vector in direction of earth's radius vector
- $R$  = Distance from earth's center to body's center of mass
- $\hat{I}$  = Moment of inertia dyadic of the body

In body coordinates the equations are

$$\begin{bmatrix} T_{Gx} \\ T_{Gy} \\ T_{Gz} \end{bmatrix} = \frac{3\mu}{R^3} \begin{bmatrix} (I_x - I_y) r_{By} r_{Bx} \\ (I_x - I_z) r_{Bz} r_{Bx} \\ (I_y - I_z) r_{Bz} r_{By} \end{bmatrix} \quad (22)$$

where  $r_{Bx}$ ,  $r_{By}$ , and  $r_{Bz}$  are the direction cosines of the unit vector from the earth's center of mass.

Computer Simulation Results. -- A complete orbit simulation was conducted; Fig. 15 is a plot of the torque. For symmetric spacecraft as we have chosen here, the y-component of torque is zero. The  $T_x$  and  $T_z$  torque components are cyclic and are the same except they are 90 degrees out of phase. Two zero torque points occur because the spacecraft principal moment of inertia is normal to the orbit plane twice per orbit. The

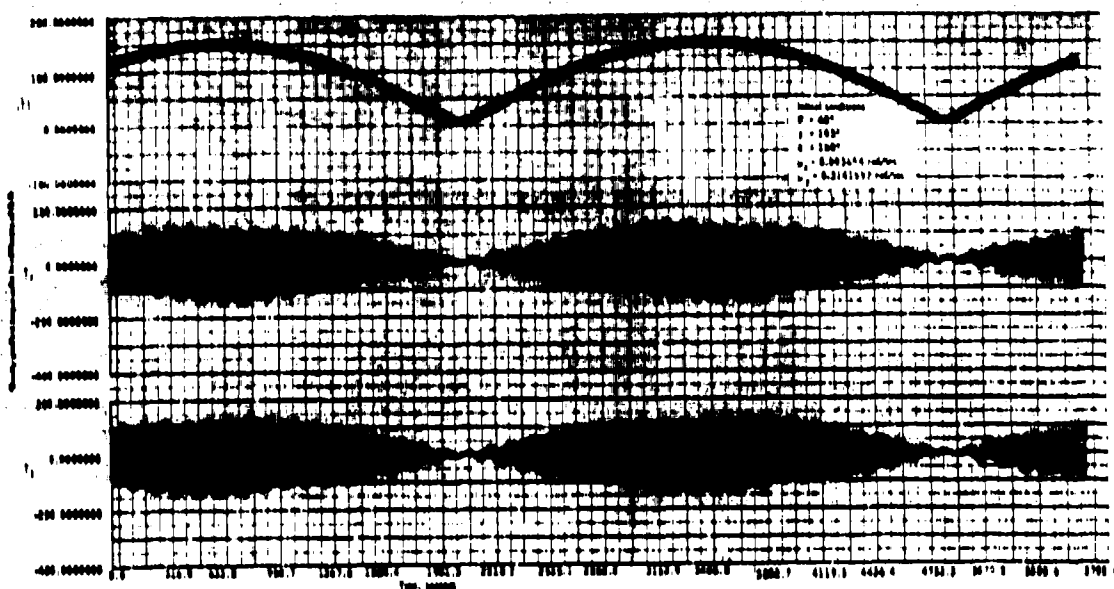


Fig. 18. Torque on Spacecraft Due to Gravity Gradient

magnitude of the torque is  $175 \times 10^{-6}$  ft-lb, which is about two orders of magnitude higher than the other five torques.

The attitude deviation due to this torque does possess variation at the spin frequency but has only a peak-to-peak variation of 2.5 arc seconds in  $\Delta\theta$  at 3500 seconds and is growing with time. For the attitude accuracy of 14 arc seconds, the torque terms that create the attitude variation at the spin frequency may be eliminated. The torque does cause a negative deviation in attitude, and at 3500 seconds the deviations in  $\theta$ ,  $\phi$ , and  $\psi$  are -17, -89, -82 arc seconds, respectively. The torque affects precession of the spacecraft,  $\phi$  and  $\psi$ , more than spin decay,  $\theta$ . Even for the relatively large value of the torque magnitude, the deviation in attitude is not correspondingly larger than the deviation due to the other torque. This is due to the attenuation of cyclic torque at spin frequencies.

#### Aerodynamic Torque

Equations -- The torque produced consists of aerodynamic pressure torque due to the spacecraft's center of mass velocity and a dissipative torque due to the spacecraft's angular rate. The torque equation including these two effects is taken from Beletskii's work (Ref. 1). The torque equation is valid when the spacecraft's angular velocity is large compared with the rotation of the atmosphere (earth's rate approximately); the linear surface velocities due to the spin of the satellite is small compared with the spacecraft's center of mass velocity; and the angle of attack of each surface encountered is less than  $\pi/8$ .

The torque equation is then given by

$$\begin{aligned} \vec{T} = & \frac{1}{2} c_{p_s} V_0^2 \int (\vec{n} \cdot \vec{e}_v) (\vec{e}_v \times \vec{r}_s) dS \\ & S(\vec{n} \cdot \vec{e}_v > 0) \\ & + \frac{1}{2} c_{p_s} V_0 \int \left[ (\vec{n} \cdot [\vec{\omega} \times \vec{r}_s]) (\vec{e}_c \times \vec{r}_s) \right. \\ & \left. + (\vec{n} \cdot \vec{\omega}) [\vec{\omega} \times \vec{r}_s] \times \vec{r}_s \right] dS \\ & S(\vec{n} \cdot \vec{e}_c > 0) \end{aligned} \quad (23)$$

where

$\vec{n}$  = unit vector in direction of normal to surface,  $dS$ .

$\vec{e}_v = \vec{V}_0 / |\vec{V}_0|$  = unit vector in direction of translational velocity of center of mass relative to incident stream

$\vec{r}_s$  = radius vector joining surface element center and spacecraft center of mass

The first term of Eq. (23) represents torque due to misalignment of spacecraft center of mass and center of pressures. The second term represents dissipative torque due to spacecraft spin. Upon examining the coefficient of each term, the torque due to center of pressure misalignment is approximately a factor of  $V_0$  larger than the dissipative torque coefficient when  $\omega r \ll V_0$ . For a 500 km-altitude orbit,  $V_0$  is  $2.524 \times 10^4$  ft/sec.

Previous investigations estimated that  $1/2 c_p V_0^2$  is  $2 \times 10^{-7}$  lb/ft<sup>2</sup>. Then, dividing by  $V_0$ , we get  $0.76 \times 10^{-11}$  lb/ft<sup>3</sup>.

Dissipative torque is a factor of  $10^{-4}$  less than pressure torque and is sufficiently small so that the second term of Eq. (23) will be neglected. Then, the aerodynamic torque equation is given by

$$\vec{T} = \frac{1}{2} c_p V_0^2 \int (\vec{n} \cdot \vec{e}_v) (\vec{e}_v \times \vec{r}_s) dS \quad (24)$$

$$S(\vec{n} \cdot \vec{e}_v > 0)$$

The domain of integration is indicated by  $S(\vec{n} \cdot \vec{e}_v > 0)$ . This means the angle of attack of each surface element is less than  $\pi/2$ . The ARPS spacecraft surfaces consist of a hexagonal cylinder and rectangular solar panels.

The direction of the stream is in the orbit plane, and for this reason the spacecraft will present a different surface to the stream, depending on the attitude of the vehicle.

Fig. 18 illustrates two orientations of the spacecraft that give two different domains for Eq. (24).

The aerodynamic torque will be represented by two equations because of the different surfaces presented to the stream as shown in Fig. 18. In Fig. 18b, the force along the y-axis due to the stream is positive. Fig. 18a illustrates that the force along the y-axis is negative.

**Derivation of Torque for  $F_y \geq 0$ :** The computation can be done on each surface and summed over the domain of integration. The spacecraft has two basically different geometries -- a hexagonal cylinder and solar panels. The hexagonal cylinder is comprised of six planes as shown in Fig. 17. The body coordinates are also shown in Fig. 17.

Torque on the cylinder is computed by integrating over each of the surfaces ( $i=1, \dots, 6$ ) and using only those torques on the surfaces which satisfy  $\vec{n}_i \cdot \vec{e}_v > 0$ .

Torque due to the solar panels is computed assuming that the solar panels can be approximated by a disk as shown in Fig. 18.

The torque equation for the disk when  $F_y \geq 0$  is given by

$$\vec{T} = \frac{1}{2} c_p V_0^2 \int (\vec{n} \cdot \vec{e}_v) (\vec{e}_v \times \vec{r}_s) dS$$

$$S(\vec{n} \cdot \vec{e}_v > 0)$$

The integration will be performed over the shaded area of Fig. 18, and the results subtracted from the integrated result over the entire disk defined between  $r_3$  and  $r_4$ .

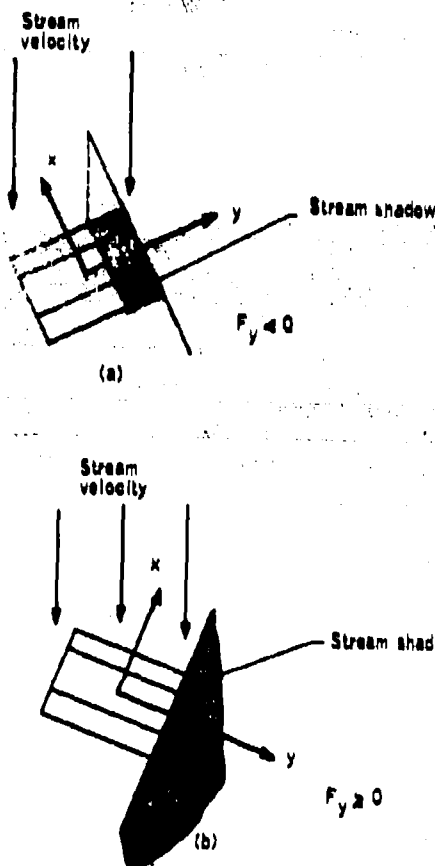


Fig. 18. Spacecraft Shadowing

The end of the cylinder contributes a torque when

$$\hat{e}_v \cdot (-\hat{j}) > 0.$$

**Derivation of Torque for  $c_{p,i} > 0$  or  $F_y \leq 0$ :** Torque due to aerodynamic pressure is different (Fig. 18a). The solar panels are not shadowed, but the cylinder is as shown in Fig. 18. The shadow, however, on the cylinder will be limited due to the attitude control limits.

The shadow on the cylinder will affect the limits of integration for the torque due to the cylinder.

In the derivation of the torque for the solar panels, we again assume a solid disk as before.

The torque on the cylinder for  $\vec{e}_v \cdot \hat{j} > 0$  is derived the same as for  $\vec{e}_v \cdot \hat{j} \leq 0$ . Only the limit of integration for  $L_2$  is changed.

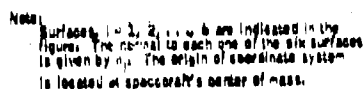


Diagram illustrating the center of mass and the shaded portion of the keel area. The diagram shows a cross-section of a ship's hull with a vertical centerline. The center of mass is labeled "CENTER OF MASS". The shaded portion of the keel area is labeled "SHADEN PORTION OF KEEL AREA". The diagram also shows the "CENTER OF GRAVITY" and the "CENTER OF BUOYANCY".

The limit of integration for  $L_2$  is a function of the spacecraft attitude relative to the stream. The new limit of integration is given by  $L_2'$ .

The torque due to the disk for  $\bar{u}_y, \hat{j} > 0$  is given by integrating over the disk of radius  $r_4$ .

Summarizing the equations for the torque, one has

$$T_0 = \begin{cases} q_1 \cdot \bar{u}_0 \cdot \left[ \sum_{i=1}^n (R_i \cdot P_i) \cdot \bar{v}_i \cdot (R' \cdot P_i) \cdot (\bar{v} + \bar{v}_0) \right] & (0 \leq P_i \leq 1, 0 \leq \bar{v} \leq 1, 0 \\ (R_1 \cdot \bar{u}_0 \geq 0) & \\ q_2 \cdot \bar{u}_0 \cdot \left[ \sum_{i=1}^n (R_i \cdot P_i) \cdot \bar{v}_i \cdot (R' \cdot P_i) \cdot \bar{v} \right] & (0 \leq P_i \leq 1, 0 \leq \bar{v} \leq 1, 0 \\ (R_1 \cdot \bar{u}_0 \geq 0) & \end{cases}$$

where

[illegible]

where

1978 1979  
 1980 1981

$v_x$ ,  $v_y$ , and  $v_z$  are the components of the  $\vec{v}$  vector in body axes and the symbol

$$\sum_{i=1}^n (R_i + \bar{R}_i \geq 0)$$

means sum over the surfaces whose angle of attack is positive.

The torque equation derived above is not an exact representation of the vehicle's aerodynamic torque. Frictional or dissipative torques were neglected.

In the derivation of pressure torque, the solar panels were assumed to be a solid disk, where in actuality, six rectangular panels are the solar panels (see Fig. 20).

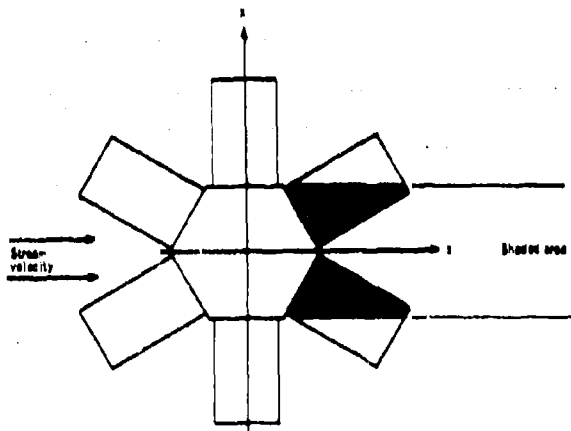


Fig. 20. Solar Panel Configuration

The torque due to the solar panels in reality is varying with a frequency six times the spin rates as opposed to the result obtained in this analysis. The result derived in this analysis is varying relative to the body axis only, but not the magnitude of the torque. In Fig. 20, the shaded area covers only part of the two solar panels, and as the spacecraft rotates, varying amounts of solar panel area are shaded. It is for this reason the magnitude of the solar panel torques is varying approximately six times the spin rate. The disk-shaped panels give a larger magnitude of torque but remain constant in absolute value.

**Computer Simulation Results** -- A simulation of one full orbit was made and the torque is shown in Fig. 21. The magnitude of the torque varies with position in orbit ranging in value from zero to  $3.0 \times 10^{-8}$  ft-lb. The x-component is cyclic at the spin frequency and possesses two nulls over one orbit. The null point occurs when the angle of attack is zero. Because spacecraft is spin stabilized, the angle of attack will become zero twice. The y-component of torque is zero.

The deviation of the attitude due to this torque is bounded over one orbit. The deviation of  $\Delta\theta$  reaches -5 arc seconds at 1200 seconds and remains constant to 2200 seconds, and the deviation then reaches +2.0 arc seconds at 3900 seconds. The attitude angles are bounded within +10 and -20 arc seconds for  $\psi$  and within +25 and +5 arc seconds for  $\theta$ . The aerodynamic torque indicates greater effect on the precession of the angular momentum vector than in the spin decay. The cyclic variation at the spin frequency is at most 2.5 arc seconds peak to peak. This suggests that cyclic terms of the torque model can be dropped.

### TORQUE MODEL LINEARITY EFFECT

For purposes of simplifying the vehicle model used in an attitude estimation algorithm, prediction times for various combinations of torque must be determined. A linearity analysis was conducted to show that the effect of each of the five torques can be summed to give the same effect as the combined five torques.

The analysis consisted of computing the attitude deviation due to the individual torques relative to an untorqued spacecraft, computing the attitude deviation due to the combined torques relative to an untorqued spacecraft, and summing the individual attitude deviations to compare with the combined attitude deviation. The initial conditions used for the analysis:

$$\begin{aligned} \Omega &= 0.78 \text{ rad} \\ i &= 1.70 \text{ rad} \\ \nu &= 3.2690 \text{ rad} \\ \psi &= 0.87 \text{ rad} \\ \theta &= 3.14 \text{ rad} \\ \varphi &= 3.27 \text{ rad} \\ I_x = I_z &= 56.68 \text{ slug-ft}^2 \\ I_y &= 65.62 \text{ slug-ft}^2 \\ \omega_x &= 0.008674 \text{ rad/sec} \\ \omega_y &= 0.314159 \text{ rad/sec} = 3 \text{ rpm} \\ P_1 &= 0.20734 \times 10^{-5} \frac{\text{ft-lb-sec}}{\text{G}} \\ P_2 &= 0.72022 \times 10^{-4} \frac{\text{ft-lb-sec}}{\text{G}} \\ P_3 &= -0.82263 \times 10^{-5} \frac{\text{ft-lb-sec}}{\text{G}} \\ M_x = M_y = M_z &= 5.17085 \times 10^{-6} \frac{\text{ft-lb-sec}}{\text{G}} \end{aligned}$$

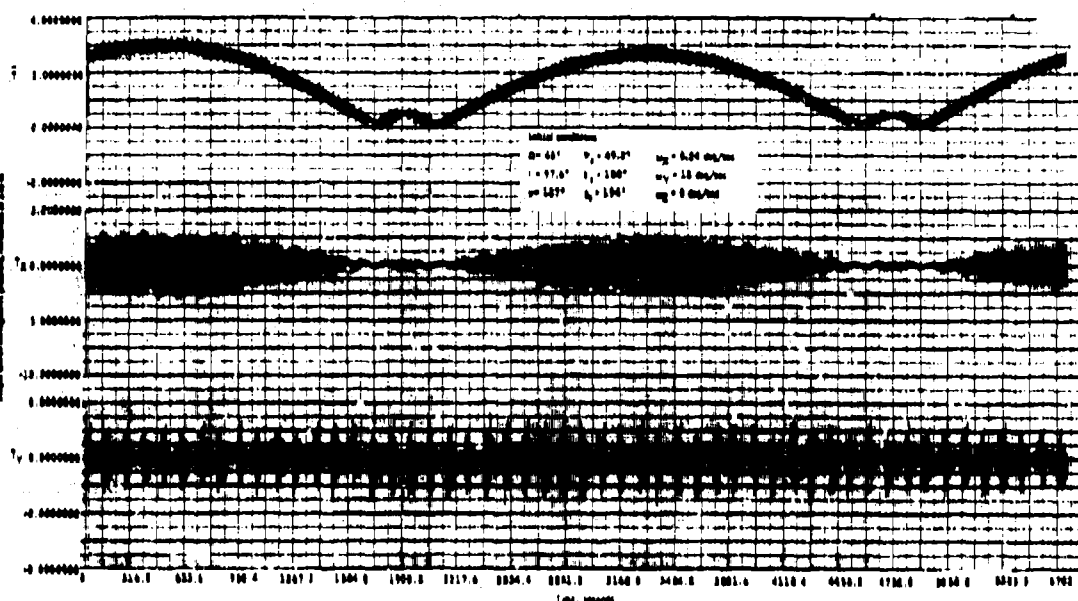


Fig. 21. Torque on a Spacecraft Due to Aerodynamic Pressure, One-Orbit Simulation

Solar pressure constant =  $1 \times 10^{-7}$   $\frac{\text{lb}_f}{\text{ft}^2}$

Aerodynamic pressure constant =  $2 \times 10^{-7}$   $\frac{\text{lb}_f}{\text{ft}^2}$

The difference,  $\Delta(\Delta\theta)$ , is approximately 0.5 arc sec after 45 minutes of orbit. This number could very well be attributed to roundoff (10th and 11th decimal place). The difference in  $\Delta(\Delta\theta)$  is at worst 0.15 arc second over 45 minutes, and  $\Delta(\Delta\psi)$  is at worst 0.5 arc second. The results demonstrate the linearity effect of the torques on the spacecraft attitude. The result allows one to quickly determine the prediction time allowed to meet the specified 14-arc second accuracy in attitude.

#### COMPARISON OF THE TORQUE EFFECTS ON ATTITUDE

Tables 2 and 3 list each torque and show the effect on spin decay ( $\Delta\theta$ ) and precession ( $\Delta\psi$ ) over 45 minute simulation. The residual magnetic moment and eddy currents cause the greatest spin decay. Solar pressure creates a spin-up which reduces the total spin decay. Table 3 shows that gravity gradient and solar pressure cause the greatest effect on precession ( $\Delta\psi$ ).

#### ATTITUDE PREDICTION TIME

The prediction time is the time elapsed when the vehicle model attitude propagation for different combinations of torque differs from the five-torque attitude propagation by 14 arc sec. Tables 4 and 5

list attitude deviation for various combinations of torque relative to the untorqued case. The last column in each table is the deviation due to the five torques. The deviations in the other columns are compared to the last for determination of the prediction time. Tables 4 and 5 show that the prediction time is less than 5 minutes when only the residual magnetic moment and eddy current models are included.

Table 2. Summary of  $\Delta\theta$  Attitude Deviation Due to Each Torque and the Total Torque

Time (min)	Residual Magnetic Moment $\Delta\theta$ arc sec	Eddy Currents $\Delta\theta$ arc sec	Gravity Gradient $\Delta\theta$ arc sec	Solar Pressure $\Delta\theta$ arc sec	Other $\Delta\theta$ arc sec	Total $\Delta\theta$ arc sec
5	-3.7	-30.3	-0.44	+0.02	-0.01	-34.4
10	-10.8	-58.7	-0.7	+0.04	-0.02	-69.8
15	-18.0	-87.1	-1.0	+0.06	-0.03	-105.2
20	-25.2	-115.4	-1.3	+0.08	-0.04	-140.6
25	-32.4	-143.8	-1.6	+0.10	-0.05	-176.0
30	-39.6	-172.2	-1.9	+0.12	-0.06	-211.4
35	-46.8	-200.6	-2.2	+0.14	-0.07	-246.8
40	-54.0	-229.0	-2.5	+0.16	-0.08	-282.2
45	-61.2	-257.4	-2.8	+0.18	-0.09	-317.6
50	-68.4	-285.8	-3.1	+0.20	-0.10	-353.0

By adding solar pressure torque to the model, the prediction time can be at least 10 minutes, based on the five torque model total environment.



Table 3. Summary of  $\Delta\theta$  Attitude Deviation Due to Each Torque and the Total Torque

(1) Time (min)	(2) Residual Magnetic Moment (10 <sup>-3</sup> arc sec)	(3) Eddy Current (10 <sup>-3</sup> arc sec)	(4) Gravity Gradient (10 <sup>-3</sup> arc sec)	(5) Aerodynamic Pressure (10 <sup>-3</sup> arc sec)	(6) Solar Pressure (10 <sup>-3</sup> arc sec)	(7) Total (10 <sup>-3</sup> arc sec)
5	8.8	0.7	1.0	0.4	8.9	18.0
10	8.4	0.6	11.9	1.1	16.8	37.0
15	14.3	0.1	13.0	8.8	36.4	64.6
20	16.8	0.1	16.4	8.7	38.8	80.9
25	18.8	0.1	19.0	10.3	48.8	98.0
30	18.4	0.1	18.0	14.8	48.8	98.2
35	7.8	0.1	18.8	18.0	37.4	84.6
40	4.8	0.1	21.3	14.7	46.7	108.8
45	0.7	0.1	22.1	18.4	72.8	114.7

### CONCLUSIONS

#### Derivation of Models

The effects of five environmental disturbances on the spacecraft have been determined for the given spacecraft mission. The torques due to the eddy currents, solar pressure, and aerodynamic pressure depend on the spacecraft configuration and were derived for the specific spacecraft configuration. The torque due to eddy currents was derived only for the spacecraft skin because of lack of definition of components and packages in the spacecraft. And in general, a closed-form solution for the eddy currents is feasible only for a few special cases. It is concluded that an exact model for the entire source is not feasible. The torques due to solar pressure and aerodynamic pressure were derived in closed form, but due to time-varying shadows in the spacecraft, the closed-form equations are very complex. The solar pressure torque model program executed four times slower than the other models because the shadowing was varying and required additional numerical computation at each integration step. Consequently, a modified version of the model was used which proved to be accurate over a half orbit.

#### Effect on Attitude

The torques due to eddy currents and the residual magnetic moments were found to have the greatest spin decay effect. The gravity gradient torque had the greatest effect on the precession ( $\phi$  and  $\psi$ ), i.e., angular momentum precession. The solar pressure created a spin-up and is third in its absolute effect on spin. And the aerodynamic torque had the least effect on the spacecraft attitude. The five torques were incorporated into a vehicle model that was used in a simulation of the true attitude determination sensor output, Ref. (10). For 5 minutes propagation time between stellar observations, the torques due to the residual magnetic moments and the eddy current are adequate for use in the attitude estimation algorithm, Ref. (10).

By adding the solar pressure to the algorithm model, the spin decay over 45 minutes is well within the accuracy of 14 arc seconds. However, the precession error limits the prediction time to

Table 4. Comparison of the Effect of Different Combinations of Torque with the Total Torque Effect

Time, min	Sum, (1)+(2), $\Delta\theta$ arc sec	Sum, (1)+(2)+(3), $\Delta\theta$ arc sec	Sum, (1)+(2)+(3)+(4)+(5), $\Delta\theta$ arc sec
5	- 28.5	- 24.9	- 24.9
10	- 109.8	- 102.9	- 102.0
15	- 284.1	- 269.9	- 268.8
20	- 388.1	- 361.7	- 360.8
25	-1028.7	- 989.1	- 988.2
30	-1569.9	-1508.8	-1508.1
35	-2176.9	-2102.8	-2101.8
40	-2890.1	-2788.2	-2780.7
45	-3616.8	-3298.9	-3294.4

(1)+(2) = Attitude deviation due to residual magnetic moment and eddy current torques

(1)+(2)+(3) = Attitude deviation due to residual magnetic moment, eddy current, and solar pressure torques

(1)+(2)+(3)+(4)+(5) = Attitude deviation due to the five torques

Table 5. Comparison of the Effect of Different Combinations of Torque on Precession ( $\phi$ )

Time (min)	Sum (1)+(2) (arc sec)	Sum (1)+(2)+(3) (arc sec)	Sum (1)+(2)+(3)+(4) (arc sec)	Sum (1)+(2)+(3)+(4)+(5) (arc sec)
5	8.8	10.8	8.6	18.0
10	8.4	24.7	19.1	37.0
15	14.3	40.7	36.4	64.6
20	16.8	48.8	37.7	80.9

(1)+(2) = Attitude deviation due to residual magnetic moment and eddy current.

(1)+(2)+(3) = Attitude deviation due to residual magnetic moment, eddy current, and solar pressure.

(1)+(2)+(3) = Attitude deviation due to residual magnetic moment, eddy current, and gravity gradient.

(1)+(2)+(3)+(4)+(5) = Attitude deviation due to all five torques.

about 10 minutes using only the magnetic and solar pressure torques.

#### Simplification of Model

The "Hat" eddy current model was found to have nearly the same effect on attitude as the spherical model. Therefore, the spherical model is adequate for the estimation algorithm. The advantage is that it has one coefficient. This reduces the number of parameters to be estimated and naturally speeds execution of the algorithm, which is important when one year of data must be processed. Purely cyclic terms in all of the torques may be removed without loss of state propagation accuracy yet gain speed in program execution. This was shown by E. C. Foudriat, Ref. (11). Due to the slow execution time for the solar pressure torque, it was modified to compute the torque due to the time-varying shadows over one spin cycle and interpolated for the entire orbit. The modified model was used in subsequent simulation, Ref. (10).

## APPENDIX A VEHICLE MODEL

The equations of motion used to analyze the effect of the torques are:

$$\dot{\omega}_x = [\omega_y \omega_z (1-C) + \tau_x] / A$$

$$\dot{\omega}_y = \omega_x \omega_z (C-A) + \tau_y$$

$$\dot{\omega}_z = [\omega_x \omega_y (A-1) + \tau_z] / C$$

$$\dot{\alpha}_1 = \frac{1}{2} (-\omega_z \alpha_2 + \omega_y \gamma_1 - \omega_x \gamma_2)$$

$$\dot{\alpha}_2 = \frac{1}{2} (\omega_z \alpha_1 + \omega_x \gamma_1 + \omega_y \gamma_2)$$

$$\dot{\gamma}_1 = \frac{1}{2} (-\omega_y \alpha_1 - \omega_x \alpha_2 + \omega_z \gamma_2)$$

$$\dot{\gamma}_2 = \frac{1}{2} (\omega_x \alpha_1 - \omega_y \alpha_2 - \omega_z \gamma_1)$$

where

$$A = \frac{I_x}{I_y} = \text{inertia ratio}$$

$$C = I_z / I_y = \text{inertia ratio}$$

$$\begin{Bmatrix} \tau_x \\ \tau_y \\ \tau_z \end{Bmatrix} = \begin{cases} \text{torques divided by } I_y \end{cases}$$

$$\begin{Bmatrix} \omega_x \\ \omega_y \\ \omega_z \end{Bmatrix} = \text{body ratios}$$

$$\begin{Bmatrix} \alpha_1 \\ \alpha_2 \\ \gamma_1 \\ \gamma_2 \end{Bmatrix} = \text{Euler symmetric parameters}$$

The two major coordinate systems used in this program are the inertial coordinate frame and the body-fixed coordinate frame. The inertial coordinate frame has its origin at the center of the earth with the  $X_I$  axis directed to the vernal equinox, and the  $Z_I$  axis along the earth polar axis. The body frame has its origin at the center of mass, and the axes defined by the principal moment-of-inertia axes. The Euler angle rotations from the inertial to the

body frame are

$\psi$  about the  $Z_I$  axis

$\phi$  about the first displaced X axis

$\theta$  about the second displaced Y axis

The transformation equation is given in Appendix B.

The equations of motion are written in terms of Euler symmetric parameter. Conversion between Euler angles and the symmetric parameter by equating the transformation matrix  $E(\psi, \phi, \theta)$  to  $E(\alpha, \alpha_2, \gamma_1, \gamma_2)$ .

The equations of motion were programmed to compute body rates and spacecraft Euler angle attitude for the untorqued case and the specified torque case. The torque in body axes and the difference in Euler angle attitude was plotted.

## APPENDIX B COORDINATE SYSTEMS

### Ecliptic System ( $X_E, Y_E, Z_E$ )

An inertial coordinate system with origin at the center of the earth. The  $X_E$  and  $Y_E$  axes are in the ecliptic plane (the plane of the earth's orbit around the sun) with the X axis directed along the vernal equinox (that point of intersection of the ecliptic and celestial equator where the sun crosses the equator from south to north and its apparent annual motion along the ecliptic). The  $Z_E$  axis is normal to the ecliptic and directed along the north pole of the ecliptic.

### Equatorial System ( $X_I, Y_I, Z_I$ )

An inertial coordinate system with origin at the center of the earth. The  $X_I$  and  $Y_I$  axes are in the earth's equatorial plane with the  $X_I$  axis directed along the vernal equinox. The  $X_I$  and  $X_E$  axes coincide. The  $Z_I$  axis is directed parallel to the earth's polar axis towards the north celestial pole.

### Body Axes System ( $X_B, Y_B, Z_B$ )

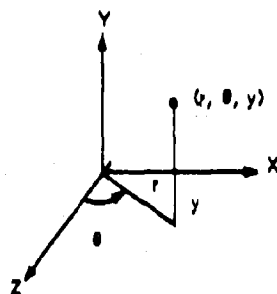
A rotating coordinate system fixed in the vehicle with origin at the vehicle center of mass. The  $X_B, Y_B, Z_B$  axes coincide with the principal axes of inertia with the  $Y_B$  axis directed along the nominal spin axis.

### The Unprimed System ( $x, y, z$ )

The coordinate system formed when the body axis system is translated without rotation a distance  $L_2$  ( $L_2 \neq 0$ ) along y-axis.

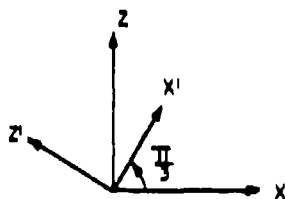
### The Cylindrical System (r, θ, y)

The coordinate system formed by letting r measure the radial distance in the x - z plane of the unprimed system, θ measure the rotation about the y-axis, and the y coordinate is the same as on the unprimed system. (See sketch below.)



### The Primed System (x', y', z')

The coordinate system formed when the unprimed system is rotated an integral multiple of π/3 about the y - axis. (See sketch below.)



### Coordinate Transformations

One rotation c defines the orthogonal transformation G(c) from the equatorial inertial system to the ecliptic inertial reference frame. This rotation is

c about the X<sub>1</sub> axis

where

c is the obliquity of the ecliptic. Its mean value in 1960 is 23° 26' 40.18". This is the angle between the ecliptic and the celestial equator. A vector  $\vec{X}_1$  in the equatorial frame is seen as the vector  $\vec{X}_2$  in the ecliptic frame where  $\vec{X}_2 = G(c) \vec{X}_1$ .

and

$$G(c) = \begin{bmatrix} 1 & 0 & 0 \\ 0 & cc & sc \\ 0 & -sc & cc \end{bmatrix} \quad (B1)$$

Successive rotations (ψ, φ, θ) define the orthogonal transformation E(ψ, φ, θ) from the equatorial inertial reference frame to the body axes reference frame. The rotations are:

ψ about the Z<sub>1</sub> axis

φ about the first displaced X axis

θ about the second displaced Y axis

A vector  $\vec{X}_1$  in equatorial inertial coordinates is seen in body coordinates as  $\vec{X}_B$ .

where

$$\vec{X}_B = E(\psi, \phi, \theta) \vec{X}_1$$

$$E(\psi, \phi, \theta) = \begin{bmatrix} c\theta c\psi - s\psi s\phi s\theta & s\psi c\theta + c\psi s\phi s\theta & s\theta c\psi \\ -s\psi c\phi & c\psi c\phi & s\phi \\ s\theta c\psi + s\psi s\phi c\theta & s\theta s\psi - c\psi s\phi c\theta & c\theta c\psi \end{bmatrix} \quad (B2)$$

One translation defines the transformation from body axes to unprimed axes:

$$\begin{bmatrix} x_B \\ y_B \\ z_B \end{bmatrix} = \begin{bmatrix} x \\ y + L_2 \\ z \end{bmatrix} \quad (B3)$$

The transformation from cylindrical coordinates to unprimed coordinates is described by the following set of equations:

$$\begin{aligned} x &= r \sin \theta \\ y &= y \\ z &= r \cos \theta \end{aligned} \quad (B4)$$

A rotation of (i - 1)  $\frac{\pi}{3}$ , i = 1, 2, ..., 6, defines the orthogonal transformation M(i) from the primed to the unprimed system.

Here,

$$M(i) = \begin{bmatrix} \cos \frac{\pi}{3} (i - 1) & 0 & \sin \frac{\pi}{3} (i - 1) \\ 0 & 1 & 0 \\ -\sin \frac{\pi}{3} (i - 1) & 0 & \cos \frac{\pi}{3} (i - 1) \end{bmatrix} \quad (B5)$$

and

$$\vec{X} = M(i) \vec{X}' \quad (B6)$$

### REFERENCES

1. Beletskii, V. V., Motion of an Artificial Satellite About Its Center of Mass, NASA TT F-429, 1966.

2. Tidwell, N. W., et al. Conceptual Mechanization Studies for a Horizon Definition Spacecraft Attitude Control Subsystem, NASA CR-66382, May 1967.
3. Vinti, John P., Theory of the Spin of a Conducting Satellite in the Magnetic Field of the Earth, Report No. 1020, Ballistic Research Labs, Aberdeen Proving Ground, Md., July 1957.
4. Smith, Louis G., A Theoretical Study of the Torques Induced by a Magnetic Field on Rotating Cylinders and Spinning Thin-Wall Cones, Cone Frustums, and General Body of Revolution, NASA TR-R-129, 1962.
5. Petrovsky, I. G., Lectures on Partial Differential Equations, Interscience Publishers, 1954, pp. 192-196.
6. "The Radiation Environment," Fourth Weather Group, United States Air Force, 4WGF-80-6-1, 1 June 1965.
7. "The Solar System," Vol. 1: "The Sun," edited by G. P. Kuiper, University of Chicago Press, 1953.
8. "The Physics of Solar Flares," AAS-NASA Symposium, NASA SP-50, Goddard Space Flight Center, 1963.
9. Dandanell, E. A., Solar Torque Model, Honeywell internal memo, dated March 1, 1968, To: D.D. James.
10. Nelson, G. D., and Arneson, G. R., The Development and Performance of an Attitude Determination Data Reduction and Analysis System, Aerospace Corporation Attitude Determination Symposium, September 30, October 1 and 2, 1969.
11. Foudriat, E. C., the Limit Memory Attitude Determination System Using Simplified Equation of Motion. Paper presented at Aerospace Corporation Attitude Determination Symposium, September 30, October 1 and 2, 1969.

A LEAST-SQUARES ATTITUDE DETERMINATION ALGORITHM UTILIZING  
STARMAPPER AND SUN SENSOR TIME PULSES<sup>1</sup>

D. K. Scharnack  
Systems and Research Center  
Honeywell Inc.  
St. Paul, Minnesota

ABSTRACT

This paper describes a feasibility study of an attitude determination scheme for the Horizon Definition Measurement Program (HDMP) satellites.

On-board instrumentation for attitude determination included a starmapper and sun sensor instrument package. The instrument outputs are time pulses, which occur whenever a star (or the sun) enters an instrument field of view. A sequence of such pulses can be interpreted as rotary motion only through integration of the model equations.

The solution of the model differential equations can be expressed as a function of the initial conditions, the model parameters, and time. The problem, then, becomes one of finding those initial conditions and parameters that best explain the observed star and sun sighting time pulses.

The method of least squares was chosen to solve this problem. It is shown that the method produces an accurate attitude estimate from noisy starmapper time pulses, even though the model equations are quite different from reality. It is also shown that with a properly designed sun sensor it is possible to determine all initial conditions and parameters except for one of the initial attitude angles. These facts determine an attitude determination algorithm that is suitable for estimating the attitude of the HDMP satellites.

INTRODUCTION

This paper describes a feasibility study of an attitude determination scheme for the Horizon Definition Measurement Program (HDMP) satellite (Ref. 1).

The HDMP satellite was conceived to be a spin-stabilized wheel configuration with the angular momentum vector nominally along the spacecraft axis of symmetry. On-board instru-

mentation for attitude determination included a starmapper and sun sensor instrument package.

The basic method for determining the attitude of a rotating vehicle from starmapper time pulses is described by Grosch in Ref. 2. He was the first to display an equation (his constraint equation) that must be true at star sighting instants. His problem was that of estimating the attitude of a spinning, rigid, torque-free, symmetric body. He was able to

<sup>1</sup>This work was done under NASA Contract No. NAS 1-6010, May, 1967.

do this with the known analytic solution for the vehicle motion, the star sighting time pulses from the starmapper, and the constraint equation. His results are extended here to the case of a spinning, rigid body under the influence of torques. A method for utilizing sun sensor time pulses is also developed.

The model differential equations for satellite rotary motion are of great importance in determining attitude with the assumed instrument package. The instrument outputs are time pulses, which occur whenever a star (or the sun) enters an instrument field of view. Assuming solution of the star-pulse matching problem, a sequence of such pulses can be interpreted as rotary motion only through integration of the model equations. The better these approximate reality, the better the time pulses can be interpreted as attitude. However, unpredictable torques, such as those produced by meteoroid impacts, produce uncertainties in the motion, so there is a limit to the accuracy of the knowledge of the motion. Moreover, the instrument time pulses themselves may be in error by random amounts, making it necessary to consider the statistics of the timing pulse error in the interpretation of the signal.

The chosen approach to the attitude determination problem is first to set up the model differential equations as accurately as possible, in order that the solution approximate, as closely as possible, the motion of the vehicle. The magnitudes of the torques in these equations are poorly known, since they depend on satellite characteristics that cannot be accurately determined before launch. Additionally, the vehicle moment of inertia ratios change slowly with time. The magnitudes and ratios can be assumed to be constant over reasonably long time intervals, and they are included as parameters to be determined. The solution of the differential equations can be expressed as a function of the initial attitude angles and angular velocities (the initial conditions), the model parameters, and time. The problem, then, becomes one of finding those initial conditions and parameters that best explain the observed star and sun sighting time pulses. The attitude estimate is recovered from integration of the differential equations with the determined set of initial conditions and parameters.

The method of least squares was chosen to solve this problem. This was a practical choice because the data reduction was to be done a posteriori on the ground. The function to be minimized is taken as the sum of the squares of the observation equation errors, where the observation equation is a relationship between the state variables that should equal zero at each observation instant. Thus, the mean error in the observation equation at each observation instant is minimized.

This paper details the development of the least squares data reduction algorithm and the results derived therefrom. It is shown, on the

basis of computer simulation results, that the method produces an accurate attitude estimate from noisy starmapper time pulses, even though the model equations are quite different from the assumed reality.

A most interesting part of the study is that of determining what parameters and initial conditions can be obtained from sun sensor data alone (viewing the sun as a fixed object in space). It is shown, on the basis of certain computer studies, that with a properly designed sun sensor it is possible to determine all initial conditions and parameters except for one of the initial attitude angles.

Finally, an attitude determination algorithm is described that uses starmapper observations during the dark part of the orbit and sun sensor pulses during the daylight part. This algorithm is suitable for estimating the attitude of the HEMP satellite.

### NOTATION

#### State Variables

$\omega_x, \omega_y, \omega_z$	Vehicle angular rates along principal body axes
$\psi, \phi, \theta$	Euler angles relating principal axes to inertial space
$t$	Time (independent variable)
$x$	State vector with components $(\omega_x, \omega_y, \omega_z, \psi, \phi, \theta)$

Subscript (o) on state variables indicates initial conditions, usually taken at  $t_o = 0$ .

#### Model Parameters

$I_1, I_2, I_3$	Vehicle moments of inertia along principal x, y, and z axes, respectively
$A, C$	Moment of inertia ratios, taken as $I_1$ and $I_3$ , respectively, divided by $I_2$
$M_x, M_y, M_z$	Vehicle magnetic moment coefficients with respect to principal coordinates
$M'_x, M'_y, M'_z$	Magnetic moment coefficients divided by $I_2$
$K$	Vehicle magnetic eddy current coefficient
$K'$	Magnetic eddy current coefficient divided by $I_2$
$\epsilon_1, \epsilon_2, \epsilon_3$	Vehicle offset angles relating experimental axes to principal coordinates

- $\epsilon$  The vector  $(\epsilon_1, \epsilon_2, \epsilon_3)$
- $a$  Parameter vector with components  $(A, C, M'_x, M'_y, M'_z, K')$
- $y$  Complete parameter vector with components  $(x_0, a, \epsilon)$

#### Orbit Parameters

- $\Omega$  Longitude of the ascending node
- $i$  Inclination
- $v$  True anomaly

#### Star Parameters

- $\alpha$  Right ascension of a given star with respect to inertial space
- $\delta$  Declination of a given star with respect to inertial space

#### Coordinate Frames and Vectors

- $i_I, j_I, k_I$  Unit vectors in the inertial  $x, y,$  and  $z$  directions, respectively.  $i_I$  points toward the first point of Aries,  $k_I$  points toward the north pole, and  $j_I$  completes the right-handed triad.
- $i_0, j_0, k_0$  Unit vectors defining the orbit coordinate frame.  $i_0$  points toward the vehicle from the center of the earth and  $k_0$  is normal to the orbit plane.  $j_0$  completes the right-handed triad.
- $i_B, j_B, k_B$  Unit vectors along the body principal  $x, y,$  and  $z$  coordinate axes, respectively.
- $i_X, j_X, k_X$  Unit vectors along the instrument or experimental  $x, y,$  and  $z$  coordinate axes, respectively.
- $i_S, j_S, k_S$  Unit vectors along the slit frame  $x, y,$  and  $z$  coordinate axes, respectively.
- $i_m, j_m, k_m$  Unit vectors for intermediate coordinate frames in the  $x, y,$  and  $z$  directions,  $m = 1, \dots, 7$ .
- $x_I$  A vector (usually a unit vector) with components along the inertial  $x, y,$  and  $z$  axes, respectively.
- $x_B$  A vector (usually a unit vector) with components along the principal body  $x, y,$  and  $z$  coordinate axes, respectively.

- $x_X$  A vector (usually a unit vector) with components along the experimental  $x, y,$  and  $z$  coordinate axes, respectively.
- $x_S$  A vector (usually a unit vector) with components along the slit frame  $x, y,$  and  $z$  coordinate axes, respectively.

#### Transformation Matrices

- $E(\gamma, \phi, \theta)$  Euler transformation from inertial space to principal body coordinates.
- $C(\epsilon_1, \epsilon_2, \epsilon_3)$  Transformation from body coordinates to experimental coordinates.
- $A(\beta, \gamma)$  Transformation from experimental coordinates to slit frame.
- $A_1(\beta, \gamma)$  First row vector in  $A(\beta, \gamma)$ , representing direction cosines of the normal to the slit plane in experimental coordinates.

#### Least Squares

- $H(t_k, y)$  Observation for  $k^{\text{th}}$  transit time as a function of parameter vector  $y$ .
- $H$  Vector of constraints for all transit times in a given interval of time.
- $G$  Matrix of partials of  $H$  with respect to  $y$ .
- $J$  Least-squares function to be minimized.

#### Miscellaneous

- $B_x, B_y, B_z$  Earth magnetic field components in principal coordinates.
- $\tau_x, \tau_y, \tau_z$  Torque components in principal coordinates divided by  $I_2$ .
- $f$  Half field of view angle (Fig. 3).
- $(\cdot)$  Time derivative  $\frac{d}{dt}$
- $(')$  The prime on a vector or a matrix represents the transpose of the vector or the matrix.

# VEHICLE MODEL

The differential equations for the rigid vehicle rotary motion may be written (Ref. 3) as

$$\begin{aligned}\dot{\psi}_x &= [\omega_y \omega_z (1-C) + \tau_x] \frac{1}{A} \\ \dot{\psi}_y &= [\omega_x \omega_z (C-A) + \tau_y] \frac{1}{B} \\ \dot{\psi}_z &= [\omega_x \omega_y (A-1) + \tau_z] \frac{1}{C}\end{aligned}\quad (1)$$

and

$$\begin{aligned}\dot{\varphi} &= [-\omega_x \sin \theta + \omega_z \cos \theta] \frac{1}{\cos \phi} \\ \dot{\theta} &= \omega_x \cos \theta + \omega_z \sin \theta \\ \dot{\phi} &= \omega_y - \dot{\varphi} \sin \phi\end{aligned}\quad (2)$$

where  $\omega_x$ ,  $\omega_y$ , and  $\omega_z$  are angular rates about the body principal axes and  $\varphi$ ,  $\theta$ , and  $\phi$  are Euler angles relating body and inertial coordinates (Fig. 1), A and C are the inertia ratios

$$\begin{aligned}A &= I_1/I_2 \\ C &= I_3/I_2\end{aligned}\quad (3)$$

and  $\tau_x$ ,  $\tau_y$ , and  $\tau_z$  are the disturbing torques divided by  $I_2$ . Preliminary studies showed that magnetic moment and eddy current torques were by far the dominant torques acting upon the HEMP vehicle. For the purposes of the feasibility study, these torques were taken as

$$\begin{aligned}\tau_x &= M_y' \omega_z - M_z' \omega_y + \\ & K' [-(\omega_y^2 + \omega_z^2) \omega_x + \omega_x (\omega_y \omega_z + \omega_z \omega_y)] \\ \tau_y &= M_z' \omega_x - M_x' \omega_z + \\ & K' [-(\omega_x^2 + \omega_z^2) \omega_y + \omega_y (\omega_x \omega_z + \omega_z \omega_x)] \\ \tau_z &= M_x' \omega_y - M_y' \omega_x + \\ & K' [-(\omega_x^2 + \omega_y^2) \omega_z + \omega_z (\omega_x \omega_y + \omega_y \omega_x)]\end{aligned}\quad (4)$$

The coefficients  $M_x$ ,  $M_y$  and  $M_z$  are magnetic moment coefficients, K is the eddy current coefficient, and the primes indicate that the coefficients have all been divided by  $I_2$ , the

moment of inertia about the principal y axis. The magnetic field components of the earth,  $B_x$ ,  $B_y$ , and  $B_z$  are assumed to be in body coordinates.

The ordering of the rotations in Fig. 1 is somewhat different than that used in Ref. 3. The ordering was selected to avoid a singular point that could occur if the precession angle were zero. Also, division of Eq. (1) by  $I_2$  eliminates a parameter in the sections that follow. This was possible because the unknown coefficients  $M_x$ ,  $M_y$ ,  $M_z$  and K are multiplicative constants in the torque equations. Division by  $I_2$  merely scales them differently.

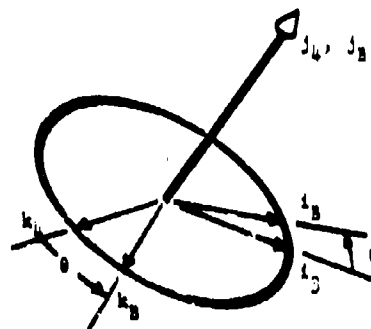
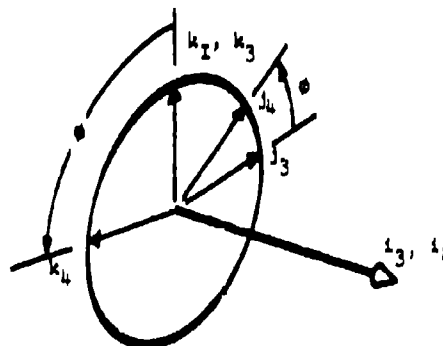
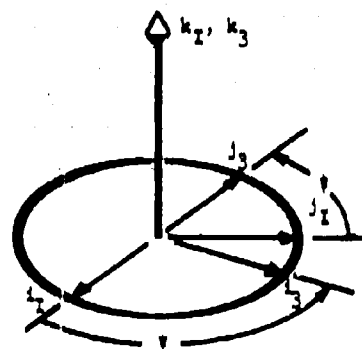


Fig. 1. Relationship of the Principal Axis Coordinate Frame to Inertial Space



### OBSERVATION EQUATION

The starmapper and the sun sensor instruments consist basically of a photocell and a plane with a straight narrow slit in it. The slit and the photocell, viewed as a line and a point, respectively, establish the "slit plane" of the instrument. The length of the slit and the distance of the photocell behind the slit determine the instrument field of view in the slit plane. The instrument is strapped to the satellite, so the slit plane sweeps the heavens as the vehicle rotates. Each time a star, viewed as a point source, enters the field of view, the photocell is triggered and an output time pulse is produced. (It is assumed that the slit plane is not normal to the vehicle angular velocity vector, so that no star remains in the field of view for a finite length of time.)

The observation equation is a relationship that should be true at timing pulse instants. At such an instant, the line of sight to the star lies in the instrument field of view. Thus, the equation states that the dot product of the slit plane normal and the line of sight to the star is zero. Now the star coordinates are known in inertial space, whereas the slit plane is tied to the rotating satellite coordinate frame. Thus, a series of rotations is required to get the two vectors into the same coordinate frame.

The first rotation relates inertial space and the body principal coordinate frame. Thus, a vector  $x_I$  in inertial space is seen in the body frame as  $x_B$ , and the transformation matrix is  $E(\psi, \phi, \theta)$ , where

$$x_B = E x_I \quad (5)$$

Matrix  $E$  can be derived from Fig. 1, and it turns out to be<sup>2</sup>

$$E = \begin{bmatrix} c\theta c\psi - s\theta s\phi s\psi & c\theta s\psi + s\theta s\phi c\psi & -s\theta c\phi \\ -c\phi s\psi & c\phi c\psi & s\phi \\ s\theta c\psi + c\theta s\phi s\psi & s\theta s\psi - c\theta s\phi c\psi & c\theta c\phi \end{bmatrix} \quad (6)$$

It is assumed that the instrument coordinate frame is displaced from the body principal coordinate system, and that the relationship between the two frames is described by rotations through the three angles  $\epsilon_1$ ,  $\epsilon_2$ , and  $\epsilon_3$ . The order of these rotations is illustrated in Fig. 2, and the transformation matrix is  $G(\epsilon_1, \epsilon_2, \epsilon_3)$ .

<sup>2</sup> $c(\ )$  and  $s(\ )$  are abbreviations for  $\cos(\ )$  and  $\sin(\ )$  in the rotation matrices of this section.

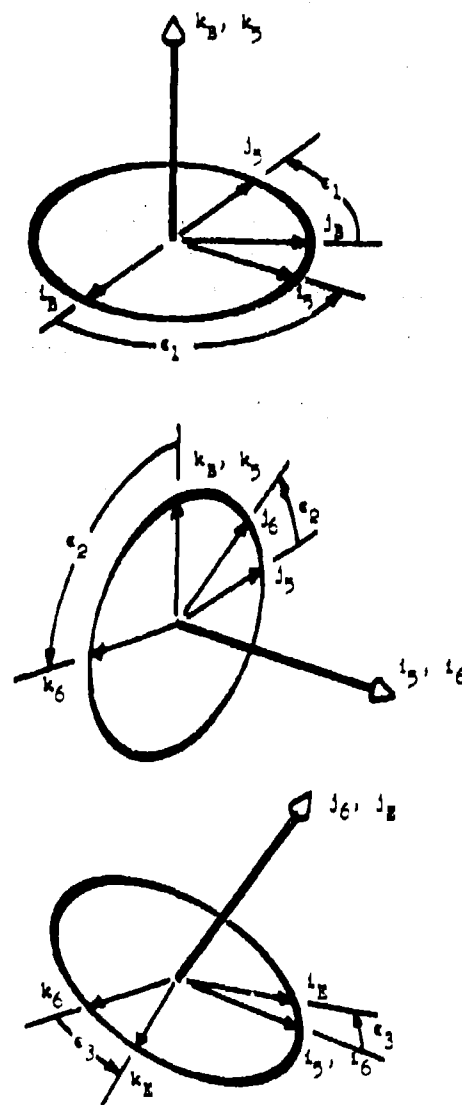


Fig. 2. Relationship of the Instrument Coordinate Frame to the Principal Axis Coordinate Frame

A vector  $x_B$  in the body frame is seen as  $x_E$  in the experimental frame, where

$$x_E = G x_B \quad (7)$$

and

$$C = \begin{bmatrix} c_3 c_1 - s_3 s_2 c_1 & c_3 s_1 + s_3 s_2 c_1 & -s_3 c_2 \\ -c_2 c_1 & c_2 c_1 & s_2 \\ s_3 c_1 + c_3 s_2 c_1 & s_3 s_1 - c_3 s_2 c_1 & c_3 c_2 \end{bmatrix} \quad (8)$$

A given slit coordinate frame of either the star mapper or the sun sensor is related to the experimental coordinate frame through rotation angles  $\gamma$  and  $\beta$ . The order of these rotations is  $\gamma$  about the experimental  $x$  axis and  $\beta$  about the new  $y$  axis (Fig. 3). If  $x_s$  is a vector in the slit frame and  $x_e$  is the vector in the experimental frame, then

$$x_s = Ax_e \quad (9)$$

where

$$A = \begin{bmatrix} c\beta & s\beta s\gamma & -s\beta c\gamma \\ 0 & c\gamma & s\gamma \\ s\beta & -c\beta s\gamma & c\beta c\gamma \end{bmatrix} \quad (10)$$

The combination of Eqs. (5), (7), and (9) is

$$x_s = ACEx_e \quad (11)$$

Let  $x_e$  be the vector  $\hat{s}$  of direction cosines of a star in inertial space. If the star has right ascension  $\alpha$  and declination  $\delta$ , then

$$x_e = \hat{s} = \begin{bmatrix} \cos \delta \cos \alpha \\ \cos \delta \sin \alpha \\ \sin \delta \end{bmatrix} \quad (12)$$

The slit plane is defined as the slit frame  $j_s - k_s$  plane. If the star is in this plane at a particular instant of time, then  $x_s$  corresponding to  $x_e$  is the vector

$$x_s = \begin{bmatrix} 0 \\ \cos \eta \\ \sin \eta \end{bmatrix} \quad (13)$$

where  $\eta$  is the angle between the line of sight to the star  $\hat{s}$  and the  $j_s$  axis (Fig. 4).

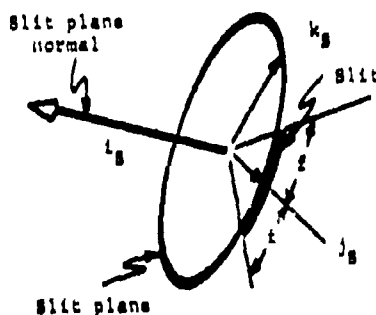
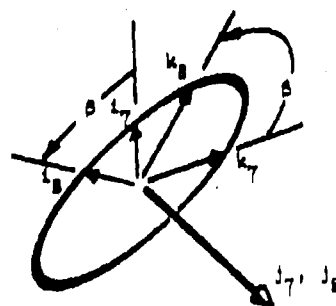
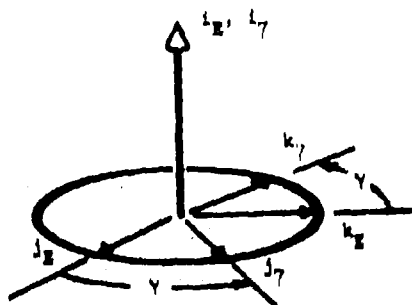


Fig. 3. Relationship of the Slit Coordinate Frame to the Experimental Coordinate Frame, Showing the Slit Plane and Slit



where  $n$  is taken as 15. If Newton-Raphson iteration (Ref. 5) is applied to Eq. (19), there results

$$\sum_{j=1}^n \left[ \frac{\partial H(t_k, y)}{\partial y_1} \frac{\partial H(t_k, y)}{\partial y_j} + H(t_k, y) \frac{\partial^2 H(t_k, y)}{\partial y_1 \partial y_j} \right] \Delta y_j + \sum_{k=1}^N H(t_k, y) \frac{\partial H(t_k, y)}{\partial y_1} = 0, \quad i=1, \dots, n \quad (20)$$

Thus, if the vector  $y$  is close enough to the minimizing value, then the  $\Delta y$  computed from Eq. (20) and added to  $y$  iteratively will cause the eventual satisfaction of Eq. (19).

The problem with Eq. (20) is the second partial derivative of  $H$  that occurs in the matrix to be inverted. This is difficult and time consuming to compute. However, its multiplier, from Eq. (17), is small, and the Newton-Raphson method is known to be relatively insensitive to errors in the matrix. Thus, one would suspect that the second partials could be neglected in Eq. (20) and that convergence would still result. This has always happened in practice, which justifies the truncated form of the equation:

$$\sum_{k=1}^N H(t_k, y) \frac{\partial H(t_k, y)}{\partial y_1} + \sum_{j=1}^n \sum_{k=1}^N \frac{\partial H(t_k, y)}{\partial y_1} \frac{\partial H(t_k, y)}{\partial y_j} \Delta y_j = 0$$

$$i = 1, \dots, n. \quad (21)$$

In matrix notation, this is

$$G'H + G'\Delta y = 0 \quad (22)$$

where

$$H = \begin{bmatrix} H(t_1, y) \\ \vdots \\ H(t_N, y) \end{bmatrix}, \quad G = \begin{bmatrix} \frac{\partial H(t_1, y)}{\partial y_1} & \dots & \frac{\partial H(t_1, y)}{\partial y_n} \\ \vdots & & \vdots \\ \frac{\partial H(t_N, y)}{\partial y_1} & \dots & \frac{\partial H(t_N, y)}{\partial y_n} \end{bmatrix} \quad (23)$$

To determine the partial derivatives required in (23), notice first that  $H(t_k, y)$  may be differentiated directly with respect to the mismatch angles  $\epsilon_1, \epsilon_2$ , and  $\epsilon_3$ . The other partials are evaluated from the expression

$$\frac{\partial H}{\partial b}(t_k, y) = A_1 C \left[ \frac{\partial \psi}{\partial b} \frac{\partial \phi}{\partial b} + \frac{\partial \psi}{\partial \phi} \frac{\partial \phi}{\partial b} + \frac{\partial \psi}{\partial \theta} \frac{\partial \theta}{\partial b} \right] \hat{s} \quad (24)$$

where  $\psi, \phi, \theta$  and their partials are evaluated at  $t = t_k$ ,  $b$  is one of  $(\omega_{x_0}, \omega_{y_0}, \omega_{z_0}, \psi_0, \phi_0, \theta_0,$

$A, C, M'_x, M'_y, M'_z, K')$  and  $\hat{s}$  is the vector in Eq. (15). The partials of  $\psi, \phi$ , and  $\theta$  come from solution of linearized versions of Eqs. (1) and (2) with torques (4). For convenience, let  $x = (\omega_x, \omega_y, \omega_z, \psi, \phi, \theta)$  and let  $a = (A, C, M'_x, M'_y, M'_z, K')$ . Then Eqs. (1) and (2) with torques (4) have the form

$$\dot{x} = f(t, x, a), \quad x(t_0) = x_0 \quad (25)$$

and the corresponding linear differential equations are

$$\frac{d}{dt} \frac{\partial x}{\partial x_0} = \frac{\partial f}{\partial x} \frac{\partial x}{\partial x_0}, \quad \frac{\partial x}{\partial x_0}(t_0) = I \quad (26)$$

$$\frac{d}{dt} \frac{\partial x}{\partial a} = \frac{\partial f}{\partial x} \frac{\partial x}{\partial a} + \frac{\partial f}{\partial a}, \quad \frac{\partial x}{\partial a}(t_0) = 0 \quad (27)$$

where the partials in Eqs. (26) and (27) are evaluated along the solution of Eq. (25). Equations (26) and (27) are solved simultaneously with Eq. (25), and values at  $t = t_k$  are used to evaluate (24).

In summary, the method proceeds as follows:

1. An initial estimate for  $y = (x_0, a, e)$  is provided.
2. Equations (25) through (27) are integrated.
3. At each star observation instant  $t_k$ ,  $k = 1, \dots, N$ , the constraint  $H$  and its partials are computed [Eq. (24) and the remarks above this equation] and inserted into Eq. (23).
4.  $\Delta y$  is computed from Eq. (22) after the last observation has been processed.
5.  $\Delta y$  is added to  $y$ .
6. Steps 2-5 are repeated until  $\Delta y$  becomes negligible.

The mathematical flow diagram of this process is shown in Fig. 5.

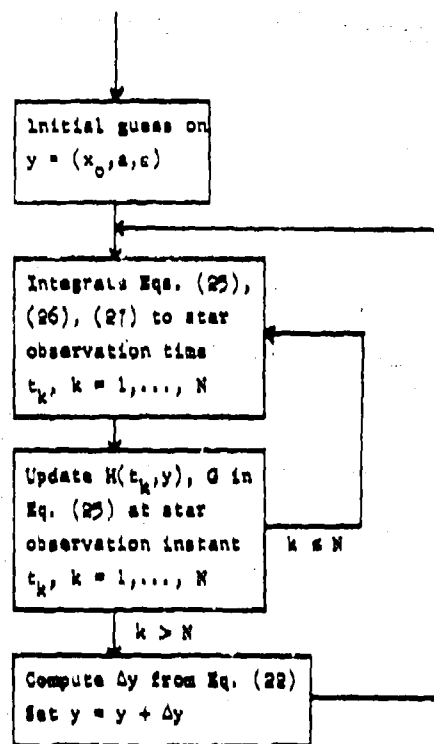


Fig. 5. Mathematical Flow Diagram of the Least-Squares Attitude Determination Simulation

#### EXPERIMENTS PERFORMED

The vehicle is assumed to be in a circular, 200 km orbit about a spherical rotating earth. The data is taken as the first day of spring, so that the sun is out the inertial x axis. The orbit parameters (see Fig. 6) are taken as  $\Omega = 45^\circ$  and  $i = 97.38^\circ$ .

Figure 7 shows the planar relationship of the sun and the orbit. Only the bottom half of the orbit is used during simulation runs, since the problem is mathematically symmetric with respect to a point halfway through the daylight portion. Therefore, demonstration of feasibility requires only a half an orbit of data. Also, simulation of a complete orbit would have resulted in excessive computer usage, since numerical integration is used in the simulation.

Computer runs start at  $t = 0$  in the center of the dark side of the orbit (Fig. 7). This corresponds to a true anomaly of  $\nu = 187.3^\circ$  (Fig. 6). The dividing point between daylight and dark (twilight) is approximately one-sixth of an orbit later, at about  $t = 940$  seconds. Star data is collected over the interval  $0 < t < 880$  seconds. Thus, a data gap of about one minute is introduced in the star data to allow for earth atmospheric refraction of sun rays and earth glow

effects on the starmapper optics. Computer results indicate that the solution from the dark side can be extrapolated over this time period within 10 arc seconds of error.

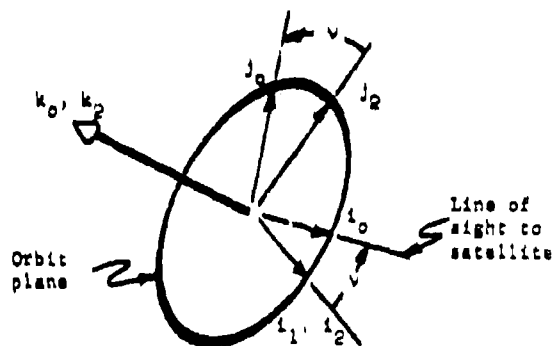
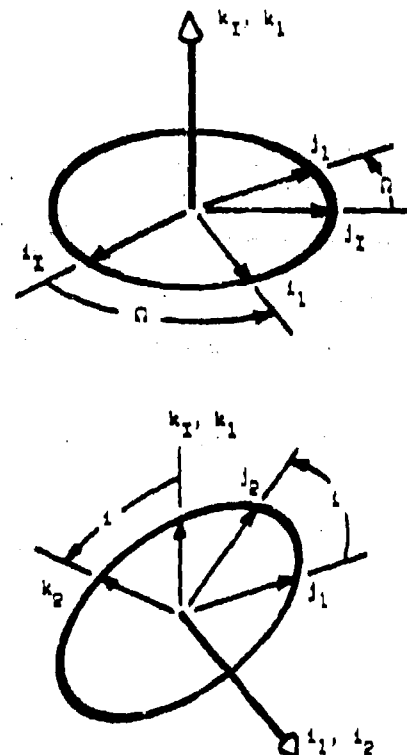


Fig. 6. Relationship of Satellite Line of Sight to Inertial Space

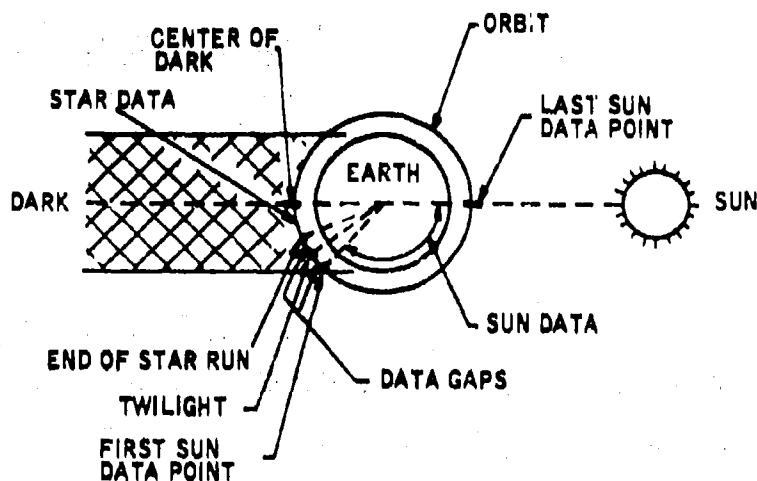


Fig. 7. Relationship of Orbit and Sun Showing Those Portions of the Orbit Over Which Star and Sun Data Are Used

An additional time gap of one minute is allowed from the twilight point to the first sun sighting data point. This is sufficient time for the vehicle to rise above the earth's atmosphere, so that refraction effects can be neglected. Sun data is collected for the remainder of the half orbit.

Initial conditions and parameter values at the center of the dark are taken as:

$$\begin{aligned} \omega_{x_0} &= .2094 \text{ deg/sec} & I_1 &= 34.68 \text{ slug} \cdot \text{ft}^2 \\ \omega_{y_0} &= 18 \text{ deg/sec} & I_2 &= 65.62 \text{ slug} \cdot \text{ft}^2 \\ \omega_{z_0} &= 0 & I_3 &= 34.68 \text{ slug} \cdot \text{ft}^2 \\ \psi_0 &= 45 \text{ deg} & \epsilon_1 &= 0 \text{ deg} \\ \phi_0 &= 190 \text{ deg} & \epsilon_2 &= 0 \text{ deg} \\ \theta_0 &= 180 \text{ deg} & \epsilon_3 &= 0 \text{ deg} \end{aligned}$$

Values for  $M_x$ ,  $M_y$ ,  $M_z$ , and  $K$  are discussed below.

From the initial conditions and parameters, it can be shown that the vehicle is symmetric ( $I_1 = I_3$ ), that it spins at roughly 3 rpm about the principle y axis, and that the cone angle is about 0.7 degrees. From the orbit parameters, the spin vector is misaligned with respect to the orbit normal by about 2.6 degrees.

The torque Eqs. (4) may not represent the exact torques acting on the vehicle. Reasons for this are (1) that the forms of the torques may only approximate the exact forms for magnetic moment and eddy current torques, (2) the earth's

magnetic field is known to about  $\pm 1$  percent of the computed value, and (3) additional torques have been neglected. To simulate these effects the magnetic field components (in local vertical coordinates) are perturbed in the data generating program (Ref. 1) by the amounts

$$\begin{aligned} \Delta B_{x_L} &= (a_1 \sin \omega_1 t) B_{x_L} \\ \Delta B_{y_L} &= (a_2 \sin \omega_2 t) B_{y_L} \\ \Delta B_{z_L} &= (a_3 \sin \omega_3 t) B_{z_L} \end{aligned} \quad (28)$$

The rates  $\omega_1$ ,  $\omega_2$  and  $\omega_3$  correspond to periods of  $1/2$ ,  $1/3$  and  $1/5$  of an orbit to simulate long period effects, and values for  $a_1$ ,  $a_2$  and  $a_3$  are discussed below.

It is also known that the magnetic moment coefficients  $M_x$ ,  $M_y$ , and  $M_z$  have different values during the sunlight portion of the orbit than they do over the dark part. To simulate this effect in the data generating program, the values of the coefficients are perturbed at the twilight point by the amounts

$$\begin{aligned} \Delta M_x &= .05 M_x \\ \Delta M_y &= -.05 M_y \\ \Delta M_z &= .05 M_z \end{aligned}$$

The data generating program generates star crossing instants for the starmapper over the dark portion of the orbit to the twilight point. Stars down to 3.4 magnitude are used. The sun-sensor slits are then used to generate sun data for the remainder of the orbit.

An editing routine is included in the least-squares attitude determination program. It reduces the number of star sightings to a given number per revolution, and corrupts the sighting times with noise. The retained stars are chosen on the basis of brightness, and the number of stars per revolution is a specified quantity. The noise is assumed to be Gaussian, with zero mean and a standard deviation of  $.155 \times 10^{-3}$  seconds. The editing routine treats the sun just like it is another star.

During runs of the least-squares attitude determination program, it became evident that the offset angle  $\epsilon_3$  in Eq. (16) was difficult to determine. The reason for this is that the last column of matrix  $G$  in Eq. (23), representing partials with respect to  $\epsilon_3$ , is approximately the same as the column containing partials with respect to  $\theta_0$ . This is especially true when  $\epsilon_1 = \epsilon_2 = 0$ . In this case  $\theta$  and  $\epsilon_3$  are additive rotations about the same axis. The vehicle is also nearly symmetric, which aggravates the situation. The result of these factors is to make the matrix  $G^T G$  nearly singular, so that poor estimates of  $\theta$  and  $\epsilon_3$  are obtained. The angle  $\epsilon_3$  was consequently set to zero during the runs described below. (A method for determining  $\epsilon_3$  is presented in Ref. 1.)

Runs of the least-squares data processing program are split into two parts, one for the dark part and one for the sunlit part of the orbit. Thus, star data (suitably edited) is used to determine the attitude from the center of the dark to approximately one minute before the twilight point. Results obtained from these computer runs are discussed first. The converged terminal conditions for these runs become the initial conditions for the sunlit portion of the orbit. It turns out that a complete solution to the attitude determination problem cannot be obtained from sun sightings alone, so problems with reduced dimension are considered for this part of the orbit. Experiments to determine the dimensionality of the problems, and the attitude results obtained are discussed below.

#### STAR SIGHTING RESULTS

Several computer runs were made to test the adequacy of the least squares approach to the attitude determination problem. The effects of model perturbations, residual magnetic moment and eddy current torque levels, and number of stars sighted per revolution were examined. The starmapper parameters for these runs are given in Table 1.

Table 1. Starmapper Parameters

Slit	$\beta$ , deg	$\gamma$ , deg
1	-20	90
2	0	90
3	20	90

During editing of the star sighting instants, only one noise set was used. The length of the set was determined from the six star per revolution case. When fewer stars per revolution were simulated (four stars and two stars) noise values at the bottom of the set were deleted.

Several of the computer runs are discussed below. All runs have 14 variables and converged to solutions.

The first three runs study the number of stars per revolution. The actual parameter values used in the data generating program are displayed in the first column of Table 2. Additionally, the magnetic field perturbation constants

$$a_1 = a_2 = a_3 = .02$$

were used during generation of the star sighting instants.

Six, four, and two stars per revolution were used in Cases I, II, and III respectively. The resulting extremum principal axis errors are displayed in Table 3, and the converged parameter values are shown in Table 2. One sees that six stars per revolution give the best results, and that two stars per revolution give the worst. Also, the magnetic moment coefficients differ the most from their actual values.

The angle differences in Table 3 compare errors in principal axes. The desired comparison is errors in instrument axes. Instrument and principal axes are the same in the data generating program, but the offset angles in Table 3 cause them to be different in the least squares program. Correction factors for  $\epsilon_1$  and  $\epsilon_2$  to be added to  $\Delta\psi$ ,  $\Delta\phi$ , and  $\Delta\theta$ , are derived in Ref. 1. They are

$$\Delta\psi = \frac{1}{\cos \theta} [\epsilon_1 \cos \theta - \epsilon_2 \sin \theta] \quad (29)$$

$$\Delta\phi = \epsilon_1 \sin \theta + \epsilon_2 \cos \theta \quad (30)$$

$$\Delta\theta = -\Delta\psi \sin \theta \quad (31)$$

These corrections do not affect Cases I and II very much since  $\epsilon_1$  and  $\epsilon_2$  are quite small. However, the effects are quite spectacular for Case III, as shown in Table 4 (compare with Table 2).

Table 2. Converged Parameter Values for Cases I, II, and III

PARAMETER	ACTUAL	CASE I	CASE II	CASE III
A	.83328	.83325	.83420	.83356
C	.83328	.83333	.83235	.83301
$M_x$ ft-lb/gauss	$5.16 \times 10^{-6}$	$-3.58 \times 10^{-5}$	$-6.42 \times 10^{-5}$	$1.74 \times 10^{-3}$
$M_y$	$5.16 \times 10^{-6}$	$3.87 \times 10^{-6}$	$5.84 \times 10^{-6}$	$-9.58 \times 10^{-6}$
$M_z$	$5.16 \times 10^{-6}$	$5.17 \times 10^{-5}$	$1.61 \times 10^{-4}$	$2.36 \times 10^{-3}$
K ft-lb-sec/gauss <sup>2</sup>	$1.42 \times 10^{-5}$	$1.42 \times 10^{-5}$	$1.44 \times 10^{-5}$	$1.54 \times 10^{-5}$
$\epsilon_1$ degrees	0	- .0021	- .0059	.036
$\epsilon_2$	0	- .0014	- .0012	- .0193

Table 3. Extreme Errors in Euler Angles Relating Principal Axes to Inertial Space at Star Sighting Instants

Case	$\Delta\gamma$ , arc sec		$\Delta\phi$ , arc sec		$\Delta\theta$ , arc sec	
	Max	Min	Max	Min	Max	Min
I	- 3.04	-13.25	4.21	- 5.90	0.31	-3.75
II	9.41	-16.83	20.23	- 8.1	1.14	-6.47
III	86.0	40.0	129.0	100.0	18.15	8.76
IV	1.85	-14.4	5.99	- 9.96	3.44	-5.84
V	0.24	-20.38	6.94	- 13.56	5.73	-6.08

Table 4. Extreme Errors in Angles Relating Experimental Axes to Inertial Space Based on a Spot Check of Results

$\Delta\gamma$ , arc sec		$\Delta\phi$ , arc sec		$\Delta\theta$ , arc sec	
Max	Min	Max	Min	Max	Min
4.2	-12.3	8	-28	3.6	-5.15



Typical errors in the pitch angle (sum of  $\phi_1$  and  $\Delta\theta$ ) are plotted in Fig. 8 for Case I. The upper and lower envelopes (dashed lines) represent the values of maximum and minimum errors at star sighting instants. The curves joining the envelopes (solid lines) are the errors over star sighting intervals. Time between these curves represents the rest of the rotation period of the vehicle, over which no data is available from this program. A similar pitch angle error curve for Case II, although with a somewhat larger spread between the dashed curves, is shown in Ref. 1. The corresponding pitch angle error for Case III is shown in Fig. 9. Also shown is a possible worst case error between star sighting instants. This was derived by assuming long term variations of the pitch angle error to be within the error envelope, and then superimposing the solution from Eq. (31). In the actual situation, there are probably compensating effects that lessen the overall error somewhat. However, these results indicate that two stars per revolution do not yield sufficient accuracy for the HEMP satellites.

Cases IV and V examine the effects of model perturbations, residual magnetic moment and eddy current torque levels. The difference between the two cases is that in Case IV the magnetic field perturbations are

$$a_1 = a_2 = a_3 = .05$$

whereas in Case V they are the negatives of these. Six stars per revolution are used in both cases.

The actual parameter values used in generating the star sightings are shown in Table 3. The magnetic moment coefficients are a factor of 10 larger than those used in the previous cases, to correspond with those estimated for the early Tiros spacecraft. The eddy current coefficient is twice that used previously, and this is the estimated value based on several satellites. The magnetic field perturbation is  $\pm 5$  percent instead of the 2 percent of the previous cases.

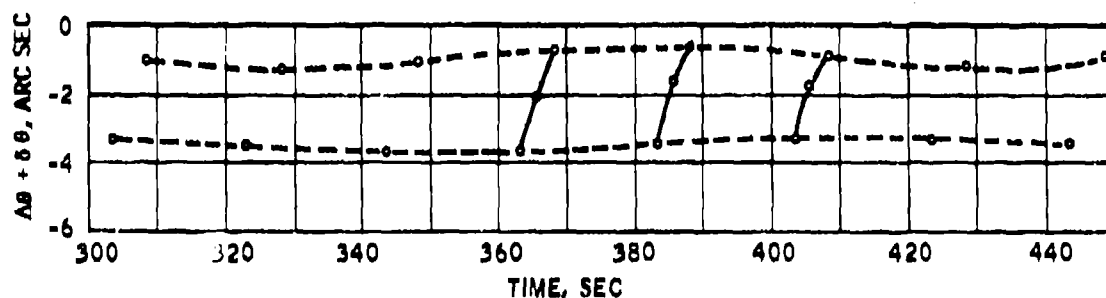


Fig. 8. Experimental Axes Pitch Angle Error for Case I

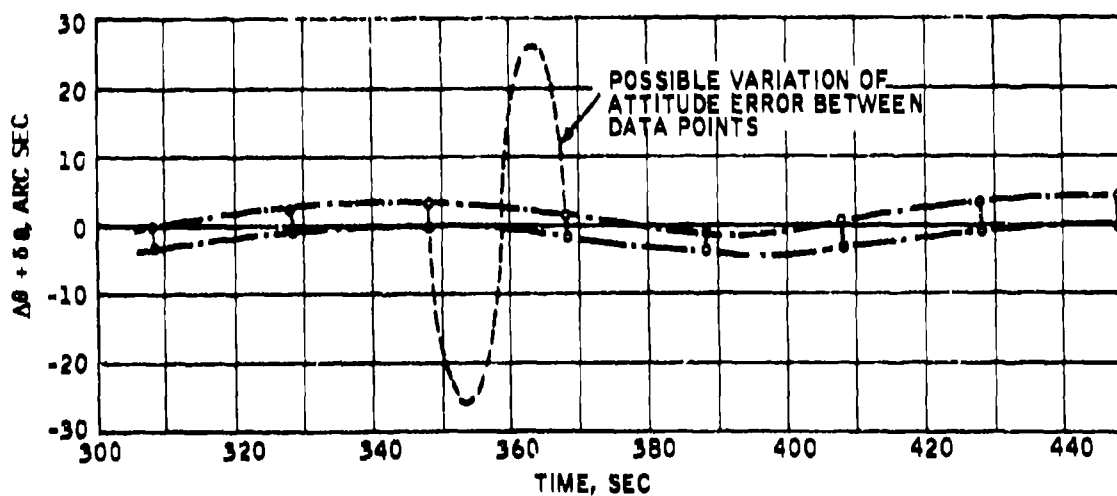


Fig. 9. Experimental Axes Pitch Angle Error for Case III

Table 3. Converged Parameter Values for Cases IV and V

PARAMETER	ACTUAL	CASE IV	CASE V
A	.83328	.83296	.83291
C	.83328	.83363	.83368
$M_x$ ft-lb/gauss	$5.16 \times 10^{-5}$	$-1.56 \times 10^{-5}$	$-3.06 \times 10^{-5}$
$M_y$	$5.16 \times 10^{-5}$	$4.95 \times 10^{-5}$	$4.74 \times 10^{-5}$
$M_z$	$5.16 \times 10^{-5}$	$1.46 \times 10^{-4}$	$1.07 \times 10^{-4}$
K ft-lb-sec/gauss <sup>2</sup>	$2.86 \times 10^{-5}$	$2.96 \times 10^{-5}$	$2.75 \times 10^{-5}$
$\epsilon_1$ degrees	0	-.0031	-.0031
$\epsilon_2$	0	-.0015	-.0016

Table 3 shows that the extremum angular errors compare favorably with those of Cases I and II. Table 3 shows how sensitive  $M_x$ ,  $M_y$ ,  $M_z$ , and K are to the magnetic field perturbations.

From the results of Cases IV and V, it is concluded that a wide range of parameter variations can be tolerated in the vehicle and model with little effect on the accuracy of the attitude estimates (at least at star sighting instances).

The conclusions drawn from the star sighting results are:

- Feasibility of attitude determination by the method of least squares is established.
- Four stars per revolution give adequate results, whereas two stars per revolution do not seem to be enough.
- Large parameter variations can be tolerated.
- Numerical integration of the differential equations is too slow.

#### SUN SIGHTING RESULTS

##### General Approach

The first problem to be solved is that of determining which of the 15 parameters in (16) can be found from observations of the sun. The approach to this problem is to apply the implicit function theorem to the normal Eqs. (19), where more than one variable has been eliminated. (The elimination merely reduces both the number of equations and unknowns to, say,  $m$ , where  $m \leq n$ . Then Eqs. (19) - (23) hold with  $n$  replaced by  $m$ .)

According to the implicit function theorem, the matrix of partial derivatives to be examined for singularity has elements given by the bracketed terms in (20). If the model and the transit times are perfect, then each  $H(t_k, y)$ ,  $k = 1, \dots, 4$  is zero. The matrix then reduces to the product  $G'G$ , where  $G$  is defined in Eq. (23), and where selected columns of  $G$  have been omitted since they correspond to the deleted variables. If the matrix is nonsingular, then the normal equations can be solved for the dependent variables in terms of the set of independent, or omitted, variables.

The matrix can be examined for singularity in only the simplest of analytic problems. For the torqued case of interest, the matrix must be examined numerically. Consequently, a computer program was constructed for this purpose.

The program starts with the complete  $15 \times 15$  matrix. The vector  $G'H$  of Eq. (22) is also in memory. An input card specifies the rows and columns to be deleted. After the matrix and vector have been condensed, the program performs the four tests described below.

1. The solution to Eq. (22) is computed. The pivot elements are output during the Gauss-Jordan reduction as an aid in estimating which rows (or columns) are dependent.
2. The solution is multiplied by the condensed matrix and compared with the condensed  $G'H$  vector. This indicates the quality of the solution.
3. The minimum rank of the condensed matrix is determined. For each numerical operation performed in the Gauss-Jordan reduction, a parallel calculation

of the maximum error in that computation is made and stored. When the errors in the elements of the working matrix become greater than or equal to the elements yet to be processed, the reduction is halted, and the rank is said to be equal to the number of rows (and columns) processed. The original matrix is assumed to be perfect. A number equivalent to  $1/8$  of the least significant bit in the computer is required for the estimate of roundoff error.

4. The eigenvalues of the symmetric matrix are computed. The method is a highly accurate one developed by Householder. The eigenvalues are examined to see if there are any close to zero, and to see if they are all positive.

The above program was used at various stages of the development to determine sets of parameters for the solution. The approach was to generate the least squares equations for a given slit geometry, and then to examine the system for several likely uses. The parameter sets were selected from the results.

Conclusions from these studies are:

- The offset angle  $\epsilon_3$  should be deleted as in the star sighting results, leaving a  $14 \times 14$  matrix to be examined.
- A single, two-slit sun sensor produces a least squares matrix with a maximum rank of 12. Thus, 12 variable solutions are possible.
- Two, two-slit sun sensors (4 slits total) produce a least squares matrix with rank 13. Thus, 13 variable solutions are possible.
- One of the initial angles ( $\psi_0$ ,  $\phi_0$  or  $\theta_0$ ) can always be deleted without reducing the rank of the matrix.

The slit parameters were taken as those of slits 1 and 3 (Table 1) of the starmapper during runs of the data generating program and the least-squares attitude determination program.

This slit configuration is illustrated in Fig. 10, where the vehicle is pictured as a spherical body. (In Fig. 10, the  $j_E$  axis is the outward normal.) The slits join together on the  $k_E$  axis. As the vehicle spins about the  $j_E$  axis, the sun-line traces the dotted line on the spherical skin of the vehicle. For the single sun sensor, the field of view is blocked off to the left of the  $i_E - j_E$  plane. In the four-slit design, the field of view is widened out to  $180^\circ$  so that the sun would cross each slit twice per revolution.

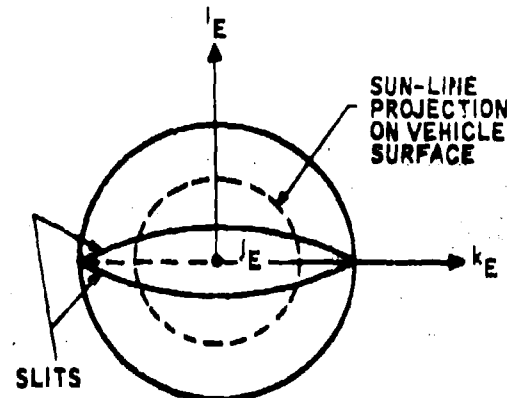


Fig. 10. Slit Configuration for the Sun Sensor Studies

It is recognized that other sun sensor designs may be more practical. The objective of the studies was to draw conclusions about a geometry that would carry over to other slit configurations, without necessitating a major reprogramming effort on the data generating program.

#### Twelve and Thirteen Variable Solutions

Several runs were made assuming the star Case II terminal values to be the starting initial conditions. Four slits were used, which allowed solutions in terms of 13 variables. The results are summarized in Table 6 in terms of angular errors in principal coordinates. All runs except the last one are for  $1/2$  the sunlit part of the half orbit. The deleted variables (specified in the table) are held fixed at their estimated values from the star sighting results.

Run I assumes a perfect model and no noise. It was included to show that a thirteen variable solution is obtained. Run II is the same run, except that the model is no longer perfect ( $a_1 = a_2 = a_3 = .02$  in Eq. (28) as in the star sighting results). The angular errors have biases, although the spreads are very small. No explanation for the bias was found. Run III adds noise to the sun transit times. It is seen that the angular bias becomes less and that the spread in extremes becomes larger.

In Run IV, angles  $\psi_0$  and  $\phi_0$  are held fixed. A somewhat better bias is obtained, but a bigger spread is found. Evidently it is best to allow as much freedom as possible to the least squares process.

Angle  $\psi_0$  was held fixed in the above runs because an error in this quantity does not affect the solution for  $\theta$  significantly (i.e., is a

Table 6. Extrema Errors in Angles Relating  
Experimental Axes to Inertial Space for 12 and 13 Variable Solutions

Run	Variables held fixed	$\Delta\psi$ , arc sec		$\Delta\phi$ , arc sec		$\Delta\theta$ , arc sec	
		Max	Min	Max	Min	Max	Min
I	$\psi_0$	0.40	- 0.41	0.41	- 0.41	0.08	- 0.08
II	$\psi_0$	10.21	8.88	55.66	54.47	55.88	53.36
III	$\psi_0$	21.39	- 8.05	49.47	29.76	48.04	31.30
IV	$\psi_0, \phi_0$	21.52	-15.11	28.07	4.94	27.37	6.82
V	$\theta_0$	15.06	-15.05	11.17	- 9.19	9.53	- 7.26
VI	$\theta_0$	5.38	- 7.46	- 1.79	- 9.84	0.40	-11.58

second-order error source). In fact, in the no torque case, the effect is to cause a bias in  $\psi$  alone, without changing the rest of the solution. However, the observation equation  $H$  is sensitive to  $\psi$ , so that poor results are obtained, even though the analytic solution to the no-torque case does not show this effect.

However, the value of  $\theta_0$  is accurately determined from star observations. Holding this constant should result in more accurate results. Runs V and VI demonstrate that this is so. Run V extends half way through the daylight part of the trajectory, whereas Run VI extends all the way. It is seen from Table 6 that the errors and the spreads in  $\psi$  and  $\phi$  are smaller for the longer run. Although the spread in the  $\theta$  error is less, the bias is larger in this case. A further comparison of the two runs is made in Table 7. Without exception, the parameter values are better for the longer run. The reason for the better accuracy may well be that twice as much data is processed to find the solution, resulting in better smoothing characteristics.

Figure 11 shows the pitch angle error for the experimental frame over a selected time period for Run VI. Data points are given and the dashed line represents the limiting values

obtained. The data appears to be fairly well bounded by these curves, as examination of the slopes of the connecting line segments yields flat slopes (maxima and minima) for at least one set of data.

These results indicate how the sun data should be merged with the star data to estimate the vehicle attitude over the entire orbit: (1) Star data should be used over the dark part of the orbit; (2) the terminal estimated value of the angle  $\theta$  (at the twilight point) from (1) should be used as the fixed initial value for the sunlit portion of the orbit; (3) the thirteen dimensional attitude determination algorithm should be used with the sun data to estimate the attitude over the sunlit part of the orbit.

This algorithm appears to be suitable for estimating the attitude of the KDMF satellite.

#### SUMMARY

The problem of estimating vehicle attitude from starmapper and sun sensor instrument time pulse measurements was considered. Star time pulses were used over the dark part of the orbit and sun sensor pulses alone were considered for the sunlit portion.

Table 7. Additional Results for Runs V and VI

Run	$\epsilon_1$	$\epsilon_2$	A	C	$M_x$	$M_y$	$M_z$	K
V	.0012°	.0033°	.83345	.83311	$1.01 \times 10^{-4}$	$4.48 \times 10^{-6}$	$6.26 \times 10^{-4}$	$1.46 \times 10^{-5}$
VI	.0004	.0006	.83323	.83334	$4.51 \times 10^{-5}$	$4.83 \times 10^{-5}$	$2.50 \times 10^{-4}$	$1.44 \times 10^{-5}$

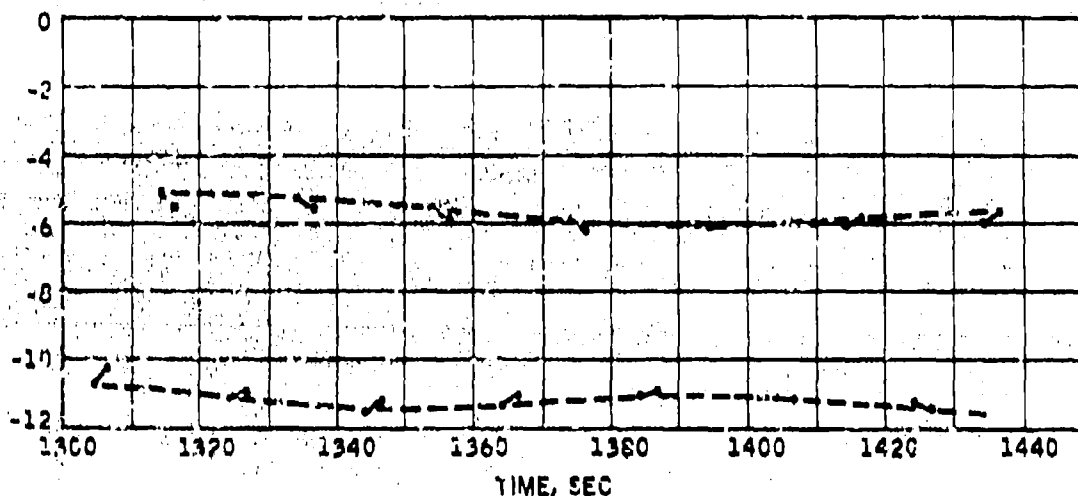


Fig. 11. Experimental Frame Piston Angle Error for Sun Sensor Run VI

An a posteriori data processing algorithm was postulated for the solution of this problem, since real-time knowledge of precise vehicle attitude is not required. It was also noted that the interpretation of the instrument measurements in terms of attitude requires a model for the vehicle motion.

The approach chosen for solution of the attitude determination problem was the method of least squares. The solution of the model equations of motion can be expressed in terms of time, the initial conditions, and the model parameters. The least-squares problem was posed as that of determining those initial conditions and parameters that best explain the observed sequence of star mapper and sun sensor time pulses.

The attitude was readily estimated on the dark side of the orbit. Four stars per revolution were sufficient for this purpose, and large parameter variations could be tolerated.

The situation was quite different on the sunlit side of the orbit. It was not clear how much information could be gleaned from sun observations alone. Computer simulations showed that everything could be determined with a properly designed sun sensor except for one of the initial attitude angles (and  $e_3$ ). This led to a thirteen dimensional attitude determination algorithm for the sunlit portion of the orbit.

Finally, a method for tying the two attitude estimates together was developed and described. This algorithm appears to be suitable for estimating the attitude of the HMM satellite.

#### REFERENCES

1. W. F. Vogelsang, J. A. Saltes, D. K. Schermack: Orbital Operations and Analysis for a 15-Micron Horizon Radiance Measurement Experiment, Horizon Definition Study, NASA CR-66376, May 1967. Prepared under Contract No. NAS 1-6010 by Honeywell Inc., Systems & Research Division, Minneapolis, Minn. for National Aeronautics and Space Administration.
2. C. B. Groesch, "Orientation of a Rigid Torque-Free Body by Use of Star Transits," J. Spacecraft, Vol. 4, No. 3, 362-366 (1967).
3. H. Goldstein, Classical Mechanics, Addison-Wesley, Cambridge, 1956.
4. E. A. Coddington, N. Levinson, Theory of Ordinary Differential Equations, McGraw-Hill, New York, 1955.
5. F. B. Hildebrand, Introduction to Numerical Analysis, McGraw-Hill, New York, 1956.

## FILTERING QUANTIZED OBSERVATIONS<sup>1</sup>

J. P. O'Malley  
Systems Design Department  
TRW Systems Group  
Redondo Beach, California

### ABSTRACT

Attitude sensor measurements may be forced to assume evenly spaced, quantized values. This effect may be caused by digital encoder truncation on-board the spacecraft or by peculiarities in sensor design. Before quantization, the observations may be error free or contaminated by normally distributed, additive noise. The method of maximum likelihood can be used to derive algorithms for processing such data. The approach and assumptions resemble those used in spacecraft navigation. When noise is absent, the estimate minimizes the quadratic form in the a priori normal density, subject to linear constraints imposed by the data. This is a linear programming problem. When noisy data are quantized, the maximum likelihood condition is transcendental. Batch processing and sequential algorithms may be derived by linearization, as the quantization vanishes, both formulations approach their more common equivalents. When the generality of the model is restricted, the quantized-normal estimate is  $\chi^2$ -minimum. The design of software incorporating these quantized data algorithms is discussed, and some simple examples are given to illustrate their accuracy advantages over suboptimal normal filters.

### 1. INTRODUCTION

Most estimation algorithms assume that the sensor observations are selected from a continuous statistical distribution. In many practical attitude determination problems, however, the measurements will be noticeably quantized. The sample values will be taken from a discrete statistical distribution. In some cases, the measurements are constrained by attitude sensor resolution limitations. In others, the analog output from the sensor is truncated, before commutation and transmission in the downlink telemetry, by the analog-to-digital format conversion process. The measurement separation, or quantization level, will be determined by the number of binary bits allocated to the sensor reading and the scaling law employed for conversion to engineering units.

When quantization is an appreciable part of the total measurement error, there may be a need

for data processing algorithms which recognize the existence of quantization constraints in the sampling process. The computational procedures most frequently used do not fulfill this requirement. In a general sense, we may conceive of four combinations of models for the observation noise and the sampling limitations. The observations may or may not contain normally distributed, additive noise. Samples of these observations may or may not be taken from a continuous set. Either of the two observation models may be combined with either of the two sampling models. Methods for processing unquantized data are relatively well known. We wish to develop feasible algorithms for processing quantized data both with and without normally distributed additive noise.

The data processing algorithm must produce an estimate of the state variables: the attitude, possibly attitude rate, and significant model constants. The state will be measured at some

<sup>1</sup>This work was company-sponsored.

epoch time. In concept, at least, updating a previous state to the current time is a trivial operation. The estimate will satisfy some criterion, but the definition and exact nature of the best criterion are topics of considerable debate. There are many camps in the field of estimation theory. There are Bayesians, who use a priori expectations, and non-Bayesians, who only believe their data. There is a non-statistical least-squares school and a partially statistical weighted-least-squares school. The least-squares advocates minimize the sum of the squares of the residuals, the differences between the measured and predicted sample values. The weighted-least-squares group gives different weights to different data types. There is a non-parametric mini-max school which believes in minimizing the maximum error without making any hypotheses about the statistical distribution on the sample values. There is a parametric mini-max school which would minimize the maximum covariance matrix of state estimation uncertainties. There is a maximum likelihood school which favors the estimate which maximizes the probability density function. Finally, there is an expected value school which advocates computing the mean of the conditional distribution defined by the a priori probability density given the data. There are particular problems which are more tractable solved one way rather than another. There are also special cases which violate the rationale behind some of these criteria. In many instances, several different philosophies will all yield the same answer. Each school contributes something to our understanding of the estimation process. The factors to be considered in selecting a criterion are the analytic tractability of the derivation, the computational complexity of the algorithm, the accuracy of the answer, and the engineering application. If we were faced with a drop-dead accuracy requirement, we would lean towards a mini-max criterion. If we lacked faith in our ability to model sensor noise, we would adopt a non-parametric, a least-squares, or a weighted-least-squares criterion. When the probability density function is symmetrical about its unique maximum, the mean and maximum coincide; either the mean value approach or the maximum likelihood approach may be used, which ever is easier. When the density distribution exhibits several relative maxima, however, the method of maximum likelihood should be avoided.

In developing algorithms for attitude determination, we shall use the maximum likelihood criterion and adopt a Bayesian outlook regarding the importance of a priori information. Bayesian algorithms are flexible and may be used for both batch processing and sequential estimation. At the last minute, a Bayesian has the option of changing his mind and de-weighting the a priori. The rationale behind the selection of the maximum likelihood method in preference to the mean value method is somewhat subjective. The use of the expected value for the state estimate insures that the variance or second moment of the probability distribution is minimized in a region near the estimate. The maximum likelihood state optimizes the probability of inclusion in a region near the estimate. The expected state and maximum likelihood state coincide if all four of the following

conditions hold:

- the a priori deviations are normally distributed
- the observation noise is additive and normally distributed
- the sampling distribution is continuous
- the observations are linearly related to the state.

When the sampling distribution is discrete, the probability density is skewed towards the a priori. The maximum likelihood estimate will be closer to the a priori than the expected state. This tendency may be in accordance with engineering judgements about the relative credibility of the a priori and a posteriori information. Also, the attitude sensor and data processing computer may both be included in the attitude control loop. The maximum likelihood estimate of attitude may be preferable to the mean, because an over correction for a return to the a priori costs more attitude control gas than an under correction.

The scope of this analysis includes the derivation of specific conditions satisfied by the maximum likelihood state estimate for quantized data, the construction of feasible algorithms for evaluating this state estimate, and the design of software incorporating these algorithms. In addition, the relative merits and demerits of such procedures will be examined.

Certainly, there are simple, sub-optimal algorithms which could be used to process quantized sensor data. Complex techniques are justifiable only when the emphasis is on accuracy enhancement. We can predict that attitude estimation algorithms which recognize quantization constraints will be more complex, and more accurate, than those which do not.

The techniques considered should be applicable to any attitude determination problem which might be encountered. The estimation equations should be expressed in a form explicitly independent of any particular dynamic model or sensor. Examples designed to guide the analyst in making preliminary decisions about the necessity for implementing these algorithms, however, should be as simple as possible.

## II. NORMAL FILTERS

A cursory review of procedures for processing continuous valued observations contaminated by normally distributed, additive noise will help codify the notation and assumptions to be employed in deriving algorithms for processing quantized observations.

Unless the attitude dynamics are badly unstable or the analyst has made a poor choice of coordinates, the propagated effect of small initial state perturbations should be approximately linear in the neighborhood of a reference solution to the dynamic equations of motion, even

though the dynamic model itself is non-linear. Also, the effect of small deviations in the current state on the nominal observations defined by the reference state should be linear, even though the observations themselves are non-linear functions of the current state. In many cases, the observations will be linearized about the a priori, but the distinction between the reference and a priori will be maintained for generality.

If a total of  $n$  attitude sensor measurements are available, their deviations  $y_1, \dots, y_n$  from the observations computed using the reference state may be arranged in an  $n \times 1$  column vector  $\tilde{y}$ . Also, the  $m$  unknown deviations between the true and reference state parameters at some common epoch time may be arranged in an  $m \times 1$  column vector and denoted by  $\tilde{x}$ . The observation vector, then, is given by

$$\tilde{y} = A\tilde{x} + \tilde{n}$$

where

$$A = \frac{\partial \tilde{y}}{\partial \tilde{x}}$$

is an  $n \times m$  matrix of first order partial derivatives of the  $n$  observations with respect to the  $m$  state components, and  $\tilde{n}$  is an  $n \times 1$  column vector of measurement noise. The noise is normally distributed, and the measurement noise covariance matrix

$$\Lambda = \overline{\tilde{n} \tilde{n}^T}$$

is presumably known. All significant measurement biases are included in the state vector.

In accordance with our Bayesian philosophy, the deviation  $\tilde{x}$  of the a priori state from the reference state and the non-singular a priori covariance matrix

$$\Lambda_0 = \overline{(\tilde{x}_0 - \tilde{x})(\tilde{x}_0 - \tilde{x})^T}$$

are assumed to be known.

The maximum likelihood state estimate  $\tilde{x}^*$  maximizes the joint probability density function  $L(\tilde{x}|\tilde{x}_0, \tilde{y})$  of the a priori state and the measurement noise. This method was used in particular cases by Gauss and introduced as a general procedure by R. A. Fisher. The value of  $\tilde{x}$  which maximizes  $L(\tilde{x}|\tilde{x}_0, \tilde{y})$  also maximizes  $\ln L(\tilde{x}|\tilde{x}_0, \tilde{y})$ . Thus, the maximum likelihood estimate may be defined by the non-trivial solutions to the likelihood equation

$$\frac{\partial \ln L(\tilde{x}|\tilde{x}_0, \tilde{y})}{\partial \tilde{x}} = 0.$$

For samples taken from a continuous distribution, the logarithm of the joint density is

$$\begin{aligned} \ln L(\tilde{x}|\tilde{x}_0, \tilde{y}) = & -\frac{1}{2} (\tilde{x}_0 - \tilde{x})^T \Lambda_0^{-1} (\tilde{x}_0 - \tilde{x}) \\ & -\frac{1}{2} (\tilde{y} - A\tilde{x})^T \Lambda^{-1} (\tilde{y} - A\tilde{x}) \\ & + \text{constant.} \end{aligned}$$

The first variation

$$\delta \tilde{x}^T [\Lambda_0^{-1} (\tilde{x}_0 - \tilde{x}) + A^T \Lambda^{-1} (\tilde{y} - A\tilde{x})]$$

must vanish at  $\tilde{x} = \tilde{x}^*$  for any choice of  $\delta \tilde{x}$ . Thus

$$\tilde{x}^* = (\Lambda_0^{-1} + A^T \Lambda^{-1} A)^{-1} (\Lambda_0^{-1} \tilde{x}_0 + A^T \Lambda^{-1} \tilde{y}) \quad (1)$$

The state estimation errors are

$$\tilde{x}^* - \tilde{x} = (\Lambda_0^{-1} + A^T \Lambda^{-1} A)^{-1} [\Lambda_0^{-1} (\tilde{x}_0 - \tilde{x}) + A^T \Lambda^{-1} (\tilde{y} - A\tilde{x})]$$

so covariance matrix of state estimation uncertainties is

$$\begin{aligned} \overline{(\tilde{x}^* - \tilde{x})(\tilde{x}^* - \tilde{x})^T} &= (\Lambda_0^{-1} + A^T \Lambda^{-1} A)^{-1} [\Lambda_0^{-1} \overline{(\tilde{x}_0 - \tilde{x})(\tilde{x}_0 - \tilde{x})^T} \Lambda_0^{-1} \\ &+ A^T \Lambda^{-1} \overline{(\tilde{y} - A\tilde{x})(\tilde{y} - A\tilde{x})^T} \Lambda^{-1} A] (\Lambda_0^{-1} + A^T \Lambda^{-1} A)^{-1} \\ &= (\Lambda_0^{-1} + A^T \Lambda^{-1} A)^{-1} \quad (2) \end{aligned}$$

By means of the matrix (Shur) identity

$$(E + BD^{-1}C)^{-1} = E^{-1} - E^{-1}B(CE^{-1}B + D)^{-1}CE^{-1}$$

which holds when the products are defined and  $E$  and  $D$  are both square and non-singular, the maximum likelihood estimate may be written in the form

$$\tilde{x}^* = \tilde{x}_0 + \Lambda_0 A^T (\Lambda_0 A^T + \Lambda)^{-1} (\tilde{y} - A\tilde{x}_0) \quad (3)$$

and the covariance matrix of estimation uncertainties is

$$\overline{(\tilde{x}^* - \tilde{x})(\tilde{x}^* - \tilde{x})^T} = \Lambda_0 - \Lambda_0 A^T (\Lambda_0 A^T + \Lambda)^{-1} \Lambda_0 \quad (4)$$

Clearly, the state estimate is a linear function of the a priori and observations, and the state estimation uncertainties are normally distributed. We shall never be this lucky again.

In some cases,  $n$  may be on the order of several thousand points, and  $m$  may include from six to sixty state variables. If Eqs. (1) and (3) were programmed directly, the core storage requirements would be excessive. If the observation errors are statistically independent, so the errors



in  $y_i$  and  $y_j$  are uncorrelated for  $i \neq j$ , then  $\Lambda$  and  $\Lambda^{-1}$  will be diagonal matrices; the  $i$ th diagonal element of  $\Lambda$  will be  $\sigma_i^2$  the variance in the  $i$ th observation, and the  $i$ th diagonal element of  $\Lambda^{-1}$  will be  $1/\sigma_i^2$ . If the  $i$ th row of  $A$  is denoted by

$$A_i = \frac{\partial y_i(t_i, \bar{x})}{\partial \bar{x}}$$

a row vector with  $m$  elements, then

$$A^T \Lambda^{-1} = (A_1^T / \sigma_1^2, A_2^T / \sigma_2^2, \dots, A_n^T / \sigma_n^2),$$

$$A^T \Lambda^{-1} \bar{y} = \sum_{i=1}^n A_i^T y_i / \sigma_i^2,$$

and

$$A^T \Lambda^{-1} A = \sum_{i=1}^n A_i^T A_i / \sigma_i^2$$

The expression for the estimate, Eq. (1), may be written in the form

$$\bar{x}^* = (\Lambda_0^{-1} + \sum_{i=1}^n A_i^T A_i / \sigma_i^2)^{-1} (\Lambda_0^{-1} \bar{x}_0 + \sum_{i=1}^n A_i^T y_i / \sigma_i^2) \quad (5)$$

and the estimation error covariance matrix is

$$(\bar{x}^* - \bar{x})(\bar{x}^* - \bar{x})^T = (\Lambda_0^{-1} + \sum_{i=1}^n A_i^T A_i / \sigma_i^2)^{-1} \quad (6)$$

Equation (5) gives the maximum likelihood estimate in the form most commonly used for processing satellite tracking data. A single estimate of the state is computed from all the data at once. Equation (5), then, is a "batch processing" algorithm. A simplified functional flow diagram is shown in Fig. 1. The program begins by reading the a priori state and state covariance matrix, the reference state estimate, the epoch time, the observation weights  $\sigma_1, \dots, \sigma_n$ , and the number of observations to be processed  $n$ . The program computes  $\Lambda_0^{-1}$ , sets the scalar  $P=0$ , and computes  $\bar{x}_0$ , the difference between the reference and a priori states estimates. The data processing loop is initialized by setting the current observation index  $i=1$ , the sum matrix  $N=0$ , the  $m \times 1$  matrix  $M=0$ , and the scalar  $T=0$ . The observations and their time tags are read off a tape or disc, the reference state is used to compute the reference observation at the time tag, the difference  $y_i$  between the actual and predicted observation, and the  $1 \times m$  row vector of observation partials  $A_i$ . Next, the running sums of

$$A_i^T A_i / \sigma_i^2, A_i^T y_i / \sigma_i^2, \text{ and } y_i^2 / \sigma_i^2$$

are computed. After processing the  $n$ th observation, the state estimate is computed via Eq. (5). At this point, we recognize that the reference

state may not have been close enough to the true state to insure linearity. Therefore, the maximum likelihood estimate is added to the reference state to define a new reference, and the calculations are repeated beginning with  $i=1$ . This iterative process does not converge until the true root-sum-square of the residuals

$$\sqrt{T} = \sqrt{\sum_{i=1}^n y_i^2 / \sigma_i^2}$$

and the predicted root-sum-square of the residuals

$$\begin{aligned} \sqrt{P} &= [(\bar{y} - A\bar{x}^*)^T \Lambda^{-1} (\bar{y} - A\bar{x}^*)]^{1/2} \\ &= [\bar{y}^T \Lambda^{-1} \bar{y} - \bar{y}^T A^T \Lambda^{-1} \bar{y} + \bar{y}^T A^T \Lambda^{-1} A \bar{x}^* - \bar{x}^{*T} A^T \Lambda^{-1} A \bar{x}^*]^{1/2} \\ &= [\sum_{i=1}^n y_i^2 / \sigma_i^2 - 2 \bar{x}^{*T} \sum_{i=1}^n A_i^T y_i / \sigma_i^2 + \bar{x}^{*T} (\sum_{i=1}^n A_i^T A_i / \sigma_i^2) \bar{x}^*]^{1/2} \end{aligned}$$

agree well enough to satisfy the criterion

$$\|\sqrt{P} - \sqrt{T}\| / \sqrt{P} \leq \epsilon.$$

For simplicity, the flow in Fig. 1 does not show logic for bounding the solution, for editing data, or for printing residuals and state after every iteration. The reduction of non-linear effects by iteration is one of the advantages of batch processing.

If Eq. (3) were used to process all the observations at one time, the core storage requirements would be gross. The dimensions of the noise covariance matrix would expand with the number of observations. There are no sneaky tricks we can play with summations to alleviate this difficulty. For sequential processing applications, however,  $\Lambda_0$  may be replaced by  $\Lambda_{i-1}$  the state estimation covariance matrix after  $i-1$  observations, the matrix  $A$  may be replaced by  $A_i$  the observation partials for the  $i$ th observation, the covariance matrix of observation errors  $\Lambda$  may be replaced by  $\sigma_i^2$  the variance on the  $i$ th observation, the a priori state  $\bar{x}_0$  may be replaced by  $\bar{x}_{i-1}$  the state estimate after processing  $i-1$  observations, and the a posteriori state  $\bar{x}^*$  may be replaced by  $\bar{x}_i$  the state estimate after  $i$  observations. With these substitutions, Eqs. (3) and (4) are

$$\bar{x}_i = \bar{x}_{i-1} - \frac{\Lambda_{i-1} A_i^T (y_i - A_i \bar{x}_{i-1})}{\sigma_i^2 + A_i \Lambda_{i-1} A_i^T} \quad (7)$$

and

$$\begin{aligned} (\bar{x}_i - \bar{x})(\bar{x}_i - \bar{x})^T &= \Lambda_i \\ &= \Lambda_{i-1} - \frac{\Lambda_{i-1} A_i^T A_i \Lambda_{i-1}}{\sigma_i^2 + A_i \Lambda_{i-1} A_i^T} \end{aligned} \quad (8)$$

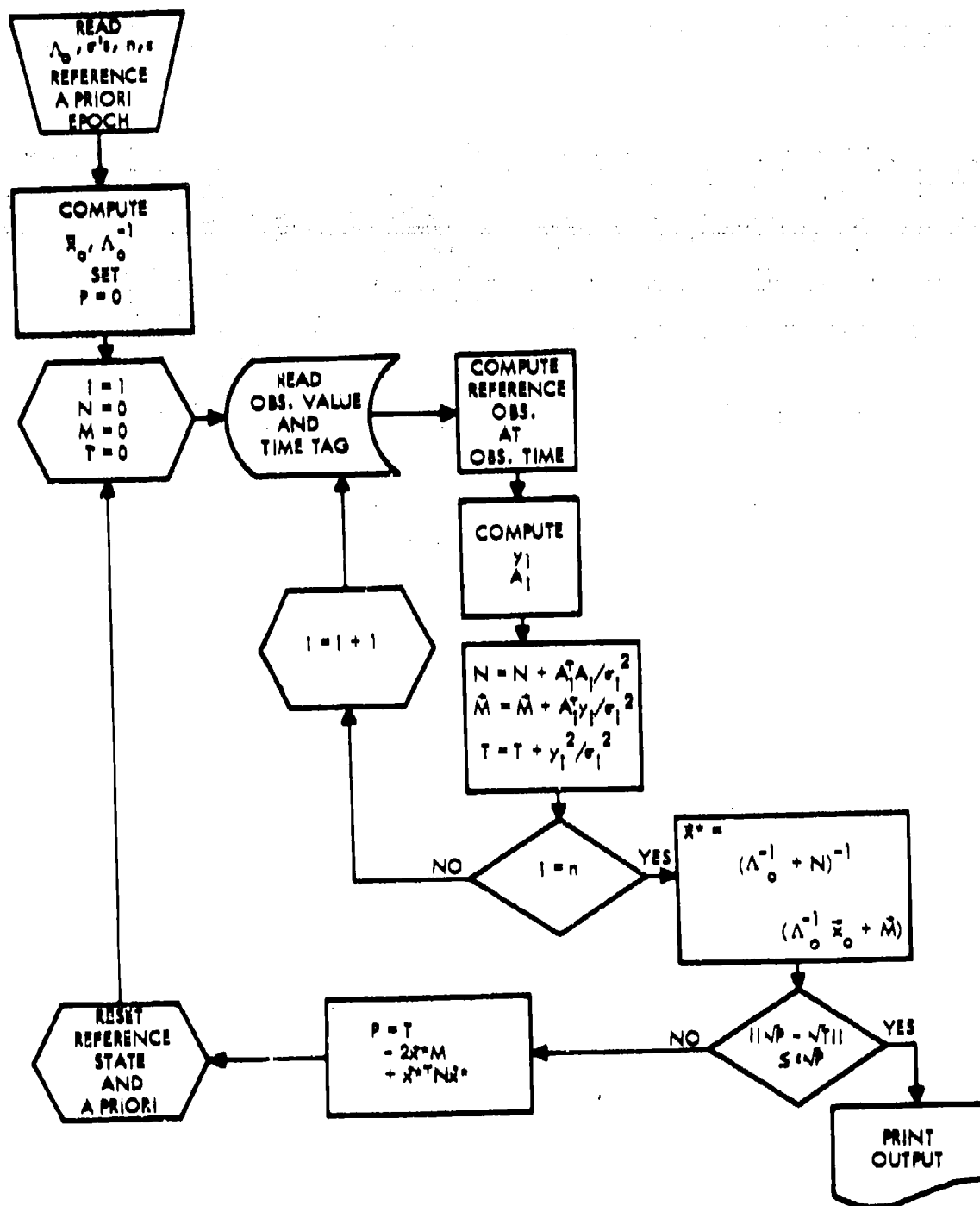


Fig. 1. Normal Batch Processing

The quantity  $\sigma^2 + A_1 A_1^T$  is a scalar, so there is no need for matrix inversions. These are the familiar Kalman filter equations for an epoch state. New values of the epoch state and epoch state covariance matrix are computed after every observation. This is a "sequential" estimation algorithm. Conversion to the current state and state covariance matrix is conceptually easy. A simplified functional flow diagram for the estimation algorithm is given in Fig. 2. One of the virtues of the sequential estimation procedure is its ability to process and discard the data as they are accumulated. The observation and observation time tag are no longer needed once they have been used to update the state. However, the sequential form can not easily be used to overcome non-linear effects by repeated iteration without compromising its main advantages.

The derivations given here follow Solloway, Ref. 1, and Cramer, Ref. 2. The treatment of correlated observations for batch processing is discussed by Magness and McGuire in Ref. 3. Morrison, Ref. 4, describes convergence criteria and bounds on the solution for non-linear iteration. Reference 5 derives the effect of unestimated biases on the estimate and gives a method for implicitly solving for biases during batch processing. The analogous state reduction for Kalman filters is outlined by Galles in Ref. 6. Most authors give the text by Shapiro, Ref. 7, as the original source for the application of batch processing methods to trajectory prediction. Bucy and Joseph, Ref. 8, have recently authored a book emphasizing sequential estimation. This text contains an extensive bibliography on the theory and applications of Kalman filters.

Simple examples sometimes help explain more complex phenomena. In the one-dimensional case where the partial of the observation with respect to the state is a scalar constant  $a$ , the maximum likelihood state estimate is given by

$$\hat{x}^* = \frac{(x_0/\sigma_0^2) + (a/\sigma^2) \sum_{i=1}^n y_i}{(1/\sigma_0^2) + n(a^2/\sigma^2)}$$

where  $x_0$  is the a priori estimate of  $x$ ,  $\sigma_0^2$  is the a priori variance,  $\sigma^2$  is the measurement noise variance, and  $n$  is the total number of observations. The estimation error variance is

$$(\hat{x}^* - x)^2 = \frac{1}{(1/\sigma_0^2) + n(a^2/\sigma^2)}$$

If the a posteriori data are of little value, the parameters  $n a^2 / \sigma^2$  and  $(a \sigma_0^2 / \sigma^2) y_i$  will be small; the a priori will dominate the solution. As the quantity of a posteriori data increases, the state estimate approaches

$$\frac{1}{na} \sum_{i=1}^n y_i = \bar{y}/a,$$

and the estimation variance approaches

$$\sigma^2/na^2.$$

### III. QUANTIZED FILTERS

At the other extreme, the a posteriori data may be free of random noise, but the samples may be restricted to a discrete set of values. Only the a priori state errors are random;  $x_0$  is normally distributed with covariance matrix  $\Lambda_0$ . For convenience, let us assume that the attitude sensor data are rounded up or down to the nearest allowed value:

$$-(\Delta/2) \leq \tilde{y} - A\tilde{x} \leq \Delta/2$$

where  $\tilde{x}$  is an  $n \times 1$  column vector of elements  $\Delta_i$  specifying the quantization for the associated observations. Cases where the data are always rounded up or always rounded down may be treated in this format by modifying the observation vector  $y$ .

The joint probability density of the a priori state estimate and a posteriori data is

$$L(\tilde{x}|\tilde{x}_0, \tilde{y}) = f(\tilde{x}|\tilde{x}_0) p_1(\tilde{x}|y_1) \dots p_n(\tilde{x}|y_n)$$

for this combination of the continuous and discrete distributions treated in Ref. 2. The a priori distribution is

$$f(\tilde{x}|\tilde{x}_0) = \frac{1}{(2\pi)^{m/2} \Lambda_0^{-1/2}} \exp \left\{ -(\tilde{x}_0 - \tilde{x})^T \Lambda_0^{-1} (\tilde{x}_0 - \tilde{x}) / 2 \right\}$$

for the  $m$  elements of the state vector  $\tilde{x}_0$ . The discrete probability for the  $i$ th observation is

$$p_i(\tilde{x}|y_i) = \begin{cases} 1/\Delta_i > 0 & \text{if } \|y_i - A_i \tilde{x}\| \leq \Delta_i/2 \\ 0 & \text{if } \|y_i - A_i \tilde{x}\| > \Delta_i/2 \end{cases}$$

where  $A_i$  is the  $i$ th row of the observation partials matrix  $A$ . The constant  $1/\Delta_i$  normalizes the integral of the distribution. The solution  $\tilde{x}$  such that

$$\sum_{i=1}^n p_i(\tilde{x}|y_i) \neq 0$$

is not necessarily unique. By the somewhat simplified conditions of the problem, there must be at least one solution such that the constraint limits are satisfied for all the observations. However, there may actually be an infinite number of solutions satisfying these constraints. The selection of the solution which also minimizes

$$f(\tilde{x}|\tilde{x}_0)$$

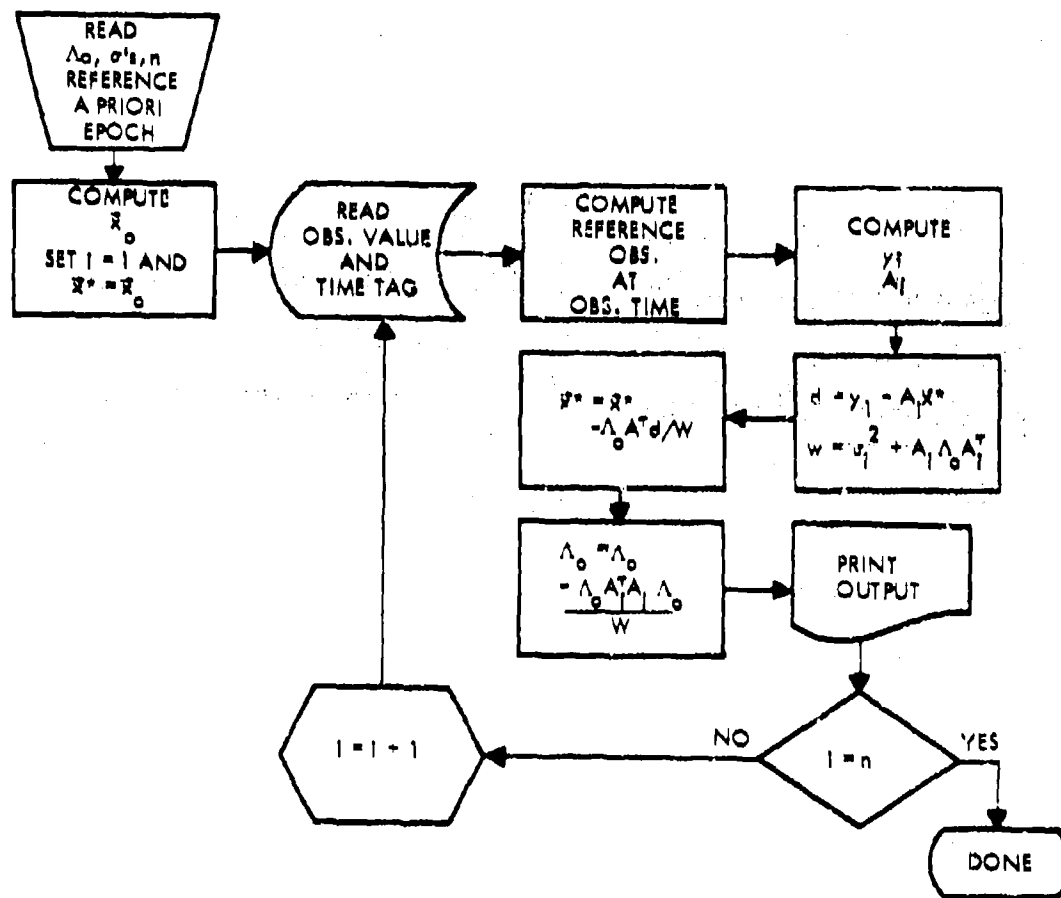


Fig. 2. Normal Sequential Processing

insures a unique estimate. When the sampling distribution is continuous, inclusion of a priori statistics is a matter of engineering judgement. If we want a unique solution when the data are quantized, we must give up this option.

The quantized maximum likelihood estimate, then, will minimize the quadratic form

$$(\bar{x}_0 - \bar{x})^T \Lambda_0^{-1} (\bar{x}_0 - \bar{x})$$

subject to the constraints

$$-\Delta/2 \leq \bar{y} - A\bar{x} \leq \Delta/2.$$

Problems of this type have been solved by Whalen, Ref. 9, using linear programming and the "simplex method" developed by Dantzig in Ref. 10. The equations required are straightforward in a formal sense. If  $\bar{z} = \bar{y} - A\bar{x}$  is a "surplus/slack" vector satisfying the quantization constraints  $|\bar{z}_i| \leq \Delta/2$ , then the maximum likelihood estimate  $\bar{x}^*$  minimizes

$$(\bar{x}_0 - \bar{x})^T \Lambda_0^{-1} (\bar{x}_0 - \bar{x})$$

subject to the linear constraints

$$\bar{z} - \bar{y} + A\bar{x} = 0.$$

The same solution minimizes the unconstrained scalar function

$$(\bar{x}_0 - \bar{x})^T \Lambda_0^{-1} (\bar{x}_0 - \bar{x}) + \bar{x}^T (\bar{z} - \bar{y} + A\bar{x}) + (\bar{z} - \bar{y} + A\bar{x})^T \bar{x}$$

where  $\bar{x}$  is a column vector of Lagrangian multipliers. The first variation must vanish at the extremal point, and the components of the first variation  $\delta\bar{x}$  are arbitrary. Thus,

$$\bar{x}^* = \bar{x}_0 - \Lambda_0 A^T \bar{\lambda},$$

and

$$\bar{z} - \bar{y} + A\bar{x}_0 - (A\Lambda_0 A^T) \bar{\lambda} = 0$$

from the constraint equations.

If we want to solve for  $\bar{\lambda}$ , we are going to have to invert the matrix  $A\Lambda_0 A^T$ . There are  $n$  observations and  $m$  state parameters, so this matrix is equal to the product of an  $n \times m$  matrix, an  $m \times m$  matrix, and an  $m \times n$  matrix. When  $n > m$ , the product is singular. When  $m = n$  and  $A$  is non-singular

$$(A\Lambda_0 A^T)^{-1} = (A^T)^{-1} \Lambda_0^{-1} A^{-1}$$

If  $n < m$  and the row vectors in  $A$  are linearly independent, then  $A\Lambda_0 A^T$  is invertible. In other words, the number of independent constraints can not exceed the state dimension without overspecifying the solution. When  $n > m$ , as is most often the case, then there will be a minimal subset with observations  $i \leq m$  such that the remaining  $n - i$  observation constraints are satisfied automatically. If  $A_i$  is a matrix with  $i \times m$  linearly independent rows taken from the set  $A_1, \dots, A_n$  and  $\bar{y}_i$  is the corresponding subset of observations from  $\bar{y}$ , then  $\bar{x}$  is an  $i \times 1$  vector given by

$$\bar{x} = (A_i \Lambda_0 A_i^T)^{-1} (\bar{z}_i - \bar{y}_i + A_i \bar{x}_0),$$

the optimal state estimate is

$$\bar{x}^* = \bar{x}_0 - \Lambda_0 A_i^T (A_i \Lambda_0 A_i^T)^{-1} (\bar{z}_i - \bar{y}_i + A_i \bar{x}_0) \quad (9)$$

and the quadratic criterion is

$$\begin{aligned} c &= (\bar{x}_0 - \bar{x}^*)^T \Lambda_0^{-1} (\bar{x}_0 - \bar{x}^*) \\ &= (\bar{z}_i - \bar{y}_i + A_i \bar{x}_0)^T (A_i \Lambda_0 A_i^T)^{-1} (\bar{z}_i - \bar{y}_i + A_i \bar{x}_0) \end{aligned} \quad (10)$$

When  $i = m$ , and  $A_i$  is invertible

$$\bar{x}^* = A^{-1} (\bar{y} - \bar{z})$$

Now, let us convert these formal results into a feasible algorithm. Given the a priori state and no observations, our best estimate of the state is the a priori state itself  $\bar{x}^* = \bar{x}_0$ . We begin by testing the attitude sensor observations  $y_1, \dots, y_i, \dots$ . As long as the sensor constraints

$$\|y_i - A_i \bar{x}^*\| \leq \Delta/2$$

are satisfied,  $\bar{x}^*$  is an adequate state estimate.

In general, each observation maps into two parallel hyperplanes:

$$y_i - A_i \bar{x}^* = \Delta/2$$

and

$$y_i - A_i \bar{x}^* = -\Delta/2$$

A sketch of the constraint boundaries is shown in Fig. 3 for a two dimensional state vector with components  $x_1, x_2$  and origin at  $\bar{x}_0$ . Only two observations are illustrated. Each observation here maps into two parallel lines.

As soon as the number of linearly independent observations equals the dimension of the state space, the region containing the optimum

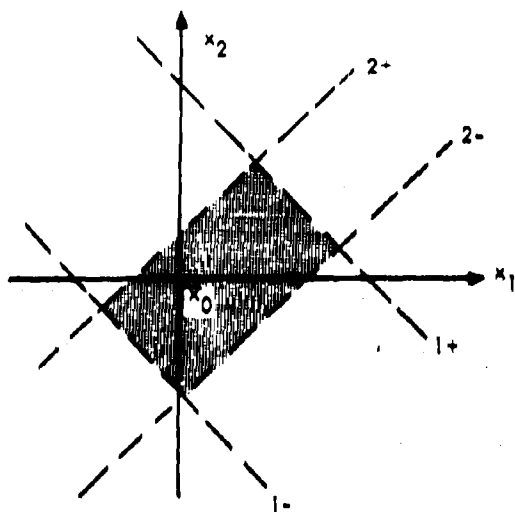


Fig. 3. Constraint Boundaries A

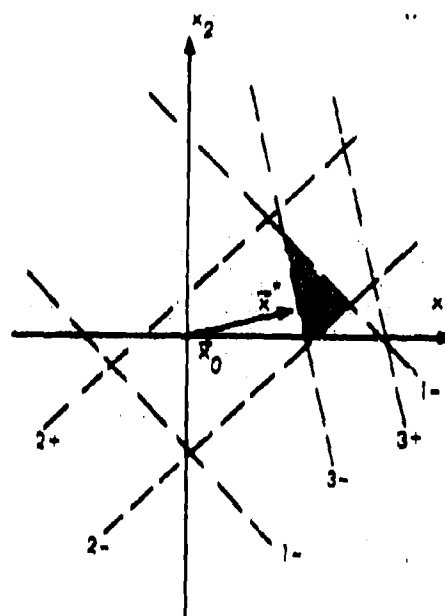


Fig. 4. Constraint Boundaries B

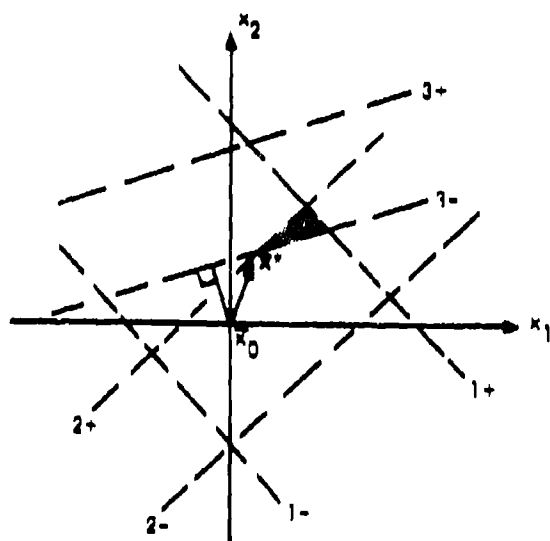


Fig. 5. Constraint Boundaries C

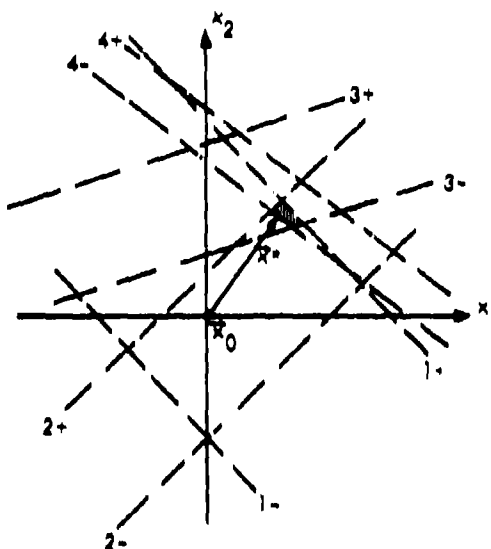


Fig. 6. Constraint Boundaries D

estimate will be bounded. We could delete any observations which lie outside the current bounds by keeping track of the vertices. However, if each observation happens to define new vertices, we might end up with more vertices than observations. Any such deletion scheme should be tailored to the data and dynamic model.

Eventually, we hope there will be an observation  $y_j$  such that

$$\|y_j - A_j \hat{x}^*\| > \Delta_j/2.$$

The new estimate of the optimum state, as defined by Eq. (9) with  $A_i, A_j$ , etc., will lie at the point of tangency between the violated constraint boundary and an a priori equiprobability ellipsoid. Figure 4 illustrates such an optimum for the third observation; the axes are scaled to make the equiprobability ellipses centered at  $\hat{x}_0$  appear circular.

The new candidate for the optimum estimate may violate some of the constraints imposed by the old observations  $1 \leq i \leq j$ . The matrices and vectors used to define the candidate state must be saved. These parameters will be denoted by a subscript  $s$ . The value of the index  $i$  which causes all the other violations to be satisfied must maximize, for all violations computed using  $\hat{x}_s$ , the minimum value of the quadratic criterion along the intersection boundary. For each value of  $i$  associated with a violation, we must define

$$A_\lambda = \begin{Bmatrix} A_s \\ A_i \end{Bmatrix}, \quad \tilde{y}_\lambda = \begin{Bmatrix} \tilde{y}_s \\ y_i \end{Bmatrix}$$

and

$$\tilde{c} = \begin{Bmatrix} \tilde{c}_s \\ c_i \end{Bmatrix}.$$

The number of constraints now is  $i+1$ . Equations (9) and (10) determine the new state estimate  $\hat{x}^*$  and criterion value  $c$  at the intersection. When the criterion value  $c$  for some observation exceeds the maximum criterion value  $c_M$  from previous violations, the current parameters should be saved using the notation  $A_M = A_i$ ,  $y_M = y_i$ ,  $c_M = c_i$ ,  $\hat{x}_M = \hat{x}^*$ , and  $c_M = c$ . Once all the violations by  $\hat{x}_s$  have been tested, we must increment the constraint dimension count and reconstruct the optimum solution by setting

$$A_s = \begin{Bmatrix} A_s \\ A_M \end{Bmatrix}$$

$$\tilde{y}_s = \begin{Bmatrix} \tilde{y}_s \\ y_M \end{Bmatrix}$$

$$\tilde{c}_s = \begin{Bmatrix} \tilde{c}_s \\ c_M \end{Bmatrix}$$

$$\hat{x}_s = \hat{x}_M$$

and

$$i = i+1.$$

A sketch showing the optimum at a vertex is included as Fig. 5. If the dimension of the constraint space  $i$  is equal to the dimension  $m$  of the state vector, then, by hypothesis, the estimate must satisfy all the constraints imposed by observations with indices less than  $i$ . If  $i < m$ , then  $i$  may not be large enough. There may be constraints which are satisfied by the old estimate  $\hat{x}_s$  and not satisfied by  $\hat{x}_M$ . At this point, we must return and begin testing the first observation with the new state estimate.

Eventually, we will either obtain a solution for some  $i < m$  which satisfies all the constraints, or we will increase the dimension of the constraint space until  $i = m$ . Once we satisfy one of these conditions, we can begin testing  $y_{i+1}, \dots$ . However, when one of the new observations in the set  $y_{i+1}, \dots$  violates the observation constraint defined by  $\hat{x}^*$ , we have no guarantee that the optimum lies on a vertex. This possibility is shown in Fig. 6. We must begin again with  $i=1$ . The computational procedure outlined is sequential. The observation base is expanded measurement by measurement, and the current state estimate is either allowed to stand or recomputed to satisfy all the preceding constraints. Unfortunately the observations, once processed, can not be discarded.

A simplified logic flow diagram for a sequential quantized filter is shown in Fig. 7. The most frequently used test loop is made as short as possible by setting  $\Delta_i = \Delta_j$  and  $\Delta_j = 0$  each time a new observation  $y_j$  violates its constraints. For the same reason,  $\Delta_i = \Delta_n$  is saved and  $\Delta_n = 0$ . The basic test on the observation is sufficient to detect the last observation in either case, and tests of  $i=j$  and  $i=n$  may be eliminated from this most frequently used portion of the computational logic.

A flow diagram for a batch version of a computer program for processing quantized data is given in Fig. 8. If the tangent point to the violation which maximizes the criterion function does not produce an estimate satisfying all the observation constraints, then the solution lies on a vertex; the constraint dimension is expanded, and a new optimum is computed. This process of testing and expanding the constraints continues until the constraint and state dimensions are

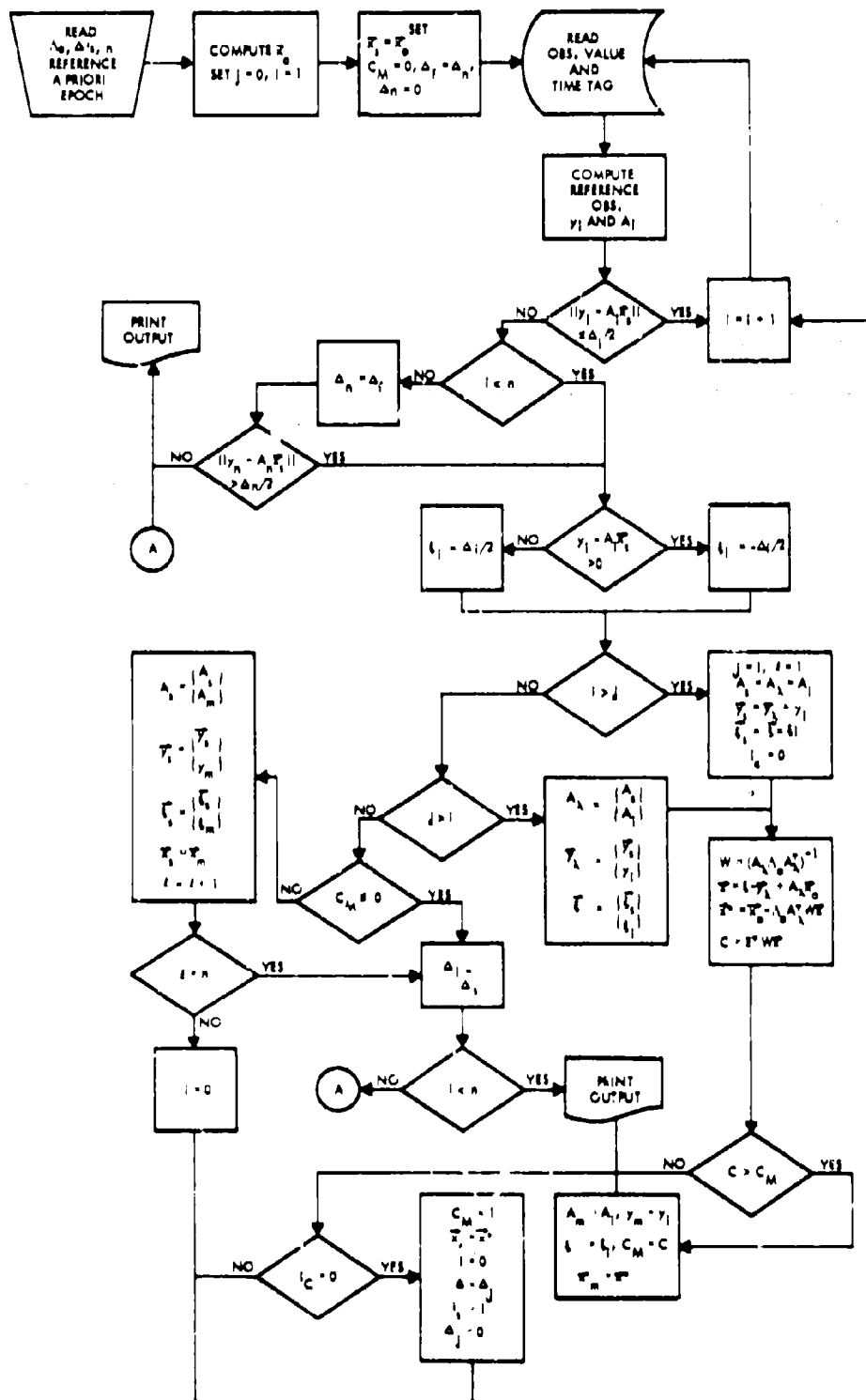


Fig. 7. Quantised Data Sequential Logic



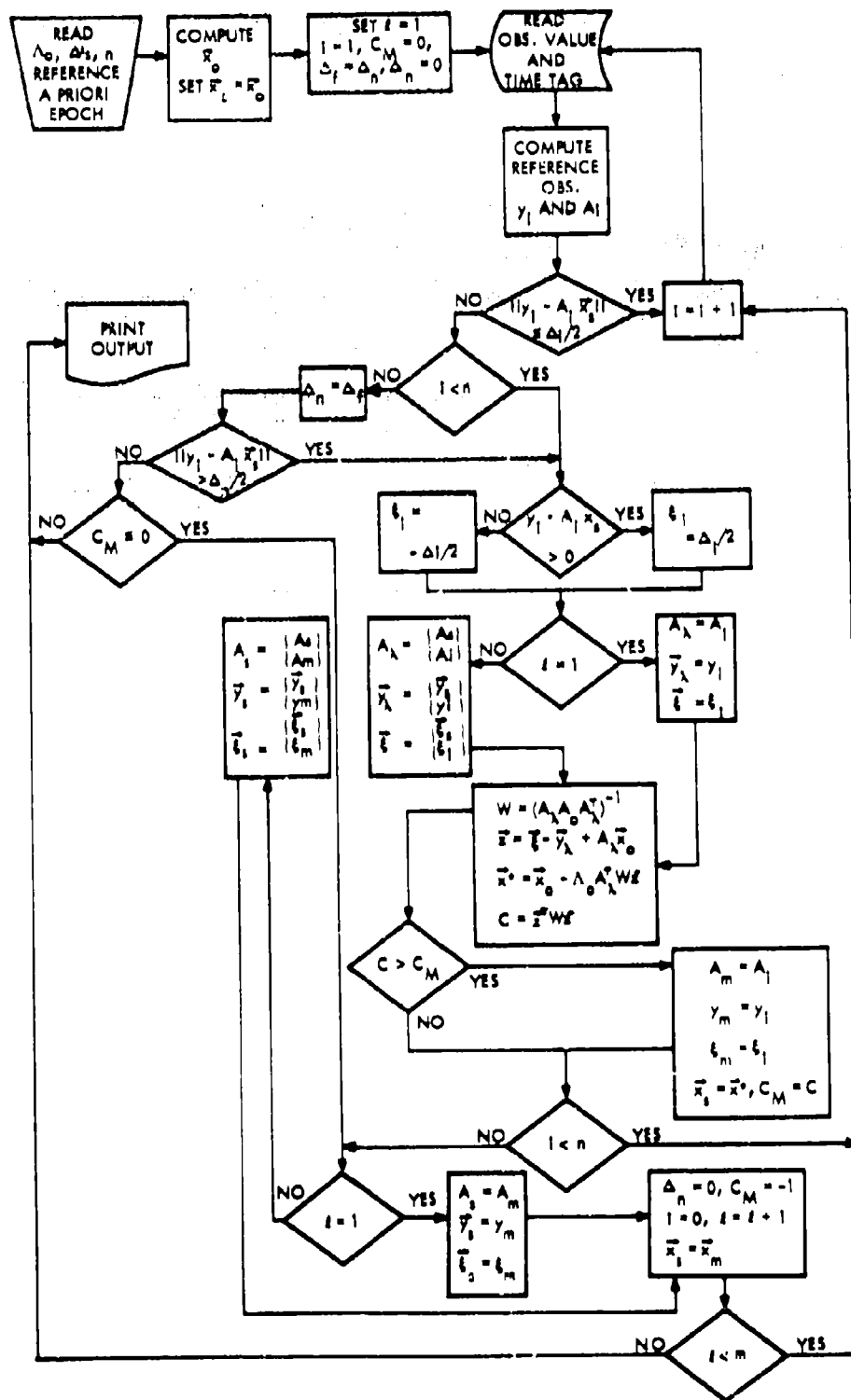


Fig. 8. Quantized Data Batch Logic

equal or until the observation constraints are satisfied. The logic required for these batch computations is a subset of the logic for the sequential algorithm.

In the general multi-dimensional case, there is no simple way to determine the error in the state estimate. The a priori normal density must be integrated over the area enclosed by the quantization constraints. The magnitude of the error is bounded by the distance from the state estimate to the furthest constraint boundary around the region of allowed estimates. A linear Monte Carlo analysis may provide the best means of determining estimation uncertainties, because of the difficulties which would be encountered in trying to construct the bounding surface.

For a one dimensional, static model, the state and observation deviations are constant. The maximum likelihood state estimate is

$$x = \begin{cases} (y - \Delta/2)/a & \text{if } y - ax_0 > \Delta/2 \\ x_0 & \text{if } -\Delta/2 \leq y - ax_0 \leq \Delta/2 \\ (y + \Delta/2)/a & \text{if } y - ax_0 < -\Delta/2 \end{cases}$$

The probability density function is

$$f(x) = \begin{cases} 0 & \text{if } |y - ax| > \Delta/2 \\ (1/\sqrt{2\pi} \sigma_0 k) e^{-(x-x_0)^2/2\sigma_0^2} & \text{otherwise, where} \end{cases}$$

otherwise, where

$$k = \frac{1}{\sqrt{2\pi} \sigma_0} \int_{(y-\Delta/2)/a}^{(y+\Delta/2)/a} e^{-(x-x_0)^2/2\sigma_0^2} dx$$

normalizes the density integral.

As a numerical example, suppose the quantization level  $\Delta/a$  is equal to the a priori standard deviation  $\sigma_0$ , and the observation  $(y/a)$  occurs  $2.5\sigma_0$  units from  $x_0$ . The density function, then, is zero when  $x$  is less than  $2.0\sigma_0$  units or greater than  $3.0\sigma_0$  units from  $x_0$ . The state estimate which maximizes the density is given by

$$x^* = 2.0\sigma_0$$

because

$$2.5\sigma_0 = (y/a) - x_0 > \Delta/a = 0.5\sigma_0.$$

The mean  $\bar{x}$  of the distribution, taken as a state estimate, minimizes the variance

$$\overline{(x-\bar{x})^2}$$

and is located  $2.32\sigma_0$  units from the a priori. The median, or 50% probability point,  $x_{50}$  minimizes the first absolute moment

$$\overline{|x-x_{50}|}$$

taken as a state estimate and is located  $2.26\sigma_0$  units from the a priori. The estimate which minimizes the maximum uncertainty is given by the arithmetic mean of the end points and is located  $2.5\sigma_0$  units from the a priori. The relative virtues of each of these measures of central location taken as a state estimate  $x^*$  depend on what one wants to maximize and where one wants the maximum to occur. The probability of inclusion in a symmetric interval

$$P(|x^* - x| \leq d) = \int_{x^*-d}^{x^*+d} f(x) dx$$

for each of these estimates is shown in Fig. 9 as a function of  $d$ . As expected, the median is the "best" estimate for this criterion up to the point where the symmetric interval extends below the break point in the density function. At high probability levels, the mini-max estimate is best. Because the lower half of the symmetric interval does not contribute anything to the probability interval, the maximum likelihood estimate is never best. On the other hand, we may be more interested in maximizing the probability of inclusion in an interval of fixed length, containing the estimate, with an arbitrary mid-point. This probability

$$P[x \in I(x^*, d)] = \int_I f(x) dx$$

is shown in Fig. 10 for our numerical example. The midpoints have been selected to maximize the probability of inclusion for each of our estimates. With this performance criterion, the maximum likelihood estimate is as good or better than any other possible estimate.

If an algorithm for processing data with normally distributed errors had been used for our example, the estimate would converge eventually to  $(y/a) = 2.5\sigma_0$ . The rate of convergence would depend on the ratio of the hypothetical measurement standard deviation  $\sigma$  to the a priori standard deviation  $\sigma_0$ .

#### IV. QUANTIZED-NORMAL FILTERS

A combination of the two data types covered in the preceding analyses occurs when the attitude sensor signal is contaminated by normally distributed, additive noise and then quantized by digital encoding. This case is particularly interesting in attitude determination problems, because the sensors are usually noisy and design limitations on the satellite communications subsystem usually preclude the use of lengthy digital words for attitude sensor information.

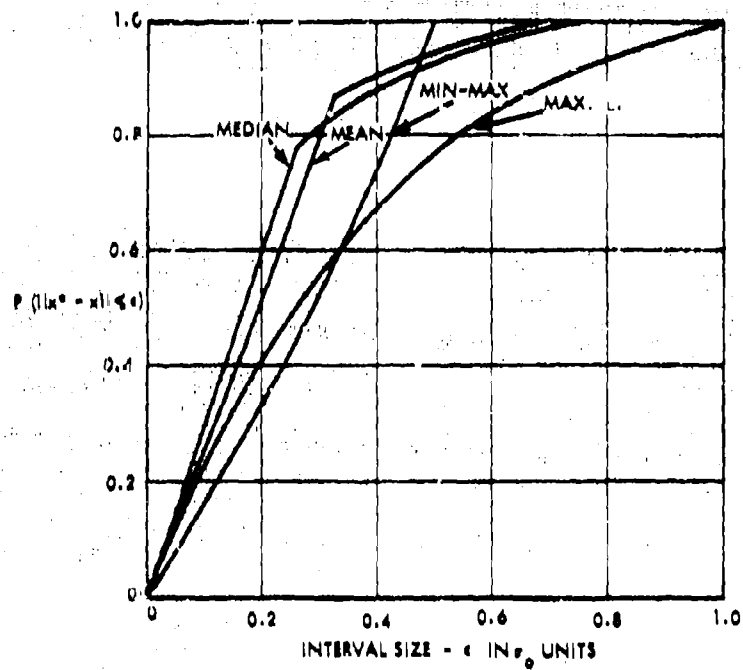


Fig. 9. Probability of Inclusion in an Asymmetric Interval

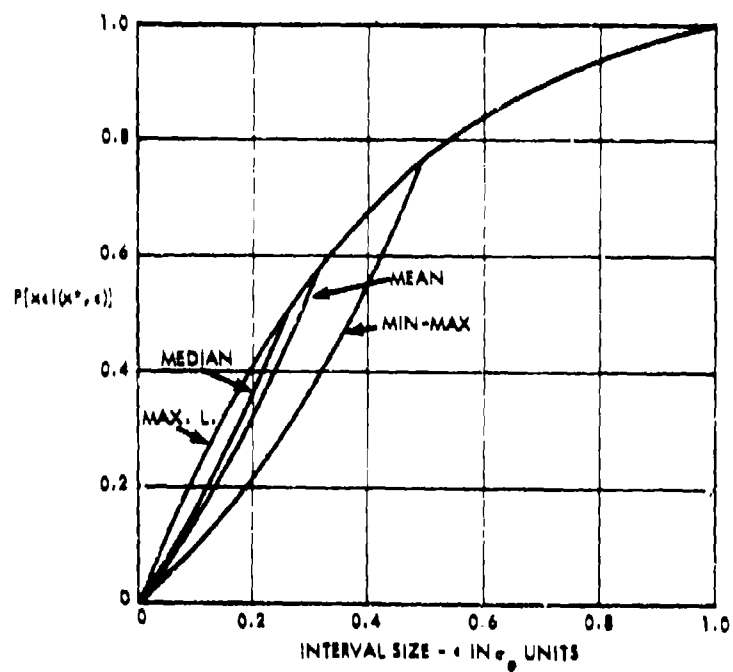


Fig. 10. Probability of Inclusion in a Symmetric Interval

The probability density function for the joint distribution on the a priori state and the quantized-normal sensor noise is given by

$$L(\tilde{x}|\tilde{x}_0, \tilde{y}) = k g_a(\tilde{x}|\tilde{x}_0) g_m(\tilde{x}|\tilde{y})$$

where  $k$  is a normalization constant,

$$g_a(\tilde{x}|\tilde{x}_0) = \exp\left\{-\frac{(\tilde{x}_0 - \tilde{x})^T \Lambda_0^{-1} (\tilde{x}_0 - \tilde{x})}{2}\right\}$$

gives the functional dependence on the a priori estimate, and

$$g_m(\tilde{x}|\tilde{y}) = \int_V \exp\left\{-\frac{(\tilde{y} - A\tilde{x})^T \Lambda^{-1} (\tilde{y} - A\tilde{x})}{2}\right\} d\psi_1 \dots d\psi_n$$

is proportional to the probability that the population parameters defined by  $\tilde{x}$  assume the sample values  $\tilde{y}$ . The volume of integration  $V$  in  $n$  dimensional measurement space is bounded by

$$\tilde{y} \pm \tilde{z}/2$$

the quantization constraints. This is again a combination of the continuous and discrete cases given in Ref. 2. If the sensor measurement errors are uncorrelated, then  $\Lambda$  is a diagonal matrix with trace elements  $\sigma_i^2$ , and

$$g_m(\tilde{x}|\tilde{y}) = \prod_{i=1}^n \int_{y_i - \Delta_i/2}^{y_i + \Delta_i/2} \exp\left\{-\frac{(\psi_i - A_i \tilde{x})^2}{2\sigma_i^2}\right\} d\psi_i$$

As before, in the derivation of the normal filter, the optimum can be found by equating the first variation of the density logarithm to zero. For the measurement contribution,

$$\frac{\delta g_m(\tilde{x}|\tilde{y})}{g_m(\tilde{x}|\tilde{y})} = \frac{\prod_{i=1}^n \int_{y_i - \Delta_i/2}^{y_i + \Delta_i/2} \exp\left\{-\frac{(\psi_i - A_i \tilde{x})^2}{2\sigma_i^2}\right\} d\psi_i}{\int_{y_i - \Delta_i/2}^{y_i + \Delta_i/2} \exp\left\{-\frac{(\psi_i - A_i \tilde{x})^2}{2\sigma_i^2}\right\} d\psi_i}$$

but

$$\begin{aligned} & \int_{y_i - \Delta_i/2}^{y_i + \Delta_i/2} \exp\left\{-\frac{(\psi_i - A_i \tilde{x})^2}{2\sigma_i^2}\right\} d\psi_i \\ &= -\delta \tilde{x}^T A_i^T \int_{y_i - \Delta_i/2}^{y_i + \Delta_i/2} \frac{(\psi_i - A_i \tilde{x})}{\sigma_i^2} \exp\left\{-\frac{(\psi_i - A_i \tilde{x})^2}{2\sigma_i^2}\right\} d\psi_i \end{aligned}$$

$$= -\delta \tilde{x}^T A_i^T \left[ \exp\left\{-\frac{(y_i + \Delta_i/2 - A_i \tilde{x})^2}{2\sigma_i^2}\right\} - \exp\left\{-\frac{(y_i - \Delta_i/2 - A_i \tilde{x})^2}{2\sigma_i^2}\right\} \right]$$

so

$$\begin{aligned} \frac{\delta g_m(\tilde{x}|\tilde{y})}{g_m(\tilde{x}|\tilde{y})} &= -\delta \tilde{x}^T \sum_{i=1}^n \frac{A_i^T \exp\left\{-\frac{(y_i + \Delta_i/2 - A_i \tilde{x})^2}{2\sigma_i^2}\right\} - \exp\left\{-\frac{(y_i - \Delta_i/2 - A_i \tilde{x})^2}{2\sigma_i^2}\right\}}{\int_{y_i - \Delta_i/2}^{y_i + \Delta_i/2} \exp\left\{-\frac{(\psi_i - A_i \tilde{x})^2}{2\sigma_i^2}\right\} d\psi_i} \end{aligned}$$

For the a priori contribution,

$$\frac{\delta g_a(\tilde{x}|\tilde{x}_0)}{g_a(\tilde{x}|\tilde{x}_0)} = -\delta \tilde{x}^T \Lambda_0^{-1} (\tilde{x}_0 - \tilde{x})$$

Thus, the maximum likelihood condition

$$\begin{aligned} \frac{\delta L(\tilde{x}^*|\tilde{x}_0, \tilde{y})}{L(\tilde{x}^*|\tilde{x}_0, \tilde{y})} &= \frac{\delta g_a(\tilde{x}^*|\tilde{x}_0)}{g_a(\tilde{x}^*|\tilde{x}_0)} + \frac{\delta g_m(\tilde{x}^*|\tilde{y})}{g_m(\tilde{x}^*|\tilde{y})} \\ &= 0 \end{aligned}$$

and the restriction that  $\delta \tilde{x}$  is arbitrary imply that the maximum likelihood state estimate  $\tilde{x}^*$  must satisfy the transcendental equation

$$\tilde{x}^* = \tilde{x}_0 - \Lambda_0 \sum_{i=1}^n$$

$$A_i^T \frac{\exp\left\{-\frac{(y_i + \Delta_i/2 - A_i \tilde{x}^*)^2}{2\sigma_i^2}\right\} - \exp\left\{-\frac{(y_i - \Delta_i/2 - A_i \tilde{x}^*)^2}{2\sigma_i^2}\right\}}{\int_{y_i - \Delta_i/2}^{y_i + \Delta_i/2} \exp\left\{-\frac{(\psi_i - A_i \tilde{x}^*)^2}{2\sigma_i^2}\right\} d\psi_i} \quad (11)$$

For the sake of brevity, this condition will be written in the form

$$\tilde{x}^* = \tilde{x}_0 - \Lambda_0 \sum_{i=1}^n A_i^T \phi_i(\tilde{x}^*)$$

where

$$\phi_i(\tilde{x}^*) =$$

$$\frac{\exp\left\{-\frac{(y_i + \Delta_i/2 - A_i \tilde{x}^*)^2}{2\sigma_i^2}\right\} - \exp\left\{-\frac{(y_i - \Delta_i/2 - A_i \tilde{x}^*)^2}{2\sigma_i^2}\right\}}{\int_{y_i - \Delta_i/2}^{y_i + \Delta_i/2} \exp\left\{-\frac{(\psi_i - A_i \tilde{x}^*)^2}{2\sigma_i^2}\right\} d\psi_i}$$

On the surface, at least, Eq. (11) seems to be amenable to solution by Newtonian iteration. We shall denote the right-hand side of Eq. (11) by  $\tilde{z}(\tilde{x}^*)$ . From a state vector estimate  $\tilde{x}_{B-1}^*$  we may compute  $\tilde{z}(\tilde{x}_{B-1}^*)$ . Expansion of  $\tilde{x}_B^*$ , the improved state estimate, in a first order series yields

$$\tilde{x}_B^* = \tilde{z}(\tilde{x}_{B-1}^*) + \left. \frac{\partial \tilde{z}(\tilde{x}^*)}{\partial \tilde{x}^*} \right|_{\tilde{x}_{B-1}^*} (\tilde{x}_B^* - \tilde{x}_{B-1}^*)$$

By differentiation of Eq. (11),

$$\begin{aligned} \frac{\partial \tilde{z}(\tilde{x}^*)}{\partial \tilde{x}^*} &= -\Lambda_0 \sum_{i=1}^n A_i^T \frac{\partial \phi_i(\tilde{x}^*)}{\partial \tilde{x}^*} \\ &= -\Lambda_0 \sum_{i=1}^n A_i^T W_i(\tilde{x}^*) A_i \end{aligned}$$

where

$$\begin{aligned} W_i(\tilde{x}^*) &= \frac{(y_i + \Delta_i/2 - A_i \tilde{x}^*) e^{-(y_i + \Delta_i/2 - A_i \tilde{x}^*)^2 / 2\sigma_i^2} - (y_i - \Delta_i/2 - A_i \tilde{x}^*) e^{-(y_i - \Delta_i/2 - A_i \tilde{x}^*)^2 / 2\sigma_i^2}}{\sigma_i^2 \int_{y_i - \Delta_i/2}^{y_i + \Delta_i/2} e^{-(\psi_i - A_i \tilde{x}^*)^2 / 2\sigma_i^2} d\psi_i} \\ &+ \left[ \frac{-(y_i + \Delta_i/2 - A_i \tilde{x}^*)^2 / 2\sigma_i^2}{\int_{y_i - \Delta_i/2}^{y_i + \Delta_i/2} e^{-(\psi_i - A_i \tilde{x}^*)^2 / 2\sigma_i^2} d\psi_i} - \frac{-(y_i - \Delta_i/2 - A_i \tilde{x}^*)^2 / 2\sigma_i^2}{\int_{y_i - \Delta_i/2}^{y_i + \Delta_i/2} e^{-(\psi_i - A_i \tilde{x}^*)^2 / 2\sigma_i^2} d\psi_i} \right] 2 \end{aligned} \quad (12)$$

Thus, the improved state estimate is given by

$$\tilde{x}_B^* = \tilde{x}_{B-1}^* + \left[ \Lambda_0^{-1} + \sum_{i=1}^n A_i^T W_i(\tilde{x}_{B-1}^*) A_i \right]^{-1} \Lambda_0^{-1} [\tilde{z}(\tilde{x}_{B-1}^*) - \tilde{x}_{B-1}^*] \quad (13)$$

This expression may be put in a more convenient form. First of all, we may let  $\tilde{x}_0 = \tilde{x}_{B-1}^*$  be our reference state estimate, substitute for  $\tilde{z}(\tilde{x}_0)$ , and perform some algebraic manipulations; then,

$$\begin{aligned} \tilde{x}^* &= [\Lambda_0^{-1} + \sum_{i=1}^n A_i^T W_i(\tilde{x}_0) A_i]^{-1} (\Lambda_0^{-1} \tilde{x}_0 + \\ &+ \sum_{i=1}^n A_i^T [W_i(\tilde{x}_0) A_i \tilde{x}_0 - \phi_i(\tilde{x}_0)]) \end{aligned} \quad (14)$$

In the limit as  $\Delta_i$  approaches zero,  $W_i(\tilde{x}_0)$  approaches  $(1/\sigma_i^2)$  and  $\phi_i(\tilde{x}_0)$  approaches  $-(y_i - A_i \tilde{x}_0)/\sigma_i^2$ . Equation (14), then, is analogous to Eq. (8) with  $W_i(\tilde{x}_0)$  replacing  $(1/\sigma_i^2)$  in the normal matrix and

$$W_i(\tilde{x}_0) A_i \tilde{x}_0 - \phi_i(\tilde{x}_0)$$

replacing  $y_i/\sigma_i^2$  in the numerator summation.

A computational procedure similar to the Kalman filter, Eqs. (7) and (8), is needed to complete the analogy between normal and quantized-normal filters. After a large number of observations have been taken, the state estimate should be fairly stable. The state estimate  $\tilde{x}_n$  after  $n$  measurements and the state estimate  $\tilde{x}_{n-1}$  after  $n-1$  measurements should be nearly equal. After  $n-1$  measurements, the transcendental maximum likelihood condition is given by

$$\tilde{x}_{n-1}^* = \tilde{x}_0 - \Lambda_0 \sum_{i=1}^{n-1} A_i^T \phi_i(\tilde{x}_{n-1}^*)$$

For  $n$  measurements,

$$\begin{aligned} \tilde{x}_n^* &= \tilde{x}_0 - \Lambda_0 \sum_{i=1}^n A_i^T \phi_i(\tilde{x}_n^*) \\ &= \tilde{x}_{n-1}^* - \Lambda_0 \sum_{i=1}^{n-1} A_i^T [\phi_i(\tilde{x}_n^*) - \phi_i(\tilde{x}_{n-1}^*)] - \Lambda_0 A_n^T \phi_n(\tilde{x}_{n-1}^*) \\ &\approx \tilde{x}_{n-1}^* - \Lambda_0 \sum_{i=1}^{n-1} A_i^T W_i(\tilde{x}_{n-1}^*) A_i (\tilde{x}_n^* - \tilde{x}_{n-1}^*) - \Lambda_0 A_n^T \phi_n(\tilde{x}_{n-1}^*) \end{aligned}$$

Solution for  $\tilde{x}_n^*$  yields

$$\tilde{x}_n^* = \tilde{x}_{n-1}^* - [\Lambda_0^{-1} + \sum_{i=1}^n A_i^T W_i(\tilde{x}_{n-1}^*) A_i]^{-1} A_n^T \phi_n(\tilde{x}_{n-1}^*)$$

This expression is not what we want to see. Because of computational difficulties, we may not wish to return and evaluate  $W_i(\tilde{x}_{n-1}^*)$  for each observation. The error introduced when  $W_i(\tilde{x}_{n-1}^*)$  is replaced by  $W_i(\tilde{x}_0)$  should be small, because  $W_i(\tilde{x}_0)$  is a first derivative. If  $W_i(\tilde{x})$  does depend strongly on the state, the linearization is invalid anyway. With this approximation, we may define

$$\Lambda_{n-1}^{-1} = \Lambda_0^{-1} + \sum_{i=1}^{n-1} A_i^T W_i(\bar{x}_{i-1}^*) A_i.$$

so

$$\begin{aligned}\Lambda_n^{-1} &= \Lambda_0^{-1} + \sum_{i=1}^n A_i^T W_i(\bar{x}_{i-1}^*) A_i \\ &= \Lambda_{n-1}^{-1} + A_n^T W_n(\bar{x}_{n-1}^*) A_n.\end{aligned}$$

By the Shur Identity,

$$\Lambda_n = \Lambda_{n-1} - \frac{\Lambda_{n-1} A_n^T \Lambda_{n-1}^{-1} A_n \Lambda_{n-1}}{A_n \Lambda_{n-1}^{-1} A_n + W_n^{-1}(\bar{x}_{n-1}^*)} \quad (15)$$

and the maximum likelihood state estimate is given by

$$\bar{x}_n^* = \bar{x}_{n-1}^* - \frac{\Lambda_{n-1}^{-1} A_n^T W_n^{-1}(\bar{x}_{n-1}^*) y_n(\bar{x}_{n-1}^*)}{A_n \Lambda_{n-1}^{-1} A_n + W_n^{-1}(\bar{x}_{n-1}^*)} \quad (16)$$

These expressions are analogous to the normal sequential filter, Eqs. (7) and (8). In the limit as the quantization vanishes,  $W_n^{-1}(\bar{x}_{n-1}^*)$  in the denominator approaches  $\sigma^2$ , while the scalar  $W_n^{-1}(\bar{x}_{n-1}^*) y_n(\bar{x}_{n-1}^*)$  in the numerator approaches  $y_n - A_n \bar{x}_{n-1}^*$ .

In view of the similarity between the normal and quantized normal filters, the batch and sequential logics described in Figs. (1) and (2) will be applicable in the quantized-normal case too. Newtonian iteration using Eq. (11) should be avoided if possible, because of the computer time cost. If non-linearities are severe, the implicit dynamic non-linearities and the explicit transcendental non-linearities in the maximum likelihood condition might be reduced simultaneously using an iterative batch logic.

Estimation uncertainties for the quantized-normal filter will not follow a normal distribution unless some simplifying assumptions are made regarding the size of the quantization. In general, a linear Monte Carlo analysis would seem to provide the most convenient means of accurately evaluating filter performance.

According to Cramer, Ref. 2, the correction to the mean for grouped data vanishes to terms of order four in  $\Delta$ . This approximation is no longer valid when the quantization and measurement standard deviation are comparable in magnitude. In theory, at least, the quantized-normal filter will converge to the correct answer as the number of observations increases. However, if the normal filter were used to process quantized-normal data, the estimate might contain residual biases, even when the number of observations is infinite. In the limit, the a priori is swamped,

and the normal filter estimate for a one dimensional static model with a single observation type approaches

$$x^* = \frac{1}{\Delta n} \sum_{i=1}^n y_i.$$

The quantized data may be broken into groups. Each group will correspond to one of the allowed observations  $y_k$ . The normal filter estimate will approach

$$x^* = \frac{1}{\Delta} \sum_k p_k y_k,$$

where

$$p_k = \frac{1}{\sqrt{2\pi} \sigma} \int_{y_k - \Delta/2}^{y_k + \Delta/2} e^{-(y - ax)^2 / 2\sigma^2} dy$$

is the probability of being in the  $k$ th group. Each group has the same quantization level  $\Delta$  and the variance  $\sigma^2$  is the same for all observations. If the samples are symmetrical about their true mean, the normal filter will be asymptotically exact. If the samples are not symmetrical, a normal filter acting on quantized-normal data will leave a bias error in the estimate. Numerical calculations have been carried out for two examples:  $\Delta/\sigma = 1.0$  with the mean offset by  $-0.25\sigma$  and  $\Delta/\sigma = 4.0$  with the mean offset by  $-1.0\sigma$ . For  $\Delta/\sigma = 1.0$ , the residual bias was  $0.045\sigma$ , and, for  $\Delta/\sigma = 4.0$ , the residual bias was  $0.37\sigma$ .

The estimation of parameters in a distribution of known form via the  $\chi^2$ -minimum method is discussed by Cramer in Ref. 2. A priori statistics are not used, the relationship between the state and sample data is static, and only one data type is considered. Under these assumptions, our transcendental maximum likelihood condition may be written in the form

$$\sum_{i=1}^k A_0 \left[ \frac{e^{-(y_i + \Delta/2 - A_0 \bar{x}^*)^2 / 2\sigma^2}}{\int_{y_i - \Delta/2}^{y_i + \Delta/2} e^{-(y - A_0 \bar{x}^*)^2 / 2\sigma^2} dy} - \frac{e^{-(y_i - \Delta/2 - A_0 \bar{x}^*)^2 / 2\sigma^2}}{\int_{y_i - \Delta/2}^{y_i + \Delta/2} e^{-(y - A_0 \bar{x}^*)^2 / 2\sigma^2} dy} \right] = 0$$

where  $A_0$  is the common value of the  $A_i$ . If the summation is taken over  $k$  quantum groups, we have

$$\sum_k v_k A_0 \left[ \frac{e^{-(y_k + \Delta/2 - A_0 \bar{x}^*)^2 / 2\sigma^2}}{\int_{y_k - \Delta/2}^{y_k + \Delta/2} e^{-(y - A_0 \bar{x}^*)^2 / 2\sigma^2} dy} - \frac{e^{-(y_k - \Delta/2 - A_0 \bar{x}^*)^2 / 2\sigma^2}}{\int_{y_k - \Delta/2}^{y_k + \Delta/2} e^{-(y - A_0 \bar{x}^*)^2 / 2\sigma^2} dy} \right] = 0$$

where  $v_k$  is the number of observations in the  $k$ th group. The integral in the denominator is

proportional to the probability of inclusion  $p_k$  in the  $k$ th group, and the product of  $A_0$  with the difference of the exponential terms in the numerator is proportional to the partial of the probability  $p_k$  with respect to the state. Thus, the condition on the estimate may be written

$$\sum_k \frac{v_k}{p_k} \frac{\partial p_k}{\partial x^*} = 0.$$

If there are  $m$  state components, this equation provides us with  $m$  conditions which the state must satisfy. The quantity  $\partial p_k / \partial x^*$  is an  $m \times 1$  row vector. This result is identical to Eq. 30.3.3a of Ref. 2.

### V. CONCLUSIONS

When estimation accuracy is critical and the attitude sensor data are subject to quantization constraints, the errors introduced by processing quantized or quantized-normal data with a sub-optimal normal filter may be intolerable. On the basis of the preceding analyses, there are promising computational procedures for finding maximum likelihood attitude state estimates in cases where quantization occurs but the data are otherwise error free and in cases where the data are quantized after being sampled from a normal population. These algorithms are comparable in generality and flexibility to the normal filters commonly used for trajectory or attitude estimation. Unfortunately, they are also more complex.

One most significant conclusion is the equivalence in form between the normal and quantized-normal logic flows. Any computer program designed to process normal data can be easily modified, if necessary, to handle quantized-normal data.

Some potentially interesting research topics, with practical applications, appear to have been discovered during this study.

- Although a linear Monte Carlo analysis does provide a way to evaluate estimation uncertainties, there may be others, less obvious but more satisfying.
- Because of their complexity, the accuracy enhancement capability of these filters should be tested for each new potential application. The estimation accuracy requirements for the application in question may not be stringent enough to warrant their use.
- The convergence properties of the proposed algorithms should be studied.
- The amount of data processed by a quantized filter could possibly be reduced by keeping track of the

bounding vertices. The logic to perform this task, if available, could also be used to provide error bounds.

- Finally, the maximum likelihood estimate may be the most desirable in some applications but not in others. For quantized and quantized-normal data, algorithms which compute the expected state or the state which minimizes the first absolute moment are not yet available, even though their potential virtues are clear.

### REFERENCES

1. C. B. Solloway, Elements of the Theory of Orbit Determination, Jet Propulsion Laboratory, EPD-265, Pasadena, California (9 December 1964).
2. Harold Cramer, Methods of Mathematical Statistics (Princeton University Press, 1961).
3. T. A. Magness and J. B. McGuire, Statistics of Orbit Determination-Correlated Observations, Space Technology Laboratories Document No. 8976-6001-RU-000 (15 December 1961).
4. David D. Morrison, "Methods for Non-Linear Least Squares Problems and Convergence Proofs," Seminar Proceedings, Tracking Programs and Orbit Determination (Jet Propulsion Laboratory, Pasadena, California, 23-26 February 1960).
5. T. A. Magness and J. B. McGuire, Statistics of Orbit Determination-Weighted Least Squares, Space Technology Laboratories Document No. 8976-6002-RU-000.
6. W. B. Galle, Elimination of States due to Bias in a Kalman Filter, A. C. Electronics Division, General Motors Corp., Memorandum 48-480-m (8 July 1966).
7. Irwin Ira Shapiro, The Prediction of Ballistic Missile Trajectories from Radar Observations (McGraw-Hill, New York, 1958).
8. R. S. Bucy and P. D. Joseph, Filtering for Stochastic Processes with Applications to Guidance (Interscience Publishers, 1968).
9. Barry H. Whalen, Linear Programming for Optimal Control (Doctoral Dissertation, University of California, Berkeley, California, 1962).
10. T. C. Koopmans, ed., Activity Analysis of Production and Allocation (Wiley, New York, 1951) Chapter XXI, G. B. Dantzig.

# APPLICATIONS OF NONLINEAR ESTIMATION THEORY TO SPACECRAFT ATTITUDE DETERMINATION SYSTEMS<sup>1</sup>

D. B. Jackson  
Space Flight Systems, Aerospace Division  
Honeywell, Inc.  
Minneapolis, Minnesota  
and  
Office of Control Theory and Application  
NASA Electronics Research Center  
Cambridge, Massachusetts

## ABSTRACT

This paper describes the application of some recent developments in stochastic estimation theory to the mechanization of strapdown attitude reference systems for spacecraft. The attitude reference problem statement and the growing need for a nonlinear formulation are briefly reviewed, along with some applicable elements of nonlinear estimation theory. Several alternate attitude reference mechanizations are outlined, and then some state variable, state measurement, and noise modeling considerations, coupled with computational estimates, are shown to dictate a clear-cut preference for a particular mechanization. A typical configuration for an advanced spacecraft attitude reference system is then postulated, and some simulation results of the performance of this system are presented. The simulation results show that the moment-approximating approach to nonlinear estimation results in better system performance than several other approaches for the class of nonlinearities found in attitude reference system equations.

## 1. INTRODUCTION

Linear optimal filtering theory (Refs. 1,2) has played an important role in the field of spacecraft trajectory determination since about 1962 (Ref. 3). Since that time, linear filtering has had important applications in the aerospace areas of celestial space navigation, aircraft navigation, reentry vehicle trajectory estimation, orbit determination, launch vehicle ascent guidance, and different types of system error analysis. There have been important non-aerospace applications as well. Recently, the need for high precision spacecraft attitude determination has led to the application of real-time linear filtering in this area (Ref. 4). The latter use of linear filtering has been made possible by the advent of the small, low power, flight-weight general purpose digital computer.

The Kalman-Bucy linear filtering theory works very well for small angle precision attitude reference, since the

necessary assumptions of linearity are very good. However, for the more general class of spacecraft attitude reference systems, assumptions of linearity break down. For all-attitude or large angle maneuvering systems, the equations of motion become highly nonlinear. For less precise systems, assumptions of small deviations from a nominal attitude trajectory break down. For gyroless systems, a nominal trajectory about which one can linearize coefficients is not available. Therefore, a universally applicable attitude reference filtering mechanization should be based on a nonlinear formulation if possible. This nonlinear formulation should also have the property that it reduces to the classical linear mechanization in the limit.

The estimation philosophy that is followed in this paper is based on entirely Bayesian models for the state and observation noise processes, and the estimation criteria will be minimum

<sup>1</sup>This work was supported in part by the NASA Electronics Research Center's Senior Residence Program in the Office of Control Theory and Application (OCTA).



variance with the best estimate defined as the conditional mean. There are a number of other estimation criteria and noise models which have been studied in the literature. For instance, Kushner (Ref. 5) and Pfeiffer, et al. (Ref. 6) have studied filters whose estimate is the mode of the conditional density (maximum likelihood estimation), and LaMay (Ref. 7) and Schweppe (Ref. 8) have studied the propagation of possible state boundaries when the inputs are describable in a set-theoretic context instead of a probabilistic framework.

However, for the attitude reference problem at hand, the Bayesian minimum variance formulation is appealing for several reasons. First, it turns out that most modern inertial component errors can be modeled nicely in terms of deterministic and probabilistic processes. Also, the minimum estimation variance criterion leads to a formal filter which involves expectations of products of process, observation, and state components. When Euler's quaternion parameters or direction cosines are used to describe the attitude state components, this expectation operation leads to integrals of products of state variables and marginal conditional densities that never have to be integrated explicitly.

When the attitude dynamics are represented by nonlinear differential equations and nonlinear state measurements are assumed, it can be shown that the state probability density function, conditioned on all the past measurements, satisfies a partial differential equation similar to Kolmogorov's forward equation. Using this result and the Itô calculus, it is possible to derive the differential equations for all the moments of the conditional density. The formal details are given in Kushner (Ref. 9).

The problem with implementing an attitude estimator based on this formulation is that expectations of functions at least cubically nonlinear in the state are involved. Therefore, these expectation terms are functions of higher moments. In turn, the differential equations for these higher moments involve still higher moments, etc., and the exact solution would require an infinite number of differential equations. In most of the literature on nonlinear estimation, the infinite dimensional problem is resolved by expanding nonlinear functions in Taylor series about the expected value of the state and truncating the series. However, for the attitude estimation problem at hand, it is unnecessary to invoke arguments about the higher order terms of series expansions being

negligible. Rather, only certain plausible arguments about the shape of the conditional probability density function are necessary.

Based on this approach, the paper describes the formulation of a comprehensive attitude reference mechanization capable of being implemented in real time in a spacecraft computer. The formulation is general enough to accommodate any combination of discrete and continuous attitude and angular rate measurements. A typical configuration for an advanced spacecraft attitude reference system is then described. The performance of this system in the face of various levels of state and observation noise is demonstrated by showing a number of results from a digital simulation of the system. Some non-theoretical questions are then briefly discussed relating to the practicality of the system postulated.

## II. ANALYSIS

### A. Attitude Reference Problem Statement and Background

The fundamental point from which most state-of-the-art precision spacecraft attitude reference system syntheses proceed is the assumption of three-axis body angular rate information, usually in the form of a three-axis, strapped down, single degree-of-freedom gyro package. Experience on a number of programs of this nature has indicated that this is the best and often the only method of achieving precision, wide bandwidth attitude information in a benign environment when the heavily weighted parameters are simplicity, high precision, and reliability. The output from this triad will be continuous analog voltages or trains of digital rebalance pulses. These output signals are then integrated on a three-axis transformation basis to obtain a continuous indication of inertial attitude.

The basic problem which must be solved in any attitude reference system of this type is the bounding of the long-term attitude errors. These errors are caused primarily by gyro drift and scale factor uncertainties and by integration algorithm imperfections. Therefore, some method of periodically injecting direct attitude information into the attitude reference system is necessary. To illustrate the dynamics of the situation, consider Fig. 1.

The system illustrated in this figure is a single-axis system which has all the salient error propagation features of more sophisticated three-axis systems.

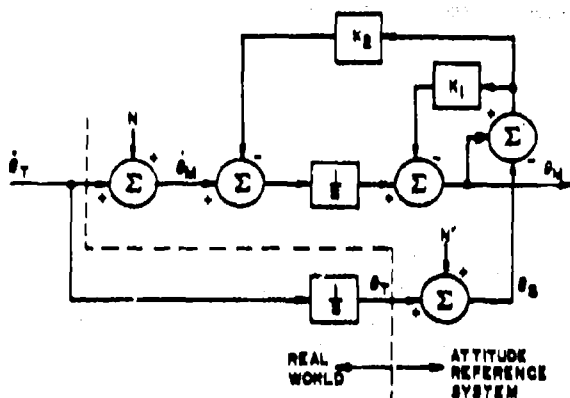


Fig. 1. Single-axis Attitude Reference System

True vehicle rate,  $\dot{\theta}_T$ , is corrupted by gyro noise and biases ( $N$ ) and appears to the system as  $\dot{\theta}_M$ . This is integrated continuously to obtain a running measure of true attitude,  $\theta_M$ . To bound  $\theta_M$ , periodic or continuous measurements are made of attitude ( $\theta_T$ ) directly. These measurements are also corrupted by sensor noise ( $N'$ ) and the attitude measurements appear to the system as  $\theta_s$ .  $\theta_s$  is then compared to  $\theta_M$  and the difference is used to generate feedback signals to trim the attitude and rate estimates. An error block diagram corresponding to the above system appears in Fig. 2.

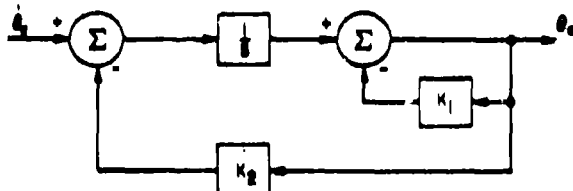


Fig. 2. Single-axis Error Block Diagram

The transfer function for systems of this type is

$$\frac{\theta_e}{\dot{\theta}_T} = \frac{1/K_2}{\frac{(1+K_1)}{K_2} + 1} \quad (1)$$

Therefore, the effect of adding the attitude measurement sequence  $\theta_M$  was to change the attitude error frequency response characteristics from those shown in Fig. 3 (a) to those in Fig. 3 (b). In other words, when attitude measurements are added the effects of low frequency and d-c rate measurement errors are no longer catastrophic. The situation is slightly more complicated when attitude

measurements are received only at discrete points in time, instead of on a continuous basis. This type of system has an error dynamics system that can be approximated as a sampled data control system. Such a representation is shown in Fig. 4.

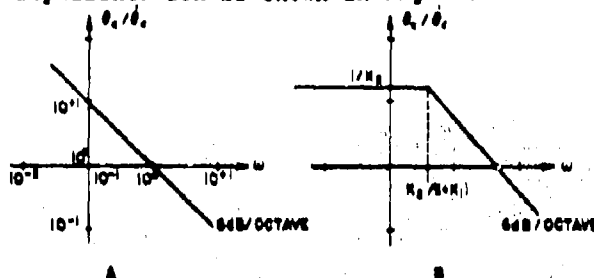


Fig. 3. Attitude Error Frequency Response Characteristics

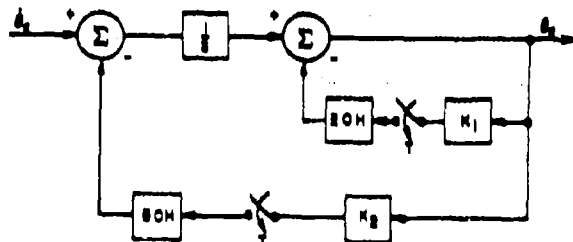


Fig. 4. Single-axis Block Diagram -- Sampled Data Case

It is possible to analyze this type of a system by s-transform and w-plane techniques. This analysis yields error frequency response characteristics that have periodic behavior at half the sampling frequency for the sampled attitude signal. For the continuous attitude error signal in this system, modified s transforms could be used to obtain the frequency response and other characteristics.

This discussion was simply included to indicate that a given attitude reference system mechanization requires knowledge not only of the magnitude of the measured angular rate null offset and noise, but also knowledge of its spectral characteristics in order to predict attitude error values of the system. It is clear from Fig. 3 that a bounded attitude reference system is less sensitive to high-frequency noise than it is to low-frequency noise, due to the inherent smoothing in the attitude integration. When mechanizing an attitude reference system of this type, the following questions must be answered.

- (1) What components of gyro drift rate and attitude measurement error influence the accuracy of

an updated attitude reference system, and what are the mathematical relationships that describe the dependence of system error on those components?

- (2) Given the answer to the first question, how should the attitude reference system be mechanized to minimize some measure of system error, i.e., how should the feedback gains be chosen as a function of initial condition errors and time?

Extensive laboratory testing and analytical modeling studies have been performed recently for precision inertial sensors (Ref. 4). The results of these studies indicate that in the frequency range of interest, precision rate and attitude instruments of the type being used in current systems have random error characteristics that can be modeled quite accurately as normally distributed white random processes. This fortunate circumstance allows one to turn effectively to the extensive literature on linear and nonlinear stochastic estimation theory to implement a system in some "optimal" sense.

## B. Applicable Elements of Nonlinear Estimation Theory

This subsection will review briefly some of the concepts of nonlinear estimation theory that have a bearing on the attitude reference problem. It should be viewed as a skimpy and nonrigorous summary. For extensive and mathematically satisfying expositions of the subject, refer to Kushner (Refs. 10, 11), Wonham (Ref. 12), Bucy (Ref. 13), Ho and Lee (Ref. 14), and Pfeiffer, et al., (Ref. 6).

As stated in the introduction, the process and observation noise models are Bayesian and the estimation criterion is minimum estimation error variance, with the best state estimate therefore being the mean of the conditional probability density function. Specifically, the differential equation describing the evolution of the state of the dynamical system is

$$dx(t)/dt = F[x(t), t] + G(t) w(t) \quad (2)$$

$$x(0) = x_0 \quad (3)$$

where  $x$  and  $F$  are  $n \times 1$ ,  $G$  is  $n \times k$ , and  $w(t)$  is a  $k \times 1$  zero-mean white Gaussian noise

process with

$$E[w(t)w'(\tau)] = Q(t)\delta(t-\tau) \quad (4)$$

where  $\delta(\cdot)$  is the Dirac delta. The case where  $Q$  depends explicitly on  $x(t)$  will not be studied, as this leads to a lengthy and subtle argument about the difference between the Itô calculus and Stratonovich calculus for the differentials of functions of solutions of stochastic differential equations. Anyway, this generality will not be needed for the problem at hand.

The problem is to continuously estimate the state  $x(t)$  from the corrupted observations

$$y(t) = H[x(t), t] + v(t) \quad (5)$$

where  $y$  and  $H$  are  $l \times 1$  and  $v(t)$  is an  $l \times 1$  zero-mean white Gaussian noise process with

$$E[v(t)v'(\tau)] = R(t)\delta(t-\tau) \quad (6)$$

$Q$  and  $R$  are assumed to be real symmetric positive definite (RSPD) matrices, and in addition it is assumed that

$$E[x(0)w'(t)] = 0 \quad (7)$$

$$E[x(0)v'(t)] = 0 \quad (8)$$

$$E[w(t)v'(\tau)] = 0, \forall t, \tau \geq 0 \quad (9)$$

$x(0)$  is a Gaussian process with mean  $\bar{x}_0$  and

$$E\{[x(0) - \bar{x}_0][x_0(0) - \bar{x}_0]'\} \triangleq P_0 = P_0 \quad (10)$$

where  $P_0$  is RSPD. Under the above assumptions, it can be shown (Ref. 11) that the probability density function, conditioned on all the past measurements, which describes the distribution of  $x(t)$  satisfies the following partial differential equation:

$$\frac{\partial p}{\partial t} = - \sum_{i=1}^n \frac{\partial}{\partial x_i} (F_i p) + \frac{1}{2} \sum_{i,j=1}^n \frac{\partial^2}{\partial x_i \partial x_j} (G_i G_j' p) + P_0 \cdot (y(t) - E[H(x, t)])' E^{-1}(t) (H(x, t) - E[H(x, t)]) \quad (11)$$

where

$$P_0 dx_1 \dots dx_n = P(x_1, \dots, x_n) C(x_1 + dx_1, \dots, x_n + dx_n) | \chi(a), 0 \leq a \leq t \quad (12)$$

(This partial differential equation without the last term (observations) is the Fokker-Plank-Kolmogorov equation for the forward evolution of the unconditional density.) Using this result and the Itô calculus, it is possible to derive the differential equations for all the moments of  $P$ . The formal details are given in Kushner (Ref. 9). The results for the first two moments can be expressed in a compact notation which is suggested by Jaswinski (Ref. 15). The conditional mean and covariance differential equations are given by

$$\begin{aligned} \frac{d\bar{x}(t)/dt}{} &= \bar{H}(t)\bar{x}(t) \\ &+ [\bar{H}(t)\bar{G}(t)\bar{G}(t)^T - \bar{H}(t)\bar{G}(t)\bar{G}(t)^T] \bar{x}(t) + \bar{H}(t)\bar{G}(t) \quad (13) \\ \frac{dP(t)/dt}{} &= [\bar{H}(t)\bar{G}(t)\bar{G}(t)^T - \bar{H}(t)\bar{G}(t)\bar{G}(t)^T] P(t) + \bar{H}(t)\bar{G}(t) \\ &+ \bar{H}(t)\bar{G}(t) + \bar{H}(t)\bar{G}(t)\bar{G}(t)^T \\ &+ [\bar{H}(t)\bar{G}(t)\bar{G}(t)^T - \bar{H}(t)\bar{G}(t)\bar{G}(t)^T] \bar{x}(t) + \bar{H}(t)\bar{G}(t) \\ &+ [\bar{H}(t)\bar{G}(t)\bar{G}(t)^T - \bar{H}(t)\bar{G}(t)\bar{G}(t)^T] \bar{x}(t) \\ &+ \bar{H}(t)\bar{G}(t)\bar{G}(t)^T - \bar{H}(t)\bar{G}(t)\bar{G}(t)^T \\ &+ \bar{H}(t)\bar{G}(t)\bar{G}(t)^T - \bar{H}(t)\bar{G}(t)\bar{G}(t)^T \quad (14) \end{aligned}$$

This filter reduces to the Kalman-Bucy continuous time filter when  $F$  and  $H$  are linear in  $x$ . The problem with implementing the above estimator is that terms like  $E(xF')$  and  $E(xH')$  are involved. Since  $F$  and/or  $H$  is nonlinear in  $x$ , these expectation terms are functions of higher moments. In turn, the differential equations for these higher moments involve still higher moments, etc., and the exact solution would require a countable infinite number of differential equations.

In most of the literature on nonlinear estimation, the infinite dimensional problem is resolved by expanding an  $f(x)$  in a Taylor's series about the expected value of  $x$ :

$$f(x) \approx f(\bar{x}) + (x - \bar{x}) \left. \frac{\partial f(x)}{\partial x} \right|_{x=\bar{x}} + \frac{1}{2} (x - \bar{x})^2 \left. \frac{\partial^2 f(x)}{\partial x^2} \right|_{x=\bar{x}} \quad (15)$$

Then the various expected values take the form

$$E[f(x)] = f(\bar{x}) + \frac{1}{2} P_2 \left. \frac{\partial^2 f(x)}{\partial x^2} \right|_{x=\bar{x}} \quad (16)$$

$$E[(x - \bar{x}) f(x)] \approx P_2 \left. \frac{\partial f(x)}{\partial x} \right|_{x=\bar{x}} \quad (17)$$

etc.

However, for the estimation problem at hand, it will be unnecessary to invoke arguments about the higher order terms of series expansions being negligible. Rather, only certain plausible arguments about the shape of the conditional probability density function will be necessary. The reason this is possible will become apparent in what follows.

The equations for updating the state estimate and covariance equations at discrete updates can be formulated from a Bayes rule approach. Ho and Lee (Ref. 14) have a very readable account of this and Jaswinski (Ref. 16) gives the results of some further studies in this area. When the discrete observations turn out to be linear in the state, which is often the case in updated attitude reference systems, the discrete Kalman filter update equations can be used to calculate the state estimate and covariance matrix discontinuities at which occur at discrete measurement time.

### C. Alternate Attitude Reference Mechanizations

The ultimate output of any attitude reference system is some periodic or continuous measure of vehicle attitude with respect to a reference coordinate system. Performance-oriented goals, when mechanizing an attitude reference system, involve minimizing a functional measure of attitude error with fixed levels of sensor error, or, conversely, maximizing the acceptable levels of sensor error consistent with meeting a fixed level of system accuracy. There are a number of alternate mathematical formulations for the attitude reference problem which are formally equivalent. However, it will be shown that the choice of a particular formulation has a profound influence on such things as the ease with which optimal or suboptimal estimation theory can be applied, computational loading, and accuracy.

The systems discussed in this report are limited to those that derive an attitude transformation matrix with respect to a coordinate system fixed in inertial space. The basic ideas, however, are easily carried over to more specialized classes of systems, such as local-vertical oriented systems.

For any arbitrary orientation of an

attitude reference system, there exists a unique real orthogonal transformation matrix  $T_{BI}$  which maps inertial vectors  $X_I$  into body vectors  $X_B$ :

$$X_B = T_{BI} X_I \quad (18)$$

where

$$T_{BI} = \begin{bmatrix} \ell_{11} & \ell_{12} & \ell_{13} \\ \ell_{21} & \ell_{22} & \ell_{23} \\ \ell_{31} & \ell_{32} & \ell_{33} \end{bmatrix} \quad (19)$$

The objective of the attitude reference system is to come up with the most accurate running estimate possible for this nine-element direction cosine matrix. There are many parametric systems which are commonly used to define uniquely the direction cosine matrix:

$$\ell_{ij} = f(x_1, x_2, \dots, x_n) \quad (20)$$

The most commonly used values of  $n$  are 3, 4, and 9. The smallest value of  $n$  sufficient to define uniquely  $T_{BI}$  is 3. The most commonly used three-parameter systems are the various Euler angle systems, a discussion of which can be found in Goldstein (Ref. 17). For an often-used spacecraft set of Euler angles in the pitch-roll-yaw sequence, the direction cosine element equations have the form

$$\begin{aligned} \ell_{11} &= \cos(x_2) \cos(x_3) + \sin(x_1) \sin(x_2) \sin(x_3) \\ \ell_{12} &= \cos(x_1) \sin(x_3) \\ \ell_{13} &= -\sin(x_2) \cos(x_3) + \sin(x_1) \cos(x_2) \sin(x_3) \\ \ell_{21} &= -\cos(x_2) \sin(x_3) + \sin(x_1) \sin(x_2) \cos(x_3) \\ \ell_{22} &= \cos(x_1) \cos(x_3) \\ \ell_{23} &= \sin(x_2) \sin(x_3) + \sin(x_1) \cos(x_2) \cos(x_3) \\ \ell_{31} &= \cos(x_1) \sin(x_2) \\ \ell_{32} &= -\sin(x_1) \\ \ell_{33} &= \cos(x_1) \cos(x_2) \end{aligned} \quad (21)$$

The differential equations relating the Euler angles to the body axis components  $p$ ,  $q$ , and  $r$  of the total angular velocity vector are in this case

$$\dot{x}_1 = \cos(x_3) p - \sin(x_3) q$$

$$\begin{aligned} \dot{x}_2 &= [\sin(x_3) p + \cos(x_3) q] \sec(x_1) \\ \dot{x}_3 &= [\sin(x_3) p \\ &\quad + \cos(x_3) q] \tan(x_1) + r \end{aligned} \quad (22)$$

The Euler angle formulations have the strong disadvantage that both the differential equations and the direction cosine equations involve nonlinear (trigonometric and product) functions of the Euler angles. Also, the differential equations have a singularity at  $x_1 = \pi/2$ . However, Euler angles are by no means the only three-parameter transformation systems. Mortenson (Ref. 18) gives a very interesting discussion of the so-called Rodrigues-Cayley parameters, which have the distinct advantage of differential and direction cosine equations which have only quadratic nonlinearities, which are computationally much simpler than trigonometric nonlinearities.

One of the most commonly used four-parameter systems is the Euler quaternion parameter system (often referred to as Euler's symmetrical parameters), a discussion of which can be found in Mitchell and Rogers (Ref. 19). For quaternions, the direction cosine element equations have the form

$$\begin{aligned} \ell_{11} &= x_1^2 + x_2^2 - x_3^2 - x_4^2 \\ \ell_{12} &= 2(x_2 x_3 + x_1 x_4) \\ \ell_{13} &= 2(x_2 x_4 - x_1 x_3) \\ \ell_{21} &= 2(x_2 x_3 - x_1 x_4) \\ \ell_{22} &= x_1^2 + x_3^2 - x_2^2 - x_4^2 \\ \ell_{23} &= 2(x_3 x_4 + x_1 x_2) \\ \ell_{31} &= 2(x_2 x_4 + x_1 x_3) \\ \ell_{32} &= 2(x_3 x_4 - x_1 x_2) \\ \ell_{33} &= x_1^2 + x_4^2 - x_2^2 - x_3^2 \end{aligned} \quad (23)$$

In this case, the differential equations relating the Euler quaternion parameters to the body-axis angular velocity components are

$$\begin{aligned} \dot{x}_1 &= 1/2 (x_4 p + x_2 r - x_3 q) \\ \dot{x}_2 &= 1/2 (x_4 q + x_3 p - x_1 r) \end{aligned}$$

$$\begin{aligned}\dot{x}_3 &= 1/2 (x_4 r + x_1 q - x_2 p) \\ \dot{x}_4 &= -1/2 (x_1 p + x_2 q + x_3 r) .\end{aligned}\quad (24)$$

With this formulation, the direction cosine equations become quadratic, nonlinear equations, and the quaternion differential equations are linear functions of the quaternions. (In the case of the Rodriguez-Cayley parameters, the differential equations are quadratically nonlinear.) There are numerous other four-parameter sets used to describe spatial rotations in quantum mechanics, such as the Cayley-Klein parameter set (Ref. 17). These parameters are computationally unappealing for the spacecraft dynamics situation, however, since the parameters are complex variables.

The most direct, and often the best way to obtain the desired transformation matrix is to deal with a non-parameter system, i.e., the direction cosines themselves. The transformation matrix  $T_{BI}$  is written directly in terms of the parameters, and the direction cosine differential equations are

$$\begin{aligned}\dot{l}_{11} &= l_{21}r - l_{31}p \\ \dot{l}_{12} &= l_{22}r - l_{32}p \\ \dot{l}_{13} &= l_{23}r - l_{33}p \\ \dot{l}_{21} &= l_{31}p - l_{11}r \\ \dot{l}_{22} &= l_{32}p - l_{12}r \\ \dot{l}_{23} &= l_{33}p - l_{13}r \\ \dot{l}_{31} &= l_{11}q - l_{21}p \\ \dot{l}_{32} &= l_{12}q - l_{22}p \\ \dot{l}_{33} &= l_{13}q - l_{23}p\end{aligned}\quad (25)$$

These equations can also be written as

$$\dot{\underline{l}} = \underline{\Omega} \underline{l}, \quad (26)$$

where  $\underline{l}$  is the 3x3 direction cosine matrix and

$$\underline{\Omega} = \begin{bmatrix} 0 & r & -q \\ -r & 0 & p \\ q & -p & 0 \end{bmatrix}. \quad (27)$$

Notice that now all the equations are linear in the attitude parameters. This, however, came at the expense of increasing the number of parameters significantly. Also, four- and nine-parameters are not all independent, and the resulting transformation matrix can become non-orthogonal because of computational errors. This is not usually a practical problem though, since an occasional orthonormalization procedure will suffice to prevent degeneration of  $T_{BI}$ .

The only thing that remains in the specification of the attitude reference algorithm (exclusive of estimation) is the determination of the body angular rate components  $p$ ,  $q$ , and  $r$  that drive the attitude parameter differential equations. For a general torque-free rigid space vehicle (the only type considered here) the differential equations for the body angular rate components are (Ref. 20) :

$$\begin{aligned}I_{xx}\dot{p} - I_{xy}\dot{q} - I_{xz}\dot{r} &= qr(I_y - I_z) + pq(I_{xz}) + (q^2 - r^2)I_{yx} - prI_{xy} \\ -I_{xy}\dot{p} + I_y\dot{q} - I_{yz}\dot{r} &= pr(I_z - I_x) + qrI_{xy} + (r^2 - p^2)I_{xz} - pqI_{yz} \\ -I_{xz}\dot{p} - I_{yz}\dot{q} + I_z\dot{r} &= pq(I_x - I_y) + prI_{yz} + (p^2 - q^2)I_{xy} - pqI_{xz}\end{aligned}\quad (28)$$

where the  $I_i$  are the moments of inertia about the rate measurement coordinate system axes and the  $I_{ij}$  are the corresponding products of inertia. It is clear that these equations can be written as the following quadratic first-order vector nonlinear differential equation:

$$\begin{bmatrix} \dot{p} \\ \dot{q} \\ \dot{r} \end{bmatrix} = \underline{I}_G \begin{bmatrix} pq \\ qr \\ pr \\ p^2 \\ q^2 \\ r^2 \end{bmatrix} \quad (29)$$

where  $\underline{I}_G$  is a constant 3x6 matrix which is a complicated, but constant, algebraic function of the moments and products of inertia. In this study, attention will be focused on the simpler principal axis equations:

$$\begin{aligned}\dot{p} &= a_1 qr \\ \dot{q} &= a_2 pr \\ \dot{r} &= a_3 pq\end{aligned}\quad (30)$$

where

$$\begin{aligned} a_1 &= (I_Y - I_Z)/I_X \\ a_2 &= (I_Z - I_X)/I_Y \\ a_3 &= (I_X - I_Y)/I_Z \end{aligned} \quad (31)$$

If the body angular rates are measured about a non-principal axis coordinate system, they can easily be transformed into a principal axis system by a constant 3x3 matrix transformation and the computations can take place in that coordinate frame, so there is no loss of generality by the principal axis assumption. If external or attitude control system torques are to be included in the dynamics, they must be modeled and included in the angular rate differential equations. However, this is beyond the intended scope of this study and will not be included here.

It is well known (Ref. 17) that the solutions of the principal axis angular rate equations are elliptic integrals of the second kind. When two of the moments of inertia are equal (disk-shaped, rod-shaped, or bodies of revolution) the elliptic integral solutions degenerate to sinusoidal solutions, and when all three moments of inertia are equal (inertial spheres) the differential equations decouple, with constant solutions. However, these facts are irrelevant to numerical integration mechanizations in real systems and are of no consequence here.

#### D. State-Variable, State-Measurement, and Noise-Modeling Considerations

There is considerable latitude in the selection of state variables, attitude reference dynamics, and component noise models for systems of the types considered here. This is a subject which can have a profound impact on system performance and often receives far too little attention. One of the dangers of optimal and suboptimal estimation is that the effects on system performance of noise and dynamics modeling errors are subtle, hard to evaluate, and sometimes disastrous. Although some work has been done in this area for linear systems (Ref. 21), the impact on complex systems is essentially an open question, and can only be resolved in a particular situation by considerable simulation work.

Consider a simple example; namely, a single-axis attitude reference system whose only sensor is a rate gyro, operating on a single axis, untorqued vehicle.

This could represent a short-term attitude reference system, or a periodically updated attitude reference system during the period between updates. Suppose, for purposes of illustration, that the only error component in the output of the gyro is additive Gaussian white noise. In this case, the dynamical system is given by

$$\begin{bmatrix} \dot{\theta}_1(t) \\ \dot{\theta}_2(t) \end{bmatrix} = \begin{bmatrix} 0 & 1 \\ 0 & 0 \end{bmatrix} \begin{bmatrix} \theta_1(t) \\ \theta_2(t) \end{bmatrix} = \underline{F} \underline{\theta}(t) \quad (32)$$

and noisy continuous observations are taken

$$\begin{aligned} y(t) &= [0 \quad 1] \begin{bmatrix} \theta_1(t) \\ \theta_2(t) \end{bmatrix} + v(t) \\ &= \underline{H} \underline{\theta}(t) + v(t) \end{aligned} \quad (33)$$

where  $v(t)$  is a scalar zero-mean white Gaussian noise process with

$$E[v(t)v(\tau)] = \sigma^2 \delta(t-\tau) \quad (34)$$

$\theta_1$  is the attitude and  $\theta_2$  is the attitude rate component of the state vector  $\underline{\theta}$ . Notice that the attitude dynamics are modeled as those of a constantly rotating untorqued vehicle.

Normally an attitude estimate  $\hat{\theta}_1(t)$  is derived from this type of system by simply integrating the gyro output  $y(t)$ . In this case, it can be shown (Appendix A) that the attitude error variance diverges as

$$E[\hat{\theta}_1(t) - \theta_1(t)]^2 = E[\hat{\theta}_1(0) - \theta_1(0)]^2 + \sigma^2 t \quad (35)$$

In other words, the standard deviation of the attitude error diverges as the square root of time. Consider, on the other hand, a mechanization based on the Kalman-Bucy continuous time linear filter. In this case, the state estimate is the solution of

$$d\hat{\underline{\theta}}(t)/dt = \underline{F} \hat{\underline{\theta}}(t) + \underline{K}(t)[y(t) - \underline{H} \hat{\underline{\theta}}(t)] \quad (36)$$

$$\text{where } \underline{K}(t) = \underline{P}(t) \underline{H}'(t) \sigma^{-2} \quad (37)$$

and

$$\begin{aligned} d\underline{P}(t)/dt \\ = \underline{F} \underline{P}(t) + \underline{P}(t) \underline{F}' - \underline{P}(t) \underline{H}' \sigma^{-2} \underline{H} \underline{P}(t) \end{aligned} \quad (38)$$

with initial conditions

$$\hat{\underline{\theta}}(0) = E[\underline{\theta}(0)] = \underline{\theta}_0 \quad (39)$$

$$\begin{aligned} \underline{P}(0) &= E\{[\hat{\underline{\theta}}(0) - \underline{\theta}(0)][\hat{\underline{\theta}}(0) - \underline{\theta}(0)]'\} \\ &= \underline{P}_0 \text{ (RSPD)} \end{aligned} \quad (40)$$

Then

$$\begin{aligned} \underline{P}(t) &= E\{[\hat{\underline{\theta}}(t) - \underline{\theta}(t)][\hat{\underline{\theta}}(t) - \underline{\theta}(t)]'\} \end{aligned} \quad (41)$$

For this simple case, this Riccati equation, although nonlinear, can be solved analytically. After some tedium, the solution is

$$\underline{P}(t) = \begin{bmatrix} P_{11}(t) & P_{12}(t) \\ P_{12}(t) & P_{22}(t) \end{bmatrix} \quad (42)$$

where

$$P_{11}(t) = P_{11}(0) \quad (43)$$

$$\begin{aligned} &+ \frac{4\sigma^2 P_{12}(0)}{P_{22}(0)} \log \left[ \frac{\sigma^2 P_{22}(0)t}{\sigma^2} \right] \\ &+ \frac{\sigma^2 P_{22}(0)t^2 - 2\sigma^2 P_{12}(0)t - P_{12}^2(0)t}{\sigma^2 + P_{22}(0)t} \end{aligned}$$

$$P_{12}(t) = \frac{\sigma^2 [P_{12}(0) + P_{22}(0)t]}{\sigma^2 + P_{22}(0)t} \quad (44)$$

$$P_{22}(t) = \frac{\sigma^2 P_{22}(0)}{\sigma^2 + P_{22}(0)t} \quad (45)$$

Consider the case where  $P_{12}(0) = 0$ , i.e., that the initial attitude and rate estimate errors are uncorrelated. This will be the case in most attitude reference systems since attitude initialization and rate information come from completely independent sources. Then the attitude error variance equation reduces to

$$P_{11}(t) = P_{11}(0) + \frac{\sigma^2 P_{22}(0)t^2}{\sigma^2 + P_{22}(0)t} \quad (46)$$

Thus, the behavior of the attitude error variance for the filter system is quite different from that of the conventional system. The time behavior of the two variances is shown in Fig. 5.

Consider the behavior of the filter system performance in the face of a dynamics model error such as a small, unknown torque  $T_s$ :

$$\begin{bmatrix} \dot{\theta}_1(t) \\ \dot{\theta}_2(t) \end{bmatrix} = \begin{bmatrix} 0 & 1 \\ 0 & 0 \end{bmatrix} \begin{bmatrix} \theta_1(t) \\ \theta_2(t) \end{bmatrix} + \begin{bmatrix} 0 \\ T_s \end{bmatrix} \quad (47)$$

where  $T_s$  is not modeled in the filter. In this case, the transient behavior of the estimate error is no longer given by the computed covariance matrix and is difficult to analyze analytically. However, the steady-state behavior of the error can be evaluated by examining the steady-state filter gain:

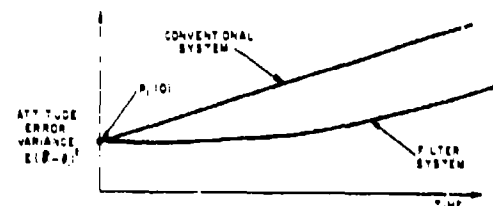


Fig. 5. Attitude Error Variances vs. Time

$$\begin{aligned} K_{\infty} &= \lim_{t \rightarrow \infty} \underline{P} \underline{H}' \sigma^{-2} \\ &= \lim_{t \rightarrow \infty} \begin{bmatrix} P_{11}(t) & P_{12}(t) \\ P_{12}(t) & P_{22}(t) \end{bmatrix} \begin{bmatrix} 0 \\ 1 \end{bmatrix} \sigma^{-2} \\ &= \begin{bmatrix} 1 \\ 0 \end{bmatrix} \end{aligned} \quad (48)$$

Thus

$$\begin{aligned} \dot{\underline{\theta}}_{\infty} &= \begin{bmatrix} 0 & 1 \\ 0 & 0 \end{bmatrix} \begin{bmatrix} \hat{\theta}_{1\infty} \\ \hat{\theta}_{2\infty} \end{bmatrix} + \begin{bmatrix} 1 \\ 0 \end{bmatrix} [y(t) - \hat{\theta}_{2\infty}] \text{ or} \\ \dot{\hat{\theta}}_{1\infty} &= \hat{\theta}_{2\infty} + (y(t) - \hat{\theta}_{2\infty}) = y(t) \\ &= \dot{e}_{2\infty} + v(t), \quad \dot{\hat{\theta}}_{2\infty} = 0 \end{aligned} \quad (50)$$



Therefore, it is clear that

$$\frac{d}{dt} [E(\hat{\theta}_{1\infty} - \theta_{1\infty})^2] = \sigma^2$$

which is the same steady-state behavior as the conventional system and the "exact" filter system. The transient behavior certainly can be no better than the "exact" filter system and for typical values of system parameters (small model errors) probably lies somewhere between the exact and conventional system performance curves. However, in certain instances it could be worse than the conventional system.

An important point is that the conventional system mechanization amounts to considering that the noise is driving the plant rather than influencing the measurement. In this case, after separating out the perfectly measured portion of the system, the state equation is of the form

$$\dot{\theta}_1 = F\theta_1 + Gw(t) \text{ with } F = 0, G = 1 \text{ and}$$

$$E[w(t)w(\tau)] = \sigma^2 \delta(t-\tau) \quad (51)$$

Then the attitude variance is

$$P_{11}(t) = p_{11}(0) + \sigma^2 t \quad (52)$$

This simple fact becomes very important for systems where rate dynamics are not taken into account, as it keeps the filter gains from approaching zero when attitude measurements are included in the system.

The point of this oversimplified example is that how one models attitude reference system dynamics, measurements, and uncertainties plays just as important a role in determining the performance of an actual system as does the skill with which one applies optimal filtering theory. Unfortunately (or fortunately, from a job security standpoint) the modeling question is one which has no pat answer, and can be resolved in an individual case only by extensive analytical and simulation studies. The question of modeling will not be broached here, since this is a more general study of attitude reference systems. Rather, plausible models will be assumed for system, measurement, and noise phenomena, and system performance will be evaluated in this constrained situation with several approaches to state variable estimation.

For the present, gyro uncertainties will be modeled as normally distributed stationary white noise processes. The question of gyro biases (constant drift rates) will not be considered here, although it is an easy extension of what follows. Essentially, the unknown biases become components of the augmented state with no dynamics or direct measurements. Thus, biases introduce no additional nonlinearities into the system or measurement equations and complicate estimation only in the sense that they increase the dimension of the state. Therefore, since the main emphasis here is to explore the nonlinear estimation aspects of attitude reference systems, biases will be assumed to be zero to keep things computationally reasonable.

Let the state of the attitude reference system be described by a sufficient set of attitude parameters and the three body angular rates. The state equation will be written in the form

$$d\mathbf{x}(t)/dt = \mathbf{F}[\mathbf{x}(t), t] \quad (53)$$

where the explicit dependence of  $\mathbf{F}$  on time is to indicate that in the general case the attitude dynamics could include known forcing terms (torques). Attention will be centered on Euler angles, Euler quaternion parameters, or direction cosines for the choice of attitude parameters. In this case,

$$\mathbf{F}[\mathbf{x}(t)] = \begin{bmatrix} x_4 \cos(x_3) - x_5 \sin(x_3) \\ \vdots \\ a_1 x_3 x_6 \\ a_2 x_4 x_6 \\ a_3 x_4 x_5 \end{bmatrix}$$

$$\text{or} \quad \begin{bmatrix} 1/2(x_4 x_5 + x_2 x_7 - x_3 x_6) \\ \vdots \\ a_1 x_6 x_7 \\ a_2 x_3 x_7 \\ a_3 x_3 x_6 \end{bmatrix}$$

$$\text{or} \quad \begin{bmatrix} x_4 x_{12} - x_7 x_{11} \\ \vdots \\ a_1 x_{11} x_{12} \\ a_2 x_{10} x_{12} \\ a_3 x_{10} x_{11} \end{bmatrix} \quad (54)$$

where

$$\begin{aligned} x_1 &= l_1 \\ x_2 &= l_2 \\ &\vdots \\ x_n &= l_n \\ x_{n+1} &= p \\ x_{n+2} &= q \\ x_{n+3} &= r \end{aligned} \quad (55)$$

and

$$\begin{aligned} a_1 &= \frac{I_Y - I_X}{I_X}, \quad a_2 = \frac{I_X - I_Y}{I_Y}, \\ a_3 &= \frac{I_X - I_Y}{I_X} \end{aligned} \quad (56)$$

The  $l_i$ ,  $i = 1, n$  are the generalized attitude parameters. The problem will be formulated so that continuous and discrete attitude and/or rate observations can be accommodated. The filter will be derived so that the conditional mean and covariance differential equations evolve including the effects of the continuous measurements, and the effects of the discrete measurements are taken into account by a separate calculation at the measurement times. Consider only continuous nonlinear measurements of the form

$$y(t) = H[x(t), t] + v(t) \quad (57)$$

where  $v(t)$  is a zero-mean continuous white Gaussian noise process with

$$E[v(t)v'(\tau)] = R(t)\delta(t-\tau), \quad R \text{ is RSPD} \quad (58)$$

Since in practically any attitude reference system the observations of attitude and rate are performed by sensors that are separate physical entities with little in common (with the possible exception of a common power supply), it is a very reasonable assumption that the attitude and rate measurement errors are uncorrelated. This permits a convenient partitioning of the measurement process and noise variance matrices:

$$y(t) = \begin{bmatrix} y_A(t) \\ y_R(t) \end{bmatrix}$$

$$y(t) = \begin{bmatrix} H_A[x_A(t)] + v_A(t) \\ H_R[x_R(t)] + v_R(t) \end{bmatrix} \quad (59)$$

where the subscripts A and R refer to attitude and rate components, respectively. Since the attitude and rate components of the measurement are uncorrelated,  $R(t)$  has the form

$$R(t) = \begin{bmatrix} R_A(t) & 0 \\ 0 & R_R(t) \end{bmatrix} \quad (60)$$

so that  $R(t)$  is invertible as

$$R^{-1}(t) = \begin{bmatrix} R_A^{-1}(t) & 0 \\ 0 & R_R^{-1}(t) \end{bmatrix} \quad (61)$$

This fact will be very useful in the sequel, since terms like

$$\{E[aH(x, t)]\}' R^{-1}(t) \{E[by(t)]\}$$

can be separated into the two terms

$$\begin{aligned} &\{E[aH_A(x_A, t)]\}' R_A^{-1}(t) \{E[by_A(t)]\} \\ &+ \{E[aH_R(x_R, t)]\}' R_R^{-1}(t) \{E[by_R(t)]\} \end{aligned}$$

This fact will permit separation of the terms involving attitude and rate measurements in the filter equations and easy evaluation of the individual contributions of these measurements.

Consider now the impact of the choice of the attitude parameter set on the ease of mechanization of the nonlinear estimator. The Euler angle differential equations given earlier have terms on the right hand side like

$$x_5 \tan(x_1) \cos(x_3)$$

Therefore, the mechanization of the nonlinear estimator leads to terms like

$$\begin{aligned} E[x_5 \tan(x_1) \cos(x_3)] &= \\ \int_{-\infty}^{\infty} \int_{-\infty}^{\infty} \int_{-\infty}^{\infty} x_5 \tan(x_1) \cos(x_3) & \\ \cdot P_M(x_1, x_3, x_5, t) dx_1 dx_3 dx_5 & \end{aligned} \quad (62)$$

where  $P_M(x_1, x_3, x_5, t)$  is the marginal conditional probability density

$$P(x_1, x_3, x_5, t) dx_1 dx_3 dx_5 = P \left[ (x_1, x_3, x_5) \in (x_1 + dx_1, x_3 + dx_3, x_5 + dx_5) \middle| Y(s), 0 \leq s \leq t \right] \quad (63)$$

If the assumption is made that the total conditional probability density,  $P(x, t)$ , is Gaussian with mean  $m$  and covariance  $E$ , then it follows from fundamental probability theory that  $P_M(x_1, x_3, x_5, t)$  is Gaussian with mean  $m_M$  and covariance  $E_M$ , where

$$m_M = \begin{bmatrix} m_1 \\ m_3 \\ m_5 \end{bmatrix} \quad (64)$$

and

$$E_M = \begin{bmatrix} E_{11} & E_{13} & E_{15} \\ E_{31} & E_{33} & E_{35} \\ E_{51} & E_{53} & E_{55} \end{bmatrix} \quad (65)$$

However, even with this simplifying Gaussian assumption, the evaluation of three dimensional Gaussian integrals involving products of trigonometric functions of the dependent variables is a formidable task. The implementation of a real time estimator which must evaluate many of these integrals numerically at each integration step would probably require a 7094 in orbit as part of the system (or some third generation counterpart).

Consider now an attitude reference system based on the Euler quaternion parameters. The quaternion differential equations have terms on the right hand side like  $x_4 x_5$ , which lead to terms in the estimator equations like

$$E(x_4 x_5) = \int_{-\infty}^{\infty} \int_{-\infty}^{\infty} x_4 x_5 P(x_4, x_5, t) dx_4 dx_5 \quad (66)$$

Now, even without any assumption on the nature of marginal conditional probability density, this can be written as

$$E(x_4 x_5) = R_4 R_5 + P_{45} \quad (67)$$

where  $R_4 R_5$ , and  $P_{45}$  are given by the solutions of the estimator equations. Thus, multidimensional numerical integrations can be dispensed with entirely in this case, which is a great advantage. The implementation of the direction cosine parameters results in this same type of quadratic nonlinearity and attendant simplification of the estimator equations. Therefore it would appear that quaternions are preferable to direction cosines, since they lead to lower dimensional state and covariance equations. However, this apparent advantage can often be more than cancelled by the computational advantages direction cosines offer when observations are taken into account.

As an example of the role that observations play in determining the structure of the attitude estimator, consider a system where the state variables are the four Euler quaternion parameters and three body angular rates, with the continuous observations consisting of attitude measurements of one inertially-fixed vector and rate measurements from three orthogonal rate gyros. The observation of the inertial vector could represent a star tracker tracking a known star for a period of time, for example. Then

$$Y(t) = \begin{bmatrix} Y_A(t) \\ \text{-----} \\ Y_R(t) \end{bmatrix} \quad (68)$$

where

$$Y_A(t) = H_A[x_A(t)] + V_A(t) \quad (69)$$

with

$$H_A[x_A(t)] = T_{BI}[x_A(t)] V_I \quad (70)$$

and

$$Y_R(t) = H_R[x_R(t)] + V_R(t) \quad (71)$$

with

$$H_R[x_R(t)] = \begin{bmatrix} x_5 \\ x_6 \\ x_7 \end{bmatrix} \quad (72)$$

$V_I$  is a known inertial vector and  $V_A(t)$  and  $V_R(t)$  are assumed to be continuous zero-mean white Gaussian noise processes with constant covariance matrices  $R_A$  and  $R_R$ , respectively, and

$$T_{BI} = \begin{bmatrix} x_1^2 + x_2^2 - x_3^2 - x_4^2 & 2(x_2x_3 + x_1x_4) & 2(x_2x_4 - x_1x_3) \\ 2(x_2x_3 - x_1x_4) & x_1^2 + x_3^2 - x_2^2 - x_4^2 & 2(x_3x_4 + x_1x_2) \\ 2(x_2x_4 + x_1x_3) & 2(x_3x_4 - x_1x_2) & x_1^2 + x_4^2 - x_2^2 - x_3^2 \end{bmatrix} \quad (73)$$

Applying the formulas given previously for the optimal nonlinear estimator yields equations for propagating the state estimate, where one of the typical component equations is

$$d\hat{x}_1/dt = 1/2(\hat{x}_4\hat{x}_5 + \hat{x}_3\hat{x}_7 - \hat{x}_3\hat{x}_6 + P_{45}P_{27} - P_{31})$$

$$\begin{bmatrix} \hat{y}_{A1} \\ \hat{y}_{A2} \\ \hat{y}_{A3} \end{bmatrix} = \begin{bmatrix} \hat{x}_1 \\ \hat{x}_2 \\ \hat{x}_3 \end{bmatrix} \hat{A}_A^{-1} \begin{bmatrix} P_{13} \\ P_{16} \\ P_{17} \end{bmatrix} + \begin{bmatrix} \hat{y}_{A1} - E(H_{A1}) \\ \hat{y}_{A2} - E(H_{A2}) \\ \hat{y}_{A3} - E(H_{A3}) \end{bmatrix} \hat{A}_A^{-1} \begin{bmatrix} E(x_1H_{A1}) - \hat{x}_1E(H_{A1}) \\ E(x_2H_{A2}) - \hat{x}_2E(H_{A2}) \\ E(x_3H_{A3}) - \hat{x}_3E(H_{A3}) \end{bmatrix} \quad (74)$$

where

$$\begin{bmatrix} H_{A1} \\ H_{A2} \\ H_{A3} \end{bmatrix} = T_{BI} \begin{bmatrix} V_{I1} \\ V_{I2} \\ V_{I3} \end{bmatrix} \quad (75)$$

So  $E(H_{A1})$  involves terms like

$$E(2x_2x_3V_{I2}) = 2V_{I2}(\hat{x}_2\hat{x}_3 + P_{23}) \quad (76)$$

and  $E(x_1H_{A1})$  involves terms like

$$E(2x_1x_2x_3V_{I2}) = 2V_{I2}(\hat{x}_1\hat{x}_2\hat{x}_3 + \hat{x}_1P_{23} + \hat{x}_2P_{13} + \hat{x}_3P_{12} + P_{123}) \quad (77)$$

One of the 49 resulting equations for propagating the second moment is

$$\begin{aligned} dp_{12}/dt &= E(F_1x_2 + P_1x_1) - E(F_1)\hat{x}_2 - E(F_2)\hat{x}_1 \\ &= \begin{bmatrix} \hat{y}_{A1} - \hat{x}_1 \\ \hat{y}_{A2} - \hat{x}_2 \\ \hat{y}_{A3} - \hat{x}_3 \end{bmatrix} \hat{A}_A^{-1} \begin{bmatrix} P_{123} \\ P_{126} \\ P_{127} \end{bmatrix} + \begin{bmatrix} \hat{y}_{A1} - E(H_{A1}) \\ \hat{y}_{A2} - E(H_{A2}) \\ \hat{y}_{A3} - E(H_{A3}) \end{bmatrix} \hat{A}_A^{-1} \begin{bmatrix} E(x_1x_2H_{A1}) - \hat{x}_1\hat{x}_2E(H_{A1}) \\ E(x_1x_2H_{A2}) - \hat{x}_1\hat{x}_2E(H_{A2}) \\ E(x_1x_2H_{A3}) - \hat{x}_1\hat{x}_2E(H_{A3}) \end{bmatrix} \\ &\quad - \hat{x}_1E(x_2H_{A1}) - \hat{x}_2E(x_1H_{A1}) + \hat{x}_1\hat{x}_2E(H_{A1}) \\ &\quad - \hat{x}_1E(x_2H_{A2}) - \hat{x}_2E(x_1H_{A2}) + \hat{x}_1\hat{x}_2E(H_{A2}) \\ &\quad - \hat{x}_1E(x_2H_{A3}) - \hat{x}_2E(x_1H_{A3}) + \hat{x}_1\hat{x}_2E(H_{A3}) \\ &= \begin{bmatrix} P_{15} \\ P_{16} \\ P_{17} \end{bmatrix} \hat{A}_A^{-1} \begin{bmatrix} P_{23} \\ P_{26} \\ P_{27} \end{bmatrix} - \begin{bmatrix} E(x_1H_{A1}) - \hat{x}_1E(H_{A1}) \\ E(x_1H_{A2}) - \hat{x}_1E(H_{A2}) \\ E(x_1H_{A3}) - \hat{x}_1E(H_{A3}) \end{bmatrix} \hat{A}_A^{-1} \begin{bmatrix} E(x_2H_{A1}) - \hat{x}_2E(H_{A1}) \\ E(x_2H_{A2}) - \hat{x}_2E(H_{A2}) \\ E(x_2H_{A3}) - \hat{x}_2E(H_{A3}) \end{bmatrix} \quad (78) \end{aligned}$$

So terms like  $E(F_1x_2)$  lead to terms like

$$E(1/2x_2x_4x_5) = 1/2(\hat{x}_2\hat{x}_4\hat{x}_5 + \hat{x}_2P_{45} + \hat{x}_4P_{25} + \hat{x}_5P_{24} + P_{245}) \quad (79)$$

and terms like  $E(x_1x_2H_{A1})$  lead to terms like

$$\begin{aligned} E(2x_1x_2x_3V_{I1}) &= 2(\hat{x}_1\hat{x}_2\hat{x}_3 + \hat{x}_1P_{223} + 2\hat{x}_2P_{123} \\ &\quad + \hat{x}_3P_{122} + 2\hat{x}_1\hat{x}_2P_{23} + \hat{x}_2^2P_{13} \\ &\quad + \hat{x}_1\hat{x}_3P_{22} + 2\hat{x}_2\hat{x}_3P_{12} + P_{1223})V_{I1} \end{aligned} \quad (80)$$

The use of the rate and attitude decomposition mentioned earlier is apparent in the above equations.

When direction cosines are used as state variables, the same form arises for the mean and second moment equations, but the expected value expansions are much less complex since in this case  $H_A$  is linear in the state instead of quadratic. Also, the highest order moments appearing are third moments, whereas with quaternions fourth moments appear in the second moment differential equations.

There are a number of other types of attitude measurements besides observations of inertial vectors which are utilized in typical attitude reference systems. For instance, if the attitude sensor has photosensitive slits across which stars transit, then the observation equation describes the fact that the dot product between the star vector and the normal to the slit plane vanishes. Derivation of the estimator equations in this and other typical cases follows along the lines indicated above for inertial vectors, and no new difficulties are encountered.

## E. Computational Considerations

In the previous section Euler angles were shown to lead to a computationally infeasible nonlinear estimator, and quaternion parameters and direction cosines yielded equations which had some hope of being implemented in real time. Quaternions led to a state of dimension seven, whereas direction cosines led to a state of dimension twelve. Now, certain assumptions will be made on the nature of the shape of the conditional probability density so that the mean and second moment equations yield "sufficient statistics" to do estimation. In the case of direction cosines, we will just have to assume that the conditional density is symmetric, whereas in the case of quaternions we will have to make the stronger assumption of normality. In other words, (see also Kushner (Ref. 15)),

$$\text{Direction Cosines: } P_{ijk} = 0 \quad (81)$$

$$\text{Quaternion Parameters: } \begin{cases} P_{ijk} = 0 \\ P_{ijk1} = P_{ij}P_{k1} \\ \quad + P_{ik}P_{j1} \\ \quad + P_{il}P_{jk} \end{cases} \quad (82)$$

The equations for the attitude estimator, examples of which were given in the previous section, can be simplified and judiciously manipulated by the application of a number of useful identities that exist between expectations of products of variables, and sums and products of moments of these variables. Some of the more useful of these identities are given in Appendix B.

Also, due to the fact that the covariance matrix initial condition is symmetric and the covariance differential equations are symmetric,  $P_{ij} = P_{ji}$ , and only the diagonal elements and one of the sets of strictly triangular elements need be solved. Thus, the mean and covariance solutions lead to 35 equations in the case of quaternions and 90 equations in the case of direction cosines.

For the present discussion, it will be assumed that  $R$  is a diagonal matrix, i.e., that all sensor errors are uncorrelated. Again, this is a reasonable assumption for random-type errors in isolated inertial components. (Anyway, in practice, correlation data are impossible to obtain from hardware people).

Within the constraints of all the qualifications listed above, a computational count was performed to determine the number of operations necessary to evaluate the right-hand sides of the estimation equations at each integration point. The results are summarized in Table 1 for the two formulations considered.

Table 1. Computational Comparison

	Quaternion Formulation	Direction Cosine Formulation
Computer Adds	6032	1495
Computer Multiplies	8309	2277

This is quite an amazing result. By increasing the dimension of the state and the number of differential equations from 35 to 90, the computational load is

lightened by more than 70%. Thus, the "curse of dimensionality" of Bellman is not a global phenomenon. The reason for the simplification due to direction cosines is, of course, due to the fact that the attitude observations are linear in the state variables, instead of quadratically nonlinear. This means that the highest moments found in the direction cosine differential equations are third moments, which are ignored, whereas the quaternion equations include fourth moments, which are approximated as sums of products of second moments.

It is emphasized that the foregoing computational estimates are conservative, in that only the most obvious common terms between equations were computed once and stored. With judicious attention to commonality, the numbers cited above could be reduced at least by 30%. Therefore, these computational estimates should be regarded as minimum memory estimates, and not maximum speed estimates.

### III. SIMULATION STUDY

#### A. Rate Estimation Mechanization

It was desirable to first evaluate the performance of the foregoing types of filters without having to study the complete attitude reference estimator. Therefore, a problem with similar dynamical and observational behavior of lower dimension was studied, namely the estimation of body angular rates in the presence of noisy continuous observations. This problem has been studied with different approaches to estimation by Detchmehdy and Bridhar (Ref. 22) and Athans and Tse at MIT. This problem has identical characteristics to the complete direction cosine formulation given earlier, e.g., quadratically nonlinear state and linear measurements.

Briefly, the problem is to estimate the state of the noise-driven system

$$\frac{d}{dt} \begin{bmatrix} x_1(t) \\ x_2(t) \\ x_3(t) \end{bmatrix} = \begin{bmatrix} \alpha_1 x_2 x_3 \\ \alpha_2 x_1 x_3 \\ \alpha_3 x_1 x_2 \end{bmatrix} + \begin{bmatrix} \sigma_P & 0 & 0 \\ 0 & \sigma_P & 0 \\ 0 & 0 & \sigma_P \end{bmatrix} \begin{bmatrix} w_1(t) \\ w_2(t) \\ w_3(t) \end{bmatrix} \quad (83)$$

$$x(0) = x_0, \quad \alpha_1 = \frac{I_Y - I_X}{I_X}, \quad \alpha_2 = \frac{I_Z - I_X}{I_Y}, \quad \alpha_3 = \frac{I_X - I_Y}{I_Z} \quad (84)$$

from the noisy continuous observations  $y_i$  of one or more of the  $x_i$  corrupted by additive noise  $\sigma_M v_i(t)$ . The  $w_i$  and  $v_i$  are unit variance zero-mean uncorrelated Gaussian white noise processes, and

$$E\{[\underline{x}(0) - \hat{\underline{x}}_0][\underline{x}(0) - \hat{\underline{x}}_0]'\} \hat{=} \underline{P}(0) = \underline{P}_0 \quad (85)$$

It will be assumed that all three moments of inertia are unequal, so that questions of state observability do not arise immediately when only one angular rate is observed. In this case, the estimator which results from applying the methods outlined in the previous section is

$$\begin{aligned} d\hat{x}_1/dt = & \alpha_1(\hat{x}_2(t)\hat{x}_3(t) + p_{23}) \\ & + \frac{p_{11}}{\sigma_M^2} [y_1(t) - \hat{x}_1(t)] \end{aligned} \quad (86)$$

$$\begin{aligned} d\hat{x}_2/dt = & \alpha_2(\hat{x}_1(t)\hat{x}_3(t) + p_{13}) \\ & + \frac{p_{12}}{\sigma_M^2} [y_1(t) - \hat{x}_1(t)] \end{aligned} \quad (87)$$

$$\begin{aligned} d\hat{x}_3/dt = & \alpha_3(\hat{x}_1(t)\hat{x}_2(t) + p_{12}) \\ & + \frac{p_{13}}{\sigma_M^2} [y_1(t) - \hat{x}_1(t)] \end{aligned} \quad (88)$$

$$\begin{aligned} d\underline{p}/dt = & \begin{bmatrix} \alpha_1(\hat{x}_2 p_{12} + \hat{x}_3 p_{13}) & \alpha_1(\hat{x}_2 p_{22} + \hat{x}_3 p_{23}) & \alpha_1(\hat{x}_2 p_{23} + \hat{x}_3 p_{33}) \\ \alpha_2(\hat{x}_1 p_{11} + \hat{x}_3 p_{13}) & \alpha_2(\hat{x}_1 p_{22} + \hat{x}_3 p_{23}) & \alpha_2(\hat{x}_1 p_{23} + \hat{x}_3 p_{33}) \\ \alpha_3(\hat{x}_1 p_{11} + \hat{x}_2 p_{12}) & \alpha_3(\hat{x}_1 p_{22} + \hat{x}_2 p_{23}) & \alpha_3(\hat{x}_1 p_{23} + \hat{x}_2 p_{33}) \end{bmatrix} \\ & \begin{matrix} \text{SYM.} & & \\ & \text{SYM.} & \\ & & \text{SYM.} \end{matrix} \\ & - \frac{1}{\sigma_M^2} \begin{bmatrix} p_{11}^2 & p_{11}p_{12} & p_{11}p_{13} \\ p_{11}p_{12} & p_{12}^2 & p_{12}p_{13} \\ p_{11}p_{13} & p_{12}p_{13} & p_{13}^2 \end{bmatrix} + \begin{bmatrix} \sigma_p^2 & 0 & 0 \\ 0 & \sigma_p^2 & 0 \\ 0 & 0 & \sigma_p^2 \end{bmatrix} \end{aligned} \quad (89)$$

The form of the equations when two or three components of rate are measured is more complicated, but of the same general form and will not be given here. The equations are similar to those given by Detchmندی and Sridhar, but additional covariance terms arise in the right-hand side of the mean equations with the Bayesian minimum variance approach.

A simulation of these rate estimation

mechanizations was coded in FORTRAN IV for the 7094. The true angular rate equations are obtained from a fourth-order Runge-Kutta solution, with a fixed 0.01-second step size. The estimation first and second order statistics are obtained from a rectangular integration, also with a 0.01-second step size. All of the runs were made with the following initial conditions, which are similar to those in the Detchmندی-Sridhar paper (Ref. 22):

$$\begin{aligned} x_1(0) &= 0.9 \text{ rad/sec} \\ x_2(0) &= 0.5 \text{ rad/sec} \\ x_3(0) &= 0.2 \text{ rad/sec} \\ I_x &= K \text{ slug/ft}^2 \\ I_y &= 2K \text{ slug/ft}^2 \\ I_z &= 4K \text{ slug/ft}^2 \end{aligned}$$

The other initial conditions for the estimator equations are given in Table 2. The assumed and actual values of the moments of inertia, plant noise, and observation noise were the same in all cases, i.e. the effect of modeling errors was not studied. The rate estimation filters were studied in situations where one and three state variables were observed in the presence of noise. Both the Bayesian minimum variance moment-approximating method and the Detchmندی-Sridhar invariant-embedding method were simulated. When only one state variable was observed, some of the estimates converged to solutions out of phase with the true solution. This behavior caused considerable consternation until the following fact was realized: Rate estimation with only one state variable observed is an unobservable problem, even if the moments of inertia are all unequal!

In general, very little is known about the observability of nonlinear differential equations. However, in this particular case, it can be said conclusively that the system is unobservable, i.e., that  $\underline{y}(t)$  for  $0 \leq t \leq T$  does not uniquely define the state  $\underline{x}(t)$  in the absence of noise. For the differential equations

$$\frac{d}{dt} \begin{bmatrix} x_1(t) \\ x_2(t) \\ x_3(t) \end{bmatrix} = \begin{bmatrix} \alpha_1 x_2(t)x_3(t) \\ \alpha_2 x_1(t)x_3(t) \\ \alpha_3 x_1(t)x_2(t) \end{bmatrix} \quad (90)$$

let the true solution be given by

$$\underline{x}(t) = \begin{bmatrix} x_1^*(t) \\ x_2^*(t) \\ x_3^*(t) \end{bmatrix} \quad (91)$$

Consider the alternate solution  $\underline{x}^{**}(t)$  given by

$$\begin{aligned} x_1^{**}(t) &= x_1^*(t) \\ x_2^{**}(t) &= -x_2^*(t) \\ x_3^{**}(t) &= -x_3^*(t) \end{aligned} \quad (92)$$

Now  $\underline{x}^{**}(t)$  clearly satisfies the differential equation, and yet if only the first state variable is observed it results in exactly the same observation time history as  $\underline{x}^*(t)$ , since

$$x_1^{**}(t) = x_1^*(t) \quad (93)$$

This explains the curious out-of-phase behavior of the second and third state variables in some of the simulation runs, since the out-of-phase solution is just as likely a candidate given the observations as the in-phase solution, given that  $\hat{x}_2(0) = \hat{x}_3(0) = 0$ . The solution that the estimator "chooses" is simply a function of the random observation noise sequence. Thus, an inertial reference unit with only one gyro would make a

rather poor three-axis platform, unless further a-priori information was available about the other two orthogonal angular rates. Therefore, the runs reported in Table 2 had all three state variables observed.

The estimation results for two selected cases are given in Figs. 6 and 7. In plot contains the true and estimated values of one of the three angular rates. (Only one is shown to conserve space.) The time histories of the true rates are marked with a "plus" sign, and the estimated rates are marked with circles. Next is a plot showing the evolution of the diagonal elements of the covariance matrix. The three time histories are marked as follows

$$\begin{aligned} P_{11} &= + \\ P_{22} &= \bigcirc \\ P_{33} &= \diamond \end{aligned}$$

The off-diagonal elements of the covariance matrix are also plotted. The coding is

$$\begin{aligned} P_{12} &= + \\ P_{13} &= \bigcirc \\ P_{23} &= \diamond \end{aligned}$$

Fig. 6 is the minimum variance moment-approximating method. The case shown here is with large observation noise, to illuminate the differences between the

Table 2. Summary of Rate Estimation Runs

Run No.	$x_1(0)$	$x_2(0)$	$x_3(0)$	$P_{11}(0)$	$P_{1j}(0)$	Method	$\sigma_P^2$	$\sigma_M^2$	Three-Axis Error (10 Run Average)
A	.9	0	0	3	1	Moment-approximating	0	0.1	0.233 rad/sec
B	.9	0	0	3	1	Invariant imbedding	0	0.1	0.278 rad/sec
C	.9	0	0	3	1	Moment-approximating	0	1.0	0.659 rad/sec
D	.9	0	0	3	1	Invariant imbedding	0	1.0	Over half of the runs diverged

performance of the two filtering methods considered. The estimate is fairly slow to converge (cautious), but it is stable and after 100 seconds is a faithful replica of the true state. Notice also that the covariance matrix elements are fairly smooth and well-behaved.

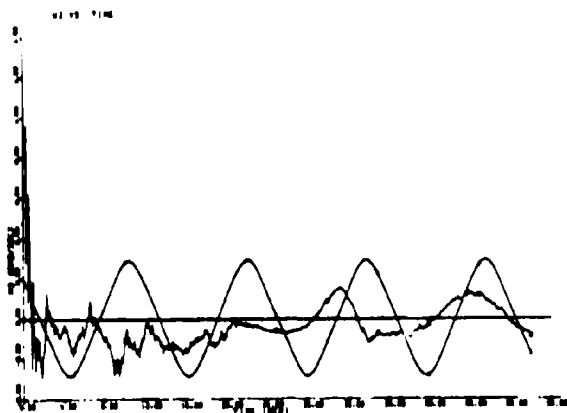


Fig. 6a. Simulation Results for Case C-1

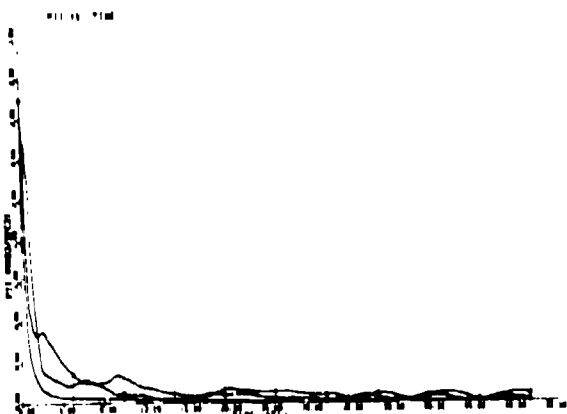


Fig. 6b. Simulation Results for Case C-1 (cont.)

Fig. 7 shows the invariant-embedding method operating under the same conditions as the moment-approximating method shown in Fig. 6, including the same pseudo-random number sequence used to derive the observation noise. The invariant-embedding method seems to be more eager to "jump to the wrong conclusion." Also, the estimate shown on Fig. 7 can be seen to be diverging, and the covariance matrix is going negative definite as indicated by the negative values of the diagonal elements. Note that the modes of the plant dynamics are much more dominant in the covariance matrix elements in this case.

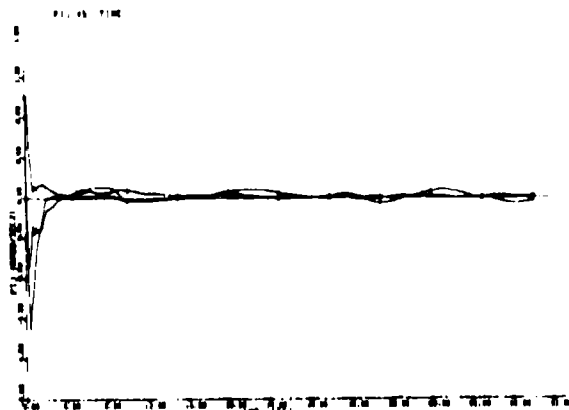


Fig. 6c. Simulation Results for Case C-1 (cont.)

Admittedly, the large values of observed rate noise tend to make this somewhat of an unrealistic example, but it does give a good comparison of the relative performances of the two approaches to estimation. Notice also that the estimation equations derived by the invariant-embedding method are the same as those resulting from the so-called extended Kalman filter approach.

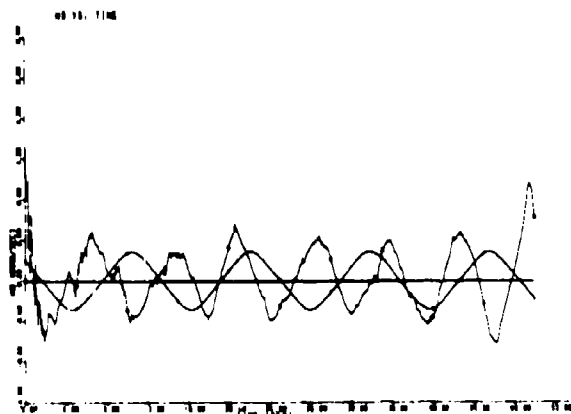


Fig. 7a. Simulation Results for Case D-1

## B. Attitude Reference Mechanization

Based on the above experience, the complete twelve dimensional direction cosine attitude reference mechanization outlined in Section 2 was simulated for a "gyroless" system. This is the type of system where continuous attitude reference information is necessary and only discrete attitude measurements are available, with no rate information available in between attitude discretizes.



system operating on a satellite in a 90 minute orbit whose primary motion is a pitch motion at orbital rate. However, the two transverse rates reach 20% of the pitch nominal amplitude. Two six degree field-of-view strapdown star sensors sweep the sky, seeing down to +3.0 visual magnitude stars with three crossed-slit detectors each.

provide interesting results.) The star sensor observation noise variance is  $0.25 \times 10^{-6} \text{ rad}^2$ . In Fig. 8a, the true attitude error  $\theta_y$  is marked with a "plus" sign and the standard deviation estimate  $\hat{\theta}_y$  is marked with a circle. The variance estimate is seen to portray quite accurately the behavior characteristics of the actual error. The three angular rate estimates are shown in Figs. 8b to 8d, tracking the noisy true rates as best they can in the absence of gyro data.

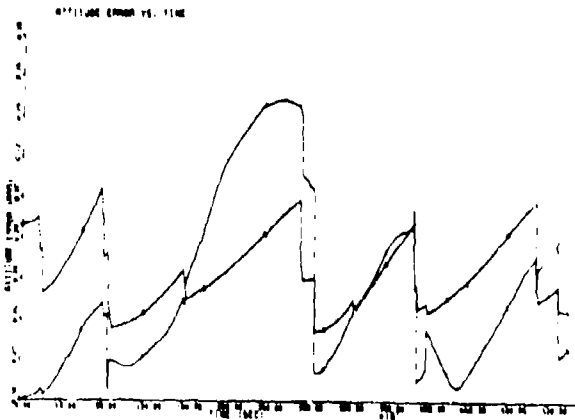


Fig. 8a. Simulation Results for Case 18A

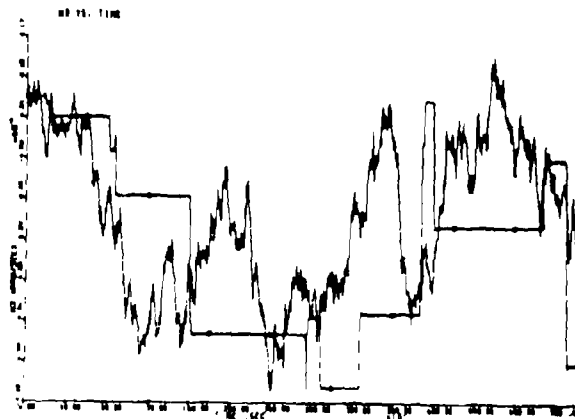


Fig. 8c. Simulation Results for Case 18A (cont.)

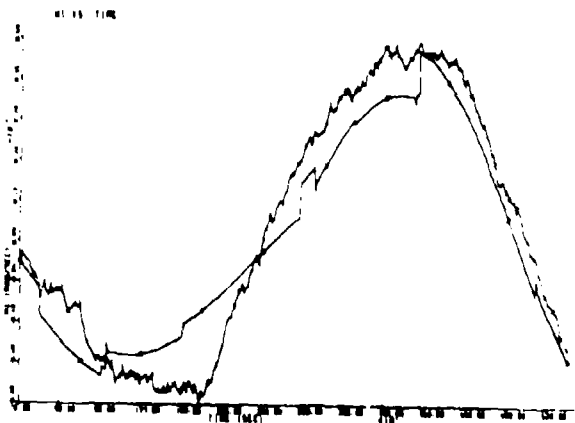


Fig. 8b. Simulation Results for Case 18A (cont.)

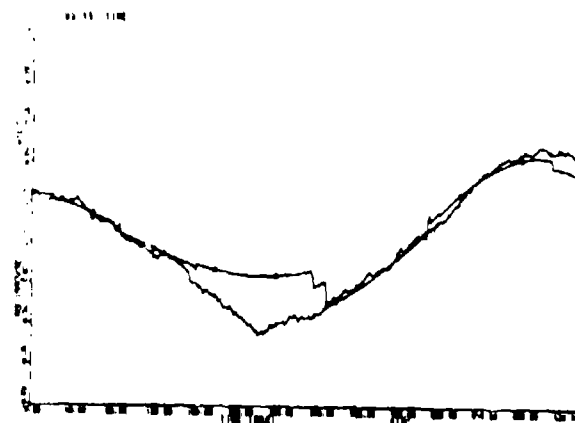


Fig. 8d. Simulation Results for Case 18A (cont.)

The unknown torque acting on the spacecraft causes a white, Gaussian angular acceleration. The angular acceleration spectral density is  $0.5 \times 10^{-11} \text{ rad}^2/\text{sec}^4/\text{Hz}$ . (This is unrealistically large to avoid classification problems and

This type of a system has been used in the past on spin-stabilized spacecraft with slit type star sensors and/or sun sensors.

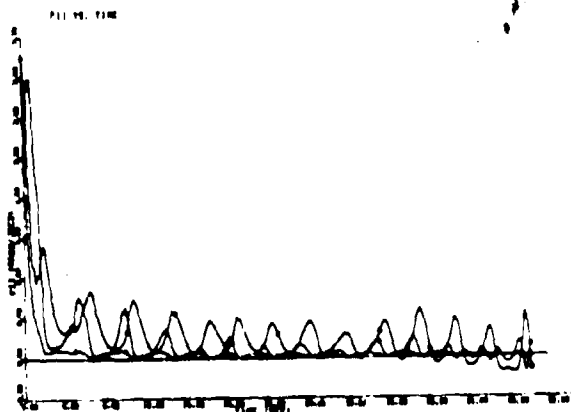


Fig. 7b. Simulation Results for Case D-1 (cont.)

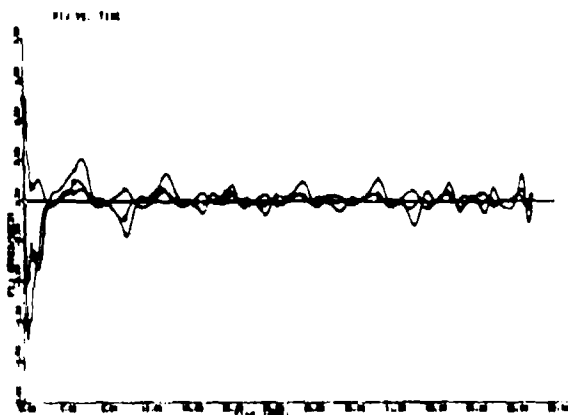


Fig. 7c. Simulation Results for Case D-1 (cont.)

Nonlinear estimation approximations are particularly attractive in this type of system, for two reasons:

1. A nominal attitude history derived from measured rate, about which one can linearize, is not available.
2. The approximate nonlinear equations are almost as easy to solve as a linear filtering solution, because all terms pertaining to continuous observations in the state and covariance equations vanish.

The equations for updating the state and covariance matrix at observation time are simply the Kalman discrete equations, because the observations are linear in the state for the dot product type of observation occurring with slit type detectors.

Many attitude error requirements specified in the last few years are in terms of the so-called three-axis attitude error. That is, small angular errors about almost orthogonal rotation axes in a small angle Euler set are treated as vectors and added, with the accuracy requirement placed on the vector sum. Let a true transformation matrix and a transformation matrix slightly in error be denoted

$$T_{BI_T} = [L_i, i = 1, 9] \quad (94)$$

$$T_{BI_E} = [\hat{L}_j, j = 1, 9] \quad (95)$$

respectively. Then it can be shown that the three-axis attitude error  $\theta_E$  existing between the two triads mapped by these two transformations is given by

$$\theta_E = \left[ (L_1 \hat{L}_4 + L_2 \hat{L}_5 + L_3 \hat{L}_6)^2 + (L_1 \hat{L}_7 + L_2 \hat{L}_8 + L_3 \hat{L}_9)^2 + (L_4 \hat{L}_7 + L_5 \hat{L}_8 + L_6 \hat{L}_9)^2 \right]^{1/2} \quad (96)$$

Also, if the elements of the covariance matrix

$$P = E[(L_i - \hat{L}_i)(L_j - \hat{L}_j)] = [P_{ij}] \quad (97)$$

are available, then it is possible to derive the estimated one sigma three-axis attitude error  $\hat{\theta}_E$ . After applying several transformation matrix identities, this error estimate can be shown to be

$$\begin{aligned} \hat{\theta}_E = \frac{1}{4} & \left[ (1-L_1^2)P_{11} + (1-L_2^2)P_{22} + \dots + (1-L_9^2)P_{99} \right. \\ & - L_1 L_2 P_{12} - L_1 L_3 P_{13} - L_2 L_2 P_{23} \\ & - L_4 L_5 P_{45} - L_4 L_6 P_{46} - L_5 L_6 P_{56} \\ & \left. - L_7 L_8 P_{78} - L_7 L_9 P_{79} - L_8 L_9 P_{89} \right]^{1/2} \quad (98) \end{aligned}$$

Figure 8 shows the results of the moment approximating method being used on a simulated gyroless attitude reference

#### IV. CONCLUSIONS AND RECOMMENDATIONS

An unified approach to the formal mechanization of nonlinear estimators applicable to a wide class of spacecraft attitude reference systems has been presented. In any given spaceborne situation, it would probably be undesired to implement the full detail of these equations, particularly the covariance matrix equations. However, if one wants to look at fixed gain mechanizations, this provides a performance level against which one can evaluate performance. If scheduled gain systems are to be considered, the behavior of the covariance matrix elements provides insight into how the scheduling should be implemented.

#### ACKNOWLEDGEMENT

The considerable help and encouragement of Prof. Harold Kushner of Brown University and the staff of the Office of Control Theory and Application of NASA/ERC are gratefully acknowledged.

#### REFERENCES

1. R. E. Kalman, "A new approach to linear filtering and prediction problems," Trans. ASME, Series D, J. Basic Engineering, Vol. 82, No. 1, pp. 35-45 (March 1960).
2. R. E. Kalman and R. S. Bucy, "New results in linear filtering and prediction theory," Trans. ASME, Series D, J. Basic Engineering, Vol. 83, No. 1, pp. 95-108 (March 1961).
3. G. L. Smith, S. F. Schmidt and L. A. McGee, "Application of statistical filter theory to the optimal estimation of position and velocity on board a circumlunar vehicle," NASA TR-135 (November 1961).
4. "Space Precision Attitude Reference System (SPARS) Phase 1A Final Report (U)," Lockheed Missiles and Space Co., Sunnyvale, California (February 1969) (Secret).
5. H. J. Kushner, "Nonlinear filtering: the exact dynamical equations satisfied by the conditional mode," IEEE Trans. on Automatic Control, Vol. AC-12, No. 3, pp. 262-267 (June 1967).
6. C. G. Pfeiffer, et al., "Sequential processing techniques for trajectory estimation," TRW Report No. 08542-6001-R0-000, TRW Systems Group, Redondo Beach California (13 December 1968).
7. J. L. LeMay, "Recoverable and reachable zones for control systems with linear plants and bounded controller outputs," IEEE Trans. on Automatic Control, Vol. AC-9, No. 4, pp. 346-354 (October 1964).
8. F. C. Schweppe, "Recursive estimation: unknown but bounded errors and system inputs" IEEE Trans. on Automatic Control, Vol. AC-13, No. 1, pp. 22-28 (February 1968).
9. H. J. Kushner, "Approximations to optimal nonlinear filters," IEEE Trans. on Automatic Control, Vol. AC-12, No. 5, pp. 546-556 (October 1967).
10. H. J. Kushner, "Dynamic equations for optimal nonlinear filtering," J. Differential Equations, Vol. 3, pp. 179-190 (1967).
11. H. J. Kushner, "On the differential equations satisfied by conditional probability densities of Markov processes," J. SIAM on Control, Vol. 2, No. 1, pp. 106-119 (1964).
12. W. M. Wonham, "Some applications of stochastic differential equations to optimal nonlinear filtering," J. SIAM on Control, Vol. 2, No. 3, pp. 347-369 (1965).
13. R. S. Bucy, "Nonlinear filtering theory," IEEE Trans. on Automatic Control (Correspondence), Vol. AC-10, No. 2, p. 198 (April 1965).
14. Y. C. Ho and R. C. K. Lee, "A Bayesian approach to problems in stochastic estimation and control," IEEE Trans. on Automatic Control, Vol. AC-9, No. 4, pp. 333-339 (October 1964).
15. A. H. Jazwinski, "Filtering for nonlinear dynamical system," IEEE Trans. on Automatic Control (Correspondence), Vol. AC-11, No. 4, pp. 765-766 (October 1966).
16. A. H. Jazwinski, "Nonlinear filtering with discrete observations," Paper 66-38, Third AIAA Aerospace Sciences Meeting, New York (January 1966).
17. H. Goldstein, Classical Mechanics (Addison-Wesley Publishing Company, Inc., Reading, Mass., 1950), Chapt. 4.
18. R. E. Mortenson, "On systems for automatic control of the rotation of

a rigid body," unpublished technical paper.

19. E. E. L. Mitchell and A. E. Rogers, "Quaternion parameters in the simulation of a spinning rigid body," Simulation, pp. 390-396 (June 1965).
20. Anon., "Dynamics of the Airframe," BU AER report AE-61-4II, Northrop Aircraft, Inc. (September 1952).
21. B. Friedlander, "The effect of incorrect gain in the Kalman filter," IEEE Trans. on Automatic Control, Vol. AC-12, No. 5, p. 610 (October 1967).
22. D. M. Detchmehdy and R. Sridhar, "Sequential estimation of states and parameters in noisy nonlinear dynamical systems," Trans. ASME. Series D, J. Basic Engineering, Vol. 88, No. 2, pp. 362-368 (June 1966).

#### APPENDIX A

##### ATTITUDE ERROR DUE TO UNCORRECTED GYRO DRIFT

Precision strapdown gyro attitude reference systems derive attitude by integrating the torque necessary to rebalance the gyro gimbal angle to zero over the time period of interest. This is accomplished by integrating a voltage proportional to the torquer current in an analog rebalanced gyro or by counting the rebalance pulses in a pulse rebalanced gyro. The error sources for attitude reference systems of this general class can be grouped as follows:

- (1) Gyro rate measurement error
- (2) Integration errors

This discussion is limited to the effects of the angular rate errors inherent in the gyro-rebalance loop combination. Integration errors, which involve such things as integration algorithm truncation and interval length, rebalance pulse quantization, finite word length, and initial condition errors, are discussed by Morgan (Ref. A1), Sullivan (Ref. A2), and others.

Gyro rate errors are usually modeled as some linear combination of constants, ramps, discrete frequency sinusoids, and weakly self-stationary random processes.<sup>1</sup> The main justification for this type of model is that its properties can usually be made to agree well with gyro rate errors measured in the laboratory. The phenomena

causing drift in precision floated gyros are not sufficiently understood at present to permit modeling these errors as functions of their sources.

The effect on attitude error of deterministic components such as constants, ramps, and discrete frequency sinusoids is straightforward. Analysis of the effects of random components of gyro drift usually begins with the assumption that the random process is stationary and ergodic. If the process has a rational power spectral density, it may be shown (Ref. A3) that the autocorrelation function may be approximated to any desired accuracy by a series

$$\phi_{xx}(\tau) = \sum_{k=1}^n A_k \exp(-c_k |\tau|) \quad (A-1)$$

Often, the process  $x(t)$  can be represented sufficiently by the first term of this series

$$\phi_{xx}(\tau) = \sigma^2 \exp(-c|\tau|) \quad (A-2)$$

where  $\sigma^2$  is the variance of the observed process and  $c^{-1}$  is the "fundamental" time constant of the autocorrelation function of the observed process.

On a single axis basis, the angular error in the attitude reference system,  $y(T)$ , which is attributable to the random process rate error is given

$$y(T) = \int_0^T x(t) dt \quad (A-3)$$

The intensity of the attitude error after a time interval  $T$ ,

$$E[y^2(T)] = \overline{y^2(T)} \quad (A-4)$$

follows from the theory of Brownian motion (Ref. A4) for particles whose velocities have an exponential autocorrelation function. Hammon (Ref. A5), and later McAllister (Ref. A6) and Frolov (Ref. A7), showed that for the gyro case the drift angle variance has the form

$$\overline{y^2(T)} = \frac{2\sigma^2}{c^2} [cT + \exp(-cT) - 1] \quad (A-5)$$

It is clear that for times long with respect to the autocorrelation function time constant  $c^{-1}$  that

<sup>1</sup>In addition, environmentally induced errors (functions of vibration, acceleration, and temperature) and dynamically induced errors (e.g., rebalance loop frequency response) are present. These sources are not considered here.

$$\overline{y^2(T)} = 2\sigma^2 c^{-1} T \text{ for } T \gg c^{-1} \quad (\text{A-6})$$

Examination of Eq. (A-2) shows that (A-5) may also be written as

$$\overline{y^2(T)} = T \int_{-\infty}^{\infty} c_{xx}(\tau) d\tau \text{ for } T \gg c^{-1} \quad (\text{A-7})$$

showing that the long period variance of the integral of any random process with a rational spectrum is equal to the product of time and the area under the autocorrelation function for the process. It may also be shown that this relation is exact for the case of white noise at the input to the integrator.

In this case

$$\phi_{xx}(\tau) = A^2 \delta(\tau) \quad (\text{A-8})$$

where

$$\delta(\tau) = \begin{cases} \infty & \text{when } \tau = 0 \\ 0 & \text{when } \tau \neq 0 \end{cases} \quad (\text{A-9})$$

and

$$\int_{-\infty}^{\infty} \delta(\tau) d\tau = 1 \quad (\text{A-10})$$

Hammon (Ref. A5) shows that (A-5) may be written as

$$\overline{y^2(T)} = 2 \int_0^T (T-\tau) c(\tau) d\tau \quad (\text{A-11})$$

Let the autocorrelation function be re-written in terms of the Gaussian pulse function (see Davenport and Root (Ref. A9))

$$c_{xx}(\tau) = A^2 \lim_{a \rightarrow \infty} g_a(\tau) \quad (\text{A-12})$$

where

$$g_a(\tau) = \frac{a}{\sqrt{\pi}} \exp[-a^2 \tau^2] \quad (\text{A-13})$$

so that

$$\overline{y^2(T)} = 2A^2 \int_0^T (T-\tau) \left[ \lim_{a \rightarrow \infty} \frac{a}{\sqrt{\pi}} \exp(-a^2 \tau^2) \right] d\tau \quad (\text{A-14})$$

Reversing the order of integration and limiting, and changing variables yields

$$\overline{y^2(T)} = \frac{2A^2}{\sqrt{\pi}} \lim_{a \rightarrow \infty} \int_0^{aT} \left(T - \frac{\tau_1}{a}\right) \exp\left[-\tau_1^2\right] d\tau_1 \quad (\text{A-15})$$

where

$$\tau_1 = a\tau \quad (\text{A-16})$$

(A-15) then reduces to

$$\begin{aligned} \overline{y^2(T)} &= \frac{2A^2}{\sqrt{\pi}} \int_0^{\infty} T \exp(-\tau_1^2) d\tau_1 \\ &= \frac{2A^2}{\sqrt{\pi}} \cdot \frac{T\sqrt{\pi}}{2} = A^2 T \end{aligned} \quad (\text{A-17})$$

which again verifies (A-7). In this case, however, the relation is exact for all T.

Relation (A-7) can be stated in a more useful form by considering the power spectral density of the exponentially correlated process  $x(t)$ .

$$\begin{aligned} G_{xx}(\omega) &= \frac{1}{2\pi} \int_{-\infty}^{\infty} c_{xx}(\tau) \exp(-j\omega\tau) d\tau \\ &= \frac{2\sigma^2 c}{2\pi(c^2 + \omega^2)} \end{aligned} \quad (\text{A-18})$$

Note that

$$G_{xx}(0) = \frac{\sigma^2 c^{-1}}{\pi}$$

so that Eq. (A-6) may be written as

$$\overline{y^2(T)} = 2G_{xx}(0) T \quad (\text{A-19})$$

In other words, the long period variance of the integral of an exponentially correlated random process is proportional to the product of the power spectral density at zero frequency and time. This result is also derived by Newton (Ref. A8) in a more rigorous manner by contour integration methods. Relation (A-19) also holds for any random process with a rational spectrum, since in this case the autocorrelation function can be represented as a sum of exponential autocorrelation functions, the Fourier transform of which (spectral density) is equal to the sum of the Fourier transforms of the individual elements.

# REFERENCES FOR APPENDIX A

- A1. A. A. Morgan, "Computational errors in the generation of the direction cosine matrix in a strapdown system," Journal of the Institute of Navigation, Vol. 14, No. 1 (1967).
- A2. J. J. Sullivan, "A solution of the critical computational problems associated with strapdown navigation systems," AIAA Guidance and Control Conference (August 1966).
- A3. J. H. Laning and R. H. Battin, Random Processes in Automatic Control (McGraw-Hill Book Company, Inc., New York, 1956.)
- A4. G. E. Uhlenbeck, and L. S. Ornstein, "On the theory of the Brownian motion," Physical Review, Vol. 36 (September 1, 1930).
- A5. R. L. Hammon, "An application of random process theory to gyro drift analysis," IRE Transactions on Aeronautical and Navigational Electronics (September 1960).
- A6. D. F. McAllister, "Lunar and Earth Orbital Navigation," Journal of British Interplanetary Society (1964).
- A7. V. S. Frolov, "Error characteristics of a gyrostabilizer with floated-type gyroscopes," Avtomatika i Telemekhanika, Vol. 26, No. 9 (September 1963).
- A8. G. C. Newton, Jr., "Inertial-guidance limitations imposed by fluctuation phenomena in gyroscopes," Proceedings of the IRE (April 1960).
- A9. W. B. Davenport, Jr. and W. L. Root, Random Signals and Noise (McGraw-Hill Book Company, Inc., New York 1958.)

# APPENDIX B

## USEFUL MOMENT IDENTITIES

There are a number of useful identities relating the expectation of products of random variables to the sums of products of moments of these variables. Judicious use of these identities can result in considerable simplification of the attitude estimation equations. Some of the more useful identities are given here. Additional identities can be easily derived from these.

$$E x_i x_j = x_i x_j + P_{ij} \quad (B-1)$$

$$E x_i x_j x_k = x_i x_j x_k + x_i P_{jk} + x_j P_{ik} + x_k P_{ij} + P_{ijk} \quad (B-2)$$

$$E x_i x_j x_k x_l = x_i x_j x_k x_l + x_i P_{jkl} + x_j P_{kli} + x_k P_{lji} + x_l P_{ikj} + x_i x_j P_{kl} + x_i x_k P_{jl} + x_i x_l P_{jk} + x_j x_k P_{li} + x_j x_l P_{ki} + x_k x_l P_{ij} + P_{ijkl} \quad (B-3)$$

$$E x_i x_j x_k - x_i E x_j x_k = x_j P_{ik} + x_k P_{ij} \quad (B-4)$$

$$E x_i x_j x_k x_l - E x_i x_j E x_k x_l = x_i E x_j x_k x_l - x_j E x_i x_k x_l + 2 x_i x_j E x_k x_l = x_k P_{jil} + x_l P_{ijk} + P_{ijkl} - P_{ij} P_{kl} \quad (B-5)$$

$$E x_i x_j x_k - x_k E x_i x_j = x_i E x_j x_k - x_j E x_i x_k + 2 x_i x_j x_k = P_{ijk} \quad (B-6)$$

SESSION II

ATTITUDE SENSORS AND SENSING TECHNIQUES

Chairman:  
Mr. R. Lillestrand  
Control Data Corporation  
Minneapolis, Minnesota

---

Two Approaches to the Star Mapping Problem for Space Vehicle Attitude Determination	115
Sub-Arc Second Star Sensors, Design and Fabrication	133
In-Orbit Startracker Misalignment Estimation on the OAO	143
Solar Attitude Reference Sensors	155
Accuracy of IR Horizon Sensors as Affected by Atmospheric Considerations	161
Instrumentation for Infrared Horizon Sensing	169

TWO APPROACHES TO THE STAR MAPPING  
PROBLEM FOR SPACE VEHICLE  
ATTITUDE DETERMINATION

Mark Gorstein and James N. Hallock  
NASA Electronics Research Center

and

Juri Valge

MIT Instrumentation Laboratory

ABSTRACT

The use of gimballed and strapped-down star trackers for spacecraft attitude determination is a well developed technology, but it presupposes some restricted degree of knowledge about the star positions and usually requires a special maneuver to obtain a favorable vehicle attitude. The paper considers the general problem of self-contained attitude determination in three axes without a priori knowledge of the star position-vehicle attitude relationship and without the need for any special maneuvers. Two approaches are discussed: The first approach concerns a search for a simple and unique star pattern and an optimum instrument geometry based upon the actual angular distribution of the stars. The second approach concerns the adaption of holography to the problem of a recognition of a star field for attitude determination.

1. INTRODUCTION

One of the quantities required by a spacecraft for guidance is its attitude. Among the several methods now employed for inertial attitude determination (horizon sensing, gravity gradient etc.), inertial gyroscope packages augmented by star tracking provide the most accurate and versatile approach. The information for determining inertial attitude is available in stellar positions, and only recently have efforts been made to utilize it beyond tracking of known stars. Various attempts have been made in the direction of fuller utilization of the stellar information by development of star mappers.

At least for this discussion, a very clear

distinction is made between star trackers and star mappers, as shown in Fig. 1. The star tracker or monitor must have attitude information sufficiently accurate to point at a star so that the star falls within its field of view. The star mapper's primary function is star identification, and it needs no a priori attitude information. It is well recognized that the area of technology between these extremes is well populated with mission oriented designs and designs geared to specific instrumentation configurations. Under consideration in this paper is the general problem of self-contained attitude determination in three axes without a priori knowledge of the star position-vehicle attitude



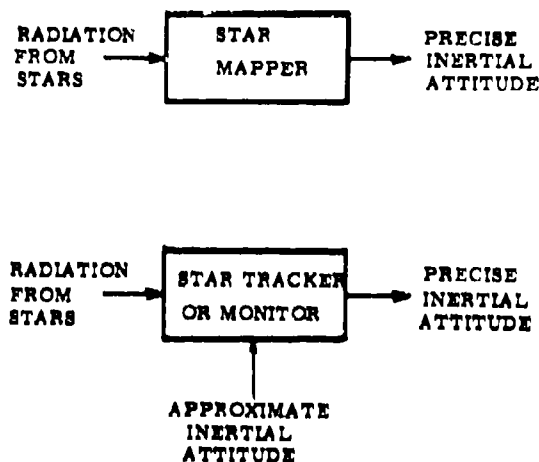


Fig. 1. Definition of Star Tracking and Star Mapping.

relationship and without the need for any special maneuvers. Two approaches will be considered. The first approach uses star catalog information for determination of a uniquely identifiable star pattern which is available in all attitudes of pointing. Minimal detector parameters are assumed from known state of the art hardware. The second approach concerns the adaptation of holography to the problem of recognition of star fields. The primary objective is a device which is completely autonomous and which will provide three-axis attitude reference information using but a single device sampling a single star field. The star position data will be processed at the speed of light without a computer.

## II. HISTORY

Autonomous space navigation has been a desirable goal for a long time, and miscellaneous approaches of stabilized attitude sensing, augmented by the use of star trackers, have been considered. There has been a continual evolution of devices, using stellar information for the purpose of vehicle attitude or position determination. The classical star trackers have been plagued by gimbal readout uncertainties and other accuracy limiting phenomena (Ref. 1) as well as the power required to articulate gimbals and activate the readout logic.

At first attempts were made to use star trackers as area scanners, and in some cases speed of response was too low, while in all cases at least two gimbals were used. Several approaches to reduce the number of gimbals were considered (Ref. 2) and some of those were evolved into star mapping schemes in

their next step of development. However, moving parts were still needed to generate information in two coordinates (Refs. 3 and 4). Some elimination of the moving parts is possible if the vehicle motion is periodic and is sufficiently stable (Refs. 5 and 6). In all these cases, the pointing direction of the instrument coordinates must be known at least in one direction. This requirement destroys the attainment of complete autonomy.

The state of the art stellar sensors of today have the above described limitations. The investigations reported below take the final step to arrive at a completely autonomous star mapper for stellar inertial attitude determination without any a priori pointing information of the mapper.

## III. FIRST APPROACH

### A. Description of the Problem

Men have used star patterns for visual identification of stars for centuries. However, it is difficult to achieve automated instrumentation on the same level of sophistication as the decision processes found in man. It is desirable therefore to find ways for simplifying the identification problem, so that it becomes a feasible task for state of the art instrumentation.

The problem at hand consists of three parts:

- Find the type of pattern into which real stars can be arranged uniquely.
- Determine its availability in all attitudes of pointing on the celestial sphere.
- Prove with a simulation program that the pattern can be used for identification of the stars that it contains.

### B. The Choice of an Identifiable Star Pattern

The basic criterion for identifying star patterns, and consequently individual stars making up the star pattern, was that star position only would be used for identification purposes. It was well recognized that there are other properties of stars which may differ sufficiently from star to star and thus aid in identification. Besides star position, the applicability of the star magnitude and spectral energy content to the problem on hand will be discussed.

#### Star Magnitude

Star magnitude is a complex quantity since it depends upon the net energy sensed by a particular detection system from a particular star. Its use

for identification imposes an accurate calibration requirement on the detection system. Calibration of radiometric sensors in practical mass-produced detection systems is possible to an absolute accuracy of 10% to 20%. Besides initial calibration, the stability of the entire detector system with time and environment will be a potential degrading factor on the detector system performance. Interference from a bright source often results in a false star detection in the detector system and discrimination by magnitude alone is not at all possible in this case. Thus there is a whole group of stars which, according to their magnitude, fall into this region and therefore no unique determination of the star identity is possible. Finally, there is considerable uncertainty about the actual spectral content of star radiation outside the earth's atmosphere. The present-day knowledge of star radiation spectral content is restricted to the atmospheric window regions and has barely been explored even in this limited region. This would restrict the magnitude identifying sensor response to the atmospheric window regions even for operation outside the atmosphere.

#### Spectral Energy Content of Stars

Another star identification scheme (Ref. 7) involves the use of the spectral energy content of the stars. Energy from a star is measured in several wavelength regions and the intensities in each region for a given star are used as the identification property. The greatest potential problem here is the basic incompatibility of detector sensitivities and star energy availability. Therefore, independent spectral measurements over restricted wavelength regions require proportionally more time to complete the measurements or need physically larger detector systems. Stars must be detected in an operational situation during a finite time period. The maximum allowable time period is very often related to the libration rates and the libration amplitudes of the base from which measurements are made. In order to overcome the effects of high libration rates, tightly controlled stabilization can be employed in some cases, but this requires auxiliary attitude sensing, and somewhat defies the purpose of the star mapper altogether. The instrumentation has the same problems with calibration and stability as the problems inherent in the systems using only magnitude. If there were a radical improvement in the available energy (such as might be found after more measurements above the atmosphere) and a major improvement in detectors, the spectral identification method may be usable, from instrumentation viewpoint, but results appear to remain plagued with ambiguities because of radiometric calibration difficulties very much like mappers using the star

magnitude.

#### Star Positions

The star positions are recorded in a star catalog more accurately than are the star magnitude and the spectral type, because astrometry in angular measurements is more advanced than in radiation measurement. This uniqueness is due to a relatively high accuracy of position measurement. Even if the star position is measured to an accuracy of only one arc minute, the absolute accuracy on a  $360^\circ$  circle is 0.00464%. This shows the potential of the angle criterion for identification, in contrast to the possibilities of the magnitude discrimination. Other factors of concern are the stability of the calibration for angle measurement and the angular distribution of the stars.

The angular stability of star position measurements in a strapped-down system is dependent upon the proper thermal and structural design of the instrument. This is one of the factors which is most often overlooked in instrument designs; the radiometry and electrical shielding problems often overshadow in emphasis the most elementary structure and thermal design requirements. With appropriate care the influence of thermal and force loads upon the structure should not contribute to the measurement system inaccuracies in excess of the above 0.00464%.

A distinction should be made here between detector stability in affecting the star measurements for pattern identification, and the inaccuracies between mapper coordinates and the operational support vehicle coordinates. Only the inaccuracies affecting the identification of stars in a pattern are of interest in the current study, since the accuracy problems affecting coordinate relationships have been adequately analyzed for star trackers.

#### Choice of an Identifiable Star Pattern

The method used here finds the stellar coordinates of the individual stars in the group by identifying the stars by their numbers and referring to the star catalog. The problem which is analyzed here is primarily concerned with identification of stars in a pattern, and therefore factors affecting this process will be emphasized.

The uncertainties which affect the identification process involve the detector resolution and the entire detection system dimensional stability. The detector resolution causes a certain number of star positions to become indistinguishable from one another. The dimensional instability of the detector system causes uncertainties in the size

of the field of view. The net result is that there will be patterns composed of different stars that appear to have similar geometries and cannot be distinguished from one another. If the number of stars in the group forming the pattern is increased, this problem will diminish. The increase in the number of stars in the group, however, increases the complexity of instrumentation and identification time. Finally, some compromise has to be reached between the uniqueness of star patterns and the complexity of information.

Another important criterion for determining the type of an acceptable pattern is the computational use of stars identified in the pattern. It is necessary to distinguish the differences involved in computational use of stars and the ability to identify them as a pattern. The magnitude of angular separation of stars in a pattern recognition problem should be sufficient to overcome the detector related problems described earlier, but has no particular lower or upper bound in value. On the other hand, it is difficult to use star positions for coordinate computations if their separation angles are less than  $10^\circ$ . The type of difficulties and their severity depend upon the navigation or attitude control problem and are generally related to the computational difficulties in establishing coordinate system relationships with nearly collinear vectors. The difficulties also depend upon how many stars are completely used in the problem. For example, two stars give enough information for a coordinate determination except for a  $180^\circ$  ambiguity, and no great precision is required to resolve this ambiguity. Therefore, if two stars were separated by an angle larger than  $10^\circ$ , the third star could be as close to one of them as allowed by the detector resolution. However, if all other factors are not relevant, a larger than  $10^\circ$  separation of stars in the pattern is desirable. If one of the separation angles were near  $90^\circ$ , the computations would be simplified. Another consideration is the availability of star pairs. For this purpose a study was made around  $80^\circ$  separation angle, to determine an optimum value. As shown in Fig. 2, the value can be chosen as  $80^\circ$ .

Practical optical systems with this field of view are not available, therefore two fields of view, separated by  $90^\circ$  center to center are used. The size of the field of view for the first tests was estimated from Kleiman's study (Ref. 8) to be  $20^\circ$ , and based on available data the sensor resolution was chosen to be 1200 lines.

The basic ground rules for the investigations to be reported here were established reflecting the criteria discussed above, and can be summarized as follows:

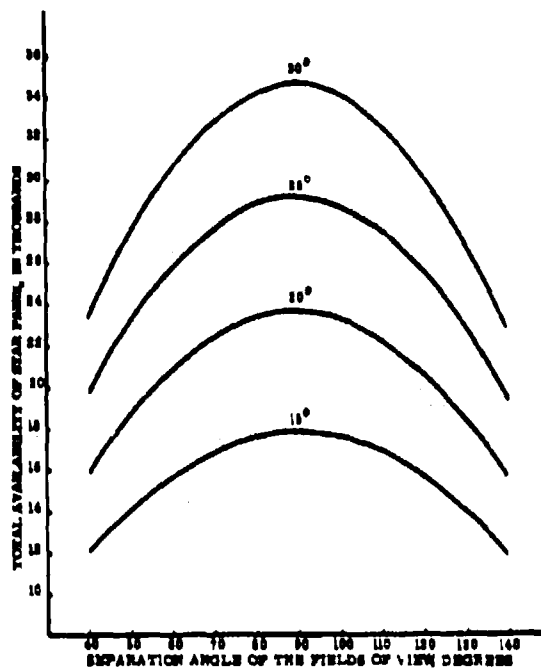


Fig. 2. Total number of star pairs plotted as a function of star separation angles for two fields of view, for various fields-of-view diameters, using stars of  $m_v = 3.8$  and brighter.

- Angular position information only may be used for searching for suitable star patterns and for identifying stars from measured information.
- The magnitude or spectrum of the stars should not be used for the purpose of identifying the stars as a pattern, or individually.
- One of the separation angles in the star pattern should be as close to  $90^\circ$  as possible.
- The measure of a star pattern usefulness in star mapper operation is the comparison of the total number of possible patterns that can be formed with the number of patterns that cannot be distinguished from each other.

#### Operational Star Catalog

The Operational Star Catalog for the star identification is a condensed format type catalog where as much information as possible is pre-processed on the ground for efficient on-board computations. The Operational Star Catalog is formed from the General Star Catalog as

follows:

- Select stars according to the energy needed by the detector system.
- Update the star positions in the coordinates suitable for the type of mission, for some mean epoch of the mission.
- Compute unit vectors in the direction of stars:

$$\underline{S}_1 = \begin{bmatrix} \cos RA \cos \delta \\ \sin RA \cos \delta \\ \sin \delta \end{bmatrix} = \begin{bmatrix} S_x \\ S_y \\ S_z \end{bmatrix}; \quad (1)$$

$\underline{S}_1$  - a unit vector in the direction of a star with identification number  $S_1$ .

RA - right ascension of a star

$\delta$  - declination of a star

- Compile the Operational Star Catalog by listing for each star  $S_x$ ,  $S_y$ ,  $S_z$  and the star identification (catalog) number  $S_i$ .

The Operational Star Catalog is entered into the storage medium of the flight computer before the launch of the vehicle. Therefore, all test and simulation operations in this study use only the Operational Star Catalog. The detector response is not specified in these studies and therefore visual star magnitude is used as a measure of the energy criterion.

#### Mapper Configuration and Analytical Formulation

In accordance with the conclusions from a. to d. above, mapper parameters were chosen for testing total availability and ambiguities of star patterns. The optical and detector systems of the mapper must form two circular fields of view, each  $20^\circ$  in diameter with a resolution of 1 minute of arc (1200 lines) and spaced  $90^\circ$  center to center.

For vehicle attitude determination without any a priori information it is necessary to have data about the positions of three stars. Therefore, three stars in a pattern is considered a minimum requirement. Furthermore, it was found that star pairs are quite ambiguous and their total number is less than the total number of star triplets formed in patterns. The number of star pairs is plotted as a function of the field of view diameter in Fig. 3, and the number of

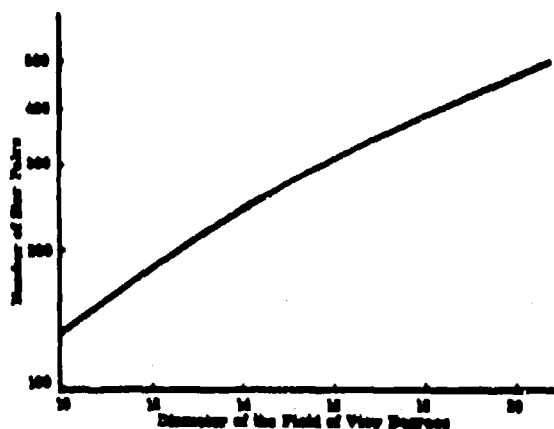


Fig. 3. Total number of available star pairs as a function of the diameter of a single field of view, using stars of  $m_v = 3.0$  or brighter.

star triplets are plotted as a function of field-of-view diameter in Fig. 4. The star triplet is formed by requiring at least two stars in either field of view, separated from each other by at least the sensor resolution, and at least one star in the remaining field of view.

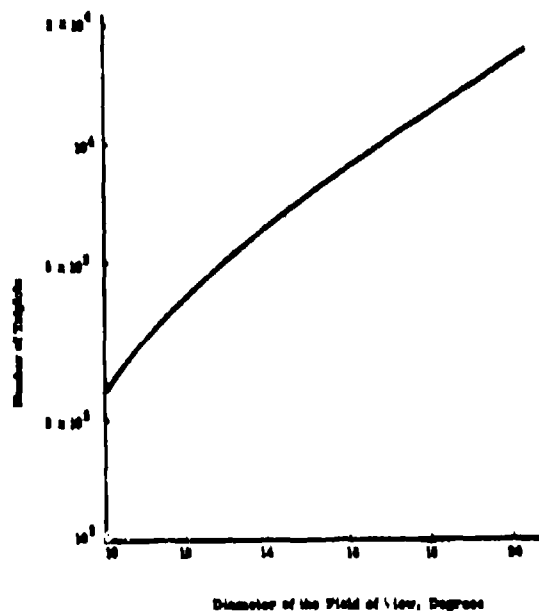


Fig. 4. Total number of three star patterns (triplets) plotted as a function of the diameter of the two fields of view. Stars of  $m_v = 3.0$  and brighter are used.

Computations for determining the star triplets formed by the stars in the Operational Catalog involve at first a test of all possible pairs for a fit in one field of view:

$$\cos(2\theta - \epsilon) \leq \underline{S}_1 \cdot \underline{S}_2 \quad (2)$$

where

$\theta$  - angular radius of each field of view

$\epsilon$  - accuracy of the field-of-view location with respect to the instrument boresight.

The pairs that fit in a field of view are then tabulated, and the entire Operational Catalog is searched for third stars corresponding to each pair. The search is carried out by performing a number of tests between the star pair and the stars in the Star Catalog in order to determine which stars could be in the second field of view. The first test consists of a comparison which eliminates most of the unsuitable candidates by requiring that both conditions below are satisfied:

$$\cos(90^\circ - 2\theta) \geq \underline{S}_3 \cdot \underline{S}_1 \geq \cos(90^\circ + 2\theta); \quad (3)$$

and

$$\cos(90^\circ - 2\theta) \geq \underline{S}_3 \cdot \underline{S}_2 \geq \cos(90^\circ + 2\theta); \quad (4)$$

- $\underline{S}_1$  - unit vector in direction of a star in first field of view, star 1.
- $\underline{S}_2$  - unit vector in direction of another star in first field of view, star 2.
- $\underline{S}_3$  - unit vector in the direction of the star which is being tested to determine if it is in second field of view, and therefore the third star in the pattern.

More tests will follow only if equations 3 and 4 are both satisfied; otherwise the next star is considered for the first test. For further tests the principle involved is that if on the celestial sphere a small circle of radius  $\theta$  contains two stars and any part of a great circle drawn with the star under test as its center, then the star under test can be a third star.

Referring to Fig. 5, if on the celestial sphere, small circles are drawn about stars  $S_1$  and  $S_2$ , the area common to both small circles must then be within angle  $\theta$  of a great circle (of radius  $90^\circ$  drawn about  $S_3$ ). The method of using circles drawn about stars on a celestial sphere for studying the angular relationship of

the stars is described in Ref. 8.

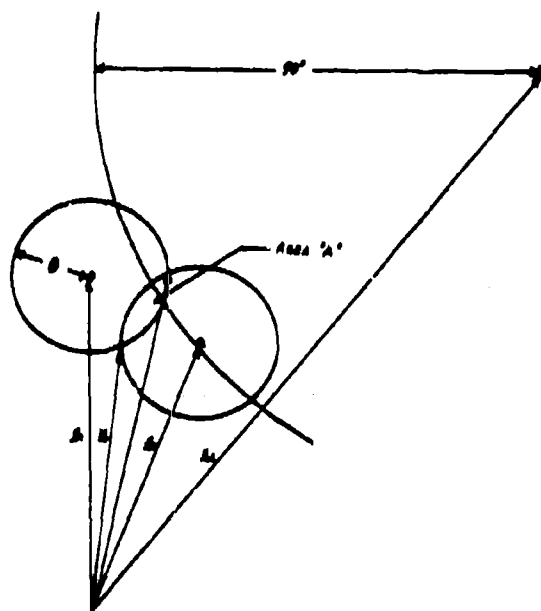


Fig. 5. Geometry of third star determination.

Ambiguous triplets are identified by actually looking at earlier computations of star pairs as potentially ambiguous patterns. The actual ambiguous triplet test then merely compares the angles of the prospectively ambiguous pair stars with the conventionally found third stars. The ambiguities arise because the accuracy of star locations specified in the catalog is much higher than the resolution of the sensor. Therefore, the sensor identifies star pairs with separation angle differences less than its resolution as being the same pair. The effect of the sensor resolution as well as the star magnitude upon the number of ambiguities and available triplets is shown in Fig. 6.

A still clearer indication of the dependence of the number of ambiguous triplets upon resolution is given in Fig. 7, where the ambiguous triplets are plotted as a function of lines of resolution for several fields of view. Special attention is called to the case of a  $20^\circ$  diameter field of view, visual star magnitude 3.0, and 1200 line resolution. This corresponds to the median star and mapper parameters assumed. The total number of triplets is equal to 16000 and of those, 80 are ambiguous, meaning there are 80 pairs of triplets which cannot be distinguished from each other by this particular mapper configuration.

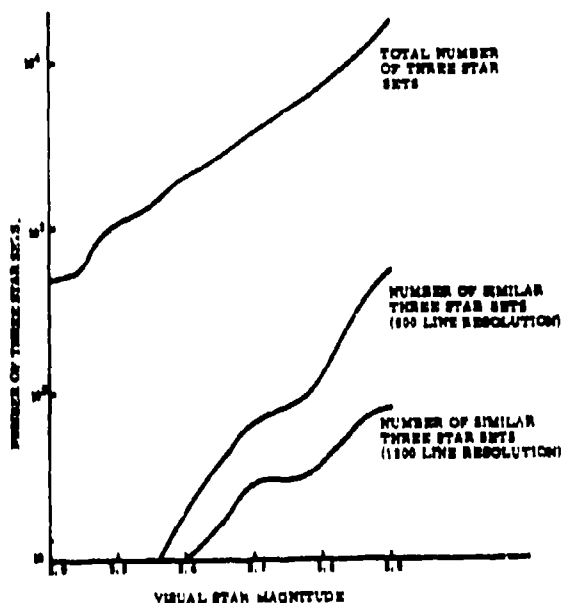


Fig. 6. Total number of three star sets, and similar three star sets plotted as a function of visual star magnitude, for two sensor resolutions.

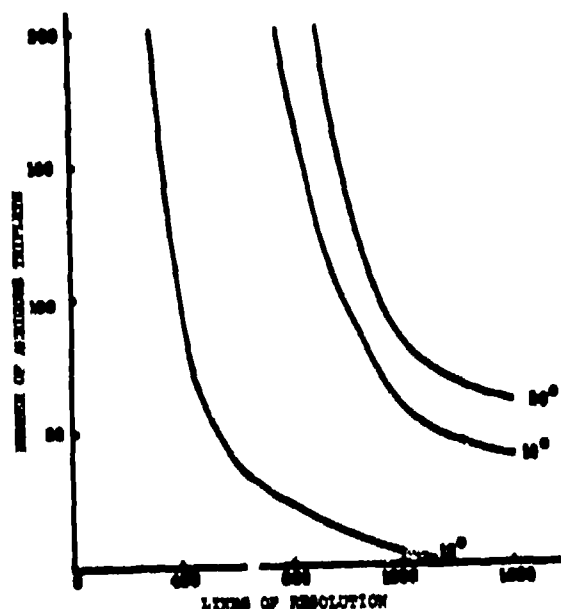


Fig. 7. The number of ambiguous star triplets plotted as a function of the lines of resolution for various fields of view.

### C. All Attitude Availability of Star Patterns

There are numerous methods which may be used to investigate the distribution of identifiable star patterns as a function of the orientation of the mapper coordinates with respect to celestial coordinates. It has not been possible to find an accurate statistical description of star positions on the celestial sphere, and therefore it is necessary to consider more deterministic although possibly laborious approaches to the solution of the star pattern availability question.

A very simple scheme was used since the analysis time was reasonable and from an estimate the computation machine time was not prohibitive (about 119,952 individual mapper orientations need to be investigated), and complete explicit information for every position of a field of view can be found.

#### Description of the Approach

Two circular fields of view, the center of each definable by two coordinates, result in a four-dimensional description of the pattern availability. In order to overcome this difficulty, the following approach will be used:

- Designate the fields of view as 1 and 2, attaching no preference as to which is which. Both fields of view are circular, with radius  $\theta$ ; the centers of the fields of view are separated by  $90^\circ$ .
- Letting one field of view (center of field of view #1) remain in place the other center is moved in steps of  $\gamma$  degrees through a complete great circle.
- At first, field of view #1 is checked and if it contains two or more acceptable stars, only one star is required in field of view #2 for each of its positions. If field of view #1 contains only one star, then field of view #2 is required to contain two stars in each of its great circle positions. If field of view #1 contains no stars, the next position is incremented without searching field of view #2. At the end of the great circle, the total number of positions in which a complete set of stars was available for pattern determination is counted and its ratio with the total number of steps, NP, will be computed:

$$NP = \frac{360^\circ}{\gamma} ; \quad (5)$$

$$C = \frac{NPI}{NP} \times 10 ; \quad (6)$$

where

C - an integer less than ten, or an asterisk showing in 10% amounts the coverage of celestial sphere by useful star patterns.

NPI- the number of positions where an identifiable star triplet was found.

Figure 8 is a schematic representation of the search routine for one point on display. For the next point field of view #1 is incremented by approximately  $\gamma$  degrees and the procedure depicted in Fig. 8 is repeated.

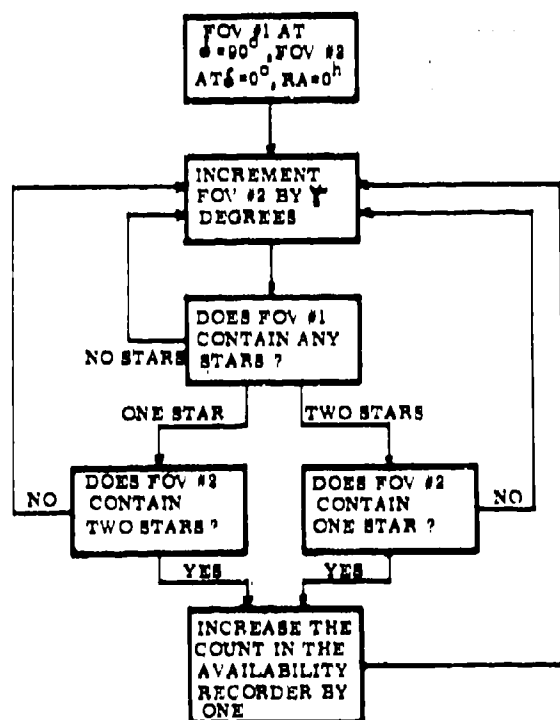


Fig. 8. Operations for availability determination.

#### Type of Display

The display of the computed information consists of symbols representing the value of C. The number of symbols in each line is the same as the number of the field of view #1 incremented positions. Four displays are incorporated into Fig. 8. Star mapper parameters and energy content of stellar information were varied, to determine the sensitivity of star set availability to these parameter changes.

Figure 10 shows the change in percent availability of star sets with magnitude. Figure 11 shows the effect of the change in the field-of-view diameter upon the three star set availability.

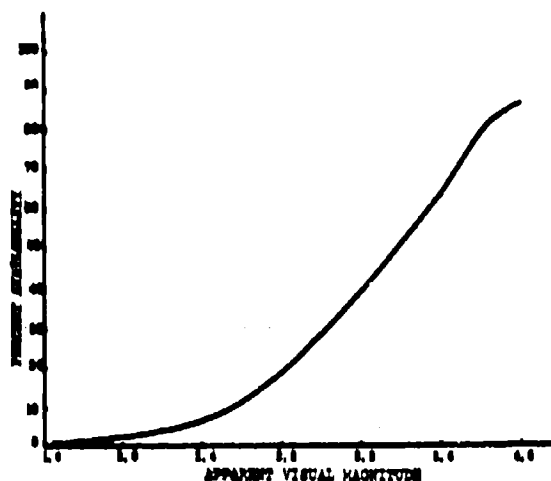


Fig. 10. Percent availability of star sets plotted as a function of star magnitude. Field-of-view diameter is  $20^\circ$ .

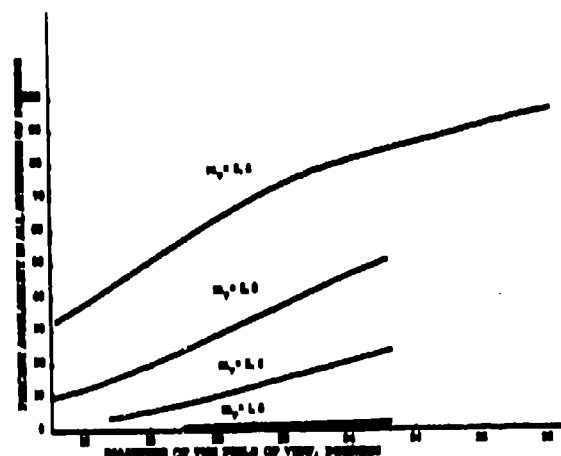


Fig. 11. Percent of availability of three star sets plotted as a function of the diameter of the two fields of view for various star magnitudes.

At first it was anticipated that a marked change in percent coverage would result from changing the test step size  $\gamma$ . However, at magnitude 3.0 and field of view diameter of  $20^\circ$ , no change at all in percent availability occurs if the test step size is varied from  $3^\circ$  to  $10^\circ$ . Hence the attained percent coverage with the  $5^\circ$  test step size is correct and there is no need to decrease the step size (and therefore increase the analysis

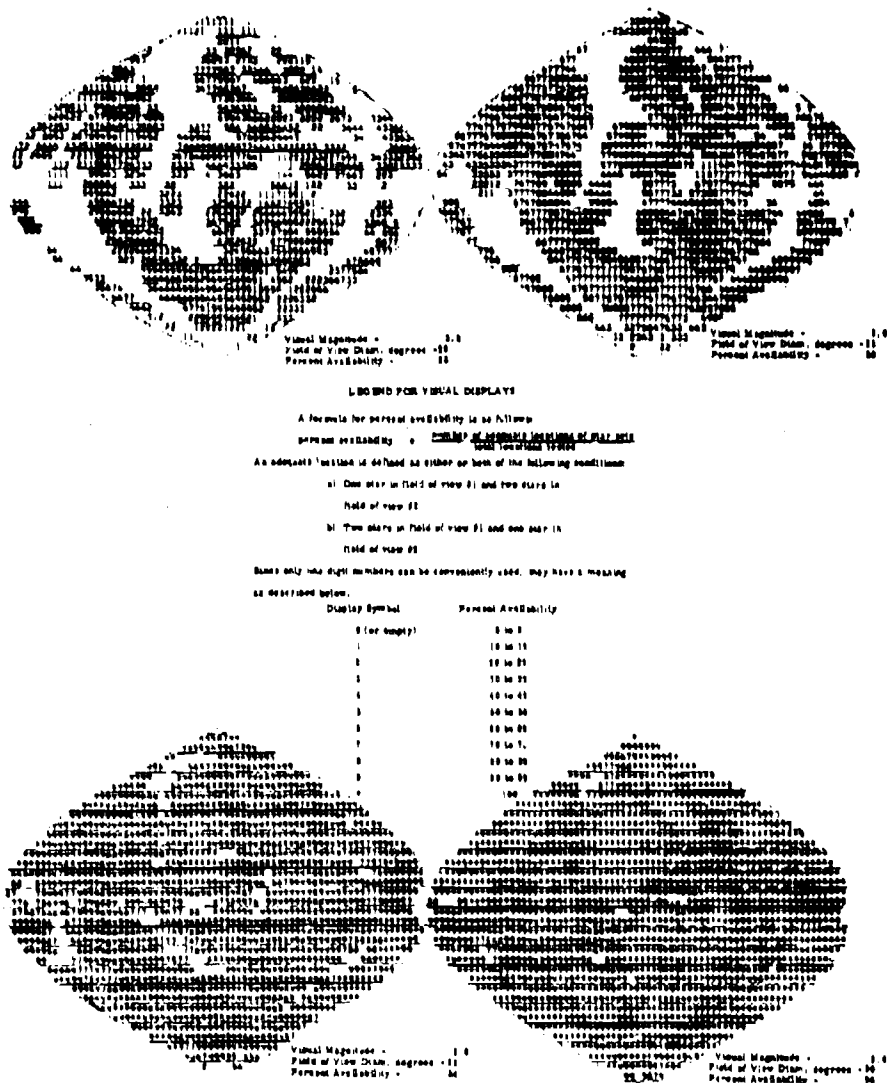


Fig. 9. Four displays of star set availability for various field of view diameters and star magnitudes.

computer time).

In conclusion for this study, acceptable percent coverage of the entire celestial sphere by star sets can be obtained with fields of view  $25^\circ$  to  $30^\circ$  in diameter and with the requirement to detect stars of visual magnitude 3.8 and brighter. The use of visual magnitude implies the use of sensors similar in response to the human eye. This is not necessarily true, and efforts are continuing in matching broad

spectral band detectors with available extra-terrestrial star data for the purpose of generating a more flexible Operating Star Catalog.

#### D. Simulation of Star Mapping

The simulation of star mapping on a computer has to be formulated in accordance with actual operating procedures of an operational star mapper system. As shown in Fig. 12, only the part concerned with the identification



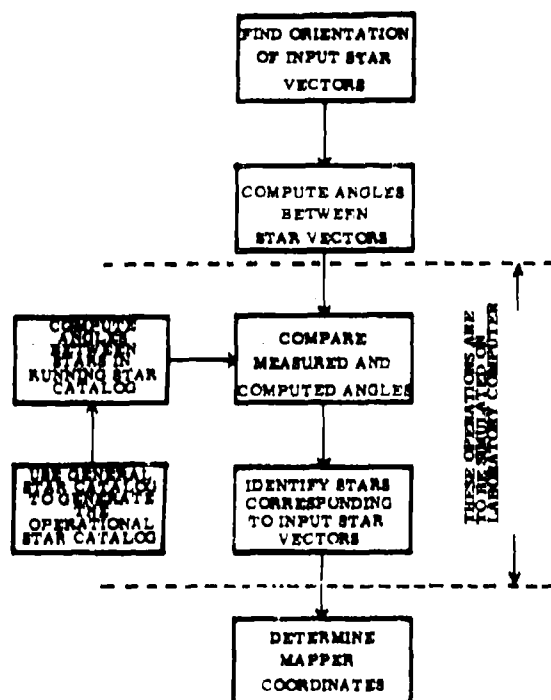


Fig. 12. Functions of an Operational Star Mapper

algorithm has been simulated.

The cosines of the separation angles between unit vectors to some known stars, designated here as  $S_1$ ,  $S_2$  and  $S_3$ , were used as input information for this simulation, and the algorithm had to find these stars from the Operational Star Catalog. This was accomplished several times, using the process described here.

The three input angle cosines are entered into computer storage media and are listed into the heads of columns in array #1, as  $\cos\beta_1$ ,  $\cos\beta_2$ ,  $\cos\beta_3$ . The separation angle cosines of the stars in the Operational Star Catalog are computed without regard to order:

$$\begin{aligned} \cos \eta_{ij} &= \underline{S}_i \cdot \underline{S}_j \\ &= S_{ix}S_{jx} + S_{iy}S_{jy} + S_{iz}S_{jz} \quad (7) \end{aligned}$$

$$j \geq i+1$$

$S_i$  - identification number of  $i^{\text{th}}$  star

$S_j$  - identification number of  $j^{\text{th}}$  star

$\eta_{ij}$  - separation angle between stars which have unit vectors designated  $\underline{S}_i$  and  $\underline{S}_j$

For the identification of individual stars a comparison of input separation angle cosines is made with the separation angles computed from data in the Operational Star Catalog. This procedure can best be described as an operation of steps for each computation.

1. Compare  $\cos \eta_{ij}$  to cosines of input separation angles:

$$\cos(\beta_1 - \sigma) \geq \cos \eta_{ij} \geq \cos(\beta_1 + \sigma) \quad (8)$$

$$\cos(\beta_2 - \sigma) \geq \cos \eta_{ij} \geq \cos(\beta_2 + \sigma) \quad (9)$$

$$\cos(\beta_3 - \sigma) \geq \cos \eta_{ij} \geq \cos(\beta_3 + \sigma) \quad (10)$$

where

$\sigma$  - resolution of the sensor

2. If  $\cos \eta_{ij}$  meets any of the criteria of 1, enter  $S_i$  and  $S_j$  into the appropriate column in array #1.

3. Find  $\cos \eta_{ij}$  for all  $i$  and  $j$ , and repeat steps 1 and 2.

Now array #1 is ready for identification of individual stars and the following discussion attempts to reason a solution.

Choose the first  $S_i S_j$  corresponding to  $\cos\beta_1$ . There  $S_i$  and  $S_j$  could be the same as  $S_1$  and  $S_2$  used for input information generation. Next choose the  $S_i S_j$  corresponding to  $\cos\beta_2$  which has one of the star numbers in common with those listed under  $\cos\beta_1$ . If no such  $S_i S_j$  corresponding to  $\cos\beta_2$  exists, the first  $S_i S_j$  corresponding to  $\cos\beta_1$  represents an ambiguous angle, and the next  $S_i S_j$  corresponding to  $\cos\beta_1$  is chosen and the same test is made. The test is then repeated until a  $S_i S_j$  is found which is formed with a star common to at least two pairs. The common star to both pairs is tentatively called  $S_2$ ; the other star in the  $\cos\beta_1$  column is called  $S_1$  and in the  $\cos\beta_2$  column,  $S_3$ .

After two pairs with one common star have been found, the remaining two stars are compared to the two star list for  $S_i S_j$  corresponding to  $\cos\beta_3$ , to see if a pair making up  $S_1 S_3$  is present. If two such stars are found, the stars

are identified. If two stars corresponding to the two stars of the pair  $S_1 S_3$  were not found among those corresponding to  $S_1 S_2$  listed under  $\cos\beta_3$ , then search must be repeated for further values of  $S_1 S_2$  corresponding to  $\cos\beta_1$  and after exhausting this column repeat the operations with  $S_1 S_2$  corresponding to  $\cos\beta_2$ , then again search the  $\cos\beta_3$  column for  $S_1 S_3$ . Several star triplets were successfully identified by this simulation, and no difficulties with the use of the algorithm were experienced.

#### E. Conclusions

The basic question of availability of unique star patterns for all pointing attitudes, and the ability of the star mapper to identify the individual stars, has been answered as shown in the two preceding sections. This means that completely autonomous stellar attitude determination by the use of a star mapper alone is possible. The mapper should have two fields of view, each  $25^\circ$  to  $30^\circ$  in diameter, and  $90^\circ$  apart center to center. It should be sensitive enough to detect stars brighter than visual magnitude 3.8; no limit in sensitivity need be imposed.

The autonomous capability does not hinder operations, if indeed the approximate pointing direction of the mapper is known, mainly from its own previous autonomous attitude determination. A priori knowledge of attitude reduces the computation time. Thus no limitations to a present systems type operation are imposed by the star mapper but the ability for autonomous attitude determination has become available. The autonomous capability allows the star mapper to operate without a gyrostabilized system, and can establish inertial attitude for such systems when they are reactivated after shutdown.

### IV. SECOND APPROACH

#### A. Introduction

The second approach is the adaption of holography to the problem of recognition of star fields for attitude determination. A primary objective is a device (hereafter to be called a star field mapper) which will be completely autonomous and which will provide three-axis inertial attitude reference information using a single device sampling a single star field. Operation of the mapper essentially will be in real-time and all the data processing required for identifying a star field will be done optically. Such a recognition device could be modified for acquisition and/or tracking. In addition to these advantages gained due to the inherent

nature of the holographic process, the star field mapper will not require an attitude control system nor will it be dependent upon ground-based information.

Holography (9, 10, 11, 12) is a means for recording a wave field on some photo-sensitive medium (typically photographic film) with sufficient completeness that the wave field can be regenerated from the record. The regenerated wave field cannot be distinguished from the original and can be focused to form an image. In the typical holographic experiment, a coherent beam of light is split into two components. One component (the object beam) illuminates the object and a portion of the Rayleigh scattered light from the object is then intercepted by photographic film. The other component (the reference beam) is directed to the film, subject to coherence length restrictions, and functions like the local oscillator signal of a superheterodyne receiver to aid in recording the phase information. To read out the recorded hologram, the developed photographic plate is returned to the original recording position and illuminated with the reference beam. If the original object position is viewed through the photographic plate, an image of the object in three dimensions will be seen.

A holographic record of a particular star pattern can be made in the laboratory using a template (with back lighting) as the star pattern and the light from a point source (a pin hole system) as the reference beam. The star field pattern may then be regenerated anywhere by presenting the point source reference beam to the hologram. A reciprocal situation can also be demonstrated in which the star pattern itself is presented to the hologram. If the star pattern is the same (or similar) as the recorded pattern, the point source will be generated and can be focused onto a detector. The presence or absence of the regenerated point source is an indication of the presence or absence of the original star pattern. This simple means of star pattern recognition is severely limited in its use for practical reasons (alignment problems) and one must introduce another level of sophistication -- the use of a lens.

#### B. Fourier Transformation Property on Lenses

One of the most remarkable and useful properties of a converging lens is its inherent ability to perform two-dimension Fourier transformations (see Reference 13, page 83, for a complete discussion). When an object is placed in the front focal plane of a lens, an exact Fourier transform relation exists between the object and the field amplitude across the back

focal plane of the lens (neglecting vignetting effects caused by the finite lens aperture). The Fourier transforms are just images but the images are defined in spatial Fourier space or, more commonly, in the spatial frequency domain.

The holographic system indicated in Fig. 13 records the information ( $\underline{a}$ ,  $\underline{b}$ ) in the focal plane of the lens. Because of the reciprocal nature of holography, either  $\underline{a}$  or  $\underline{b}$  may be considered as the object and the other as the reference. Let  $T$  be the operator which generates a Fourier transform -- then  $T$  represents the action of the lens. If:

$$\underline{A} = T(\underline{a}) \quad (11)$$

$$\underline{B} = T(\underline{b}) \quad (12)$$

then the field amplitude in the back focal plane of the lens is:

$$T(\underline{a} + \underline{b}) = \underline{A} + \underline{B} \quad (13)$$

by invoking the linearity of Fourier transforms. The hologram is recorded on film which has a square-law characteristic (film is analogous to a mixer) and thus the recorded information is:

$$(\underline{A} + \underline{B})(\underline{A}^* + \underline{B}^*) \quad (14)$$

where \* indicates complex conjugate.

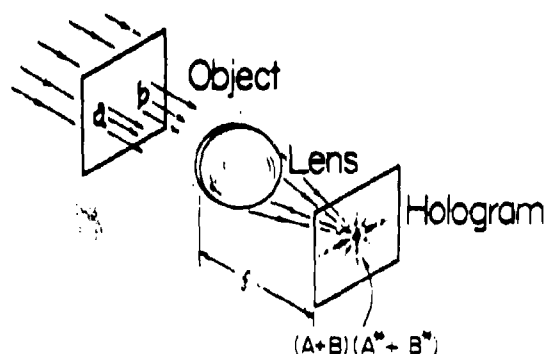


Fig. 13. A holographic system to record ( $\underline{a}$ ,  $\underline{b}$ ) in the focal plane of a lens.

In Fig. 14 the symbol  $\underline{a}$  is presented to the hologram and an additional lens is used to perform another Fourier transformation. With an appropriate choice of coordinate systems (Ref. 14), the second Fourier transformation will yield the same result as the inverse

Fourier transform operation:

$$TT(\underline{a}) = T\underline{A} = \underline{a} \quad (15)$$

$$TT(\underline{b}) = T\underline{B} = \underline{b} \quad (16)$$

(A theorem of Fourier transforms says that:

$$\begin{aligned} TT f(x, y) &= T^{-1} T^{-1} f(x, y) \\ &= f(-x, -y) \end{aligned} \quad (17)$$

for all points of continuity of  $f(x, y)$ . The coordinate system is redefined in a reflected geometry.) The field amplitude in the hologram plane is:

$$\underline{A}(\underline{A} + \underline{B})(\underline{A}^* + \underline{B}^*) \quad (18)$$

and in the image plane the field amplitude is:

$$\begin{aligned} T(\underline{A}(\underline{A} + \underline{B})(\underline{A}^* + \underline{B}^*)) \\ = T(\underline{A}^2 \underline{A}^* + \underline{A}^2 \underline{B}^* + \underline{A} \underline{A}^* \underline{B} + \underline{A} \underline{B} \underline{B}^*) \end{aligned} \quad (19)$$

The term of interest is  $T(\underline{A} \underline{A}^* \underline{B})$  which is the holographically generated image of  $\underline{b}$ . Obviously using  $\underline{b}$  as the input would generate  $T(\underline{B} \underline{B}^* \underline{A})$ , the holographic image of  $\underline{a}$ , along with other terms. If  $\underline{a}$  were a given star pattern and  $\underline{b}$  a point source serving as a reference beam, then presenting  $\underline{a}$  to the hologram will generate the point source as long as  $\underline{a}$  is identical (or similar) to the pattern which was used to make the hologram. Also, the desired term will be generated off-axis and will be separated from the other three terms.

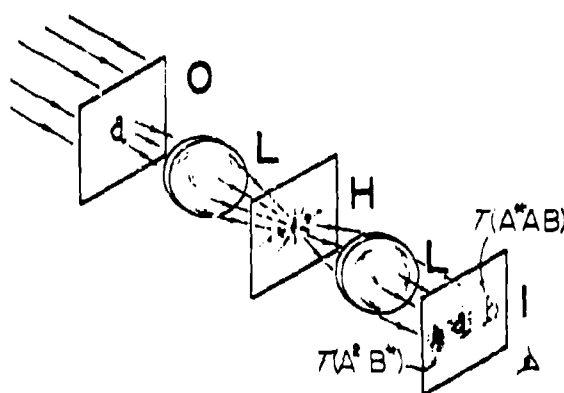


Fig. 14. A simple optical recognition system.

Now, why introduce the lenses in the first place? A hologram constructed without the

lenses requires an accurate alignment between the unknown pattern and the original recording position of the stored pattern. The problem is similar to trying to prove that a small section cut from one of two identical photographic negatives will match some portion of the uncut negative - a trial and error search may or may not work. By transforming to the spatial frequency domain, an object can be "compared" anywhere in the field of view of the lens without precisely overlaying the images. No matter where in the field of view of the lens the pattern is located, the information (assuming a perfect lens) will pass through the focal region of the lens. The information retained in this process is the relative positions of *a* and *b* (see Fig. 13) in the output plane. Thus, if the pattern *a* is moved about in the input plane (just translations, not rotations), the reconstruction of *b*, the point source, will move correspondingly in the output plane. The prospect of tracking is meaningful if a position sensitive detector (mosaic detector for instance) can be used to sense the presence of the point source.

Suppose that a pattern composed of the letters A through Y arranged in five rows of five letters each is recorded in the focal plane of a lens. A point source is used as the reference wave. Assume the letter E is in the "upper right-hand corner" of the input pattern. If just the letter E is presented to the optical system (see Fig. 14), then the holographically generated point source would appear in the "upper right-hand corner" of the output plane. Alternatively, if the input is any one of the twenty-five possible letters, an identification can be realized by applying the input to a bank or memory of twenty-five filters (each matched to one of the possible input characters) and examining the output - ideally only one will reconstruct the point source.

#### C. Star Field Mapper

The star field mapper under development will use a memory composed of optically generated Fourier transforms of the "universe" (see Fig. 15). A modified Rayleigh interferometer is used to record the diffracted images. Once the Fourier transform has been recorded, it is placed in a similar optical system (recognition mode of Fig. 15) to serve as a memory unit -- a matched filter in the spatial domain. The star mapper presents an unknown star field to the optical memory which, in turn, modifies the star field's spatial frequency spectrum; the output is an altered image of the star field. The transform lens converts the optical signals to spatial frequencies by diffraction and they are then passed through the spatial filter. The

correct frequencies pass almost unattenuated while the other frequencies are largely suppressed. The transmitted frequencies then are reconstructed to form a normal image while the leakage of other frequencies reconstructs a noise background. Since the memory unit was constructed holographically using a point reference, the output is a spot of light (a correlation) whose coordinates in the output plane bear a one-to-one correspondence with the location of the unknown star field in the optical memory. With a position sensitive detector, the coordinates of the unknown star field are obtained directly.

#### D. Implementation of Star Mapper

One possible means of implementing a star field recognition system is indicated in Fig. 16. The figure is intended only to depict the seven major research and/or component areas.

##### Telescope

The telescope provides the star field image to be identified. In the laboratory, photographic positives are used in place of the telescopic system and the film transport system. An ideal star field mapper will have its angular resolution determined solely by the diameter of the collecting aperture of the telescope via the Rayleigh criteria. For the ensuing discussion it is assumed that diffraction limited collecting optics will be available. About a 45 degree field of view (fourth magnitude stars being the limiting magnitude) is anticipated (Ref. 8); it is known that Schmidt-Cassegrain and Bouwers-Maksutov systems have no field distortions over wide fields and their field curvatures can be improved.

##### Imaging Medium

A film transport system is shown (Fig. 16) as the means of presenting the star field image to the recognition system. An ultimate design would employ a reusable medium which could store the input star image during the recognition phase and be erasable and ready for use when another attitude measurement is required. The optical recognition system is not able to operate directly on the temporally incoherent and mutually spatially incoherent star field. An input medium would transfer the incoherent star field to a density or phase modulation which could be accepted by the optical system. Presently, various solutions to the recording problem are being examined: rapidly developed silver halide films, thermoplastics, photoplastics, free radical films, dry silver films, photochromics, etc.

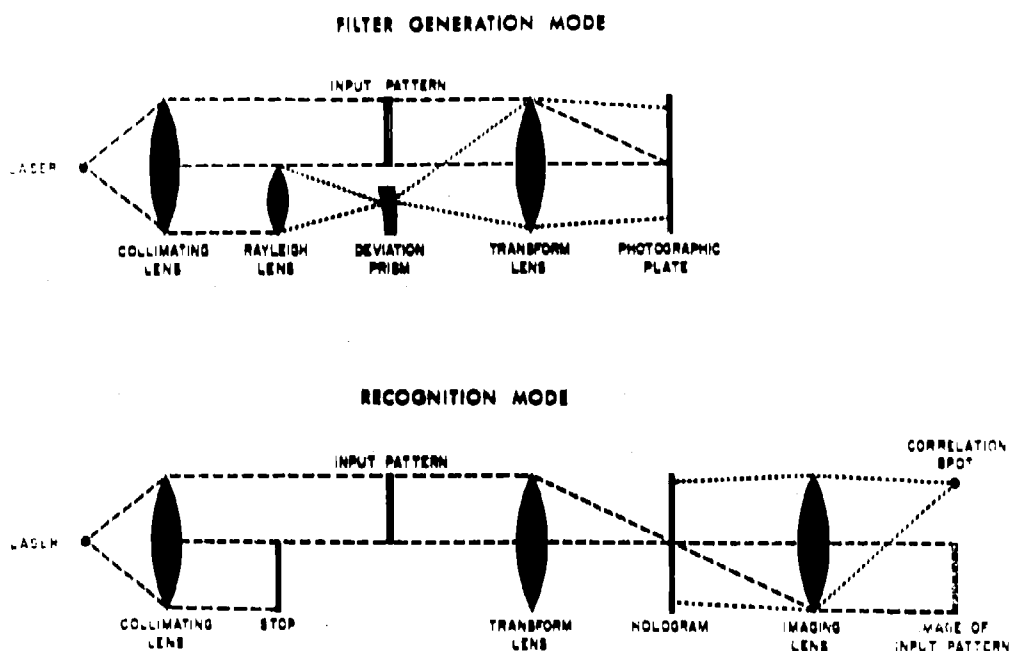


Fig. 15. The spatial filter generation and recognition optical systems.

### Laser

A laser is used to provide a source of high-intensity, coherent, monochromatic illumination for the optical processing system. In the laboratory simulation, a twelve milliwatt Helium-Neon gas laser is used. For space application, both small solid state lasers and incoherent sources are being considered, although some partially coherent sources show considerable promise.

### Lens

In choosing the lenses, particularly the transform lens, the effect of the lens must be considered. If the lens is essentially infinite, a strict Fourier transform relationship will exist between the object and hologram planes. The effect of the lens may be seen by examining the response of the lens to a point object: the amplitude distribution in the hologram plane will be just a Fresnel diffraction pattern (Ref. 14). Thus, only spatial frequencies lower than the

resolution limit will be passed by the lens. (The maximum spatial frequency that may be passed by a lens is simply  $D/2\lambda$  where  $D$  is the diameter of the lens,  $\lambda$  is the wavelength of light, and  $f$  is the focal length of the lens.) Typically, for laboratory simulation, the transform lens is between  $F/10$  and  $F/15$  with between 10 and 15 centimeter aperture; imagers are usually aerial photographic objectives of about  $F/4$  and 60 centimeter focal length.

### Position Sensitive Detector

A position sensitive detector, such as a mosaic detector, is required to read out the location of the correlation or point spot. A vidicon could be used in conjunction with a deflection system and pulse center detection logic. Any detector will require some sort of intensity threshold detection circuitry in order to distinguish a "recognition" from a "noise." The output is an interpolated position of the reconstructed point source in digital form.

## POSSIBLE IMPLEMENTATION

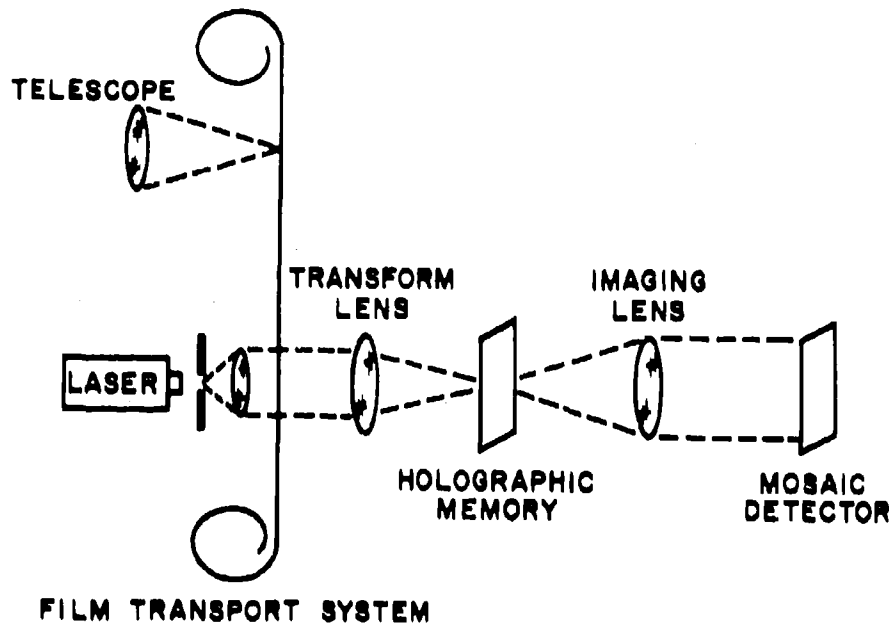


Fig. 13. Schematic of a possible holographic star mapping system.

### Holographic Memory

The holographic memory, its formation and read-out, is the most critical aspect of the recognition system. The concept of a bank of filters (one for each possible scene) with each scene stored on a separate hologram implies a lot of equipment. For instance, if all the holograms were to be mounted on a filter wheel, an additional means would be required to allow a rotation of the hologram for an angle search plus a means to record the angle (angle encoder). For any general instrument to be used in a space mission, the number of holograms could become impractical. If equal radius circular fields of view are stored, then  $8n^2$  ( $n$  is an integer greater than unity) circles are required to completely cover a unit sphere with circles of radius  $90/(2^{1/2}n)$  degrees (about  $64/n$  degrees). In the interest of eliminating moving parts in the space environment, multiple storage techniques were investigated.

A three-beam technique (Ref. 15) has been

developed to superimpose a number of patterns in the same plane of a hologram with the ability to uniquely identify each individual pattern. In contrast to prior techniques, the readout process does not require any movement of parts, e. g., the hologram is not rotated through a Bragg angle nor is the direction of the input beam changed in any manner. The solution is to introduce another lens which comes to a focus before the photographic plate (see Fig. 17). Mathematically, the hologram is:

$$H(x) = \left| S e^{i(\Phi + \alpha x)} + e^{-i\alpha x} + 1 \right|^2 \quad (20)$$

where, for simplicity, the reference beam has been assumed to be on-axis and the obliquities of the star pattern (amplitude  $S$ ) and the third beam are opposite and differ by the angle  $\Phi$ . Expanding:

$$H(x) = (2 + S^2) + (1 + S e^{i\Phi}) e^{-i\alpha x} + (1 + S e^{-i\Phi}) e^{i\alpha x} + S e^{-i\Phi} e^{i2\alpha x} \quad (21)$$

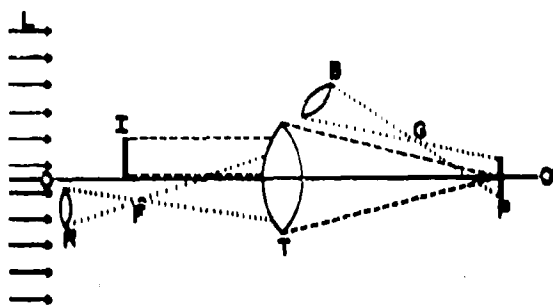


Fig. 17. Three-beam concept for the recording of multiple star fields.

When the hologram is illuminated by the star pattern (assume  $\Phi$  to be small), the first and second order reconstructed beams consist of the interferograms of the star pattern (or its conjugate) with the third beam and with the reference beam. By choosing appropriate obliquities, the reconstructions of the third beam and the reference beam can be confined to well-defined regions of the output plane.

When a new pattern is to be stored, the location of lens B is changed in such a manner as to keep constant the distance from the center of lens B to the axis  $O-O'$  as well as the distances from the center of the plate P to point G (the focal point of lens B) and from point G to the center of lens B (i. e., a rotation about the  $O-O'$  axis). Now there are three beams interfering at the photographic plate P. The exposure time for each pattern varies roughly as the reciprocal of the total number of patterns to be stored. The non-linearity of the amplitude transmittance curve causes each pattern to be recorded in its entirety (Ref. 16).

The distinct advantage of the three-beam technique can be seen in Fig. 18 which displays the readout process of the images stored on the photographic plate P. An unknown pattern is placed in a window formed by the stops  $S$ ; the transform lens performs the Fourier transform of the pattern, and in the plane of the photographic plate the Fourier transform is multiplied with the previously recorded Fourier transforms. Lens A then performs another Fourier transform and exhibits the cross correlation of the input pattern with all the stored patterns as a point of light  $F'$ . Using just the prior art, one would have to rotate the photographic plate in order to search for the

formation of point  $F'$ , and the angle of the plate P would indicate which of the stored patterns is matched by the input pattern. In the three-beam technique, point  $F'$  will be present without any movement of plate P; there will also be another point of light  $G'$  which is the image of point G (Fig. 17). The position of point  $G'$  indicates which of the stored patterns matches the input pattern (if any).  $F'$  and  $G'$  come to a point focus in different planes which is convenient for readout purposes. Thus, the three-beam technique allows one to interrogate the stored patterns for a matching pattern in one operation, without the previously required need for moving the photographic plate.

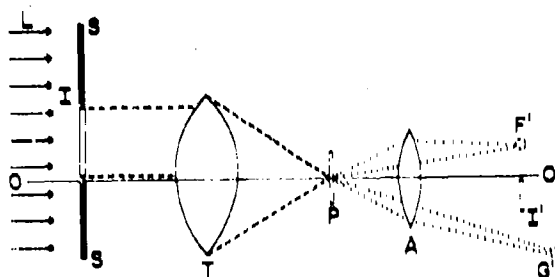


Fig. 18. Readout process of the three-beam technique.

It is now proposed to store the  $6n^2$  patterns required to cover the celestial sphere in each of the angular orientations needed to be sure that a recognition is always obtained. Regeneration of the point source will give the  $(x, y)$  coordinates of the center of the unknown star field with respect to a stored pattern. A ring of photodiodes will be used to intercept the regeneration of the third beam and thus identify which of the many stored patterns correlates with the unknown pattern. The voltage signals can then be used directly to monitor and/or update a gyro inertial frame.

#### E. Laboratory Simulation

The apparatus for the star field mapper is in the development stage. At present, the holographic memory is being constructed and studied. The three-beam technique and appropriate bleaching techniques appear to have considerable potential for extending the holographic memory capability. At this writing, thirteen patterns have been recorded and the crosstalk is barely detectable with an unshielded photomultiplier. The signal-to-noise ratios have

always been better than 40:1 and at times nearly 1000:1. If an input medium can be found or developed and if the three-beam technique can be extended to map the universe, an autonomous star field mapper can become a practicality. If a mission restricts the fields of view to only selected stellar areas or landmarks, a tracking mode is certainly feasible using the same optical system.

#### F. Conclusion

Optical mated filtering has a great potential in the pattern recognition field, especially when the objects are stars. Critical registration problems inherent in conventional recognition systems are eliminated in the spatial frequency domain. The star field mapper will be a completely self-contained automatic device which will provide three-axis attitude reference information in either analog or digital form. The optical system processes the star conditions without a computer and at the speed of light. A holographic star mapper could provide greater accuracy than known autonomous navigation techniques.

#### V. SUMMARY

As more far reaching space voyages are undertaken and for future Earth-orbiting vehicles, the need for self-contained navigation systems based on electro-optical technique is decidedly increased. The attitude information provided by such systems is essential for the proper reduction of meteorological, geophysical, and many other types of data gathered by a space vehicle.

This paper has discussed two new approaches to the problem of rapid determination of directions in inertial space. Though both systems have the desirable property of being able to perform the required star pattern match without moving parts or spacecraft slewing (i. e., they both operate in the strapped-down model), the complement of equipment and the speed at which attitude is determined is markedly different for the two approaches.

The conventional approach employs a computer and is within the state of the art so that hardware may be configured which will meet space qualification. For precise pointing information, the use of two sensing heads is required. The two heads may have arbitrarily skewed or orthogonal pointing axes.

The desirable approach using the holographic technique with its inherent advantage

of speed in processing the information (due to the elimination of the computer) and the simplified optical system is presently in the development stage. Although initial feasibility has been demonstrated in the laboratory, the determination of the accuracy to which a star field can be located as a function of the spacecraft stabilization and the size of the holographic memory have yet to be determined. Also, further development is needed for an erasable input medium exhibiting recognition capabilities with signal-to-noise ratios of several hundred to one. It is expected, however, that these problems can be solved within the next few years and that modern optical methods will be a demonstrated powerful technique for spacecraft navigation and guidance.

#### Acknowledgements

Constructive suggestions from Mr. J. Bellantoni in designing the Operational Star Catalog and the contributions of Dr. K. Soosaar and Mr. H. Iuzzolino for the analysis and programming in Part III of this paper are gratefully acknowledged.

#### REFERENCES

1. F. D. Grant, "Inflight Alignment Errors of the IMU Stable Member," MIT Instrumentation Laboratory Report E-1482, December 1963.
2. R. C. Hutchison, "Geometrical and Astronomical Aspects of Employing a Star Tracker to Correct the Attitude of a Stable Platform," MIT Instrumentation Laboratory Report R-323, February 1961.
3. P. Gevas, J. Abate and J. Gulbenkian, "Design, Fabrication and Test of a Feasibility Model Relative Star Angle Comparator," Technical Documentary Report No. ASD-TDR-63-586.
4. Research Division, Control Data Corporation, "Feasibility Investigation of a Wide Angle Celestial Reference for Space Navigation," Technical Report AFAL-TR-66-10, April 1966.
5. T. M. Walsh and R. L. Kenimer, "Analysis of a Star Field Mapping Technique for Use in Determining the Attitude of a Spin Stabilized Spacecraft," NASA TND-4637.



6. T. M. Walsh, W. C. Dixon Jr., D. E. Hinton and J. A. Holland, "A Celestial Attitude Measurement Instrument for Project Scanner," NASA TN D-4742,
7. AF Avionics Lab., R & TD Division AFSC, Wright-Patterson AFB, Ohio, "Star Identification by Optical Radiation Analysis," TDR No. AL TDR 64-13, January 1964,
8. L. A. Kleiman and R. A. Archart, "An Analytical Approach to the Determination of Stellar Fields of View," NASA TR R-257,
9. J. B. DeVelis and G. O. Reynolds, "Theory and Applications of Holography," Addison-Wesley, 1967,
10. G. W. Stroke, "An Introduction to Coherent Optics and Holography," Academic Press, 1969,
11. E. N. Leith and J. Upatnieks, J. O. S. A. 52, 1123, 1962,
12. E. N. Leith and J. Upatnieks, J. O. S. A. 54, 1285, 1964,
13. J. W. Goodman, "Introduction to Fourier Optics," McGraw-Hill, 1968,
14. J. B. DeVelis and G. O. Reynolds, "Theory and Applications of Holography," Addison-Wesley, 84, 1967,
15. J. N. Hallock, NASA Tech Brief 68-10347,
16. J. N. Hallock, Amer. J. of Physics 36, 782, 1968.

## SUB-ARC SECOND STAR SENSORS, DESIGN AND FABRICATION<sup>1</sup>

Joseph E. Carroll  
Control Data Corporation  
Edina Space and Defense Systems  
Minneapolis, Minnesota

### ABSTRACT

Current and future requirements for star sensors in the sub-arc second region favor Starmappers over Star Trackers because of the latter's mechanical complexity. Work at Control Data has concentrated since 1961 on Starmappers in which star images transit slits in the focal surface of a wide-angle optical system. The variety of space vehicle motions causes a corresponding variety in star sensor designs, including the choice between an internally driven reticle and a non-moving-parts system which uses vehicle motion for scan generation. Inherently concentric optical systems (catadioptric or all mirror) are required to maintain high quality images throughout the field. Image diameters will probably not become smaller than a few arc seconds, thereby necessitating interpolation of the star transit pulse from the photodetector. Successful thermal design of the sensor avoids temperature gradients and permits operation over wide ambient ranges. Finally, the type of photodetector chosen significantly influences the design of the pulse processing electronics. Both solid state (photodiode, CdS, CdSe) and photoemissive (PMT) detectors are examined.

### I. INTRODUCTION

Extremely precise star sensors can find use in a broad array of applications from scientific research to operational systems; from ground-based installations to spacecraft components.

Spacecraft attitude detection is of most interest in the present conference, but there are also positioning requirements in space--location within the solar or satellite system via triangulation, distance from an extended body, and direction to a target body. There are also a host of terrestrial tasks which require star sensing: astronomical surveys, north azimuth determination, polar motion and atmospheric tilt studies, continental drift, star position determination; then on other planets: position fixing, determination of spin dynamics, studies of internal mass distributions (vertical deflection)--the possibilities are almost endless.

<sup>1</sup> Control Data Corporation has performed numerous programs under Department of Defense, NASA, and company sponsorship. The results of those programs are pertinent to the conclusions drawn in this paper.

All of these applications--in space and ground based--require the sensing of the direction to a star relative to a coordinate frame located within a star sensor. We consider in this paper only those sensors capable of performing this task in its most precise form--that is, with errors from one or two arc seconds down to one- or two-tenths of an arc second. We thus intend to discuss sensor performance which we believe feasible in the 1970's in the areas of:

- (a) operational spacecraft, and
- (b) automated tools for astronomical surveying and research.

In addition to the requirement for sub-arc second accuracy, we will treat only those sensors which are automatic in the sense that no manual intervention is required in their operation. This eliminates such star sensors as observatory telescopes, theodolites, photographic zenith tubes, and similar equipment which use the eye or photography for the basic sensing element or is manually directed, even if aided by servos.

We have thus restricted ourselves to two types of star sensors: Star Trackers and

Starmappers, and the purpose of this paper will be to compare these two in terms of ultimate accuracy (concluding that in some applications the latter would be a better choice) and to review those optical design and star detection (electronic) techniques employed in Starmapper systems to maximize performance.

We will not discuss system aspects in any depth. Suffice it to say that sensors such as these are capable--through multiple measurements and math modeling--of providing system accuracies which improve upon individual star sightings by as much as an order of magnitude (Refs. 1 and 2).

## II. STARMAPPERS AND STAR TRACKERS

The two major categories of star sensors (after telescopes, etc., are eliminated as discussed above) are the relatively conventional Star Tracker--a descendant of the theodolite--and the newer Starmapper--an outgrowth (principally at GDC) of early work in astrometrics in Russia and satellite tracking in this country.

### A. Star Tracker

The Star Tracker, as shown in Fig. 1, is composed of a telescope gimbaled in two axes so that it can point in any direction. (Practical limitations usually limit this to one hemisphere.) It is very much like a theodolite except that the vertical and horizontal circles have been replaced by angle encoders and the focal plane of the telescope contains photoelectric sensors for determining the location of the star within the optical field of view.

Servos are also mounted on each axis for the purpose of acquiring the star on command from the computer and driving the star to the center of the field of view based on error signals from the telescope detection electronics. Thus, an approximate knowledge of the orientation of the vehicle is used to point the telescope in the general direction of the desired star (usually a few minutes of arc to one degree) from whence the internal control loop takes over to precisely point the telescope. When this is complete, the angle encoders are read into the computer as a measurement.

Alternately, the photodetectors themselves can provide a vernier on the angle encoder readings, thereby eliminating the need for precise control of final pointing.

An extensive literature exists on Star Trackers, their application, limitations, construction, etc. References 3, 4, and 5 are perhaps representative of the current state of the art.

### B. Starmapper

Also shown in Figure 1 is a sketch of the major Starmapper concepts. Briefly, a wide-angle camera type of optical system images a field of stars onto a slit pattern at the focal surface,

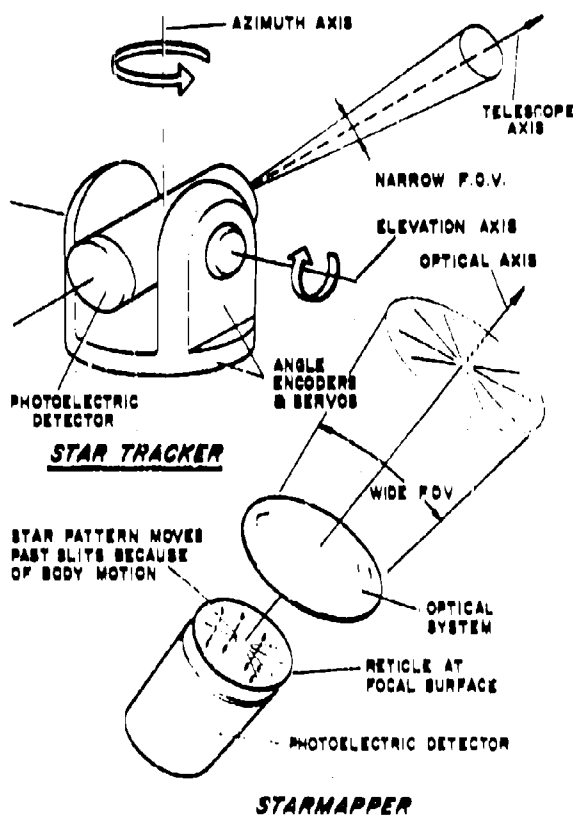


Fig. 1. Schematic Diagrams of Two Automatic Star Sensors

The Starmapper has no gimbals but is rigidly attached to the vehicle. As the latter rotates, the star images are carried across the slit pattern producing a series of pulses from the photoelectric detector(s). This pulse sequence is then timed and relayed to the computer which identifies the transiting stars and computes a pointing direction and/or determines the values of various motion parameters (spin rate, precession, moments of inertia, etc.).

There are two types of Starmappers: one having no moving parts and depending upon the body for motion through the star field, and the other containing an internal reticle drive to scan the slits past star images which are relatively stationary when body rotation is slow.

A number of articles (far less than for Star Trackers) have been published concerning Starmappers and their antecedents. Early Russian astrometric work involving star transits is reviewed in Ref. 6. The use of slits in the Baker-Nunn satellite tracking camera is discussed in Ref. 7. Astronomical surveying applications using theodolites are discussed in Refs. 8, 9,

and 10. A completely automatic surveying system is outlined in Refs. 2 and 11. Satellite attitude determination is discussed principally in Refs. 1, 12, 13, 14, 15, and 16. More detailed references are cited later.

### C. Tracker/Mapper Comparisons

The fundamental differences between a Star Tracker and a Starmapper are listed in Table 1. Generally, the Starmapper is a much simpler instrument mechanically due to the absence of servo loops, gimbal axes, and angle encoders. But to accomplish an essentially similar task, it must possess a wide field of view (measured in degrees rather than minutes) in order to scan a sufficient number of stars, and it is very important that image quality remain high over the entire field since stars can pass through the field at any point and must be detected with equal accuracy. The Star Tracker need only have good image quality near the center of the field since it is only with the star centered that the angle encoders are read.

Table 1. Comparison of Star Sensor Characteristics

Characteristic	Star Tracker	Starmapper
Control loop	Control loop, star and angle encoders in center of field of view	None
Angle precision	Intercept pointing accuracy (2 axis) equal to body	None required if body motion sufficient to stop, or enough stars in field of view to allow only one star precision required
Optical field of view	Narrow angle	Approaching that of a camera, image quality throughout field of view is important
Field of view accuracy	Equal to body from which stars are seen	Equal to body from which stars are seen
Image quality	A few stars sufficient to allow body to be seen	All stars in field of view must be seen with equal accuracy
Device complexity	Relatively low with appropriate optical design	Relatively high with appropriate optical design

On the Star Tracker ledger are its greater versatility relative to star field density, its applicability to daytime operation, its more intuitive operation (almost identical to the theodolite), and its reduced load on the computer.

Thus, on the one hand, we have an instrument of great mechanical simplicity (to the point of no moving parts), and, on the other hand, an instrument of apparently more versatile usage and certainly one of longer historic acceptance.

However, when viewed in terms of system accuracy, and when that accuracy requirement is specified in tenths of an arc second, then one must conclude--provided the particular application by itself does not favor one instrument form over the other--that the elimination of moving

parts is a definite advantage. Moving parts mean varying stresses, changes in lubrication films, slow wearing of the surfaces, and torques applied to other members of the system (altering perhaps the orientation ever so slightly). The requirements for mechanical balance and cancellation techniques is nearly unsurmountable. Constant calibration becomes much more involved because of the many configurations of the sensor which must be checked.

In short, tiny systematic errors (a too large ball in the race, e.g.) which refuse to relent to calibration, are present in all measurement systems but get rapidly out of hand when moving parts are encountered.

Thus it is the author's point of view that for certain of the most precise applications--in space or on the planets--the Starmapper possesses an ultimate accuracy potential which the Star Tracker lacks.

Another comparison between Star Trackers and Starmappers (and one far less likely to get the author boiled in oil) can be made on the basis of body spin rate as shown in Fig. 2. Vehicles with rapid rotation rates are ideally suited to Starmappers whereas those applications tending toward inertially stable platforms are more suitable for Star Trackers or require Starmappers with internal scan.

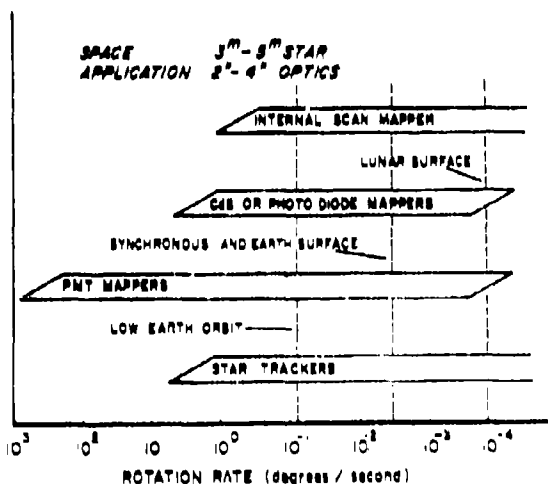


Fig. 2. Applicability of Star Trackers and Starmappers to Vehicles with a Wide Range of Spin Rates

2

The above accuracy comments apply also to internal scan Starmappers (though only one part is involved). It could be that a body with no motion whatsoever relative to the star can have its orientation precisely measured (automatically) only with very great difficulty.

### III. STARMAPPER DESIGN

The Starmapper sensor achieves its sub-arc second performance through a combination of high quality optics and electronic interpolation of the transit pulse.

Analysis (Refs. 17 and 18), experiment (Ref. 19), and flight performance (Refs. 1 and 20) demonstrate that the image of a star can be interpolated--that is, have its center located to within some fraction of the total image size--by a factor approximately equal to the signal to noise ratio. Thus, if, for example, individual star transits were desired to 0.5 arc second, and the aperture were such as to provide a  $S/N = 10$ , then the diameter of the optical image can be five arc seconds.<sup>3</sup> Furthermore, for 0.5 arc second individual transits, a system accuracy of 0.1 arc second or better can be achieved through over-determination. Thus, system accuracies are often 50 times better than optical image diameter!

This complementary role--optics/detection--requires excessive performance from neither component. The electronics need be stable only over the time duration of the transit and the optical image can be much larger than the final desired system performance.

In the following two sections we examine each of these major components of the Starmapper system, illustrating various design techniques and pointing out their relative merits and penalties. Quite obviously we will not cover all aspects of Starmapper design. The optical and detection systems, however, have undergone considerable development over the past few years and thus merit special attention at the present time though there should be no implication that these developments are complete.

#### A. Optical System

The optical system for a precision Starmapper must have both a camera-type field of view (from a few degrees to a few tens of degrees) and an image diameter of a few arc seconds throughout this field. This combination is usually contradictory since image quality, in the classical sense, is a strong function of off-axis angle. The image diameter (arc seconds) for a single lens increases as  $\theta$ , where  $\theta$  is the off-axis angle. For a parabola, the dependence is  $\theta^2$ . (See Ref. 21.) With good imagery over a wide field, however, the sensor encounters a sufficient number of stars and each is measured with equal accuracy. The optical design possessing these properties, while at the same time remaining simple and easy to manufacture, is the concentric optical system of Bouwers and Maksutov.

In the 1930's and 40's it was recognized by a number of investigators that a spherical mirror with the aperture stop placed at the center of

curvature was by definition completely free of coma, astigmatism, distortion, and chromatism as well as having a very nearly 180 degree field of view. Its disadvantages are spherical aberration, curvature of field, and a focal surface located within the optical system itself. In terms of Starmapper usage, curvature of field is circumvented by conforming the photodetector to the focal surface. (This is discussed later near Fig. 9.) An internal focal surface is detrimental in that it blocks light entering the aperture and it is relatively inaccessible. The latter is no problem for electronic photodetectors since access is required only for initial assembly; light blocking is one of the inevitable negatives present in any design though it can usually be kept to 25% or 30% of the total aperture.

Thus, the spherical mirror with centered aperture seems well suited to the Starmapper concept if spherical aberration can be eliminated. During the 1940's several publications--most notably that of Maksutov (Ref. 22) and Bouwers (Ref. 23), demonstrated that a concentric meniscus could correct the spherical aberration of the mirror without affecting any of the other useful properties except for a small amount of color introduced by the meniscus itself. This color is then reduced by using an achromatic meniscus, also discussed by Maksutov, Bouwers, and especially Taylor (Ref. 24). Finally, a Schmidt-type aspheric corrector plate (invented as early as 1929 (Ref. 25)) can be located at the aperture to eliminate the residual spherical aberration at the expense of slight off-axis degradation. The configuration recommended for a particular Starmapper depends on the required field of view,  $f$ /number, and photodetector spectral region.

#### 1. Example Design

A numerical example will help to illustrate these features of the concentric optical system. Let us start with the basic optical configuration shown in Figure 3. Let it be an  $f/2.0$  system which we wish to design for an 8-11 detector response (3200 to 6200 Angstroms) which peaks at

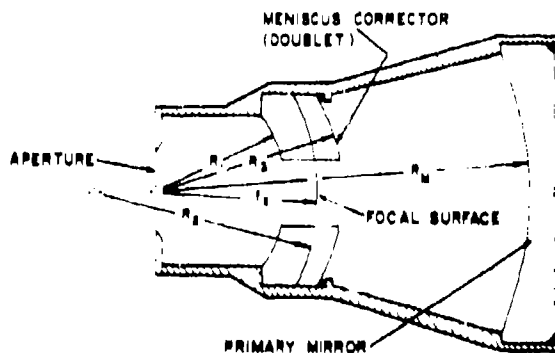


Fig. 3. Illustrative Cross-Section of Starmapper Concentric Design

<sup>3</sup> This is the diffraction limit for a 1.6 in. diameter aperture.

4200 Angstroms. (For the moment we leave the maximum off-axis angle unspecified.)

Looking ahead to the correction for color, we must first choose a pair of glasses whose indices cross near 4200 Angstroms. While not necessary, the advantage to this selection is that the meniscus becomes, at the selected wavelength, a solid piece of glass whose radii can be varied to optimize monochromatic performance. The correction for color in the neighboring wavelengths then becomes easier because one is already guaranteed good performance for at least one wavelength. Systems have been designed for wavelength regions quite different from that at which the indices are equal. However, this considerably complicates the decision process and is not as all-intuitive as designing near a "crossing" wavelength.

A review of the Schott glass catalog (or any glass catalog having the requisite data) shows that several glass pairs have indices which are equal near 4200 Angstroms.<sup>4</sup> Let us choose ZK5 and LLF6, whose indices are plotted in Figure 4.

First order optical design then shows that the system focal length  $f_s$  (positive), mirror radius  $R_M$  (negative), and meniscus radii  $R_1$  and  $R_2$  (negative) of a concentric system are related at the design wavelength by

$$\frac{1}{f_s} + \frac{2}{R_M} = - \left( \frac{1}{R_1} - \frac{1}{R_2} \right) \left( \frac{n-1}{n} \right) \quad (1)$$

where  $n$  is the (common) index of refraction.<sup>5</sup> If

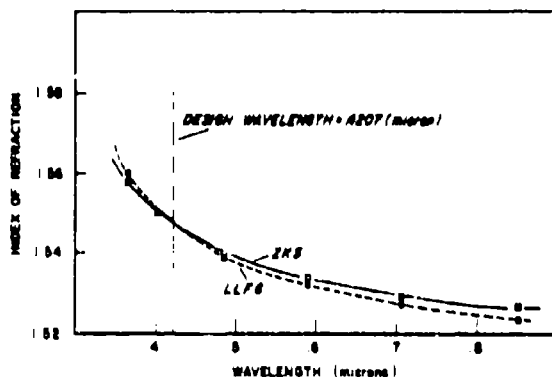


Fig. 4. Glass Pairs are Chosen for the Meniscus Based upon Their Indices Being Equal at the Design Wavelength

<sup>4</sup> Such a review is best carried out via a computer program which uses the index coefficients published in the catalog. At CDC a table of all such glass pairs together with their dispersions and common indices has been published from 3650 Angstroms to 8532 Angstroms.

<sup>5</sup> Equation (1) can be derived from any standard optical text, e.g., Ref. 26, p. 57

this is normalized relative to the aperture, then  $f_s = f/\text{no.} = 2.0$ . Let us choose  $R_M = -4.5^\circ$  for a specific design. Then

$$- \left( \frac{1}{R_1} - \frac{1}{R_2} \right) = 0.156966 \quad (2)$$

The advantage of this equation lies in the fact that, while it is derived only for paraxial rays, it is a true relationship even for rays of large aperture height. In the ray-trace program, a concentric element combination of  $R_1$ ,  $R_2$ ,  $R_M$ , and meniscus index  $n$  is found to focus marginal rays at the point  $f_s$  given by Eq. (1). Thus, for a given  $f_s$ ,  $R_M$ , and  $n$  (the parameters usually chosen first), Eq. (2) reduces the design task to the systematic investigation of only one parameter, not two.

To be specific, we merely choose a series of  $R_1$  values, compute  $R_2$  from the above equation, and perform a computer ray-trace on each resulting system. For the numerical example, Fig. 5 is the outcome from which we immediately see that  $R_1 = -1.6250$ ,  $R_2 = -2.1814$  is the preferred

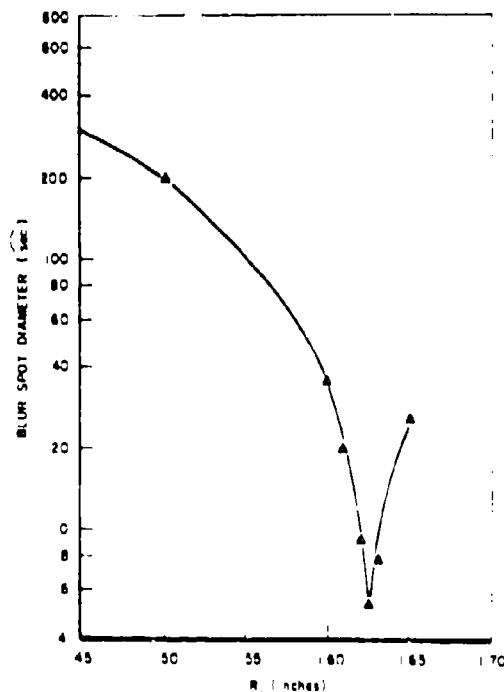


Fig. 5. Monochromatic Meniscus Design

<sup>6</sup> The closer  $R_M$  comes to  $-2 \times f_s$ , the thinner will be the meniscus.

<sup>7</sup> The ray-trace program most used at CDC was originally designed by S. Braver of the Aerospace Corporation and adapted to our needs through frequent add-ons and revisions. This is a continuous process, as is to be expected, and the program lends itself very nicely to these changes.

design which minimizes blur spot size even though all points in the figure satisfied Eq. (1). (This is an excellent illustration of analytical tools being used to reduce the computational load.)

We have thus found a monochromatic design with very good imagery at any off-axis angle. The spherical aberration of the mirror alone amounted to 1600 arc seconds. We have thus achieved a factor of 400 improvement by the addition of the concentric meniscus. The blur spot can be further reduced at this point (and at this wavelength) by placing an aspheric corrector plate at the aperture stop. (See below.) However, the blur spot size achieved in Figure 5 is sufficient for the present illustration.

To extend this performance to other colors, we need to select an interface position and radius of curvature. This is a much more difficult task requiring investigation of many wavelengths and decisions whether to sacrifice some portion of the spectrum for another. The ray-trace program is run at 30 uniformly spaced wavelengths in the range 3150 Angstroms to 6200 Angstroms. The maximum blur spot dimension is automatically plotted as a function of wavelength. Figure 6 shows some of the results for several values of the radius of curvature  $R_2$  of the meniscus interface. A design near  $R_2 = 7.5$  and  $t_1 = 0.2$  would probably be a good combination producing image diameters under six arc seconds from 4000 Angstroms to 5000 Angstroms.

The introduction of an interface into the meniscus destroys the pure concentricity of the

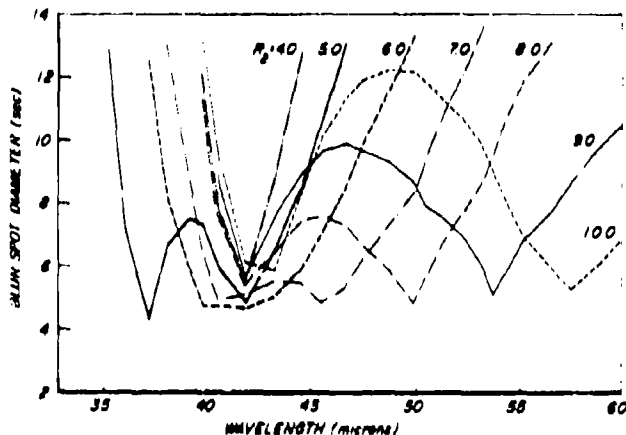


Fig. 6. Optical System Color Analysis as a Function of Meniscus Interface Radius of Curvature

A controlled method of evaluating color correction is to integrate the product of the detector spectral response and the maximum percent of blur spot energy passing through the slit. The design task is then to maximize this integral through manipulation of the surfaces.

original design. That this is a very minor problem with concentric systems is shown by the spot diagrams of Figure 7.

## 2. Aspherics

There is usually not much point in depressing the blur circle diameter below a few arc seconds since this is the diffraction limit for apertures of a few inches. The simple meniscus discussed above is thus sufficient for optical systems with  $f/\text{no.} \geq 2$ . Should the  $f/\text{no.}$  approach one, the requisite image quality becomes harder to achieve, as shown in Fig. 8 (taken from page 453 of Ref. 21).

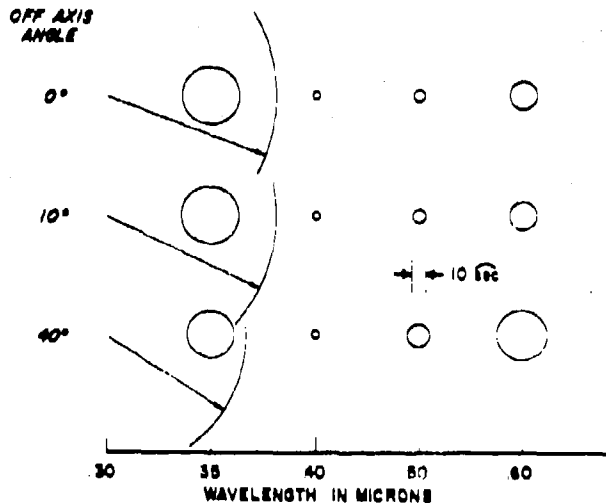


Fig. 7. Off-axis and Color Performance of Example Design

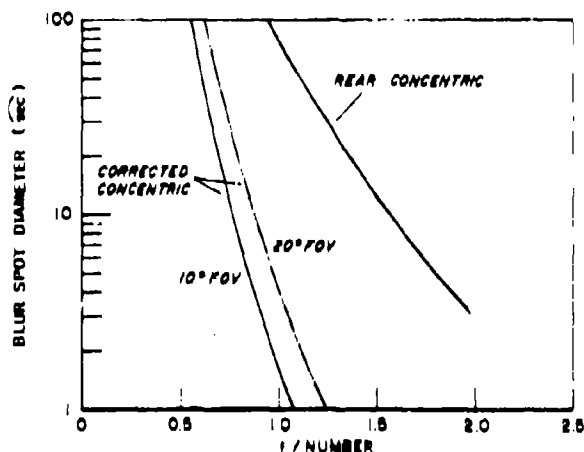


Fig. 8. Spot Diameter is a Strong Function of  $f/\text{no.}$  and Can Be Greatly Reduced by Using an Aspheric Corrector

An aspheric plate placed at the aperture stop can significantly reduce image size as also seen in Fig. 8. The aperture is the proper place for the aspheric as it is there that the least effect on off-axis images will occur. To understand this, note that the aspheric surface is designed to correct rays that are a given distance radially from the aperture center. If the design is tailored to the on-axis bundle of rays, then a bundle of rays arriving from some other angle will strike the aspheric at slightly different positions; thereby undergoing slightly different (and perhaps not optimum) corrections. With the aspheric somewhere else, however, (e.g., on the mirror surface) the difference in correction would be significant since the effective "height" of a ray striking the surface at a given point would vary with the off-axis angle.

In summary, the use of any aspheric degrades the "concentricity" of the design. The least penalty is paid, however, by locating this surface at the aperture stop or the center of curvature of the other elements.

In terms of color correction, the aspheric appears to subtract an amount from the blur circle diameter which is the same for all wavelengths. Thus the degree of color correction provided by the meniscus interface is approximately preserved when an aspheric is added.

### 3. Optical System Fabrication

The concentric optical system discussed here contains only three elements: two pieces of glass and one mirror. All five surfaces are spherical, making the fabrication task quite inexpensive relative to the usual 9 to 11 element refractive systems. However, some new techniques for measuring precisely the radius of curvature of the surfaces have had to be developed. These consist of a combination of gauge blocks and large diameter spherometers to obtain accuracies of better than one mil. Theoretical tolerance analysis shows that two and, for some surfaces, three mils can be permitted without serious degradation in image quality, but a few critical parameters (especially the entrance face of the meniscus) should be within .0005 in. of the design value.

Fabrication of the aspheric is a more difficult task but is again aided by the computer and by the fact that the aspheric is required only to perform very slight "corrections." Thus very little deviation from a plane is required which makes possible the use of interference fringes as a measuring technique. During the design of the aspheric, the computer can also produce the desired fringe pattern (via e.g. a Cal-Comp plotter). This pattern can then be used as a direct overlay to check the work.

The design and fabrication of the lens housing is vitally important from the standpoint of maintaining proper separation between the mirror and the focal surface (mounted integrally with the meniscus corrector). This distance--the back focal length--must be held constant over as wide a

temperature range as possible. For the concentric system the glass lands can be located in such a way that housing expansion is counteracted by meniscus expansion to produce a constant back focal length.

### 4. Physical Size

Narrow field, high resolution telescopes, such as used in Star Trackers, are usually of quite long focal length. The reason for this is that the photodetector (such as an array of diodes or an image dissector) has resolution usually less than 1,000 lines/in. If each such element is to be, say, five arc seconds, a focal length of  $10^{-3}/(5 \times 5 \times 10^{-6}) = 40$  in. is required. To maintain reasonable physical size for aerospace applications, folded and cassegrain systems are, therefore, normal.

Starmapper systems, on the other hand, make excellent use of short focal lengths for equally compelling reasons. In the first place, the wide field of view would create an excessively large focal surface for long focal lengths. A 40 in. focal length and  $20^\circ$  field of view means that the photodetector would be 13 in. in diameter! An order of magnitude smaller is desired. Furthermore, the resolution element is defined as the fineness of the slit edge. This can be held to 20 to 40 microinches which, over a one inch surface, is a lines/inch equivalent of 25 to 50 thousand. Thus, not only is it desirable to have short focal lengths in Starmappers; it is quite possible also.

Since the barrel length of a concentric system is roughly two and one-half times the focal length, we have the general result that the folded or cassegrain system is approximately the same size as a concentric system.

### 5. Detection and Image Interpolation

As the star image moves across the slit, the photodetector output rises to a maximum and falls back to its steady state value in a manner which is delayed and perhaps distorted from the original light pulse. This original pulse is highly symmetric due to the care taken in designing the optical system and in arranging the slits. This symmetry is maintained if (a) the detector is fast (such as a PMT or photodiode), and (b) the following electronics is designed to preserve the original shape. For slow detectors (in relation to the star transit time), the output pulse will probably not be symmetric. In that case, detection must rely on a single side of the pulse, such as the leading edge.

Before discussing specific electronic techniques used to time the transit of a star across a slit, let us first cover the problem of matching a (generally flat) photodetector to a curved focal surface.

#### 1. Curved Focal Surface

The wide field usually used in the concen-



tric system makes the focal surface curved, thereby requiring that photodetectors or other defining elements--such as slits--must conform to this curvature to remain in focus.

Approximating the curved surface by a plane severely restricts the focussed field of view. If an image size increase of  $\alpha$  radians is allowable, then it can be shown that the focussed FOV is

$$FOV \leq 4/\sqrt{\alpha}$$

where  $F$  is the f/no. For  $F = 2$  and  $\alpha = 1$  sec,  $FOV < 3/4$  deg. Thus, for FOV values of several degrees or more, some means must be found to affect physical curvature of the detection elements.

Figure 9 illustrates several methods of dealing with a curved focal surface. Others can probably be invented. Each requires careful consideration of such things as the photodetector, detector or slit pattern, fiber optic technology, and crystal deformation possibilities.

All of the methods shown in Figure 9 have been tried. b and D have been most successful to date. A and C appear promising since for A, fractional deformation is usually small, and for C, the fibers are already part of a larger face-plate, thus eliminating the handling required in alternate E.

## 2. Detector/Amplifier

Figure 10 illustrates three detector/electronics associations. Each has its own set of advantages, disadvantages, and special requirements. The classical photomultiplier, of course, has the advantage of a built-in high-gain, low-noise amplifier which, in addition, is very fast, thereby preserving the pulse shape of the incoming light. In addition to this, and most important for low-light-level work, the basic photo-conversion process--the photoemissive surface--is essentially photon noise limited. That is, the surface itself contributes very little noise due to "dark" current. Against this are size and high voltage.

Both the CdS and photodiode detectors are quite small and require only low voltages, but their fabrication problems are not trivial (Ref. 27). Electrically, carefully designed amplifiers must be added to each system, and noise calculations show that the detector itself is the primary source.

A further concern with solid-state devices is their high impedance which makes them especially susceptible to electromagnetic interference. The signals are so tiny that the least amount of EMI gets amplified along with the signal, thereby creating additional noise. To counteract this, preamplifiers are micro-packaged and placed as close to the detecting element as possible. The net effect is to produce a package behind the

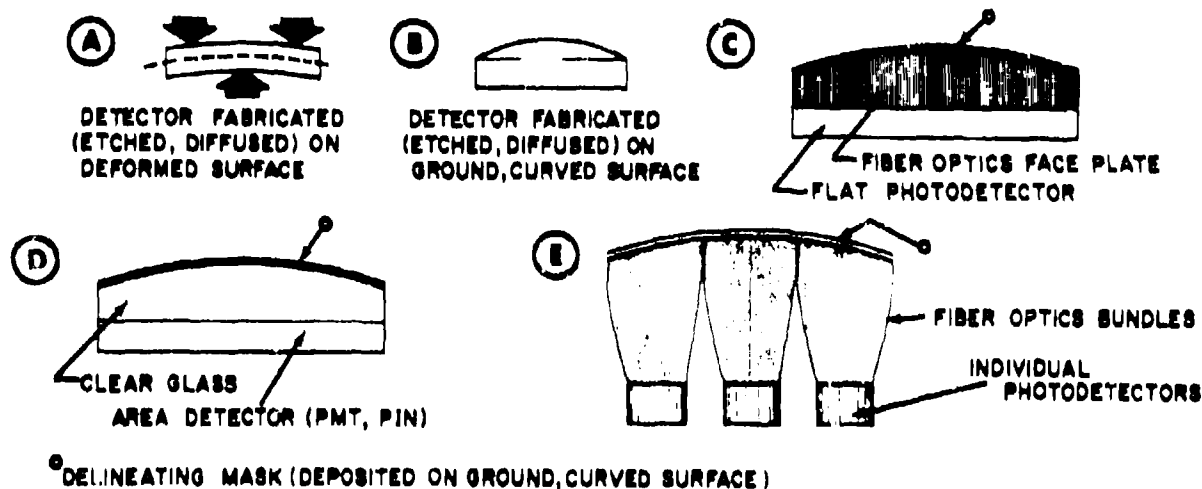


Fig. 9. Various Methods of Matching Photodetector to a Curved Focal Surface

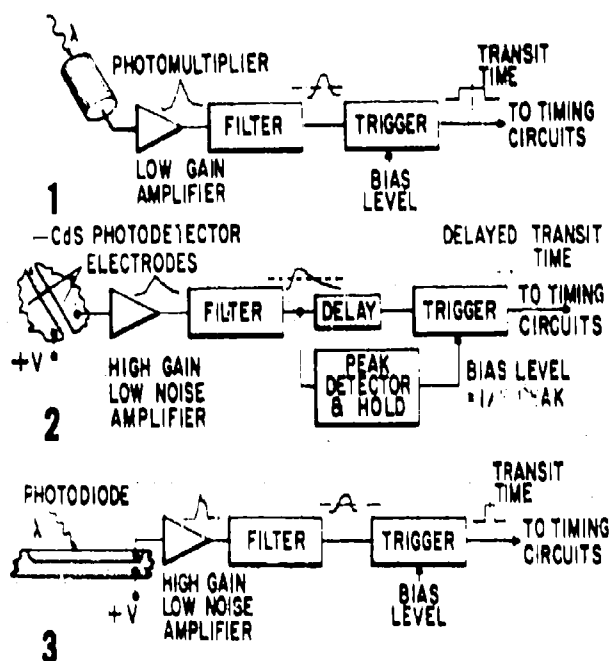


Fig. 10. Three Star Detection Schemes for Starmappers

focal surface which is, in most cases, approximately the same size as a PMT.

From a systems standpoint, the solid state detection method can identify the slit which the star crossed--the PMT generally cannot. This identification can be of significant benefit--reducing computation load--when the approximate attitude is only poorly known and when solutions are desired quickly. If sufficient computing capacity is available (either in volume or length of time allowed) then such a benefit is of less importance. Either solid state or PMT detectors

are, of course, equally useful if the system is closely following the true attitude or after initial identification is achieved. The reason is obvious: the transits themselves are occurring at relatively widely separated times, thus making the occurrence of an ambiguity (two transits for one possible star or two stars for one transit) almost impossible.

### 3. Transit Timing

A special requirement for timing the transit of a star in a Starmapper is the wide dynamic range required. If star magnitudes are desired from  $+3^m$  to  $0^m$ , this represents a factor of 100 in signal range. This can be cut to about 16 if stars brighter than  $2^m$  are allowed to saturate the system. This results in only a 2.7% loss of targets.

A variety of timing methods are possible, two of which are shown in Fig. 10--fixed and variable bias levels. For symmetric pulses, the times of the rise and fall of the pulse bear the same relationship to the peak and, therefore, can be averaged to determine the time of the peak. The significant advantage here is that no special stability criteria need be applied to the bias level. Stability is only required during the pulse itself.

To handle the dynamic range, several levels could be established so that detection would occur near enough to the pulse midpoint to encounter a rapidly changing signal.

If the pulse is unsymmetric, the above scheme has to be abandoned because a fixed bias level would give transit times which depended on pulse height (see Fig. 11). Such a system could be calibrated if the detector output were sufficiently uniform, but for solid state devices (especially narrow-slit CdS) it is not.

To avoid such problems the second illustration in Fig. 10 shows a scheme in which the pulse traverses two channels: one delayed and the other which detects and holds the peak. A fixed

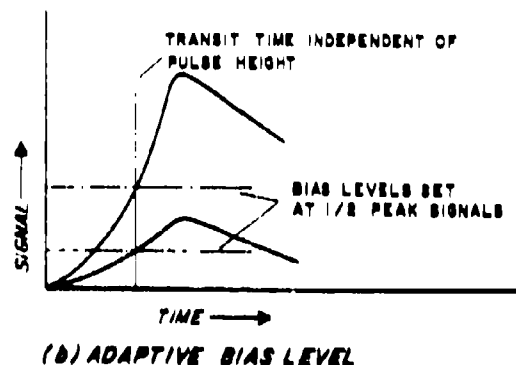
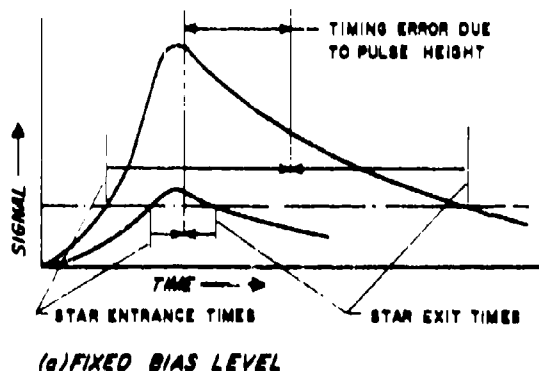


Fig. 11. Transit Time Measurement of Asymmetric Pulse

fraction of the peak value (e.g., one-half) is then used as a bias voltage for detection of the delayed pulse. The pulse is then detected on its leading edge only and at a certain percentage of the peak regardless of this peak value. Such a scheme takes care of variations both from star intensity and detector response by the introduction of a calibratable delay. The accuracy of such a scheme is dependent upon two characteristics of the pulse: consistency of shape independent of height and reaching its peak when the star image has a fixed relationship relative to the slit.

#### REFERENCES

1. A. E. LaBonte, et al., "The SCNS Attitude Determination Experiment on ATS-III," presented at the Spacecraft Attitude Determination Symposium, The Aerospace Corporation, El Segundo, Sept. 30-Oct. 1-2, 1969.
2. J. E. Carroll, "An Automatic Instrument for the Determination of Astronomic Position," Surveying and Mapping, Sept. 1969.
3. R. desJardins, "In-Orbit Star Tracker Misalignment Estimation on the OAO," presented at the Spacecraft Attitude Determination Symposium, The Aerospace Corporation, El Segundo, Sept. 30-Oct. 1-2, 1969.
4. A. F. W. Parr and M. R. Dachs, "Day/Night Shipborne Test Range Star Tracker," presented at the Electro-Optical Systems Design Conference, New York, Sept. 16-18, 1969.
5. G. Quasius and F. McCanles, Star Trackers and Systems Design, Spartan Books, Washington, D. C., 1966.
6. Pavlov, N. N., "The Photoelectric Registration of Star Transits," Trudy GAO, Leningrad, Publications of the GAO, Series II, Vol. LIX, 1946.
7. A. P. Willmore, "A New Method of Tracking Artificial Earth Satellites," Nature, 128, 1008 (1938).
8. Liang Tseng-Yung, "Determination of Time, Longitudes, Latitudes, and Azimuths by the Photoelectric Method," Geodesy and Aerophotography, 1, 32-38, 1963.
9. R. L. Moreau, "Photoelectric Observations in Geodetic Astronomy," Canadian Surveyor, Vol. 20, no. 4, 282-291, 1966.
10. D. G. Abby, "Development of an Electro-Optical Theodolite," presented to the XI Pan American Consultation on Cartography, Washington, D. C., 1969.
11. J. E. Carroll, "An Automatic Instrument for the Determination of Astro-Azimuth," presented at the AIAA Guidance, Control and Flight Mechanics Conference, Princeton, New Jersey, August 18-20, 1969. Preprint No. 69-861.
12. R. L. Lillestrand and J. E. Carroll, "Self-Contained System for Interplanetary Navigation," American Astronautical Society, San Francisco, August 1-3, 1961. Preprint 61-95.
13. R. L. Lillestrand et al., "Celestial Successor to Inertial Guidance," Electronics, March 21, 1966. Also, "Automatic Celestial Guidance, part 2: New Challenge to Designer's Ingenuity," April 4, 1966.
14. C. B. Grosch, "Orientation of a Rigid Torque-Free Body by Use of Star Transits," J. of Spacecraft & Rockets, Vol. 4, no. 3, p. 362, August 1968.
15. T. M. Walsh, G. C. Keating, D. Hinton, "Attitude Determination of a Spin-Stabilized Project Scanner Spacecraft," NASA TND-6740, August, 1968.
16. R. Hertel and I. Lowen, "Scanning Celestial Attitude Determination System for a Stabilized Satellite," presented at the Electro-Optical Systems Design Conference, New York, September 16-18, 1969.
17. D. C. Harrington, "Noise Error Analysis of an Optical Star and Planet Scanner," NAECON, IEEE, Dayton, May, 1963.
18. E. J. Farrell and C. D. Zimmerman, "Information Limits of Scanning Optical Systems," Optical and Electro-Optical Information Processing, MIT Press, 1965.
19. Feasibility Investigation of a Wide Angle Celestial Reference for Space Navigation, Technical Report AFAL-TR-66-10, Control Data Corporation, April, 1966.
20. Self-Contained Navigation Experiment, Final Report, Contract No. NAS3-9883, Control Data Corporation, July 10, 1969.
21. Handbook of Military Infrared Technology, U. S. Government Printing Office, Washington, D. C., 1965.
22. D. D. Maksutov, "New Catadioptric Meniscus Systems," J. Opt. Soc. Amer., Vol. 34, no. 3, p. 270, May, 1944.
23. A. Bouwers, Achievements in Optics, Elsevier, 1950.
24. P. H. Taylor, "Reflecting Telescope," U. S. Patent No. 2,538,593, June 26, 1951.
25. B. Schmidt, Mitt. Hamb. Sternwarte, Bergedorf, 7 (1932) 36.
26. F. A. Jenkins and H. E. White, Fundamentals of Optics, McGraw-Hill, 1950.
27. R. T. Scott and J. E. Carroll, "Development and Test of Advanced Strapdown Components for SPARS," presented at Spacecraft Attitude Determination Symposium, Sept. 30-Oct. 1-2, 1969.

## IN-ORBIT STARTRACKER MISALIGNMENT ESTIMATION ON THE OAO

R. deJardins  
Goddard Space Flight Center  
Greenbelt, Maryland

### ABSTRACT

The present Orbiting Astronomical Observatory (OAO-A2) is designed to point its optical axis to any location on the celestial sphere, and then maintain that pointing within one minute of arc while making astronomical observations. This is accomplished under control of six two-axis gimballed startrackers. In order to ensure this precision the startrackers must be properly aligned relative to each other and to the spacecraft structure. Since this alignment can change due to thermal and launch stresses, the alignment must be performed after the spacecraft is in orbit.

Four misalignment parameters are modeled for each startracker: the three rotational misalignments about the coordinate axes, and a null shift in the inner gimbal. Then two procedures for estimating these parameters from in-orbit telemetry are analyzed. The special procedure, which applies when the spacecraft attitude is perfectly known, involves expressing the known true direction cosines of the guide star in terms of the measured gimbal angles and the four unknown misalignment parameters. The general procedure, which applies when the spacecraft attitude is known only to be near nominal, involves considering the trackers by pairs. For each pair, the known true angle between the pair of guide stars is expressed in terms of the measured gimbal angles and the eight unknown misalignment parameters.

Some problems encountered in the use of these procedures are briefly described, and the actual misalignment parameters estimated in-orbit on the OAO-A2 are presented.

### I. INTRODUCTION

The Orbiting Astronomical Observatory (OAO) is designed to maintain precise pointings in space within one minute of arc under the control of six two-axis gimballed startrackers. Such precision cannot be maintained unless the startrackers are aligned relative to one another and to the spacecraft structure to the same order of magnitude. Launch vibration and thermal stresses cause alignment deviations which must be calibrated out while the spacecraft is in orbit.

In this paper, the mathematical analysis of techniques for performing this calibration on the OAO is

developed. Then some problems peculiar to the OAO are discussed briefly, and actual misalignment parameters estimated in-orbit on the OAO-A2 are presented.

### II. GENERAL DISCUSSION

The Orbiting Astronomical Observatory (OAO) was launched successfully on December 7, 1968. Two days later, its six gimballed startrackers were turned on, directed through a computer-controlled star search pattern, and successfully acquired their predetermined guide stars. Thus began one of the most complex control procedures ever attempted, as the Support Computer Program System (SCPS) at Goddard Space Flight

Center took on the 24-hour-a-day task of directing and maintaining the spacecraft pointing axis to preassigned targets within one minute of arc. This is the design pointing accuracy in the coarse-pointing mode, in which control is derived from the gimballed startrackers.<sup>1</sup>

Any desired attitude in space can in theory be maintained simply by calculating the gimbal angles required to point two or more startrackers at predetermined noncollinear guide stars. If the trackers are then directed at these guide stars and the actual gimbal angles required to do this are observed, the error angles between the observed and computed gimbal angles can be processed to provide control signals for restoring the spacecraft to the nominal attitude.

Many practical problems arise to complicate the picture. Lack of control stability arises for some tracking configurations, especially near collinearity of two trackers. Occulting bodies are troublesome, specifically the "effective" earth, which has a diameter of 164' at the 500-mile orbital altitude of the OAO. As seen from the spacecraft, the earth revolves about the OAO once every orbital period (about 100 minutes). This makes it necessary for the SCPS to provide alternate startracker-star pairs, which are switched out of or into the control loop as various guide stars become occulted or unocculted.

The practical problem being addressed in this paper is the post-launch alignment of the gimballed startrackers. Prior to launch, the startrackers are precisely aligned, in the sense that the directions of their optical and gimbal axes are fixed in the control coordinate system. The misalignments from nominal (perfect orthogonality) are then entered into the computational model of the spacecraft in the SCPS, so that corrections to the gimbal commands can be computed which will ensure that the startrackers are accurately pointed. During launch, however, violent stresses occur which change these misalignments. On OAO-A2, these changes have been as large as five arcminutes. Even in the orbital environment, thermal stresses cause measurable changes in the misalignments. On OAO-A2, a 180° roll about the spacecraft optical axis causes changes greater than one arcminute in some misalignments. It is clear that such misalignment discrepancies are intolerable if the desired coarse pointing accuracy of one arcminute is to be maintained. Even if pointing accuracy were not a problem, pointing precision is. Data quality is greatly degraded when misaligned trackers, dropping out of or coming into the control loop as their stars become occulted or unocculted, cause large movement of the spacecraft pointing axis.

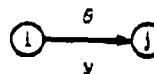
### III. MATHEMATICAL MODELS

#### A. Notational Preliminaries

The mathematics employed in the ensuing analysis is almost exclusively the algebra of rotations, since abstractly the problem is one of locating various three-dimensional rectangular coordinate systems, with a common origin, with respect to one another. A notation of the form



will mean that a rotation  $R$  transforms vectors from some coordinate system  $i$  to some other coordinate system  $j$ . Computationally this means that if  $\vec{v}^i$  is an ordered triple representing a fixed abstract vector  $\vec{v}$  in some coordinate frame  $i$ , and  $j$  is some other coordinate frame, then  $R$  is the matrix such that  $\vec{v}^j = R \vec{v}^i$ . Obviously then  $\vec{v}^i = R^T \vec{v}^j$ , where the superscript  $T$  signifies the transpose. The notation



will mean that the transformation from the  $i$  coordinate system to the  $j$  coordinate system is effected by rotating the  $i$  coordinate system in the positive sense (right-hand rule) about its  $y$ -axis through an angle  $\theta$ , i.e.,

$$\vec{v}^j = \begin{pmatrix} c\theta & 0 & -s\theta \\ 0 & 1 & 0 \\ s\theta & 0 & c\theta \end{pmatrix} \vec{v}^i$$

where  $c\theta = \cos \theta$ ,  $s\theta = \sin \theta$ .

#### B. Mathematical Model of Spacecraft

The present application concerns only the relationships among directions in space; hence the OAO spacecraft will be adequately modeled by considering only its body-fixed axes, the "control" coordinate system  $c$ . This is a standard right-hand orthogonal triad of axes  $x_c, y_c, z_c$  (Fig. 1). The Wisconsin Experiment Package (WEP) experiment optics on OAO-A2 are nominally aligned to the  $+x_c$ -axis; the Smithsonian

<sup>1</sup>The follow-on spacecraft OAO-B and OAO-C will have a fine-pointing capability, in which control is derived from the experimenter's sensor. These spacecraft have design pointing accuracies in the one arcsecond range.

Astrophysical Observatory (BAO) cameras are nominally aligned to the  $-x_k$ -axis.

The six startrackers are oriented one at each end of the three coordinate axes, as shown in Fig. 1. Local tracker coordinate systems  $x_k, y_k, z_k, k = 1, 2, \dots, 6$ ,

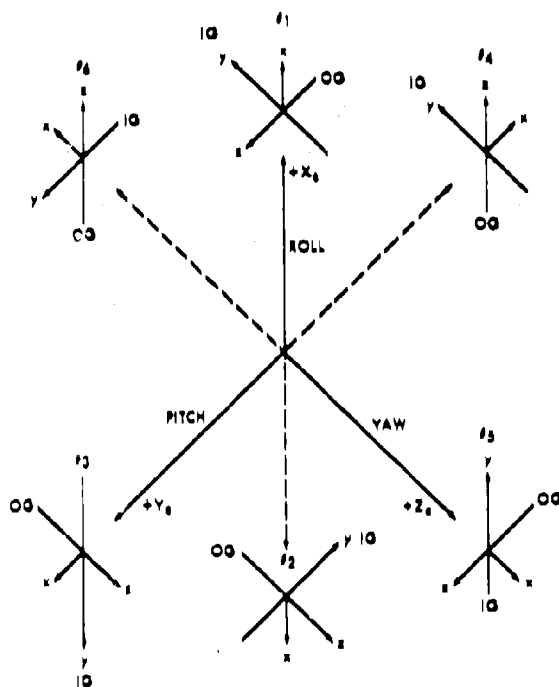


Fig. 1. Control Axis System and Star Tracker Gimbal Locations

are defined such that the zenith position of tracker  $k$  lies along the  $-x_k$ -axis, the inner gimbal axis at zenith<sup>2</sup> coincides with the  $y_k$ -axis, and the outer gimbal axis coincides with the  $z_k$ -axis. Within the local tracker  $k$  coordinate system, the outer and inner gimbal phasing is defined according to the right ascension-declination convention: outer gimbal motion about the  $z_k$ -axis is positive counterclockwise, inner gimbal motion about the inner gimbal axis is positive clockwise.<sup>3</sup> These relationships are shown in Fig. 2.

Hence a star in the field of view of tracker  $k$  with gimbal angles  $\sigma_k, \mu_k$  (outer, inner, resp.) has

<sup>2</sup>The inner gimbal rides in the outer gimbal, so that the inner gimbal axis rotates with the outer gimbal. Hence the inner gimbal axis coincides with the  $y_k$ -axis only for zero outer gimbal angle.

<sup>3</sup>Phasing is defined in this way for the mathematical model; phasing in the physical spacecraft is slightly different from that defined here.

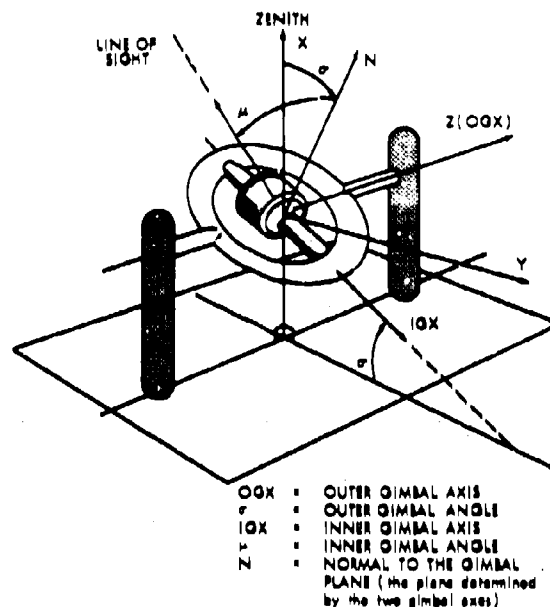


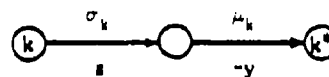
Fig. 2. Gimbal Angles

local coordinates

$$\begin{pmatrix} x_k \\ y_k \\ z_k \end{pmatrix} = \begin{pmatrix} c\sigma_k & s\sigma_k & 0 \\ -s\sigma_k & c\sigma_k & 0 \\ 0 & 0 & 1 \end{pmatrix}^T \begin{pmatrix} c\mu_k & 0 & s\mu_k \\ 0 & 1 & 0 \\ -s\mu_k & 0 & c\mu_k \end{pmatrix}^T \begin{pmatrix} 1 \\ 0 \\ 0 \end{pmatrix}$$

$$= \begin{pmatrix} c\sigma_k c\mu_k \\ s\sigma_k c\mu_k \\ s\mu_k \end{pmatrix}$$

This transformation is represented by the following coordinate-transformation diagram:



As each of the six local coordinate systems is nominally aligned parallel to some control set of axes, the

nominal transformation  $R_k$  from the control axis  $c$  to the system  $k$  has a matrix composed only of 0,  $\pm 1$ :

$$\begin{aligned} R_1 &= \begin{pmatrix} 1 & 0 & 0 \\ 0 & 0 & -1 \\ 0 & 1 & 0 \end{pmatrix} & R_2 &= \begin{pmatrix} -1 & 0 & 0 \\ 0 & -1 & 0 \\ 0 & 0 & 1 \end{pmatrix} \\ R_3 &= \begin{pmatrix} 0 & 1 & 0 \\ -1 & 0 & 0 \\ 0 & 0 & 1 \end{pmatrix} & R_4 &= \begin{pmatrix} 0 & -1 & 0 \\ 0 & 0 & -1 \\ 1 & 0 & 0 \end{pmatrix} \\ R_5 &= \begin{pmatrix} 0 & 0 & 1 \\ 1 & 0 & 0 \\ 0 & 1 & 0 \end{pmatrix} & R_6 &= \begin{pmatrix} 0 & 0 & -1 \\ 0 & 1 & 0 \\ 1 & 0 & 0 \end{pmatrix} \end{aligned}$$

Each such transformation is represented by the following diagram:



#### C. Mathematical Model of Misalignments

The misalignments modeled were, first, rotational misalignments  $d\phi_k$ ,  $d\theta_k$ ,  $d\psi_k$  (taken positive in the conventional right-hand sense) about each of the tracker  $k$  coordinate axes  $x_k$ ,  $y_k$ ,  $z_k$ , resp. These represent an arbitrary misalignment of the tracker  $k$  gimbal platform relative to the spacecraft structure as a whole. Making the usual small-angle (first-order) approximations

$$\cos \alpha \approx 1, \quad \sin \alpha \approx \alpha \quad (|\alpha| \ll 1)$$

the misalignments can be represented by a small-angle rotation matrix

$$I + d\phi_k = \begin{pmatrix} 1 & d\psi_k & -d\theta_k \\ -d\psi_k & 1 & d\phi_k \\ d\theta_k & -d\phi_k & 1 \end{pmatrix}$$

Second, there were also modeled shifts of the null position in the inner and outer gimbals. A null shift in the outer gimbal cannot be distinguished from a misalignment about the tracker  $x_k$ -axis, since the outer

gimbal axis is always parallel to the  $x_k$ -axis. Hence no separate parameter is necessary to represent this shift.

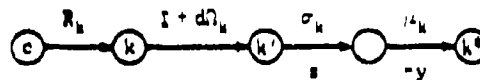
However, a null shift  $d\delta_k$  in the inner gimbal can be separated from a misalignment about the tracker  $y_k$ -axis by taking a large outer gimbal angle, since this separates the inner gimbal axis from the  $y_k$ -axis. (The inner gimbal axis is parallel to the  $y_k$ -axis only when the outer gimbal axis is zero.)

Because  $d\delta_k$  masquerades as  $d\phi_k$  for zero outer gimbal angle, the sense of  $d\delta_k$  has been taken as that of  $d\phi_k$ , viz., positive in the usual right-hand sense. This is opposite to the sense of the inner gimbal angle itself, which is that of declination (declination is negative in the usual right-hand sense).

There are of course some misalignments present at launch. These misalignments are measured during pre-launch calibration, and are included in the software in the following way. First, the initial rotational misalignments are measured for each tracker and incorporated as an initial constant small-angle rotation matrix  $I + d\Omega_k$ . Second, the initial inner gimbal null shift is incorporated in such a way that the inner gimbal command issued includes this null shift.

#### D. Summary

Thus we have defined the following coordinate transformation models for each tracker. In the nominal case, the outer and inner gimbal angles  $\sigma_k$ ,  $\mu_k$ , resp., are computed based on the known attitude of the spacecraft and the known misalignments  $d\Omega_k$ .

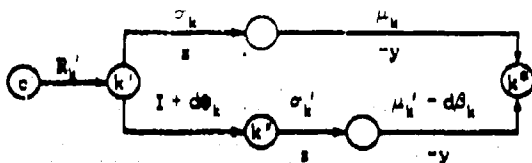


These gimbal angles would nominally point the star-tracker  $k$  line-of-sight directly at the target star. Due to unknown misalignments  $d\phi_k$ ,  $d\theta_k$ , however, and to the fact that the true spacecraft attitude could be somewhat removed from nominal, the tracker will not in general find the target star at the commanded angles  $\sigma_k$ ,  $\mu_k$ , but rather at measured angles  $\sigma'_k$ ,  $\mu'_k$  slightly different from  $\sigma_k$ ,  $\mu_k$ . Hence including misalignments, we have the following situation:



(The negative sign before  $d\delta_k$  is due to the fact that its sense is opposite to that of  $\mu_k$ .) Thus for a

given star being tracked by a given tracker, we have the following:

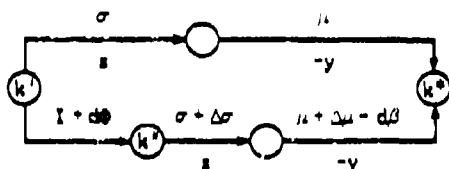


where  $R_k' = (I + d\eta_k)R_k$ .

#### IV. MISALIGNMENT EQUATIONS

##### A. Known Spacecraft Attitude

First, consider the situation which would prevail if the spacecraft attitude were perfectly known. Suppose that at this attitude a certain startracker  $k$  views a fixed star, at nominal gimbal angles  $\sigma, \mu$  (outer and inner, resp.). Due to misalignments, however, the star is actually found at measured gimbal angles  $\sigma' = \sigma + \Delta\sigma, \mu' = \mu + \Delta\mu$ .



In coordinate system  $k^*$ , the viewed star has coordinates  $(1, 0, 0)$ ; in coordinate system  $k'$ , the viewed star has some coordinates  $\bar{v}$ . Working backwards from system  $k^*$  to system  $k'$  by either path should lead to the same coordinates  $\bar{v}$ . Hence we have the equation:

$$\begin{pmatrix} \cos \sigma & -\sin \sigma & 0 \\ \sin \sigma & \cos \sigma & 0 \\ 0 & 0 & 1 \end{pmatrix} \begin{pmatrix} \cos \mu & 0 & -\sin \mu \\ 0 & 1 & 0 \\ \sin \mu & 0 & \cos \mu \end{pmatrix} \begin{pmatrix} 1 \\ 0 \\ 0 \end{pmatrix}$$

$$= \bar{v} = \begin{pmatrix} 1 & -d\psi & d\theta \\ d\psi & 1 & -d\phi \\ -d\theta & d\phi & 1 \end{pmatrix}$$

$$\begin{pmatrix} \cos(\sigma + \Delta\sigma) & -\sin(\sigma + \Delta\sigma) & 0 \\ \sin(\sigma + \Delta\sigma) & \cos(\sigma + \Delta\sigma) & 0 \\ 0 & 0 & 1 \end{pmatrix}$$

$$\begin{pmatrix} \cos(\mu + \Delta\mu - d\theta) & 0 & -\sin(\mu + \Delta\mu - d\theta) \\ 0 & 1 & 0 \\ \sin(\mu + \Delta\mu - d\theta) & 0 & \cos(\mu + \Delta\mu - d\theta) \end{pmatrix} \begin{pmatrix} 1 \\ 0 \\ 0 \end{pmatrix}$$

Now for an arbitrary angle  $a$  and a small angle  $\Delta a$ , we can make the first-order approximations:

$$\cos(a + \Delta a) \approx \cos a - \Delta a \sin a,$$

$$\sin(a + \Delta a) \approx \sin a + \Delta a \cos a$$

The misalignments  $d\phi, d\theta, d\psi, d\beta$  are assumed small, and the errors  $\Delta\sigma, \Delta\mu$  must therefore likewise be small. Hence the right-hand member of the above equation can be put in the form:

$$\begin{pmatrix} 1 & 0 & 0 \\ 0 & 1 & 0 \\ 0 & 0 & 1 \end{pmatrix} + \begin{pmatrix} 0 & -d\psi & d\theta \\ d\psi & 0 & -d\phi \\ -d\theta & d\phi & 0 \end{pmatrix}$$

$$\begin{pmatrix} \cos \sigma & -\sin \sigma & 0 \\ \sin \sigma & \cos \sigma & 0 \\ 0 & 0 & 1 \end{pmatrix}$$

$$+ \Delta\sigma \begin{pmatrix} -\sin \sigma & -\cos \sigma & 0 \\ \cos \sigma & -\sin \sigma & 0 \\ 0 & 0 & 0 \end{pmatrix}$$

$$\begin{pmatrix} \cos \mu & 0 & -\sin \mu \\ 0 & 1 & 0 \\ \sin \mu & 0 & \cos \mu \end{pmatrix}$$

$$+ (\Delta\mu - d\theta) \begin{pmatrix} -\sin \mu & 0 & -\cos \mu \\ 0 & 0 & 0 \\ \cos \mu & 0 & -\sin \mu \end{pmatrix} \begin{pmatrix} 1 \\ 0 \\ 0 \end{pmatrix}$$

Retaining only terms to first order in the small angles, we have:

$$\begin{pmatrix} \cos \sigma \cos \mu \\ \sin \sigma \cos \mu \\ \sin \mu \end{pmatrix} \approx \begin{pmatrix} \cos \sigma \cos \mu \\ \sin \sigma \cos \mu \\ \sin \mu \end{pmatrix}$$

$$+ \begin{pmatrix} 0 & -d\psi & d\theta \\ d\psi & 0 & -d\phi \\ -d\theta & d\phi & 0 \end{pmatrix} \begin{pmatrix} \cos \sigma \cos \mu \\ \sin \sigma \cos \mu \\ \sin \mu \end{pmatrix}$$



$$+ \Delta\sigma \begin{pmatrix} -\sin\sigma \cos\mu \\ \cos\sigma \cos\mu \\ 0 \end{pmatrix} + (\Delta\mu - d\beta) \begin{pmatrix} -\cos\sigma \sin\mu \\ -\sin\sigma \sin\mu \\ \cos\mu \end{pmatrix}$$

which leads to

$$\begin{pmatrix} 0 & \sin\mu & -\sin\sigma \cos\mu & \cos\sigma \sin\mu \\ -\sin\mu & 0 & \cos\sigma \cos\mu & \sin\sigma \sin\mu \\ \sin\sigma \cos\mu & -\cos\sigma \cos\mu & 0 & -\cos\mu \\ \sin\sigma \sin\mu & \cos\sigma \sin\mu & \cos\mu & 0 \end{pmatrix} \begin{pmatrix} d\phi \\ d\theta \\ d\psi \\ d\delta \end{pmatrix} = \begin{pmatrix} \sin\sigma \cos\mu & \cos\sigma \sin\mu \\ -\cos\sigma \cos\mu & \sin\sigma \sin\mu \\ 0 & -\cos\mu \end{pmatrix} \begin{pmatrix} \Delta\sigma \\ \Delta\mu \end{pmatrix}$$

Thus if for a particular tracker, one reading of the telemetry  $\sigma, \mu, \Delta\sigma, \Delta\mu$  is given, one can generate three equations in that tracker's four unknown misalignments  $d\phi, d\theta, d\psi, d\delta$ . If two readings are given representing different pointings (and in particular, different values of  $\sigma$ ), one can generate six equations in the four unknowns, and in general four of these will be independent, so that a unique solution may be obtained. If more than four equations are available, one may obtain a least-squares solution.

## B. Operational Considerations

The situation described above prevails only under very artificial circumstances. On OAO-A2 the above procedure was used to obtain initial rough estimates of the post-launch misalignments as follows. There is another startracker, the boresighted startracker, in addition to the gimballed startrackers, mounted on the spacecraft. Its optical axis is aligned nominally along the  $+x_c$ -axis. This startracker was directed at a suitable star, then commanded to hold the spacecraft in pitch and yaw, while one of the side-looking gimballed startrackers was directed at a suitable star and commanded to hold the spacecraft in roll. The following assumptions are made:

- I. The boresighted startracker is aligned to the  $+x_c$ -axis
- II. The side-looking tracker is aligned in the roll-controlling gimbal
- III. The control system holds the spacecraft fixed

Then one can in theory direct any of the five remaining gimballed startrackers to several stars as outlined in the previous section, and determine the misalignments as described. This procedure was actually used during the early orbital checkout to identify any large misalignments present.

The assumptions made do not hold rigorously, of course, and hence the method has limited precision.

The first assumption, that the boresighted startracker is aligned to the  $+x_c$ -axis, is not too serious for OAO-A2, for the axis of interest is the WEP optical axis, and the experimenter has the capability of measuring the pitch and yaw deviations of his optics from the boresighted startracker optics. These deviations can then be propagated through all the six gimballed startrackers as artificial misalignments in such a way that the experimenter optics are properly pointed.

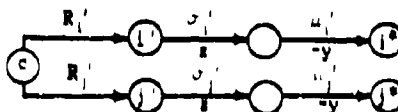
The second assumption, that the particular side-looking tracker chosen accurately controls the roll coordinate, is also not serious for the OAO-A2, for the experiment optics are not roll-sensitive. The roll coordinate is used to maximise solar paddle power output by rolling so as to align the solar paddle as nearly normal to the sunline as possible. But the power output varies like the cosine of the deviation from this optimum roll angle, and hence is not sensitive to first-order variations.

The final assumption mentioned above, that the control system holds the spacecraft fixed, creates a lower bound on the precision obtainable with the method, of about 15 arcseconds. This order of precision has actually been obtained under very tightly constrained operations.

## C. Unknown Spacecraft Attitude

The design pointing accuracy of the OAO-A2 under gimballed startracker control was one minute of arc. To achieve this accuracy, gimballed startracker misalignments must be known to at least the same order of magnitude. Hence it is desired to create an alignment estimation technique which does not depend on knowing the spacecraft attitude precisely.

This is accomplished by considering the tracking startrackers by pairs. On the one hand, the angle between two stars individually being tracked by two corresponding startrackers is known precisely from star catalogs. On the other hand, the angle between the tracking startrackers as computed from the gimbal measurements will differ from the true angle, and this discrepancy is assumed to be due to misalignments of the trackers involved. Consider the following diagram:



The computed dot product between the trackers  $i$  and  $j$  is given by

$$b' = \bar{s}_j^{(c)} \cdot \bar{s}_i^{(c)}$$

where  $\bar{s}_i^{(c)}$  are the measured (') coordinates of star  $i$  in the control coordinate system ('). From the diagram:

$$\bar{s}_i^{(c)} = R_i^T \begin{pmatrix} c\sigma_i' & s\sigma_i' & 0 \\ -s\sigma_i' & c\sigma_i' & 0 \\ 0 & 0 & 1 \end{pmatrix}^T$$

$$\begin{pmatrix} c\mu_i' & 0 & s\mu_i' \\ 0 & 1 & 0 \\ -s\mu_i' & 0 & c\mu_i' \end{pmatrix}^T \begin{pmatrix} 1 \\ 0 \\ 0 \end{pmatrix} = R_i^T \begin{pmatrix} c\sigma_i' & c\mu_i' \\ s\sigma_i' & c\mu_i' \\ s\mu_i' \end{pmatrix}$$

Similarly for tracker  $j$ .

On the other hand, the true dot product between the stars is known from the star catalog, and may be expressed as a function of the (unknown) misalignments and the (known) measured angles:

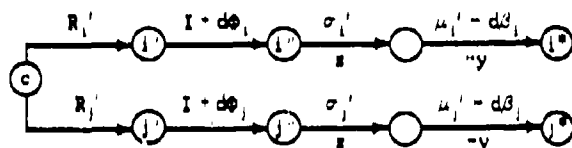


Fig. 3.

Taking the dot product in the  $1'$  coordinate system:

$$b = \bar{s}_j^{(1')} \cdot \bar{s}_i^{(1')}$$

The difference  $\Delta b = b - b'$  is a function of the eight unknown misalignments  $d\phi_i, d\theta_i, d\psi_i, d\delta_i, d\phi_j, d\theta_j, d\psi_j, d\delta_j$ , and hence may be expressed to first order in differential form:

$$\Delta b = \left( \frac{\partial \Delta b}{\partial d\phi_i} \right)_0 d\phi_i + \left( \frac{\partial \Delta b}{\partial d\theta_i} \right)_0 d\theta_i + \dots + \left( \frac{\partial \Delta b}{\partial d\delta_j} \right)_0 d\delta_j$$

$$= \begin{bmatrix} \left( \frac{\partial \Delta b}{\partial d\phi_i} \right)_0 & \left( \frac{\partial \Delta b}{\partial d\theta_i} \right)_0 & \dots & \left( \frac{\partial \Delta b}{\partial d\delta_j} \right)_0 \end{bmatrix} \begin{bmatrix} d\phi_i \\ d\theta_i \\ \vdots \\ d\delta_j \end{bmatrix}$$

where the differential coefficients are all evaluated in the nominal state, i.e., assuming zero misalignments. For any given data reading, the discrepancy  $\Delta b = b - b'$  is computed from the known coordinates of the stars and the data (the measured angles  $\sigma_i', \mu_i', \sigma_j', \mu_j'$ ). The differential coefficients are also computed from the data, as follows:

$$\Delta b = b - b' = \bar{s}_j^{(1')} \cdot \bar{s}_i^{(1')} - \bar{s}_j^{(c)} \cdot \bar{s}_i^{(c)}$$

$$\frac{\partial \Delta b}{\partial d\phi_i} = \frac{\partial}{\partial d\phi_i} (\bar{s}_j^{(1')} \cdot \bar{s}_i^{(1')}) = \bar{s}_j^{(1')} \cdot \frac{\partial \bar{s}_i^{(1')}}{\partial d\phi_i}$$

Now

$$\bar{s}_i^{(1')} = \begin{pmatrix} 1 & d\psi_i & -d\theta_i \\ -d\psi_i & 1 & d\phi_i \\ d\theta_i & -d\phi_i & 1 \end{pmatrix}^T \bar{s}_i^{(1')}$$

(The coordinate system  $1'$  is that of the misaligned star-tracker  $i$  gimbal platform. Cf. Fig. 3.) Hence

$$\frac{\partial \bar{s}_i^{(1')}}{\partial d\phi_i} = \frac{\partial}{\partial d\phi_i} \begin{pmatrix} 1 & -d\psi_i & d\theta_i \\ d\psi_i & 1 & -d\phi_i \\ -d\theta_i & d\phi_i & 1 \end{pmatrix} \bar{s}_i^{(1')}$$

$$= \begin{pmatrix} 0 & 0 & 0 \\ 0 & 0 & -1 \\ 0 & 1 & 0 \end{pmatrix} \bar{s}_i^{(1')}$$

Evaluating  $\bar{s}_i^{(1')}$  in the nominal state, this becomes

$$\left( \frac{\partial \bar{s}_i^{(1')}}{\partial d\phi_i} \right)_0 = \begin{pmatrix} 0 & 0 & 0 \\ 0 & 0 & -1 \\ 0 & 1 & 0 \end{pmatrix} \bar{s}_i^{(1')}$$

$$= \begin{pmatrix} 0 & 0 & 0 \\ 0 & 0 & -1 \\ 0 & 1 & 0 \end{pmatrix} \begin{pmatrix} c\sigma_i' & c\mu_i' \\ s\sigma_i' & c\mu_i' \\ s\mu_i' \end{pmatrix}$$

$$= \begin{pmatrix} 0 \\ -s\mu_i' \\ s\sigma_i' & c\mu_i' \end{pmatrix}$$

Hence

$$\begin{aligned} \left( \frac{\partial \Delta b}{\partial d\phi_i} \right)_0 &= \bar{s}_i^{(1)} \cdot \begin{pmatrix} 0 \\ -s\mu_i' \\ s\sigma_i' c\mu_i' \end{pmatrix} \\ &= (R_i' R_i'^T \bar{s}_i^{(1)})^T \begin{pmatrix} 0 \\ -s\mu_i' \\ s\sigma_i' c\mu_i' \end{pmatrix} \\ &= \begin{pmatrix} c\sigma_i' c\mu_i' \\ s\sigma_i' c\mu_i' \\ s\mu_i' \end{pmatrix}^T R_i' R_i'^T \begin{pmatrix} 0 \\ -s\mu_i' \\ s\sigma_i' c\mu_i' \end{pmatrix} \end{aligned}$$

In a similar way,

$$\begin{aligned} \left( \frac{\partial \Delta b}{\partial d\theta_i} \right)_0 &= \bar{s}_i^{(2)} \cdot \begin{pmatrix} s\mu_i' \\ 0 \\ -c\sigma_i' c\mu_i' \end{pmatrix} \\ \left( \frac{\partial \Delta b}{\partial d\psi_i} \right)_0 &= \bar{s}_i^{(3)} \cdot \begin{pmatrix} -s\sigma_i' c\mu_i' \\ c\sigma_i' c\mu_i' \\ 0 \end{pmatrix} \end{aligned}$$

Finally,

$$\begin{aligned} \frac{\partial \bar{s}_i^{(1)}}{\partial d\beta_i} &= \frac{\partial}{\partial d\beta_i} \begin{pmatrix} 1 & d\psi_i & -d\theta_i \\ -d\psi_i & 1 & d\phi_i \\ d\theta_i & -d\phi_i & 1 \end{pmatrix}^T \\ &= \begin{pmatrix} c\sigma_i' & s\sigma_i' & 0 \\ -s\sigma_i' & c\sigma_i' & 0 \\ 0 & 0 & 1 \end{pmatrix}^T \begin{pmatrix} c\mu_i' & 0 & s\mu_i' \\ 0 & 1 & 0 \\ -s\mu_i' & 0 & c\mu_i' \end{pmatrix}^T \\ &= \begin{pmatrix} 1 & 0 & -d\beta_i \\ 0 & 1 & 0 \\ d\beta_i & 0 & 1 \end{pmatrix}^T \begin{pmatrix} 1 \\ 0 \\ 0 \end{pmatrix} \\ &= \begin{pmatrix} 1 & -d\psi_i & d\theta_i \\ d\psi_i & 1 & -d\phi_i \\ -d\theta_i & d\phi_i & 1 \end{pmatrix} \begin{pmatrix} c\sigma_i' s\mu_i' \\ s\sigma_i' s\mu_i' \\ -c\mu_i' \end{pmatrix} \end{aligned}$$

At zero misalignments,

$$\left( \frac{\partial \Delta b}{\partial d\beta_i} \right)_0 = \bar{s}_i^{(1)} \cdot \begin{pmatrix} c\sigma_i' s\mu_i' \\ s\sigma_i' s\mu_i' \\ -c\mu_i' \end{pmatrix}$$

The coefficients

$$\left( \frac{\partial \Delta b}{\partial d\phi_i} \right)_0, \left( \frac{\partial \Delta b}{\partial d\theta_i} \right)_0, \left( \frac{\partial \Delta b}{\partial d\psi_i} \right)_0, \left( \frac{\partial \Delta b}{\partial d\beta_i} \right)_0$$

can be computed using the above formulas, due to the symmetry of  $i$  and  $j$ , simply by interchanging  $i$  and  $j$ . Hence the following equation in eight unknowns has been generated:

$$[C_{11} \mid C_{12}] \begin{bmatrix} d\phi_i \\ d\theta_i \\ d\psi_i \\ d\beta_i \\ d\phi_j \\ d\theta_j \\ d\psi_j \\ d\beta_j \end{bmatrix} = b - b' \quad (1)$$

where  $C_{11}, C_{12}$  are  $1 \times 4$  matrices:

$$\begin{aligned} C_{11} &= \begin{pmatrix} c\sigma_i' c\mu_i' \\ s\sigma_i' c\mu_i' \\ s\mu_i' \end{pmatrix}^T R_i' R_i'^T \\ &= \begin{pmatrix} 0 & s\mu_j' & -s\sigma_j' c\mu_j' & c\sigma_j' s\mu_j' \\ -s\mu_j' & 0 & c\sigma_j' c\mu_j' & s\sigma_j' s\mu_j' \\ s\sigma_j' c\mu_j' & -c\sigma_j' c\mu_j' & 0 & -c\mu_j' \end{pmatrix} \end{aligned}$$

Altogether in the system of the six gimballed star-trackers, there are 24 unknowns, and the above Eq. (1) may be regarded as one equation in 24 unknowns. Each pair of tracking startrackers generates one such equation for each data reading. A set of three tracking star-trackers taken by pairs generates three such equations, and in general a set of  $n$  tracking startrackers generates  $\binom{n}{2}$  such equations (some redundant).

Data readings are collected representing many different values of  $\sigma, \mu$  for all trackers, and the equations described above are generated. In this way a large

number of equations in the 24 unknown misalignments are generated. This system of equations is then solved in the least-squares sense. The solutions represent the least-squares estimates sought.

The quality of the estimates obtained is controlled by processing several sets of data, so that the consistency of each estimate may be monitored. Several interesting characteristics have appeared as a result of this quality evaluation. Some of these features are discussed in the next section.

## V. SPECIAL FEATURES

### A. Tracker in or out of Control Loop

There are two tracking modes of startracker operation. In both modes, the startracker is locked onto a star (its guide star), and continuously reads out its error angles "measured-minus-commanded" in both gimbal.

In the usual operational mode, the Auto Track Mode, these error signals are then resolved into components of error about each of the three spacecraft control axes, and averaged with similar components from the other tracking startrackers. The average error signals then control the spinning up or down of inertia wheels to restore the spacecraft to its nominal attitude. It is then clear that the error signals from a tracker operating in the Auto Track Mode by themselves give no information about the misalignments of that tracker relative either to nominal or to any other tracker. The spacecraft takes on attitudes near nominal in response to all the errors seen by all the tracking startrackers in the control loop; these attitudes are away from nominal and hence generate additional errors in all the trackers in the loop, including the perfectly aligned trackers. Hence it is not possible in the Auto Track Mode to separate errors due to misalignment from errors due to other sources simply by observing the errors from one startracker.

Another tracking mode of startracker operation, the Forced Track Mode, is also available. If a startracker is tracking in this mode, its error signals are not mixed into the control loop. (The spacecraft attitude must be controlled by some other means, such as by other gimballed startrackers, by the Rate and Position Sensor (RAPS) accelerometer package, etc.) If attitude reference can be maintained in a sufficiently precise way, then the gimbal error signals read out will actually represent the misalignments of the tracker with respect to the reference coordinates being maintained. If conditions are right, this mode can be used to obtain gross misalignment estimates fairly quickly, as discussed in Section IV.A.

### B. Misalignment Reference

The 24 unknown misalignments are not all determined by the estimation procedure. Since only the

angles between pairs of startrackers are involved, there is no fixed reference in the body axes to which all the trackers can be aligned. Hence normally startracker #1, the forward-looking tracker, is chosen as a reference and assigned zero rotational misalignments  $d\phi_1 = d\theta_1 = d\psi_1 = 0$  (it may still have a nonzero inner gimbal null shift  $d\beta_1$ ). Then the remaining misalignments are estimated by the procedure described. The experimenter has the capability of determining the deviation in pitch and yaw of his optics from the startracker #1 line-of-sight. It has already been noted that the experiment is not roll-sensitive, so from that point of view it is permissible to leave the roll reference arbitrary.

### C. Separation of $d\beta$ from $d\theta$

It has turned out to be more difficult than anticipated to separate  $d\beta$  from  $d\theta$ , that is, to decide what portion of the error appearing about the inner gimbal axis is due to null shift  $d\beta$  in the inner gimbal and what portion is due to rotational misalignment  $d\theta$  of the gimbal platform about the tracker y-axis.

From Eq. (1), assuming that the other misalignments have been determined, the pertinent equation for some tracker  $i$  has the form

$$\begin{aligned} \vec{u}_i' &= \begin{pmatrix} s\mu_i' \\ 0 \\ -c\sigma_i' \ c\mu_i' \end{pmatrix} d\theta_i \\ &+ \vec{u}_i' \cdot \begin{pmatrix} c\sigma_i' \ s\mu_i' \\ s\sigma_i' \ s\mu_i' \\ -c\mu_i' \end{pmatrix} d\beta_i = \text{constant} \end{aligned}$$

When  $\sigma_i' = 0$ , the inner gimbal axis and the  $y_i$ -axis coincide:

$$c\sigma_i' = 1, \quad s\sigma_i' = 0$$

$$\vec{u}_i' \cdot \begin{pmatrix} s\mu_i' \\ 0 \\ -c\mu_i' \end{pmatrix} (d\theta_i + d\beta_i) = \text{constant}$$

Thus only the sum  $d\theta_i + d\beta_i$  can be determined. To separate  $d\beta_i$  from  $d\theta_i$ , it is necessary to take large values of  $\sigma_i'$ , so that the coefficients

$$\vec{u}_i' \cdot \begin{pmatrix} s\mu_i' \\ 0 \\ -c\sigma_i' \ c\mu_i' \end{pmatrix}$$

And

$$\bar{\mu}_1' = \begin{pmatrix} c\sigma_1' \mu_1' \\ s\sigma_1' \mu_1' \\ -c\mu_1' \end{pmatrix}$$

are sufficiently distinct.

If  $\sigma_1'$  is small, then the difference between these coefficients can be approximated to first-order:

$$\begin{aligned} \bar{\mu}_1' &= \begin{pmatrix} s\mu_1' \\ 0 \\ -c\sigma_1' c\mu_1' \end{pmatrix} - \bar{\mu}_1' = \begin{pmatrix} c\sigma_1' s\mu_1' \\ s\sigma_1' s\mu_1' \\ -c\mu_1' \end{pmatrix} \\ &= \bar{\mu}_1' + \begin{pmatrix} s\mu_1' - c\sigma_1' s\mu_1' \\ -s\sigma_1' s\mu_1' \\ -c\sigma_1' c\mu_1' + c\mu_1' \end{pmatrix} \\ &\approx \bar{\mu}_1' + \begin{bmatrix} s\mu_1' (\sigma_1')^2 \\ -s\mu_1' (\sigma_1')^2 \\ c\mu_1' (\sigma_1')^2 \end{bmatrix} = \sigma_1' \bar{\mu}_1' + \begin{pmatrix} \sigma_1' s\mu_1' \\ -s\mu_1' \\ \sigma_1' c\mu_1' \end{pmatrix} \end{aligned}$$

which is first order in the small angle. If in addition,  $\mu_1'$  is small, this becomes approximately

$$\sigma_1' \bar{\mu}_1' = \begin{pmatrix} \sigma_1' \mu_1' \\ -\mu_1' \\ \sigma_1' \end{pmatrix}$$

which is second order in small angles. Now in the course of collecting data, a considerable portion of the data will have both gimbal angles small enough to cause difficulty in separating these parameters, since the procedure followed by the computer in selecting guide star patterns favors small gimbal angles.

#### D. Optimal Estimation

The above feature points out one of the limitations of least-squares estimation in this application. Functional dependence between parameters is not taken into account. Furthermore the data are assumed to be representative of all the parameters equally. Due to the

manner in which the data are collected, this requirement cannot be assured. For these reasons, it may be necessary in the continuing development of this estimation system to perform minimal variance estimation on the data rather than simple least squares. Most of the analysis for such a procedure can be found in Ref. 1.

## VI. RESULTS

### A. Launch-induced Misalignments

Table 1 lists the misalignments estimated to have been caused by launch stresses. The figures given are the differences between the pre-launch calibration measurements and the early in-orbit estimates. These values were determined by a variety of techniques and data fits, and are given relative to startracker #1.<sup>4</sup> The entries in Table 1 are given to the nearest 0.2 arcminute although their accuracy is probably not better than 0.4 arcminute.

Table 1. Launch-induced Misalignments (arcmin)

Tracker #	Misalignment Parameter			
	dφ	dθ	dψ	dχ
1	0	0	0	0
2	0.4	0.4	-1.0	1.4
3	-5.6	3.0	-1.0	0
4	-1.6	-3.0	-2.8	0
5	-0.6	-0.2	1.0	0.8
6	-3.0	-0.8	-5.6	0

These are significant misalignments. Allowing for 0.4 arcminute error in the entries in Table 1, and even assuming a complete inability to separate dφ from dθ, the rotational misalignments exceed 2.2 arcminutes rms and 5 arcminutes maximum.

### B. Thermal-induced Misalignments

The misalignments given in Table 1 produced exceptionally good pointings in the early orbits, with gimbal errors consistently down in the 10-20 arcsecond range. But when operations with the alternate experimenter (BAO) commenced, the pointings degraded markedly. The degradation is due in some part to

<sup>4</sup> A shift in the pointing of tracker #1 relative to the experiment optics has been removed from the misalignments reported in Table 1, although it is included in the misalignment table for spacecraft operations.

thermal fluctuation. In the early orbits, the operations staff was gingerly in their movements of the spacecraft and tended to operate in a restricted region of the sky. Over a period of several orbits, the misalignments stabilized at or near the values given in Table 1 above.<sup>5</sup>

The SAO experimenter operates out of the opposite end of the spacecraft from WEP, however. Since both stay well away from the sun, this tends to expose the opposite extremities of the spacecraft to the sun's rays. The thermal bending which then takes place is felt to contribute substantial additional misalignment to that given in Table 1. Hence it was deemed advisable to develop an additional (B) set of misalignments for SAO operations. The differences B-A between this modified set and the original (A) set are given in Table 2. These are considered to be in some part thermal-induced misalignments.

Table 2. Misalignment Differences B-A (arcmin)

Tracker #	Misalignment Parameter			
	$d\phi$	$d\theta$	$d\alpha$	$d\delta$
1	0.4	1.0	0	0.4
2	-1.8	-0.2	-1.6	1.4
3	0.8	-1.2	-1.8	0.4
4	0.2	3.0	0.8	-1.6
5	-0.8	-0.8	0.2	-1.8
6	0	0.8	0.8	1.2

It should be noted that these B misalignments have not succeeded in reducing the gimbal errors to those experienced in the early orbits. The errors currently run in the 30-60 arcsecond range. One explanation for this may be that the experimenter is currently ranging over a much larger region of the celestial sphere due to a spacecraft problem which is not of concern here. It may be that the thermal fluctuations due to this activity are contributing substantial variation in the misalignments.

The misalignment differences given in Table 2 may be conservatively characterized as were those in Table 1. Allowing for an error of 0.2 arcminute in these entries, and not separating  $d\phi$  from  $d\theta$ , the figures

still represent rotational misalignments in excess of 0.6 arcminute rms and 1.6 arcminutes maximum.

### C. Conclusions

Significant gimballed startracker misalignments on the order of 2 to 5 arcminutes due to launch stresses and 0.5 to 1.5 arcminutes due in part to thermal stresses have been estimated on the OAO-A2 using techniques described in this report. This magnitude of misalignments, if uncorrected, would have represented a substantial limitation to high-precision pointing under gimballed startracker control. Using rather crude data collection and estimation techniques, however, misalignment parameters have been obtained of sufficient precision to maintain (and in some constrained operations, to improve on) the OAO-A2 design pointing accuracy of one arcminute. Using improved data collection techniques and optimal misalignment estimation, a theoretical pointing capability under gimballed startracker control of close to one-half arcminute in constrained operations is indicated.

### VII. ACKNOWLEDGMENT

This paper would not be complete without acknowledging the people who made it possible: J. Howard Wright, Sal Soscia, and especially Paul Davenport, who were farsighted enough to recognize the problem area, and who provided the support and encouragement needed for me to make a contribution.

### REFERENCES

1. Specification of Computer Program for Determination of OAO Startracker Bias Errors, Contract No. NAS5-9753-14, prepared by Westinghouse Electric Corporation for Goddard Space Flight Center, October 13, 1966.
2. Final Report for OAO-OCCS Problem #1, "Mathematical Modeling of Factors Causing Bias Errors in Pointing of OAO-A1 Spacecraft", Contract No. NAS5-9753-7, prepared by Westinghouse Electric Corporation for Goddard Space Flight Center, March 17, 1966.
3. Mathematical Analysis of a Proposed Technique for Calibrating Gimballed Startracker Misalignments, Goddard Space Flight Center OAO-SCPS Technical Memorandum T-68-28, R. deJardins, October 26, 1966.

<sup>5</sup>The thermal inertia of the spacecraft is such that light-dark variation of misalignments during one revolution is negligible.

# SOLAR ATTITUDE REFERENCE SENSORS<sup>1</sup>

D. A. Koso and J. C. Kollodge  
Honeywell Radiation Center  
Lexington, Massachusetts

## ABSTRACT

The use of sun sensors for space craft attitude systems is reviewed. Effects of solar activity and solar constant uncertainty are considered. It is shown that with proper design sun sensors with arc second accuracy can be built. However, to achieve high accuracy, thermal considerations and physical optics considerations have to be introduced into sensor design.

## I. INTRODUCTION

### Solar Attitude Reference Sensors

The problem of the selection of navigational references is a complex one and the approach to its solution varies considerably with mission applications. For some missions it is possible to find a "natural" set of coordinate systems. For example, for a synchronous attitude satellite, an earth sensor and polaris tracker form a natural reference. For planetary exploration, the sun and the Star Canopus form a natural reference as illustrated in Fig. 1. Most missions, however, are flown in low earth orbit and it becomes necessary to sense various navigational references during different parts of the mission.

One possibility is the use of various guide stars and planets. The latter are usually excluded, because their use requires additional ephemeris computation.

The sun has been used as a navigational reference for missions of this type. However, due to its size, tracking of the sun carries with it several problems, which have to be considered in detail, before accurate sun sensors can be designed.

This work was performed at the Honeywell Radiation Center

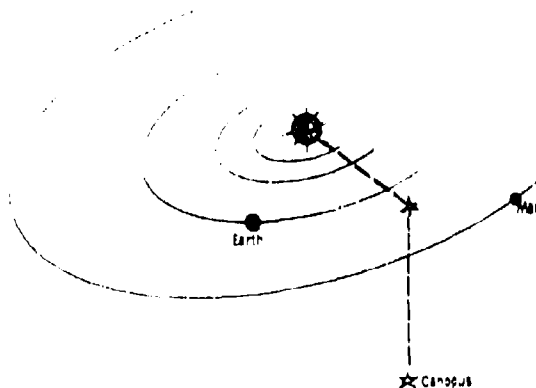


Fig. 1. Sun Canopus Measurement Geometry

A general pictorial representation of the sun is shown in Fig. 2. The first important factor is the diameter of the solar disc. In a 10 micro-radian sensor, the center of the solar disc has to be determined to an accuracy of approximately 1 part in 1000. This can be achieved with proper selection of operating spectra because the sun is a disc of uniform brightness. However, since solar activity causes light emission outside of the solar disc, and sun spots cause darkening of the solar disc in various areas, as in most systems, careful selection of operating wavelengths and compromises between linearity and null stability are necessary.

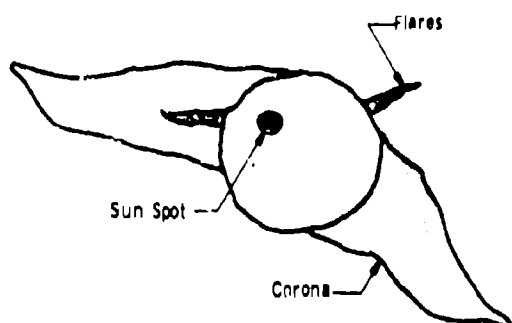


Fig. 2. Sun Activity

## II. DIFFERENCES BETWEEN THE STAR SENSING AND SUN SENSING PROBLEMS

The star tracker designer has a very serious problem with signal levels. Most tracker designs are signal limited, requiring high sensitivity low noise detectors. The optical systems generally are large to collect the necessary stellar energy.

The sun represents a source of interference to the star tracker designer. To understand the difference between star tracker and sun sensor design one has to realize that the energy received from the sun is approximately  $10^{10}$  greater than the energy received from Sirius.<sup>(1)</sup>

Thus from the signal processing standpoint, the sun sensor designer can work with extremely small apertures. As a matter of fact, the signal - or really total energy - from the sun is so high, that severe thermal distortions within the structure can cause misalignments and errors.

Very often sun sensors are used in an offset pointing mode as shown in Figure 3. This type of a system requires accurate knowledge of the linearity of the sun sensor output and of the gradient of the sensor.

For star trackers, measurements of this type are relatively easy. The sun sensor designer though is faced with the problem of sun simulation.

The brightness of the sun is extremely difficult to simulate. Thus the sun sensor designer may either test with a source which provides the correct total energy at the sensor and thus subtends a larger angle than the actual sun, use a source with the proper subtended angle and lower total energy or actually go outside and use the real sun.

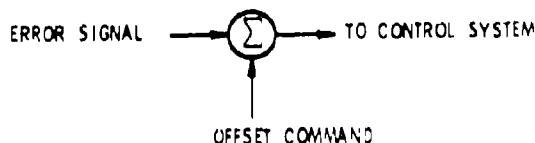
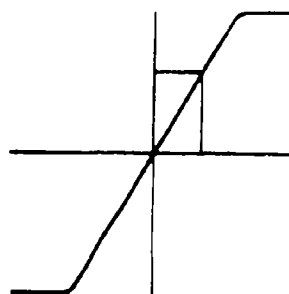


Fig. 3. Offset Pointing Mode

In many cases all three approaches have to be used to measure various aspects of the sun sensor performance. To overcome problems of exact calibration systems are often designed to provide for simple automatic gain circuitry to insure that the unknowns in the testing and calibration process do not contribute to systematic errors of the sensor.

In the following section, some generic types of sun sensors are described, to indicate approaches which have been taken in the design process. The last section of the paper describes some of the properties of the sun and how these properties relate to the design of high accuracy sun sensors.

## III. SENSOR CONFIGURATIONS

### A. Shadow Mask System

One of the simplest sensor configurations is shown in Figure 4. The system consists of two detectors, two masks, and structure to which the detector and masks are attached. As the sun moves through an angle  $\theta$ , a larger portion of detector 1 and a smaller portion of detector 2 are illuminated. The current generated by the two detectors varies with incident sun angle; thus an error signal is generated.

The assembly can be divided along the vertical demarcation line and the two halves can be mounted on separate areas of the spacecraft. The field of view of the sensor and linear range can be varied by the detector-mask spacing and by the size of the two detectors.



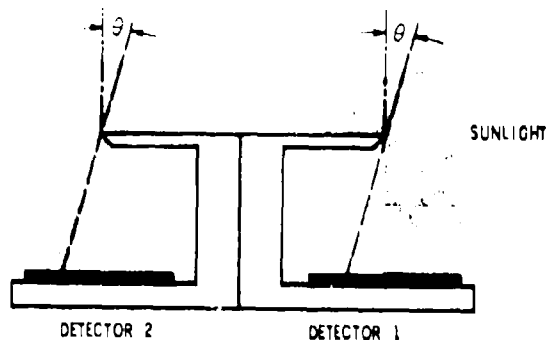


Fig. 4. Shadow Mask Sensor

The circuitry commonly used with these detectors is shown in Fig. 5. (Assuming that silicon detectors are used, Cadmium Sulfide or Cadmium Selenide can also be used. In this case the detectors are generally used as two arms of a bridge circuit.)

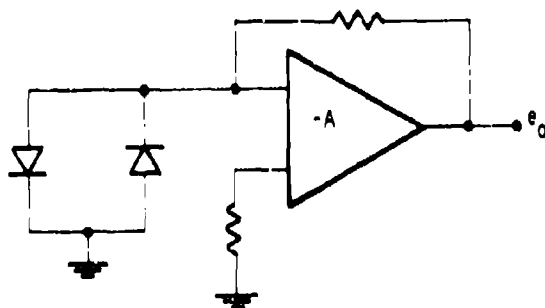


Fig. 5. Detector Difference Amplifier

The major problem with this system, when one tries to use the sensor as a high accuracy sensor, is the thermal stability of the assembly

A second technique, which limits the field of view and produces a more compact unit which can be shielded with greater care from thermal transients, is shown in Fig. 6. The sun is imaged through a slit on two detectors, which are shaped according to the desired transfer function of the sun sensor. As the solar image moves across the sensor, differing areas of detector 1 and detector 2 are illuminated, providing an error signal output when used with the circuitry shown in Figure 5

These two configurations are only a small sample of the possibilities.

Keeping the sum of the signals from the two detectors constant throughout the operating

field of view, does provide the designer with the possibility of using an AGC system as shown in Figure 7.

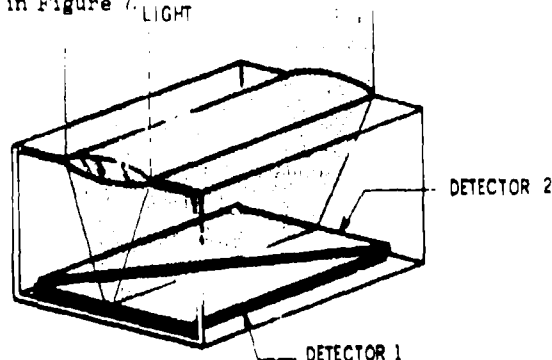


Fig. 6. Sensor with Cylinder Lens

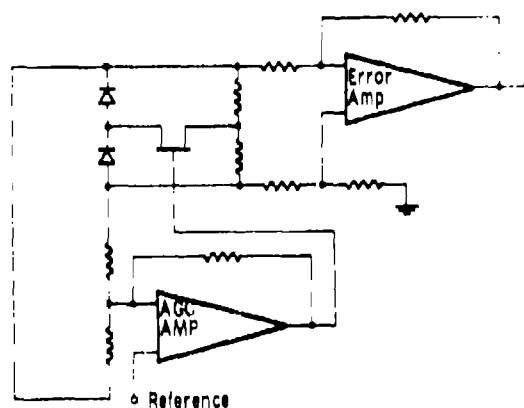


Fig. 7. AGC System

As noted before, this alleviates the problems encountered in simulation, especially in systems designed for offset pointing.

## B. Imaging Systems

In the previous section approaches were considered where either a mask forms the defining geometry or a lens images the sun on a detector and the detectors define the field of view and tracking geometry of the system.

Another combination provides both as shown in Fig. 8. (2,3) Two sensors of the type shown can be mounted on a common base or separated on the spacecraft.

## C. Critical Angle Prism

The sensors described above require stable alignment of at least two parts: the mask or lens and the detector.

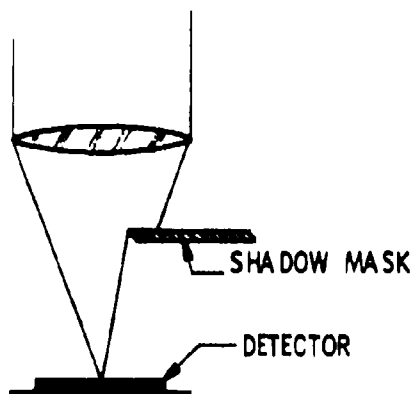


Fig. 8. Imaging System with Shadow Mask

To reduce the number of pieces which have to be controlled relative to the reference surface, a critical angle prism can be used. In this case a single piece of glass (or quartz) controls the null axis of the sensor. Light enters the sensor as shown in Fig. 9. The back surface of the prism is cut at the critical angle. The transmission through the prism near the critical angle is shown in Figure 10. For small angles near the critical angle the transmission is proportional to the square root of the angle and passes through zero with an infinite slope. Thus extremely high sensitivity can be obtained in addition to the advantages mentioned above.

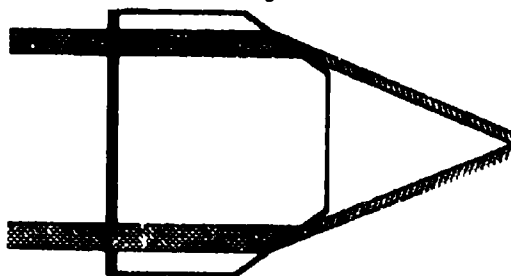


Fig. 9. Critical Angle Prism

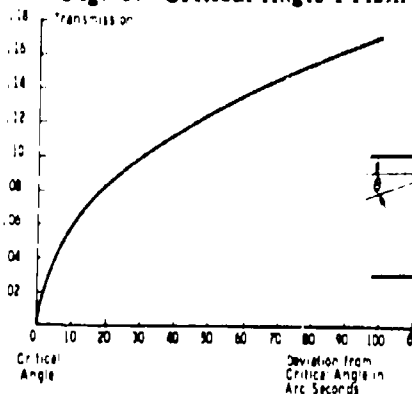


Fig. 10. Critical Angle Prism Transmission

In a simple DC system, the detectors can be mounted directly on the back surface of the critical angle prism as shown in Figure 11. If variation in detector sensitivity is sufficiently critical, a single detector and chopper as shown in Figure 12 can be used.

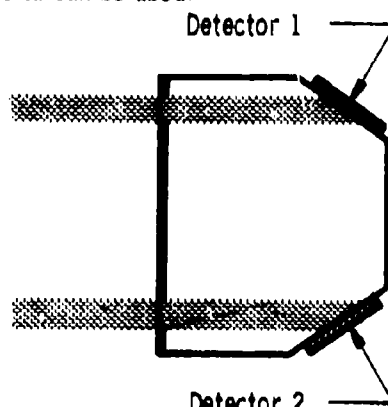


Fig. 11. DC Caps System

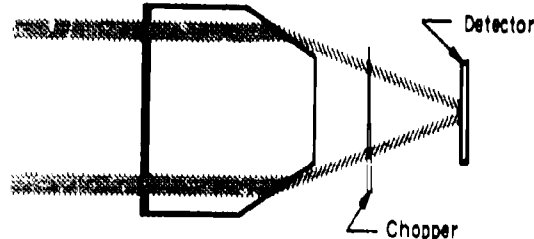


Fig. 12. AC Caps System

#### D. Digital Sensors

Due to the high energy which is available from the sun, it is possible to replace the analog detectors shown in Figure 6 with a Grey coded set of detectors. This type of system provides direct readout of the sun position. Since the solar diameter is approximately  $1/20^\circ$ , the system shown in Figure 13 is limited to a resolution of  $1/20^\circ$ . For certain missions, and especially during attitude acquisition portions of a mission, this type of a system can provide the required accuracy.

Since the position output is carried as a parallel digital word, interface problems are simple and offset pointing is very easy.

If higher accuracy is required, it can be obtained directly at discrete times when the state of one of the digital outputs is changing or by either analog or digital interpolation.

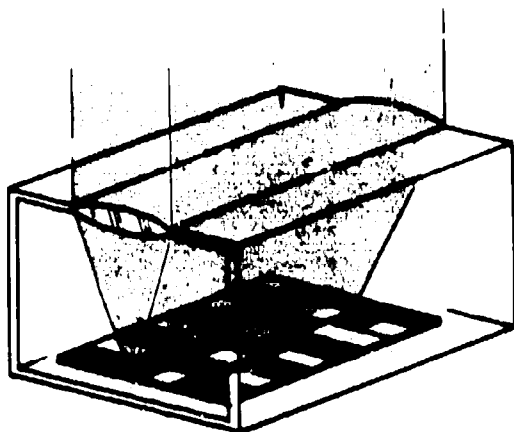


Fig. 13. Digital Sensor

#### IV. ERROR SOURCES IN SUN SENSORS

First let us consider solar activity and the corona to determine whether or not high accuracy sun sensing is feasible.

Most of the solar activity is photographed through very narrow filters, because very little activity is easily observable within the white continuum. The brightness of the sun decreases very rapidly at the edge, with the white corona having a brightness of approximately  $10^{-6}$  of the sun. The corona does extend to about 3 solar radii, thus it can contribute  $\approx 10^{-5}$  of the energy compared to the sun.

Flares generally cannot be seen against the photosphere though one flare (July 25, 1948) added 10% to the continuum but only in the 4000-6000  $\text{\AA}$  region.<sup>(1)</sup>

Typical flares provide less than 1% to the continuum output.<sup>(1)</sup>

To avoid the regions of high solar activity, it is therefore necessary to choose a band of operation in the red region of the spectrum looking at the red to near infrared spectrum of the sun. A spectral region choice of this type allows achievement of the highest accuracy within present knowledge of the sun.

Let us now consider the error terms within the sun sensor shown in Fig. 6. The complete image of the sun falls on both detectors. Consider a displacement of 10 micro-radians (the sun diameter is approximately 9 milli-radians) as shown in Fig. 14

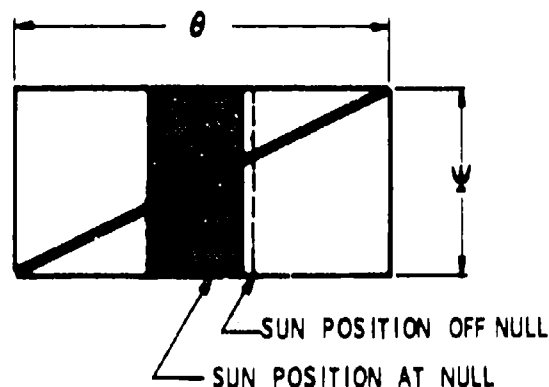


Fig. 14. Error Sensitivity

The total field of view of the system is 9 milli-radians. The comparable width of the detector is  $\psi$ .

At null the current from each detector is proportional to  $9\psi/2$ . The change in the current for a 0.01 milli-radian displacement is  $0.01 \times 9\psi/8$ . Thus the fractional change in the detector current for a 10 micro-radian displacement is  $0.02/\theta$ .

If it is assumed that the two detectors will have a differential sensitivity drift of 1% after initial calibration, then the field of view of the sensor,  $\theta$ , can be 0.2 milli-radians (considerably smaller than the solar diameter). For a 1 degree ( $\approx 20$  milli-radian) field of view the relative stability of the detectors has to be 0.1 per cent.

This relationship is independent of the sun diameter and depends only on the total field of view.

If one assumes that 0.1% matching over an extended period is feasible, then the accuracy and field of view limits of this type of system are set. If these numbers are not compatible, it becomes necessary to remove a portion of the energy at null.

As a first approximation, assume a 9 milli-radian mask (essentially a complete masking of the sun). The primary error source is now the corona.

As a worst case, assume that the corona extends to three times the solar radius and that it is all located on one side of the solar disc.

A quick calculation shows that errors introduced by this factor are negligible for reasonable (less than 180 degree) fields of view.

Prominences which average 0.5 arc min by 2 arc sec also represent negligible sources of error in a sun sensor system.

Thus, in conclusion, one can assume that the sun is an object with uniform brightness in the 0.8 to 1.0 micron range.

#### V. DESIGN CONSIDERATIONS

Due to the high energy which is available from the sun the apertures of solar attitude sensors are usually very small when compared to the apertures used in star trackers. 1 cm<sup>2</sup> of solar energy is more than sufficient for very easy data processing.

However, the Airy disc diameter of an optical system with 1 cm aperture operating at 1 micron is approximately 50 arc sec. Thus the order of magnitude approximations used in the previous section require much more detailed analysis<sup>(4)</sup> than is provided by simple geometrical optics arguments.

While one type of sun sensor was used to illustrate the design parameters, the same analysis is required for imaging, shadow mask or critical angle prism systems.

The designer has to realize from the beginning that he is working on a system with an expected accuracy of 1 or 2 arc seconds. The problems are not in the circuit design, but in the mechanical, thermal and physical optics aspects of the system.

#### REFERENCES

1. G. P. Kuiper, The Sun (The University of Chicago Press, Chicago, Illinois, 1953).
2. Staff of Goddard Space Flight Center, Orbiting Solar Observatory Satellite, The Project Summary, NASA SP-57, 1965.
3. NASA Design Criteria Office, Sun Sensor Design Criteria, NASA SP to be assigned.
4. H. Nagaoka, Diffraction Phenomena in the Focal Plane of a Telescope with Circular Aperture, due to a Finite Source of Light, Philosophical Magazine, V. 45, no. 1898.

## ACCURACY OF IR HORIZON SENSORS AS AFFECTED BY ATMOSPHERIC CONSIDERATIONS\*

John A. Dodgen and Howard J. Curfman, Jr.  
NASA Langley Research Center  
Hampton, Virginia

### ABSTRACT

(U) The effects of atmospheric variability on IR horizon sensors are illustrated using experimental data and analytical study results obtained or supported by Langley Research Center. It is shown that proper selection of spectral interval minimizes horizon sensor problems caused by low-level atmospheric effects. The best spectral interval was found to be the 14.0- to 16.3-micron band associated with CO<sub>2</sub> absorption in the atmosphere. This band effectively shields a sensor from clouds and other low-altitude effects, however, makes it sensitive to relatively slowly varying temperature changes in the atmosphere above 20 km, thereby introducing variations caused by seasonal and geographic effects. The results of a study of these variations over a 3-year span shows that a deterministic trend with latitude exists, which changes with season. It is shown that a simply implemented, single beam, horizon sensor in the CO<sub>2</sub> band can be expected to experience approximately 3 km random variation of the horizon about the deterministic mean, primarily at the higher latitudes. It is concluded that the use of a three- or four-beam horizon sensor, with simple "oblateness" type corrections for systematic effects, will provide attitude determination accuracy of 0.05° (1σ) for spacecraft at altitudes above 100 nautical miles.

### INTRODUCTION

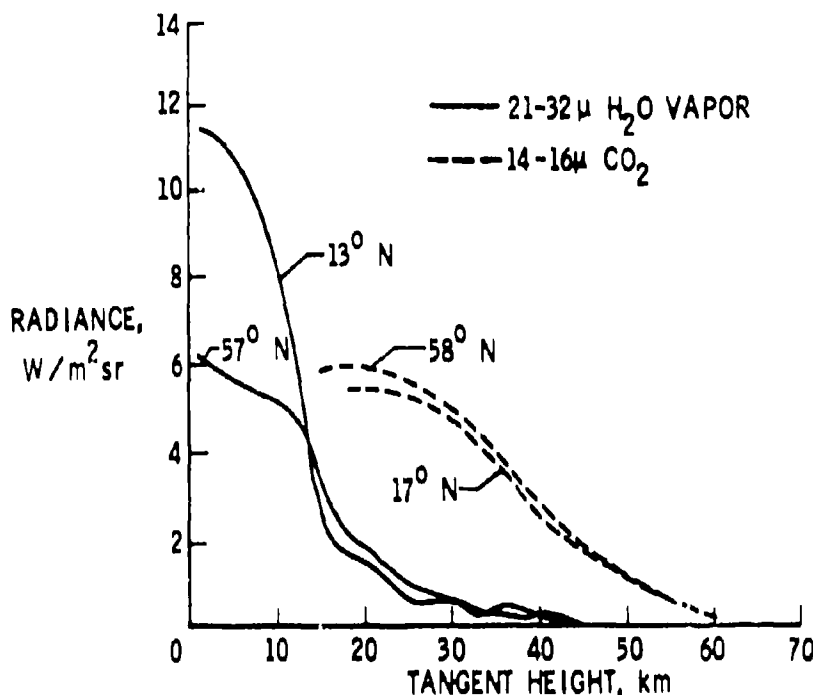
(U) For the past several years, the Langley Research Center has been conducting research on horizon sensing as a means of measuring spacecraft attitude. This work was directed primarily toward describing more accurately the input to such horizon sensors, namely, the horizon radiance profile. The research includes both experimental measurements and analytical studies, and covers a wide spectral range from the ultraviolet to the far infrared (Refs. 1-12). We feel quite strongly that the horizon data being obtained establishes fundamental design considerations for any future horizon sensor developments. This paper will review briefly parts of the Langley research including results. Data from the Project Scanner flight experiment will be used to demonstrate the effects of spectral interval selection and of geographical position. The results of an analytical study utilizing available

atmospheric data to predict horizon variance as seen by a horizon sensor will be shown, and some conclusions drawn as to the accuracy obtainable.

### BACKGROUND

(U) Early in this work, LRC decided to concentrate on the thermal infrared spectral region, in order to provide "full-time" horizon sensor use, in both sunlit and dark portions of the orbit; a feature not possible with spectral intervals dependent on solar illumination. As a result of analytical work by several investigators (Refs. 13, 14, and 15) we further concentrated on two spectral intervals, namely, the 15-micron CO<sub>2</sub> band and the rotational water vapor band beyond 20 microns, where the absorption characteristics of the atmosphere move the apparent horizon to higher altitudes, thereby minimizing the effects of low-altitude phenomena such as clouds. Project Scanner obtained experimental data in the 14-16μ CO<sub>2</sub> band and in the 21-32μ water vapor band which indicated the CO<sub>2</sub> band to be more promising from the standpoint of minimizing the effects of low-altitude atmospheric vagaries. Figure 1 presents radiance profiles from Project

\*This work was done at NASA Langley Research Center, Hampton, Virginia



(U) Fig. 1. Measured Radiance Profiles From Project Scanner for 14-16 $\mu$  and 21-32 $\mu$  Spectral Bands

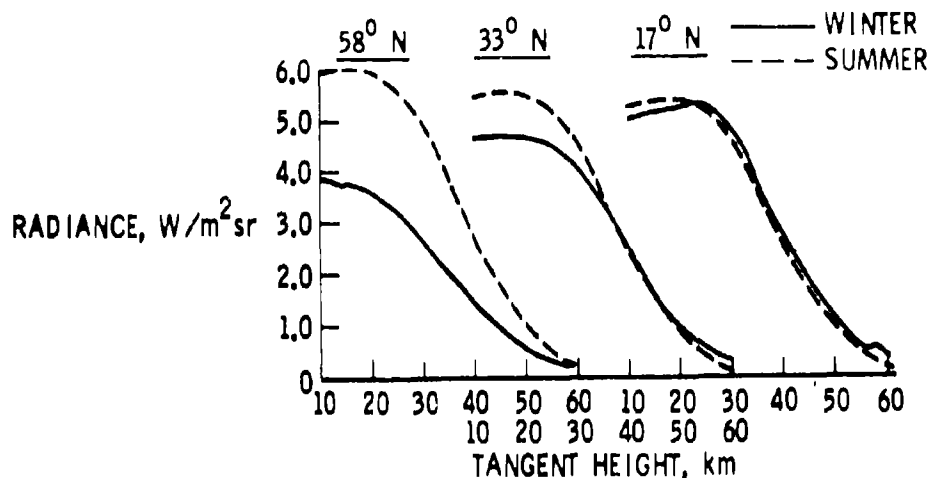
Scanner (Ref. 6), illustrating a version of the so-called "cold-cloud" problem in the 21-32 $\mu$  profile. The solid-line water-vapor profile marked 13° N was obtained from an area known to be clear, while that marked 57° N came from an area known to have high clouds. The radiance observed in the cloudy area is seen to be roughly one-half that in the clear areas. The two dashed-line curves are CO<sub>2</sub> profiles from the same areas and show little or none of the effect and indicate the radiance levels are governed only by the temperature structure of the atmosphere. The effects that the temperature structure has on the horizon are illustrated on Fig. 2 where measured radiance profiles for both winter and summer conditions (Ref. 7) are shown for three latitudes. The dashed profiles are for summer conditions, and a trend of increasing radiance with latitude is noted. The solid profiles were obtained on the winter flight and show a more prominent and opposite trend with latitude. The agreement between the winter and summer profiles at 17° N falls within the experimental measurement accuracy, so no seasonal effects are evident. Thus it is seen that a horizon sensor operating in the 15 $\mu$  CO<sub>2</sub> band is effectively decoupled from cloud problems, however, it would probably be sensitive to high-altitude atmospheric variations which occur as a function of season and the position on the earth.

#### STUDY APPROACH

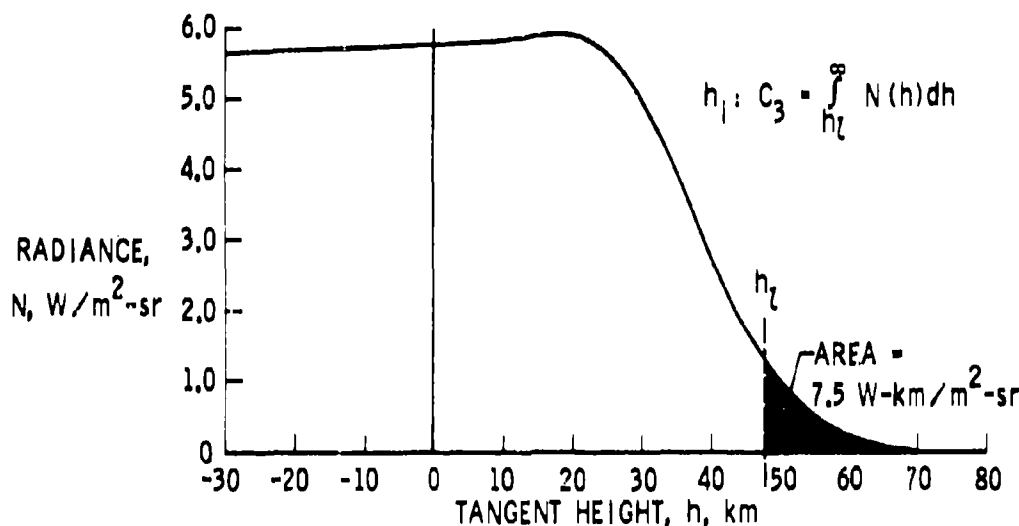
(U) In order to evaluate the sensitivity of horizon sensors to the geographical and seasonal

changes which occur, it was found necessary to develop an analytical means of synthesizing radiance profiles from available atmospheric information by solving the radiative transfer problem. This was due to the lack of experimentally determined profiles having the required temporal and geographic coverage. Honeywell, Inc., under contract to Langley, developed a model (Ref. 10) which included such factors as gas mixing ratio, atmospheric transmittance, refraction, Doppler broadening, and the absence of thermodynamic equilibrium at higher altitudes. While it was recognized that other analytical methods existed (Refs. 14 and 15), no single one appeared to incorporate all of the factors deemed important. Profiles obtained from the developed analytical model compared very favorably with experimental Project Scanner results, giving added confidence to the ensuing analysis of atmospheric effects on horizon sensors.

(U) A second problem then arose, namely, how can we get the computer to "see" or "think" like a horizon sensor in order to determine the sensitivity to radiance profile changes? Honeywell developed what we call the "locator" concept for this purpose (Ref. 12). A "locator" defines, in a simple way, how an idealized horizon sensor operates to detect (or locate) an altitude which is characteristic of a radiance profile. This concept is illustrated on Fig. 3. A horizon sensor having a wide field of view would, in effect, integrate the energy under the profile as it is scanned down across the horizon. The located horizon altitude ( $h_l$ ) would be as shown



(U) Fig. 2. Seasonal Variations of Measured CO<sub>2</sub> Radiance Profiles (Project Scanner)



(U) Fig. 3. Located Horizon for a Threshold Value on the Integral of Radiance

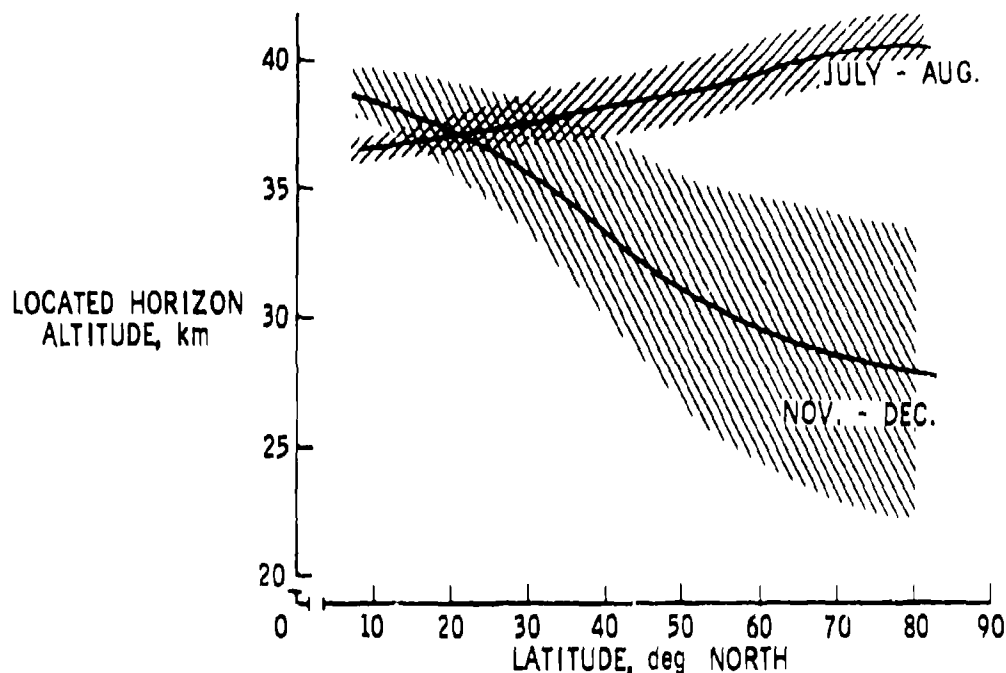
for the specified threshold on the value of the integral. A number of other "locators" have been devised, some using radiance level, others tending to normalize the profiles. The important thing is that any profile, defined by season, latitude, time-of-day, and so forth, can be reduced to a single number, an indicated horizon altitude, for a given locator. In this way, variations due to the perturbing functions can be conveniently analysed.

(U) To examine the effects of seasonal and geographical changes, a body of atmospheric data from radiosondes and MRN rocket flights was compiled (Ref. 9), and used to synthesize radiance profiles for a number of synoptic situations (Refs. 16-18) covering various seasons and several years, for the geographical area which

can be generally described as the northern hemisphere near North America. A number of locators were identified and applied to this body of data, and the variations of indicated altitudes were examined. For practical horizon sensor use, it was deemed best to view any systematic variations as a function of latitude for a specified season. This then constitutes an oblateness-type correction which could be rather easily implemented.

#### STUDY RESULTS

(U) The method of analysis just described was used to examine the performance of a sensor which located the horizon at the altitude where a 3-watts-meter<sup>-2</sup>-sr<sup>-1</sup> radiance level exists. The



(U) Fig. 4. Variation of the  $3 \text{ m-m}^2\text{-sr}^{-1}$  Altitude Point With Latitude for Two Seasons (Data Based on 3 Years)

results are shown on Fig. 4. The ordinate is altitude in km, the abscissa is north latitude in degrees, and data for July and for late November are presented to show the seasonal change. The solid lines represent the mean for all data for the date, and the shaded zone represents the  $1\sigma$  variation about the mean. The upper curve for the July data shows the summer trend and is seen to be relatively flat, but shows the tendency toward a higher altitude (greater radiance) at the upper latitudes seen earlier in the Scanner curves in Fig. 2. The winter data show a much more pronounced trend (approx 11 km deviation of the mean) which is accompanied by a much wider random variation,  $\pm 5.5$  km at the higher latitudes. It is interesting to note, however, that the trend lines appear to pivot about a latitude near  $20^\circ$  which might explain the close agreement between the Project Scanner winter and summer profiles at  $17^\circ$  N latitude. The data of Fig. 4 cover the 3-year span 1964 to 1967, and the variance for any single year is considerably reduced from that shown here. In fact, the November data for 1965 and 1966 tended to agree, and averaged together provided a systematic variation (or trend) of 12 km and a maximum  $1\sigma$  value of approximately 4 km, while 1964 was a bland year having a systematic variation of 5.5 km with a  $1\sigma$  value of little more than 1.0 km. We are not yet convinced that a deterministic biennial cycle exists which would allow some reduction in the random  $1\sigma$  variance. When it is realized that 1.0 km at the horizon corresponds to  $0.02^\circ$  displacement for a

single horizon sensor beam from 300 n. mi. altitude, this locator is not too promising. If the locator is modified to normalize the profile using peak radiance levels, considerable improvement is obtained. For example, using the half-radiance level, or "half-power point," locator moves the located altitude to approximately 40 km, with an indicated systematic variation of 6 km and a  $1\sigma$  variance of 1.5 km, resulting in an improvement of about a factor of 3.

(U) The data just discussed, while interesting from a synoptic view as to what is happening, do not represent what is felt to be a realistic horizon sensor.

(U) The characteristics of the single beam of a more practical sensor are shown on Fig. 5. An edge tracker dithering at 2 Hz is postulated, utilizing a thermistor bolometer in a 2-inch-diameter optical system. This device with a  $1^\circ$  vertical by  $4^\circ$  horizontal field of view integrates the energy in the horizon profile as it sweeps onto the earth, therefore operating on an integral-of-radiance locator. The radiance sensitivity of the device corresponds to slightly less than 2 km indicated altitude at the horizon. Addition of a sample-and-hold circuit and comparator will allow use of a normalized integral locator.



EDGE TRACKER -  $5^{\circ} \times 2\text{Hz}$  VERTICAL DITHER

DETECTOR : THERMISTOR BOLOMETER

OPTICS : 2 INCHES DIAMETER

FIELD OF VIEW :  $1^{\circ} \times 4^{\circ}$

RADIOMETRIC EFFICIENCY : 18%

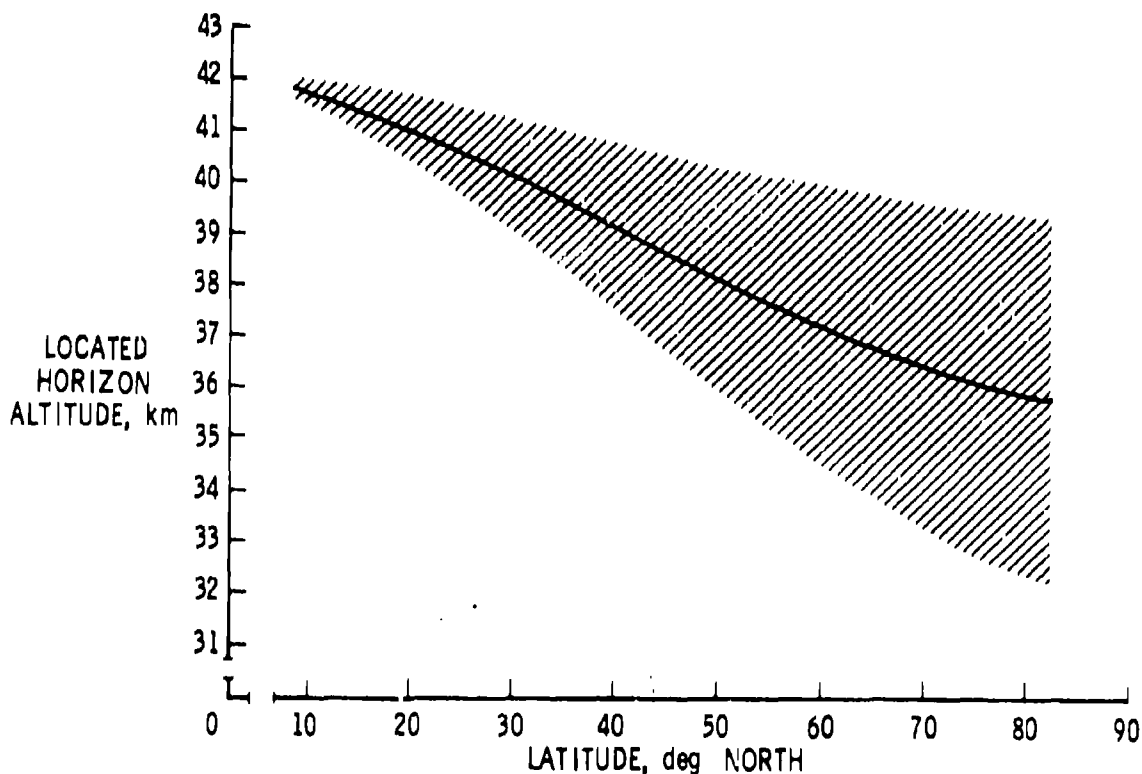
DETECTION LOGIC : 1. THRESHOLD OF INTEGRATED  
RADIANCE

2. THRESHOLD OF NORMALIZED  
INTEGRATED RADIANCE

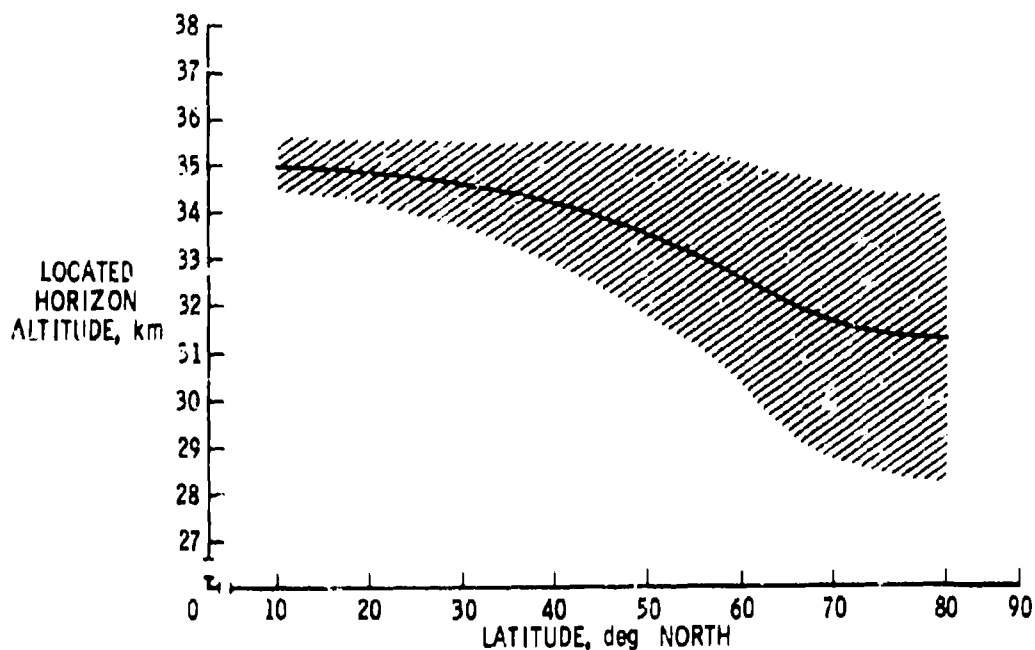
NER :  $\approx 0.025 \text{ W/m}^2 \text{sr}$

HORIZON SENSITIVITY :  $\approx 2\text{km}$ ,  $\text{S/N} = 10$

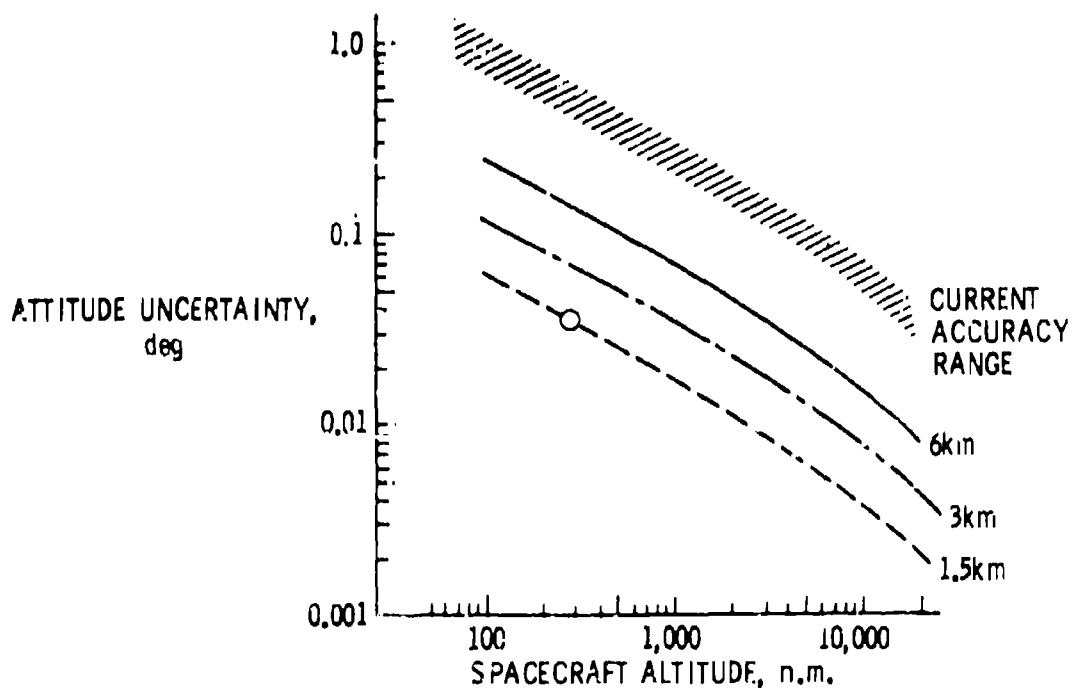
(U) Fig. 5. Single-Beam Horizon Sensor Design Characteristics



(U) Fig. 6. Variations of the Located Altitude for a  $20\text{-Watt-km-Meter}^{-2}\text{-sr}^{-1}$  Threshold on Integrated Radiance With Latitude for November



(U) Fig. 7. Variations of the Located Altitude for a Normalized Integral of Radiance With Latitude for November (Data Based on 3 Years)



(U) Fig. 8. Single-Beam Horizon Sensor Angular Uncertainty Caused by Horizon Radiance Variations

(U) Representative performance for such a sensor as described, during the November season (3-year average), as a simple threshold of integrated radiance device is shown on Fig. 6. Note that the average trend with latitude is reduced to 6 km with a maximum 1σ uncertainty about the mean of approximately 3.5 km. The change in performance due to the approach used in "normalizing" the locator is shown on Fig. 7. The trend of the average was reduced to about 4 km, however, the random variation was reduced only to about 3 km, indicating the major advantage to be suppression of the systematic effects, with little improvement in random scatter. These data should only be considered as illustrative, and do not represent an attempt to optimize the normalization technique.

(U) The significance of the results just discussed is illustrated on Fig. 8. The ordinate of this plot is the attitude uncertainty in degrees, and the abscissa shows the spacecraft altitude in nautical miles. The curves show the effects of several values of horizon variance in kilometers on the accuracy of a single-beam horizon sensor. The values of horizon variance are near those which were obtained as 1σ values in the earlier results. For reference purposes, the top zone represents the accuracy range reported by several users of horizon sensors. The line showing the angular uncertainty for a 3-km variation corresponds to the performance of the single-beam horizon sensor just presented, where correction has been made for latitude. If the attitude measurement were obtained by a two-beam horizon sensor, the effective uncertainty would roughly correspond to the 1.5 km value also plotted. For a spacecraft operating at 300 n. mi. altitude, it is seen that an angular accuracy of approximately 0.035° (1σ) is indicated.

(U) The results just presented are based on a study which utilized a model to synthesize radiance profiles from upper atmospheric data. There are indications that some further improvement in horizon sensor accuracy may be available if more sophisticated compensations are allowed, however, the question arises as to the validity of the synthesized data for purposes of improved accuracy. Project Scanner experimental data used to check the model were limited to approximately 1.5-2.0 km resolution. Further experimental data of improved radiometric accuracy, and wider coverage, would be necessary to verify, or replace, the model for purposes of improved accuracy.

#### CONCLUDING REMARKS

(U) The work done at the Langley Research Center on the variability of the earth's infrared horizon indicates that proper selection of spectral interval can minimize horizon sensor problems due to low-level atmospheric effects. The best choice of spectral interval was found to be the 14.0- to 16.3-micron band associated with CO<sub>2</sub> absorption in the atmosphere. This band effectively shields a sensor from cloud problems and variable sources of stray radiation. It

does make the sensor sensitive to relatively slowly varying temperature changes in the atmosphere above 20 km and, consequently, introduces variations due to seasonal and geographical effects. A study of these changes indicates that a deterministic effect with latitude exists which varies with season. Based on a study of atmospheric changes covering 3 years, a simply implemented, single-beam, horizon sensor in the CO<sub>2</sub> band can expect to experience about 3 km random variance of the horizon at higher latitudes. Use of a three- or four-beam horizon sensor of the type discussed, and making "oblateness type" corrections for the systematic horizon effects, should provide attitude determination accuracy to 0.05° (1σ) or better. While the results of the horizon variance study showed a possibility of further accuracy improvements, additional high-resolution experimental measurements of the horizon would be required to fully exploit the potential.

#### ACKNOWLEDGMENTS

(U) The authors gratefully acknowledge the work of R. E. Davis, of Langley Research Center, whose analyses provided much of the data presented, and A. Jalink, Jr., for verifying the horizon sensor design characteristics.

#### REFERENCES

1. Dodgen, J. A.; and Gurfman, H. J., Jr.: Summary of Horizon Definition Studies Being Undertaken by Langley Research Center. Proceedings of the First Symposium on Infrared Sensors for Spacecraft Guidance & Control, Barnes Eng. Co., c. 1962, pp. 233-239.
2. Dodgen, J. A.; McKee, T. B.; and Jalink, A., Jr.: NASA-LRC Program to Define Experimentally the Earth's IR Horizon. Proceedings of the Second Symposium on Infrared Sensors for Spacecraft Guidance & Control, Barnes Eng. Co., c. 1968, pp. 113-129.
3. Hrasaky, W. C.; and McKee, T. B.: Radiance of the Earth and Its Limb in the Middle Ultraviolet. NASA TN D-2355, July 1964.
4. McKee, T. B.; Whitman, R. I.; and Engle, C. D.: Radiometric Observations of the Earth's Horizon From Altitudes Between 300 and 600 Kilometers. NASA TN D-2328, December 1964.
5. Jalink, A., Jr.; Davis, R. E.; and Hinton, D. E.: Radiometric Measurements of the Earth's IR Horizon From the X-15 in Three Spectral Intervals. NASA TN D-4654, July 1968.
6. McKee, T. B.; Whitman, R. I.; and Davis, R. E.: Infrared Horizon Profiles for Summer Conditions From Project Scanner. NASA TN D-4741, August 1968.
7. Whitman, R. I.; McKee, T. B.; and Davis, R. E.: Infrared Horizon Profiles for Winter Conditions From Project Scanner. NASA TN D-4905, December 1968.

8. Kirk, R. J.; Watson, B. F.; Brooks, E. M., and Carpenter, R. O. B.: Infrared Horizon Definition - A State-of-the-Art Report. NASA CR-722, Honeywell, Inc., April 1967.
9. Peterson, E. E.; Schuetz, J.; Shenk, W. E.; and Tang, Wen: Derivation of a Meteorological Body of Data Covering the Northern Hemisphere in the Longitude Region Between  $60^{\circ}$  W and  $160^{\circ}$  W From March 1964 Through February 1965. NASA CR-723, Honeywell, Inc., April 1967.
10. Bates, J. C.; Hanson, D. S.; House, F. B.; Carpenter, R. O. B.; and Gille, J. C.: The Synthesis of  $15\mu$  Infrared Horizon Radiance Profiles From Meteorological Data Inputs. NASA CR-724, Honeywell, Inc., April 1967.
11. Thomas, J. R.; Jones, E. E.; Carpenter, R. O. B.; and Ohring, G.: The Analysis of  $15\mu$  Infrared Horizon Radiance Profile Variations Over a Range of Meteorological, Geographical, and Seasonal Conditions. NASA CR-725, Honeywell, Inc., April 1967.
12. Thomas, J. R.: Derivation and Statistical Comparison of Various Analytical Techniques Which Define the Location of Reference Horizons in the Earth's Horizon Radiance Profile. NASA CR-726, Honeywell, Inc., April 1, 1967.
13. McGee, R. A.: An Analytical Infrared Radiation Model of the Earth. Applied Optics, Vol. 1, No. 5, September 1962, pp. 649-653.
14. Hanel, R. A.; Andeen, W. R.; and Conrath, B. J.: The Infrared Horizon of the Planet Earth. J. of the Atmospheric Sciences, Vol. 20, No. 2, March 1963, pp. 73-86.
15. Wark, D. Q.; Alishouse, J.; and Yamamoto, G.: Calculations of the Earth's Spectral Radiance for Large Zenith Angles. U.S. Department of Commerce Weather Bureau Meteorological Satellite Laboratory Report No. 21, October 1965.
16. Honeywell, Inc.: Compilation of Atmospheric Profiles and Synthesized  $15\mu$  IR Horizon Radiance Profiles Covering the Northern Hemisphere in the Longitude Region Between  $60^{\circ}$  W and  $160^{\circ}$  W From March 1964 Through February 1965 - Part I. NASA CR-66184, October 1966.
17. Honeywell, Inc.: Compilation of Atmospheric Profiles and Synthesized  $15\mu$  IR Horizon Radiance Profiles Covering the Northern Hemisphere in the Longitude Region Between  $60^{\circ}$  W and  $160^{\circ}$  W From March 1964 Through February 1965 - Part II. NASA CR-66185, October 1966.
18. Bradfield, L. G.; and Nelson, G. D.: Located Horizon Variation Study - Final Report. NASA CR-66748, Honeywell, Inc., January 1969.

## INSTRUMENTATION FOR INFRARED HORIZON SENSING

Robert W. Astheimer  
Defense and Space Division  
Barnes Engineering Company  
Stamford, Connecticut

### ABSTRACT

The characteristics of the earth's horizon in various infrared spectral regions are presented in another paper. This paper will discuss the instrumentation necessary for sensing this radiation signature and processing it to produce an electrical output indicative of the angular location of the horizon.

Basically, all horizon sensing instruments are comprised of an optical system including any optical-mechanical scanning mechanisms, one or more IR detectors, and processing electronics. The most sensitive IR detectors are the cryogenically cooled photodetectors. However, these have been rarely used in horizon sensors because of the practical difficulties of cooling, and because instrument accuracy is generally limited by factors other than detector sensitivity. The detectors commonly used are the immersed thermistor bolometer and the thermopile, both of which are thermal detectors and do not require cooling.

Usually the information desired is the position of the local vertical, from which pitch and roll attitude can be derived. Therefore, it is not necessary to locate the actual ground horizon but rather any level in the atmosphere bearing a constant relation to the ground horizon. At low altitudes the structure of the horizon profile becomes of great importance and the instrument must contain logic to identify such an invariant point on the profile. This logic is called a "locator" and a variety of locator techniques have been studied and used. At high altitudes where the angular subtense of the entire atmosphere is less than the accuracy desired, the horizon profile becomes unimportant.

Horizon sensing instruments can be classified into three types: wide angle scanners, edge trackers, and radiance balancers. The relative advantages of each are discussed and typical instruments of each type described. The factors limiting accuracy and the results achieved in practice are discussed.

## I. INTRODUCTION

A number of methods have been developed for determining the attitude of a space vehicle. They all require some instrument for sensing the angular orientation of spacecraft coordinates with respect to some external reference such as the sun, the stars, the magnetic field of a planet, or an inertial platform which stores the orientation of some external coordinate system. For orbiting vehicles the local vertical or horizon of the planet is a useful reference and in this paper, I will discuss instrumentation for sensing this horizon from the thermal discontinuity between the planet and the essentially absolute zero space background. The horizon can obviously be detected in other spectral regions such as the visible during the daylight phase, but the infrared has proven to be the most useful since it is independent of phase, so I will restrict my remarks to this type. Our general problem then is to design hardware that will measure angles between spacecraft coordinates and the planetary horizon at several points. Neglecting planetary oblateness this amounts to sensing the position of the local vertical with respect to the spacecraft.

The major factors entering into the design of a horizon sensor are tabulated in Table 1.

Table 1

### A. SYSTEM REQUIREMENTS

1. Acquisition Capability
2. Accuracy
3. Linear Range
4. Response Time

### B. HORIZON CHARACTERISTICS

1. Angular Subtense (Altitude)
2. Radiance Variations
3. Horizon Profile

### C. SENSOR PARAMETERS

1. Detector Type
2. Detector Field of View
3. Aperture Requirements
4. Scanning or Tracking Mechanisms
5. Electronic Logic and Processing

First, we must consider the system requirements. This involves the type of information we require from the horizon sensor and the use to which it is to be put. The system must, at some

point, acquire the horizon. This may be accomplished by some other system such as an inertial reference, or a search mode may be necessary. Once the horizon is acquired, there are two possible modes of operation. The horizon sensor output may be used as an error indicator to control the spacecraft, in which case only a narrow proportional range around the null position is required. Alternately the sensor may be required to accurately read out the position of the local vertical independently of the spacecraft attitude, in which case a wide linear or proportional range is necessary.

The principal target parameters of interest are the angular subtense, the temperature and emissivity of the planetary surface, and in the case of a planet with an atmosphere, the limb profile. Finally, the sensor parameters are the design decisions which must be made to construct hardware to fulfill the system requirements. In the following sections some of these factors will be considered in more detail.

## II. CHARACTERISTICS OF THE INFRARED HORIZON

Fundamental to obtaining high accuracy are the characteristics of the infrared horizon. This is discussed in more detail in another paper but it is necessary at this point to indicate briefly how and why they affect the horizon sensor design and accuracy. The true or hard horizon of the earth can only rarely be seen from space, being obscured by clouds, haze, and atmospheric absorption. Therefore, the thermal horizon appears as a radiance gradient fading into the space background, which can subtend as much as  $2^\circ$  at low orbiting altitudes. This gradient has a different appearance and stability in various spectral regions. From experimental and theoretical studies of these profiles, stable characteristics have been found which permit identification of a point on the profile which is always a fixed altitude above the true horizon. A signal processing technique to detect such a point has been called a "locator." It has been shown that by spectral filtering to the 14.5 - 15.5 micron band, and use of a suitable locator, an accuracy of  $0.02^\circ$  can be achieved from low orbiting altitudes.

This problem is non-existent on the moon because of the absence of an atmosphere; however, another and equally disturbing phenomenon occurs, namely, the large variation in horizon radiance over the lunar disc. In practical sensors, a horizon "locator" is required to overcome this effect as well.

We shall first consider the simpler problem of identifying the so-called "hard" horizon where there is no gradient caused by the atmosphere. This is the situation with the moon, or the earth at long distances where the angular subtense of the atmosphere becomes negligibly small. The worst case is encountered on the moon where the surface temperature range of 120°K to 390°K will produce a radiance range of 50/1 in the 14-35 $\mu$  spectral region. A simple horizon location example for this case is sketched in Figure 1. Consider the field of view of an infrared detector scanning across the edge of the moon. The horizon will be identified as the angular position where the signal exceeds a pre-established threshold level which, in this example, is taken as 1/2 the full cold moon signal. If the field of view is infinitesimally small, the correct horizon position P will be identified regardless of the temperature of the horizon. However, if a wide field is used as shown, the horizon will be identified at A on a hot horizon and at B on a cold one, which will produce an error equal to almost half the field of view. Thus if the field were 2°, an error up to 1° could result depending upon the temperature of the lunar horizon.

An obvious means of reducing the error is to lower the threshold, since A and B approach P as the threshold approaches zero. This is called a minimum threshold locator technique. In practice, a limit is reached by the detector noise and the threshold must be placed well above the noise level. The threshold can be made as low as desired by increasing the optical collecting aperture to improve the signal/noise ratio.

Another technique is to adjust the threshold to a fixed percentage of the full edge radiance. This could be accomplished by using two detectors separated so that the field of one was completely filled below the horizon before the second reached the horizon. The signal developed by the first detector would then be used to set the threshold for the second. In scanning systems, the edge radiance could be stored on one scan and used to adjust the detection threshold for the following scan - the process continuously updating itself. For example, if the threshold were always adjusted to 50% of the edge radiance the horizon would always be identified at point B for any edge temperature. The true horizon position P can then be determined since the displacement B-P is a known constant, in this case half the field of view  $\theta$ . This technique is called a normalized threshold locator.

In practice other factors enter to distort the idealized situation shown in Figure 1, and must be considered. The sensitivity over the field of view will not be perfectly uniform because of

spatial variations in detector responsivity and optical aberrations. Also the frequency response of the detector and associated electronics will tend to round off the corners of the waveshape, which is a further limitation to use of a very low threshold.

When we consider the earth from low altitudes an added complexity develops; the infrared horizon no longer appears sharp but is diffuse because of the emission of the atmosphere. The plot of radiance seen from space vs. altitude above the earth's surface is called the horizon profile and is dependent upon the local atmospheric conditions, and the spectral region in which it is viewed. Figure 2 shows calculated profiles for the 8-12 $\mu$  atmospheric window. The profiles are computed for different atmospheric structures dependent upon latitude, season and weather conditions. Since clear air is fairly transparent in this region the horizon is determined by the surface, or clouds; - usually the latter because of the long tangent slant path through the atmosphere. The variations in cloud height with different weather conditions strongly affect the shape of the profiles and make this a poor spectral region if high accuracy is desired.

Figure 3 shows profiles for the same range of atmospheric conditions in the carbon dioxide absorption band between 14 and 16 $\mu$ . The surface and clouds are veiled in this region by the opaque CO<sub>2</sub> in the upper atmosphere and consequently the profiles are much more uniform. The differences are almost entirely caused by the change in stratospheric temperature with latitude. If these profiles are normalized with respect to the peak radiance, they almost perfectly overlay each other. This indicates that the normalized threshold locator technique described previously would identify a point a fixed distance above the true horizon, which is independent of weather conditions or latitude. For establishing attitude this is equivalent to sensing the true horizon.

Because of the stability of the horizon profile and the uniformity of radiance over the surface, the 14-16 $\mu$  band is the best spectral region for obtaining high accuracy attitude information with respect to the earth. By using suitable locator techniques, an accuracy of 0.6 km can be obtained which corresponds to 0.02° from a 300 km altitude. However, use of this band provides no advantage in attitude sensing against the moon, and the narrow spectral filtering only reduces the radiation signal. Because of the low temperature of the dark side of the moon, it is necessary to collect as much radiation as possible. Thus it is desirable to use a wide spectral bandwidth extending out to long wavelengths. The spectral band from 14 to 35 $\mu$  is a good compromise for

combined operation with the earth or the moon. The short out-off at  $14\mu$  reduces the dynamic range of lunar radiance from the hot to cold sides and also blocks the atmospheric window where cloud effects from the earth are most troublesome. The earth atmosphere is opaque in the  $14-35\mu$  region because of  $\text{CO}_2$  and water vapor absorption.

### III. DETECTOR CHARACTERISTICS

As has been mentioned, at least for the earth and moon, the range of apparent planetary temperatures to be sensed extends from  $120^\circ\text{K}$  to  $380^\circ\text{K}$ . Detectors sensitive to such thermal radiation must respond to long wavelengths from 8 to 40 microns. Photoconductive detectors highly sensitive in this region have been developed such as copper or zinc doped germanium, but these all must be cooled to temperatures in the neighborhood of liquid helium. Reliable cooling to these temperatures for long periods of time is difficult in space systems and the most suitable detectors are the thermal types, such as thermistor bolometers and thermopiles which do not require cooling. Of these the thermistor bolometer is the most sensitive and has found greatest use. They are usually immersed in a germanium lens for increased detectivity.

The thermal detectors operate by virtue of the heating effect when incident radiation is absorbed on the sensitive element. The very small temperature change resulting affects some physical parameter such as the resistance which can be read out electrically. An inherent difficulty in the use of such detectors is the identification or separation of the temperature change caused by the desired radiation from the very much larger ambient temperature variations. For example, in a typical horizon sensor the change in radiation, when the field of view scans from space onto the earth, increases the detector element temperature about  $0.001^\circ\text{C}$ . The sensor must be designed so that this temperature differential may be detected in spite of ambient temperature variations 10,000 to 100,000 times greater.

The most common way of separating the desired temperature change from unwanted internal effects is by optical-mechanical scanning or chopping. This modulates the external radiation signal at a relatively high frequency, and spurious signals produced by the slowly changing ambient temperature can be removed by capacitance coupling to the electronic amplifier. It is important to notice that such modulation must be done on the radiation signal before detection and not on the electrical output. Electronic chopping will modulate both external and internal signals and is of no value in this respect.

Thermal detectors which depend upon a resistance change for signal generation, such as thermistor or metal bolometers, are much more subject to internal temperature effects than thermocouple types. The reason for this is that in order to sense the resistance change a bias current must be used to convert it to a voltage signal. The desired signal thus appears as a very small change superimposed on the much larger bias voltage. Bridge arrangements of detector elements may be used to buck out the large bias voltage, but it is practically impossible to maintain the degree of balance necessary over a wide ambient temperature range. Optical modulation, of course, solves the problem since the d.c. bias voltage is filtered out, therefore these detectors are seldom used without optical modulation.

Thermocouple detectors do not require biasing and are thus free of this problem. The only voltage appearing is the thermoelectric EMF produced by the radiant heating of the junction, and this is not superimposed on a biasing voltage. Unmodulated optical systems are therefore feasible with thermocouple or thermopile detectors. However, even with these detectors, care must be taken in the design to eliminate spurious signals from internal temperature gradients and self-emission of optical parts. Also thermocouple detectors sufficiently rugged for space applications are much slower and less sensitive than thermistor detectors.

The elimination of optical chopping and scanning mechanisms is highly desirable for space missions where very long life and low power are necessary. The spurious signals or drifts, inherent in unmodulated systems, make them relatively less accurate than optically scanned systems. Therefore, thermopile detectors are most suitable for applications where low power and long life are paramount, and where restrictions in other performance characteristics can be tolerated.

### IV. BASIC SENSING TECHNIQUES

The detector must be employed in an optical arrangement to provide information from which the coordinates of the center of the planetary disc can be determined to the degree of accuracy desired. A number of systems have been developed for this purpose. These can all be shown to be versions of three general categories which we shall designate as follows:

- (1) Wide Angle Scanning Systems
- (2) Edge Tracking Systems
- (3) Radiometric Balance Systems



The detector field of view and scan pattern associated with these techniques are shown in Figure 4. In the conical scan, which is typical of the wide angle scanning systems, the instantaneous detector field is relatively small and is caused to scan through a large cone whose apex angle may be as much as  $180^\circ$ , although an apex angle between  $50^\circ$  to  $120^\circ$  is more usual. The detector signal generated will be an approximately rectangular waveshape repetitive at the scan frequency. This waveshape is usually limited in some fashion to eliminate amplitude dependence, and then position information is derived by a phase or pulse width comparison technique. Two sensors are used to generate pitch and roll attitude information.

Most horizon sensor systems flown to date have been of the conical scan type because it possesses a number of very significant advantages. It has excellent acquisition capability, attained without additional search modes because of the wide scan angle. The attitude information is derived from time characteristics of an amplitude limited waveshape and is therefore relatively insensitive to radiance variations over the surface of the planet. Another advantage is that because of the wide field scanned it is certain that some portion of the scan will leave the planet and view space. This provides an absolute zero radiance level against which any portion of any planet must give a positive contrast. Use can be made of this reference in setting limiting levels so as to prevent the system from confusing radiance discontinuities on the planetary surface, such as may be produced by the terminator or clouds, with the true horizon. This can be a serious problem with edge tracking systems. The primary disadvantage of the conical scan sensor is the need for high speed rotating elements which restrict life and cause lubrication complications in spaceborne applications.

The basic concept of the edge tracking system is shown in Figure 4-B. A small detector field of view is caused to lock onto the radiance discontinuity at the edge of the planetary disc. This is usually accomplished by oscillating the detector field through a small angle normal to the horizon edge and moving the entire sensor or the oscillating field until a balanced waveshape is obtained. Multiple sensor heads may be used, in which case at least three are necessary, or a single oscillating field may be caused to trace around the edge. In either case, the horizon position is determined by reading out the position of the center of the oscillating field with respect to spacecraft coordinates, i.e., angles  $\theta_1$ ,  $\theta_2$ ,  $\theta_3$ , and  $\theta_4$  in Figure 4-B.

For equivalent optics and detectors, this type of system will have a better signal-to-noise ratio than the wide angle scanning types because of narrower electronic bandwidth. It leads to a much more complicated system, however, because separate search and edge tracking movements must be provided on each sensing head along with precision position readouts.

A high price is paid for this narrow bandwidth and consequent greater sensitivity. Without the wide angle scan, the previously mentioned space reference is lost, and there is no convenient way for the system to sense whether the signal is from the true horizon or some other discontinuity such as a cloud edge or terminator which can be much greater than the horizon signal. Various devices such as auxiliary detectors may be employed to prevent locking on false edges, but they further complicate the system. The edge tracking type of system would appear best suited for application where spectral filtering to a narrow atmospheric absorption band such as the  $15\mu$   $\text{CO}_2$  band can eliminate radiance variations over the planetary disc. The increased detectivity of this type system would compensate for the large reduction in signal caused by the spectral filtering.

The former two systems employ optical modulation by mechanical means. It should be pointed out, however, that a stationary array of detectors could be used whose outputs are electronically sampled. For example, in a conical scan system, instead of mechanically causing a small detector field to scan over a wide circle, a stationary array of detector elements can be placed to view the same circle, and the array sequentially sampled electronically. Thermopile detectors are particularly well suited for this technique, and a system of this type has been developed.

The radiometric balance type sensor is a non-scanning system and operates by comparing the radiation received from opposite portions of the planet. Wide fields of view are necessary to achieve a proportional output. A possible arrangement of detector fields is shown in Figure 3C. Four wide angle stationary fields are employed designated a, b, c, and d; and attitude information is obtained by the difference in radiant power received from opposite fields, i.e.,  $P_c - P_a$  and  $P_b - P_d$ . This obviously only gives accurate results if the planet is uniformly radiant, and therefore this system is primarily suited for use with planets of uniform radiance such as Venus or where only coarse pointing information is necessary.

The great virtue of this system is its extreme simplicity and consequent high reliability. By using thermopile detectors no moving parts are necessary and very long life can be achieved. Non-uniform radiance effects can sometimes be minimized by spectral filtering.

In the remainder of this paper, several examples of operational sensors employing these principles are described.

#### V. WIDE ANGLE SCANNING SYSTEMS

The conical scanning horizon sensor has been the most commonly used system of this type. A cross sectional view of a typical sensor of this type is shown in Figure 5. The conical scan is produced by a germanium prism mounted on a hollow barrel which is driven through gearing by a small motor. An internal phase reference signal is developed by a semicircular iron vane on the hollow barrel and a stationary magnetic pick-up. The detector is a germanium immersed thermistor detector. The sensor is filled with dry nitrogen and hermetically sealed to prevent evaporation of lubricants. A germanium front window is used with a multilayer interference filter to define the spectral band. Overall dimensions are approximately 3-1/2" diameter and 7" long.

A typical scan geometry is shown in Figure 6. Two sensor heads are usually used. In this configuration, pitch attitude is determined by phase comparison between the detector signal which is of a rectangular waveshape, and an internal square wave reference generated by a magnetic pick-up. Roll attitude is obtained by pulse width comparison between the detector signals from the two sensor heads. An alternate arrangement is to direct one of the sensor heads along the direction of travel in which case, the same phase detection processing is used for both pitch and roll.

Figure 7 shows a typical wave shape produced by the conical scan. The earth pulse amplitude is irregular because of radiance variations over the surface and is cleaned up by clipping. The sun may also appear in the scan and must be rejected, which can be done by several methods such as pulse width or amplitude rejection, inhibiting the output when the threshold crossing rate is doubled, or the use of an auxiliary short wavelength detector for identifying and rejecting the sun pulse.

Figure 8 shows the component of a conical scan horizon sensing system manufactured by Barnes Engineering Company for use on the Agena spacecraft. It consists of two sensor heads and an electronic processing box mounted on a common

base structure. The other unit on the base is an inertial reference package.

If a satellite is spin stabilized, the motion of the vehicle itself can be used to generate a wide angle scan, and the internal scanning mechanism can be eliminated. In this case the sensor becomes very simple, consisting only of a lens, detector and processing electronics. As its field of view crosses the horizon a pulse is generated, thus such sensors are usually called horizon crossing indicators. They are used to measure spin rate, inclination of the spin axis, or to trigger other instruments when they arrive at the proper position.

Figure 9 is a photograph of a horizon crossing indicator used on the INTELSAT and TACSAT vehicles. The sensor is about 2" x 2" x 4" in overall dimensions.

#### VI. EDGE TRACKING SENSOR

The horizon sensing system used with the Orbiting Geophysical Observatory (ProjectOGO) is a good example of an edge tracking system. A cross-sectional view of the basic sensor head is shown in Figure 10. A germanium immersed thermistor bolometer at the focal point of a fixed telescope views the earth by a reflection from a mirror mounted on the rotor of an electro-magnetic actuator called a Positor. This is shown in Figure 11 and is essentially a permanent magnet type torquer with a set of auxiliary coils excited at several kilocycles to accurately read out the rotor position in a manner similar to a resolver. It permits the mirror to be positioned at any point over a 45° angle and also superimposes a small rapid sinusoidal oscillation or "dither" at a frequency of 30 cps and a peak to peak amplitude of 3". The rotor is mounted to the frame by a pair of flexure pivots to eliminate lubrication and wear problems. The telescope aperture is 2 cm and the instantaneous field of view of the detector is 1° x 1° which can be positioned over a 90° angle by the Positor.

The sensor has two modes - search and track. In the search mode the instantaneous field of the telescope is slowly scanned over a 90° arc. When the horizon is reached a 30 cps signal will be generated on the detector by the small 30 cps dither oscillation superimposed on the Positor mirror. The position of the horizon within the limits of the dither oscillation amplitude is indicated by the 2nd, harmonic content of the detector signal, which goes to zero when the horizon is centered within the dither oscillation. The Positor mirror is servoed by adjusting its average angle so that the 2nd harmonic vanishes. The angle to the horizon is then read out from

the average Positor-mirror position by the read-out windings.

The complete system is comprised of four such sensor heads oriented  $90^\circ$  apart. These measure the angles from a reference axis to four points equally spaced around the horizon from which the attitude of the reference axis with respect to the earth is determined. Actually only three heads are required, the fourth giving redundancy in case of a failure. Also if the sun appears within the field of view of any of the four sensor heads, that head is removed from the computation without any loss of performance. Pairs of heads are packaged together in a single casting, the entire system consisting of two such dual tracker head castings and an electronic package. Its total weight is 13.2 lbs. and it consumes 8.5 watts of power (average).

The basic system has been extended and applied by TRW Corporation to other spacecraft. In one version for synchronous altitude operation, the Positor dither motion is increased such that the sensor scans completely across the earth. In this mode the system is no longer an edge tracker but becomes a wide angle scanner.

Another ingenious edge tracking system has been developed by Quantic Industries. In this system the tracking mirror is mounted on crossed thermostated bimetallic springs. The arrangement allows the mirror to rotate about the crossover of the bimetal springs as if it were mounted on a shaft with bearings. Mirror position is controlled by heating one or the other of the bimetallic springs. The mirror position is read out optically. The horizon is sensed by an array of three thermopile detectors. Such detectors are capable of DC radiometric response as mentioned previously and, therefore, no dither motion need be superimposed on the tracking mirror.

## VII. RADIOMETRIC BALANCE SENSORS

Because of their basic inaccuracy as discussed previously, such systems have found little application although several experimental systems have been constructed. A unique system of this type has been used on the Micrometeoroid Measurement Capsule of Project Pegasus. This is an unstabilized spacecraft which very slowly tumbles in a random manner and the problem was to read out its attitude with respect to the earth upon ground interrogation.

The attitude readout system employed consists of six identical sensor heads, each having two narrow fields of view pointing in opposite directions along the same optic axis. The fields of view are  $2^\circ \times 2^\circ$ . On the space vehicle the

sensor heads are placed in such a manner that their optical axis are normal to the surfaces of an imaginary dodecahedron encompassing the vehicle as shown in Figure 12. This produces an angular separation between fields of  $63^\circ 26'$ .

The presence or absence of earth signal within the twelve fields of view is used to establish the orientation of the vehicle relative to the earth. The system is only suitable for use at lower altitudes such that at least one sensor field will always view the earth. At an altitude of 625 km ( $130^\circ$  subtense angle) a single interrogation will give an attitude readout accuracy of  $\pm 10^\circ$  about each axis. By successive interrogations, the vehicle's tumbling motion can be determined and the accuracy improved to about  $\pm 1^\circ$ .

A photograph of one of the six sensor heads is shown in Figure 13. Two inch diameter germanium objective lenses are mounted at opposite ends of an optical tube focusing radiation onto a pair of thermopile detectors at the center of the tube. The thermopiles are connected in series opposition so that a positive, negative, or zero signal will result depending upon whether the earth is seen in one field, the other, or neither.

The long life capability of this type of system has been amply demonstrated on this program since one of these spacecraft is still in orbit and the earth altitude sensing system working after about 4 years.

In conclusion, it may be stated that infrared horizon sensors have and are being effectively used on a wide variety of earth orbiting space missions and it is expected that they will find additional use in the future on orbiting missions to the moon and other planets.

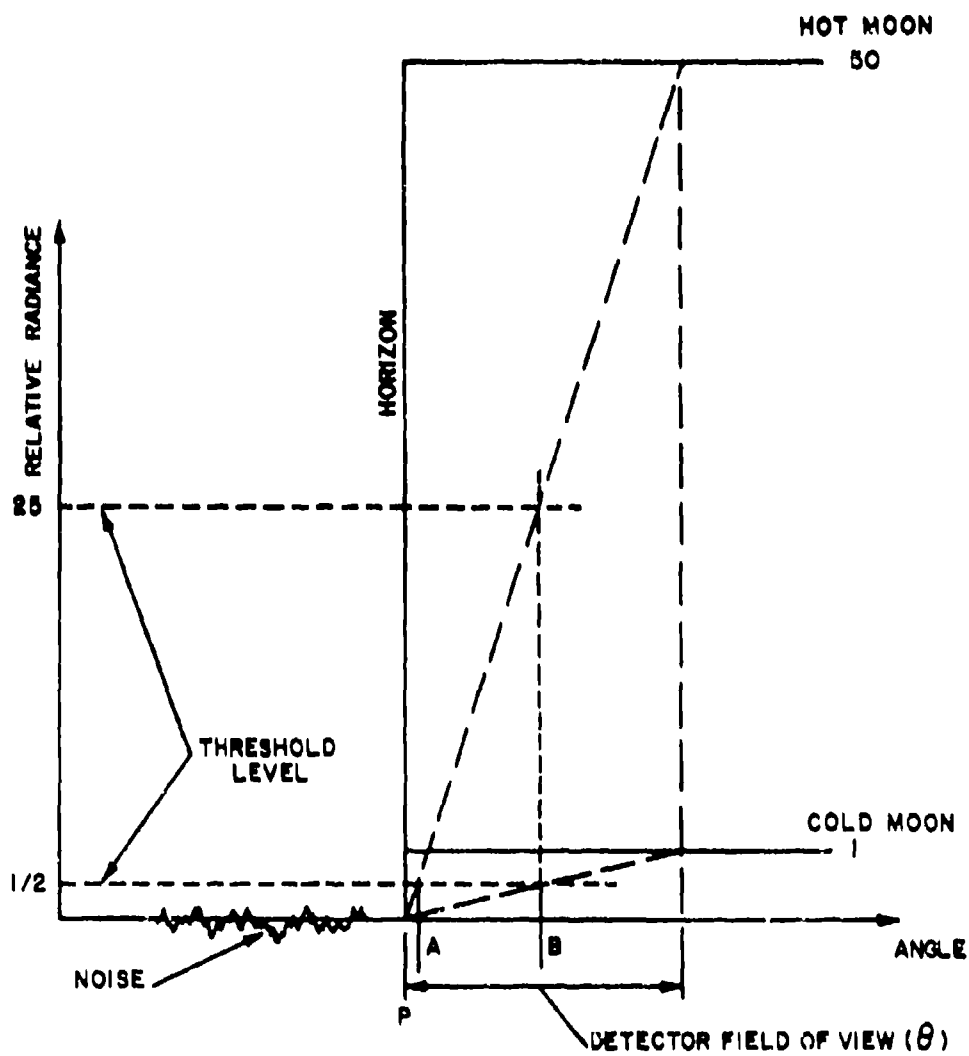


Figure 1. ERRORS CAUSED BY THRESHOLD LEVEL

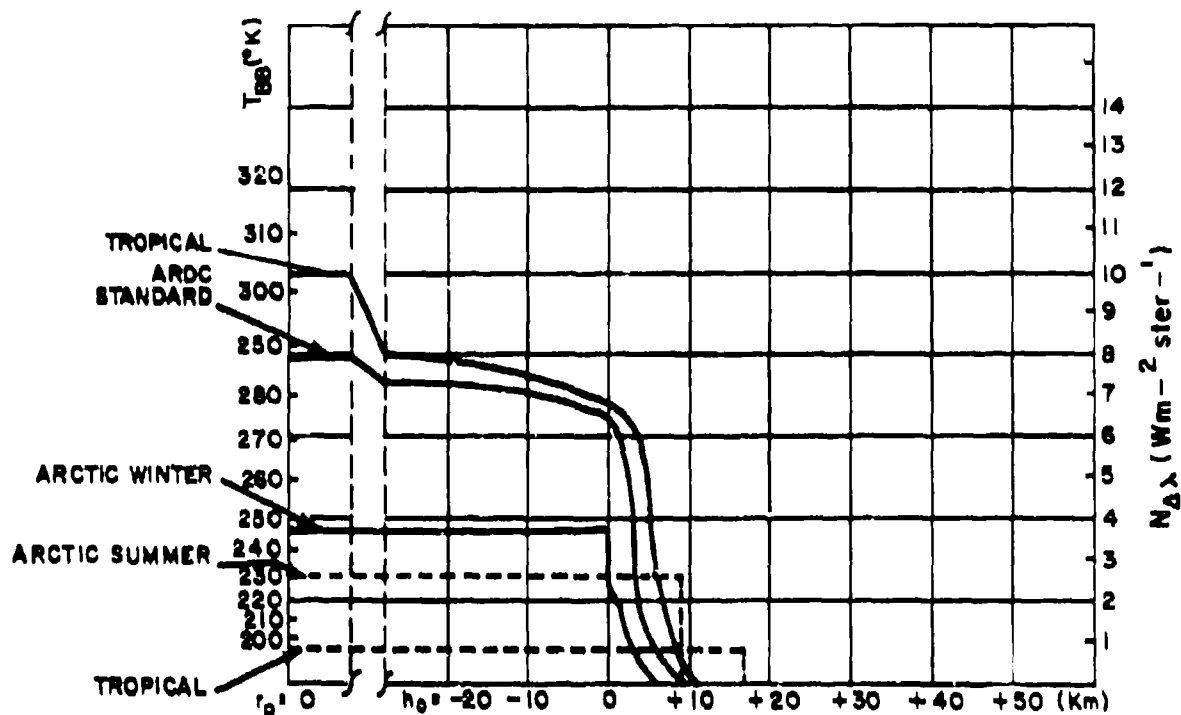


Figure 2. HORIZON PROFILES IN THE 8-12 $\mu$  SPECTRAL BAND

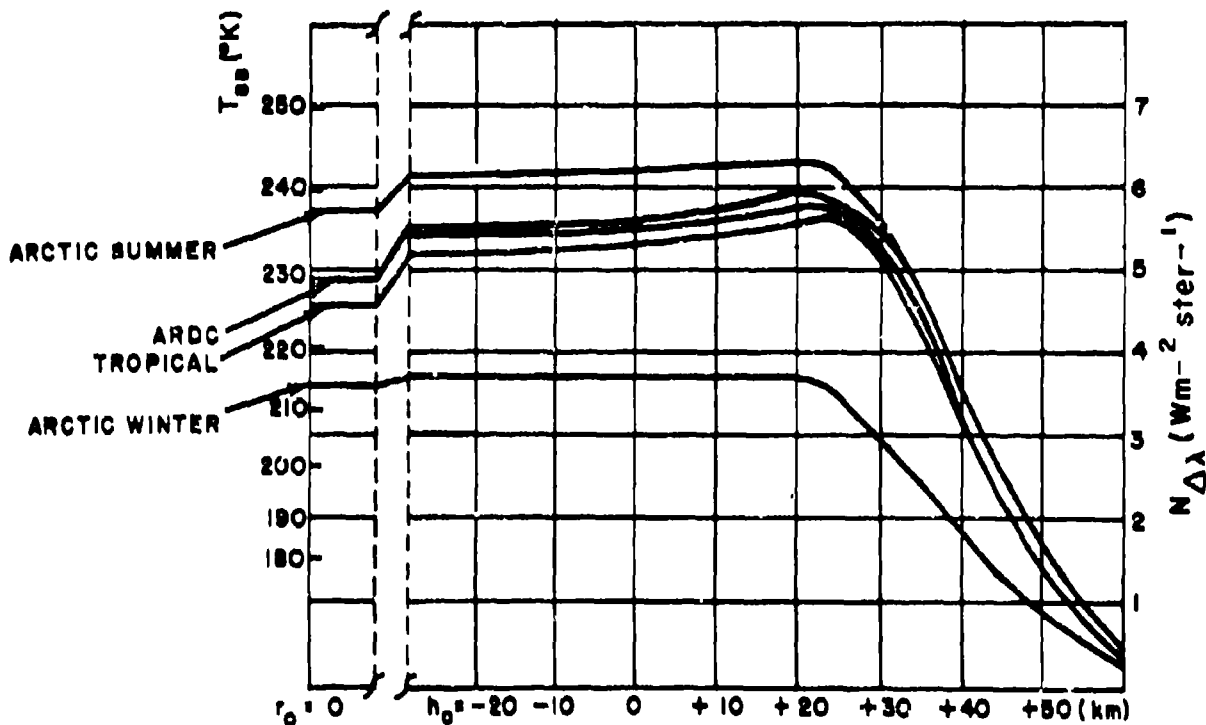


Figure 3. HORIZON PROFILES IN THE 14-16 $\mu$  SPECTRAL BAND

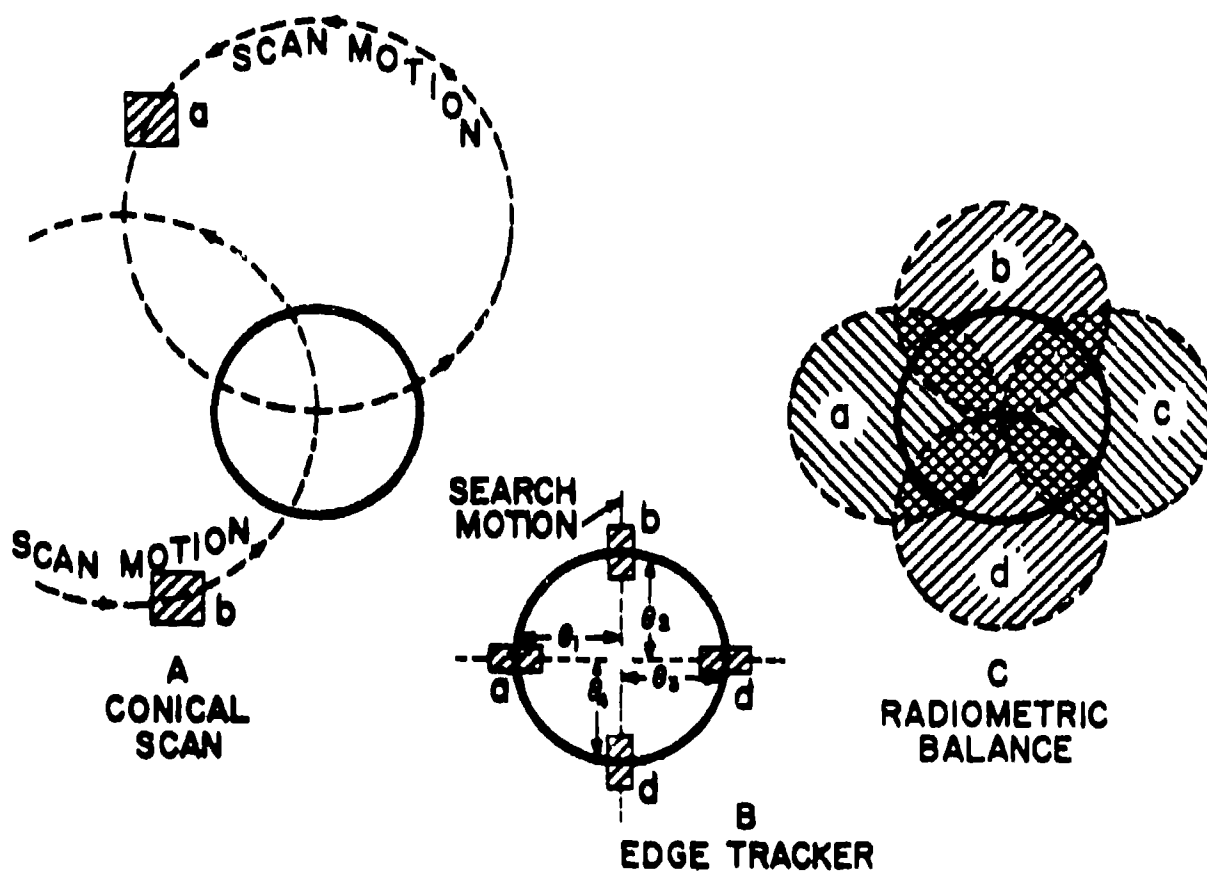


Figure 4. BASIC SENSING TECHNIQUES

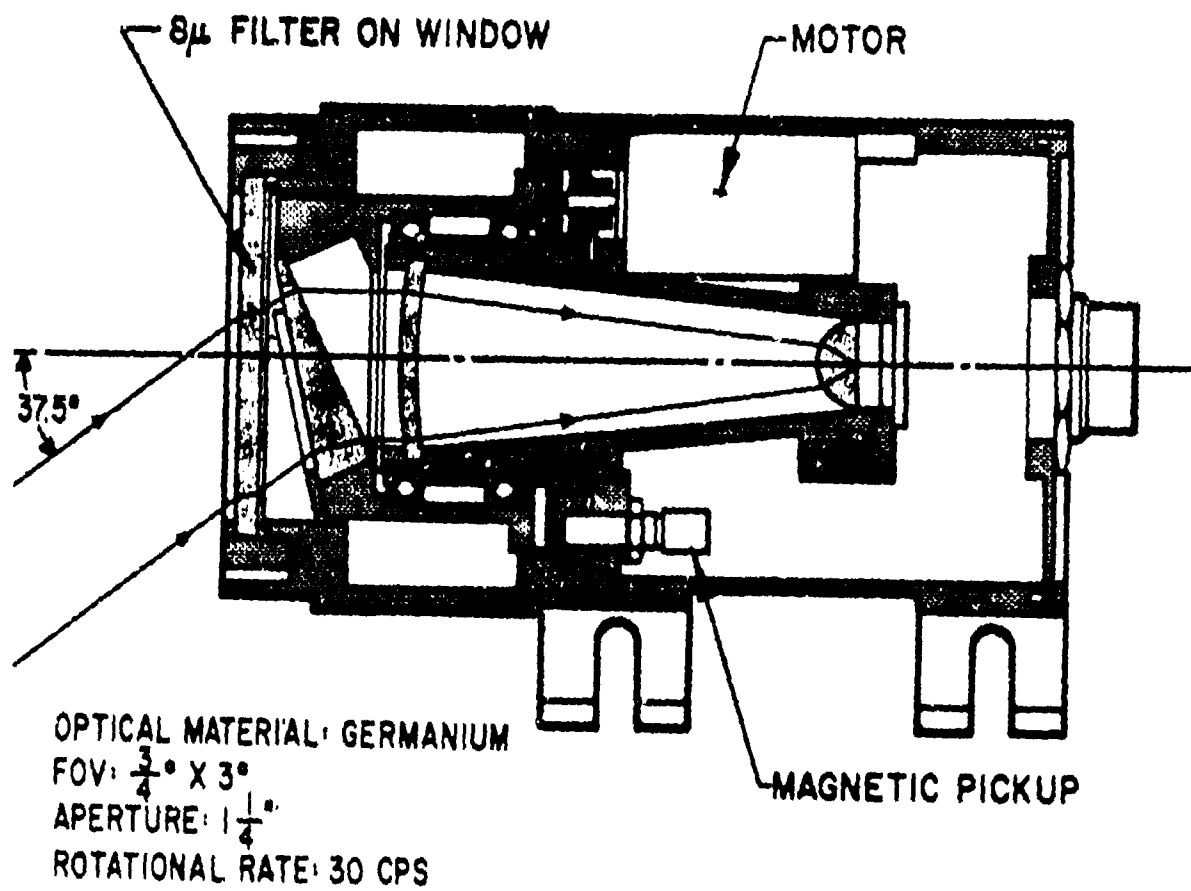


Figure 5. TYPICAL CONICAL SCANNER

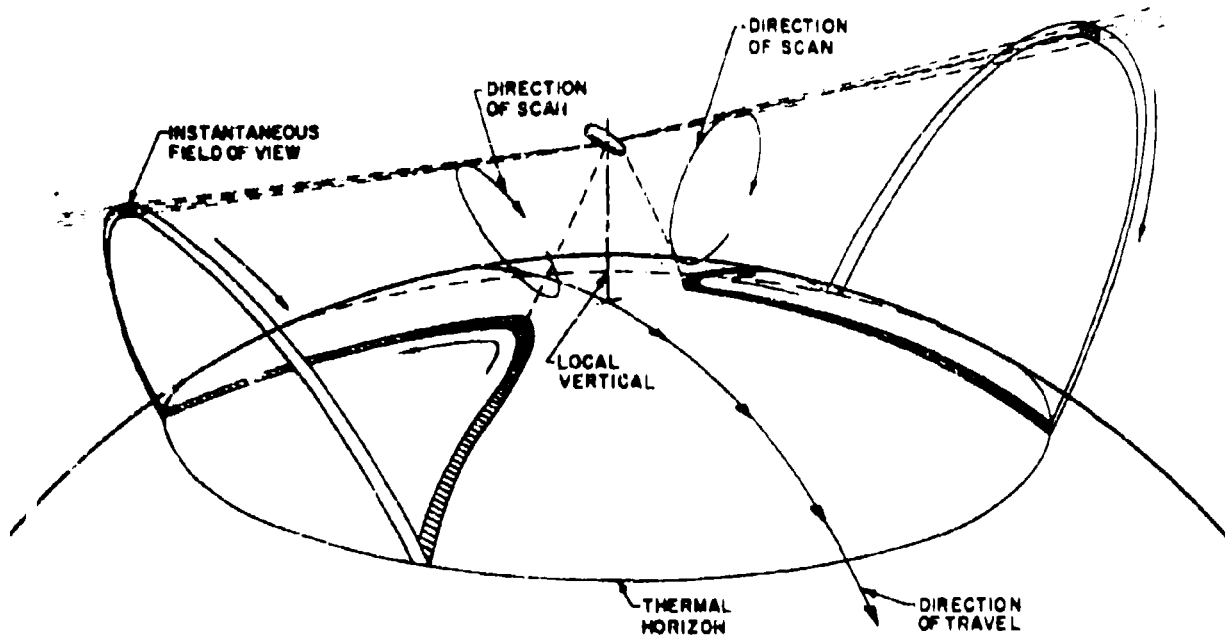
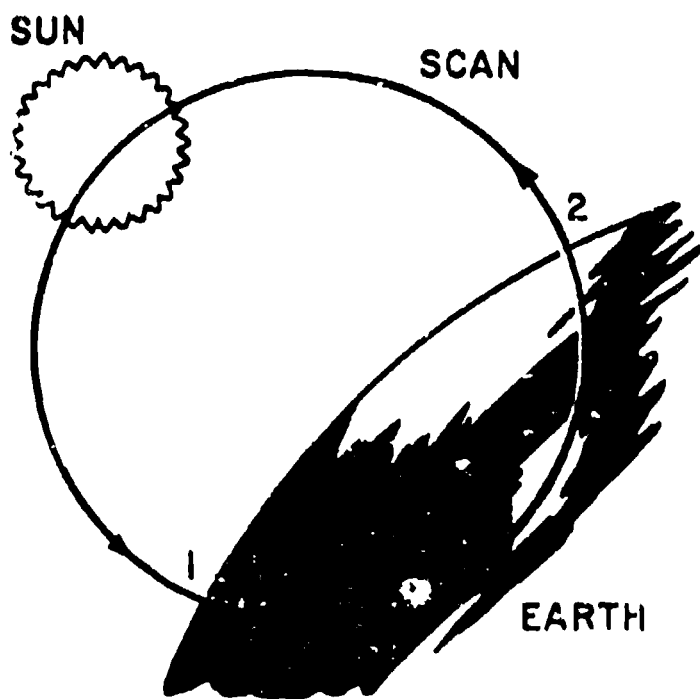
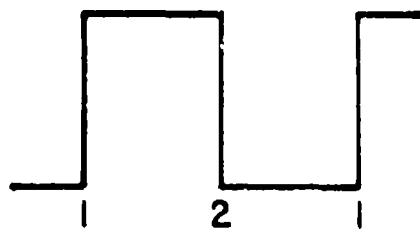


Figure 6. CONICAL SCAN GEOMETRY



A - RISE / FALL TIME  
B - CONTRAST  
C - SUN

IDEAL:



ACTUAL:

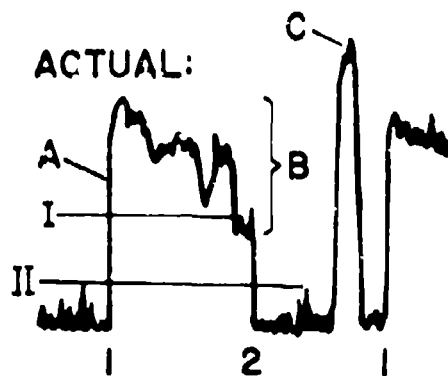


Figure 7. CONICAL SCAN WAVESHAPES



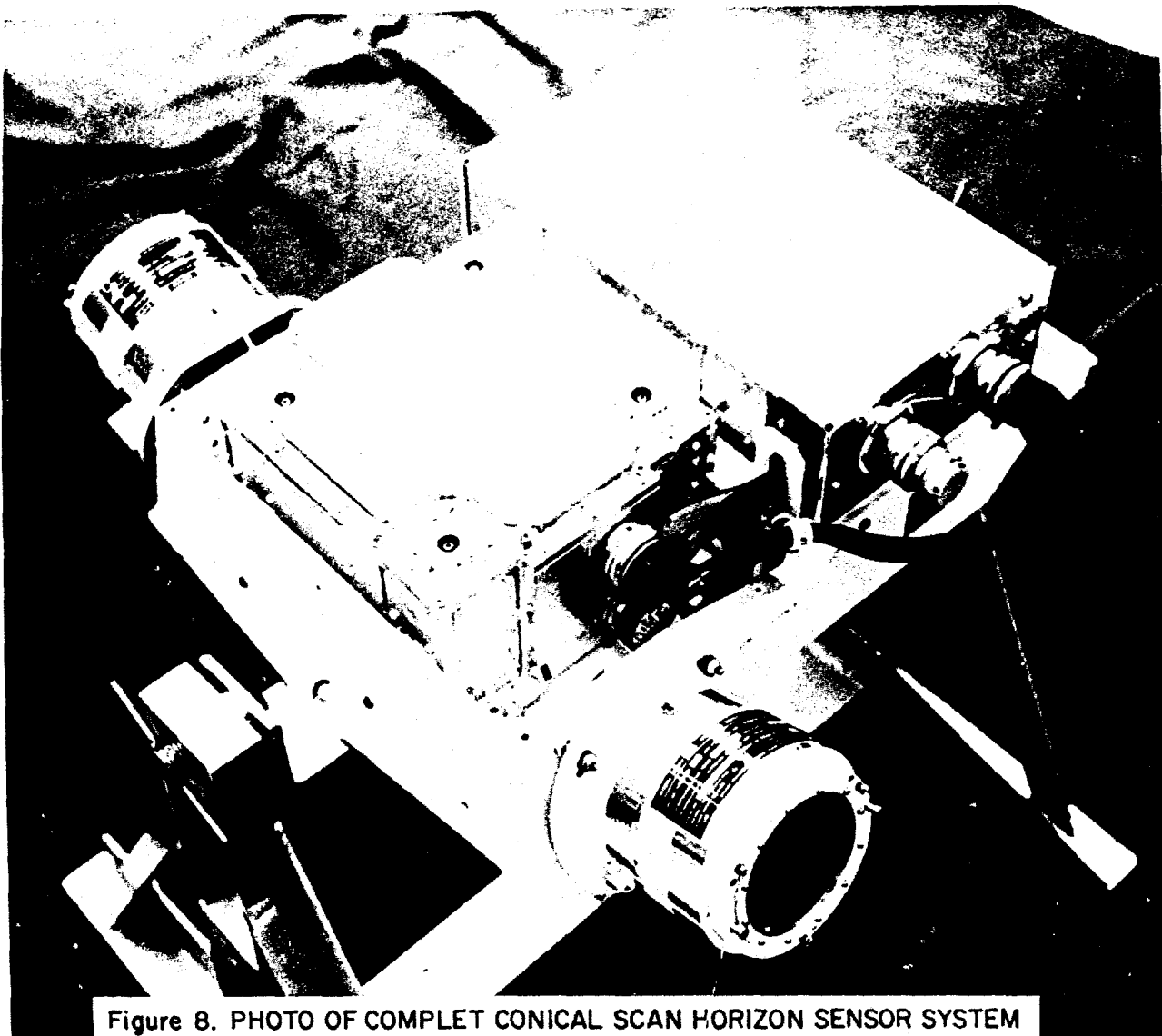


Figure 8. PHOTO OF COMPLET CONICAL SCAN HORIZON SENSOR SYSTEM

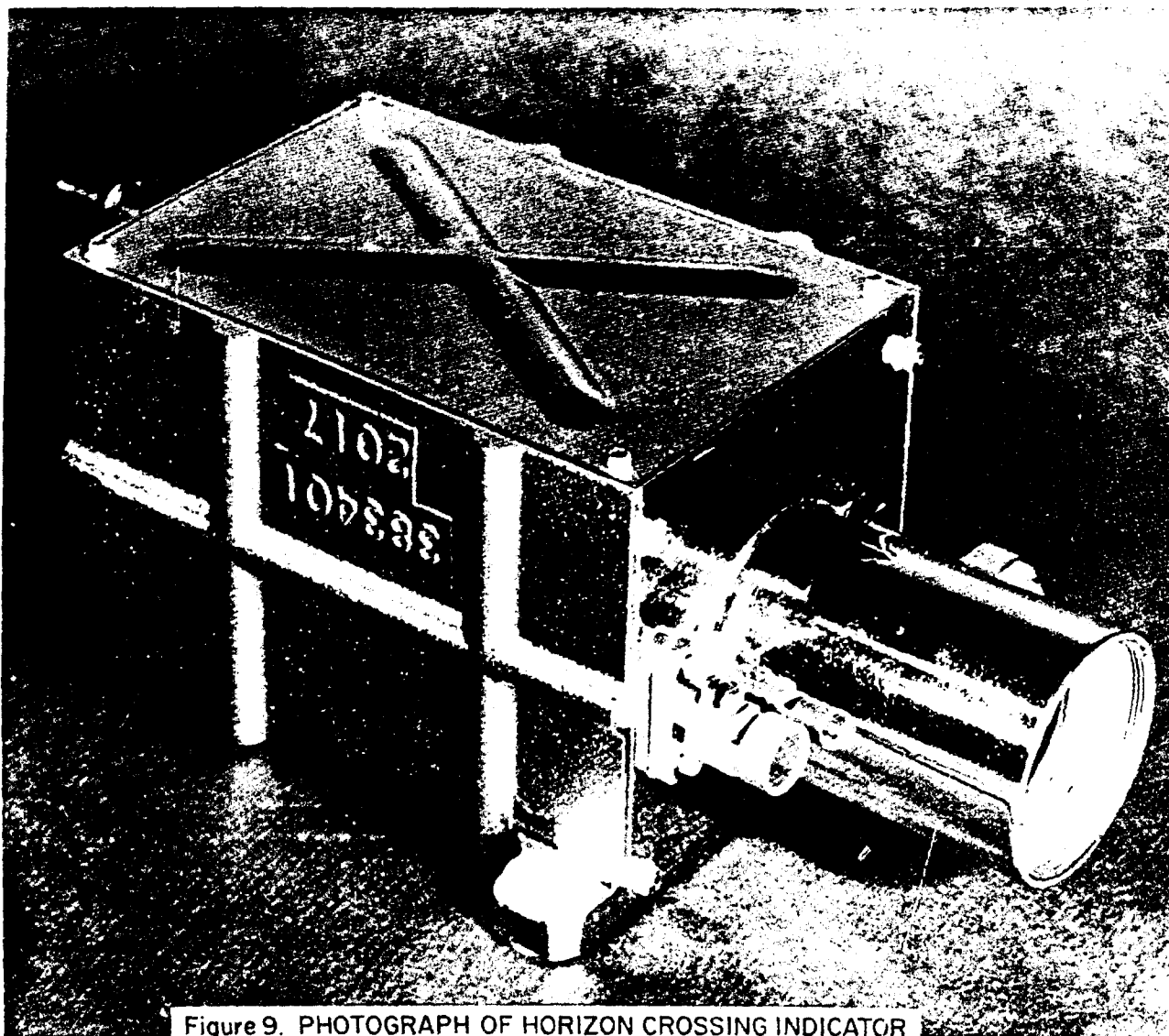


Figure 9. PHOTOGRAPH OF HORIZON CROSSING INDICATOR

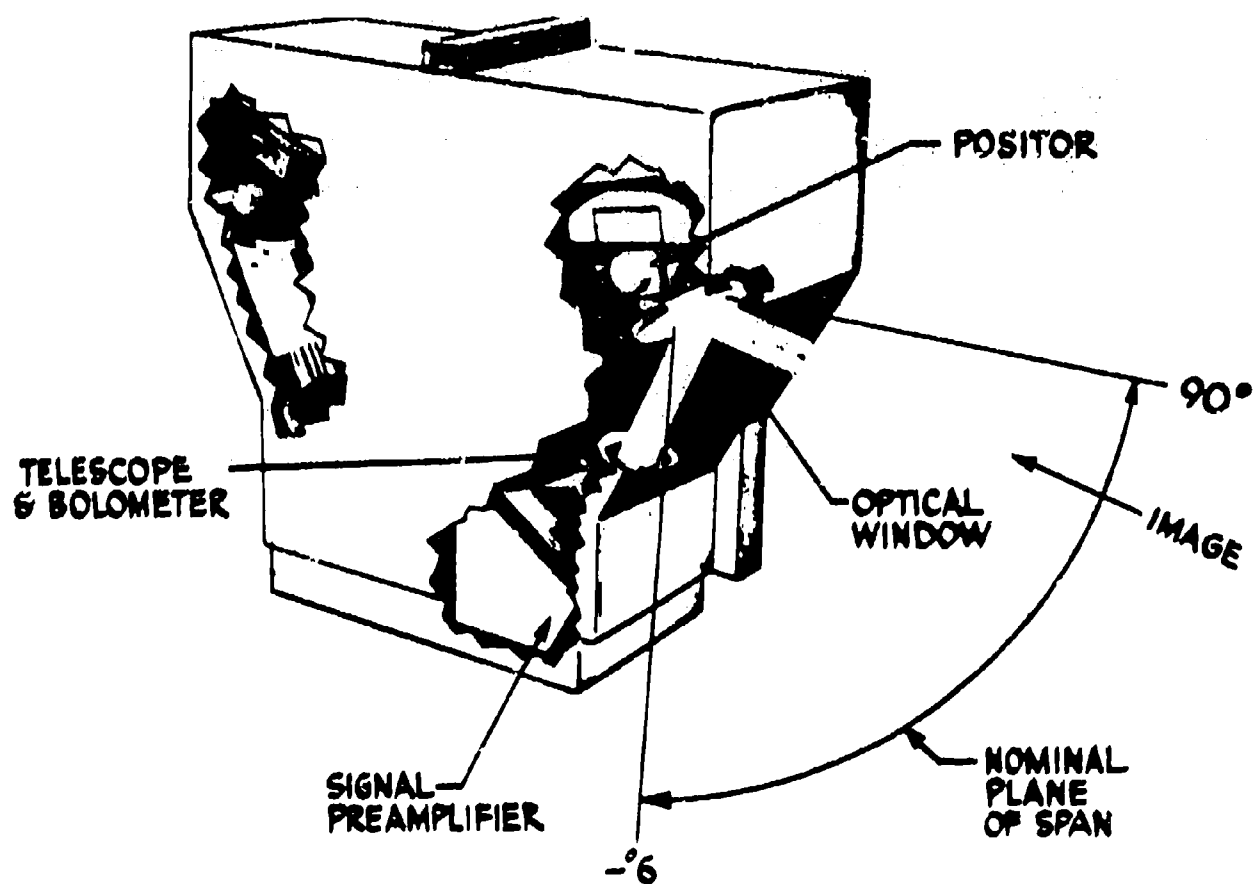


Figure 10. OGO TYPE TRACKING SENSOR

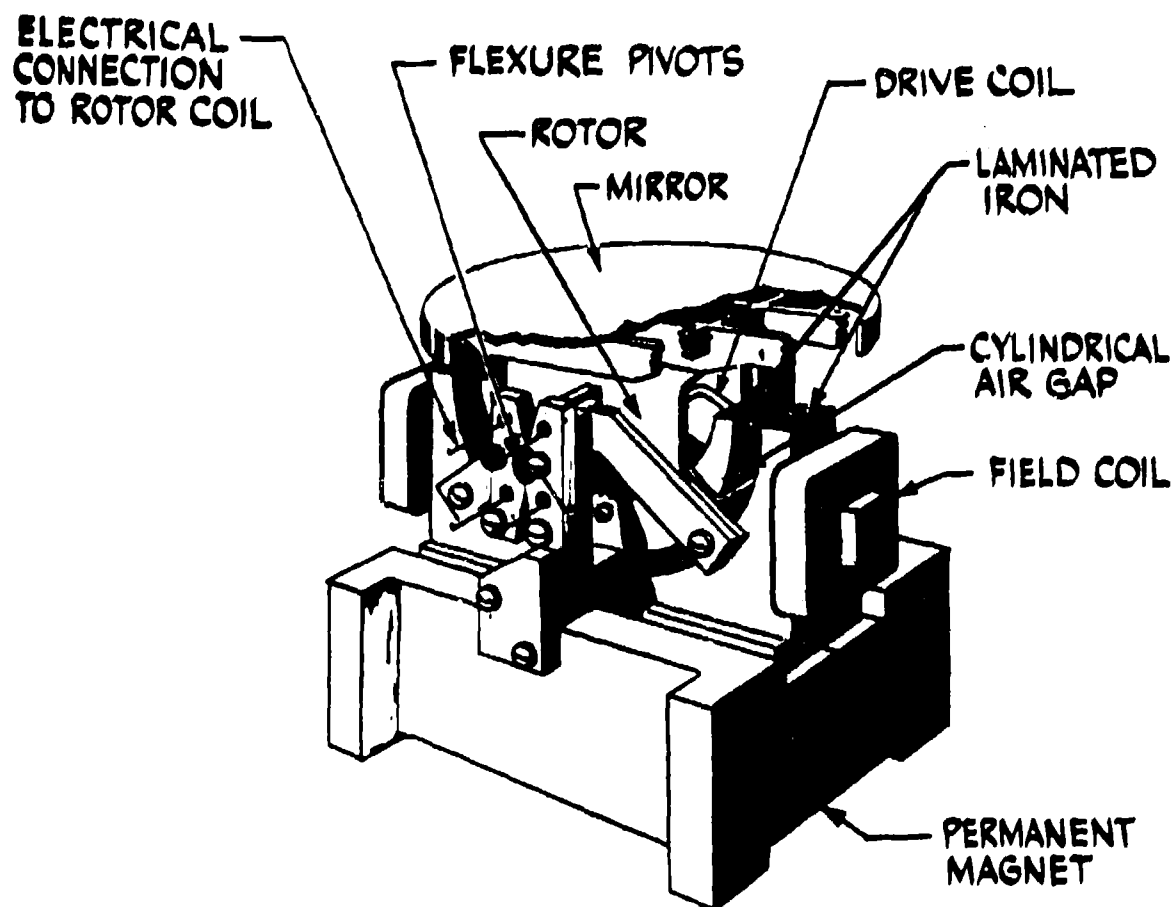


Figure II POSITOR ASSEMBLY

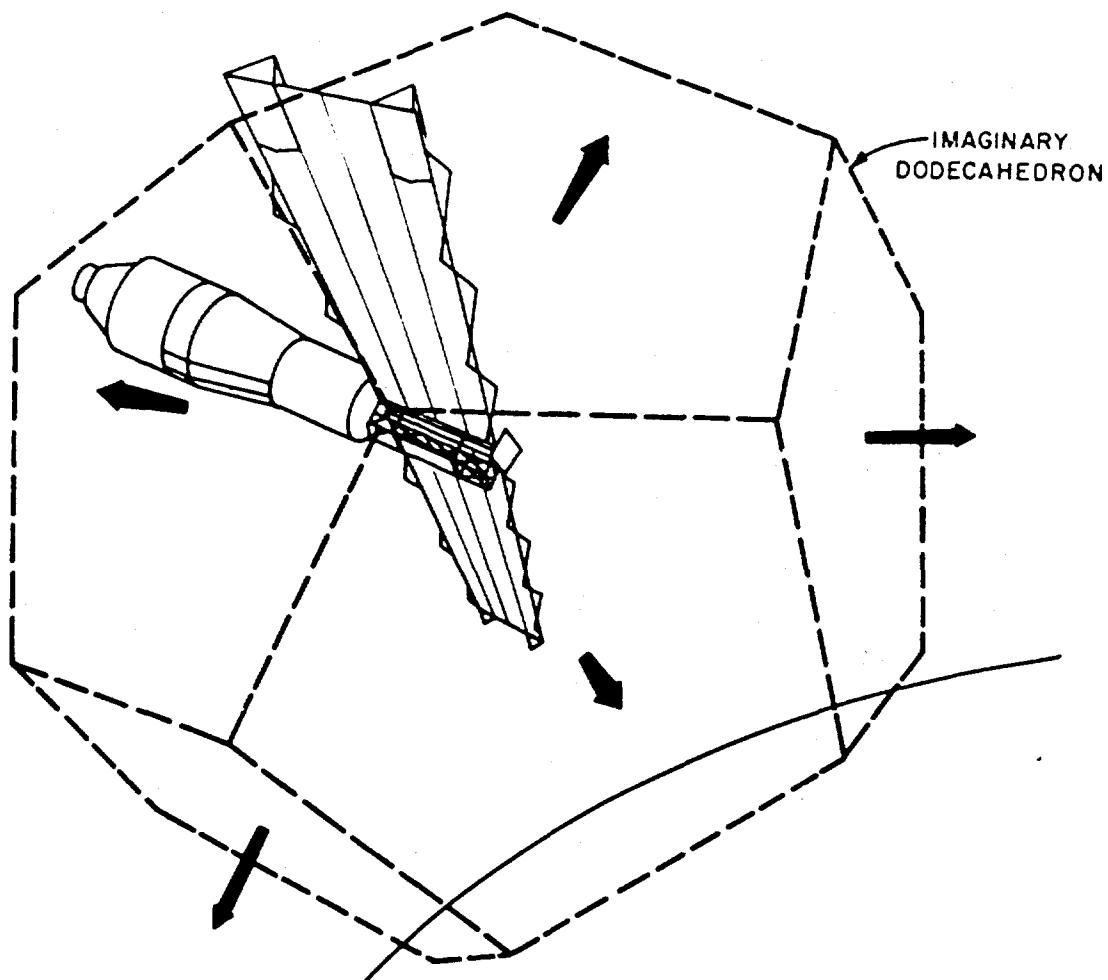


Figure 12. ORIENTATION OF MMC SENSOR FIELDS

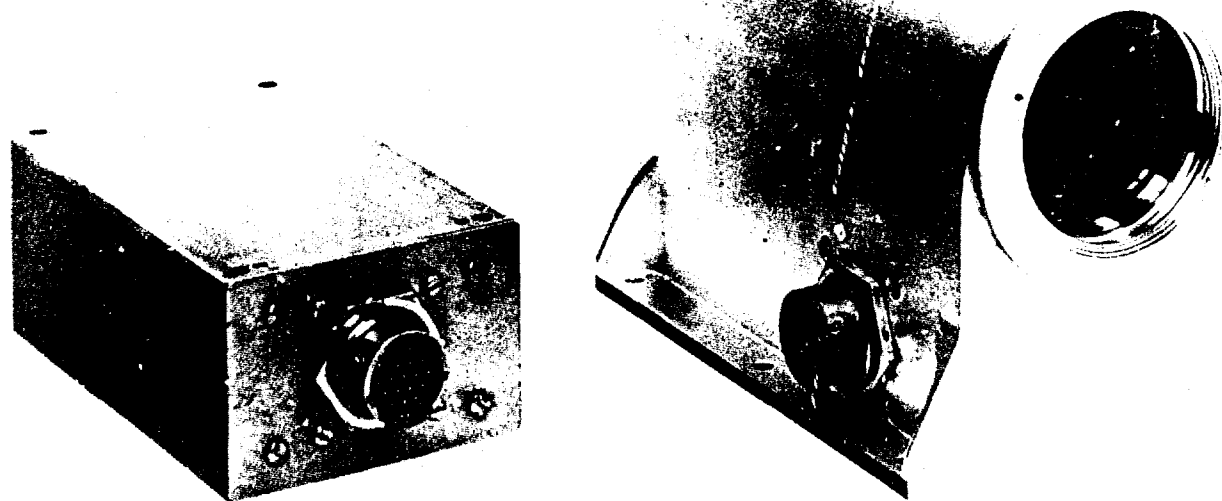


Figure 13. MMC SENSOR HEAD

SESSION III

ATTITUDE DETERMINATION SYSTEMS I

Chairman:  
Dr. J. D. Gilchrist  
The Aerospace Corporation  
El Segundo, California

---

Development and Application of a Star-Mapping Technique to the Attitude Determination of the Spin-Stabilized Project Scanner Spacecraft	189
The SCNS Attitude Determination Experiment on ATS-III	207
The Development and Performance of an Attitude Determination Data Reduction and Analysis System	223
TACSAT Attitude Determination	235
The Attitude Determination System for the Orbiting Astronomical Observatory	249
Attitude Determination and Prediction for a Class of Gravity-Stabilized Satellites	257
Estimation and Prediction of the Attitude of a Passive Gravity Stabilized Satellite from Solar Aspect Information	267

DEVELOPMENT AND APPLICATION OF A STAR-MAPPING TECHNIQUE TO THE ATTITUDE DETERMINATION OF  
THE SPIN-STABILIZED PROJECT SCANNER SPACECRAFT\*

Thomas M. Walsh and Dwayne E. Hinton  
NASA Langley Research Center  
Hampton, Virginia

ABSTRACT

(U) Determination of the positions of the infrared radiance profiles of the earth's horizon measured during two suborbital Project Scanner flights required that the instantaneous spacecraft attitude be determined with an accuracy (1 $\sigma$ ) of 0.016°. This requirement led to the development of a celestial attitude determination procedure using a star-mapper. This procedure was successfully applied to flights on August 16, 1966, and December 10, 1966, with an estimated accuracy of 0.01°. The instrument design and data processing techniques are discussed.

(U) A summary of flight results including signal and noise characteristics, signal detection, time measurement accuracies, and examples of attitude determination of selected axes is also presented.

INTRODUCTION

(U) A research program at the Langley Research Center, directed to defining the radiance signature of the earth's horizon, has included several flight experiments which obtained data in a wide spectral range. One of these experiments, called Project Scanner, which utilized a spin-stabilized spacecraft launched into a suborbital trajectory, was designed to obtain high-resolution measurements of the earth's horizon radiance profile in the carbon dioxide and water vapor spectral regions and to position these measurements relative to the solid earth with a 1 $\sigma$  accuracy of 0.022°. Determination of the positions of these profiles required that the instantaneous spacecraft attitude be determined with an accuracy (1 $\sigma$ ) of 0.016° (Ref. 1). This requirement led to the development of a celestial attitude measurement procedure using a star-mapping technique. Figure 1 illustrates the application of this technique to the Project Scanner experiment. As shown in the figure, spacecraft spin motion scans the field of view of an optical system about the celestial sphere. Detection and identification of stars falling

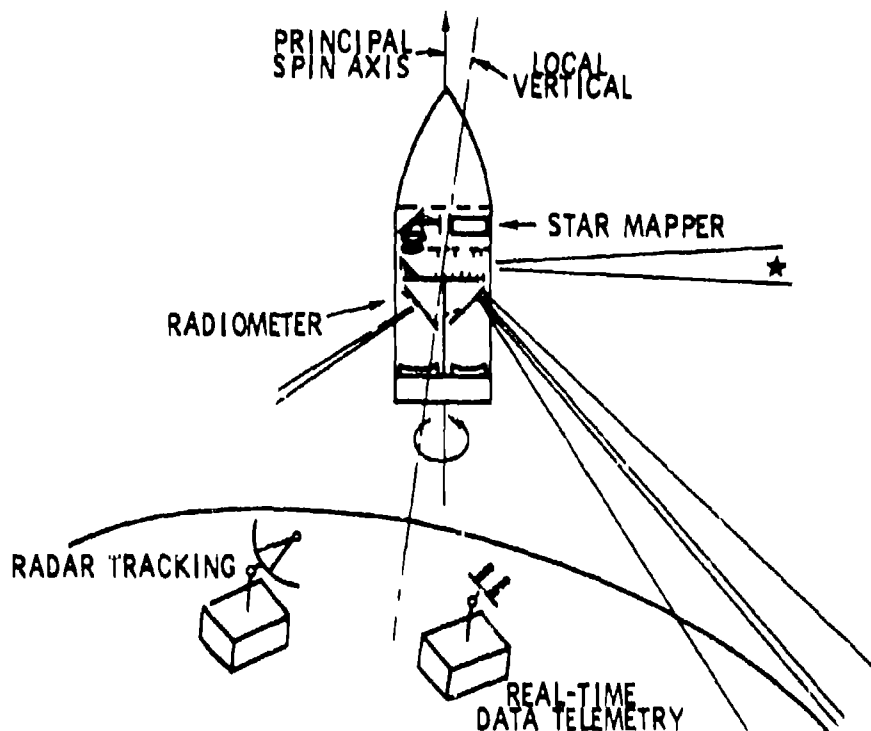
within the field of view result in a star map that is descriptive of spacecraft attitude relative to the celestial sphere.

(U) The design of the star-mapper is discussed and a description of its basic elements such as the optics, photomultiplier, reticle, electronics, and sun shield is included. A brief discussion of the techniques used for processing the Project Scanner star-mapper signals is also included. Results from Scanner flights 1 and 2 of August 16, 1966, and December 10, 1966, are summarized.

STAR-MAPPER CONCEPT

(U) The measurements used to obtain attitude information were provided by a passively scanned star-mapper, which is described in detail in Ref. 2. A schematic of the star-mapper is shown in Fig. 2. The instrument mounting positioned the star-mapper optical axis normal to the expected principal spin axis of the spacecraft. A coded reticle, shown in Fig. 2, was centered in the focal plane of the instrument. A photo-detector was placed behind the reticle, which was principally opaque and contained a pair of

\* This work was done at NASA Langley Research Center, Hampton, Virginia



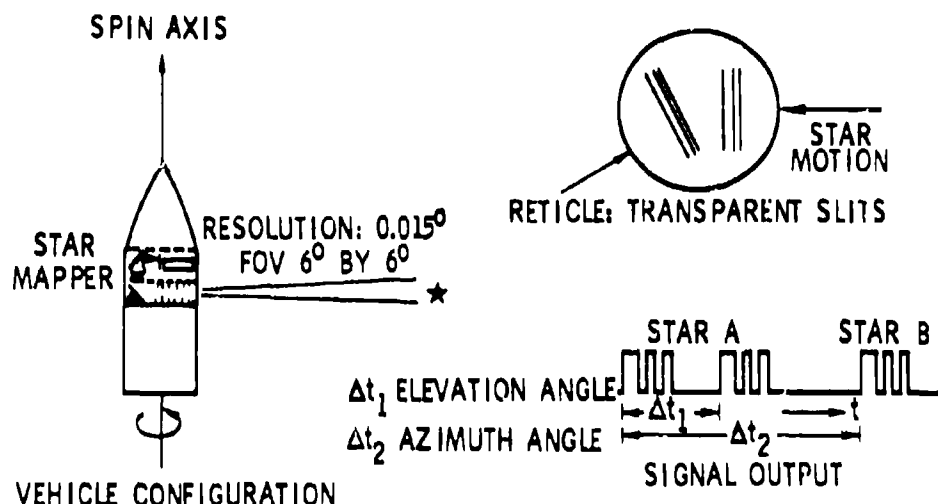
(U) Fig. 1. Scanner Spacecraft Operational Schematic

identically coded sequences of transparent slits, one vertical group and one slanted group. Each sequence of transparent slits in the star-mapper was designed to generate an output code group indicating the passage of a star across the reticle. The elapsed time ( $\Delta t_1$ ) between a pair of pulse groups produced by a single star is related to the elevation angle of that star in the field of view of the star-mapper. The elapsed time ( $\Delta t_2$ ) between pulse groups produced by a pair of stars is related to their azimuth angle separation.

(U) The coding feature of the reticle was used to reduce the system response to instrument noise and to background noise due to the multitude of stars dimmer than a selected threshold visual magnitude. This feature permitted limiting of the

number of detected stars by adjustment of the threshold magnitude and reduction of false detections due to spurious noise by adjustment of the detection logic (Refs. 2 and 3). Limiting of the number of detected stars and reduction of false detections eased the problem of identification of the sighted stars. Spin motion of the spacecraft caused star images to travel across the reticle and produced two coded sequences of radiant energy which were sensed by the photodetector and transmitted to a ground receiving station. The ground-received coded star signals were tape recorded simultaneously with range time signals. Processing of the recorded star signals consisted of four major operations: time detection of apparent star sightings, manual pairing of star sighting times to reduce the number of false star





(U) Fig. 2. Star-Mapper Concept

sightings, identification of detected stars, and identification of the parameters of the dynamical equations of motion describing the spacecraft attitude. A brief description of these operations is given in this paper.

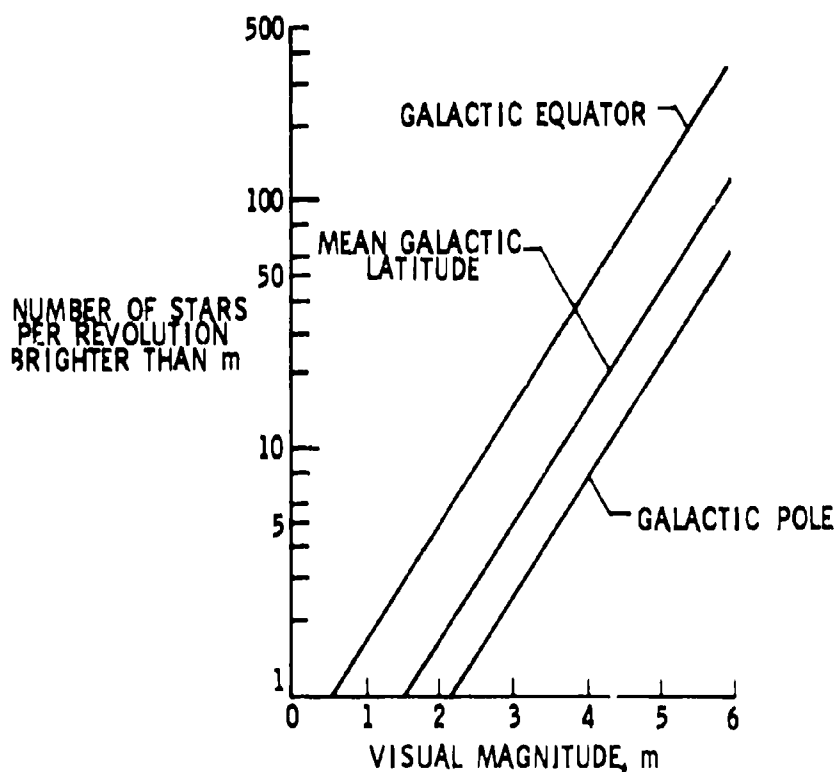
#### INSTRUMENT DESIGN CONSIDERATIONS

(U) Since the basic star-mapper measurement is the time a star image transits a reticle slit, the instrument accuracy is determined by the resolution of time detection of a star pulse. Therefore, in design, it is necessary to consider not only the optical field distortion and reticle inaccuracies but also the optical image quality and electronic system fidelity that affect the star-signal pulse shape. The optical and electronic design requirements are further constrained by the specific flight requirements. On Project Scanner, these requirements were a  $270^\circ$  per sec spin rate, a day or night operation, a mechanical envelope of 40.64 by 25.40 by 54.61 cm, and a mass limitation of 18 kg.

(U) A major problem involved in a system of this type is signal detection in the presence of system and external noises. The signal levels are principally a function of the number of required star sightings for identification purposes. The noise sources investigated for the instrument design were: external noise due to background starlight, noise of the photomultiplier tube, and electronic noise of the system. The noise due to starlight was considered to originate from the

dimmer or nonprominent stars. This external light was assumed to be of a diffuse nature; hence, the noise as sensed by the photomultiplier is dependent upon the effective field of view of the telescope. Effective field of view is defined here as the total clear opening of the reticle in the focal plane. The background light may be considered as an equivalent signal in terms of total integrated starlight, and expressed in effective number of tenth-magnitude stars per square degree of effective field of view (Refs. 4 and 6). This equivalent signal can then be handled in a manner similar to the star signal to determine the effective noise level as sensed by the photomultiplier. Noise sources such as the electronic noise of the airborne equipment and radio frequency noise are negligible, as compared with the other noise sources mentioned here.

(U) For positive identification of a scanned star field, it is necessary to insure that an adequate number of detectable stars will be scanned in a given star field. It has been determined that a  $6^\circ$  field of view scanned through  $360^\circ$  of the celestial sphere will satisfy a three-body sighting requirement when the density of the stars contained within the scanned field of view approximates the star density of the mean galactic latitude, as shown in Fig. 3 (Ref. 3). The launch windows for both flights were selected to insure that the density of stars viewed by the star-mapper would approximate this density for the brighter stars.



(U) Fig. 3. Spatial Density of Stars Per Revolution of a  $6^\circ$  Vertical Field of View

(U) The star signals generated by the photomultiplier are dependent upon the spectral radiant intensity of the star source and the spectral characteristics of the optics and photomultiplier. The spectral radiant intensities of star sources were determined by using equivalent source-temperature approximations and assuming blackbody spectra for +3 visual magnitude and brighter stars. A survey of the literature indicated that the majority of stars of +3 visual magnitude and brighter have source temperatures of  $6,000^\circ$  and

hotter (Refs. 4 and 5). In addition, the "average" source temperature of the myriad of stars which make up the sky background is  $6,000^\circ$  K or colder (Refs. 4 and 6). The representative source temperatures clearly indicated that the peak spectral response of the star-mapper should lie toward the short-wavelength region relative to the visual spectrum. Based on available glass for the optical system and photomultipliers, the short-wavelength cutoff of the instrument was selected to be 3,200 angstroms as

a design goal. The long-wavelength cutoff of the instrument was selected to be 6,000 angstroms to provide a sufficient amount of star irradiance integration for star-signal detection and to reduce the response of the instrument to background light.

(U) The Project Scanner experiment required that the spacecraft attitude be determined continuously with an accuracy (1 $\sigma$ ) of 0.016°. As a means of insuring that the experiment accuracy requirement was met, a 1 $\sigma$  accuracy of 0.006° was established for sightings of individual stars. This accuracy of 0.006° included the effects of optical resolution, reticle slit widths, and a 10-microsecond time resolution of range-time measurements.

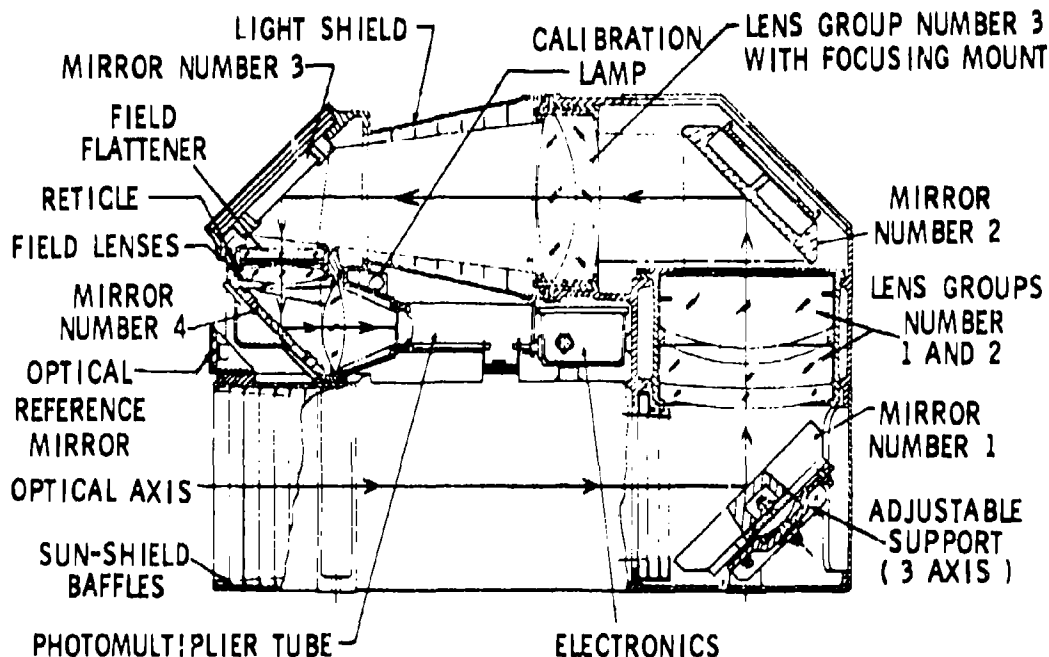
(U) Ideally, the optical resolution and basic slit width would have been equal to achieve a matched-filter relationship. However, a possible need arose for star-signal amplitude measurements for purposes of magnitude classification to aid the star identification problem. Therefore, a slit width of 0.015° and an optical resolution of 0.01° were selected as a compromise between matched-filter characteristics and amplitude-measurement requirements. The resolution of

range-time measurements was expected to be 10 microseconds or 0.003° when the spacecraft nominal spin rate of 270° per sec was considered. The 1 $\sigma$  error in sighting an individual star was determined to be 0.006° by computing the root-sum-square of the error due to range-time resolution and convolution of the optical resolution with the basic slit width.

(U) The design of a star-mapper unit followed a series of trade-offs between optical transmission, detector sensitivity, optical distortion, reticle design or curvature, background noise, electronic bandwidth, detector dark-current noise, vehicle spin rate, resolution requirements, size, and weight (mass). In the following section, the star-mapper design is presented along with the more significant trade-offs.

#### INSTRUMENT CONFIGURATION

(U) The final design layout of the star-mapper is shown in Fig. 4. As indicated in this figure, it was necessary to use folding mirrors to meet the Scanner vehicle space limitation. For this configuration, the overall optical efficiency, using measured transmissivity of all elements, was computed to be approximately 60 percent.



(U) Fig. 4. Star-Mapper Assembly Layout

(U) The refractive optical system chosen for the Project Scanner star-mapper was a modified Petzval design with a 38.1-cm focal length and a 12.7-cm clear aperture. The lens layout consisted of a cemented doublet, a large lens with an aperture stop located midway through the lens, a second cemented doublet, and a field flattener just in front of the reticle. Behind the reticle were two field lenses which spread the light to cover 75 percent of the photomultiplier cathode surfaces. This design provided a maximum blur circle of  $0.01^\circ$  over the field of view. Since it was not possible to obtain a distortion-free image plane, the slits on the reticle were curved slightly to adjust for this problem. The first transparent vertical slit was  $0.03^\circ$  wide, followed by an opaque slit width of  $0.015^\circ$ . The second transparent vertical slit was  $0.015^\circ$  wide with an opaque slit width of  $0.045^\circ$  being next, and the third transparent vertical slit was  $0.015^\circ$  wide. This grouping provided a two-level eight-bit pseudo random code sequence of 1-1-0-1-0-0-0-1. The choice of this code sequence was made to provide a high probability of discriminating stars of +3 visual magnitude and brighter against the expected background (Refs. 1 and 3).

(U) A ruggedized photomultiplier tube having an approximate 8-11 spectral response was selected as the photodetector. This tube had a dark current of  $1.5 \times 10^{-15}$  amperes, a responsivity of 65 microamperes per lumen, and used 14 dynodes to develop a gain of  $10^6$  at a nominal supply voltage of 2,800 volts dc. The output of the photomultiplier tube was amplified by a bandpass amplifier to obtain the desired gain and pulse fidelity. The low-frequency cutoff was required because of slowly varying levels of spatial background noise. The high-frequency cutoff was a function of time of star passage over the narrowest reticle slit, optical resolution (blur circle), and telemetry system filtering. The telemetry system required that the maximum output of the star-mapper be 3 volts. To remain within this output level, a dynamic range of 0.256 to 4.0 volts was established for +3 to 0 visual magnitude stars of the A0 spectral class (11,000° K), respectively. An in-flight calibration lamp was installed so that a one-point calibration check could be made periodically throughout the flight to evaluate the system gain stability.

(U) In order to assure recognition of a +3 visual magnitude A0 star, it was required that the signal levels produced by stray light be less than or equal to the signal level produced by a +4 visual magnitude A0 star. For sunlight, this specification required an attenuation factor of  $10^{-12}$  for all rays entering at angles of  $25^\circ$  or greater from the optical axis. The sun-shield baffles were knife edged, with a  $60^\circ$  bevel, and were spaced 1.27 cm apart over the length of the sun shield. All baffles were coated with a high-quality black paint. The assembled star-mapper flight unit is shown in Fig. 5.

(U) The effectiveness of the sun-shield attenuation was evaluated for off-axis light sources using

the QAO test facility. A summary of the measured data indicated the sun-shield attenuation at  $25^\circ$  off the optical axis was approximately  $4 \times 10^{-10}$  rather than the required  $10^{-12}$ . Since the Scanner launch could be changed to a dark-of-night firing without compromising the experiment objectives, no attempt at a redesign was undertaken.

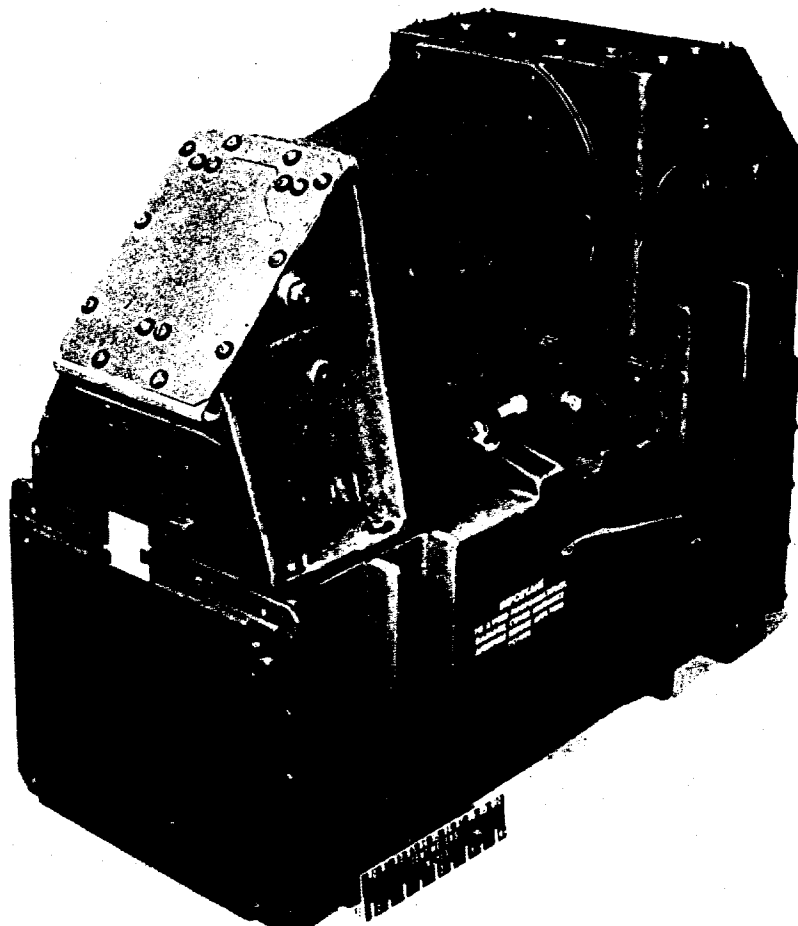
#### CALIBRATION AND TESTING

(U) Operational tests were performed before, during, and after environmental stresses. Optical and alignment degradations were evaluated after each environmental test. The results of several system tests including field-of-view mapping accuracy and photometric calibration are discussed briefly. A more detailed presentation may be found in Ref. 2.

(U) The field-of-view mapping accuracy test was designed to determine the effects of optical inaccuracies on angular position measurements in the field of view. The basic method employed to determine these inaccuracies was a reconstruction of the reticle through star-mapper measurements and comparison of this reconstructed reticle with the reticle design. The results of this test demonstrated that the reconstructed reticle agreed with the theoretical reticle within  $0.01^\circ$  at all points.

(U) The ideal means of calibration for a photometric device of this type would be exposure to several stars of different visual magnitudes and spectral classes. However, present knowledge of atmospheric attenuation at any particular time and the presence of scintillation make this method questionable. Therefore, a star simulator was constructed to calibrate the Scanner star-mapper. Three spectral filters were used to match three selected star spectral classes. The selected classes were A0, G0, and M0, which were approximated by blackbody temperatures of 11,000°, 6,000°, and 3,100° K, respectively. A study was performed to estimate the response of the star-mapper to the simulated stars and to the ideal blackbodies of exact temperatures. The results of this study showed that spectral errors in the simulated blackbodies caused the output of the star-mapper to be slightly less when viewing a simulated star than when viewing true blackbodies of the same visual effective irradiance. The differences in star-mapper output varied between 3 and 10 percent, depending on the star spectral class.

(U) The absolute levels of the star simulator spectral output were adjusted by use of neutral density filters. The transmission values of the neutral density filters were selected to control the effective visible irradiance of the star simulator when used with the test collimator. Corrections were made to the data to compensate for irregularities in the flatness of the spectral characteristics of the neutral density filters. Tests were performed to determine the attenuation factors for each class necessary to achieve an irradiance value of  $3.1 \times 10^{-15}$  watts/cm<sup>2</sup> for a star with a visual magnitude of 0. These tests were performed by using a standard photocell and



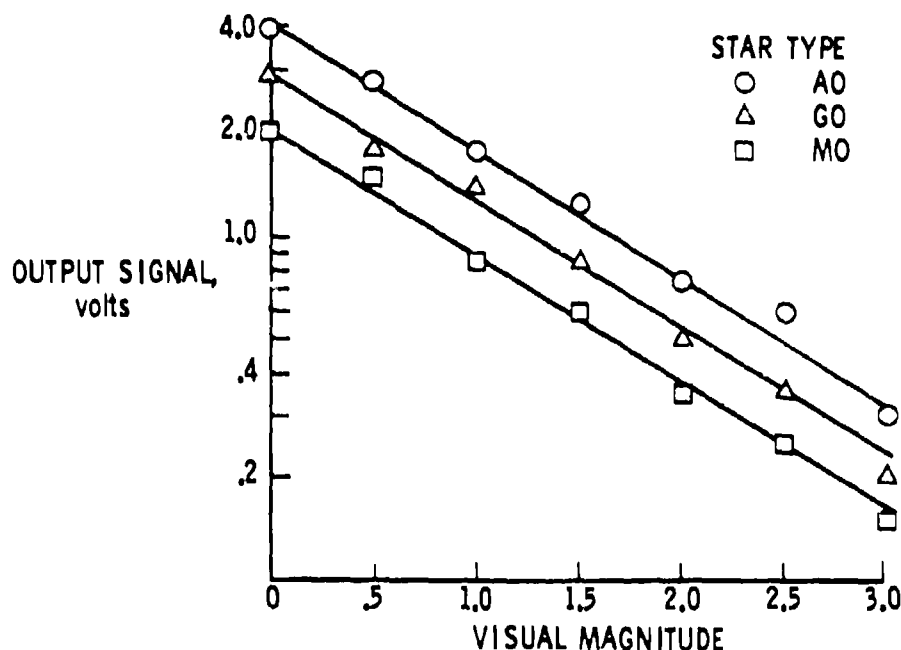
(U) Fig. 5. Project Scanner Star Mapper

filter combination with a spectral response equivalent to the human eye. For the AO star with visual magnitude of 0, the system gain was adjusted until the star-mapper output signal reached a value of 4 volts. For each spectral class, the irradiance was varied from an equivalent star with  $m_v = 0$  to a star with  $m_v = +3$  in half-magnitude steps. The signal-to-noise ratio (exclusive of background noise) was found to be approximately 13:1 for the stars with a visual magnitude of 0 of the AO class. A summary of the calibration of the star-mapper is shown in Fig. 6. An error analysis of this calibration method was performed, and results indicated that a variation of  $\pm 25$  percent could be expected for in-flight irradiance measurements.

#### TRANSIT-TIME DETECTION

(U) The data processing required to detect and identify the stars sighted by the instrument will be briefly described. A detailed discussion of the data processing may be found in Ref. 1.

(U) A simplified diagram of the data processing procedure is shown in Fig. 7. The raw star-mapper signals, range time, and two reference frequencies of 1 kilohertz and 100 kilohertz were tape recorded. The 100-kilohertz signal was used as a 10-microsecond vernier during 1-millisecond intervals. The raw star-mapper signals were converted to a two-level digital pulse train by use of an adjustable threshold. This two-level coded-pulse sequence was compared in a correlator with a reference pulse sequence consisting of an equal number of bits. Detection of a star transit across a sequence of transparent slits was acknowledged provided that comparison of the reference code sequence with a given sequence of nine basic bits produced agreement of any two ones and all five zeros or three ones and four zeros. Acknowledgment of transit detection was in the form of a gating signal which enabled digital recording of range time of detection, threshold setting, and peak amplitude of the first pulse in a signal-pulse sequence. The peak-amplitude detector was reset to zero after



(U) Fig. 6. Star-Mapper Calibration

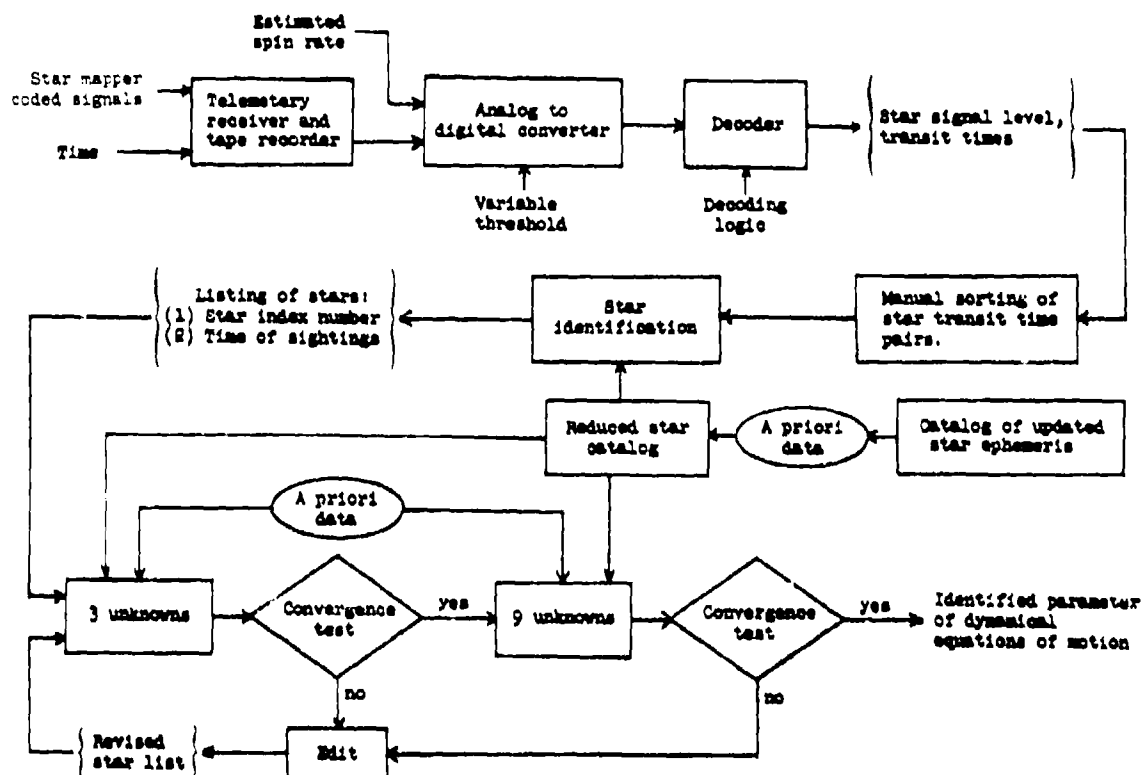
each code-sequence recognition. The variable threshold and the tape recording feature permitted manual selection of a limited number of stars per vehicle revolution. This capability reduced the number of possible ambiguities in the subsequent star identification program. Detection times were set for the trailing edge of each code sequence. Detection-time resolution was limited by the time duration of one element of the code sequence and range-time uncertainties. The time duration of each bit of the code sequence was controlled by a variable-clock pulse generator which was adjusted for the best estimate of vehicle spin rate and the angular resolution of the smallest transparent slit of the reticle. The spin-rate estimate was readjusted as attitude-determination results became available (Ref. 1).

(U) The results of the transit-time-detection processing were stored in a digital listing of apparent-star transit times and amplitudes of each apparent-star signal. This listing was hand sorted

by pairing transit-time differences between apparent-star signals with the aid of the signal amplitude measurements. All transit-time differences that exceeded the constraints established by the geometry of the reticle slit configuration and estimated vehicle spin rate were rejected as false star indications. This modified listing of star transit times was then used in the routine of star identification.

#### STAR IDENTIFICATION AND PARAMETER ESTIMATION

(U) The two primary operations of the star-mapper data processing procedure shown in Fig. 7 are the identification of the detected stars and estimation of the parameters of the dynamical equations of motion describing the spacecraft attitude. The listing of star transit-time pairs was operated upon in a star identification program which produced a listing of identified



(U) Fig. 7. Star-Mapper Data-Processing Procedure

stars and their sighting times. The listing was used as input data to a parameter estimation program, its resulting output being a set of the parameters which defines the dynamical equations of motion of the spacecraft. A priori data were used in both the star identification and parameter estimation programs in the form of estimates of nominal vehicle trajectory, vehicle moments of inertia based on preflight measurements, and an approximation of vehicle spin rate based on successive sightings of identified stars. The following sections describe in detail the spacecraft attitude geometry, the mathematical model assumed for the dynamical equations of motion, the star identification program, and the parameter estimation program.

#### Star Identification

(U) A star identification program was used to identify each star associated with each pair of transit times detected in the decoding routine.

One of the primary requirements of the program was that the transit times be in chronological order and that the times appear in pairs, each pair being from the same star. The equatorial coordinates of the reference stars used in this program were obtained from the Boss catalog (Ref. 7) and updated to the nearest 0.1 day of the time of flight by use of the astronomical techniques described in Ref. 8. The reference star listing was reduced by elimination from consideration all stars dimmer than a visual magnitude of +3.5 (Ref. 2). The star listing was further reduced by selecting all stars falling within a selected band of the celestial sphere established by the launch window.

(U) All stars of the reduced reference list were considered as candidates for the transiting stars. An additional listing of all these candidate stars was made in the form of a catalog of angular separation of each pair of stars in the reference list. Star identification was

principally a process of finding a cataloged angular separation which agreed to within a fixed tolerance of an estimated angular separation of a pair of observed stars.

#### Space Attitude Geometry

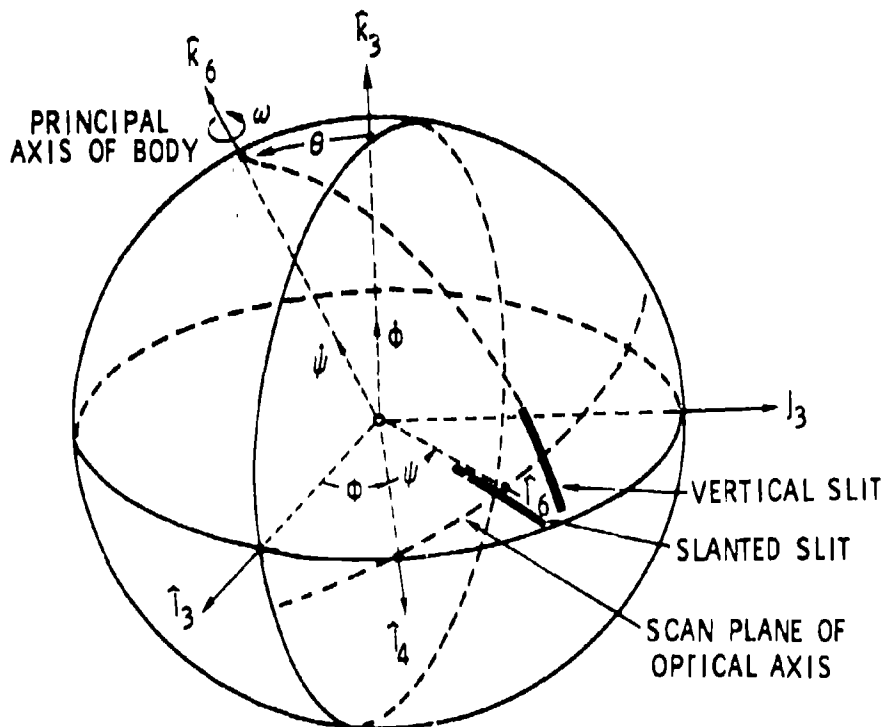
(U) The general problem considered here is one of a geometrical formulation of the celestial attitude of a reference frame fixed in a spinning, torque-free, prolate, symmetrical rigid body. The problem is further defined as one for which the orientation of the body-fixed reference is to be determined at instants of time at which known stars are observed and as a function of time for periods during which no stars are observed. The basic measurements which are used to determine vehicle orientations are the times at which known

stars appear in the transit slit planes of the star-mapper reticle. A simplified schematic of the problem geometry is shown in Fig. 8.

#### Vehicle Dynamics

(U) The relationship between the coordinates of an identified star in the celestial reference frame and the coordinate of the star as sighted in a slit-plane reference frame may be determined by use of the defined Euler angular rotations

$$\underline{R} = (\phi)(\theta)(\psi)(\phi_1)(\phi_2)(\gamma)(\beta)\underline{I} \quad (1)$$



(U) Fig. 8. Relationship of Vehicle Principal Axes to Inertial Reference Frame



The parameters  $\theta$  and  $\Theta$  define the location of the angular momentum vector in celestial coordinates;  $\phi$ ,  $\theta$ , and  $\psi$  are the standard Euler angle rotations for the principal body axes;  $\epsilon_1$  and  $\epsilon_2$  represent misalignment rotations of the optical axis relative to the principal spin axis; and  $\gamma$  and  $\beta$  are rotations which define the location of the coded slits relative to the optical axis.

(U) The vector  $\underline{R}$  may also be written in the celestial reference frame as

$$\underline{R}^T = (\cos \alpha \cos \delta, \sin \alpha \cos \delta, \sin \delta) \quad (2)$$

where  $\alpha$  and  $\delta$  are the right ascension and declination of the identified star. The vector  $\underline{r}$  in the star-mapper reference frame is defined as

$$\underline{r}^T = (\cos \eta, 0, \sin \eta) \quad (3)$$

where  $\eta$  is defined as the elevation angle of the star in a slit plane. For the case of a spinning torque-free symmetrical rigid body, the angles  $\phi$  and  $\psi$  of Eq. (1) are defined as

$$\phi = \dot{\phi}t + \phi_0 \quad (4)$$

$$\psi = \dot{\psi}t + \psi_0 \quad (5)$$

and the rates  $\dot{\phi}$  and  $\dot{\psi}$  are defined as

$$\dot{\phi} = \frac{I_3 \omega}{I_1 \cos \theta} \quad (6)$$

$$\dot{\psi} = \frac{(I_1 - I_3)\omega}{I_1} \quad (7)$$

where  $I_3$  is the moment of inertia about the principal spin axis of the vehicle;  $I_1$  is the moment of inertia about either one of a pair of axes which are mutually orthogonal and orthogonal to the principal spin axis of the body; and  $\omega$  is the total spin velocity about the principal spin axis of the body.

(U) If all parameters of Eq. (1) were uniquely defined, the attitude of any set of axes would be known. However, only the  $\gamma$  and  $\beta$  angles of Eq. (2) were assumed to be well known before flight. Of the remaining parameters in Eq. (2),  $\epsilon_1$ ,  $\epsilon_2$ ,  $\theta$ ,  $\phi_0$ , and  $\psi_0$  were assumed to be unknown; estimates of  $\theta$  and  $\Theta$  were available from launch data; and estimates of  $\omega$ ,  $\dot{\phi}$ , and  $\dot{\psi}$  were available from preliminary examination of star-mapper data. With the use of identified

stars, their sighting times, and least-square techniques, the parameters of Eq. (1) were estimated.

### Parameter Estimation

(U) In the development of the spacecraft attitude determination geometry, Eq. (2) was derived to show the relationship between the celestial coordinates of an identified star and the coordinates of the star in either the vertical or slanted slit plane reference frames. Substituting Eqs. (2) and (3) into Eq. (1) results in

$$\begin{pmatrix} \cos \delta \cos \alpha \\ \cos \delta \sin \alpha \\ \sin \delta \end{pmatrix} = (\theta)(\Theta)(\phi)(\psi)(\epsilon_1)(\epsilon_2)(\gamma)(\beta) \begin{pmatrix} \cos \eta \\ 0 \\ \sin \eta \end{pmatrix} \quad (8)$$

The nine undetermined parameters of Eq. (8) are  $\theta$ ,  $\Theta$ ,  $\phi$ ,  $\phi_0$ ,  $\theta$ ,  $\psi$ ,  $\psi_0$ ,  $\epsilon_1$ , and  $\epsilon_2$ . An observed star produced two equations such as Eq. (8), one each for the slanted and vertical slit planes. Since a large number of star observations were expected, a least-squares technique was selected for estimation of the undetermined parameters.

### DEVELOPMENT OF DATA-REDUCTION ACCURACY CRITERIA FROM PREFLIGHT ANALYSIS

(U) Before application of the attitude determination technique to flight data reduction, the accuracy of the parameter estimation method had to be ascertained in order to establish expected accuracies for the Project Scanner flights. In addition, criteria had to be developed in order to assess the adequacy of any estimate as determined from flight data. To establish the expected accuracy of spacecraft attitude determination, a simulation study was performed. Criteria for assessing the adequacy of estimates were developed by using the results of this study. In this study, simulated flight data were generated by using the expected launch and flight conditions of Project Scanner flight 1. The mathematical model of simulated spacecraft equations of motion was identical to that which was assumed for the flight vehicle. Simulated flight data were in the form of a time list of transited stars and the right ascension and declination values of these stars updated to the expected launch time. These simulated data were used to estimate the values of the previously described parameters in the same manner as for flight data. These estimates were used to generate pointing direction time histories of selected axes. The errors in these pointing directions, specifically the pointing direction errors of the optical axis, were the basis of assessing the accuracy of the attitude determination solution.

(U) The accuracy of the attitude determination procedure was determined by calculating the standard deviation of the pointing direction error  $\sigma_p$  at selected times from data representing multiples of a precession period, number of star sightings per spin period, and angular displacement of stars within a spin period. The results of these calculations showed that star placement within a spin period was a major factor, since with poorly placed stars (i.e., all stars in a spin period are placed within half a period) precession information is not well defined. The accuracy of attitude determination increased as the data-fit period used in the least-squares program increased and as the number of star sightings per spin period increased for the one-precession-cycle case. The one-half precession-cycle case also indicated evidence of this trend. The one-and-one-half precession-cycle case showed no particular trend, and the results for this case were interpreted to mean that the errors in the estimates of the undetermined parameter were in the noise level for any considered number of stars per spin period. Based on these calculations, the predicted Scanner star-mapper accuracy was estimated to have a maximum 1 $\sigma$  value of approximately  $0.004^\circ$ . The values obtained in the simulation study gave assurance that the attitude determination technique would meet the experimental requirement of  $0.016^\circ$  with a confidence level of 99 percent.

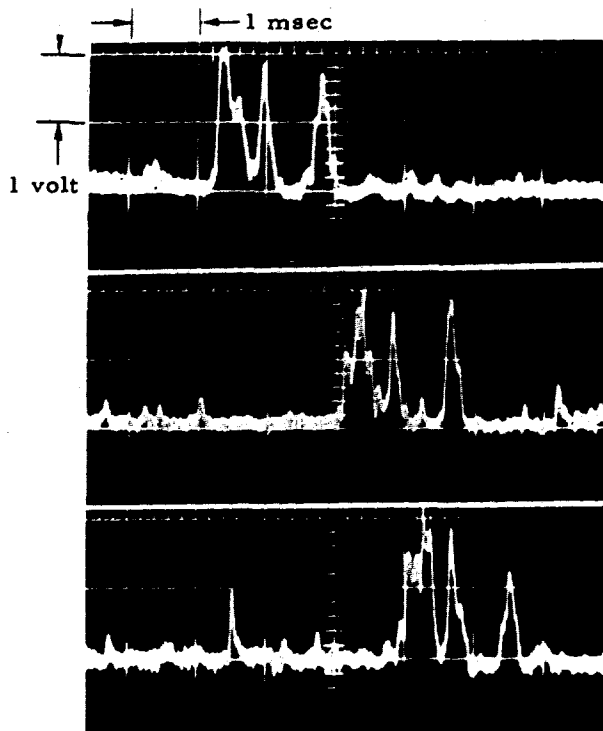
#### Relation of Transit-Time Errors to Least-Squares Functional Residuals

(U) To evaluate the accuracy of attitude determination resulting from use of the estimates as computed in the least-squares program, time errors were added to the simulated star transit times. These errors had an equal probability of having values of +26, 0, or -26 microseconds and a standard deviation  $\sigma_t$  of approximately 21 microseconds. Since it is not possible to measure  $\sigma_t$  for flight data, it was necessary that some other parameter be used to estimate the magnitude of transit time errors. The functional residuals of the least-squares solutions resulting from simulated data were examined for this purpose. The convergence factor used in the least-squares program was adjusted until a least-squares iteration resulted in time residual values which agreed with the time errors to within an accuracy of 5 microseconds. In this study, the standard deviation of the time residuals  $\sigma_{tr}$  was calculated for each set of star sightings used in a least-squares solution and found to be approximately 20 microseconds for all cases in the study. For  $\sigma_{tr} \approx 20$  microseconds, the accuracy of the computed vehicle attitude orientation was well within the specified requirements. This parameter was the factor which was used to assess the adequacy of a least-squares solution for flight data. In the case of flight data, the convergence factor was adjusted until  $\sigma_{tr}$  was near its minimum value. When  $\sigma_{tr}$  was at an acceptable minimum value, a least-squares solution was accepted as an adequate one.

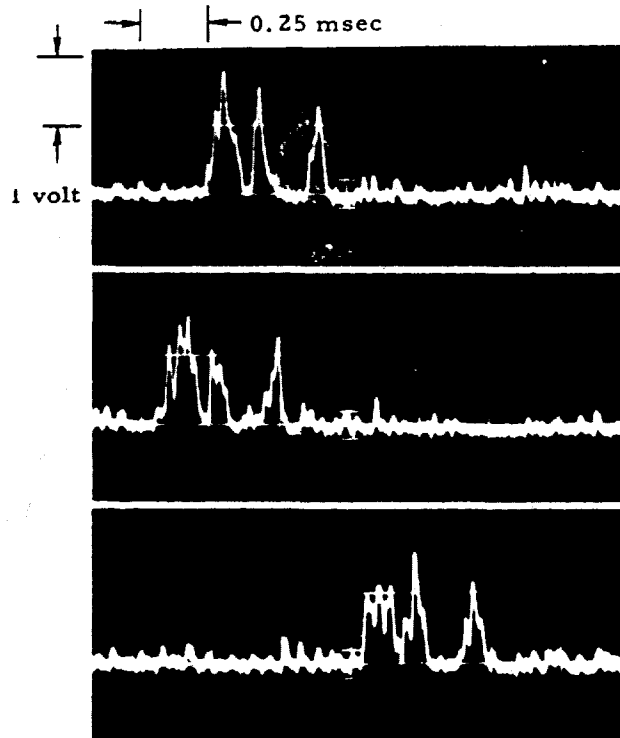
#### POSTFLIGHT EVALUATION OF STAR-MAPPER OPERATION

(U) A check of the star-mapper calibration was attempted by using two randomly selected identified stars of flight 1. Photographs of the coded star signals for the selected stars Alkaid and Alphecca are shown in Fig. 9. This figure shows star signals generated by the vertical group of slits for three different sighting times to demonstrate the severe noise problem introduced by background and signal-generated noise. In all cases, the coded pattern is clearly evident and indicates the advantages of coded reticles for star signal detection purposes. Alkaid and Alphecca are +1.91 visual magnitude B5 and +2.31 visual magnitude A0 stars with predicted star-mapper signal levels of 0.90 and 0.60 volt, respectively. Averaging 10 sightings of each star resulted in output signal levels of 1.65 volts for Alkaid and 0.85 volt for Alphecca. Several other stars were examined in a similar manner and results indicated that the star-mapper had a sensitivity which was 1.5 to 1.75 times greater than that expected from the preflight calibration results. A check of the star-mapper calibration over its dynamic range was not possible, since none of the stars identified during the first flight were predicted to produce outputs greater than 1 volt.

(U) The average background noise was expected to be approximately equivalent to the signal produced by a +4 visual magnitude A0 star. No attempt was made to verify this expected background noise because of the existence of numerous low-intensity stars that were identifiable as star signals although not identified for attitude determination purposes. However, a rough approximation of the peak-to-peak noise level due to background noise may be determined from an examination of Fig. 9. In this figure, the average peak-to-peak background noise level is approximately 0.3 volt or a root-mean-square (rms) value of 0.11 volt. By using the signal and noise definitions of Ref. 3, the ratio of average signal level to rms background level was predicted to be in the range of 8.5:1 to 13.5:1 for an assumed +2.3 visual magnitude A0 signal star and a background level equivalent to a range of +3 to +4 visual magnitude A0 star, respectively. The average in-flight signal of 0.85 volt obtained for Alphecca and the average rms background level of 0.11 volt indicate a signal-to-noise ratio of 8:1. These values agree favorably and indicate validity of the assumed signal and noise models used in the design of the star-mapper. A listing of all stars identified during Project Scanner flight 1 is given in Fig. 10. These stars are listed according to their Boss catalog number, star name, Bayer name, constellation, visual magnitude, and spectral class. The lowest intensity visual magnitude star identified from the star-mapper data of the first flight was a B5 star with a visual magnitude of +3.30; the lowest intensity star, relative to



(a) Alkaid



(b) Alphecca

(U) Fig. 9. Typical Star Signals

the instrument spectral response, identified from data of the first flight, was an M3 star with a visual magnitude of +3.19. The results of Project Scanner flight 2 were very similar and a listing of all stars used to determine attitudes for both flights is shown in Fig. 11.

(U) The number of stars per spin period sighted by the star-mapper during each data period varied from 3 to 14. Ambiguities in associating raw data with vertical or slanted slit transits and in star identification were encountered when two or more stars with small angular separations were present in the field of view of the star-mapper. Such problems usually resulted in unusable data from one or both stars, in which case the questionable stars were eliminated from the star identification list. As a result, the number of stars actually used for attitude determination of the Scanner vehicles was considerably smaller than the number identified.

(U) Preliminary data revealed that several stars consistently exhibited large time residuals. Subsequent checking traced the cause of these high residuals to errors in the updated star positions based on values listed in the Boss catalog. The

positions of these stars ( $\delta$  Orionis,  $\eta$  Ursae Majoris, and  $\alpha$  Piscis Austrini) were cross checked with positions taken from the apparent place tables (Ref. 9) and updated to the nearest 0.1 day of the flight. Discrepancies of the order of  $0.01^\circ$  in the star positions taken from the Boss catalog and updated to the nearest 0.1 day of flight were found. When the stars' positions determined from the apparent place tables were used for these stars, the time residuals for these stars dropped to acceptable limits.

(U) An analysis of all solutions of the nine vehicle-motion parameters determined from flight data showed a time residual  $\sigma_{tr}$  of approximately 30 microseconds. In the simulation study described in an earlier section, star transit time errors having a standard deviation of approximately 21 microseconds were added to the simulated star transit data. These time errors resulted in a standard deviation of the time residuals  $\sigma_{tr}$  of approximately 20 microseconds when data were fitted over an interval of 0.5 to 1.50 precession cycles. The corresponding maximum standard deviation of the pointing direction error,  $\sigma_a$ , was found to be approximately  $0.004^\circ$ .

Boss catalog number	Name	Bayer name	Apparent visual magnitude	Spectral class
*3584	Acamar	$\theta$ Eridani	3.06	A2
6274	Cursa	$\beta$ Eridani	2.92	A3
6668	Bellatrix	$\gamma$ Orionis	1.70	B2
6847	Mintaka	$\delta$ Orionis	2.48	O9
8208	Tejat Posterior	$\mu$ Geminorum	3.19	M3
12407	Talitha	$\iota$ Ursae Majoris	3.12	A4
15145	Merak	$\beta$ Ursae Majoris	2.44	A0
16268	Phekda	$\gamma$ Ursae Majoris	2.54	A0
17518	Alioth	$\epsilon$ Ursae Majoris	1.68	A0
*18133	Mizar	$\zeta$ Ursae Majoris	2.17	A2
18643	Alkaid	$\eta$ Ursae Majoris	1.91	B3
20947	Alphecca	$\alpha$ Corona Borealis	2.31	A0
22193	Kornephoros	$\beta$ Herculis	2.81	G8
25180	Kaus Borealis	$\lambda$ Sagittarii	2.94	K0
25661		$\phi$ Sagittarii	3.30	B8
25941	Nunki	$\sigma$ Sagittarii	2.14	B3
*26161	Ascella	$\xi$ Sagittarii	2.71	A2
30942	Alnair	$\alpha$ Gruis	2.16	B5

\*Double star.

(U) Fig. 10. Identified Stars of Project Scanner Flight 1

It can be shown that there is a linear relationship between  $\sigma_a$  and  $\sigma_t$ . Since it has been shown that  $\sigma_a$  and  $\sigma_{tr}$  have very close agreement, it can be said that there is approximately a linear relationship between  $\sigma_a$  and  $\sigma_{tr}$ . Therefore, the expected accuracy in pointing direction determined from flight data is approximately  $0.006^\circ$ . Although the time residuals were somewhat larger than the transit time errors used in the simulation study, the accuracy of the data still remained within acceptable limits for the flight experiment.

(U) On both flights, a cold-gas reaction jet control system was used to erect the vehicle to within  $12^\circ$  of the local vertical at four definite times during the flight in order to maximize the data gathering of the primary horizon definition experiment. During the intervals between these erection times, the controls were turned off and the spin-stabilized vehicle was assumed to be free of external and control torques. Star-mapper data for each of the two Scanner flights consisted of four such data periods, each of which was approximately 2-1/2 minutes in duration. Had

the vehicle actually been a symmetrical, rigid, torque-free spinning body, the vehicle's motion for an entire data period could have been represented by a single set of nine vehicle motion parameters. Under this assumption, the single set of nine vehicle motion parameters could have been determined by performing a least-squares fitting of all the star transit times in an entire data period. Preliminary evaluation of the results of the attitude determination procedure for both flights indicated that some undefined source produced small disturbing torques during the data periods. Desired accuracies in the determination of vehicle attitude were obtained with the assumed model by reducing the time periods covered by a least-squares solution to approximately three-fourths of a precession cycle in order to minimize the effects of these torques and possible vehicle asymmetries. For example, the second data period of Scanner flight 1 was divided into 12 time intervals and 12 sets of nine vehicle motion parameters were used to define the vehicle's motion during that data period. The discrepancy between the model assumed for the motion of the

Boss catalog number	Name	Bayer name	Apparent visual magnitude	Spectral class
Scanner flight 1				
*3584	Acamar	$\theta$ Eridani	3.06	A2
6274	Cursa	$\beta$ Eridani	2.92	A3
6668	Bellatrix	$\gamma$ Orionis	1.70	B2
6847	Mintaka	$\epsilon$ Ursae Majoris	1.68	A0
15145	Merak	$\beta$ Ursae Majoris	2.44	A0
16268	Phekda	$\gamma$ Ursae Majoris	2.54	A0
17518	Alioth	$\epsilon$ Ursae Majoris	1.68	A0
18643	Alkaid	$\eta$ Ursae Majoris	1.91	B3
20947	Alphecca	$\alpha$ Coronae Borealis	2.31	A0
22193	Kornephoros	$\beta$ Herculis	2.81	G8
*26161	Ascella	$\zeta$ Sagittarii	2.71	A2
Scanner flight 2				
519	Ankaa	$\alpha$ Phoenicis	2.44	G5
9188	Adara	$\epsilon$ Canis Majoris	1.63	B1
9443	Wezen	$\delta$ Canis Majoris	1.98	G3
9886	Aludra	$\eta$ Canis Majoris	2.43	B5
13926	Regulus	$\alpha_1$ Leonis	1.34	B7
*14177	Algieba	$\gamma$ Leonis	2.61	K0
18643	Alkaid	$\eta$ Ursae Majoris	1.91	B3
25466	Vega	$\alpha$ Lyrae	0.14	A1
30491	Deneb Algiedi	$\delta$ Capricorni	2.98	A5
32000	Fomalhaut	$\alpha$ Piscis Austrini	1.29	A2

\*Double star.

(U) Fig. 11. Stars Used to Determine Attitude of Scanner Vehicles

vehicle in the parameter identification program described earlier and the actual vehicle motions may be seen by observing the total angular spin rate  $\omega$ , which is defined by

$$\omega = \dot{\psi} + \dot{\theta} \cos \theta$$

For a symmetrical, rigid, spinning, torque-free body, this angular spin rate should remain constant. Spin rate determined by succeeding solutions of approximately three-fourths of a precession cycle over an entire data period slowly but constantly increased. This was characteristic of all four data periods of both Scanner flights.

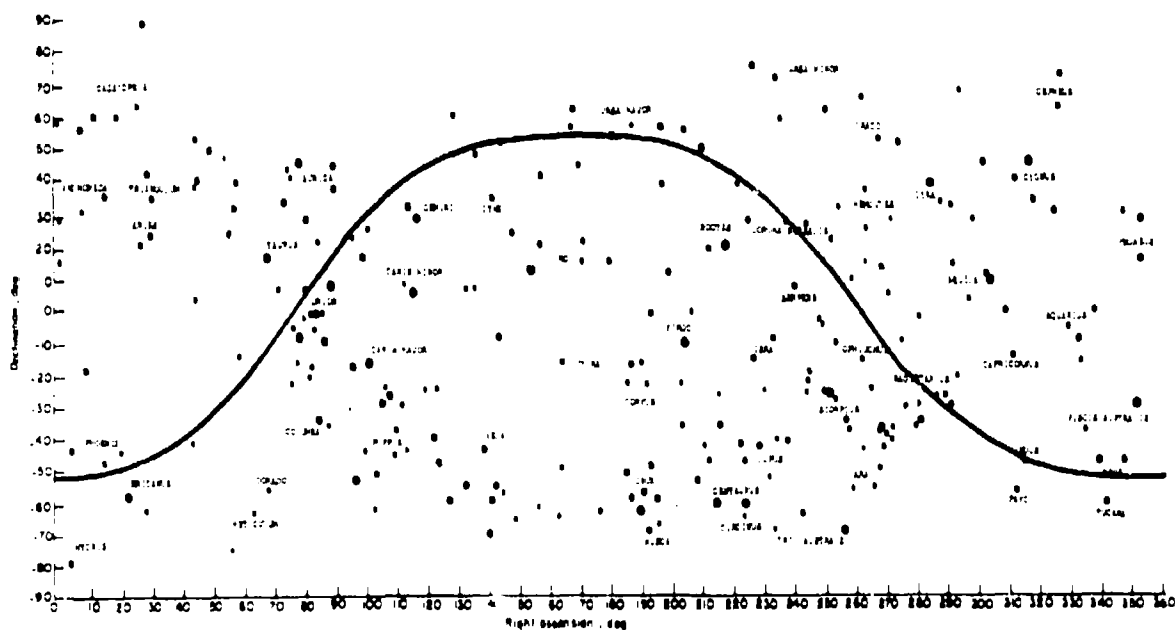
The spin rate obtained for the second data period of flight 1 increased by 0.04 percent over this time period. This percentage of increase for  $\omega$  was approximately the same for all data periods of both flights. No attempt was made to determine the source of this variation in the assumed model. A possible source of the small disturbing torques could have been incomplete closure of the control valves in the reaction jet control system during the data period.

(U) To illustrate the use of the nine vehicle motion parameters, a set of these parameters was selected from the second data period of Scanner flight 1 and was used to generate time histories of the star-mapper optical axis ( $i_g$ ) and the

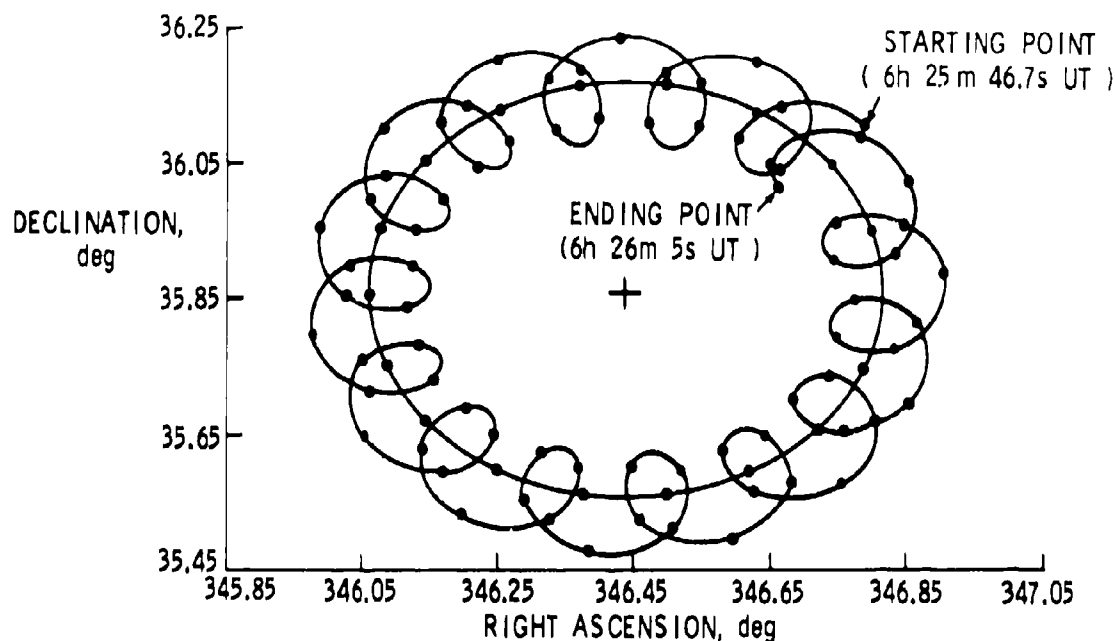
vehicle principal spin axis ( $\hat{e}_3$ ). The results of these computations are shown in Figs. 12 and 13 in which the pointing directions of these two axes are plotted in terms of declination and right ascension for selected time periods. Figure 12 represents the pointing direction of the optical axis during one spin period and Fig. 13 represents the pointing direction of the vehicle principal spin axis during a precession cycle. Also shown in Fig. 13 is the pointing direction of the  $\hat{e}_2$  axis during a precession cycle. This plot illustrates the effects of the misalignment angles,  $\epsilon_1$  and  $\epsilon_2$ . The complete listing of all the sets of nine parameters for each data period and for both flights was used in a similar manner to generate time histories for the  $\hat{e}_3$  axis. These results along with the preflight measured angular relationship between the star-mapper  $\hat{e}_3$  axis and each radiometer optical axis were used to determine the time history of each radiometer optical axis in celestial coordinates.

#### CONCLUSIONS

(U) The star-mapper system and the associated data reduction techniques described provided a highly accurate method for determining the instantaneous attitude of a spinning vehicle. Dispersions in attitude angles determined by this method for Project Scanner were less than  $0.01^\circ$ . The flight results also demonstrated that the design goal of detecting and identifying +3 visual magnitude stars was achieved and the laboratory photometric calibration was sufficiently accurate to permit use of signal amplitudes for slit-to-slit and scan-to-scan correlation of star transits to aid in the identification procedure. A significant problem that was not resolved was the design and construction of a sun shield having the required attenuation of stray sunlight to allow daylight operation.



(U) Fig. 12. Pointing Direction of the Star-Mapper Optical Axis ( $\hat{e}_3$ ) for One Vehicle Spin Period Based on the Set of Nine Vehicle Motion Parameters Selected From the Second Data Period of Project Scanner Flight 1 for Time Beginning 6h 25m 46.7s UT on August 16, 1966



(U) Fig. 13. Pointing Direction of Vehicle Principal Spin Axis  $R_6$  and the  $R_8$  Axis for One Precession Cycle Based on the Set of Nine Vehicle Motion Parameters Selected From the Second Data Period of Project Scanner Flight 1 for Time Beginning 6h 25m 46.7s UT on August 16, 1966

#### REFERENCES

1. Walsh, T. M.; Keating, Jean C., and Hinton, Dwayne E.: Attitude Determination of Spin-Stabilized Project Scanner Spacecraft. NASA TN D-4740, 1968.
2. Walsh, T. M.; Dixon, William C., Jr.; Hinton, Dwayne E.; and Holland, James A.: A Celestial Attitude Measurement Instrument for Project Scanner. NASA TN D-4742, 1968.
3. Walsh, T. M.; and Kenimer, Robert L.: Analysis of a Star-Field Mapping Technique for Use in Determining the Attitude of a Spin-Stabilized Spacecraft. NASA TN D-4637, 1968.
4. Chapman, R. M.; and Carpenter, R. O.: Effect of Night Sky Backgrounds on Optical Measurements. OCA Tech. Rep. 61-23-A, Geophys. Corp. Amer., May 22, 1961.
5. Kauth, Richard: Backgrounds. Handbook of Military Infrared Technology, William L. Wolfe, Ed., Office Naval Res., Dept. Navy, 1963, pp. 95-173.
6. Roach, F. E.; and McGill, Lawrence R.: Integrated Starlight Over the Sky. Astrophys. J., Vol. 133, No. 1, January 1961, pp. 228-242.
7. Boss, Benjamin: General Catalogue of 33 342 Stars for the Epoch 1950. Publ. No. 468, Vols. II-V, Carnegie Inst. of Washington, 1937.
8. Anon.: Explanatory Supplement to the Astronomical Ephemeris and the American Ephemeris and Nautical Almanac. H. M. Nautical Almanac Office, 1961.
9. Anon.: Apparent Places of Fundamental Stars, 1966. Astron. Rechen-Inst., Heidelberg, 1964.

## THE SCNS ATTITUDE DETERMINATION EXPERIMENT ON ATS-III<sup>1</sup>

C. E. Grosch, A. E. LaBonte, and B. D. Vannelli  
Edina Space and Defense Systems  
Control Data Corporation  
Minneapolis, Minnesota

### ABSTRACT

The attitude determination portion of the SCNS experiment flown on ATS-III is traced from the original concept formulation through operational data reduction and interpretation of the attitude results. The basic concepts related to the determination of spacecraft attitude from the stellar transit time information provided by a completely passive strapped-down star scanner are briefly reviewed. A sketch of the complete SCNS attitude determination system and its information flow is provided. The effects of celestial noise sources--faint star background, bright objects, and hard radiation--are examined. Results of a detailed evaluation of star detection performance are also presented. Finally, the attitude results and estimates of their accuracy are discussed. In cases of good stellar target geometry, the root sum square three-axis attitude error was found to lie in the range from 12 to 20 seconds of arc.

### I. INTRODUCTION

The characteristics of the stellar-based, completely passive, strapped-down attitude determination system which was flown on ATS-III are described. The attitude motion of the satellite can be approximated as that of a spinning, torque-free, rigid symmetric body. The attitude determination instrumentation employs three slits which are located behind a lens system which is rigidly mounted to the satellite. The rotational motion of the satellite causes the stars to sweep across these slits. The brighter stars in the instrument's field of view are sensed by a photomultiplier located behind the slits and the time they transit each slit is recorded. These transit times together with a description of the orientation of the slits with respect to the satellite axes and a knowledge of the star which produces each recorded transit time is sufficient to determine the attitude of the satellite as a function of time.

Unfortunately, not all recorded times are produced by known stars. Celestial noise sources such as faint star background, the sun, sunlit

moon, sunlit Earth, and hard radiation yield a significant number of recorded times. Moreover, statistical fluctuations in the radiant output of any given star cause legitimate transits to be undetected with a significantly high frequency. In addition, the recovery time duration following a bright source encounter causes a large portion of the azimuthal directions to be lost to usable detections.

Before examining the nature and solution of these various difficulties, a brief description of the basic method used to compute the attitude from transit times of known stars will be given. More complete discussion may be found in Refs. 1 and 2.

The general problem is to find the orientation of a coordinate system fixed in the spacecraft with respect to a stationary coordinate system. The basic input measurements which yield this orientation, or attitude, are the times of transit of known stars across a slit.

Consider a transparent slit etched on the otherwise opaque focal plane of an optical system as shown in Fig. 1. If the slit is a straight line segment and the optical system is free of distortion, then a portion of a plane will be defined which contains the slit and the

<sup>1</sup>This work was carried out for the Goddard Space Flight Center of NASA under Contract No. NAS5-9683.



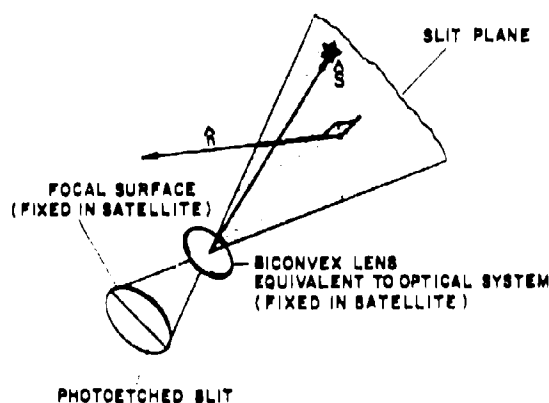


Fig. 1. The Relationship Between the Slit Plane and the Target Star at the Instant of Transit

nodal point of the lens system. Given a distant bright point source, this source will be sensed by a detector behind the slit if, and only if, it lies on the plane defined by the slit and optical system. If a point source crosses the plane, the source transits the slit. The instant the point source lies in the plane is called the transit time.

For any transit time of a star, the following equation may be written

$$\hat{n} \cdot \hat{S} = 0 \quad (1)$$

where

$\hat{n}$  = unit vector normal to the slit plane at the instant of transit, and

$\hat{S}$  = unit vector in the direction of the star.

But to specify the vehicle orientation at any specific instant requires three independent angles while Eq. (1) yields only one condition. Additional equations are obtained as the vehicle motion causes the sensor to scan the celestial sphere and other stars are encountered. This results in a set of conditions

$$(\hat{n}(t_i) \cdot \hat{S}_i = 0) \quad (2)$$

If no further information is introduced, this simply adds one equation and three unknown angles at each isolated transit time. However, the physics which governs the motion of the satellite may be invoked to develop a time-dependent characterization of the attitude which involves just a few unknown parameters. This "attitude model" may then be used to internally couple the conditions in Eqs. (2).

Observe that since the optical system is fixed within the satellite,  $\hat{n}$  is also fixed within the satellite. Its components are therefore most easily written in a coordinate system fixed in the satellite. On the other hand,  $\hat{S}$  is most easily written in a celestial coordinate system (a system in which the star directions are cataloged).<sup>2</sup> In order that these vectors may be written in the same coordinate system, parameters which specify the orientation of the coordinate system fixed in the satellite with respect to the celestial system must be introduced. However, these are precisely the unknown attitude model parameters which are to be determined. Solution for these parameters yields a state vector, which, when inserted in the attitude model, results in a time history of the attitude over the interval spanned by the transit time data in Eqs. (2).

Two additional observations may be made. First, each stellar target will yield two spatially independent measures--e.g., azimuth and elevation--if more than one slit is employed in the sensor. The set of basic constraint equations then takes the form

$$(\hat{n}_j(t_i) \cdot \hat{S}_i = 0) \quad (3)$$

where  $j$  indexes the set of slits. The additional information per star which is gained from a multi-slit system may be exploited to reduce the number of required stellar targets or to increase the data sampling rate. Second, if the number of independent conditions in Eqs. (3) exceeds the dimensionality of the state vector, then this set of equations is redundant and may be solved in a least-squares sense. The internal consistency of the resulting solution is a measure jointly of the adequacy of the attitude model and the accuracy of the transit times.

The remainder of the paper emphasizes the implementation of these concepts in the attitude determination portion of the SCNS (Self-Contained Navigation System) experiment flown on the ATS-III satellite. The discussion begins with a brief description of the characteristics of ATS-III which are pertinent to this problem.

## II. ATS-III

The orbit of the ATS-III satellite is circular, equatorial, and synchronous. Hence, as viewed from the spacecraft, the earth subtends a relatively small angle (17°). This implies that the vehicle will be in the sunlight continuously except for very brief eclipses (of approximately one hour duration) on orbits which occur around the time of the Spring and Fall equinoxes. However, the great altitude required for synchronous orbits also means that Earth-related torques on the satellite will be very small.

<sup>2</sup>At this point it is assumed that the star has been identified, although such identification is not a trivial problem.

A pictorial view of the ATS-III spacecraft itself is displayed in Fig. 2. Also shown is the relative location of the flight instrumentation for the SCNS experiment. Although the satellite is quite massive, it is seen to have a very compact shape which tends to make it insensitive to even those small forces which are present. Further, the vehicle is spinning very rapidly--100 rpm--and thus possesses a high degree of attitude "stiffness."

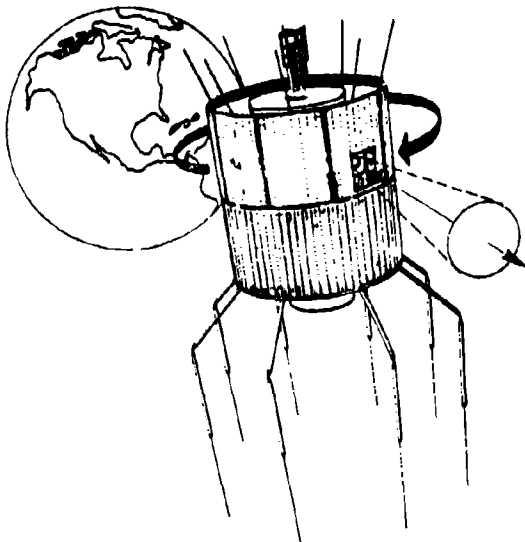


Fig. 2. The ATS-III Satellite Showing the Location of SCNS Flight Instrumentation

As a consequence of the characteristics described above, the dynamics of ATS-III were initially assumed to correspond to the general case of a rigid, torque-free, symmetric body. The basic attitude parameters in this description (referred to henceforth as Model 1) are:

$\alpha, \delta$  - right ascension and declination, respectively, of the angular momentum vector,

$\theta$  - nutation or half-cone angle,

$\psi = \psi_0 + \dot{\psi}t$  - spin angle, and

$\phi = \phi_0 + \dot{\phi}t$  - precession angle.

However, after gaining some experience with the actual operation of the satellite, two changes were made in the model. First, the precession and nutation damper on the spacecraft was found to be very effective; the half-cone angle  $\theta$  was held to less than 0.5 arc-minute. Thus, the spin axis and total angular momentum vectors were essentially coincident. Under these conditions, only the sum of  $\alpha$  and  $\delta$  has significance; no separation of the spin and precession can be

effected. Second, much of the SCNS attitude data was collected in the brief eclipse periods and a positive acceleration of the vehicle rotation was observed. This was attributed to the change in the spacecraft thermal environment as the satellite passed out of direct sunlight and into the earth's shadow. As the spacecraft cooled, it shrank and consequently sped up to conserve angular momentum. A constant acceleration was found to provide an adequate description over a time period of a few minutes (several hundred rotations). For longer periods, an acceleration which is linear in time was required. The revised attitude characterization (Model 2) assumed that the satellite spins about a fixed axis with a rate which may be a quadratic in time. Along with  $\alpha$  and  $\delta$ , the attitude parameters for Model 2 enter as

$$s = s_0 + \dot{s}t + \frac{1}{2}\ddot{s}t^2 + \frac{1}{6}\dddot{s}t^3 - \text{simple spin angle.}$$

Two additional features of ATS-III require mention here. The nominal direction for the spin axis was very close to the South Celestial Pole. Since a characterization in terms of  $(\alpha, \delta)$  has a singularity at that point, an alternative pair of angles with the singularity at the First Point of Aries was used internal to the data reduction to avoid possible convergence problems. The final solution was, however, converted to standard celestial coordinates before output. The other feature relates to the ATS-III telemetry. A wide band (5 MHz) channel was available so it was possible to transmit the analog star signal from the scanner directly to the ground receiving station for pulse detection and digital transit time encoding. This permitted significant simplification of the flight instrument and provided considerably more flexibility in system operation.

### III. THE SCNS EXPERIMENT

The SCNS experiment had two primary objectives--demonstration of precision attitude determination capability and investigation of the feasibility of a self-contained celestial navigation system. The stellar attitude determination system--the subject of this paper--is patterned after the concepts outlined in the Introduction. The navigation system extends these concepts to the detection of the apparent motion of a nearby body with respect to the fixed field of stellar targets. This apparent motion is created both by the actual motion of the target body--the moon and/or a small probe ejected from the spacecraft--and the motion of the spacecraft itself. Thus, if data is gathered over a significant segment of the orbital path, it may be reduced to obtain the orbits of both spacecraft and target or of the spacecraft alone if the target orbit is known a priori. The latter case holds, of course, if the target is the moon.

## A. Experiment Geometry

In Fig. 3, some fundamental aspects of the relative geometry of the experiment are shown as a projection on the celestial sphere. The optical axis of the SCNS instrument is nominally canted away from the positive spin axis of the vehicle by an angle of  $65^\circ$  and the optical field of view is approximately  $30^\circ$ . Since the direction of the spacecraft spin axis lay very close to the South Celestial Pole, the scanning motion swept out an effective field of view covering the annulus between declinations  $-10^\circ$  and  $-40^\circ$ . The large field of view and large cant angle were dictated primarily by the target acquisition requirements of the navigation experiment. As can be seen from Fig. 3, however, this leads to a configuration in which the sun lies directly in the path of the scan during the winter months. Figure 3 also illustrates the fact that the sun will be eclipsed by the earth only for times of the year near the equinoxes and then only for spacecraft orbital positions such that the satellite nadir is near that same equinoctial point. Note finally that the sun is never more than  $34^\circ$  from the edge of the annular field, even at summer solstice.

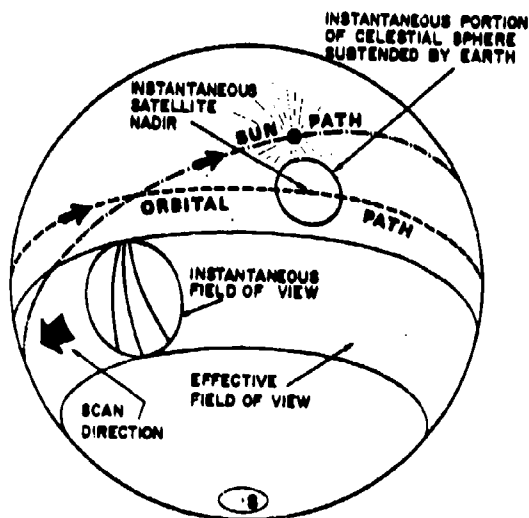


Fig. 3. Principal Geometric Relationships of the SCNS Experiment as Projected on the Celestial Sphere

The SCNS slit configuration as projected on the celestial sphere is shown in Fig. 3. The location of these slits with respect to the satellite spin axis is critical and is pictured in Fig. 4. The slits were fabricated to intersect at a point so that the center slit bisects the angle formed by the outer slits. The unit vector  $\hat{k}_B = \hat{k}_S$  is in the direction of the spacecraft's spin axis, while  $\hat{i}_B$  is fixed in the body of the spacecraft such that the  $(\hat{i}_B, \hat{k}_B)$  plane contains the direction which images at the point of slit

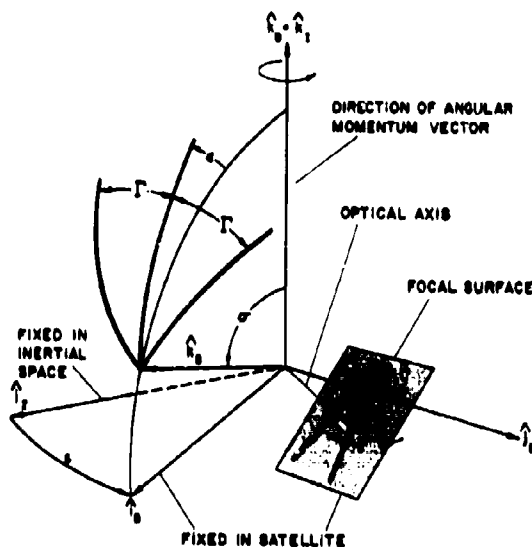


Fig. 4. Orientation of the Slits as Defined by  $\Gamma$ ,  $\epsilon$ , and  $\sigma$ . The body fixed system  $(\hat{i}_B, \hat{j}_B, \hat{k}_B)$  is such that the  $(\hat{i}_B, \hat{k}_B)$  plane contains the point of slit intersection.

intersection.

The unit triad  $\hat{i}_B, \hat{j}_B$ , and  $\hat{k}_B$  have defined directions, which are fixed in the spacecraft. In general, it would require six angles to define the orientation of the three slit planes; however, for the case here, only three angles are required as shown in Fig. 4. These three angles cannot be considered known beforehand for they depend upon the spacecraft's spin axis. This alignment cannot be accomplished with the accuracy to which it may be computed from star transits. Thus, the three angles  $\Gamma$ ,  $\epsilon$ , and  $\sigma$  which define the orientation of the slits with respect to a preferred coordinate system fixed in the spacecraft are parasitic unknowns in the total problem.

The general state vectors for the two attitude models may now be summarized as follows:

Model 1  
precession



Model 2  
simple accelerated spin



## B. The Sensor

The on-board equipment pertinent to the attitude determination experiment consists of an optical system, detector, and analog electronics assembly. A schematic section of the sensor head is presented in Fig. 5. Because of severe experiment space limitations, it was necessary to fold the optical system as shown. Furthermore, only a minimum light baffle sufficient to block stray scattered light from the adjacent spacecraft structure could be provided. The absence of an elaborate sunshade was partially offset by the experimental nature of the program which permitted restriction of operation to favorable configurations of the bright celestial sources--the sun, sunlit Earth, and moon. However, as will be described below, the instrument was operated with fair success when the satellite was fully sunlit and with excellent results with the moon directly in the annular field of view.

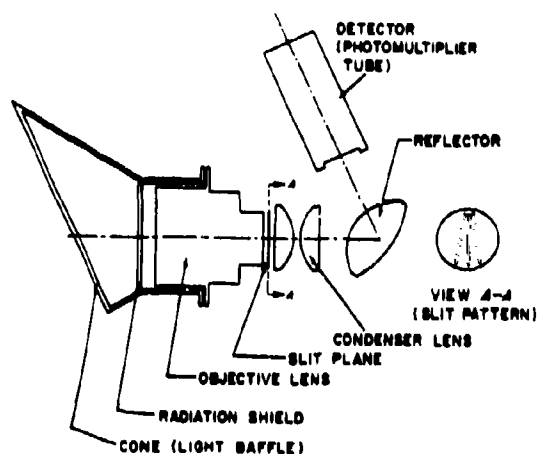


Fig. 5. SCNS Optical Assembly and Detector Schematic

The objective is an off-the-shelf Super-Ferron lens assembly with a  $30^\circ$  nominal field of view, a 76 mm focal length, and an 88.5 mm aperture. Because of this wide field angle and very small  $f/\text{number}$ , the system exhibits rather strong vignetting. Further, computer ray traces based on the lens prescription indicate that the blur spot diameter varies from 5 to 80 arc minutes as the off-axis angle grows from  $0^\circ$  to  $10^\circ$ . The efficiency for off-axis sources is reduced even more by the optical complications inherent in the folded light collection system. The net effect of this pattern of attenuation is to reduce the useful field for typical stellar detections to about  $12^\circ$ . This, however, remains ample for attitude target acquisition for almost any orientation of the annular field on the celestial sphere. In addition, the full field is still available for the bright lunar transits required for moon navigation.

The rotational slit width of each of the three photo-etched slits in the focal plane reticle is approximately 7.6 arc-minutes. Here, "rotational slit width" is defined as the angle through which the satellite must rotate to cause a point image to pass from the leading to the trailing edge of the slit. A constant rotational slit width along the length of each slit and among the slits implies a constant stellar dwell time. This, in turn, simplifies specification of the optimum signal filter electronics.

The detector is an Electro-Mechanical Research Model 341-E-01-14 photomultiplier with an integral high voltage power supply. The electronics following the photomultiplier provide on-board amplification and filtering of the analog star pulse output. A combination of two high voltage settings plus eight gain steps in the on-board amplification results in 16 levels of system sensitivity which can be selected by telemetry command. The overall range of these levels corresponds to approximately five stellar magnitudes. The final amplified star signal output is then fed directly to the ground station over the wide-band telemetry link.

## C. Data Encoding

After the analog sensor signal is received at the tracking station it is fed immediately to an electronics complex which implements a variety of signal processing steps. A copy of the analog signal is recorded on a video tape unit. This recording provides a back-up source in the event of a malfunction in the direct digital encoding of the star data; the signal can be replayed and digitized from the copy. The tape version may also be replayed to a high speed chart recorder to generate a visual display of the signal for more detailed study. Another copy of the signal is directed to the operator's real-time visual display. This unit is centered around an oscilloscope with trace storage capability. It permits the operator to estimate the quality of the signal and provides him with information on which to base his selection of a detection threshold level.

The primary path for live data, however, is shown in the over-all chart of SCNS information flow presented in Fig. 6. The sensor output is fed directly into the threshold detection electronics and all analog pulses which exceed the threshold level setting are detected. The threshold system initially employed a level which was operator selectable but otherwise constant in time. This approach proved entirely adequate for operation in the nearly dark-sky conditions of the eclipses. However, the extreme changes in the background light levels encountered during sunlit operation required development of baseline following circuitry. The threshold was then set at a fixed level above the resultant time-varying baseline.

For either type of level, the output of the threshold system is a new train of rectangular pulses. The leading edge of each rectangular

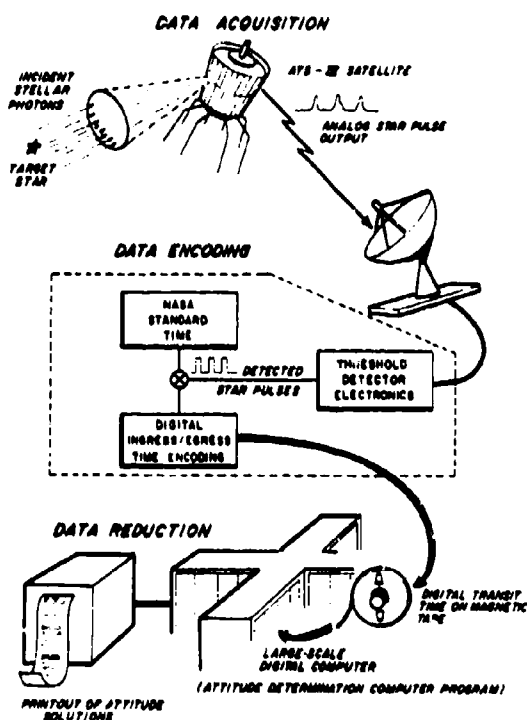


Fig. 6. Principal Path of Information Flow Through the Complete SCNS Attitude Determination Experiment

pulse corresponds to transit "ingress"--the instant at which the analog pulse just exceeds the threshold.

Similarly, the trailing edge of the rectangular pulse corresponds to transit "egress"--the instant at which the analog pulse just drops below the threshold.

The train of rectangular pulses, in turn, is used to control the transfer of digital clock times. The basic clock is derived from NASA standard time and is carried to a time encoding granularity of one microsecond. At the instant corresponding to the leading edge of a rectangular pulse, the contents of the clock and a tag indicating transit ingress are transferred to a small digital computer which serves as a data buffer at the tracking site. In analogous fashion, the transit egress time and its tag are transferred at the occurrence of a rectangular-pulse trailing edge. Note that the star "transit time" as defined above is taken as the mean of the ingress and egress times. The small computer then simply transfers the data it has collected to digital magnetic tape. The remaining series of steps in the attitude determination process may now be implemented by reducing this transit data offline in a large-scale digital computer.

#### D. Data Reduction

In the absence of a high incidence of spurious transits, the stellar target identification (and subsequent attitude determination) process would be relatively simple and straightforward. Almost every star detected would appear as a unique triplet of star signals. Time separations of triplet pulses for a given star could be compared unambiguously to known separations of candidate stars, and a matching of triplets to corresponding stars accomplished.

Because of the positioning of the SCNS instrument on the ATS vehicle and the direction of the spin axis of the satellite, the optical field of view swept close to the earth and Earth-occulted sun on each scan. In addition, the annular field of view crossed the Milky Way at two points. Consequently, the sensor picked up a great deal of spatial noise which resulted in many spurious detections. This high incidence of noise necessitated the use of digital filtering techniques which were applied as a pre-processing step in the ground-based computer data reduction.

A computer program was written to perform the necessary digital filtering, to identify stars from their transit times, and to calculate the attitude parameters. The principal operations in this program are outlined in the flow chart presented in Fig. 7. These operations are briefly described as follows:

1. From the raw transit time data, determine the scan period to within approximately one part in  $10^5$ . This is accomplished by constructing a histogram of transit time differences of all (reasonable) differences near the approximate spin period (an estimate of the period good to one part in about  $10^5$  was usually available). Then all entries in the most heavily populated cell are averaged to obtain the spin period estimate.
2. Reduce all transit times within an interval covering approximately 20 scans modulo the scan period estimate from Step 1. This "folds" all of the data back to the first scan interval, and a pulse count histogram is built up over the scan. Peaks in the histogram are then selected as corresponding to repeatable transits. In effect, a multi-scan correlation is performed and used to reject random spurious detections. For each selected cluster of repeatable transits, the reduced average transit time (in the first scan) is computed.
3. Search through the set of reduced average transit times to locate triplets of repeatable pulse clusters. Triplet selection is based on the symmetry of the slit pattern about the center slit; equal spacing from

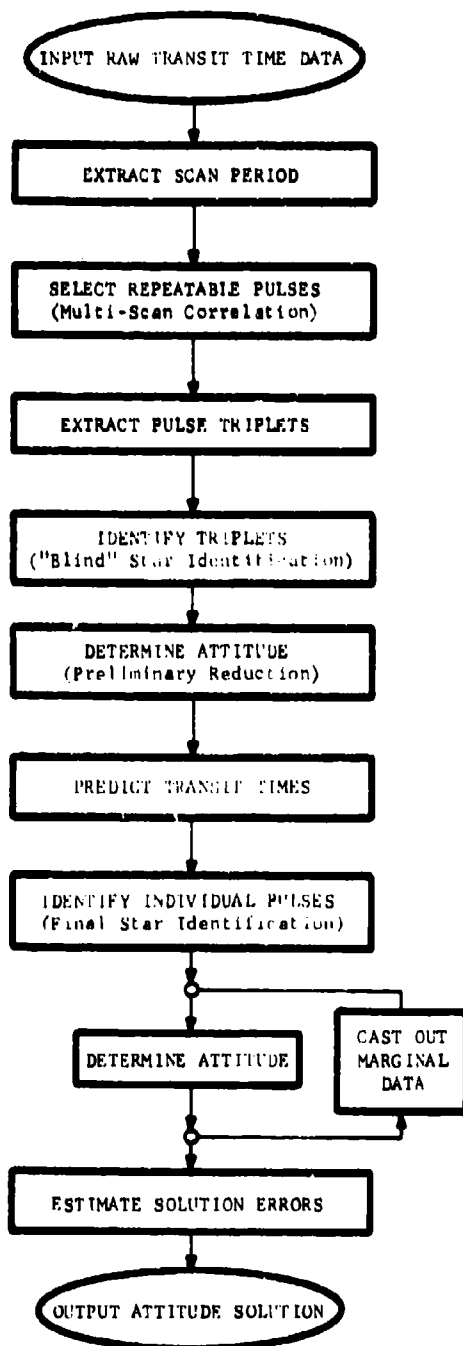


Fig. 7. Flow Chart of the Major Steps in the SCNS Attitude Determination Computer Program

first-to-second and second-to-third pulses is sought. The triplets which arise are then regarded as candidate stellar detections. This step completes the preprocessing phase.

4. Identify as many triplets as possible with known stars. This is the "blind" star identification operation and its implementation may be illustrated by reference to Fig. 8. The apparent

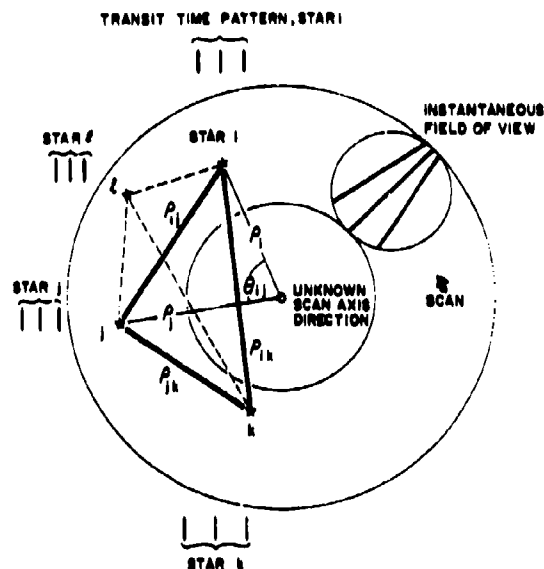


Fig. 8. Geometry of the "Blind" Star Identification

co-elevation,  $\rho_i$ , of target  $i$  with respect to the as yet unknown scan axis direction may be inferred from the pulse-to-pulse separation internal to triplet  $i$ , the scan period estimate, and the known slit geometry. Further, the azimuth separation,  $\theta_{ij}$ , between targets  $i$  and  $j$  may be inferred from the scan period and the reduced average transit times of the corresponding center slit transits. Once  $\rho_i$ ,  $\rho_j$ , and  $\theta_{ij}$  are known, only a simple application of spherical trigonometry is required to compute the angular separation,  $\rho_{ij}$ , on the celestial sphere between targets  $i$  and  $j$ . But this apparent separation on the celestial sphere between any two stars is an invariant quantity independent of the particular scan axis from which they are sensed. Thus, a catalog listing star pair separation is searched and all pairs which agree with  $\rho_{ij}$  to within some tolerance are listed as potential matches with targets  $i$  and  $j$ . This procedure is also applied to

target pairs (i, k) and (j, k). The lists of potential matches are then searched for a linkage of three stars which closes on itself as follows:

Target separation	$P_{ij}$	$P_{jk}$	$P_{ik}$
Potential star-pair	a-c	b-c	f-h
matches (a, b, ...	f-r	d-m	p-w
are star index	q-s	h-r	t-x
numbers)	...	...	...

The corresponding targets are then identified with the stars in the linkage. If additional triplets are present (such as  $l$  in Fig. 8), then confidence in the identification is greatly strengthened by matching these new triplets with catalog stars. For the case shown in Fig. 8, the star identified with target  $l$  must have three matching separations with the corresponding three stars already identified with i, j, and k. After as many triplets are identified as possible, the identifications of both star number and slit number are assigned to each original transit time which entered into the corresponding repeatable pulse cluster.

5. Perform a least squares solution of the set of constraint equations [Eqs. (3)] associated with these identified transit times; the result is a preliminary attitude state vector determination. Note that the components of the state vector enter Eqs. (3) in a non-linear manner so the equations are first linearized and an iterative solution is required.
6. Predict transit times for all possible target stars in the annular field of view on the basis of the attitude solution obtained in Step 5.
7. Match the predicted times with individual measured transit times. This step comprises the final detailed star identification operation.
8. Perform the least squares iterative attitude determination on the final set of identified transit time data. Once the solution has converged, the residuals for the individual transit times are examined and data which fits the solution rather poorly is cast out. This process tends to delete misidentified or inaccurately detected transits. The attitude solution is then repeated with the restricted data set.
9. Estimate the errors in the attitude parameters from the internal consistency (functional residuals) of the overdetermined system of equations. The process is then completed with the output of the

attitude state vector and its estimated standard deviation.

The background description is concluded with a brief history of the operation of the SCNS attitude experiment.

#### E. Experiment Operation

ATS-III was launched in November of 1967. However, operation of the SCNS experiment was not attempted until 13 March 1968 when the satellite was in the shadow of the earth and thus completely shielded from direct sunlight for a brief segment of each orbit. Indeed, up to that time the spacecraft was continually sunlit and the sun's position lay directly in the SCNS annular field of view.

Data was then collected with the SCNS equipment on 31 separate days over a period spanning 203 days from 13 March 1968 through 4 October 1968. The specific dates of experiment operation and key operational conditions are summarized in Table 1 where the "Day" number is measured from the beginning of 1968. "Eclipse" operation corresponds to the celestial configuration when ATS-III is in the earth's shadow; also, unless it is explicitly noted, the moon is not in the annular field of view.

Table 1. History of SCNS  
Attitude Determination Experiment Operation

Day	Date	Operational Conditions
73	13 March	Spring Eclipse (preliminary experiment check)
93-97	4-6 April	Spring Eclipse
131-133	10-14 May	Spacecraft Sunlit Moon in Annular Field (no useful transit time data obtained)
151	30 May	Spacecraft Sunlit (test of baseline following circuitry)
170-171	18-19 June	Spacecraft Sunlit
193	11 July	Spacecraft Sunlit Moon in Annular Field (moon detection tests)
201-204	19-22 July	Spacecraft Sunlit
249-250	3-6 September	Fall Eclipse Moon in Annular Field (data for lunar navigation experiment)
263	19 September	Fall Eclipse
268-278	24 September -4 October	Fall Eclipse Moon in Annular Field (data for lunar navigation experiment)

As noted in the table, no useful transit time data was obtained for the period covering Days 131 through 135. However, oscilloscope observations of the analog signal from the sensor revealed that star pulses were present in the portion of the scan away from the sun or moon; they were not being adequately detected by the fixed threshold level because of large baseline fluctuations induced by the high light levels from the moon and scattered sunlight. The detection electronics were modified to include a baseline following threshold level which was tested on Day 151 (30 May). This modification successfully solved the detection problem and useful stellar data was obtained under all following operational conditions--with the spacecraft in direct sunlight or in the earth's shadow and with the moon in or out of the annular field of view. The stellar detection performance of the SCNS instrument is the subject of the next section.

#### IV. DETECTION CHARACTERISTICS

The locations and visual magnitudes of the principal stellar targets in the SCNS annular field of view are shown in Fig. 9. The two clusters consisting of Sirius, Adhara, Wesaen, and Mirzam on one side and Antares, Nunki, and Deneb on the other correspond to the two regions in which the SCNS annulus crosses the Milky Way. The remaining bright star, Fomalhaut, is in a relatively sparsely populated region of the celestial sphere. In addition to these eight bright stars, most of which are also very close to the center of the optical field of view, the full annulus contains 26 more stars down to third

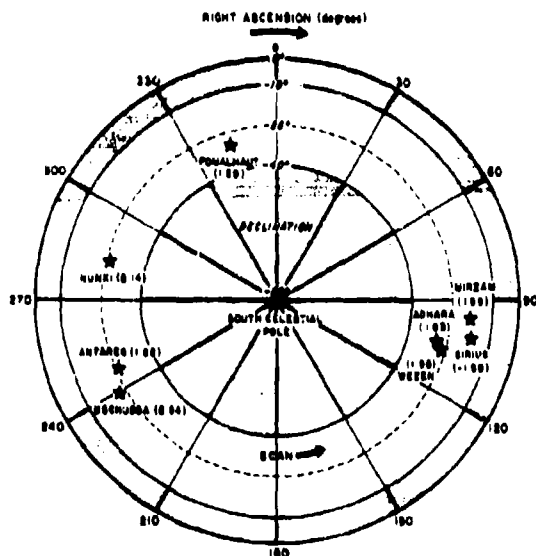


Fig. 9. Target Geometry of the SCNS Effective Annular Field of View Showing the Eight Stars (Plus Visual Magnitudes) Which Were Regularly Detected Under Dark Sky Conditions

magnitude (visual). However, very few of these added stars are near the center of the field and the strong off-axis optical attenuation makes them appear effectively fainter. Further, those few fainter stars which are near the center of the field are fairly red in color; the spectral response differences between the relatively blue-sensitive SCNS instrument and the visual magnitude scale also make these stars effectively fainter. Even so, many of these fainter targets were detected with modest repeatability.

The first observation which strikes one upon examining a set of raw transit time data is that there are many more apparent transits than can be accounted for on the basis of the potential stellar targets--even if all of the moderately bright stars are considered. The results in Fig. 10 were derived after the problem of extracting the stellar information from the spurious

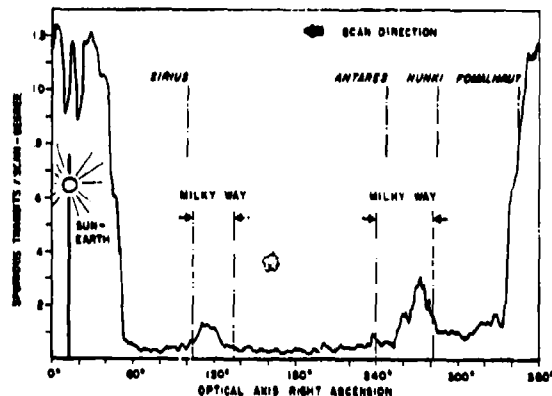


Fig. 10. Typical Noise Pulse Histogram for Dark Sky Conditions (based on data remaining after all transits from identified stellar targets have been removed).

transit background had been solved with the pre-processing correlation described in Section III-D. Nevertheless, these results illustrate the sources of the excess transits. The spurious detection rate (in pulses per degree per scan) which is plotted in Fig. 10 was obtained in the following series of steps:

1. Transit times from highly repeatable detections were extracted from the noisy raw data using multiscan correlation.
2. These transit times were identified and then used to obtain a precise attitude determination on the basis of Model 2.
3. This attitude solution was next used to predict the transit times for all stars which were in the annular field of view and brighter than fourth magnitude.



4. The solution generated times were then compared against the raw transit data and a match was accepted whenever the predicted and measured times agreed to within a tolerance equivalent to the rotational slit width. All data "identified" in this manner was deleted from the list. The original transit times which remained after this matching process were assumed to be spurious.
5. Finally, the distribution of this noise data was found as a function of position in the scan and normalized to a noise frequency in spurious transits per scan degree.

For the results in Fig. 10 (acquired on Day 96), the rate of spurious detections is quite low over the right ascension range from  $30^\circ$  to  $330^\circ$  although there are clearly discernible increases correlated with the two crossings of the Milky Way. The noise sources in this region appear to be primarily the background of faint stars (supported by the Milky Way correlation) and random hard radiation events at the sensor. In particular, visual examination of Visicorder chart recordings of the analog signal reveals occasional isolated pulses of very large amplitude but short duration. These are thought to be due to very compact showers of photoelectrons produced by a single hard radiation event. Indeed, the narrow transit width of such pulses was used to delete them in the preprocessing phase of the data reduction.

The dominant noise detection rates for eclipse operation, however, are correlated with the position of the earth and the earth-occulted sun relative to the scan (see Fig. 10). Although the body of the earth is dark and is not directly in the SCNS field, the edge of the annulus passes within  $1^\circ$  of the earth's south pole. Two effects are significant here. First, because of the great altitude of ATS-III in its synchronous orbit, sunlight may be refracted and scattered to the spacecraft by the earth's atmosphere. The earth will thus have a halo around it which can be seen from the spacecraft. Further, even though direct sunlight is blocked by the earth, the SCNS annulus will cross the zodiac very close to the sun and the scan will sweep to within  $10^\circ$  of the solar position at closest approach. Thus, the SCNS instrument will scan directly through a region of the sky where the background due to zodiacal light will be more than an order of magnitude brighter than the background of faint stars. These two sources, then, may account for the tremendous increase in false detections near the "dark" earth and occulted sun.

As a concluding note to the discussion of the level of spurious data acquired during eclipse operation, it may be observed from Fig. 10 that on Day 96, Fomalhaut was embedded in the edge of the band of sun- and earth-related noise. Nevertheless, this star was regularly detected and its transits were extracted from the background by the multi-scan correlation. Thus,

the preprocessing techniques described here were found to be very effective in isolating the useful data. Indeed, it was found that the entire problem could be solved automatically in cases where there were five times as many spurious transits as reliable stellar detections!

The noise environment became significantly worse for SCNS operation when the satellite was in full sunlight. Although the sun was some distance from the annular field (but never more than  $34^\circ$  away at closest approach), sunlight was directly incident on the inner surface of the minimal baffle over a significant fraction of the scan. Light scattered directly into the optics under these conditions obliterated nearly half the scan. In addition, the detector high voltage supply and the following amplification electronics were saturated by this burst of light and required a time equivalent to approximately 30 additional degrees of the scan to recover after each solar encounter. Thus, a segment of the scan nearly  $210^\circ$  long was lost for data acquisition during sunlit operation. Nevertheless, those bright stars which lay in the remainder of the scan were regularly detected with only a small increase in the transit time variation. This latter decrease in accuracy is attributed to the general increase of internal noise excitation in the detector and following electronics; the spin period was sufficiently rapid so that the system was unable to return completely to a quiescent state before receiving another burst of scattered sunlight.

In addition to the significant level of spurious transits just described, another problem related to the selection of reliable stellar data was encountered. The moderately bright stars in the annular field--Wesen, Mirzam, Nunki, and Deneb--were not regularly detected in every slit on every scan. Indeed, although each star-slit combination was detected with significant frequency when considered alone, a complete triplet of transits from any of these stars was observed only occasionally. The detectability of a particular star on a particular scan exhibited only weak correlation from slit to slit. These intrascan detection fluctuations imply, then, that much of the useful stellar data cannot be located by searching for individual triplets of uniformly spaced transits. Fortunately, however, the multi-scan correlation technique first establishes the repeatability of individual star-slit combinations and only then seeks to locate triplets among these pulse clusters. Thus, the automatic preprocessing in the data reduction deals simultaneously with the problems of extra noise transits and missing stellar transits.

Before turning to the detailed results characterizing the detection performance of the system on individual stellar targets, a brief discussion of effective or "instrument" stellar magnitudes is needed. As noted above, both the SCNS spectral response and the varying off-axis optical attenuation affect the apparent magnitudes of potential target stars. In order to obtain a reasonable spectral correction, the equivalent

black body temperature and intensity coefficient were derived for each candidate star from the visual magnitude and B-V color index for that star. This black body characterization was then combined with spectral information on the lens and photomultiplier to obtain a new relative magnitude. The zero point of this new scale was chosen such that a star of zero visual magnitude and zero B-V index would transform to zero instrument magnitude at the center of the optical field. These color-corrected magnitudes were then modified for off-axis attenuation using measurements obtained during pre-flight tests. Here, all corrections were expressed in a manner such that the final "instrument" magnitudes were normalized to an equivalent magnitude for a star on the optical axis. The specific attenuation corrections could be made, of course, only after the attitude problem had been solved and the off-axis crossing angles were known. It may also be observed here that the side slit transits were further from the optical axis than the center slit transit; thus, the stars were effectively fainter in the side slits. A summary of the instrument magnitudes for the eight principal target stars and for the specific attitude results on Day 263 is given in Table 2.

Table 2. Instrument Magnitudes of SCNS Target Stars

Star	Visual Magnitude	Instrument Magnitude	
		Center Slit	Side Slits
Sirius	-1.58	-0.68	-0.63
Antares	1.22	1.60	1.78
Fomalhaut	1.29	1.41	1.62
Adhara	1.63	1.50	1.70
Wexen	1.98	2.23	2.38
Mirzam	1.99	2.37	2.43
Nunki	2.14	1.97	2.13
Dechubba	2.54	2.28	2.39

There are two key indices of stellar detection performance--the frequency with which individual star-slit combinations are detected and the transit time variation within the set of detections for a particular star and slit. In Fig. 11, observed detection frequencies are plotted as a function of star-slit instrument magnitude for data taken on Day 263. Individual frequencies are simply the ratio of the number of scans on which a particular star-slit was detected and identified to the total number of scans in the data set; the results in Fig. 11 correspond to approximately 650 scans. Only "conflict-free" points have been plotted here. A "conflict" arises when more than one potential target is in the slit pattern (but not necessarily in the same slit) at the same time. This can have two effects. If the targets are very nearly centered in the slits simultaneously, then the apparent detection rate for each is artificially enhanced by the other. On the other hand, if one target is just entering a slit as the other is leaving then the detection frequency for the combined pulse is enhanced but the transit time is distorted and

the identification may be missed. Precisely this type of conflict arose between Sirius and Adhara for one of the three transits of each; a detection was regularly present near the expected location but was paired with Sirius only 12% of the time and was never associated with Adhara in the final star identification.

Figure 11 illustrates the expected gradual detection cut-off as a function of magnitude. The three bright stars--Fomalhaut, Adhara, and Antares--all have nearly the same instrument magnitude and are detected very regularly. The four stars of intermediate brightness are also somewhat clustered in instrument magnitude and are typically seen from 35% to 65% of the time. The group of points beyond magnitude 2.5 and below frequency 0.2 in Fig. 11 represents data from the fainter, marginally detectable stars in the SCNS annulus. Although the clustering of instrument magnitudes into three fairly distinct and compact sets precludes an unambiguous interpretation, the results in the plot do suggest that the cut-off extends over approximately one stellar magnitude. This broad range of intermediate frequencies may be attributed to a combination of statistical variations in the additive

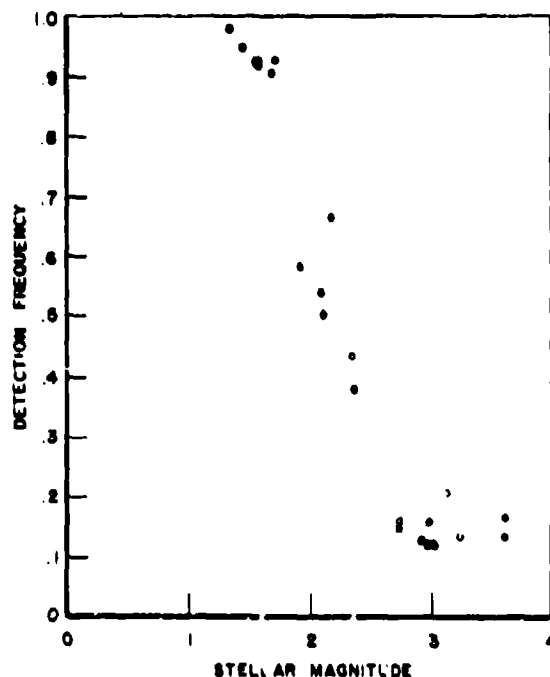


Fig. 11. Star Detection Frequency as a Function of Effective Stellar Magnitude for Typical Dark Sky Operation.

(The "effective" magnitudes have been corrected both for the relative spectral response of the SCNS sensor and for varying off-axis optical attenuation. The latter correction differs from slit to slit on the same star.)

background noise and to fluctuations in the photon arrival rate from the individual moderate-brightness target stars. The rapid spin rate of the ATS-III spacecraft provides a very short "integration time" for the collection of stellar photons as each slit transits the star.

Results for the complementary index of stellar detection performance--viz., transit time accuracy--are shown in Fig. 12. Here, the RMS transit time residual for the center slit detections of each of the eight principal SCNS targets is plotted against the corresponding instrument magnitude. Again, the results are taken from Day 263 and involve several hundred detections per star. Since each individual transit time residual is a measure of the accuracy with which the associated transit time "fits" the final least-squares attitude solution, the data in Fig. 12 demonstrates the rather strong correlation between target intensity and transit time variation for stars in the vicinity of detection cut-off. In terms of scan azimuth angle, the detection variation ranges from 23 arc-seconds for transits of Sirius to 36 arc-seconds for transits of Fomalhaut and finally to 76 arc-seconds for transits of Mirzam. Since the rotational slit width is 7.6 arc-minutes, these detection variations correspond to effective slit interpolation factors of 20, 12.5, and 6, respectively. Thus, the use of a moderately wide slit to improve the photon integration capabilities of the sensor while still maintaining accuracy in the resulting detected transit times is clearly demonstrated.

One aspect of detection performance--the recovery of the system after an encounter with a

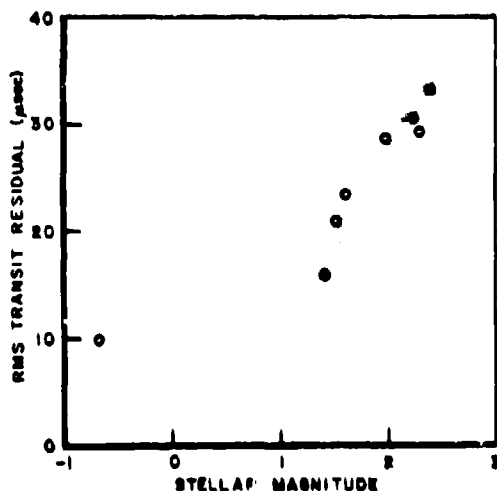


Fig. 12. Transit Time Residuals as a Function of Instrument Magnitude--Data for Center Slit Transits Only, Day 263. One microsecond of time corresponds to 2.3 arc-seconds of scan rotation.

bright source--remains to be discussed in more detail. The effects of operation with the spacecraft in full sunlight have already been briefly described. However, much of the experiment operation was carried out with the moon directly in the annular field of view (see Table 1) and the associated sensor behavior was extensively investigated. In particular, during the data collection operations on Days 249 through 250 and again over the entire period from Day 268 through 278, the moon occupied a sequence of positions in the vicinity of Dschubba, Antares, Nunki, and Fomalhaut. Each of these stars was completely obliterated by the effects of the moon for some of these configurations; the results are summarized in Fig. 13. Here, the relative detectability of each star is plotted as a function of its azimuth separation from the moon. The "relative detectability" values were obtained through two normalization steps applied to the original detection frequencies for each star and each data collection operation. On a given day, all of the detection frequencies for the four stars of interest were divided by the detection frequency for the center slit of Adhara. This latter star was well away from the location of the moon, and it was therefore used as a detection standard to eliminate the effects of slight variations in threshold settings from day to day. The second normalization consisted of dividing each of the detections for a particular star by the detection frequency observed for that star on Day 263 (each divisor was also normalized with respect to detections of Adhara on Day 263). The moon was completely out of the field on the latter date. Thus, the frequencies for Day 263 were treated essentially as measures of the intrinsic detectability of each star. From Fig. 13, it may be observed that the scan prior to the moon is affected only when the moon has essentially entered the optical field. Following the lunar encounter, however, the system sensitivity remains degraded over a larger azimuth angle. This is attributed to the time required for the detector, its power supply, and the following electronics to recover from saturation; the recovery angle is similar to the value noted above for the recovery from a strong burst of scattered sunlight. In any event, the presence of the moon directly in

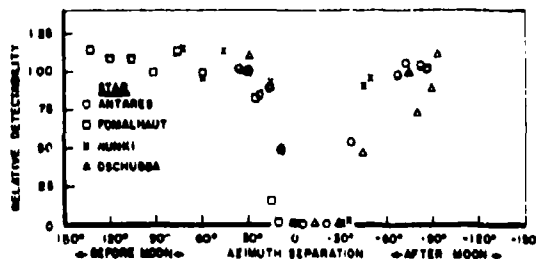


Fig. 13. Relative Stellar Detectability as a Function of the Azimuth Separation from the Moon to the Target Star. In all cases, the moon is in the field of view.

the annular field appears to delete about 50° of azimuth from the useful scan (except, of course, for moon transits) but to leave the remainder of the scan essentially unaffected. This is a remarkably short time for full recovery given the rapid spin rate of ATS-XII.

#### V. ATTITUDE RESULTS

The aspects of the system described up to this point are all significant but subsidiary to the primary goal--precision determination of the time dependent spacecraft orientation. It was anticipated that the spacecraft might exhibit significant precession so the preliminary data taken on Day 73 (13 March 1968) was reduced using attitude Model 1. The results for four different intervals of data, each covering approximately 25 rotations of the satellite, are summarized in Table 3. A number of features emerge. First, the direction of the total angular momentum is seen to lie very close to the South Pole--within 14 arc-minutes. Second, the results for the nutation cone angle,  $\theta$ , are bounded by 0.5 arc-minute. Also, Cases 1 and 2 (or 3 and 4) use a common initial time and one would expect the values for both  $\dot{\phi}_0$  and  $\dot{\psi}_0$  to remain the same from one solu-

tion to the next. Since they do not, it is concluded that the precession and nutation damper is very effective and that the determination of  $\theta$  is in the noise; the effects of precession and spin cannot be reliably separated. It may be observed, however, that the sums  $(\dot{\psi}_0 + \dot{\phi}_0)$  and  $(\dot{\psi} + \dot{\phi})$  are well defined. Thus, the general precession model was abandoned in favor of Model 2 which assumes that the satellite spins about a fixed axis. This latter model was employed in all subsequent reductions of attitude data, and its use was justified by the small residuals associated with the solutions.

Typical solutions obtained using Model 2 with data taken during the spring eclipses are presented in Table 4. For these reductions, the time interval over which the data was gathered was sufficiently long to exhibit a non-negligible spin acceleration ( $\ddot{\phi}$ ) due to the cooling and contraction of the spacecraft in the earth's shadow. The  $\ddot{\phi}$  term, however, was assumed to be identically zero.

Also shown in Table 4 are estimates of the standard deviations of the eight variable components in the state vector; these were obtained

Table 3. Solution for Precession Model (Day 73 Data, 10 Unknowns)

	Half Cone (Nutation) Angle	Initial Spin Angle	Spin Rate	Initial Precession Angle	Precession Rate	Angles Which Define Location of Slits			Right Ascension & Declination of Angular Momentum	
Case No.	$\theta$ deg	$\psi_0$ deg	$\dot{\psi}$ deg/sec	$\phi_0$ deg	$\dot{\phi}$ deg/sec	$\sigma$ deg	$\Gamma$ deg	$\epsilon$ deg	$\alpha$ deg	$\delta$ deg
1*	.008	-68.720	-21.935	-34.255	598.042	84.272	-11.057	.192	64.81	-89.782
2*	.003	51.419	-18.211	185.589	594.318	84.294	-11.170	.186	66.53	-89.768
3**	.005	106.187	-22.589	117.065	598.595	84.373	-11.122	.186	62.42	-89.772
4**	.003	104.132	-22.445	119.117	594.451	84.391	-11.114	.184	60.43	-89.773

\*, \*\* indicate cases which had common initial times.

Table 4. Summary of Attitude Results from Data Taken on Days 73 and 96.  
(Simple Accelerated Spin Model with  $\ddot{\phi} = 0$ ,  $\Sigma$  = RMS Value of Residuals of Least Squares Solution ( $\mu$ sec))

Day	$\theta_0$ deg	$\dot{\theta}_0$ deg/sec	$\ddot{\theta}_0$ deg/sec <sup>2</sup>	$\Gamma$ deg	$\epsilon$ deg	$\sigma$ deg	$\alpha$ deg	$\delta$ deg	No. of Transits	$\Sigma$ $\mu$ sec	Total Data Interval sec
73	256.694	575.9005	.00012	-11.1688	.193	84.280	61.27	-89.748	444	31.8	104
96	47.497	576.3982	.00010	-11.0834	.220	84.436	78.548	-89.530	867	34.9	84

Day	$\sigma(\theta_0)$ deg	$\sigma(\dot{\theta}_0)$ deg/sec	$\sigma(\ddot{\theta}_0)$ deg/sec <sup>2</sup>	$\sigma(\Gamma)$ deg	$\sigma(\epsilon)$ deg	$\sigma(\sigma)$ deg	$\sigma(\alpha)$ deg	$\sigma(\delta)$ deg
73	9.44	.446	.0078	32.26	29.33	54.17	.621	12.93
96	11.92	.391	.0089	35.13	26.65	67.26	.211	10.62

from the residuals of the final solutions. It is seen that all parameters are quite accurately determined except for  $\sigma$  (the co-elevation of the slit vertex) and  $\alpha$  (the right ascension of the spin direction). The slit parameter,  $\sigma$ , is poorly determined because the angle between the center slit and each outer slit is relatively small (11°10'20") while the useful target stars have a very small spread in co-elevation with respect to the spin direction. For precisely these same reasons, however, the other unknowns in the state vector are insensitive to errors in  $\sigma$ . The large estimate for the standard deviation in  $\alpha$  arises simply from the fact that the spin axis is close to the South Celestial Pole; the right ascension is poorly determined there but a large error in  $\alpha$  results in a rather small error in the pointing direction.

One further observation may be made from the results in Table 4; the spin axis direction changes significantly between Days 73 and 96. This change is attributed to a spacecraft maneuver which was performed on Day 82. The entire history of the ATS-III spin axis pointing direction as determined by the SCNS experiment is traced in Fig. 14. Note that the spin axis was never further than 1.1° from the South Celestial Pole, but its right ascension varied by almost 180° over the time interval from Day 73 to Day 278. No spacecraft maneuvers were performed during the period from Day 171 to 278 so the drift in pointing direction must be attributed to small external torques acting on the satellite. A more detailed plot of the right ascension and

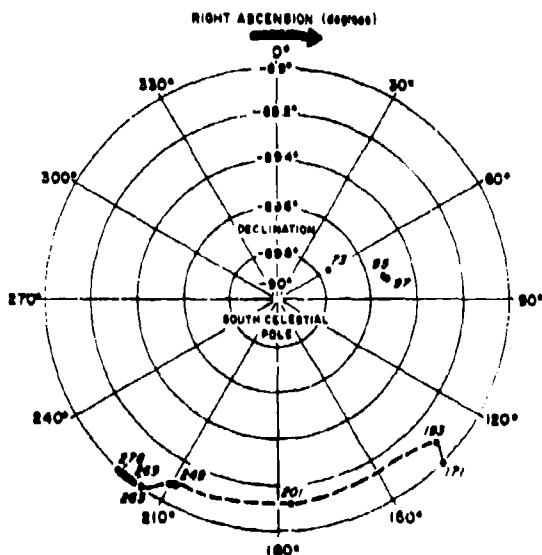


Fig. 14. Direction of the ATS-III Spin Axis as Determined by the SCNS Experiment for Various Dates in 1968. No spacecraft maneuvers were performed from Day 95 to 97, nor from Day 171 to 278.

declination of the spin axis on Days 269 through 277 is presented in Fig. 15. These results also clearly demonstrate the small but significant systematic change in both  $\alpha$  and  $\delta$ .

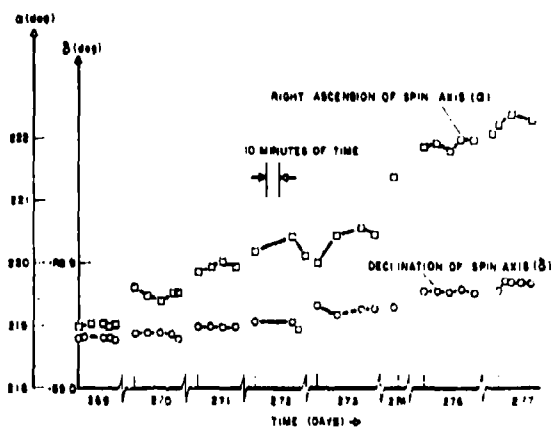


Fig. 15. Direction of Satellite Spin Axis as a Function of Time on Days 269 to 277. (Time measured from the beginning of 1968.)

The attitude results as just described are of fundamental interest to the total operation of the spacecraft. However, from the standpoint of the experimental nature of SCNS, the attitude solution error characteristics are more interesting. Of course, an attitude reference of higher precision than SCNS is not available on the spacecraft so error estimates can only be obtained by examining the internal consistency of the SCNS results. Two methods of obtaining such estimates were used.

The first approach exploited the fact that the least-squares solutions involved hundreds of transits from eight independent targets. Thus, both the spatially independent variables (the spin axis direction, the azimuth at the reference time, and the slit parameters) and the time related rates and accelerations were highly overdetermined. Under these conditions, the residuals in the least-squares solutions may be used to estimate the standard deviations in the determinations of the state vector components. An example of this approach has already been exhibited in Table 4 in connection with results from operation in the spring eclipses. Note that when the full scan is available, the target geometry is excellent (Fig. 9) and the errors in each of three spacecraft axes is on the order of ten arc seconds (Table 4).

During the summer months, when the satellite was in full sunlight, only two or three of the stars were acquired from the set consisting of Dachubba, Antares, Nunki, and (occasionally) Fomalhaut. This resulted in significantly poorer target geometry. Also, as has already been

mentioned, the variation in the transit times from those star-slit combinations which were detected was increased by the noise environment. Under these circumstances, it was not possible to solve for the slit parameters--they were treated as known. Even so, the estimate for the standard deviation in the pointing direction determination is only 1.5 minutes of arc.

Finally, the alternative approach to evaluating internal consistency in the attitude solutions was applied to data obtained during the full eclipses. This method consists of separating the original transit time data into subsets of completely independent but interleaved detections. The solutions based on these various subsets are then independent of one another and the spread in the determination of each unknown is a measure of the solution consistency. The results for a set of five such determinations from the data acquired on Day 263 are displayed in Table 5. Here, a significant and reasonably repeatable  $\delta$  term has been determined. Note also that spreads in the determinations of the three spacecraft axes-- $\Delta\alpha_0$ ,  $\cos \delta \Delta\alpha$ , and  $\Delta\delta$ --are each on the order of ten arc seconds. These values are thus very consistent with the standard deviation estimates described above. In conclusion, then, the root sum square three-axis attitude errors appear to fall in the range of 12 to 20 seconds of arc.

## VI. CONCLUSIONS

The attitude determination portion of the SCNS experiment on ATS-III was successfully operated on a number of different dates spread over a 205 day period from 13 March to 4 October 1968. Data was acquired both when the satellite was within and out of the earth's shadow. This data was reduced off-line but with an operational computer program which fully automated the tasks of pre-processing data selection, star identification, attitude determination, and error estimation.

For operation in full sunlight, it was found that the sensor was able to recover from its extensive solar encounter on each scan and to detect two or three bright stars within a narrow azimuth band. Even, in this case of very poor target geometry, the accuracy of the determination of the spin axis direction was on the order of 1.5 arc minutes. For an operational as opposed to experimental system, however, more elaborate sun shielding would clearly be desirable and is recommended. Finally, when the spacecraft was in the earth's shadow, both the number and distribution of useful stellar targets improved and the full potential of the system was more nearly demonstrated. In these cases of good target geometry and reasonably dark sky conditions, the root sum square three axis attitude errors decreased to lie within the range from 12 to 20 arc seconds.

## ACKNOWLEDGMENT

The authors wish to express their thanks to Mr. Forrest H. Waincott of the ATS Project Office, Goddard Space Flight Center, for his helpful insights and active participation during the course of this effort.

## REFERENCES

1. Final Report: Self-Contained Navigation Experiment, Contract No. NAS5-9683, prepared by Control Data Corporation, for NASA-Goddard, July, 1969.
2. C. F. Groch, "Orientation of a Rigid Torque-Free Body by Use of Star Transits," Journal of Spacecraft and Rockets, Vol. 4, No. 5, pp. 562-566.

Table 5. Attitude Solutions for Completely Independent but Interleaved Sets of Data (Day 263, 9 Unknowns)

Group	$\alpha_0$ deg	$\dot{\alpha}$ deg/sec	$\ddot{\alpha}$ deg/sec <sup>2</sup>	$\dddot{\alpha}$ deg/sec <sup>3</sup>	$\Gamma$ deg	$\epsilon$ deg	$\sigma$ deg	$\alpha$ deg	$\delta$ deg
(1)	266.170	637.0246	$1.247 \times 10^{-4}$	$-2.485 \times 10^{-8}$	-11.0964	0.463	84.203	216.551	-88.999
(2)	266.168	637.0246	$1.247 \times 10^{-4}$	$-2.379 \times 10^{-8}$	-11.0904	0.458	84.220	216.668	-88.999
(3)	266.170	637.0246	$1.247 \times 10^{-4}$	$-2.304 \times 10^{-8}$	-11.0985	0.463	84.209	216.643	-88.999
(4)	266.169	637.0246	$1.246 \times 10^{-4}$	$-1.926 \times 10^{-8}$	-11.0916	0.458	84.213	216.604	-89.002
(5)	266.167	637.0246	$1.248 \times 10^{-4}$	$-2.566 \times 10^{-8}$	-11.0937	0.459	84.211	216.760	-89.000
Spread	0.003	--	$0.002 \times 10^{-4}$	$0.640 \times 10^{-8}$	0.0081	0.005	0.015	0.209	0.003

# THE DEVELOPMENT AND PERFORMANCE OF AN ATTITUDE DETERMINATION DATA REDUCTION AND ANALYSIS SYSTEM<sup>1</sup>

G. R. Arneson and G. D. Nelson  
Honeywell Inc.,  
Minneapolis, Minnesota

## ABSTRACT

An Attitude Determination (A/D) data reduction and analysis system is described. The system's basic capabilities are: The reduction of starmapper and sun sensor data to estimates of spacecraft state, generation of simulated starmapper and sun sensor data, and an on-line analysis capability. A nonlinear Kalman-type estimation algorithm is used in the system to reduce sensor outputs to estimates of vehicle rates, attitude, and parameters. Conceptually, the spacecraft is spin stabilized and uncontrolled during data gathering with the spin axis nominally oriented normal to the orbit plane. A discussion of the spacecraft dynamics and estimation algorithms is included, along with results which demonstrate attitude accuracy as a function of such parameters as instrument noise and number of celestial sightings per vehicle spin period.

## INTRODUCTION

For the purpose of this paper, the Attitude Determination problem is defined to be the estimation of spacecraft rates, attitude, and parameters by means of ground-based data processing of starmapper and sun sensor data. Conceptually, the A/D system under consideration consists of a passive starmapper and sun sensor instrument system fixed in the spacecraft, an on-board data handling and filtering subsystem, and ground data processing of the starmapper and sun sensor outputs to yield estimates of spacecraft attitude. Within this context, two topics are discussed. First, the capabilities of an attitude determination system simulation are described. Second, results of studies using the simulation are presented.

The simulation is designed to simultaneously satisfy several requirements:

- Operational Requirement - Missions of a year's duration or longer are contemplated. Thus, to prevent backlogging of data, the chosen estimation algorithms must be capable of providing estimates of spacecraft state in significantly faster than real time on existing computers.

- General Applicability - The contract objectives are to provide a simulation applicable to a class of applications rather than to a specific mission. Consequently, a system treating a wide selection of parameters as variables for data reduction studies is required.
- Display Capability - A computer system with a versatile display is necessary to enable the analyst to realize a thorough understanding of the operation and performance of the data reduction algorithms.

To satisfy these requirements the following features have been incorporated into the simulation:

- An accurate and computationally efficient mathematical model of the spacecraft dynamics and torques affecting the spacecraft rotational dynamics. External disturbance torques due to eddy currents, residual magnetic moment, gravity gradient, and solar and aerodynamic pressure are included in the model to generate simulated star and sun sensor outputs. For the attitude determination data reduction the first two torques are included in the spacecraft model.

<sup>1</sup>This work done under Contract NAS1-8801, August 1969

- Kalman filtering of sensor outputs to yield estimates of spacecraft rates, attitude, and parameters.
- Identification of stars causing sensor outputs by using algorithm estimates of attitude during the normal sequential data processing.
- An on-line analysis and control utilizing cathode ray tube display to provide access to any variable of interest and simulation control functions.

### NOTATION

$t$	Time, independent parameter
$t_s$	Star (or sun) transit times
$\omega_x, \omega_y, \omega_z$	Spacecraft angular rates, principal body axes
$\psi, \phi, \theta$	Euler angles parameterizing the rotation from inertial to body coordinates
$I_1, I_2, I_3$	Spacecraft moments of inertia
$A, C$	Inertia ratios $I_1/I_2$ and $I_3/I_2$
$\bar{M}$	Spacecraft residual magnetic moment coefficient vector divided by $I_2$
$K$	Spacecraft eddy current coefficient, divided by $I_2$
$\bar{X}$	Variable dimension estimation state vector
$\bar{f}(\bar{X})$	Functional representation of $\dot{\bar{X}}$
$P$	Covariance matrix
$( )^T$	Denotes matrix or vector transpose
$f_x$	Jacobian matrix, $\partial \bar{f} / \partial x$
$e$	Measurement error
$H$	Measurement model
$\bar{H}_x$	$\left[ \frac{\partial H}{\partial x_1}, \dots, \frac{\partial H}{\partial x_n} \right]$
$\sigma_H^2$	Measurement variance
$\Phi(k, k-1)$	State $n \times n$ transition matrix relating linearized state from time $t_{k-1}$ to time $t_k$
$W$	Square root of covariance $P = WW^T$
$( )_b, ( )_a$	Denotes quantity before and after application of corrections due to measurement error
$(^*)$	Denotes unit vector
$\hat{U}$	Unit normal to slit plane
$\hat{S}$	Star (or sun) vector in inertial space

$\sigma_I^2$	Variance of instrument noise
$( )_B$	Denotes vector in body coordinates
$( )_I$	Denotes vector in inertial coordinates
$\hat{O}$	Optical axes of starmapper (sun sensor)
fov	Field of view of starmapper (sun sensor)
$\epsilon_1, \epsilon_2, \epsilon_3$	Angles parameterizing the offset of the experimental w.r.t. the spacecraft axes
$\gamma$	Cant angle, with zero offset, the angle between the optical axis, and the y body axis
$\beta$	Rotation angle of slit plane about the optical axis
$\alpha, \delta$	Right ascension, declination of star (sun)

### SIMULATION DESCRIPTION

Two major functions are performed by the simulation. The primary function is the reduction of starmapper and sun sensor measurements to spacecraft attitude estimates. Secondly, in lieu of actual transit data, simulated transit data is generated. Thus the simulation, which exists as a single operational computer program, encompasses both the major hardware and software aspects of the problem.

Because of its simplicity and non-iterative structure, the nonlinear Kalman filter mechanized to process transit data sequentially in time is used for the estimation algorithm. Sequential processing of transit data, as opposed to batch processing, provides a distinct advantage when applied to an operational system. In such a system the identification of stars causing the transit is in itself a formidable problem and one that must be solved before the data can be used for attitude estimation. However, after an initial period of convergence, the attitude estimates generated by the sequential estimation provide the necessary information to perform the star identification in parallel with, rather than prior to, the estimation. Two formulations of the filter are mechanized in the simulation - a conventional mechanization and the so called "square root" formulation in which all covariance computations are performed with the square root of the covariance matrix rather than with the covariance matrix itself. While the conventional formulation and the square root are analytically equivalent if additive noise is not considered, numerical errors do not cause the covariance matrix to become negative definite in the latter, thus circumventing one formidable problem in the practical application of the filter.

Estimation of vehicle rates, Euler angles, inertia ratios, and magnetic moment and eddy current coefficients is possible with the simulation.



The following paragraphs provide a detailed description of the system.

#### Spacecraft Model

Vehicle motion and orientation are described by the angular rates about the principal body axes and Euler angles parameterizing the rotation sequence from inertial to body coordinates. A yaw, roll, pitch sequence given by rotations

- $\psi$  about the inertial z axis
- $\phi$  about the first displaced x axis
- $\theta$  about the second displaced y axis

is used for the parameterization. A right-hand inertial coordinate system defined by the x axis pointing toward the first point of Aries and the z axis pointing toward Polaris is assumed.

These variables satisfy the first-order non-linear differential equations:

$$\dot{\omega}_x = [\omega_y \omega_z (1 - C) + \tau_x] / A$$

$$\dot{\omega}_y = [\omega_x \omega_z (C - A) + \tau_y]$$

$$\dot{\omega}_z = [\omega_x \omega_y (A - 1) + \tau_z] / C$$

and

$$\dot{\psi} = [-\omega_x \sin \theta + \omega_z \cos \theta] / \cos \phi$$

$$\dot{\phi} = \omega_x \cos \theta + \omega_z \sin \theta$$

$$\dot{\theta} = \omega_y - \dot{\psi} \sin \phi$$

where  $\tau$  represents the total external disturbance torque acting upon the spacecraft and A and C are the inertia ratios  $I_1/I_2$  and  $I_3/I_2$ .

Distinct torque models are employed for the generation of simulated transit data and the attitude determination data reduction. For the latter, the two most prominent torques, magnetic moment and eddy current (single coefficient) are included in the model. For the former, the gravity gradient, solar pressure, aerodynamic pressure, three coefficient eddy current and magnetic moment torques are modeled. Ref. 1 contains a detailed description of these torques.

From the rotations described it is seen that a vector in inertial space is given in body coordinates by the transformation

$$\bar{X}_B = P(\psi, \phi, \theta) \bar{X}_I$$

where

$$P = \begin{bmatrix} \cos \psi \cos \phi - \sin \psi \sin \phi \sin \theta & \cos \psi \sin \phi + \sin \psi \sin \phi \sin \theta & -\sin \psi \cos \theta \\ \sin \psi \cos \phi + \cos \psi \sin \phi \sin \theta & \sin \psi \sin \phi - \cos \psi \sin \phi \sin \theta & \sin \theta \\ \sin \phi \cos \psi + \cos \phi \sin \psi \sin \theta & \sin \phi \sin \psi - \cos \phi \cos \psi \sin \theta & \cos \theta \end{bmatrix}$$

Figure 1 illustrates these rotations.

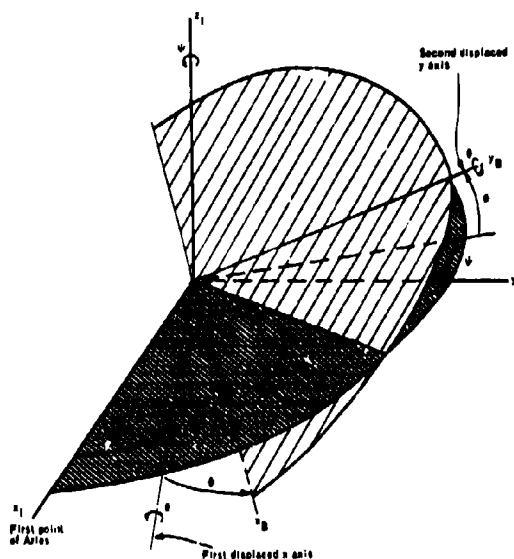


Fig. 1. Rotations from Inertial to Body Coordinates

Since in practice the experimental frame, defined by the starmapper and sun sensor instruments, may differ from the desired body axes frame, small displacements of this frame from the body frame are treated by the introduction of the following sequence of rotations

- $\epsilon_1$  about the z body axis
- $\epsilon_2$  about the first displaced x axis
- $\epsilon_3$  about the second displaced y axis

These relate a vector in body coordinates to the experimental frame by

$$\bar{X}_E = D(\epsilon_1, \epsilon_2, \epsilon_3) \bar{X}_B$$

where

$$D = \begin{bmatrix} \cos \epsilon_1 \cos \epsilon_2 - \sin \epsilon_1 \sin \epsilon_2 \sin \epsilon_3 & \cos \epsilon_1 \sin \epsilon_2 + \sin \epsilon_1 \sin \epsilon_2 \sin \epsilon_3 & -\sin \epsilon_1 \cos \epsilon_3 \\ \sin \epsilon_1 \cos \epsilon_2 + \cos \epsilon_1 \sin \epsilon_2 \sin \epsilon_3 & \sin \epsilon_1 \sin \epsilon_2 - \cos \epsilon_1 \sin \epsilon_2 \sin \epsilon_3 & \sin \epsilon_3 \\ \sin \epsilon_2 \cos \epsilon_1 + \cos \epsilon_2 \sin \epsilon_1 \sin \epsilon_3 & \sin \epsilon_2 \sin \epsilon_1 - \cos \epsilon_2 \sin \epsilon_1 \sin \epsilon_3 & \cos \epsilon_3 \end{bmatrix}$$

It is noted that these rotations are identical to those relating inertial to body coordinates.

Orientation of each starmapper or sun sensor slit is specified with respect to the experimental coordinate frame by the cant angle  $\gamma$  and slit plane rotation angle  $\beta$  about the optical axis. Fig. 2 illustrates the orientation of a given slit.

The geometry shows that in the experimental frame the slit normal  $\hat{U}$  and optical axis  $\hat{O}$  are the first and second rows of the matrix, respectively,

$$B = \begin{bmatrix} \cos \beta & \sin \beta \sin \gamma & -\sin \beta \cos \gamma \\ 0 & \cos \gamma & \sin \gamma \\ \sin \beta & -\cos \beta \sin \gamma & \cos \beta \cos \gamma \end{bmatrix}$$

whereas the third row is a unit vector lying in the slit plane and normal to  $\hat{O}$ .

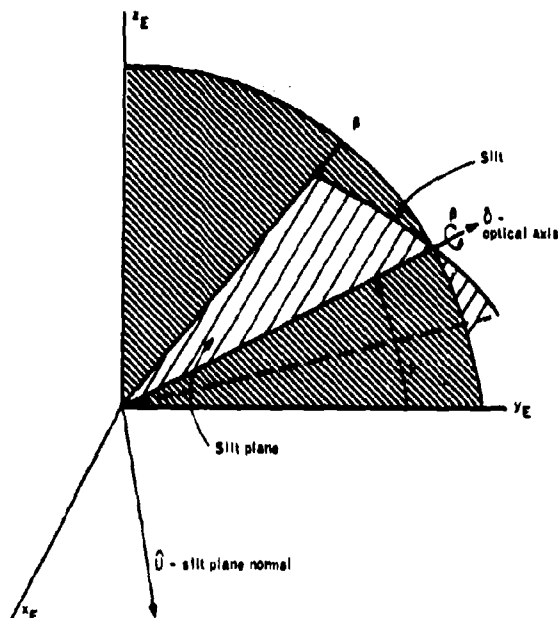


Fig. 2. Slit Plane Orientation

The zenith vector  $\hat{Z}$  from the center of the earth through the spacecraft is specified by the usual orbital parameters - longitude of the ascending node  $\Omega$ , inclination  $i$ , and true anomaly  $u$ . For the nominal case defined by the  $y$  body axis normal to the orbital plane, the Euler angles  $\psi$  and  $\phi$  would equal  $\Omega$  and  $i-90^\circ$ , respectively. The geometry is illustrated in Fig. 3.

#### Measurement Model

Starmapper and sun sensor transits provide the raw data from which spacecraft attitude is deduced. The nonlinear estimation algorithms used for attitude determination require that these transit measurements be modeled analytically to provide a measurement error at the time of transit. The error is computed as the difference between a predicted measurement value and the observed. Since at a transit time the line of sight to the star lies in a plane defined by the slit and optical axis of the instrument, a natural measurement model to employ is the equation which

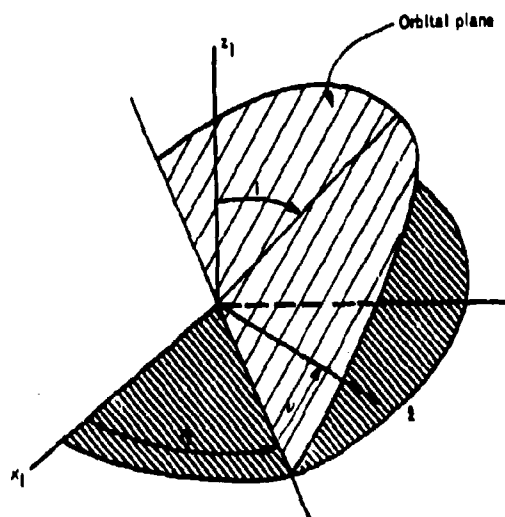


Fig. 3. Orbital Geometry

states that the projection of the vector along the line of sight to the star on the vector normal to the slit plane vanishes analytically,

$$0 = \hat{U} \cdot \hat{S}_B$$

where  $\hat{U}$  is the normal to the slit plane and  $\hat{S}_B$  the star vector, both in body axes. In view of the coordinate transformations described, it is seen that

$$\hat{U} = B_1 D$$

and

$$\hat{S}_B = E(t) \hat{S}$$

Thus, the measurement model which follows is the scalar form

$$H(t) = B_1 D E(t) \hat{S}$$

This provides a measurement error at a transit time given by

$$e(t_y) = 0 - \hat{H}(t_y)$$

where  $\hat{H}$  is the predicted, generally nonzero, value of the measurement.

Alternately, the time at which a transit will occur can be predicted and the error term taken to be the difference of the predicted and measured time. To first order such a measurement model is

$$\dot{H}'(t) = -H(t)/\dot{H}(t)$$

Both models are implemented since the latter exhibits a nonzero sensitivity to the rate variable, whereas the geometric constraint  $H(t)$  does not.

Beside the measurement error, the filtering algorithms require the variance of the measurement. This is derived from an assumed instrument noise  $\sigma_v$ . For the time constraint model  $H'(t)$  the measurement variance is

$$\sigma_H^2 = (\sigma_v / |\bar{w}|)^2$$

while for the geometric constraint

$$\sigma_H^2 = \sigma_H^2 (R_x \dot{X})^2$$

#### Estimation Algorithm

Two formulations of the nonlinear Kalman filter are mechanized in the simulation - a conventional formulation using additive noise and a square root formulation. Both state estimation techniques are implemented to process transit data sequentially in time and as such can be conveniently stated in two parts (Ref. 2). Between transit measurements, the state and covariance are extrapolated by a numerical solution of the differential equations which describe, in some sense, their motion. At a transit measurement, both the extrapolated state and covariance are extrapolated by a numerical solution of the differential equations which describe, in some sense, their motion. At a transit measurement, both the extrapolated state and covariance are updated using the Kalman estimation formula appropriate to the formulation. For state extrapolation, a variable time step, variable order (second, third, or fourth) Runge-Kutta numerical integration is used to solve

$$\dot{X} = f(X), \quad X(t_g) = X_a$$

Covariance extrapolation is accomplished by a variable time step second-order Euler integration. In the mechanization of the conventional estimation formulation covariance is extrapolated by a numerical solution of

$$\dot{P} = P f_x^T + f_x P + Q, \quad P(t_g) = P_a$$

where  $Q$  is an  $n \times n$  diagonal "noise" matrix, determined empirically to prevent the covariance from becoming negative definite. At a transit measurement the state and covariance are updated with

$$X_a = \bar{X}_b + K e$$

and

$$P_a = P_b - \bar{K} \bar{H}_x^T P_b$$

where the gain vector  $\bar{K}$  is

$$\bar{K} = P_b \bar{H}_x^T / (\bar{H}_x P_b \bar{H}_x^T + \sigma_H^2)$$

With the square root formulation (Ref. 3) the covariance

$$P = W W^T$$

is updated implicitly by

$$W_a(s) = W_b(s) - c \bar{K} \bar{g}$$

where

$$\bar{g}^T = W_b^T(s) R_x^T$$

$$c = [1 + \sigma_H (\sigma_H^2 + \bar{g} \bar{g}^T)^{-1/2}]^{-1}$$

with the gain given by

$$\bar{K} = W_b(s) \bar{g}^T / (\bar{g} \bar{g}^T + \sigma_H^2)$$

The covariance is propagated from transit to transit by

$$W_b(s) = \bar{W}(s, s-1) W_a(s-1)$$

where  $W(s-1)$  is the "after" update covariance from the previous transit and  $W_b(s)$  is the "before" update for the current transit and  $\bar{W}(s, s-1)$  is determined by numerical solution of

$$\dot{\bar{W}}(k, k-1) = f_x(t_k) \bar{W}(k, k-1), \quad \bar{W}(k, k) = I.$$

It is noted that initial conditions

$$\bar{X}(t_0) = \bar{X}_0$$

$$P(t_0) = P_0 \text{ (diagonal)}$$

or

$$W(t_0) = \sqrt{P_0}$$

are assumed.

#### Transit Time Model

In lieu of actual transit data, simulated hardware outputs in the form of a sequence of transit time pulses from the starmapper and sun sensor are employed in the data reduction algorithms.

The generation of simulated starmapper and sun sensor outputs requires a simulation of considerable complexity. Its outputs are a series of time values representing the times at which the images of various stars or the sun cross slits in the focal planes of the respective instruments as the instruments are scanned across the celestial sphere by the spacecraft's motion. The situation is illustrated in Fig. 4. It is seen that each transit is characterized by the following conditions.

The line of sight to the celestial body causing the transit lies in a plane defined by the optical axis of the instrument and the slit, or

$$\hat{U}_i \cdot \hat{S} = 0$$

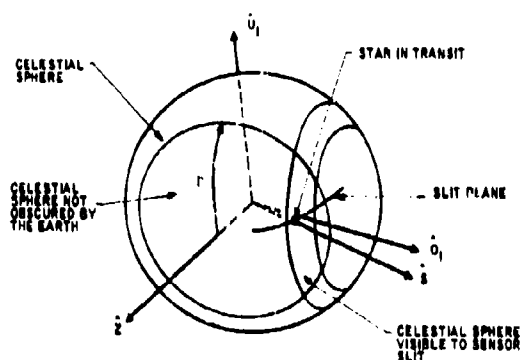


Fig. 4. Transit Geometry

which states that the normal to the slit plane  $\hat{U}_1$  is perpendicular to the star (sun) vector  $\hat{S}$  at the instant of transit.

The celestial body must lie within the field of view (fov) of the instrument, analytically given by

$$-fov \leq 2 \cos^{-1} (\hat{\delta}_1 \cdot \hat{S}) \leq fov$$

This states that the angle subtended by the star vector and the optical axis  $\hat{U}_1$  is less than half the fov of the sensor. The celestial body must not be blocked by the earth, or

$$\hat{S} \cdot \hat{Z} \leq \cos \tau$$

This earth blocking condition is expressed in terms of the zenith vector  $\hat{Z}$  through the vehicle and the earth blocking angle  $\tau$ , which defines the visible region of the celestial sphere not obscured by the earth.

Since the simulated sequence of transit times must depict a "real world" situation, all five torques described in Ref. 1 are normally included in the spacecraft model. The resulting complexity, of course, precludes a closed-form solution of the equations and requires an iterative technique to determine the times of transit. Iteration is accomplished as follows -- a reference solution of the spacecraft equations of motion is established at evenly spaced time increments by numerical integration. Fourth order Runge-Kutta is used. Once per spacecraft rotation crude estimates are made of all transit times which will occur in the next spin period. The crude estimate is determined by solving the equation of motion of the slit normal

$$\dot{\hat{U}}_1 = \bar{\omega}_1 \times \hat{U}_1$$

assuming a constant rate  $\bar{\omega}_1$ . This equation is integrated numerically by trapezoidal rule. The integration is terminated when the Newton Raphson integration step

$$\Delta t = - \frac{\hat{S} \cdot \hat{U}_1}{\hat{S} \cdot (\bar{\omega}_1 \times \hat{U}_1)}$$

becomes sufficiently small for a solution  $\hat{U}_1$  at a test. As the reference solution is generated, the crude time estimates are refined by the same procedure over shortened time spans. Spacecraft attitude is evaluated at each refined estimate and an estimate is accepted as a transit on the condition

$$|\hat{U}_1 \cdot \hat{S}| < \epsilon'$$

for an arbitrary tolerance  $\epsilon'$ .

### On-Line Analysis

To expedite analytical studies with the simulation, an on-line analysis capability utilizing the cathode ray tube (CRT) display is used. This feature is mechanized so that all variables of interest are available for display during a simulation. Beside the basic display capability, considerable simulation control is exercised through the CRT by light pen.

Specific on-line control functions provided by the light pen are: 1) initiation of a simulation, 2) the capability to change variables for display by selection from a displayed directory of variable names with the light pen, 3) the capability to interrupt the simulation at any time during the course of a run whereupon all variables may be observed or parameter changes may be input into the simulation, and 4) a case-to-case display capability permitting the superposition of variables from different simulation cases. Fig. 5 illustrates the display format, showing the display directory, plotted simulation variable, and light-pen control mechanization. Other features incorporated in the display are automatic scaling and variable display window length for modifying the resolution of displayed variables.

Parameter changes necessary for case-to-case studies may be input into the system via teletype at the beginning of a simulation.

As implemented the display provides an extremely versatile and powerful on-line analysis tool, enabling rapid engineering decisions to be made on-line and allowing complete monitoring of the entire simulation.

### SIMULATION RESULTS

In the following paragraphs simulation results are presented which are intended to provide insight into the performance of the attitude determination system which has been described. Some problems in the estimation of inertia ratios are delineated and results given showing attitude accuracy as a function of number of celestial sightings per vehicle spin period, as a function of instrument noise, and as a function of instrument noise uncertainty.

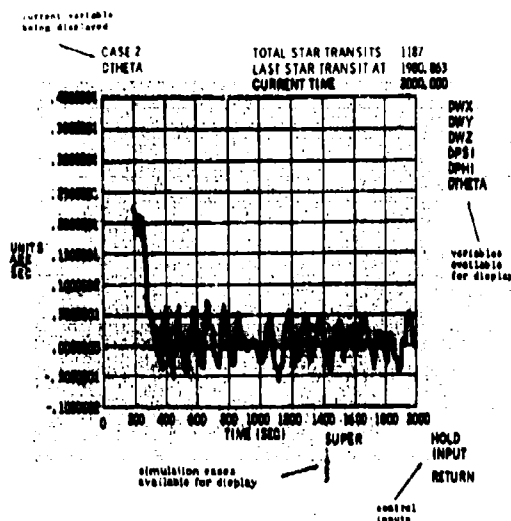


Fig. 5. CRT Display

Transit data for these simulations is described by the following spacecraft initial conditions and parameter values:

$$\dot{\omega} = (0.2094 \text{ deg}, 18 \text{ deg}, 0)/\text{sec}$$

$$\psi = 45 \text{ deg}$$

$$\phi = 190 \text{ deg}$$

$$\theta = 82 \text{ deg}$$

$$I_1 = 54.68 \text{ slug-ft}^2$$

$$I_2 = 65.62 \text{ slug-ft}^2$$

$$I_3 = 54.38 \text{ slug-ft}^2$$

$$\bar{M} = (0.516) 10^{-5} (\hat{i}, \hat{j}, \hat{k})_B \text{ ft-lb/G}$$

$$K = (0.143) 10^{-4} \text{ ft-lb-sec/G}^2$$

All five torques are included in the model. Orbital parameters used are:

$$\Omega = 45 \text{ deg}$$

$$i = 87.38 \text{ deg}$$

$$\omega_0 = 86 \text{ deg}$$

$$\alpha_{\text{sun}} = 0$$

$$\delta_{\text{sun}} = 0$$

with a circular orbit assumed.

It is noted from the initial conditions that the vehicle is spinning at approximately three rpm, is misaligned with respect to the orbit plane by approximately 2.6 deg and has a cone angle of 0.5 deg.

The starmapper is characterized by the cant angle

$$\gamma_{\text{star}} = 110 \text{ deg}$$

and the slit plane rotations

$$\beta_1 = -20 \text{ deg}, \beta_2 = 0 \text{ deg}, \beta_3 = 20 \text{ deg}$$

the sun sensor by

$$\gamma_{\text{sun}} = 45 \text{ deg}, \beta_4 = -20 \text{ deg}, \text{ and } \beta_5 = 20 \text{ deg}$$

A 30-deg fov is assumed for each instrument. A star catalog consisting of the first one-hundred brightest stars (limiting "visual" magnitude of 2.74) is used.

For the data reduction simulations initial condition errors for rates and Euler angles are taken as

$$\Delta \dot{\omega} = (0.2094 \text{ deg}, -0.1 \text{ deg}, -0.1 \text{ deg})/\text{sec}$$

$$\Delta \psi = 0.5 \text{ deg}$$

$$\Delta \phi = 1 \text{ deg}$$

$$\Delta \theta = -1 \text{ deg}$$

These values are arbitrarily chosen since initial condition errors have a negligible effect on the steady-state errors. Although the error limits from which convergence can be obtained are not completely defined, convergence from 5-deg errors in pitch ( $\theta$ ) is possible. Other vehicle parameters values for the data-reduction simulations are

$$\bar{M} = (0., 0., 0)$$

and

$$K = (0.2) 10^{-4} \text{ ft-lb-sec/G}^2$$

Thus, for estimation purposes no knowledge of the spacecraft magnetic moment characteristics is assumed and the eddy current coefficient is grossly in error. Estimation of these parameters is possible with the system. However, the accuracy to which it is possible to estimate these parameters is as yet an unresolved question. Consequently, the above values are used.

## Inertia Ratio Determination

In an operational environment, it can be assumed that, initially at least, the spacecraft principal moments of inertia will not be known with sufficient precision to permit accurate extrapolation of the spacecraft equations of motion. Thus, estimation of the inertia ratios will have to be performed using the algorithms discussed. The following paragraphs describe simulation experiments undertaken specifically to obtain estimates of these parameters.

Results of a first cut at the estimation of the inertia ratios are shown in Figure 6, where the errors in  $A$ ,  $\psi$ ,  $\phi$ , and  $\theta$  labeled DA, DPSI, DPHI, DTHETA, respectively, are plotted. Although the errors are converging at the termination of the simulation, these results are not satisfactory for the mission being simulated. For this mission the spacecraft is in the earth's shadow slightly less than 2000 seconds; consequently, it is desirable to obtain good convergence in this period of time. The poor performance exhibited by the filter in this simulation is due primarily to the relatively large updates experienced by the inertia ratios  $A$  and  $C$  at the first few transit measurements. As seen from Figure 6, the update is not only large but incorrect in sign. This is not too surprising since the initial measurement error primarily reflects the large initial uncertainties in attitude and not the uncertainty in inertias. Since the initial corrections are proportional to the initial assumed variance values, this problem can be controlled by suitably modifying the variances on  $A$  and  $C$ . However, such an approach is undesirable since it is initial condition dependent, and by reducing the initial variances on  $A$  and  $C$  the sensitivity of the filter to uncertainties in the inertias may be lost.

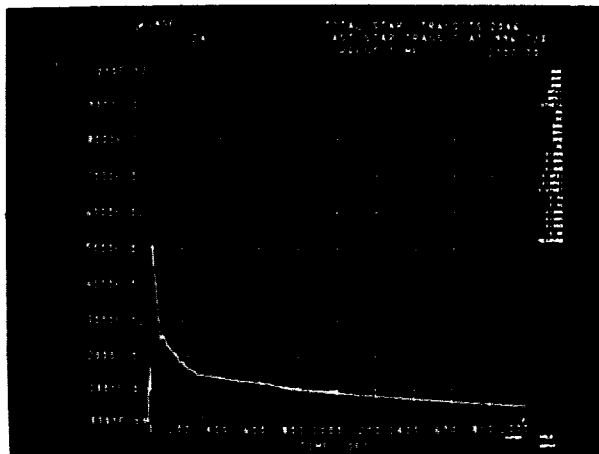


Fig. 6. First Cut Inertia Ratio Estimation Results. (Euler Angle Units are Arc Seconds) -- Continued

Fig. 6. Continued

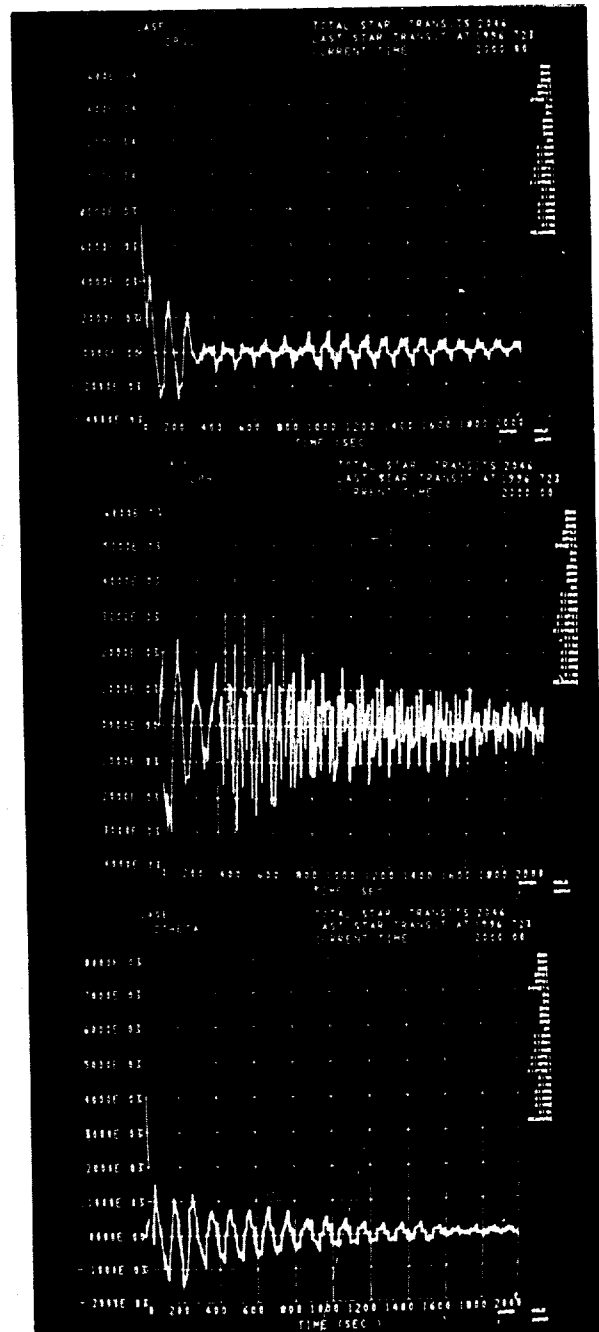


Fig. 6. First Cut Inertia Ratio Estimation Results. (Euler Angle Units are Arc Seconds)

Alternately, estimation of these parameters can be initiated at some time later than the time at which estimation of the vehicle rates and attitude is initiated. With this approach, the objective is to obtain convergence to a measurement error which is primarily due to the uncertainty in the inertia values. Results of two simulations

using this approach are shown in Figures 7 and 8 where errors in  $A$ ,  $\psi$ ,  $\phi$ ,  $\theta$  are plotted for two values of initial uncertainty in  $A$  and  $C$  (not shown). The first 200 seconds of the simulation are not plotted to permit a better choice of scaling. The results indicate the virtue of this approach.

For comparative purposes, it is noted that the simulations illustrated in Figures 6 and 7 are identical in every respect except for the time at which the estimation of the inertia ratios was initiated.

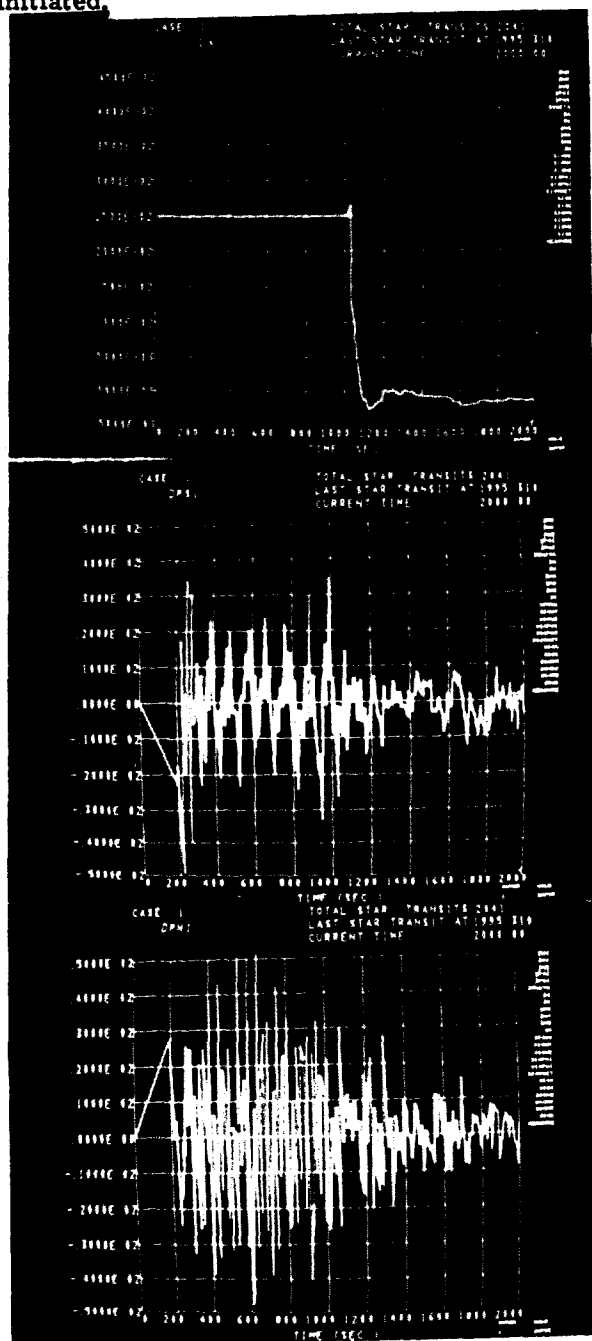


Fig. 7. Inertia Ratio Estimation Results,  $\Delta\Lambda_0 = 0.0025$  -- Continued

Fig. 7. Continued

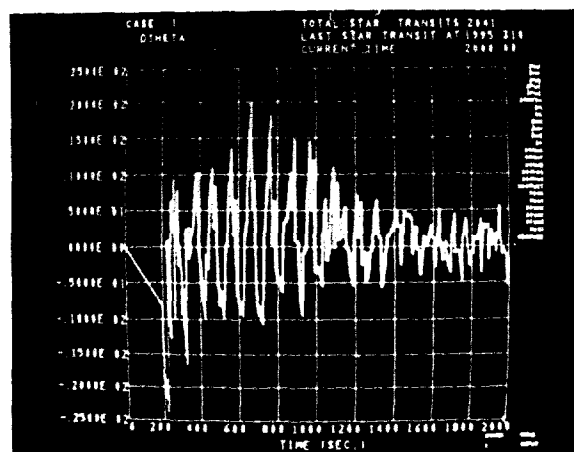


Fig. 7. Inertia Ratio Estimation Results,  $\Delta\Lambda_0 = 0.0025$

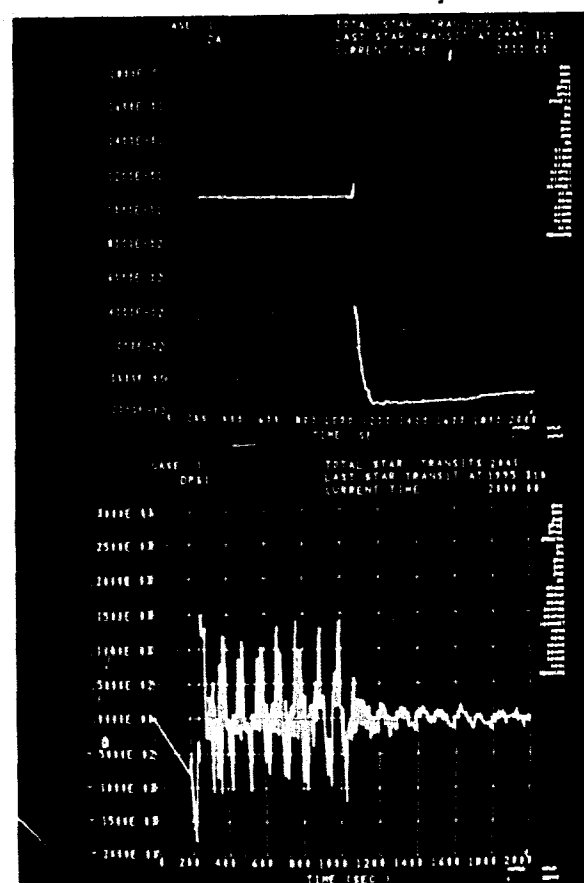


Fig. 8. Inertia Ratio Estimation Results,  $\Delta\Lambda_0 = 0.011$  -- Continued

Fig. 8 Continued

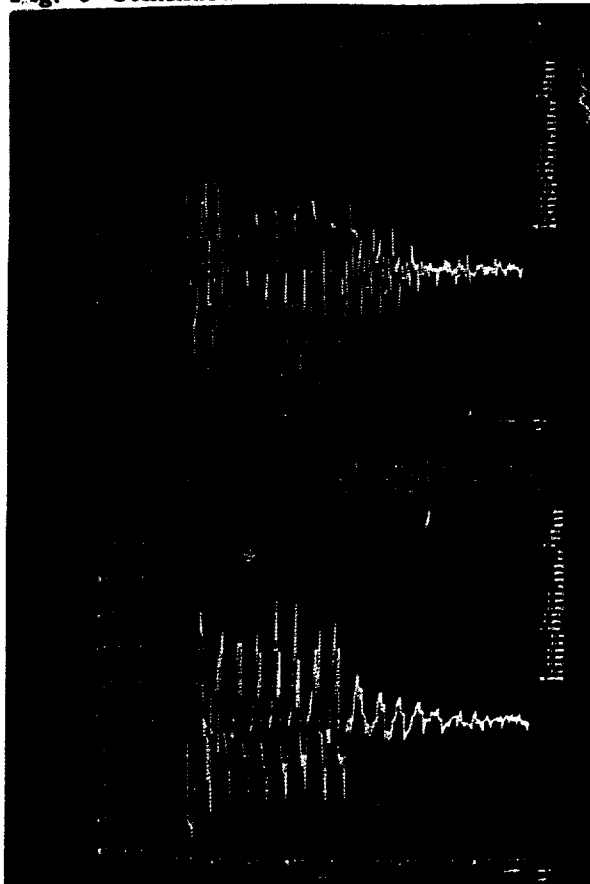


Fig. 8. Inertia Ratio Estimation Results,  
 $\Delta A_0 = 0.011$

#### Celestial Sighting Results

Because of the impact upon onboard data storage requirements and sensor detection limits, attitude accuracy as a function of the number of celestial sightings per vehicle spin period is an extremely critical design parameter. Results of simulations undertaken to evaluate this for instruments of varying quality are presented in Figures 9 through 11. These graphs show the mean  $\mu$  and standard deviation  $\sigma$  about the mean of the errors  $\Delta\psi$ ,  $\Delta\phi$ , and  $\Delta\theta$  respectively, plotted as a function of instrument noise  $\sigma_I$ . Two values are presented for each statistic. These represent the error before and after state is updated by the transit measurement and thus are plotted as the upper and lower limits of error bands. The larger error values are from simulations using approximately three celestial sightings per vehicle spin period while the smaller use approximately six. Limiting star magnitudes of 1.7 and 2.5 are used in the two cases. It is noted that for these simulations six-state estimation ( $\omega, \psi, \phi, \theta$ ) is used with values of the inertia ratios determined by the convergence demonstrated in Figure 7.

Two points worthy of mention in these results are that the pitch ( $\theta$ ) error is significantly smaller than the roll and yaw errors and that attitude errors are not linear functions of instrument noise. The first is observed in all simulation results and is due to the higher sensitivity

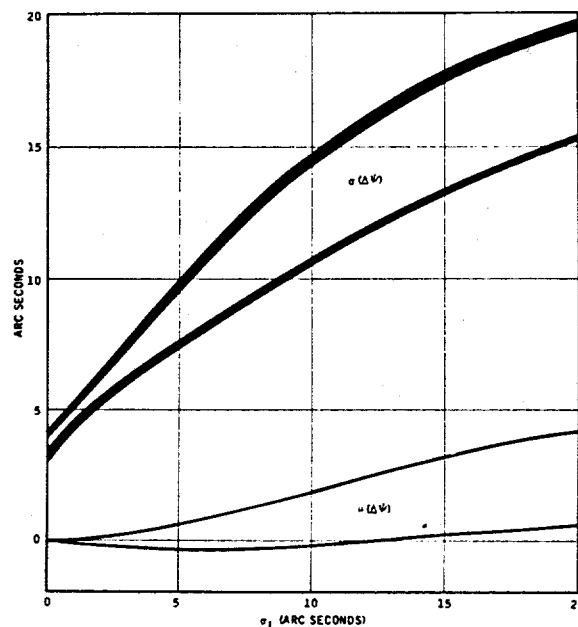


Fig. 9. Error in Yaw,  $\psi$

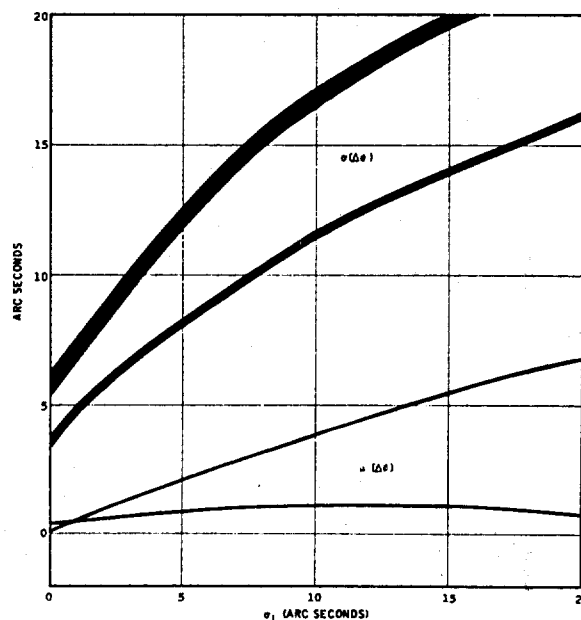


Fig. 10. Error in Roll,  $\phi$



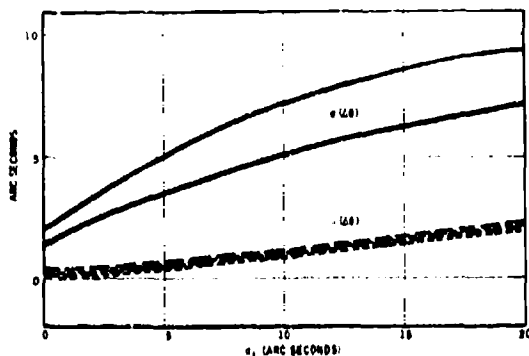


Fig. 11. Error in Pitch,  $\theta$

of the measurement error to errors in pitch. The second is due to uncertainties caused by unmodeled torques and inertia ratio errors.

#### Instrument Noise Uncertainty

Beside simplicity of implementation, the explicit appearance of the measurement statistics in the estimation equations provides a strong motivation for the selection of the Kalman filter over such techniques as least squares fitting to solve the attitude determination problem. However, in practice the noise level of the instrument under operational conditions may not be known precisely. Thus, it can be expected that the estimation will be degraded by the use of a value of instrument variance which does not represent the measurement error.

Normalized simulation results are presented in Figure 12 which demonstrate the effect of instrument noise uncertainties. Normalized attitude errors are shown for two values of actual instrument error. It is encouraging to note that the minimum variance value generally occurs at the point where the assumed variance equals the actual, or in the case of the pitch error for  $\sigma_1 = 10$ , is not significantly different than the minimum value. These results indicate that in an operational data reduction system it is safer to underestimate, rather than overestimate, the quality of the instrument.

#### SUMMARY

Simulation results presented in the preceding section show the attitude accuracies possible with a spin-stabilized (3 rpm) spacecraft and demonstrate the capabilities of the attitude determination system simulation described earlier. From the standpoint of meeting the simulation design requirements stated in the introduction of the paper it is noted that the estimation algorithms and computer programs used in the simulation execute on the CDC 6600 computer in from 10 to 20 times faster than real time, depending upon the dimension of the estimation state. Thus,

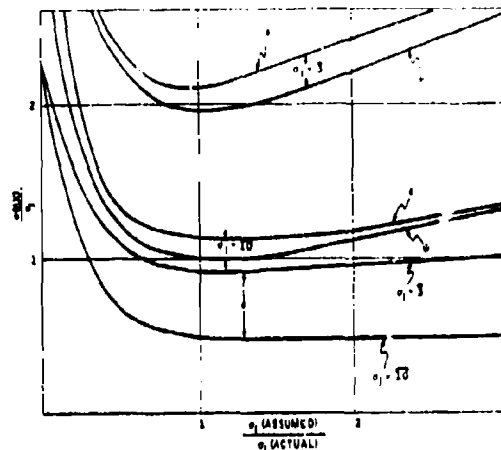


Fig. 12. Noise Uncertainty Results

they provide the basis for an operational data processing system. Further, as an analysis system, all system parameters are treated as simulation variables and can be readily varied for design studies. The on-line analysis capability implemented in the system provides instant access to simulation results and permits computer turnaround not possible with other input/output media.

The basic contract (Ref. 4) accuracy design goal is 15 arc seconds (3 sigma) in pitch and 100 arc seconds in each of the other two orthogonal axes. The simulation results indicate that there is little difficulty in meeting the latter goal. However, the pitch requirement is much more difficult but can be achieved with 3-5 arc second (1 sigma) instruments capable of sensing three to six stars per vehicle spin period.

#### REFERENCES

- (1) Tidwell, N. W., "Modeling of Environmental Torques of a Spin-stabilized Spacecraft in a Near Earth Orbit," Proceedings of the Spacecraft Attitude Determination Symposium, Aerospace Corp., El Segundo, California, September 1969.
- (2) Schmidt, S. F., "Compensation for Modeling Errors in Orbit Determination Problems," Rep. No. 67-16, NAS5-11048, November 1967.
- (3) Bellantoni, J. F., and Dodge, K. W., "A Square Root Formulation of the Kalman-Schmidt Filter," AIAA paper No. 67-90, 5th Aerospace Sciences Meeting, New York,
- (4) Attitude Referenced Radiometer Study, Statement of Work, Nov. 1968, Langley Research Center, NASA, Hampton, Va.

## TACSAT ATTITUDE DETERMINATION

Warren H. Sierer  
Staff Engineer  
Hughes Aircraft Company

Joseph Del Riego  
Member Technical Staff  
Hughes Aircraft Company

### TACSAT MISSION: GENERAL

The TACSAT Military Communications Satellite is a large, spinning spacecraft built on the Gyrostat stabilization principle. Hughes Aircraft Company designed and built the satellite under the auspices of the Air Force for tactical communications experiments in both the UHF and SHF bands. Under contract to the Air Force, Hughes has supplied in-orbit control support since the successful launch in February 1969.

TACSAT is in synchronous, equatorial orbit with its spin axis directed along the orbit normal, close to the direction of the earth's north polar axis. This orientation is critical to mission performance; the despun communication antennas have only east-west or azimuth freedom (by virtue of the despun control system) and depend on control of spacecraft spin axis orientation for north-south control.

The spacecraft and its communications repeater are designed to support an experimental military communication test program involving small, low-performance ground stations for eventual triservice use. The primary purpose of these tests is to demonstrate the feasibility of satellite communications using very small to medium-sized terminals and to further define ground station and spacecraft requirements for a future operational mission.

The experimental communication environment is characterized by several simultaneous, direct links to and from low-performance ground stations operating in two radio frequency bands (UHF and SHF). The large communication repeaters required for this program are a direct consequence of the multilink mission and limited ground station performance.

In addition to the experimental ground terminals, which will be operated under simulated field conditions, the communications experiments are supported using a large terminal with both UHF and SHF capability. This high-performance ground terminal (located at Camp Parks, California) is used for quantitative measurements of satellite communication

performance for correlation with field test results. Support activities at Camp Parks are currently scheduled to extend through 3 years of satellite orbital life.

### SATELLITE CONFIGURATION

Figure 1 shows a cutaway view of the spacecraft illustrating all primary subsystem hardware. As indicated, the mission requirements have been implemented using a dual spin configuration utilizing the spinning rotor angular momentum to stabilize the spacecraft in pitch and yaw (axes normal to vertical cylinder axis) and employing despun control to point a preferred axis in the despun section toward earth. The satellite's communication antennas are mounted on the despun section, allowing the utilization of pencil-beam (high-gain) antenna patterns necessary to meet the very high communication power (ERP) and receive sensitivity requirements associated with the experimental communication mission. Figure 2 is a representation of the total spacecraft.

The design of the spacecraft's attitude sensors (sun and earth) utilize the rotor spin to provide a built-in scan and allow the use of simple fixed sensors with no moving parts. Similarly, the execution of all required propulsive maneuvers can be accomplished using two fixed jets (axial and radial) pulsed over a selected (by command) segment of the rotor spin cycle. In addition, the rotor spin provides an artificial (centrifugal) gravity field maintaining the  $H_2O_2$  liquid propellant in the tanks at the orifice location, which avoids the problems associated with handling liquids in a zero g environment. The arrangement of the attitude control and station-keeping hardware is shown in Figure 3. Four earth sensors and two sun sensors are provided where one of each is sufficient to support all critical functions. In addition, the RCS subsystem incorporates two completely independent propulsion systems with the on-board  $H_2O_2$  propellant in either system sufficient to complete the mission once station acquisition has been achieved. Figure 4 and 5 show the TACSAT sun sensor and earth sensor units.

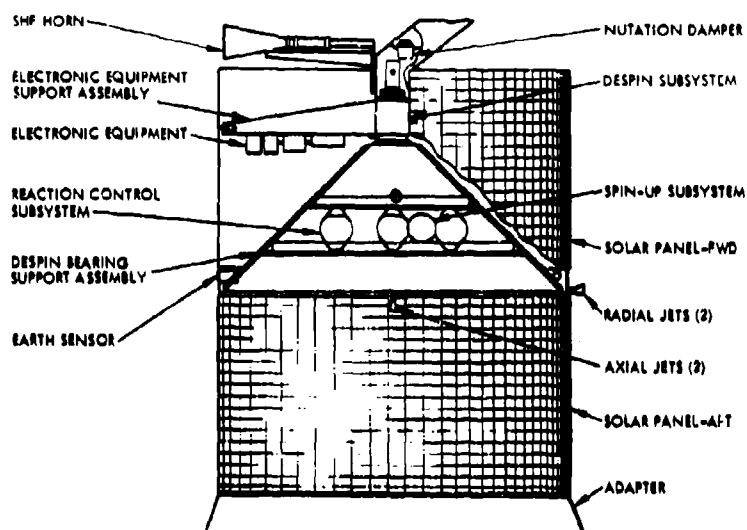


Figure 1. Satellite Configuration

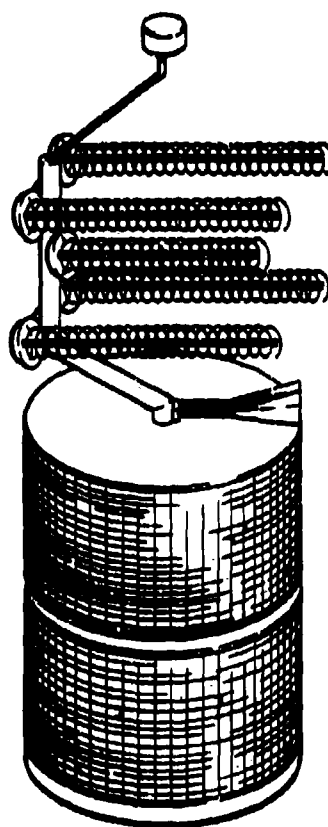


Figure 2. TACSAT Military Communications Satellite

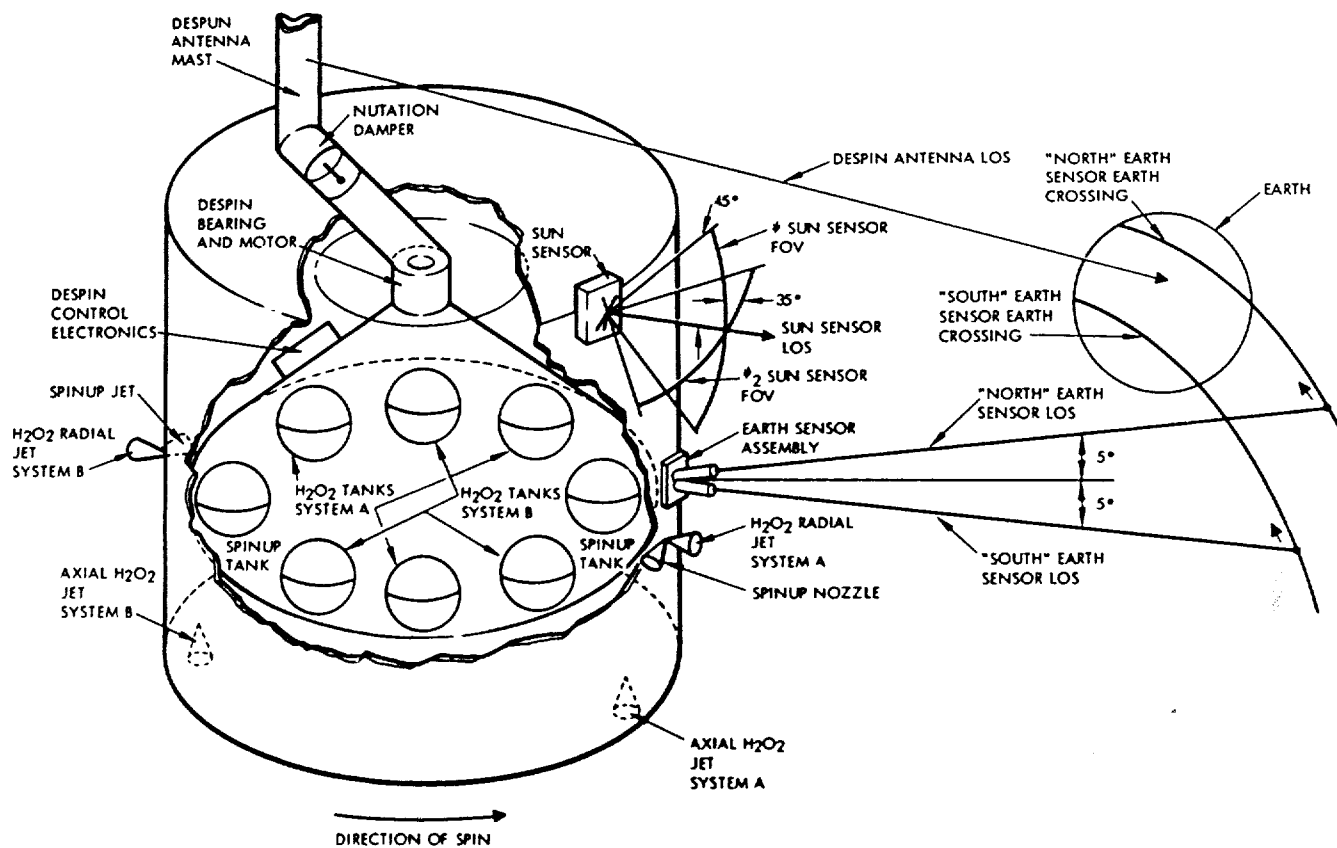


Figure 3. Attitude Control Hardware

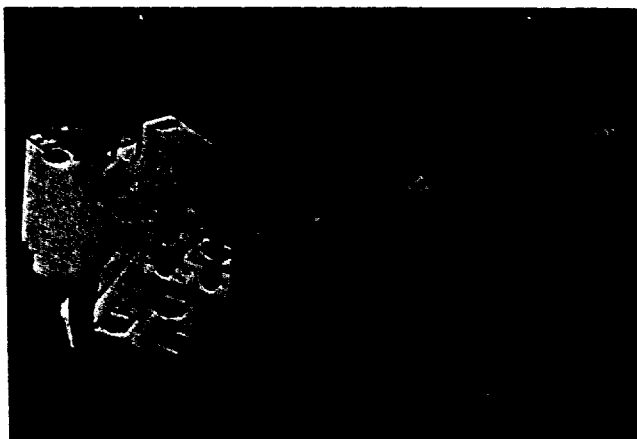


Figure 4. Sun Sensor  
(Photo ES 00057)

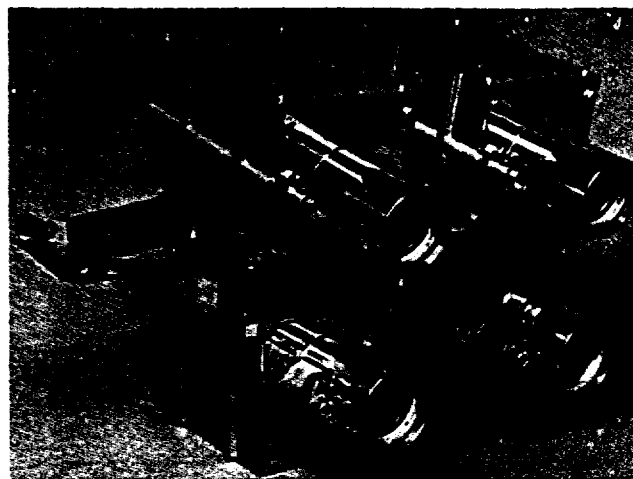


Figure 5. Earth Sensor Assembly  
(Photo ES 00314)

## ATTITUDE CONTROL\*

A dual-spin-stabilized spacecraft will maintain its spin axis fixed with respect to inertial space in the absence of external torques, in accordance with the law of conservation of angular momentum. Since detailed discussion of the dynamics of the dual-spin-stabilized configuration is not called for, only a brief description, with emphasis on the control aspects, is presented here for completeness.

The hydrogen-peroxide control system consists of two sets of body-fixed axial and radial jets. The radial jets fire outward at an angle of 26 degrees to the spin plane. The spacecraft center of gravity (cg) can be varied such that the radial jets may or may not fire through the cg, as dictated by maneuver requirements. The jets are pulsed in synchronism with the spin speed, which allows velocity only or simultaneous velocity and attitude corrections to be performed on the vehicle (see Figure 6).

The axial jets, aligned parallel to the spin axis, are mounted near the periphery of the spacecraft. In performing a reorientation maneuver, a precession torque is applied to the spinning spacecraft by one of the body-fixed axial jets, which is pulsed in synchronism with the spin speed over a given sector of the spin cycle (Figure 7). In accordance with Newton's second law of (angular) motion,

$$T = (d/dt)H = \omega \times H \quad |H| = \text{const}$$

where  $T$  is the applied torque vector,  $H$  is the angular momentum vector, and  $\omega$  is the

precession rate vector. In this pulsed-jet method of generating torque, the vectors  $T$ ,  $H$ , and  $\omega$  are mutually perpendicular.

It can be shown that the nutation induced by the axial jet during the pulsing mode is small for a reasonable rotor spin speed (~55 rpm) and the TACSAT inertia configuration. Thus, for all practical purposes, the motion of the geometric spin axis follows that of the angular momentum vector during the precession process.

The reference signal for synchronous pulsing is obtained from the earth sensor. Knowledge of the spacecraft orbital elements is sufficient to generate spin phase information for the axial and radial jets. Thus, with very simple spacecraft sensor instrumentation and body-fixed thrusters, both attitude and velocity control are provided.

## TACSAT ATTITUDE DETERMINATION REQUIREMENTS

Pointing errors directly affect communication performance through a reduction of the earth coverage antenna gain, thereby lowering the ERP ~1/2 dBw per degree (Figure 8). Since the spacecraft is essentially in a circular synchronous equatorial orbit, pointing errors may be resolved into north-south (latitude) and east-west (longitude) components (Figure 9). North-south errors are caused by the following:

- Attitude measurement errors
- Antenna mirror to bearing and power transfer assembly mechanical spin axis perpendicularity

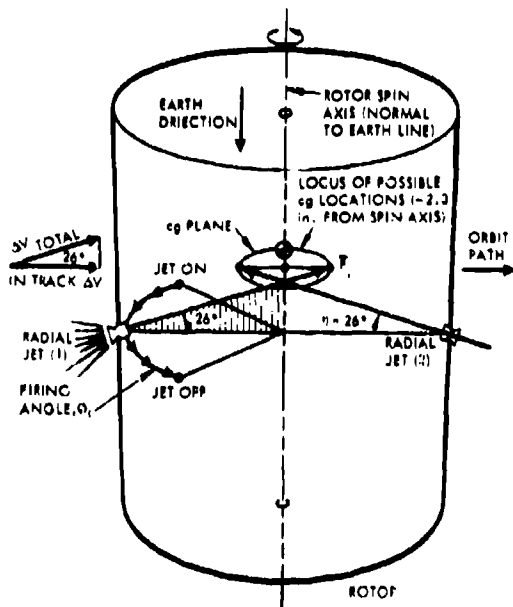


Figure 6. Radial Jet Firing Geometry

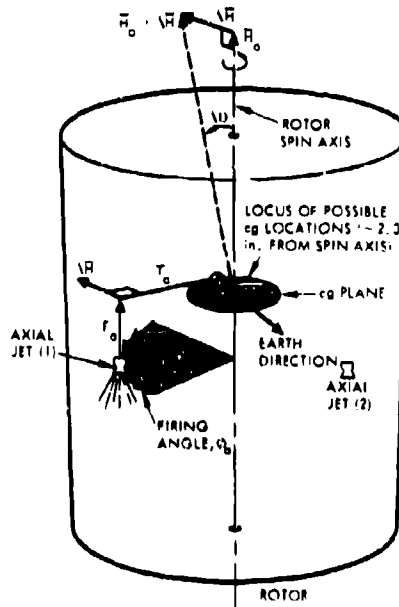


Figure 7. Axial Jet Firing Geometry

\*See Reference 1.

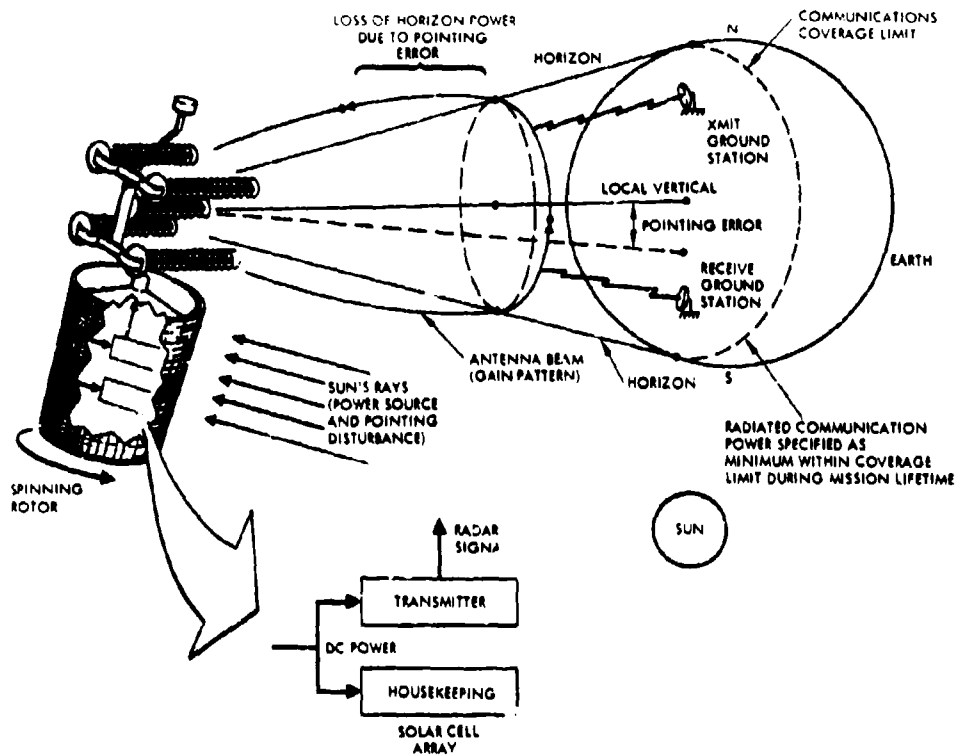


Figure 8. Attitude Error Effects on Communication Performance

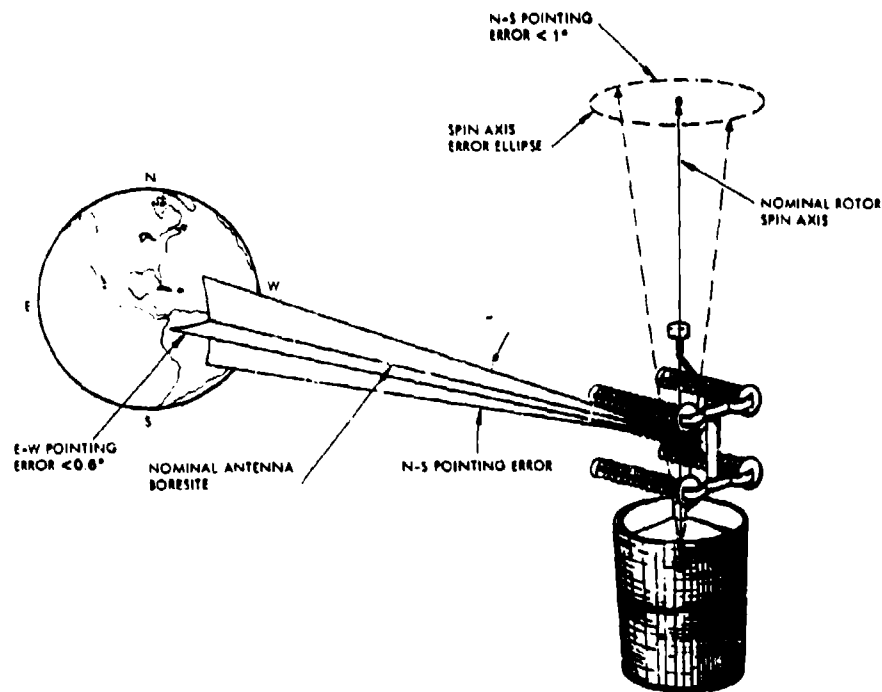


Figure 9. Pointing Errors in Steady Operation

- Antenna electrical boresight
- Antenna boresight variation
- Dynamic unbalance
- Bearing and power transfer assembly mechanical axis wobble (runout)
- Attitude deadband
- Reaction control system execution errors

Errors in the east-west direction generally result from two sources:

- Inaccuracies in detection of deepin pointing error due to manufacturing tolerances
- Noise input to servo loop

In addition to these effects, the attitude of the spacecraft cannot be maintained so that the angular momentum vector is always perpendicular to the earth-satellite line. This is due to two causes: 1) attitude measurement and control inaccuracies, and 2) secular variations in the angular momentum vector due to solar torque disturbances.

To meet platform pointing accuracy requirements of 0.6 degree east-west and 1 degree north-south, attitude determination accuracy on the order of 0.1 degree is required. In-flight data indicates that this accuracy has been easily achieved even under worst case geometrical conditions.

#### ATTITUDE DETERMINATION PROBLEM

To this point, no distinction between the spacecraft mechanical spin axis (i. e., deepin bearing axis) and the total spacecraft angular momentum vector has been made. The difference is a subtle but very important one. The average spacecraft spin vector lies along the angular momentum vector which may be regarded as constant in inertial space (over short periods of time). However, a multitude of effects may cause the rotor mechanical spin axis to deviate from this direction.

Nutation is the coning motion of the bearing axis around the momentum vector caused by a transverse torque. A nutation damper is mounted on the antenna tower to cause such transient motion to decay. Wobble is the spin frequency coning caused by the center of gravity not lying on the spin axis or by rotor cross products of inertia. Higher frequency deviations are caused by bearing runout. For true three-axis definition of spacecraft orientation, each of these effects, and others, must be considered in detail. However, the magnitude of these effects (<0.02 degree) in steady-state operation is small enough to be neglected for the earth coverage TACSAT mission.

It can be argued that the average direction of the mechanical spin axis is along the angular momentum vector. Hence, in determining the angular momentum vector direction, many individual sensor readings will "average out" in the least squares fit. This was demonstrated during periods of TACSAT nutation.

Estimation of the angular momentum direction alone is not enough however, since other unknowns enter the problem. Solar radiation pressure introduces a disturbance torque resulting in a steady precession of the spin axis direction. Thus, analogous to orbit determination, the spin axis direction is estimated at some point in time. Certain coefficients of the solar torque equations of motion also must be estimated (similar to geopotential coefficients in orbit determination). Finally, the attitude sensors may have constant biases in their alignment and/or their electronic response which introduce data bias errors. These biases must be estimated.

#### SUN SENSORS

The TACSAT takes advantage of its rotor spin (~55 rpm), which allows simple, non-articulated sensors to be scanned in a cone about the spacecraft spin axis. Earth and sun sensors are used that allow immediate determination of inertial orientation by measuring the co-elevation between the spin axis and the two celestial reference bodies.

The sun sensors are identical to those flown on previous Hughes synchronous spacecraft (see Reference 2). The sensor is composed of two photo-voltaic elements, each mounted behind a separate slit aperture (see Figure 4). Each slit allows a fan-shaped field of view. The primary slit is mounted such that the plane of its field of view contains the spin axis, while the second slit is twisted 35 degrees about a radial line through the first. Thus, the angular difference,  $\psi_2$ , between receipt of a sun pulse from each slit is related to the coelevation of the sun,  $\phi_s$ , by the following spherical trigonometric relationship (see Figure 10).

$$\cot \phi_s = \cot \xi \sin \psi_2 \quad (1)$$

where

- $\phi_s$  = angle between spin axis and sun line
- $\psi_2$  = angular separation of two slit crossings
- $\xi$  = cant angle between slits

While all Hughes' slit-type sun sensors flown to date have been canted at  $\xi = 35$  degrees, it is none the less interesting to discuss the tradeoffs made in selecting this angle. By intersecting the plane formed by each slit with a unit sphere centered at the spacecraft, the two resulting great circles may be drawn on a projection of the sphere, as shown in Figure 11a. Neglecting sensor physical characteristics and

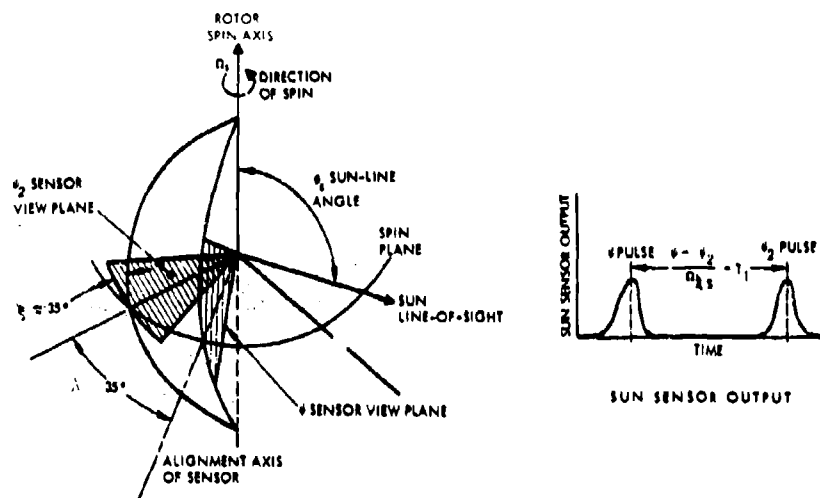


Figure 10. Sun Sensor Characteristics

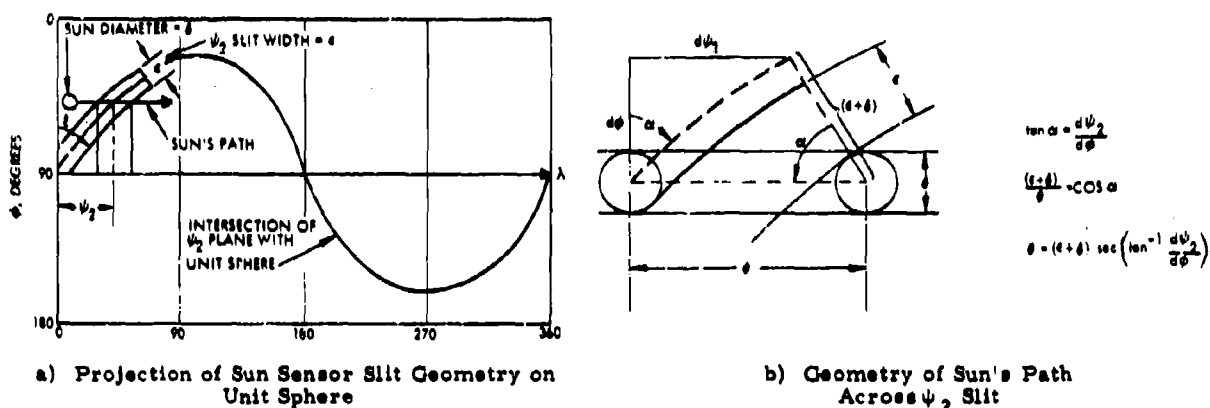


Figure 11. Sun Sensor Slit Geometry

mission requirements,  $\xi$  is to be chosen so as to maximize the sensitivity of the data,  $\psi_2$ , to the coelevation angle,  $\phi_s$ . That is, the derivative of  $\psi_2$  with respect to  $\phi_s$  should be maximized with  $\xi$  as a parameter. Immediately, from Equation 1,

$$\frac{d\psi_2}{d\phi_s} = -\tan \xi \sec \psi_2 \csc^2 \phi_s \quad (2)$$

As is expected intuitively,  $\xi = \phi_s$  maximizes Equation 2 with the constraint that Equation 1 be physically meaningful ( $\sin \psi_2 \leq 1$ ); this constraint is equivalent to saying that for  $\xi > \phi_s$ , the second slit will never pass through the sun, as is obvious in Figure 11a. The conclusion to be drawn is that if data sensitivity were the only constraint, the sensor should be canted the maximum amount consistent with the mission sun angle ( $\phi_s$ ) history.

Several physical characteristics of the sensor make the choice of  $\xi = \phi_s$  impractical. First, the slits do not have a total planar field of view, or even a half-plane, but are optically limited to a total of about 90 degrees, giving them the true fan-shaped field of view as shown in Figure 10. Second, they have a finite angular width,  $\epsilon$ ; and more important, the sun is not a point source, but has a finite diameter,  $\delta$ . The effect of both these factors is to produce a broader, less sharply defined voltage pulse to be processed by spacecraft (or ground) electronics.

Returning to Figure 11a, define "longitude" as  $\lambda$ . Since the projection is spacecraft centered, consider the sun to be moving left to right at some "latitude",  $\phi_s$ , and at some angular rate,  $\omega$ , the spacecraft rotor spin rate. It is required to determine the total angle  $\theta$  during which the sun is visible in the slit as a function of  $\phi_s$ , with  $\xi$  as a parameter. Referring to Figure 11b,



recognize that  $\tan \alpha$  has already been calculated in Equation 2 as

$$\tan \alpha = \frac{d\psi_2}{d\phi_s} \quad (3)$$

which leads immediately to the required equation for  $\theta$ .

$$\theta = (\epsilon + \delta) \sec \left( \tan^{-1} \frac{d\psi_2}{d\phi_s} \right) \quad (4)$$

where

$\theta$  = total spin angle through which the sun is visible in the canted slit

$\epsilon$  = slit width

$\delta$  = diameter of the sun

( $\psi_2$ ,  $\phi_s$  as defined in Equation 1)

As expected, this relationship yields

$$\theta = (\epsilon + \delta) \sec \xi \text{ at } \phi_s = 90 \text{ degrees} \quad (5)$$

but more important, it shows  $\theta$  degenerating rapidly as  $\phi_s \rightarrow \xi$ , and finally results in

$$\theta = \infty \text{ at } \phi_s = \xi \quad (6)$$

From a design point of view, Equation 4 shows that excessively long solar viewing by a slit may be controlled by making the slit width,  $\epsilon$ , as small as possible consistent with minimum solar input energy requirements. Use of Equations 2 and 4, along with sensor characteristics (signal-to-noise ratio, slit width, etc.) and mission constraints, allows proper selection of  $\xi$ .

As a final note, recognize that the longitudinal ( $\lambda$ ) intercept of the canted slit need not necessarily be zero, but that the sensor will function in an identical manner with an arbitrary intercept longitude,  $\lambda_0$ . This results in a simple modification of Equation 1 to

$$\cot \phi_s = \cot \xi \sin (\psi_2 - \lambda_0) \quad (7)$$

where  $\lambda_0$  is the longitudinal intercept of canted sun sensor beam and  $\phi_s$ ,  $\xi$ , and  $\psi_2$  are as previously defined.

Data sensitivity and other functional properties are unaffected; however, proper selection of  $\lambda_0$  can prevent the two voltage pulses from ever overlapping, which may allow simpler processing electronics.

The sun sensor has been extremely reliable (no failures in 40 satellite-years in orbit) but yields data of only medium quality. TACSAT experience indicated random measurement deviations of 0.03 degree, but constant bias

errors on the order of 0.10 degrees. Calibration of these bias errors is discussed later.

## EARTH SENSOR

The earth sensor is a small telescope with an infrared-sensitive chip mounted at the focal point. The optics allow an effective bandpass of 14 to 16 microns in the infrared band, the so-called  $\text{CO}_2$  window. The earth sensor provides both leading and trailing edge pulses, using derivative thresholding, with the leading edge pulse serving as a despin and control jet reference in addition to providing attitude information. (By measuring the spin period as the time between successive leading edge earth pulses, all other time interval measurements can be converted to equivalent angles.) The earth sensors are mounted in pairs, one 5 degrees above the satellite spin plane and one 5 degrees below (or equivalently, 85 and 95 degrees, respectively, from the spacecraft spin axis). Two such pairs are included for redundancy; however, only one is used at any time.

The basic information content from a single earth sensor is the earth chord width observed as indicated by the time interval between leading and trailing edge pulses (see Figure 12). For a known satellite position (hence, known radius), the earth chord width may be calculated from the co-elevation between the spacecraft spin axis and the earth center direction by the following spherical trigonometric relationship, which is derived immediately from the law of cosines and is illustrated in Figure 13.

$$\cos \alpha_1 = \frac{\cos \alpha_0 - \cos \gamma \cos \eta_1}{\sin \gamma \sin \eta_1} \quad (8)$$

where

$\alpha_1$  = one half the angular chord width seen by the  $i$ th sensor

$\alpha_0$  = semidiameter of the earth's disk as seen from the satellite

$\gamma$  = co-elevation of the spacecraft spin axis and a line toward the earth's center

$\eta_1$  = angle between the spacecraft spin axis and the optical axis of the  $i$ th sensor (85 and 95 degrees on TACSAT)

While the sun sensor response is nearly linear over the range of sun angles encountered during TACSAT mission life ( $\phi = 90 \pm 23.5$  degrees), earth sensor response is highly nonlinear, reflecting the relatively small earth size (17.8 degrees diameter) seen from synchronous altitude. An analysis similar to that described for the sun sensors can be made for the earth sensors leading to an optimal selection of the mounting angles,  $\eta_1$ , for both earth sensors. Since the earth sensor pulse is used additionally for a despin and

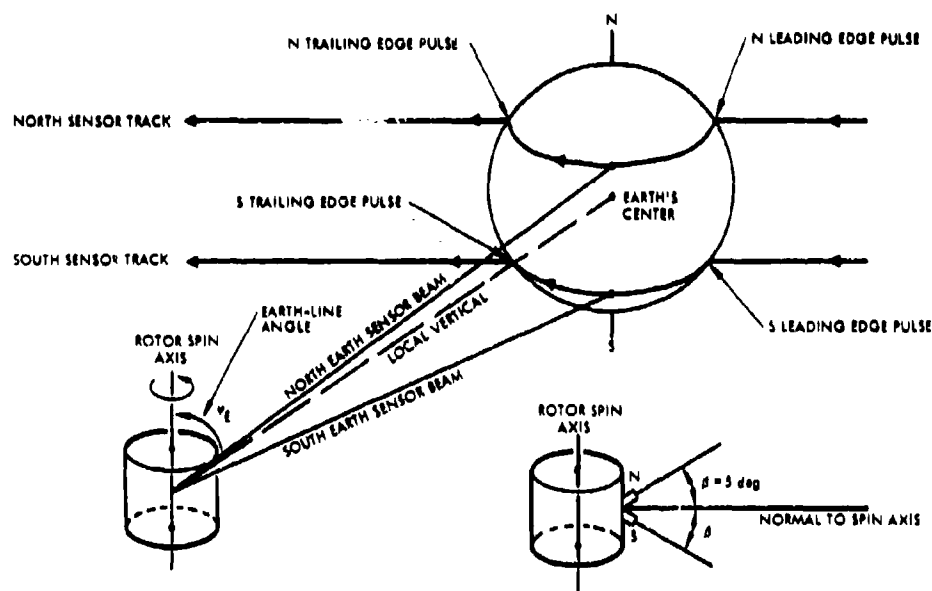


Figure 12. Earth Sensor Geometry

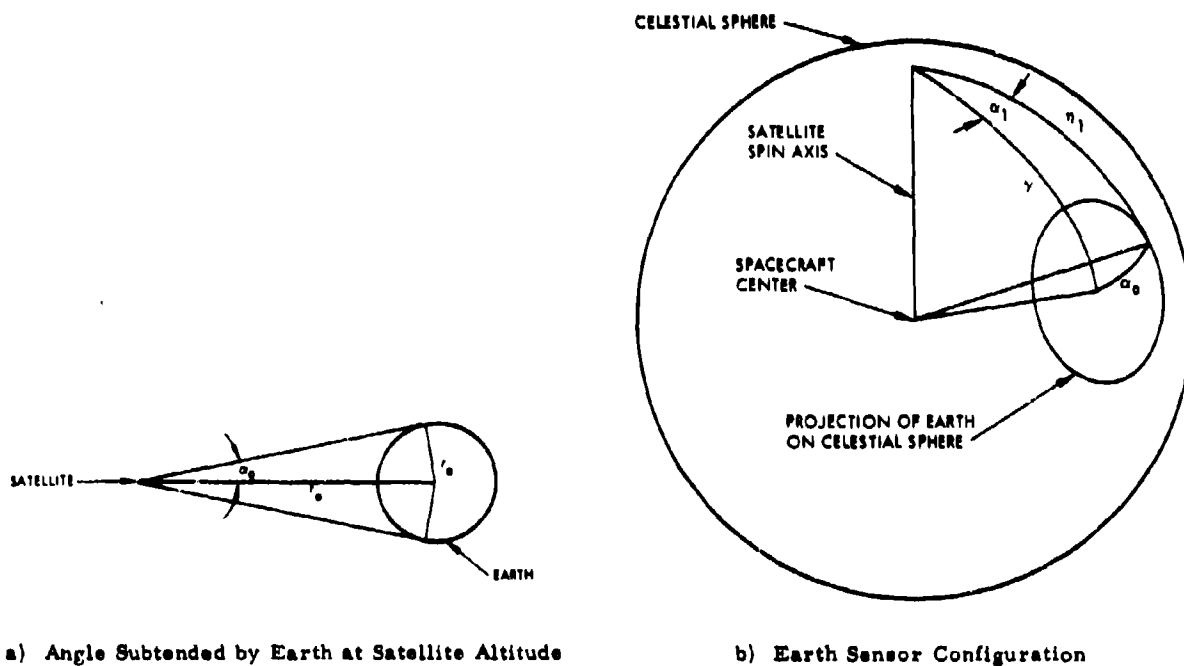


Figure 13. Earth Chord Width Calculation

jet control reference, these individual requirements for pulse stability must be included in any analysis.

Two earth sensors used concurrently offer several interesting variations in data processing. Instead of processing their measurements as two independent readings of earth co-elevation angle, it is possible to difference their measurements and process the difference as a measure of the angle between the spacecraft spin axis and the plane orthogonal to the radius vector. This concept can be likened to monopulse radar and has the similar advantage of doubling the error sensitivity of the single measurement where error is interpreted as a deviation from orthogonality to the radius vector. Another variation based on the same theme is that of differencing only the leading edge (or trailing edge) pulses. This would prove effective where the accuracy of one type of pulse was in doubt.

Neither method can create information that did not already exist in the data, and the authors contend that processing the two readings as independent co-elevation measurements utilizes the data to its full advantage. Additionally, two important benefits are derived: 1) data processing algorithms work equally well whether data from both sensors is available or not, hence, are valid if either sensor fails or is off the earth, while other schemes cannot handle this situation; 2) bias calibrations (described later) can be done on an individual sensor basis, allowing better sensor performance analysis and utilization if other sensors fail.

The TACSAT earth sensors returned data of 0.03 degree rms deviation, but with biases of up to 0.38 degrees. These biases were determined in the attitude determination least squares estimate and caused no significant problems.

#### SUN-EARTH SEPARATION

A third, independent data type is available "free of charge" by virtue of the sun and earth sensors: sun-earth separation angle,  $\psi_c$ . By telemetering the time delay between receipt of the sun pulse (from the vertical slit) and the midpoint between the leading and trailing edge earth pulses, the angular separation between the two bodies, as measured about the spacecraft spin axis, is available.

This data has unique properties and is often overlooked as a potential data source. The data has its maximum sensitivity when the spin axis, the spacecraft-sun line, and the spacecraft-earth line are coplanar and the two coelevation angles,  $\phi$  and  $\gamma$ , are each as far from 90 degrees as possible. As described in Reference 3, this data can be particularly valuable during the launch and ascent phase of a mission when the spin axis may not be orthogonal to the orbit plane.

\*Right ascension and declination themselves are singular near the pole and hence unsuitable for differential correction. A local coordinate system using the current estimate of the spin axis as the 3-axis is defined and the estimate is differentially corrected along the orthogonal 1- and 2-axes.

#### DATA FLOW

Figures 14, 15 show the attitude data flow from the TACSAT vehicle to the Hughes Data Processing Facility (HDPF).

The data is measured as a sequence of time differences on-board, is digitized, and is then telemetered to the ground. The remote tracking station (RTS) receives and preprocesses the raw telemetry bit stream and records it on magnetic tape. The RTS then converts the telemetry to engineering units and edits it according to any of several processing modes. The edited telemetry is then transmitted to the satellite test center (STC) Bird Buffer.

The STC Bird Buffer processes the edited telemetry to provide a printout of data for real-time monitoring, and generates history tapes of the edited telemetry. The history tapes are processed through the MUNCH program, which produces paper tapes for teletype transmission directly to the HDPF, where the transmitted data is automatically stored on magnetic tape by the OE 635 computer to await processing by the attitude determination program.

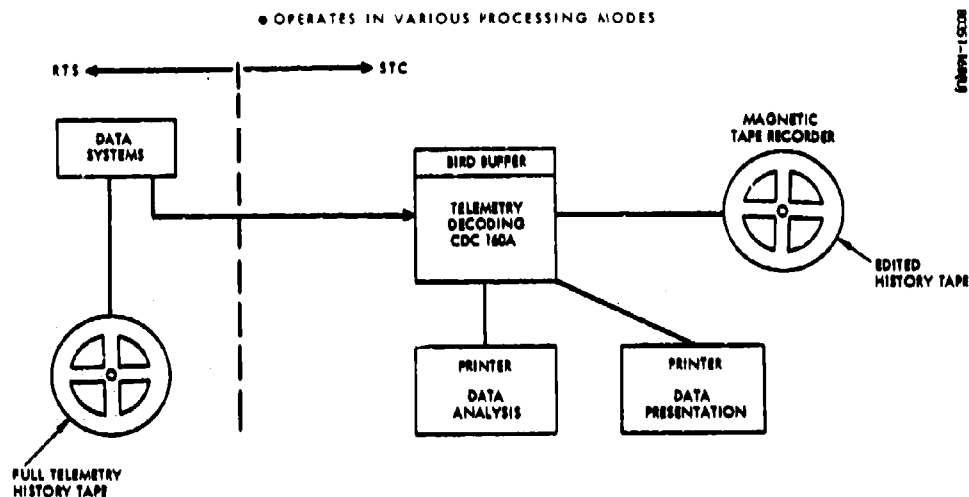
#### THE ATTITUDE DETERMINATION PROGRAM

The attitude determination algorithm was implemented on the HDPF OE 635 large scale digital computer. Program and data storage are on magnetic tape and are operated from the TACSAT Operations Center via a remote terminal.

An attitude determination differential correction algorithm was developed which handles up to nine parameters in its state vector: two attitude parameters (the equivalent\* of right ascension and declination), three solar torque coefficients, and four attitude sensor biases. Any subset of the total vector may be selected for differential correction, the others being held constant.

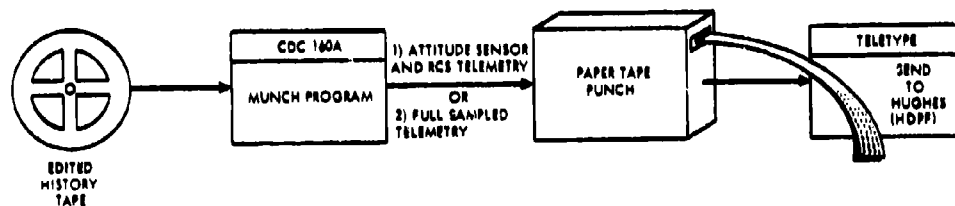
The initial estimate of the state vector may be weighted with an a priori covariance matrix. The program itself will output the covariance matrix of the final attitude state vector estimate on request at the end of each run. This previous covariance matrix may be used in conjunction with subsequent data, resulting in a stage-wise estimate being built up as data is received. This capability reduces data storage and reprocessing requirements.

A straightforward least-squares estimator with a variety of data weighting and culling options is used. The data can be shown to be uncorrelated, both between data types and between sequential readings of the same type, by virtue of the way it is measured and telemetered. A fixed point state estimate (based on work by I. A. Gura, see Reference 4) is obtained with all



- REQUIREMENTS DURING MANEUVER EXECUTION MODE:
- REAL TIME PRINTOUT OF ATTITUDE SENSOR AND RCS INFORMATION
  - RECORD HISTORY TAPE FOR MUNCH PROGRAM

Figure 14. SCF On-Line Telemetry Processing System



MUNCH PROGRAM:

- 1) EDITS TELEMETRY HISTORY TAPE TO:
  - PROVIDE ATTITUDE SENSOR AND RCS TELEMETRY
  - PROVIDE FULL SAMPLED TELEMETRY
- 2) FORMATS TELEMETRY FOR PAPER TAPE
- 3) PUNCHES PAPER TAPE FOR TELEMETRY TRANSMISSION TO HUGHES

Figure 15. SCF Off-Line Telemetry Processing System

the data related back to a single reference epoch of the state vector. As described in the Reference, this technique is applicable to situations where the differential equations describing the state vector are known and the system is not driven by "forcing noise". Forcing noise may be described in this application as disturbance torques which are not modeled or are modeled incorrectly. A fixed point state estimate can be contrasted to a Kalman-type filter where covariance matrix terms are increased to reflect errors made in mapping the state vector forward.

The differential equations governing spin axis motions due to solar torque were integrated analytically after substitution of some simplifying approximations. (These approximations introduce a completely negligible error over periods of up to several months.) The torque itself was modeled as a quadratic in solar aspect angle,  $\phi_s$ , with the three coefficients as terms in the state vector. The analytic integrals result in a considerable saving in computation time over a numerical integration scheme.

Four constant biases arise from the four data types available in each data vector: sun sensor, north earth sensor, south earth sensor, and sun-earth separation angle. The biases are modeled as sensor misalignments. It is conceivable that the bias errors are, in fact, due to electronic timing delays, etc., but it is impossible to determine the source from the data alone. Hence, it makes no difference how they are modeled as long as the end result - correct determination of attitude - is achieved.

In general, the algorithm has worked quite well. Convergence of the differential correction iteration is generally rapid (2 to 3 iterations) and is not strongly initial - estimate dependent due primarily to the relative linearity of the problem. Determination of biases is only possible when the data available meets certain geometric criteria. The determination of solar torque coefficients requires that data be gathered over a considerable time span (so as to allow the motion of the spin axis to be measurable in the data).

The program was developed with considerable operating flexibility in mind and has not required any major modifications to respond to actual mission situations.

## RESULTS OF IN-FLIGHT EXPERIENCE

Actual experience with flight data has been quite successful. The earth and sun sensors have returned data with random noise of approximately 0.03 degrees (1 $\sigma$ ), but with larger than expected bias errors of up to 0.4 degree on certain of the redundant sensors (see Table 1).

These bias errors were determined quickly, and caused no major concern in mission operations. The accurate determination of sensor biases is quite important. In theory, for a gaussian or purely random distribution of measurement errors, the uncertainty in attitude should decrease as  $N^{-1/2}$  where  $N$  is the number of measurements. This assumption is implicit in the weighted least-squares method of estimation. However, the biases in these measurements dominates the certainty of the solution, so that an accurate attitude solution is dependent on knowing the data biases with a high degree of confidence.

In light of modeling uncertainties, which are felt to be the limiting factor in attitude determination accuracy, the overall certainty in attitude estimates is approximately 0.03 degree.

Several phenomena have become apparent. Attitude determination accuracy does not suffer significantly when data is taken during periods of spacecraft nutational activity (TACSAT has undergone random periods of nutation with amplitudes up to ~1.5 degrees). Though the variation in sensor output is actually sinusoidal and regular in nature due to spacecraft nutation, the attitude estimator successfully treats this sensor output variation as random noise and eliminates the effects on the solution almost completely. Larger data residuals result, but attitude determination results agree to within ~0.01 degree of results obtained immediately before or after periods of nutation (after accounting for the effects of solar torque).

An accurate orbit ephemeris generator is mandatory. In particular, a 1- to -1 correspondence exists between error in orbit normal direction (orbit inclination and right ascension of ascending node) and attitude determination error. Operationally, orbit determination and/or updating must occur frequently enough so that the orbital elements reflect the correct orbital inclination and right ascension of the ascending node corresponding to the time at

TABLE 1. TACSAT ATTITUDE SENSOR BIASES

Sensor	Bias, degrees	Description
Earth sensor		
North A	0.38 $\pm$ 0.05	Toward equator (down)
North B	0.37 $\pm$ 0.05	Toward equator (down)
South B	-0.06 $\pm$ 0.05	Toward equator (up)
South A	-0.02 $\pm$ 0.05	Toward equator (up)
Sun sensor	-0.024 $\pm$ 0.05	Decreased azimuth separation of sensor planes

which the data was taken. Correct inclination is more important than correct in-track position (mean anomaly).

The "strength" of the earth-sun-sensor geometrical relationships varies with time of day and time of year. The time of day and time of year at which attitude data is taken is crucial. Close to the equinoxes, the sun sensor data becomes less sensitive to attitude changes. During

periods close to local (spacecraft) noon and midnight when the earth, sun, and spacecraft are essentially colinear, earth sensor data and sun sensor data are, to a large extent, redundant and no longer provide separate attitude information. It is therefore advantageous to collect attitude data at times when the earth-spacecraft line is as close to perpendicular to the sun-spacecraft line as possible.

#### REFERENCES

- 1) M. J. Neufeld, and B. M. Ansel, "Synchronous Satellite Station Keeping," Communications Satellite Systems Technology, edited by R. B. Marsten, Academic Press, New York, 1966.
- 2) W. H. Sierer, and W. A. Snyder, "Attitude Determination and Control of Syncom, Early Bird, and Applications Technology Satellites," Journal of Spacecraft and Rockets, Vol. 6, No. 2, pp. 162-166, February 1969.
- 3) "Hughes Multipurpose Synchronous Communications Satellite Study," Vol. 2, Part III, August 1967.
- 4) I. A. Gura, "Extension of Linear Estimation Techniques to Nonlinear Problems," Journal of the Astronautical Sciences, Vol. XV, No. 4, pp. 194-206, July-August 1968.

## THE ATTITUDE DETERMINATION SYSTEM FOR THE ORBITING ASTRONOMICAL OBSERVATORY

Paul B. Davenport  
Goddard Space Flight Center

### ABSTRACT

Various applications of attitude estimation as applied to the operation of the Orbiting Astronomical Observatory are enumerated and explained in some detail. The techniques used, the results of these techniques, and the problems encountered during the first nine months of the mission are delineated. The operation of the Orbiting Astronomical Observatory including the spacecraft and the supporting ground system is briefly described.

### INTRODUCTION

On December 7, 1968 the NASA's Orbiting Astronomical Observatory (OAO) was placed into a near circular orbit inclined 35 degrees from the equator by an Atlas-Centaur booster. The OAO, orbiting 480 miles above the earth's surface, doubled existing stellar data clear of the earth's absorbing atmosphere in its first thirty days of operation. After nine months of successful operations this first astronomical observatory in space has made over 3000 observations of stellar objects and has attained some 8000 different attitudes distributed over the entire celestial sphere.

Two experiments are aboard the OAO spacecraft: One designed by the University of Wisconsin and the other by the Smithsonian Astrophysical Observatory (SAO). The Wisconsin Experimental Package (WEP) includes four stellar photometers, two scanning spectrometers, and one nebula photometer. The primary function of the WEP is to gather spectral energy distributions on selected stars and nebulae in the ultraviolet range of 1000 to 4000 Angstrom (A). The SAO experiment contains four 12-inch telescopes each of which images a star field onto an ultraviolet sensitive photocathode. The scientific objective of SAO is to measure the brightness of many celestial bodies in four separate ultraviolet spectral bands ranging between 1100 A and 3000 A.

### THE SPACECRAFT AND ITS CONTROL

The OAO spacecraft is an octagonally shaped aluminum structure ten feet long and six and two-thirds

feet across any two parallel sides of the octagon. There is a hollow central tubular area four feet in diameter running the length of the spacecraft which is used to house the experimental equipment. Two hinged sunshades approximately four feet square are attached to each end of the spacecraft to protect the experimental equipment from sunlight. Attached to each of two opposite sides of the octagon at an angle of 34 degrees from the longitudinal (optical) axis are four solar cell paddles whose combined dimensions are nearly eleven feet by nine feet. Solar cells are mounted on both sides of all eight paddles. The major subsystems of the OAO are stabilization and control, data processing, communications, and power. Thermal control is passive. The entire spacecraft weighs over two tons which includes 1000 pounds of experimental equipment.

The primary mode of control is by stellar guidance so as to point either of the experiments to within one arc-minute of a specified target star. Control perpendicular to the optical axis is also required for maneuvering, power, thermal, and shading considerations. This three dimensional control is accomplished by using various combinations of six orthogonally mounted gimbaled startrackers each having a field of view of one degree and an excursion of approximately forty degrees in any direction. A seventh tracker, bore-sighted with the optical axis, is also available which provides single axis (optical) control. Averaged error signals from the trackers drive three orthogonally mounted "fine" momentum wheels which absorb the extraneous torques that would cause attitude errors. The momentum in the fine wheels is continuously "dumped" by a magnetic unloading system consisting

of three flux gate magnetometers, three torquer coils (electromagnets), and a processor. The momentum in the fine wheels may also be removed by a gas jet system.

The OAO may also be controlled by three rate gyros which actuate either the fine momentum wheels (Hold On Wheels) or the gas system (Hold On Jets). The maximum drift rate for any one gyro as obtained from in-flight data is about 0.2 degree per hour.

The spacecraft is maneuvered from one attitude (two axes) to another by means of three "coarse" inertia wheels in an open loop manner. Two or more trackers are required to track continuously during the slew and averaged errors from preset gimbal angles settle the spacecraft when the slew has terminated. Slewing plus settling times vary with the axis and angle of rotation but is usually better than three degrees per minute. Small closed loop slews (several degrees) may also be accomplished with the fine wheels by changing the commanded gimbal angles.

The OAO has two special modes of control: "sun-bathing" and "sun-pointing." In the former, sun sensors are used to actuate gas jets which align the normal of the solar cell array to the sun when in sunlight. Rate gyros then hold this position while in darkness. Sun-pointing is similar except in this case the optical axis is pointed toward the anti-sun line. This is the pointing the spacecraft automatically obtains upon separation from the launch vehicle.

In addition to the sensors mentioned above there are four sun sensors mounted so as to give solar aspect data at any attitude. It is the purpose of these sensors to provide independent attitude information while in sunlight.

The data processing subsystem can accept 168 different control commands in addition to the gimbal and slewing commands. All commands may be executed in real time or stored (up to 256 commands) and executed at a specific time later as a function of an on-board clock.

### THE GROUND SYSTEM

For the most part, the actual functions performed by the OAO are initiated by one of the experimenters although several major elements of the ground system lie between his request and the commands executed by the spacecraft. The experimenter specifies a sequence of target stars (pointings) and the associated experimental equipment commands necessary to obtain the desired scientific objectives. This information (Experimenter's Target List) is passed on to the Mission Computing Group where it and other inputs are entered into a complex computing system known as the Support Computer Program System (SCPS). The SCPS (which resides in a large scale-high speed computer) determines the total attitude as a function of the target and

other geometric considerations. From this, the number of turns for each inertia wheel required to slew from the previous attitude to the present one is then determined. The gimbal angles for each tracker and their on-off schedule as a function of occultations by sun, moon, or earth are also generated. One of the final outputs of the SCPS is the ordered list of commands in spacecraft format which are to be executed and their time of execution. Based upon the schedule of ground contacts with the spacecraft, the number of commands to be executed, and the current memory assignments the SCPS also determines when and where the commands are to be loaded into the spacecraft memory.

The image of the OAO command memory along with certain ground procedures generated by the SCPS is then routed to the OAO Operations Control Center (OCC) which in turn transmits this "contact message" to one of five remote sites. These sites are: Rosman, North Carolina; Quito, Ecuador; Santiago, Chile; Tananarive, Madagascar; and Orrorel, Australia. At the scheduled contact the remote station establishes communications with the OAO, loads new commands in memory (if necessary), and gathers telemetered data (real time and stored). The OCC monitors these contacts (in the case of a Rosman contact it also replaces the remote station functions), and displays the returning telemetered data. During the contact, real time commands already at the remote site may be executed and real time commands from Goddard Space Flight Center (where the SCPS and OCC are located) can be received by the site and relayed to the spacecraft.

### ATTITUDE ESTIMATION APPLICATIONS

The applications for attitude estimation techniques in the OAO program range from coarse estimates (several degrees) from the solar and magnetic sensors to a precise attitude determination (seconds of arc) from as many as six star trackers.

A coarse attitude estimate is used as an intermediate step in obtaining stellar guidance. The transition between the coarse attitude estimate and stellar control is obtained by generating a sequence of star-tracker gimbal angles consistent with a sequence of attitudes. This sequence of attitudes sweeps out the most probable region associated with the coarse attitude estimate. Stellar guidance is then obtained when two or more trackers acquire their preassigned stars during the search maneuver.

The coarse estimate of the OAO's attitude is obtained by placing the spacecraft in an attitude hold using the rate gyros and fine momentum wheels. Sun sensor and magnetometer data are then collected while the spacecraft is in contact with a ground station (approximately ten minutes). This data is then relayed, by high speed data links, to the control center where it is passed to the SCPS. Since the attitude of the spacecraft



is fairly stable during the collection of the data (relative to the accuracy of the data), it is assumed that all the data refers to the same attitude and is thus used collectively to obtain a weighted least squares estimate of that attitude. The star search commands, based upon the attitude estimate, are then generated by the SCP8 and transmitted (via the total ground system) to the spacecraft at some subsequent contact in real time.

Even though the magnetometers were not calibrated and give noisy data (their original purpose was solely to unload momentum from the fine wheels) the above procedure yields an adequate solution and has been used to place the OAO under stellar control approximately thirty times in a nine month period. The success of this technique has saved valuable time and extended the life of the OAO's gas supply since it is applicable at any orientation whereas the original design concept required a reorientation to align a particular axis with the sun. Stellar control would then be accomplished by rolling about this axis until two or more startrackers simultaneously acquired stars.

The OAO's capability to hold an unknown attitude under gyro control has also been used to derive an estimate of attitude using only magnetometer data. To date such rough estimates have had very limited application. However, on one occasion such an estimate was used to verify that the telemetry from a sun sensor had been misinterpreted. With calibrated magnetometers this capability could provide useful attitude information while the spacecraft is in darkness.

When under stellar control, attitude determination techniques using startracker data have been used for an independent verification of the commanded attitudes and to determine the accuracy of the various sensors. Least squares solutions using all tracker data (usually from two to four trackers) as an aggregate and in various combinations provides an excellent means for evaluating the performance of each tracker and whether any misalignments exist between them.

More sophisticated techniques have been employed to determine the values of the tracker misalignments from inflight data. This has been necessary since shifts due to launch stresses and other effects have been greater than expected. By use of this procedure the pointing accuracy has been better than the design specification of one arc-minute.

Attitude determination from tracker gimbal angles is also performed in the processing of the experimental data. This allows a correlation of the data to a known star and aids in the evaluation of the scientific results.

Stellar control has provided the opportunity to study the correlation between the errors of the sensors and the resulting error in attitude. In this manner a good deal of experience has been obtained in the selection of weighting factors for the various sensors as well as

interpreting the results based on residual errors and the angular separation between the solar and magnetic vectors. A technique has recently been developed which will determine from in-flight data any systematic errors caused by: the misalignment of the magnetometers, the permanent magnetic moment of the spacecraft, and the effects of the torquer coils on the magnetometers. It is felt that this information will help eliminate the present wide dispersion in the magnetic data.

### THE ATTITUDE ESTIMATE

All of the attitude estimates referred to in the preceding sections are obtained from the same mathematical algorithm which yields a weighted least squares estimate of attitude. The only difference between the various applications is the selection of the weights and/or the type of data to be used.

The method (delineated in an appendix) is based upon two different vector parametrizations of three-dimensional rotations. One vector has been referred to as the Gibbs vector and the other's components are three of Euler's symmetrical parameters. The direction of both vectors defines the axis of rotation and their lengths are trigonometric functions of the angle of rotation. One vector has a length equal to the tangent of the half-angle of rotation and is denoted as the Y vector. The other vector is denoted as Z and has length equal to the sine of the half-angle of rotation.

The Z vector is used to obtain a vector expression for the "smallest" rotation which will align an estimate of a rotated vector to its true value. A generalized weighted least squares criterion is thus established by requiring the sum of squared lengths of all such Z's (premultiplied by a symmetric weight matrix) to be a minimum. The resulting equation is then simplified by assuming that the weight matrix is the identity times a scalar (this implies that the component errors of each Z vector are equal and independent).

The Y vector is used to express the least squares condition in vector notation where the only variables are the three components of the Y vector. The necessary conditions for an extremum are then applied to this function and the result is a vector equation in terms of the Y vector. The least squares solution can then be obtained by finding the largest zero of a fourth degree polynomial and then solving a linear system of three equations. In practice, this approach is not taken since the vector equation is also amenable to a simple successive substitutions iteration which converges rapidly. Thus an approximate solution is constructed to start the iteration.

When only two data vectors are given the least squares rotation can be expressed as a product of two rotations, each of which is obtained by juxtaposing vectors that are linear combinations of the given vectors. The scalar coefficients of these linear combinations

are explicitly given as functions of the lengths and dot products of the given vectors. This method yields the attitude estimate when only two data vectors are available and provides the first approximation when more than two vectors have been measured.

### RESULTS AND PROBLEMS

Attitude error signals from the experiments are not available on the present OAO. Therefore, it is difficult to ascertain the absolute error in attitude while under stellar control. However, attitude determination using telemetered gimbal angles from several trackers over a ten minute interval usually yields residual errors of one arc-minute or less (the smallest command increment is twenty arc-seconds). To maintain this precision, however, it has been necessary to occasionally re-evaluate the misalignments between the trackers. More elaborate misalignment models are being considered to eliminate this minor problem and

to improve the overall accuracy. Since the misalignments have been as good as thirty arc-seconds over extended periods it is felt that much of the variation can be accounted for with additional parameters in the model.

In the following table are the results of fifteen typical attitude estimates using only sun sensor and magnetometer data. Column one contains the number of data points used in the estimate—each data point gives two vectors (solar and magnetic). The second column shows the angular separation between the solar and magnetic vectors. The length of time over which the data were taken is given in column three. Columns four and five give the actual angular error of the solar and magnetic data respectively (the attitude obtained from tracker data serves as the reference). The next two columns display the solar and magnetic errors using the solar-magnetic estimate as a reference. The last column contains the angle of that rotation necessary

No. of Data Points	Angular Separation	Duration min: sec.	Actual Sun Error	Mag. Error Mean, Max.	Residual Sun Error	Mag. Residual Mean, Max.	Attitude Error
6	36 to 38	0:47	0.02	3.9, 4.9	0.18	3.9, 4.8	1.1
6	62 64	1:03	0.25	6.4, 6.6	0.32	5.8, 6.0	1.1
10	39 44	1:50	0.14	3.6, 4.5	0.20	3.4, 4.4	1.2
11	37 29	9:42	0.06	2.6, 4.0	0.06	2.2, 3.3	1.8
11	56 49	2:21	0.06	4.7, 6.0	0.37	4.4, 5.9	1.8
14	81 82	4:11	0.06	7.1, 9.2	0.31	6.8, 9.9	2.8
16	40 50	3:28	0.26	2.2, 3.5	0.15	2.3, 3.8	0.9
17	37 28	3:56	0.06	3.4, 5.4	0.16	2.6, 5.3	3.5
18	47 26	8:23	0.02	1.4, 3.3	0.05	1.4, 3.3	0.5
24	69 46	7:52	0.06	4.5, 6.3	0.30	4.2, 6.0	0.3
26	80 107	7:07	0.36	5.4, 6.4	0.31	5.4, 6.4	0.8
26	88 78	7:52	0.09	6.1, 8.1	0.32	5.8, 8.1	1.0
26	29 41	6:49	0.22	1.7, 3.4	0.08	2.2, 4.0	1.5
26	61 46	6:34	0.21	6.1, 8.5	0.33	5.4, 8.4	1.9
26	74 61	6:49	0.26	5.5, 8.1	0.30	4.7, 7.6	2.1

All errors and angular separation are in degrees.

In all attitude estimates the sun sensor data was given a weight of 4 and the magnetometer data a weight of 1.

to bring the solar-magnetic estimate in agreement with the stellar determination. These figures clearly show the dispersion in the magnetic data that was referred to previously. The errors range from as good as our capability to predict the magnetic vector (the time of the data is only known to within 16 seconds) to a factor of five times worse. This makes it very difficult to determine the accuracy of the estimate in practice, especially when the angular separation is poor (less than twenty degrees). In this case, small residual errors do not necessarily mean a good estimate. On the other hand, a separation of less than twenty degrees may yield a good estimate if the magnetic data are good.

It is rather apparent from the table that attitude estimates based upon the magnetic data only would be quite poor in general. However, we made such an estimate for what was considered to be the best case (the one with eighteen data points) merely to see what type of accuracy could be obtained by this method. The attitude error in this case was 0.96 degree. Thus, if the larger errors in the magnetic data can be eliminated, useful attitude estimates could be obtained while the spacecraft is in darkness.

Of the thirty some star searches attempted, only three have failed due to poor attitude estimates. The present search capability, due to a ground constraint, is about 3.5 degrees which is the maximum error of the fifteen cases discussed earlier. However, in the failure cases data was limited to a small interval of time where the angular separation was also small. Two searches have also failed because one or more trackers looked onto wrong stars (a bright neighbor of the selected star). Normally, logic aboard the OAO prevents this by requiring simultaneous acquisition of stars. This logic which is set whenever all trackers lose their stars, has been by-passed several times by ground commands when it was apparent that stellar control had been lost (only one tracker tracking). This action is justifiable in that it also prevents further loss of control.

The occasional large errors in the magnetic data have alerted us to a potential problem in estimating attitude from multiple data representing essentially only two directions. When one direction is weighed heavily over the other the solution is weak in one dimension geometrically and in another statistically. The net result is that there is another solution (a saddle point) to the necessary conditions for extremum near the desired least squares solution. This is especially troublesome for small angular separations.

#### CONCLUSION

In every respect, the present OAO mission must be considered a resounding success. Although the OAO is the most complex scientific satellite ever built it has operated almost flawlessly for nine continuous months.

The ground system has been able to keep the satellite productive around the clock and both experimenters are continuing to receive valuable scientific data. The problems, thus far, have been minor and solved with work-around procedures on the ground.

With future OAO spacecraft carrying such equipment as integrating as well as rate gyros, ultra precision experiments, and an on-board computer it appears that the OAO program will continue to offer challenging and exciting possibilities in the field of attitude determination and control.

#### ACKNOWLEDGMENT

I would like to take this opportunity to express my sincere thanks to the many hundreds of people who have contributed to the success of the Orbiting Astronomical Observatory which has made this paper possible. A special "thank you" goes to Mr. and Mrs. Joseph Hennessy for the computer programs associated with this effort.

#### REFERENCES

1. Korn and Korn, Mathematical Handbook for Scientists and Engineers (McGraw-Hill Book Company, Inc., New York, 1968), 2nd ed., chap. 14, p. 472.
2. P. B. Davenport, A Vector Approach to the Algebra of Rotations with Applications, NASA Tech. Note, TN D-4696 (Aug. 1968).
3. P. B. Davenport, Mathematical Analysis for the Orientation and Control of The Orbiting Astronomical Observatory Satellite, NASA Tech. Note, TN D-1668 (Jan. 1968).
4. J. L. Farrell, et al., "A Least Squares Estimate of Satellite Attitude," SIAM Review, Vol. 8, No. 3, p. 384 (1966).

## APPENDIX

### A VECTOR APPROACH TO WEIGHTED LEAST SQUARES ATTITUDE ESTIMATION

Given the angle of a rotation,  $\theta$ , and the rotation axis defined by the unit vector  $X$  it is well known that the matrix,  $R$ , of the rotation can be expressed as

$$R_X(\theta) = \cos \theta I + (1 - \cos \theta) XX^T - \sin \theta \tilde{X} \quad (1)$$

Here  $\tilde{X}$  denotes the skew-symmetric matrix formed from the components of  $X$  such that for any vector  $V$ ,  $\tilde{X}V = X \times V$  ( $I$  is the  $3 \times 3$  identity matrix and the superscript  $T$  denotes transpose). Furthermore, any orthogonal matrix with determinant equal to plus one can be expressed in the form of Eq. (1). Except when otherwise stated, it is assumed that  $X$  has been selected so  $0 \leq \theta \leq \pi$ .

If we define the vectors  $Y$  and  $Z$  as

$$Y = \tan(\theta/2)X, \quad Z = \sin(\theta/2)X.$$

then we find, by standard trigonometric identities, that  $R$  may be written as

$$R = \frac{1}{1 + Y \cdot Y} [(1 - Y \cdot Y)I + 2YY^T - 2\tilde{Y}].$$

or

$$R = (1 - 2Z \cdot Z)I + 2ZZ^T - 2\sqrt{1 - Z \cdot Z}\tilde{Z}.$$

In this manner, the vector components relative to a rotated system can be expressed, by vector relations, as a function of  $Y$  or  $Z$  and the components relative to a fixed system. For every rotation there exists a  $Z$  vector, uniquely except for 180 degree rotations. A unique  $Y$  vector exists for any rotational matrix whose trace is different from minus one.

With the above definitions it then follows that if  $T$  and  $U$  are any two vectors the rotation,  $R$ , which will align  $U$  and  $RT$  with the minimum angle of rotation can be expressed by the  $Z$  rotation vector as

$$Z = \frac{1}{\sqrt{2(1 + U_n \cdot T_n)}} U_n \times T_n,$$

where  $U = |U| U_n$  and  $T = |T| T_n$ . In other words, the angle of the rotation is the angle between  $U$  and  $T$ , and the rotation axis is perpendicular to the plane containing these two vectors. If  $|U| = |T|$  then  $U = RT$ . In particular, if  $U$  is a measurement (including error) of vector components relative to a local right-handed orthonormal coordinate system,  $T$  is the same physical vector but relative to a fixed reference system (also right-handed and orthonormal), and  $R$  is an estimate of the rotation (attitude) relating the two systems, then the vector error that can be corrected by a rotation is given by

$$\Delta Z = \frac{1}{\sqrt{2(1 + U_n \cdot RT_n)}} U_n \times RT_n. \quad (2)$$

The quantity  $U - RT$  is the error in a true vector sense—it cannot be removed, in general, by a rotation.

For each such measurement,  $U_i$ , there corresponds a  $\Delta Z_i$ . Thus, the weighted sum of "rotational errors" squared is given by

$$f(R) = \sum_{i=1}^m (P_i \Delta Z_i)^T P_i \Delta Z_i. \quad (3)$$

where  $m$  is the number of measured vectors and  $P_i$  is the weight matrix for the  $i^{\text{th}}$  measurement. If  $P_i = p_i I$  ( $p_i$  a scalar) and equation (2) is substituted into equation (3) we obtain

$$f(R) = \sum_{i=1}^m (w_i - RV_i)^2. \quad (4)$$

where

$$W_i = \frac{p_i}{2} \frac{U_i}{|U_i|}$$

and

$$V_i = \frac{p_i}{2} \frac{T_i}{|T_i|}$$

The function  $f(R)$ , the weighted squared error, is minimized when the function

$$g(R) = \sum_{i=1}^n W_i \cdot RV_i$$

is a maximum. This expression may be written as

$$g(R) = \sum_{i=1}^n (RV_i) W_i^T = \sum_{i=1}^n \text{tr}(RV_i W_i^T)$$

$$\text{tr} \left[ R \sum_{i=1}^n V_i W_i^T \right] = \text{tr}(RA)$$

where  $\text{tr}$  denotes "trace of" and

$$A = \sum_{i=1}^n V_i W_i^T$$

Hence, the least squares rotation is obtained by maximizing the function  $g(R) = \text{tr}(RA)$ .

Except for notation, Eq. 4 is the same as the equation in Ref. 4 to be minimized and the solutions there may also be applied to Eq. 4. There is, however, considerable difference in the definitions of the vectors used in the equations. As applied to attitude estimation, the vectors in Ref. 4 are direction cosines (although the solution also applies to unnormalized vectors) whereas here they are generated from the measurements (normalized or not) so as to minimize the weighted rotation error. The following solution to minimizing Eq. 4 is similar to that given in Ref. 4.

The matrix  $A^T A$  is symmetric and positive-semi-definite. Let  $d_i^2$  denotes the  $i^{\text{th}}$  ordered ( $d_1^2 \geq d_2^2 \geq d_3^2 \geq 0$ ) non-negative eigenvalue of  $A^T A$  corresponding to the normalized eigenvector  $N_i$ . The vectors  $AN_i$  ( $i = 1, 2, 3$ ) then constitute an orthogonal system of vectors with  $|AN_i| = d_i$ . Thus, an orthonormal system of vectors  $T_i$  ( $i = 1, 2, 3$ ) can be constructed such that  $AN_i = d_i T_i$ . If  $d_i = 0$  then  $T_i$  may be any arbitrary unit vector; otherwise

$$T_i = \frac{AN_i}{d_i}$$

$T_2$  and  $T_3$  are then similarly constructed. Let  $N$  and  $T$  denote the orthogonal matrices obtained by juxtaposing the vectors  $N_i$  and  $T_i$  respectively. Then from the constructions above it follows that  $T^{-1}AN = D$ , where  $D$  is a diagonal matrix with entries  $d_i$  (ordered). Introducing the orthogonal matrix  $M = N^{-1}RT$  ( $R$  is the desired least squares rotation) we find that the expression  $\text{tr}(RA)$  as a function of  $M$  becomes

$$\text{tr}(RA) = \text{tr}(NMT^{-1}A) = \text{tr}(MD) = \sum_{i=1}^3 m_{ii} d_i$$

For  $M$  orthogonal and  $d_i \geq 0$ , the maximum value of  $\text{tr}(RA)$  is obtained when  $M = I$ . Since  $|M| = |N| |R| |T|$ ,  $R$  will be a rotation matrix when  $M = I$  if  $|N| |T| = 1$ . If  $|N| |T| = -1$  then the maximum value of  $\text{tr}(RA)$  for  $|R| = 1$  is obtained when

$$M = \begin{pmatrix} 1 & 0 & 0 \\ 0 & 1 & 0 \\ 0 & 0 & -1 \end{pmatrix}$$

This latter case is equivalent to changing the sign of  $T_3$  in the definition of  $T$ . Thus,  $R = NT_0^T$ , where  $T_0 = (T_1, T_2, |N| |T| T_3)$  is the desired solution to the least squares condition. This solution can easily be generalized for vectors of arbitrary dimensions.

When only two measured vectors are given it can be shown that

$$\begin{aligned} N_1 &= \frac{W_1 - yW_2}{|W_1 - yW_2|} & N_2 &= \frac{W_1 + xW_2}{|W_1 + xW_2|} \\ T_1 &= \frac{xV_1 - V_2}{|xV_1 - V_2|} & T_2 &= \frac{yV_1 + V_2}{|yV_1 + V_2|} \end{aligned}$$

$N_2 = N_1 \times N_2$ , and  $T_2 = T_1 \times T_2$  gives the least squares solution if  $x$  and  $y$  satisfy the condition  $x + y > 0$  as well as the simultaneous equations:

$$(V_1 \cdot V_1)xy + (V_1 \cdot V_2)(x - y) - V_2 \cdot V_2 = 0$$

$$(W_1 \cdot W_1) + (W_1 \cdot W_2)(x - y) - xyW_2 \cdot W_2 = 0$$

The solution to this pair of equations is given by

$$x = \frac{a \pm \sqrt{a^2 + 4bc}}{2c}$$

$$y = \frac{-a \pm \sqrt{a^2 + 4bc}}{2c}$$

with

$$a = (V_2 \cdot V_2)(W_2 \cdot W_2) - (V_1 \cdot V_1)(W_1 \cdot W_1)$$

$$b = (V_1 \cdot V_2)(W_1 \cdot W_1) + (W_1 \cdot W_2)(V_2 \cdot V_2)$$

$$c = (W_1 \cdot W_2)(V_1 \cdot V_2) + (V_1 \cdot V_2)(W_2 \cdot W_2)$$

If Eq. 4 is written as a function of the  $Y$  rotation vector and the conditions for an extremum applied, the resulting three scalar equations can be expressed by a single vector equation as

$$2 \left[ \sum (W_1 \cdot V_1) \cdot Y + (V_1 \cdot Y)(W_1 \cdot Y) + V_1 \cdot W_1 \right] Y$$

$$= (1 + Y \cdot Y) \sum [(V_1 \cdot Y)W_1 + (W_1 \cdot Y)V_1 + W_1 \times V_1]$$

Ref. 2 gives a solution of this equation which requires obtaining the largest zero of a fourth order polynomial and then solving a linear system of three equations. It has also been solved successfully by a successive substitutions iteration (divide both sides of the equation by the coefficient of  $Y$  on the left side). In this case, the  $V_i$  are first rotated by an approximation of  $R$ . The rotation corresponding to  $Y$  is then the correction to the approximation necessary to obtain the least squares solution.

# ATTITUDE DETERMINATION AND PREDICTION FOR A CLASS OF GRAVITY-STABILIZED SATELLITES

M. G. Lyons and E. D. Scott  
Lockheed Missiles & Space Company  
Sunnyvale, California

## ABSTRACT

A relatively straightforward procedure for determining and predicting the attitude of gravity-stabilized satellites from incomplete attitude information is presented. The satellites considered were semi-passively stabilized with viscously damped control moment gyros. Closed form solutions for determining gyro parameters through flight data processing and for obtaining vehicle yaw measurements from sun sensor data are given. Techniques for processing on-orbit flight data and obtaining perturbed responses are described which permit evaluation of the vehicle torque environment using minimum squared error criteria. Finally, flight data from a recent series of gravity-stabilized satellites is presented with a comparison of on-orbit versus prelaunch parameters and a demonstration of the modelling accuracy and effectiveness of the attitude prediction method.

## SYMBOLS

$M_T$	Total external torque (3 x 1)	H	Time derivate of H with respect to body axes (3 x 1)
M	External torque exclusive of gravity torque (3 x 1)	I	Satellite's rigid body moment of inertia matrix (3 x 3)
$M_G$	Gravity-gradient torque $M_G = 3kR \times IR/r^3$ (3 x 1)	$\omega$	Angular velocity of body (3 x 1)
$H_B$	Satellite's rigid body portion of angular momentum $H_B = I\omega$ (3 x 1)	$\dot{\omega}$	Total time derivative of $\omega$ with respect to inertial space $\dot{\omega} = \dot{\omega} + \omega \times \omega = \dot{\omega}$ (3 x 1)
$\dot{H}_B$	Total time derivative of $H_B$ with respect to inertial space $\dot{H}_B = I\dot{\omega} + \omega \times I\omega$ (3x1)	R	Unit radius vector (3 x 1)
H	Total angular momentum of the CMGs (3 x 1)	r	Magnitude of radius vector
$\dot{H}$	Total time derivative of H with respect to inertial space $\dot{H} = \dot{H} + (\omega \times) H$ (3 x 1)	k	Earth's gravity field constant $k = 1.4077 \times 10^{16} \text{ ft}^3/\text{sec}^2$
		( $\omega \times$ )	Cross product matrix of $\omega$ (3 x 3)
		( $R \times$ )	Cross product matrix of R (3 x 3)
		A	Direction cosine matrix relating the body frame relative to the orbital reference frame (3 x 3)

$\omega_D$	Relative angular velocity between the body frame and the orbital frame $\omega_D = \omega - A\omega_R$ (3 x 1)
$\omega_R$	Angular velocity of orbital frame WRT $(X_o, Y_o, Z_o)$ (3 x 1)
$(\omega_D X)$	Cross product matrix of $\omega_D$ (3 x 3)
$(\omega_R X)$	Cross product matrix of $\omega_R$ (3 x 3)
$\sigma_1$	Gimbal angle of CMG <sub>1</sub>
$D_1$	Viscous gain of CMG <sub>1</sub>
$K_1$	Spring constant of CMG <sub>1</sub>
$\tau_1$	Gimbal torque due to torque generator and drift on CMG <sub>1</sub>
$O_1^t$	Transpose of the unit vector representing the output axis of CMG <sub>1</sub> (1 x 3)
$I_x, I_y, I_z$	Principal moments of inertia
$\omega_x, \omega_y, \omega_z$	Components of $\omega$ w. r. t. body axes
$H_x, H_y, H_z$	Components of $H$ w. r. t. body axes
$h_1, h_2$	Magnitude of angular momentum of CMG <sub>1</sub> , CMG <sub>2</sub>
$A_{13}, A_{23}, A_{33}$	Components of $A$
$M_x, M_y, M_z$	Components of $M$ w. r. t. body axes
$\beta$	Vee angle - one half the total included angle between the spin axes of the two CMGs in the vertical VCMG system
$\omega_o$	Average orbital angular rate $\omega_o = 2\pi/\text{Period}$ (scalar)
$c, s$	Abbreviation of cosine, sine
$e$	Eccentricity of the orbit
$\mu$	True anomaly
$E$	Unit 3 x 3 matrix (3 x 3)

## I. INTRODUCTION

The success of many satellite missions depends on how well vehicle attitude is controlled or, at least, on how well it is known. Employing an attitude determination system is often, especially for passive and semi-passive control systems, the most cost-effective way of performing mission objectives. Over the past year, such a system has been successfully used to estimate and predict the attitude librations of a gravity-stabilized Agena satellite in a low altitude orbit. Satellite motion was controlled with a pair of viscously-damped control moment gyros placed in a vertical vee configuration (Refs. 1, 2, and 3). Although four gyros were available for redundancy, two were normally operated at one time. Attitude sensing, in pitch and roll, was provided by a dual-head horizon sensor, and some yaw information was provided indirectly by three sun sensor units. All sensor outputs were contaminated with noise from both on-board systems and down-link telemetry processing such that pointwise attitude readings were unreliable. Furthermore, the sun was not always visible from the satellite which made it impossible to calculate yaw directly from the sensor data throughout each orbit. Since qualification of additional flight control hardware was neither feasible nor warranted, an attitude determination system, employing ground data processing, was developed.

Although the solution to this problem, as posed, can be obtained in a very abstract setting, it is the purpose of this paper to present a relatively straightforward method of solution and to give results obtained from processing actual flight data. The contribution is not one of new theoretical work but rather one of interesting experimental results.

The attitude determination system to be described employs a model, implemented with a digital computer simulation, of the gravity-stabilized satellite and the environmental disturbances due to magnetic, solar, and aerodynamic interactions. In order that the simulation accurately portrays actual vehicle motion, parameters describing the spacecraft must be determined. Usually, such parameters as center of gravity, CMG angular momentum, and vehicle moments of inertia are accurately known. Also, intensities of external disturbances such as solar pressure, aerodynamic effects, and magnetic fields can be calculated for particular orbits of interest. What is unknown about the system are those parameters describing the interaction of the vehicle with the environment, e. g., area and magnetic moments, and drag coefficients. Once the satellite is placed in orbit, however, observed vehicle motion can be used together with the simulation to estimate these unknown parameters. Since



attitude motion for this type of satellite is a somewhat periodic forced oscillation produced by complex environmental disturbance torques (Ref. 1), a digital simulation provides an appropriate solution; disturbance complexity is easily handled and convergence problems in the numerical integration are of little concern.

The determination procedure is organized into four main areas: flight attitude data is processed to remove telemetry channel noise; this data is used to compute closed form, equivalent on-orbit gyro parameters and sun sensor yaw values; perturbed vehicle responses are obtained for variations in disturbance torques to compute area moments using minimum squared error criteria; and, finally, a simulated response for past, present, and future satellite motion is generated. Relevant details of these techniques are discussed in the sequel, beginning with system modelling and concluding with some actual results and comments on system accuracy.

## II. SYSTEM MODELING

Since the attitude determination technique depends on an accurate simulation model, some characteristics of the disturbance environment and a brief description of the non-linear vehicle dynamics are given for later reference. A similar derivation of the equations of motion has been given in Ref. 1.

Magnetic, aerodynamic, and solar environmental disturbances were incorporated into the simulation. The earth's magnetic field was represented, for computational efficiency, with a twelve offset dipole approximation to 1960 earth field data (Ref. 4). The fitting error was less than two percent for low altitude orbits. Aerodynamic torques were accounted for with a modified Poe atmosphere (Ref. 5), incorporating solar bulge effects. Satellite position and relevant sun orientation were given with sun and satellite ephemerides including second order earth oblateness terms. Solar pressure disturbances were provided from structural models incorporated as part of the simulation. Frequently, however, uncertainties in the reflectance and specularities of structural components required that additional solar torque components be added "open-loop."

The roll-skewed VCMG control system is a semi-passive system used to constrain vehicle librations and is described in detail by numerous references, recently in (Ref. 1). As shown in Fig. 1, the spin vectors of the gyros form a vee in the vertical plane with the pitch axis bisecting the vee. The resulting angular momentum vector is nominally aligned to the orbital angular velocity vector. Both gyros are electrically torqued to maintain the vee and prevent alignment of orbit rate and gyro angular momenta. Gyro

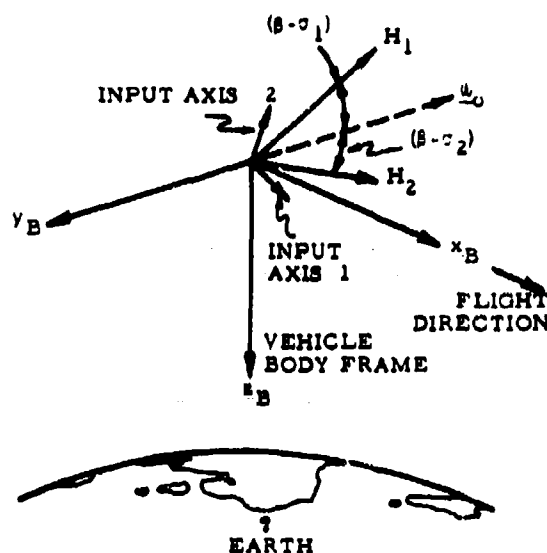


Fig. 1. Roll Skewed VCMG System Gyro Orientation

scissor motion provides pitch damping, while cascade motion produces yaw damping and, by roll-yaw cross coupling, damping in the roll axis. The system equations of motion are now briefly developed.

From Euler's equation of motion one obtains

$$\begin{aligned} M_T &= M + M_G = H_B + \dot{H} \\ M &= I\omega + (\omega \times) I\omega \\ &\quad + H + (\omega \times) H \\ &\quad - 3 \frac{k}{r^3} (R \times) I R. \end{aligned} \quad (1)$$

The kinematics of attitude motion will be specified in terms of the direction cosine matrix  $A$ , rather than some of the more usual kinematic representations (i.e., Euler angles, Euler parameters, Gibbs parameters, Cayley-Kline parameters, etc.) in order to minimize notation and geometric developments. The direction cosine matrix  $A$  relates the body frame  $(X, Y, Z)$  roll, pitch, and yaw axes, respectively, relative to an orbital reference frame. The orbital reference frame  $(X_o, Y_o, Z_o)$  is established by the unit velocity  $\omega_o$  (for circular orbit), unit negative orbital angular velocity, and unit gravity vectors, respectively. The time derivative of  $A$  can be determined from Coriolis's law as

$$\dot{A} = -(\omega_D X)A$$

$$\dot{A} = -(\omega X)A + A(\omega_R X); \quad (2)$$

the second line of Eq. (2) comes about through the similarity transformation of A on the cross-product matrix  $(\omega_R X)$ , coordinating it in the body frame rather than the orbit frame.

With the body frame selected to coincide with the satellite's principal axes, the moment of inertia matrix is diagonal with elements  $I_x, I_y, I_z$ , so that Eq. (1) can be written as

$$\begin{aligned} M_x &= I_x \dot{\omega}_x - (I_y - I_z) \omega_y \omega_z + H_x + \omega_y H_z - \omega_z H_y \\ &\quad + \frac{3k}{r^3} (I_y - I_z) A_{23} A_{33} \\ M_y &= I_y \dot{\omega}_y + (I_x - I_z) \omega_x \omega_z + H_y + \omega_x H_z - \omega_z H_x \\ &\quad - \frac{3k}{r^3} (I_x - I_z) A_{13} A_{33} \\ M_z &= I_z \dot{\omega}_z + (I_y - I_x) \omega_x \omega_y + H_z + \omega_x H_y - \omega_y H_x \\ &\quad - \frac{3k}{r^3} (I_y - I_x) A_{13} A_{23}. \end{aligned} \quad (3)$$

If the orbital motion is that of the undisturbed central force field two-body problem where the earth's oblateness, atmospheric drag, sun and moon effects are ignored, the angular velocity of the orbital reference frame becomes

$$\omega_D = \begin{bmatrix} 0 \\ \dot{\mu} \\ 0 \end{bmatrix} \quad (4)$$

where,

$$\dot{\mu} = \frac{\omega_0}{(1-R^2)^{3/2}} (1 + e \cos \mu)^2 = \omega_0 (1 + 2e \cos \mu) \quad (5)$$

and

$$k/r^3 = \dot{\mu}^2 / (1 + e \cos \mu) = \omega_0^2 (1 + 3e \cos \mu). \quad (6)$$

CMG dynamics may also be derived from Euler's equation of motion. Since the CMG is constrained to rotate only about its output axis, its dynamic

equation is scalar. The effect of the polar moment of inertia of the gyro's gimbal can be neglected, since the normal gimbal time constant is in the order of milliseconds while the vehicle time constant is in the order of kiloseconds. The equation of motion for the  $i^{\text{th}}$  CMG (CMG<sub>i</sub>) is

$$D_i \sigma_i + K_i \sigma_i = \tau_i - O_i^T (\omega_R) H_i \quad (7)$$

Equations (3) and (7) can now be written explicitly for the roll-skewed VCMG system. For this system, the X-component of H is zero, since the output axes of each gyro lie along the roll or X-axis. Assume that both gyros are oriented symmetrically above and below the minus Y-axis, in the vertical plane, by the angle  $\beta$  and CMG<sub>1</sub> has its output axis along negative X-axis with its spin above the horizontal plane, and CMG<sub>2</sub> has its output axis along positive X-axis with its spin below the horizontal plane (Fig. 1). The angular momentum of each CMG is then

$$\begin{aligned} H_1 &= h_1 \begin{bmatrix} 0 \\ -c(\beta - \sigma_1) \\ -s(\beta - \sigma_1) \end{bmatrix} \\ H_2 &= h_2 \begin{bmatrix} 0 \\ -c(\beta - \sigma_2) \\ -s(\beta - \sigma_2) \end{bmatrix} \end{aligned} \quad (8)$$

Thus the set of equations that specify the dynamics of the roll-skewed VCMG system is

$$\begin{aligned} M_x &= I_x \dot{\omega}_x - (I_y - I_z) \omega_y \omega_z \\ &\quad - \omega_y h [s(\beta - \sigma_1) - s(\beta - \sigma_2)] \\ &\quad + \omega_z h [c(\beta - \sigma_1) + c(\beta - \sigma_2)] \\ &\quad + \frac{3k}{r^3} (I_y - I_z) A_{23} A_{33} \\ M_y &= I_y \dot{\omega}_y + (I_x - I_z) \omega_x \omega_z \\ &\quad - \dot{\sigma}_1 h s(\beta - \sigma_1) - \dot{\sigma}_2 h s(\beta - \sigma_2) \\ &\quad + \omega_x h [s(\beta - \sigma_1) - s(\beta - \sigma_2)] \\ &\quad - \frac{3k}{r^3} (I_x - I_z) A_{13} A_{33} \end{aligned}$$

$$M_z = I_z \omega_z + (I_y - I_x) \omega_x \omega_y \quad (9)$$

$$\begin{aligned} & + \dot{\sigma}_1 h c (\beta - \sigma_1) - \dot{\sigma}_2 h c (\beta - \sigma_2) \\ & - \omega_x h [c(\beta - \sigma_1) + b(\beta - \sigma_2)] \\ & - \frac{3k}{r^3} (I_y - I_x) A_{13} A_{23}, \end{aligned}$$

and

$$\begin{aligned} D_1 \dot{\sigma}_1 + K_1 \sigma_1 &= \tau_1 - \omega_y h c (\beta - \sigma_1) + \omega_z h c (\beta - \sigma_1) \\ D_2 \dot{\sigma}_2 + K_2 \sigma_2 &= \tau_2 - \omega_y h c (\beta - \sigma_2) - \omega_z h c (\beta - \sigma_2) \\ \tau_1 = \tau_2 &= -\omega_0 h s \beta \end{aligned} \quad (10)$$

where the electrical torque generator commands on each CMG,  $\tau_1$ ,  $\tau_2$ , are adjusted to cause the gyro gimbal to operate about its null. With these results, some preliminary flight data processing may be accomplished.

### III. INFORMATION OBTAINED DIRECTLY FROM FLIGHT DATA

#### A. Gyro Parameters

Before evaluation of the interaction of the spacecraft and the environment can be accomplished, modeling for the control system must be made more precise. Although the structural properties of the vehicle are usually known quite accurately prior to launch, the gyro parameters are subject to large uncertainty since accurate measurements in earth gravity are not valid for this type of gyro. Therefore, it is advantageous to calculate the damping coefficients and torque generator biases for the CMG's installed in the spacecraft. The calculation proceeds by eliminating  $\omega_z$  from Eq. (10), which yields for zero spring constant,  $K_1$ ,

$$\begin{aligned} & \begin{bmatrix} \dot{\sigma}_1 c(\beta - \sigma_2), \dot{\sigma}_2 c(\beta - \sigma_1), -c(\beta - \sigma_2), -c(\beta - \sigma_1) \end{bmatrix} \begin{bmatrix} D_1 \\ D_2 \\ \tau_1 \\ \tau_2 \end{bmatrix} \\ & = \omega_y h s (\sigma_1 - \sigma_2) \end{aligned} \quad (11)$$

Evaluating (11) at  $n$  discrete times, letting

$$r^t = \begin{bmatrix} \dot{\sigma}_1(t_1) c(\beta - \sigma_2(t_1)), \dot{\sigma}_2(t_1) c(\beta - \sigma_1(t_1)), -c(\beta - \sigma_2(t_1)), -c(\beta - \sigma_1(t_1)) \\ \vdots \\ \dot{\sigma}_1(t_n) c(\beta - \sigma_2(t_n)), \dot{\sigma}_2(t_n) c(\beta - \sigma_1(t_n)), -c(\beta - \sigma_2(t_n)), -c(\beta - \sigma_1(t_n)) \end{bmatrix} \quad (12)$$

and weighting the parameters equally, (11) is inverted, for minimum squared error (Ref. 6) by

$$\begin{bmatrix} D_1 \\ D_2 \\ \tau_1 \\ \tau_2 \end{bmatrix} = (F^t F)^{-1} F^t \begin{bmatrix} \omega_y(t_1) s(\sigma_1(t_1) - \sigma_2(t_1)) \\ \vdots \\ \omega_y(t_n) s(\sigma_1(t_n) - \sigma_2(t_n)) \end{bmatrix} h, \quad (13)$$

All quantities except  $[D_1, D_2, \tau_1, \tau_2]^t$  are known functions of time. A unique solution for the unknown parameters is obtained when (11) is evaluated at four or more discrete times. With gyro characteristics determined, (10) can be used to compute  $\omega_z$ , whence yaw follows by integration. The integration constant is not known, however, so that the yaw obtained is only the oscillatory component, denoted  $\psi$ . It can be shown, in fact, that yaw motion is not observable from just horizon sensor and gyro gimbal data. Both  $\psi$  and gyro parameters are subject to errors in CMG modeling. Deviations from an ideal gyro such as spring restraint and gimbal sticktion effects could introduce appreciable errors into the calculation. Furthermore, the gyros used for this particular system are known to possess strongly temperature dependent damping coefficients,  $D_i$ . The solution (13), then, must be considered to describe average system parameters and not to give valid point-wise evaluation of gyro performance. The only method for eliminating the bias error from  $\psi$ , and hence, determine system yaw, is to provide independent yaw measurement at discrete times throughout the orbit. To this end, a sun sensor is employed and the necessary data processing is now described.

## B. Construction of Yaw From Sun Sensor Data

Before any sun direction sensor system can be used to determine yaw attitude, a sun reference direction must be established. To this end satellite and sun ephemerides are constructed which are valid over the time span when sun sensor data is available. The sun direction can now be defined with respect to orbit reference axes ( $X_o, Y_o, Z_o$ ) as shown in Fig. 2. This direction is, of course, independent of vehicle attitude. The sun sensor data may now be introduced. For the experiments considered here, the sensor hardware consisted of three sensor heads, each with a pair of orthogonal recticles positioned over a grey coded light-sensitive surface, oriented at various angles to the vehicle body frame. Attitude and azimuth readings from the recticles are converted to direction cosines; the sun direction is then transformed to the vehicle body frame ( $X_B, Y_B, Z_B$ ) through a set of Euler rotations specified by the alignment of the appropriate sensor. Finally, the sun direction in the body frame is transformed to a control frame ( $X_c, Y_c, Z_c$ ) defined as the body frame with pitch and roll rotations removed, i.e., a reference frame including only the yaw rotation about the local vertical. The relevant geometry is shown in Fig. 2. The vehicle horizon sensor pitch and roll time history determines this last transformation everywhere in the orbit. The sun direction is now projected onto the osculating plane of the orbit in both orbit and control reference axes. If  $S_{yo}$  and  $S_{yc}$  denote these projections then vehicle yaw is simply

$$\psi = \psi_o - \psi_c = \tan^{-1} \left( \frac{S_{yo}}{S_{xo}} \right) - \tan^{-1} \left( \frac{S_{yc}}{S_{xc}} \right) \quad (14)$$

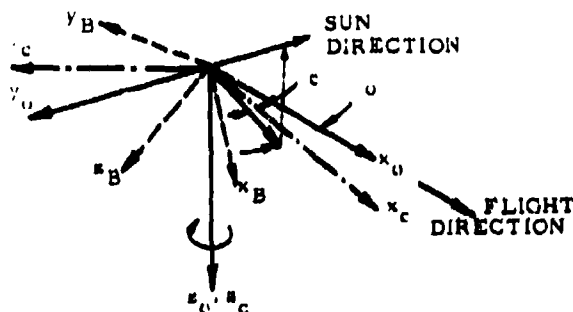


Fig. 2. Yaw Determination Geometry

The oscillatory yaw component,  $\bar{\psi}$ , discussed in the previous section, can now be combined with the measured yaw, which may be provided only infrequently throughout an orbit. To determine the bias or constant yaw offset,  $\bar{\psi} - \bar{\psi}$  is made small in the sense of minimum squared error following Eq. (13). The computed bias can then be added to  $\bar{\psi}$  giving a yaw time history valid over the entire orbit.

Although simple to implement, the sun sensor technique of yaw determination possesses some serious shortcomings. Errors introduced into the computations from inaccurate ephemerides are usually less than 0.1 deg; the principal errors are due to sensor quantization error and uncertainty in sensor alignment on the vehicle. For the present system, outputs in 0.5 deg increments with interpolation to 0.25 deg were available and the least squares estimation, between  $\bar{\psi}$  and  $\bar{\psi}$ , reduces this error. Sensor misalignment uncertainty, the most serious error, must be determined on-orbit while the vehicle is stabilized to a known attitude in three axes using a control system other than the CMO's. If such a calibration check cannot be made, there is no way to determine actual sensor alignment since vehicle and sensor yaw biases are indistinguishable. For the data given in Section V, no such alignment check was possible and alignment information from pre-flight measurements was employed. The errors observed are discussed in Section V.

## IV. PERTURBATION METHODS

Once the characteristics of the Control Moment Gyros are obtained (Section III), it remains to describe the interaction of the disturbance environment with the satellite. The effects of solar pressure, aerodynamic drag, and the earth's magnetic field must be considered. Thus, area moments and magnetic moments must be identified for each vehicle. If solar pressure disturbances are not accounted for directly in the dynamic model, additional external torques may have to be determined. The basic perturbation technique for accomplishing these tasks will now be described.

Flight data for the orbiting satellite giving vehicle roll, pitch, and CMO gimbal angles as functions of time over one complete orbit is obtained. Some additional details of the flight data processing will be given in the next section. For convenience in handling this data, these time functions are converted to the frequency domain with a modified Fourier series such that

$$\chi(t) = a_0 + \sum_{i=1}^5 a_i \cos \omega_0 i t + \sum_{i=1}^5 b_i \sin \omega_0 i t + a_{12} \frac{\omega_0 t}{2\pi} \quad (15)$$

where

$\underline{y}(t)$  is the flight data vector and  $t$  is time, usually taken from the ascending node.

The calculation is affected over a set of time points  $[t_j]_{j=1}^N$  by rewriting Eq. (15):

$$\underline{y} = \begin{bmatrix} \underline{y}(t_1) \\ \vdots \\ \underline{y}(t_N) \end{bmatrix} = \underline{A} \underline{x} \quad (16)$$

where  $\underline{x}$  is the vector of coefficients  $a_1, b_1$ , so that

$$\underline{x} = (\underline{A}^t \underline{A})^{-1} \underline{A}^t \underline{y} \quad (17)$$

for an unweighted minimum squared error (Ref. 6). The satellite motion due to disturbances can now be evaluated.

Perturbations to satellite motion are found using a dynamical simulation of the non-linear equations of motion. System response over the orbit represented by the flight data is converted to a set of modified Fourier coefficients given by (17). Let the basic librations due to eccentricity be given by coefficients  $\underline{x}_0$ , for area moments  $\underline{x}_{AX}, \underline{x}_{AY}, \underline{x}_{AZ}$ , and for magnetic moments  $\underline{x}_{MX}, \underline{x}_{MY}, \underline{x}_{MZ}$ . The coefficients, which will be referred to generally as  $\underline{x}_j$ , are produced with a nominal perturbation (e.g., area moment)  $\underline{P}_j$ , repeated simulation runs, and application of (17). If the system is assumed linear, it is then possible to write

$$\underline{x} - \underline{x}_0 = \sum_{j=1}^M \alpha_j \underline{x}_j \quad (18)$$

where the  $\alpha_j$ 's are to be determined.

Using a quadratic error criterion, (18) is solved in the presence of noise and model inaccuracies by

$$\underline{\alpha} = (\underline{X}^t \underline{X})^{-1} \underline{X}^t (\underline{x} - \underline{x}_0) \quad (19)$$

where the  $\underline{x}_j$  are the columns of  $\underline{X}$ . Hence, the desired vehicle parameters are given by

$$\underline{P}_j = \alpha_j \hat{\underline{P}}_j \quad (20)$$

These parameters are set in the simulation and the vehicle response to all the perturbations is observed. If this response matches flight data within allowable limits, modelling is complete and estimation and prediction of attitude motion is accomplished by running the simulation. If not, this motion, generated by  $\underline{P}_j$ , is used as a new  $\underline{x}_0$ , and the procedure using (18) is repeated until the simulated and actual motions agree to within an acceptable error bound. Actual processing has shown that more than one or two iterations produce little improvement in the fit.

## V. SYSTEM PERFORMANCE

The flight data results given below include evaluation of the fitting and simulation procedure for a four-hundred orbit time span. System parameters were initialized with the fitting procedure for orbit 742. The flight data and the simulated response using parameters obtained with the perturbation technique are shown in Fig. 3. Table 1 gives a numerical evaluation of the errors between the flight and simulated responses. Specific time points are not shown for the flight data in that this data has been processed to remove telemetry channel noise. The most noticeable error in the fit is between processed flight yaw and simulated yaw. A bias on the order of 0.5 deg can be observed. This is principally due to the new sensor misalignment uncertainty previously discussed. Figures 4 and 5 illustrate the deterioration of the simulation over subsequent orbits 773 and 1142, a full 400 orbits beyond the initial fit, and Table 2 gives an evaluation of the errors between simulation and flight data.

The deterioration in simulation accuracy as one moves away from the initial orbit is due to errors in modelling the system. To examine this problem consider the comparison of system parameters given in Table 3 for orbits 742 and 1142. The first column gives the results of the fit on 742, and the second column presents results of a refit done on 1142. Notice there is a substantial increase in gyro damping coefficients (four gyros were operating throughout this work). The nominal damping coefficient, based on ground measurements, is  $D_1 = 1.67$  ft-lb-sec. Ground measurements of this parameter cannot be made closer than  $\pm 50\%$ , however, so that the results obtained for 742 are not unreasonable. The gyro compartment was exposed to full sun on 742 and was partially shaded on 1142 which would cause an increase in damping for the latter orbit. (The temperature differential was  $20^\circ\text{C}$ .) Additionally, aging on-orbit for this type gyro has been

Table 1. Errors in Initial Fit,  
Rev 742

	Mean	Std Dev	Max Error
Roll	.0286	.0544	.3083
Pitch	-.0750	.1542	-.789
Yaw	-.0373	.1141	-.4919
CMG1	-.0101	.0734	-.2705
CMG2	-.0073	1.0625	.2396
CMG3	.0186	.1133	.5985
CMG4	.0127	.0965	.5246

All errors in degrees.

Table 2. Errors in Predicted  
Responses  
Rev 773

	Mean	Std Dev	Max Error
Roll	.1031	0.0818	.3230
Pitch	-.3673	0.3669	-.10090
Yaw	-.2947	0.1202	-.6742
CMG1	-.0104	0.1756	-.3158
CMG2	.0431	0.1631	.3242
CMG3	.0564	0.1822	.4118
CMG4	.1423	0.1630	.4955

Rev 1142

Roll	0.1	0.09	.29
Pitch	0.05	1.09	-1.88
Yaw	0.7	.76	-2.02
CMG1	-0.4	.80	-1.91
CMG2	-0.4	.74	-1.81
CMG3	-0.8	.46	-1.58
CMG4	-1.2	.43	-1.87

observed to create severe sticktion problems. Since sticktion is not explicitly modeled, variations in damping will attempt to account for this effect.

For this satellite, closed-loop calculation of solar pressure disturbances was not available, and these torques were added open-loop for orbit rate and twice orbit rate terms as shown in Table 3. This modeling error results in the wide variation of the solar torques and, consequently, of the magnetic torques. At the flight altitudes used, system response was quite insensitive to changes in yaw area moments. Thus the deviation in this quantity is not unexpected.

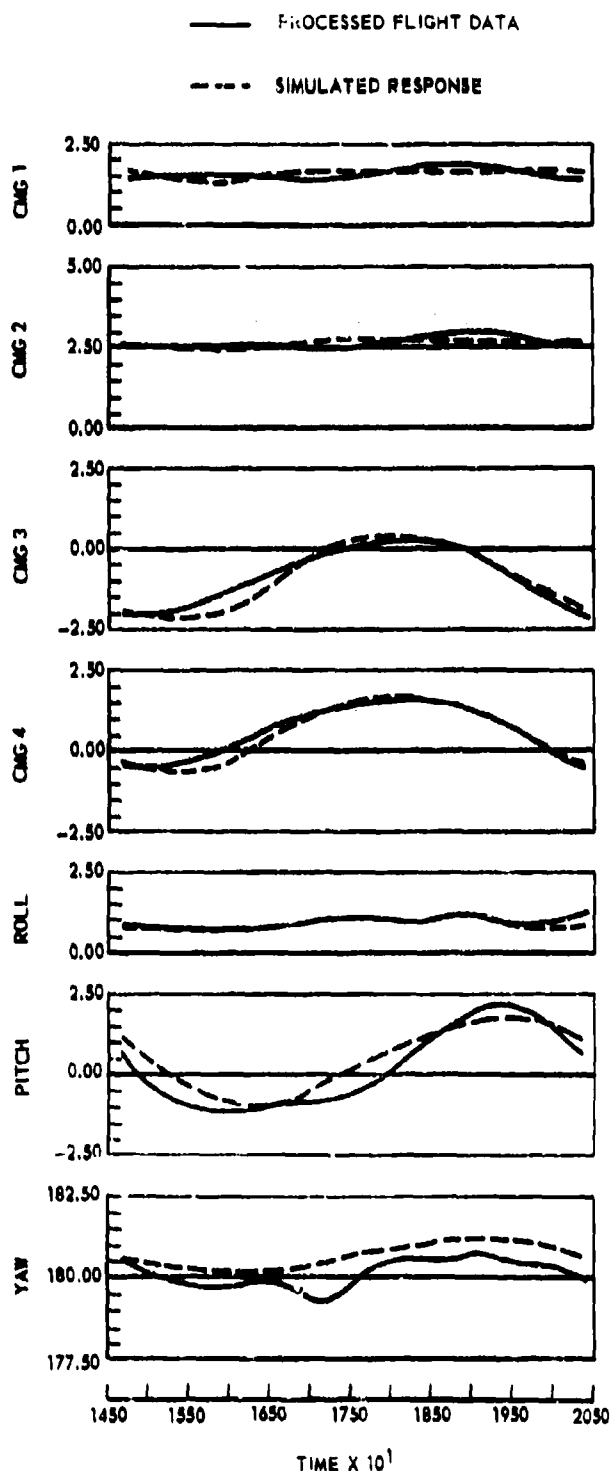


Fig. 3. Flight Data and Simulation for a Fit  
on Orbit 742

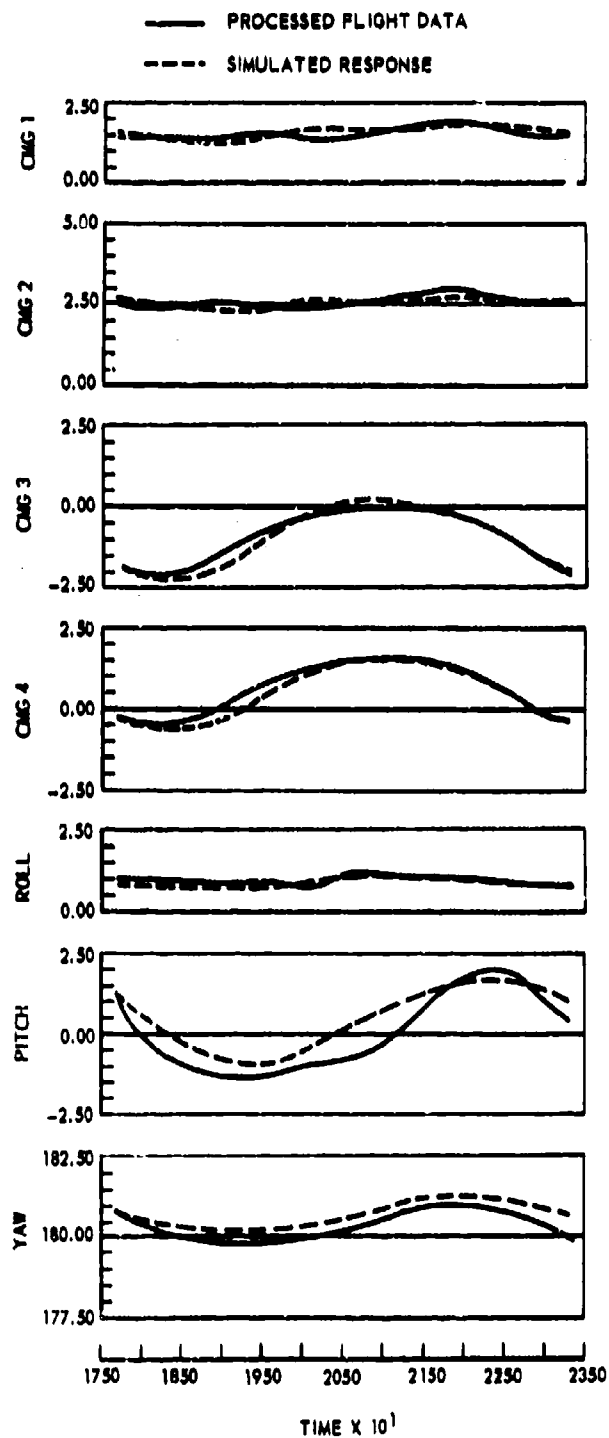


Fig. 4. Flight Data and Simulation for a Prediction on Orbit 773

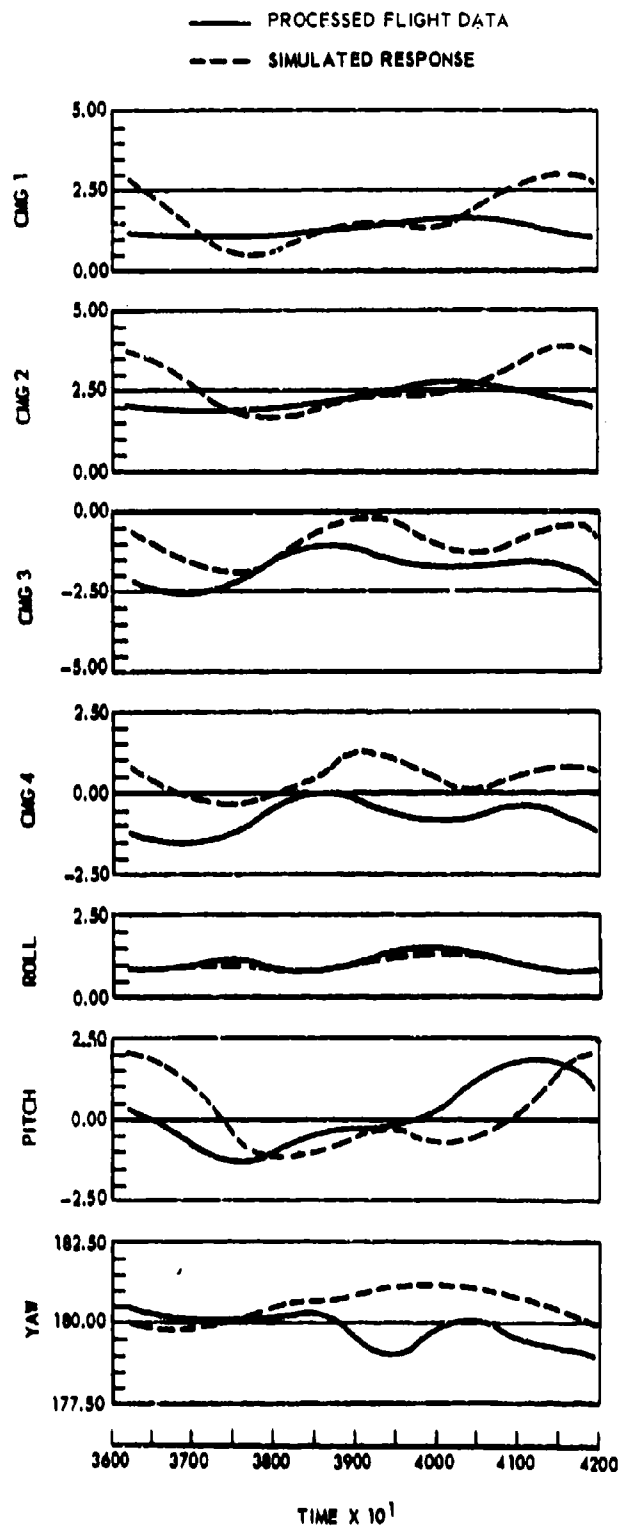


Fig. 5. Flight Data and Simulation for a Prediction on Orbit 1142

Table 3. Vehicle Parameters for  
Orbits 742 and 1142

Parameter	742	1142
$D_1$ ft-lb-sec	1.33	2.71
$D_2$	2.03	2.36
$D_3$	1.72	2.35
$D_4$	1.89	2.35
$\tau_1$ rad/sec	$-4.03 \times 10^{-4}$	$-4.09 \times 10^{-4}$
$\tau_2$	$-3.85 \times 10^{-4}$	$-3.91 \times 10^{-4}$
$\tau_3$	$-6.82 \times 10^{-4}$	$-6.95 \times 10^{-4}$
$\tau_4$	$-6.60 \times 10^{-4}$	$-6.80 \times 10^{-4}$
roll torque: constant	$7.0 \times 10^{-5}$	$-0.4 \times 10^{-5}$
ft-lb $c\omega_o t$	$-3.0 \times 10^{-5}$	$-9.8 \times 10^{-5}$
$c\omega_o t$	$-1.3 \times 10^{-5}$	$3.2 \times 10^{-5}$
$s\omega_o t$	$-1.6 \times 10^{-4}$	$-3.3 \times 10^{-4}$
$ss\omega_o t$	$-0.3 \times 10^{-5}$	$0.8 \times 10^{-5}$
area moments: $x$	951	858
$ft^3$ $z$	-512	-227
magnetic $M_x$	$5.0 \times 10^{-4}$	$7.4 \times 10^{-4}$
moments $M_y$	$0.9 \times 10^{-4}$	$3.3 \times 10^{-4}$
ft-lb/ oerst $M_z$	$5.0 \times 10^{-4}$	$-1.5 \times 10^{-3}$

#### REFERENCES

1. E. D. Scott, and J. J. Rodden, "Performance of gravity-gradient VCMG systems," Proceedings of the AIAA Guidance, Control and Flight Mechanics Conference (Princeton, New Jersey, 18-20 August 1969).
2. E. G. C. Burt, "On the attitude control of earth satellites," Eighth Anglo-American Aeronautical Conference (London, Sept. 1961).
3. E. D. Scott, "Control moment gyro gravity stabilization," Progress in Astronautics and Aeronautics (Academic Press, 1964), Vol. 13, Guidance and Control -II, p. 103.
4. J. J. Rodden and E. D. Scott, "Dyadic representation of the earth's magnetic field," DCA/2257/6221, Communication to Ekotech, Inc., Washington, D. C., 13 Nov. 1967.
5. NASA Monographs on Space Vehicle Design Criteria, Guidance and Control, Spacecraft Aerodynamic Torques, to be published.
6. R. Deutsch, Estimation Theory (Prentice-Hall, Inc., Englewood Cliffs, N. J., 1965), p. 58.

In conclusion, it has been seen that even for simplified gyro and environmental modeling, the capability of the simulation is characterized by fitting mean errors less than 0.1 deg and by attitude prediction errors of less than 1.0 deg mean over a four-hundred orbit span. Furthermore, gyro parameters determined during the fitting process agree with relatively inaccurate measurements made in the earth's gravitational field, and exhibit behavior which can be at least qualitatively explained. For many missions of interest, such prediction and determination capability is of definite value. The results are especially important if the vehicle horizon sensors should fail. For such an occurrence, mission life might be greatly extended with the prediction system. More precise modeling of course will improve the accuracy, and, in fact, prediction to the above accuracies was made for time spans one order of magnitude larger than those given here.



ESTIMATION AND PREDICTION OF THE ATTITUDE OF A PASSIVE GRAVITY STABILIZED  
SATELLITE FROM SOLAR ASPECT INFORMATION

Bruce E. Tinling and Vernon K. Merrick  
Ames Research Center, NASA  
Moffett Field, Calif., 94035

ABSTRACT

Essential to the estimation and prediction technique is the selection of a simple observable set of satellite parameters which, if known, permits the disturbance torques to be approximated. The values of the parameters were established by analyzing a large number of imperfect observations and the attitude was subsequently calculated by integration of the equations of motion. A significant result of the study is that the parameters can be estimated solely from solar aspect information.

The technique was evaluated by a simulation study. The simulated satellite was assumed to be in a polar orbit at an altitude of 1400 km and to have solar aspect sensors digitized to have a sensitivity of  $0.5^\circ$  per digit. The results indicated that past attitude history could be estimated to within  $0.1^\circ$ . Application of the technique to long range prediction produced the same errors in earth pointing, but the yaw errors were approximately doubled.

I. INTRODUCTION

The accuracy of any attitude determination scheme depends upon the accuracy of the satellite attitude sensors and upon the technique employed to process their readings. Measurements taken at a given instant contain random errors, and considerably better accuracy can be achieved when some smoothing technique is applied. An efficient smoothing, or attitude estimation, scheme can be based on the premise that the steady-state motion can be computed when the variation of the external disturbance torques with time is known. Successful implementation requires that the satellite dynamics and environment be known, and that sufficient information can be obtained from observing the attitude motion to deduce those remaining unknown quantities, such as the residual magnetic dipole, essential to the calculation of the disturbance torques.

The estimation scheme is readily applied to improving the knowledge of the attitude motion of passively controlled satellites. In theory, the

scheme can be applied regardless of the type of control system in use. However, passive systems are unique in that they are subject only to forces caused by interaction with the environment. In contrast, active systems are subject to forces caused by less predictable control activity. Further, since the disturbances to passive satellites are almost exclusively steady or periodic, it should be possible to predict future attitude motion based on the analysis of past attitude history. If it is required that a satellite direct its sensors earthward, the natural choice of passive attitude control is gravity stabilization. In addition to long life, zero power consumption, and excellent reliability, this stabilization technique provides a vibration-free sensor platform with angular rates much lower than its active counterparts.

Attitude estimation and prediction has already been demonstrated by Scott and Rodden (Ref. 1) who analyzed the motion of a gravity stabilized satellite that used control moment gyros to provide damping and yaw stiffness. The present

study was initiated to determine the feasibility of applying estimation techniques to predict the attitude of a completely passive gravity stabilized satellite. The aims of present study differ somewhat from those of Scott and Rodden. In particular, major objectives of the present study are to compare the estimation accuracy for various sets of instruments and to determine the simplest set of instrument sufficient to yield the necessary information.

More specifically, the estimation technique was applied to an inertially coupled satellite that relies solely upon the gravitational field for damping as well as restoring torque (Ref. 2). In the absence of suitable data from an actual satellite, it was necessary to analyze simulated attitude motions. The simulation assumed the satellite to be in a polar orbit at an altitude of 1400 km such as might be specified for meteorological or earth resources missions. It is, of course, not possible to determine if the model of the steady-state disturbances used in the simulation is adequate or if important errors will be caused from those nonsteady disturbances that are encountered in orbit. This type of study can, therefore, never prove that attitude estimation will be successful when applied to an actual satellite. Conversely, if attitude estimation is infeasible with a simulated satellite, it is certain to be infeasible for an actual satellite.

## II. NOTATION

$A(t)$	time varying matrix of partial derivatives of the attitude angles with respect to the unknown parameters
$\bar{b}_j$	unit vectors defining orthogonal reference frame fixed in main satellite body; for zero attitude errors $\bar{b}_j = \bar{o}_j$
$d_j$	components of the unknown vector from the center of mass to the geometrical center of the satellite; measured in the $\bar{b}_j$ frame
$e(t)$	instrument errors
$H(t)$	time varying matrix of partial derivatives of the instrument readings with respect to the unknown parameters
$I_{ij}$	moments and products of inertia of main satellite body relative to the $\bar{v}_j$ frame
$i, j$	1, 2, 3
$m_j$	components of the unknown magnetic dipole, moment; measured in the $\bar{b}_j$ frame
$\bar{o}_j$	unit vectors defining orthogonal reference frame fixed at satellite orbit: $\bar{o}_3$ is directed toward center of earth; $\bar{o}_1$ is in the direction of motion
$p$	parameters describing physical characteristics of the satellite

$Q$	covariance matrix of the observations
$q$	quantization of digital sensors
$r$	vector function describing satellite environment
$t$	time
$\bar{v}_j$	unit vectors defining orthogonal reference frame coincident with principal inertia axes of entire satellite; in equilibrium $\bar{v}_j = \bar{o}_j$
$x$	unknown parameters composed of the elements $a_j$ , $d_j$ , and $m_j$
$y(t)$	instrument readings
$z$	state vector composed of attitudes and angular velocities
$\Delta()$	increment
$()$	ensemble
$()^*$	estimated quantity
$a_j$	unknown angles giving orientation of $\bar{b}_j$ frame relative to $\bar{v}_j$ frame
$\beta$	acute angle between boom axis and $\bar{b}_3$ axis
$\gamma$	angle the sunline makes relative to the orbit normal
$\epsilon_s$	error in the subscripted quantity
$\theta_{ds}$	bias of damper spring from zero position in absence of gravity torques
$\lambda$	angle of the sunline relative to the first point of Aries measured in the ecliptic plane
$\sigma_e$	variance of normally distributed errors in the edges of the region assigned to each digit of sensors
$\phi, \theta, \psi$	Euler angle sequence relating $\bar{b}_j$ frame to $\bar{o}_j$ frame
$\Omega$	longitude of the ascending node of the orbit measured from the first point of Aries in the equatorial plane

## III. ESTIMATION AND PREDICTION TECHNIQUE

The estimation technique is based on the premise that the dynamics of a gravity stabilized satellite and all of its disturbance sources are understood. The estimation technique seeks to establish the hitherto unknown values of certain quantities through analysis of the observed attitude sensor readings. Once the unknowns are established, a complete model of the

dynamics and disturbance sources is available and past and future attitude motion can be simulated.

#### A. The Model

All of the information, both known and unknown, that constitutes the complete model required for the simulation can be placed in three general categories: the equations of motion, the physical characteristics of the satellite, and the environment. These are discussed in the following sections.

##### 1. The Equations of Motion

The equations of motion must include all of the significant dynamical effects if precise estimation of future attitude motion is to be achieved. For this study, the dynamics were assumed to be adequately represented by the dynamics of a pair of connected rigid bodies. For some gravity stabilized satellites, rigid-body dynamics are not an adequate representation because the flexural modes of boom motion couple significantly with the librational motion. This is true, for instance, in the analysis of the motion of the Radio Astronomy Explorer Satellite which has boom lengths of the order of 200 meters (see Ref. 3). In other instances, the variation of the mass distribution with time caused by thermal distortion may invalidate the assumption of rigid-body dynamics (see Ref. 4). These effects will not be present if newly developed booms are used which theoretically have no thermal distortion (Ref. 5), or if the satellite has a symmetrical arrangement of the booms.

The satellite considered in this study has symmetrically oriented booms whose lengths are such that their natural frequencies are large compared with the libration frequencies. For such a satellite the rigid-body equations are considered to provide an adequate representation of the steady-state dynamics. This representation requires an eight-dimensional state space: three coordinates each for the attitude and angular velocity of the main satellite body, and two coordinates to represent the relative attitude and angular velocity of the single degree-of-freedom damper body (see Ref. 2). The state equation is

$$\dot{z} = f_1[t, z, p, r(t)] \quad (1)$$

The form of  $f$  is known explicitly;  $p$  represents the parameters defining the particular physical characteristics of the satellite;  $r$  represents the environment which reacts with the spacecraft to produce the external disturbances. The solution of Eq. (1) for initial conditions  $z = z_0$  and  $t = t_0$ , will be denoted by

$$z(t) = f_2(t, t_0, z_0, p, r) \quad (2)$$

Equation (1) was used in generating the various quantities required by estimation procedure and

in simulating the unknown motion to be analyzed. It is obvious, therefore, that the results of the study can provide no conclusions concerning whether or not the rigid-body equations are adequate for use in the estimation procedure. Such conclusions must await application to a real, rather than to a simulated, satellite.

##### 2. The Environment

The estimation procedure is based upon a perfect knowledge of the environment. Essential to the knowledge of the environment is knowledge of the orbital parameters. This permits the effects of eccentricity on the attitude motion to be accounted for and establishes the relationship between satellite-, solar-, and earth-centered coordinates. This information along with the known energy density of sunlight and a model of the geomagnetic field, defines the solar pressure and magnetic environment of the satellite. For near earth orbits, such as considered in this study, the assumption that the magnetic field is known perfectly appears to be reasonable. For the purpose of this study the field was assumed to be that due to a tilted dipole, although more accurate models are available.

##### 3. Physical Characteristics of the Satellite

The attitude behavior of the satellite can be calculated only if the set of parameters  $p$  defining its physical characteristics are known accurately. Many of these parameters, such as the mass distribution and geometry of the stabilized package, are known in the sense that they can be measured accurately prior to launch and are certain to remain constant thereafter. Others, such as the residual magnetic dipole, although they may be measured accurately prior to launch, vary unpredictably during the period of launch and deployment. Still others, such as solar pressure torques, cannot be measured adequately on the ground and must be estimated.

Provided the model of the satellite system is adequate, errors in the calculated attitude will arise because of deviations in the measured or estimated values of the unknown and poorly known parameters. An obvious approach to the attitude estimation problem is to select all the parameters whose value is uncertain and try to estimate better values using measured data. One difficulty with this approach is that measurements may not permit all the parameters to be uniquely distinguished from each other. Another difficulty, of a more practical nature is that the amount of computation and numerical round off errors increase rapidly with the number of parameters considered. A more realistic and certainly more practical approach is to limit the number of parameters to be estimated. The set of parameters selected must have two properties. First, the effect of each of the parameters on the attitude must be distinguishable from the effect of all the others. Second, it must be possible to find a set of values for the parameters that will produce an approximation to all the expected disturbance torques. For the particular low-altitude satellite under consideration,

the parameters selected were the misalignment angles between the principal axes of inertia and the reference axes, the distance between the center of mass and center of area, and the magnitude and direction of the residual magnetic dipole. A total of nine quantities is needed to define these error sources.

The selection of the nine parameters to be estimated implies that all other parameters and the environment are assumed to be known perfectly. Let  $p = (x, p_0)$  where  $x$  denotes the nine parameters to be estimated, and  $p_0$  denotes all those assumed to be known. The motion of the system then only depends upon  $t$  and the unknown parameters  $x$ . Thus:

$$z(t) = g_1(t, x) = f_2[t, t_0, z_0, (x, p_0), r] \quad (3)$$

### B. Instrumentation

Attitude instrumentation for earth oriented satellites is usually selected so that the attitude can be resolved from a set of data taken at a given instant. Most earth oriented satellites have some combination of earth sensors magnetometers, and solar aspect sensors. Each sensor can determine the coordinates of some line relative to the satellite reference system; thus two different types are required to determine the attitude at any given instant. With the introduction of the estimation procedure, the criterion for the selection of instruments is different and less stringent. The only requirement is that the unknown parameters can be found from some set of observations taken at selected times. Using the estimation procedure to determine attitude therefore affords an opportunity to simplify the instrument system. The identification of the simplest set of instruments that would yield satisfactory attitude information was one of the goals of the study.

The instruments considered were combinations of solar aspect sensors, a horizon scanner, and a damper boom angle indicator. Five solar aspect sensors are required for spherical coverage. Three were placed 120° apart in the plane that nominally coincides with the orbital plane and the remaining two were pointed in either direction normal to the orbital plane.

The general form of the equations characterizing the set of instrument readings can be expressed as:

$$y(t) = g_2(t, z) + e(t) \quad (4)$$

where  $e$  represents instrument errors. Consequently, sensor outputs are related to the unknown parameters by the composite of Eqs. (3) and (4). That is,

$$y(t) = g_3(t, x) + e(t) \quad (5)$$

where

$$g_3(t, x) = g_2[t, g_1(t, x)]$$

### C. Estimation of Unknown Parameters

The estimation procedure seeks to improve the knowledge of the parameters assumed to be imperfectly known. The process is similar to quasi-linearization described in Ref. 6. As illustrated in Fig. 1, the process starts with an initial guess of the parameters  $x_1$ . From this estimate, an estimate of the subsequent instrument readings is calculated from the dynamic model of the satellite and its disturbances, and is compared with the actual instrument readings from the satellite. The difference between the actual and estimated instrument readings is then used to improve the knowledge of the parameters  $x_1$ . The desired quantities, the attitude angles, are obtained from the dynamic model of the satellite and its disturbances. Knowledge of  $x_1$  therefore implies that not only can past motion be estimated but future motion can be predicted.

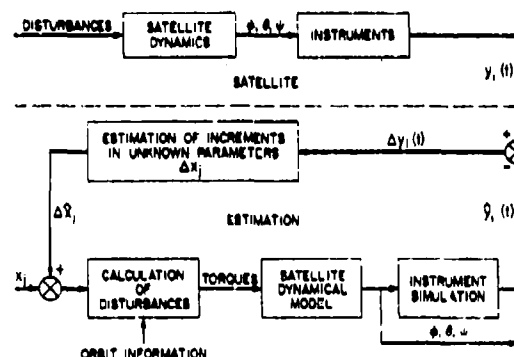


Fig. 1. Block diagram of the estimation procedure.

The estimation technique relies upon making a large number of imperfect observations to establish the value of the unknown parameters. Since the parameters are assumed to be invariant with time, the problem is tractable and consists in finding the minimum variance solution of a system of linear equations. The system of equations can be expressed as

$$\Delta y = H \Delta x + e \quad (6)$$

where

$$\Delta y = \begin{pmatrix} \Delta y(t_1) \\ \vdots \\ \Delta y(t_n) \end{pmatrix}$$

$$H = \begin{pmatrix} H(t_1) \\ \vdots \\ H(t_n) \end{pmatrix}$$

$$e = \begin{pmatrix} e(t_1) \\ \vdots \\ e(t_n) \end{pmatrix}$$

and

$\Delta y(t)$  the deviation of the instrument readings from those corresponding to the attitude at time  $t$  given the prior estimate of the unknowns  $x$

$\Delta x$  deviations in the unknown parameters from the prior estimate

$H(t)$  a matrix of partial derivatives relating  $\Delta y(t)$  to  $\Delta x$

$e(t)$  the instrument errors at time  $t$

It was not feasible to calculate the elements of the matrix  $H(t)$  analytically from the nonlinear equations of motion of the two-body satellite. Instead, the elements of the matrix were evaluated through simulation of the attitude motion. A reference motion was first obtained assuming a prior estimate of the unknown parameters. A subsequent motion was then calculated with an increment in one of the components of  $x$ . The magnitude of the increment was chosen to be equal to the expected deviation. The derivative was then evaluated assuming the variation of the instrument reading with the change of state to be linear. Thus,

$$h_{ij} = \frac{g_j(t, x + \Delta x_i) - g_j(t, x)}{\Delta x_i}$$

The elements of the matrix  $H(t)$  therefore depend on the prior estimate of  $x$  and the magnitude of the increment  $\Delta x$ , as well as time. However, the primary dependence is upon time which determines the orbital position and therefore the relationship of the satellite to the sun and the magnetic field. The dependence upon  $x$  arises solely from nonlinearities.

The minimum variance solution of Eq. (6) for the deviations of the unknowns from the prior estimates,  $\Delta x$ , is well known (see, e.g., Ref. 7) and is given as

$$\Delta x = (H^T Q^{-1} H)^{-1} H^T Q^{-1} \Delta y \quad (7)$$

where  $Q$  is the covariance of the instrument errors (i.e.,  $Q = E(ee^T)$ ). It is assumed in the derivation of Eq. (7) that the instrument errors are uncorrelated, have zero mean, and are independent of the measurements.

#### IV. SIMULATION

The unknown attitude motion and the corresponding instrument readings were generated by a digital computer simulation. The characteristics of the simulated satellite were obtained

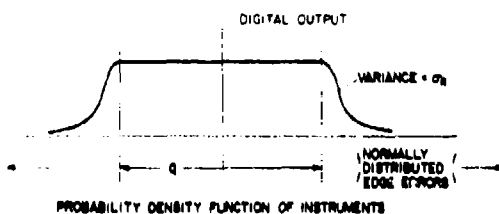
by assuming random deviations of its physical characteristics from a known satellite. The characteristics of the known and the unknown satellites are given in Table I. These deviations were intended to simulate the unknown error sources that might be present after the spacecraft has been launched and the booms erected. The deviations included the angle that the individual booms make with the vertical reference axis, the reflectivity of the booms, the radius of curvature due to thermal distortion, the erected boom length, the damper bias angle, and the residual magnetic dipole.

A complete simulation of a satellite would require that the relationship of the orbit to the sunline change slowly with the seasons and with any motion of the line of nodes. For purposes of simulation, the orbit was assumed to be polar, and its relationship to the sunline was assumed to be fixed for any one data sample. The effect of changes in the relationship of the orbit to the sunline on the estimation procedure was studied through simulation of separate cases. These were achieved by arbitrary changes in  $\Omega$ , the angle the line of nodes of the orbit makes with the first point of Aries, and  $\lambda$ , the angle measured in the ecliptic between the sunline to the earth and the first point of Aries. The following cases were studied:

Case	$\Omega$	$\lambda$	Sun angle relative to orbit
I	0	0	Orbit plane contains sunline
II	60°	0	Sunline 30° from orbit normal
III	30°	0	Sunline 60° from orbit normal
IV	120°	90°	Sunline -60° from orbit normal

All the instruments were assumed to be representative of those currently available. Their output readings were assumed to be digital and were simulated by calculating their exact value and assigning the appropriate digital value. Each instrument was assumed to have some randomness in the location of the edges of the regions assigned to each digit. This randomness can arise from errors in the quantization (i.e., errors in the location of the edge of the region assigned to each digit), and from randomness in the digit assigned by the sensor electronics when the exact reading approaches the edge. In the simulation, the errors were considered to be of the latter type and were simulated by adding a random number to the exact reading prior to assigning the digital value. If quantization errors are present, the assumptions inherent in the solution of Eq. (7) will be violated because the error distribution associated with a particular digit will not have zero mean. Consequently, there will be a correlation between the sensor reading and its errors.

The characteristics of each of the instruments simulated is given in the following sketch and table. Note that the quantization of the solar aspect sensor is given as approximately 0.5°. The exact quantization of the solar aspect sensor varies with the angles sensed. This variation,



INSTRUMENT	Q	$\sigma_1$
HORIZON SCANNER	0	0.1
SOLAR ASPECT SENSORS	-0.85	0.1
DAMPER BOOM ANGLE	0	0.1

as well as the edge errors, were taken into account in calculating the instrument variances for use in Eq. (7).

## V. RESULTS AND DISCUSSION

### A. Observability

The first result to be established is the identification of those sets of instruments that will permit a solution of Eq. (7) for the values of the unknown parameters. A necessary condition for solving this equation is that all attitude angles must influence the readings of the sensors at some time during a given orbit. As in the case of determining attitude at a given instant, this rules out the possibility of using the horizon scanner alone, since yaw angle cannot be sensed. The additional information possibly could be supplied by a damper boom angle indicator if the damper boom responds to steady and oscillatory yawing motion. It will so respond provided that either the neutral position of the damper or the hinge axis does not lie normal to the yaw axis. However, the damper boom and the hinge axis of the satellite analyzed were located in the horizontal plane. For this position, the damper does not respond to a steady yaw, thereby preventing the evaluation of the steady yaw offset,  $\alpha_3$ . It follows that solar aspect sensors must be included in any combination of the available instruments if Eq. (7) is to be solved.

With the exception of a single orientation of the orbit relative to the sunline, the solar aspect sensor measurements are influenced by all the attitude errors at some time during an orbit. This is necessary, but not sufficient, to insure that a solution to Eq. (7) exists. To establish that a solution exists it is required that the determinant of  $\mathbf{H}^T \mathbf{H}$  be nonzero for some series of measurements. With the exception of one situation described below, this condition was satisfied for solar aspect measurements alone. Hence, except for one condition, solar aspect measurements will provide sufficient information to solve for the unknown increments in the unknown parameters.

This exception occurs when the orbit plane is normal to the sunline. Then the complete list of unknowns is unobservable by any combination of instruments because the solar pressure torques that result from the center-of-mass shift,  $d_1$ ,

produce steady angular offsets that are indistinguishable from the variables,  $\alpha_1$ . The estimated values of either set of parameters will therefore produce both effects and one set could be eliminated if the satellite orbit were to remain normal to the sunline.

This particular orbit is also unique in that solar aspect sensors alone do not provide sufficient information to solve for even the reduced list of unknowns. The reason is that a satellite with a steady attitude error will have no change in its orientation relative to the sun as it moves along the orbital path. The sun sensors will yield information on two angles required to describe the orientation of the satellite relative to the sun. Since it is required to evaluate three variables to describe the steady attitude angle offset, no solution is possible. This difficulty could be resolved by using the damper boom angle for additional information if the bias of the damper from its nominal position,  $\theta_d$ , is known. Otherwise, the bias must be included in the list of unknowns to be determined. In this event, one more unique equation and one more unknown are added to the system of equations and a solution does not exist.

Although the test for observability establishes that, with the above exception, solar aspect sensors alone yield a unique solution for the unknowns, it gives little insight into the accuracy of the estimation technique when a limited number of imperfect measurements are processed. Therefore, estimation was attempted with several instrument systems. These included solar aspect sensors alone, solar aspect sensors in combination with a damper boom angle indicator, and solar aspect sensors in combination with a horizon scanner.

### B. Short-Term Estimation

The unknown parameters were estimated from a data sample that covered about five orbits. Typical results showing the motion calculated given initial estimates of the unknowns are shown in Fig. 2. In this instance, the unknown parameters were initially estimated to be zero ( $x = 0$ ). The first iteration then seeks to minimize the variance of the difference between the actual instrument readings and the exact instrument readings corresponding to motion when  $x = 0$ . As can be seen from the results, integration of the equations of motion with the new estimate of the unknowns results in reasonable agreement between the estimated and the actual motion. Some improvement in the estimated motion results if a second estimate of the unknowns is made. In practice, this estimate would be based upon a subsequent data sample. For purposes of this study, the same data were reprocessed.

The errors in the second iteration of the pitch, roll, and yaw for the period covering the data sample are shown in Fig. 3. The estimated motion matched the actual motion to within 0.1° except for a few points in yaw. This result was obtained regardless of the instrument system in

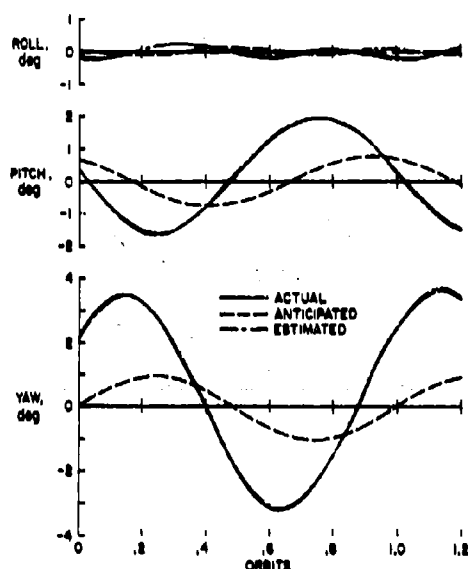


Fig. 2. Typical results of the estimation procedure.

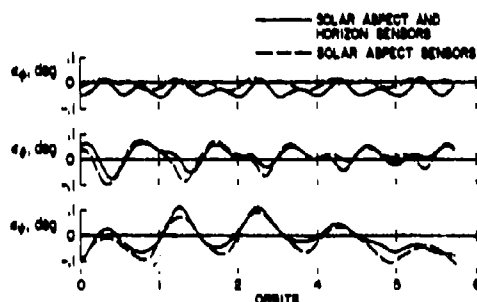


Fig. 3. Typical errors in the estimation after two iterations over the entire period of the data sample;  $\Omega = 0$ ,  $\lambda = 0$ .

use. As indicated by Fig. 3, no improvement in the estimate based on solar aspect sensors alone resulted when horizon scanner measurements were included. A similar conclusion was reached concerning the addition of damper angle measurements to the solar aspect sensor measurements.

An examination was made of various error sources that can influence the accuracy of the estimation. These sources include: insufficient number of observations, nonlinearities in the variation of the instrument readings with the unknowns, imperfections in the model, and poor observability. These error sources will be discussed in turn.

#### 1. Effect of Number of Observations

Ideally, sufficient observations should be taken to reach the point where additional observations would cause little or no change in the

solution for the unknowns. The observations were arbitrarily taken 0.3 of a radian apart along the orbital path, and the maximum number of observations for any solution was limited to 100. For the set of 100 observations, the number of discrete instrument readings varied with the set of instruments in use and with whether or not the satellite passes through the earth's shadow, thereby eliminating solar aspect sensor readings.

To test if 100 observations were sufficient to estimate the unknowns accurately, estimations were made with fewer observations and the variation noted as the number of observations was increased. To eliminate the possible effects of other sources of error, the data analyzed corresponded to a perfect linear model. Exact instrument readings were generated by multiplying the matrix  $H$  by an arbitrary set of values for unknowns. These readings were quantized as outlined to the section on simulation.

The error in estimating the unknown parameters for various numbers of observations is shown in Fig. 4. When the horizon scanner was used, little change in the estimate of the unknowns occurred after about 50 observations. When the solar aspect sensors alone were used, 100 observations appeared to be marginal in that some of the unknowns were still changing. Note, however, that the errors for 100 observations were very nearly the same for both instrumentation systems. The addition of horizon scanner measurements did nothing to improve the knowledge of the variables  $a_2$  and  $a_3$  which correspond to steady roll and yaw. The horizon scanner would not be expected to improve  $a_3$  since it does not sense yaw. The reason that no improvement in the estimate of  $a_1$  occurred is that the roll angle

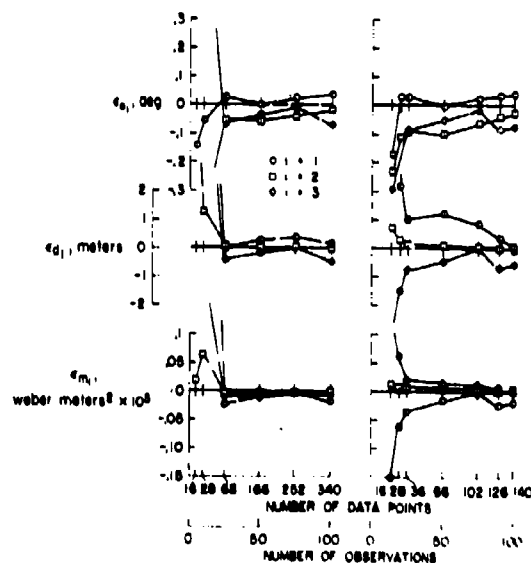


Fig. 4. The effect of the number of observations on the estimate of the state after one iteration.

typically never exceeded  $0.5^\circ$ . All readings of the digital horizon scanner, accordingly were zero. Therefore, in effect, the horizon scanner contributed information only on the pitch motion.

## 2. Effect of Nonlinearities

The matrix  $H$  was calculated with the assumption that the variation of the instrument readings with each of the unknowns was linear. The fact that several iterations are necessary to get the best fit to the actual motion indicates that the variation is not linear. This nonlinearity is clearly demonstrated in Fig. 5, where a comparison is made of the errors for the first and second estimates. Two curves are shown for each estimate. The curves designated as linear are the estimation errors when the attitude is assumed to vary linearly with  $\Delta x$  and is given by  $A(t)\Delta x$  summed with the reference motion upon which the estimate was based. The curve designated as simulated, is the error incurred when the estimated unknowns are used as an input to the integration of the equations of motion. The nonlinearity is evident in the first estimate given in Fig. 5(a). The second estimate eliminated the errors from nonlinearity, for all

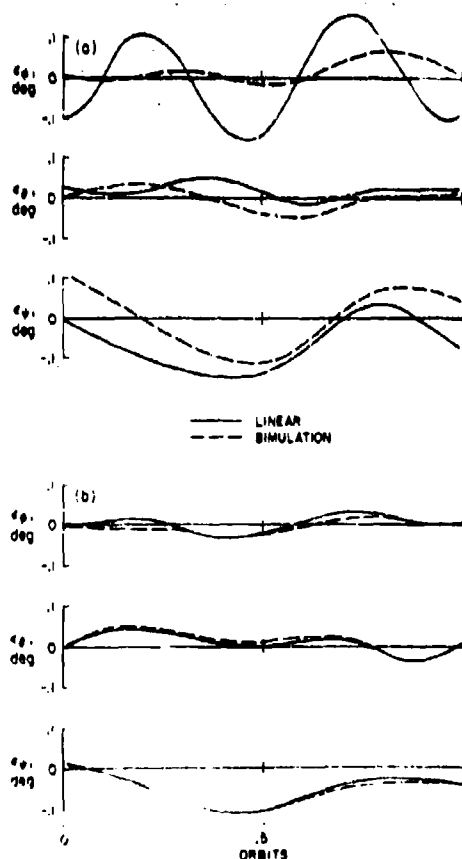


Fig. 5. Comparison of the errors in the first and second linear estimates with the errors from simulations.

practical purposes, as illustrated in Fig. 5(b). Figure 6 shows the expected result, that a third estimate produced no further change in the unknowns.

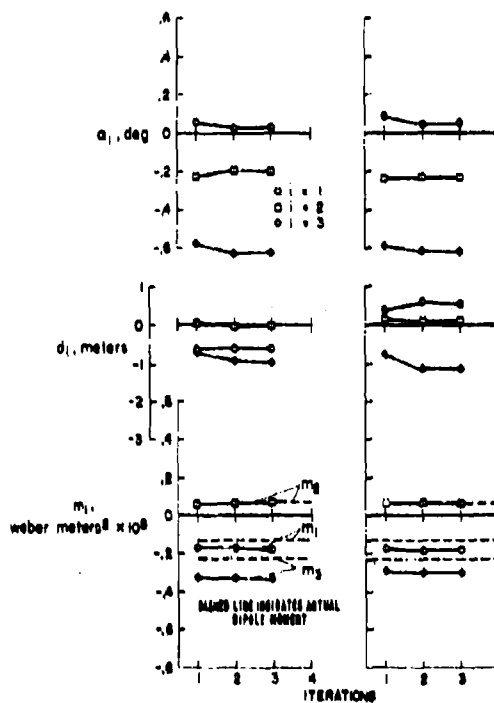


Fig. 6. Convergence of the estimated parameters with number of iterations to eliminate nonlinearities.

## 3. Effect of Model Imperfections

The principal source of difficulty in applying the estimation technique appears to be imperfections in the model of the unknown disturbances. These imperfections impair the accuracy of the short-term estimation and degrade the prediction of future motions, particularly when seasonal variations and orbital regression change the relationship of the orbit to the sunline.

If the model is perfect it should be possible to estimate the unknowns precisely, because the effects of instrument errors can be eliminated by taking a sufficiently long data sample, and the effects of nonlinearities can be accounted for through an iterative procedure. However, consider the results shown in Fig. 6, which gives the estimates of the parameters corresponding to an unknown motion generated by simulation of the satellite whose physical characteristics are listed as "Actual" in Table I. For this simulation, the magnetic dipole is the only variable that enters directly. Other sources of attitude error, which are represented in the estimation by the variables  $\alpha_1$  and  $d_1$  are unknown solar pressure torques and rotations of the principal axes relative to the instrument package. These



torques and rotations are generated by errors in boom lengths, boom angles, surface reflectivities, etc., rather than directly by changes in the variables  $a_i$  and  $d_i$  such as used in computing the H matrix. The results indicate that the estimated dipole is different from that known to be present (see Fig. 6). The error in the estimation is not small, the largest component being underestimated by roughly 50 percent. The corresponding errors in the attitude motion are those shown in Fig. 3. These latter errors, however, are small, being almost always less than  $0.1^\circ$ .

The apparent contradictory results, that is, good estimation of the attitude motion, but poor estimates of some of the unknowns, can arise from two sources. One possibility is that the motion may be insensitive to change in a particular unknown. The other possibility is imperfect representation of the attitude error sources by the model. The model used is an attempt to represent all of the disturbances with a few distinct variables and is known to be an approximation. For instance, including the unknown distances,  $d_i$ , is an attempt to allow for unknown variations in the solar pressure torques. These variations are a consequence of variations in the geometry and surface properties as well as deviation of the center of mass from its stated position. Even though deviations in the center-of-mass position will produce solar pressure torques with the same frequencies as actually occur, it is unlikely that a combination of the distances,  $d_i$ , will produce a solar pressure torque variation that would have the correct Fourier series representation about all axes. Also, the use of  $a_i$  to allow for variations in the relationship between the principal axes of inertia and the instrument axes, does not allow for changes in the magnitude of the principal moments of inertia. If the moments of inertia are changed, the response of the satellite to disturbance will be different from that given by the calculated H matrix.

The estimation procedure will find the best fit to the data sample. In the example cited, the shortcomings of the model were compensated by estimating a dipole different from that known to be present. For short-term estimates this compensation is of little consequence. However, the compensation required to yield the best estimate of the motion would be expected to be altered as

the relationship of the orbit to the sun changes, thereby presenting some difficulty in the long-term prediction of attitude motion.

#### 4. Effect of Poor Observability

As has been previously noted, when the orbit is oriented so that the sunline lies along the orbit normal, three components of the state become unobservable by any set of instruments. When the sunline lies close to the orbit normal, all the elements of the state are observable in that the determinant of  $HH^T$  is nonzero. However, Eq. (1) becomes poorly conditioned and the states differ wildly from those estimated for other orbits. This condition was found to prevail even when the orbit normal was as far as  $30^\circ$  from the sunline. Typical results of the first estimate are shown in the table below. The data in the first column for estimates when the sunline was  $30^\circ$  from the orbit normal ( $\Omega = 60^\circ$ ,  $\lambda = 0$ ) show results quite different from those obtained when the sunline was in the orbital plane ( $\Omega = 0$ ,  $\lambda = 0$ ). This is particularly true of the values of  $a_3$  and  $d_1$ . These variables produce steady motions which are compensating so that the linear fit to the unknown trajectory obtained from the product  $|A(t)||\Delta X|$  was comparable to other results of a first estimate of the unknowns. Better definition of the state might be obtained if the data sample were lengthened, thereby reducing the effect of instrument errors. Evidence of this type of improvement is given by the results shown for perfect solar aspect data.

The fact that one unknown parameter is poorly distinguished from another, or is poorly observable, can be viewed as evidence that each produces nearly the same effect on the motion. Insofar as short-term estimation is concerned, it is expedient to eliminate one of the unknowns. In this instance, it was decided to eliminate all three of the distance elements,  $d_i$ . The resulting short-term estimate (see third column of table) yielded attitude estimation errors comparable to those shown in Fig. 2 for the case when the sun was in the orbit plane and all nine unknown parameters were estimated.

Variable	$\Omega = 60^\circ, \lambda = 0$			$\Omega = 0, \lambda = 0$
	Simulated Solar Aspect Sensor, 9 Variables	Perfect Solar Aspect Data, 9 Variables	Simulated Solar Aspect Sensor, 6 Variables	Simulated Solar Aspect Sensor, 9 Variables
$a_1$	0.054	0.072	0.030	0.067
$a_2$	-.219	-.254	-.230	-.210
$a_3$	-5.45	-1.24	-.227	-.575
$d_1$	3.94	.73	Not estimated	-.62
$d_2$	.07	.04	Not estimated	.04
$d_3$	.32	.51	Not estimated	-.66
$m_1$	$-1.22 \times 10^{-6}$	$-1.21 \times 10^{-6}$	$-1.28 \times 10^{-6}$	$-1.67 \times 10^{-6}$
$m_2$	$.67 \times 10^{-6}$	$.57 \times 10^{-6}$	$.58 \times 10^{-6}$	$.67 \times 10^{-6}$
$m_3$	$-2.02 \times 10^{-6}$	$-3.42 \times 10^{-6}$	$-3.49 \times 10^{-6}$	$-3.28 \times 10^{-6}$

### C. Prediction

The goal of the estimation procedure is to be able to predict attitude motion well into the future so that the user of the satellite will know, in advance, the geocentric coordinates of the center of the field of view of the sensors. The results discussed so far indicate that the unknown parameters can be evaluated from analysis of a short data segment such that simulation provides a fit to the attitude motion to within  $0.1^\circ$ . However, it is clear that the model is not perfect. There is, therefore, no assurance that the same set of parameters will provide satisfactory simulation of the motion for some future time when orbital regression and seasonal variations have changed the relationship between the solar, geomagnetic, and orbital coordinate systems.

The results of the short-term estimation were used in an attempt to predict the motion for other orbits with a different angle of the orbit normal relative to the sunline. In particular, it was attempted to predict the motion for the time of the vernal equinox ( $\Omega = 0$ ) from the parameters evaluated when  $\Omega = 60^\circ$  and vice-versa. The results are shown in Fig. 7. In each case, the pointing error was predicted to within nearly  $0.1^\circ$ , but the prediction of the yaw motion was poor. Curiously, the predictions of yaw based on estimations when  $\Omega = 60^\circ$  were somewhat the better of the two, even though three of the unknown parameters were not estimated.

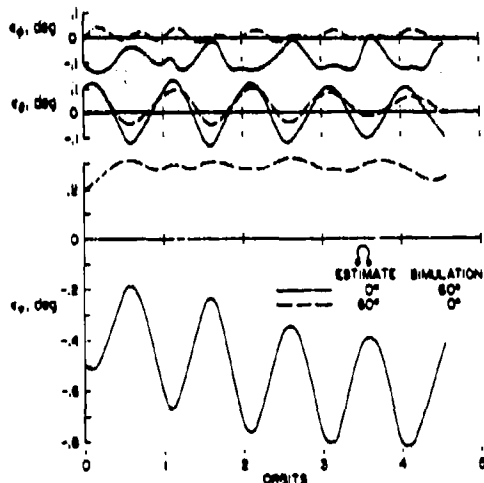


Fig. 7. Errors when a short term estimate of the unknown parameters is used in the prediction of attitude for a different orbit-sun relationship.

In practice, satisfactory long-term prediction might be achieved in a variety of ways. The most obvious is to determine the time period for which an estimate of the unknown parameters yields satisfactory accuracy. The duration of this period will depend upon the orbit and its regression rate. After a number of successive estimates of the parameters have been made, the estimation frequency might be reduced through

interpolation or extrapolation, depending upon whether one cycle of the variation of the sunline relative to the orbit has been completed. An alternative technique is to analyze data that encompasses the entire range of conditions that have been encountered in the past. After one complete cycle of these conditions has been covered, the estimate will yield a set of parameters for a best fit to all of the attitude motion. This possibility was explored in a rudimentary fashion by analyzing a data segment composed of 80 observations when  $\Omega = 60^\circ$  and 80 when  $\Omega = 0$ . The results are shown in Fig. 8. The estimation of roll and pitch for either condition was equivalent to the estimate when all 160 pieces of data were

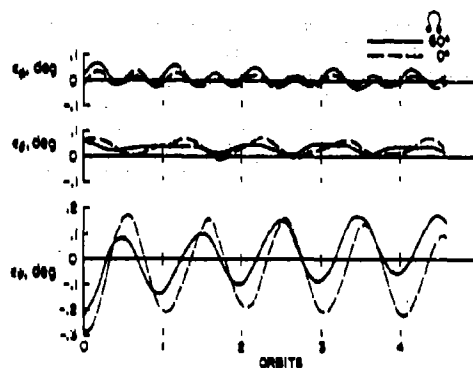


Fig. 8. Errors when the solar aspect measurements for two different orbit-sun relationships are analyzed as one data sample,  $\lambda = 0$ .

taken from a single condition. The yaw error, though about doubled, was considerably smaller than the error encountered under the condition of Fig. 9. The parameters estimated from a combination of the two data segments were used to predict the motion for other orbits. Results of predictions when the orbit-sun relationship was midway between the two data samples are shown for 24-hour periods in Fig. 9. Two cases are shown, one corresponding to the time of the equinox, and one to the time of the solstice. In each case, the errors in pitch and roll are the same magnitude as estimated for a particular data sample. The error in yaw is roughly twice that estimated for a short-term data sample and shows a 24-hour variation indicative of an error in estimation of the components of the magnetic dipole.

The results presented are limited in that they are based entirely upon simulation, rather than flight results, and in that a single example satellite confined to a particular orbit was studied. If the results can be considered to be typical, it is indicated that the pitch and roll attitude can be predicted with an accuracy about five times better than the accuracy of a single measurement of an attitude sensor. For the particular satellite studied, the prediction, along with an accurate satellite ephemeris, should yield the geographic location of the earth oriented instrument axes to within 3 km. The errors in the long-term prediction of the yaw errors was about twice that for roll and pitch. Better yaw information

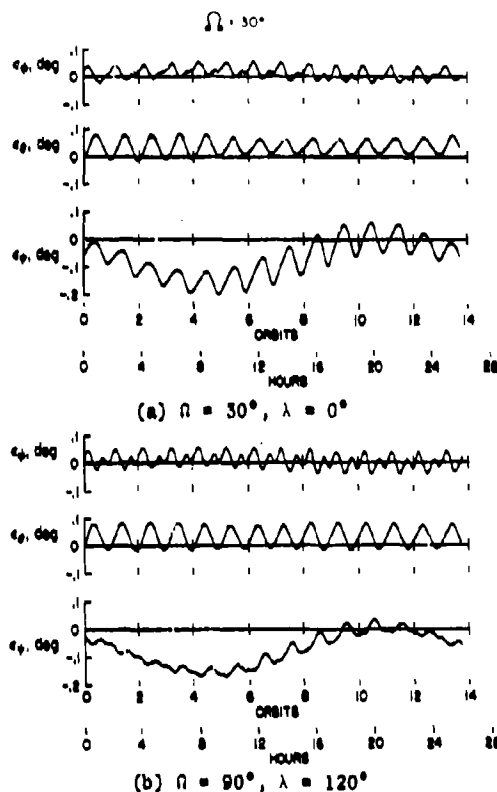


Fig. 9. Errors in attitude prediction when  $\gamma = 60^\circ$  from parameters estimated from data when  $\gamma = 90^\circ$  and  $\gamma = 30^\circ$ .

might be obtained through estimation with advance prediction limited to periods encompassing only a small change of the orbit relative to the sunline.

#### VI. CONCLUDING REMARKS

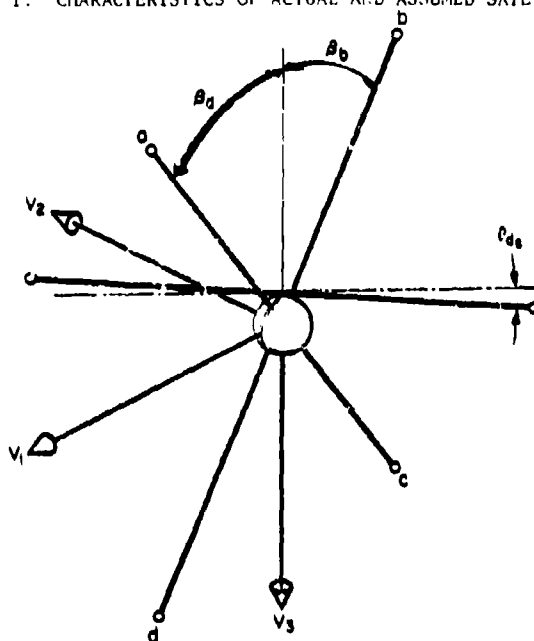
The steady-state attitude of a passive gravity stabilized satellite can be determined if the forces caused by the interaction of the satellite with the environment are known. It has been shown that these forces can be adequately defined in terms of a small number of parameters. Furthermore, by applying the techniques of estimation, the value of these parameters can be determined from solar aspect measurements only.

Simulation studies have indicated that the attitude can be estimated to within  $0.1^\circ$  from data from digital solar aspect sensors having a sensitivity of  $0.5^\circ$ . It must be recognized, however, that it is not possible to determine from the study if the model of the steady-state disturbances is adequate or if important errors will be caused by those nonsteady disturbances that are encountered in orbit. Final evaluation of the method therefore must await the launch of a suitable satellite to which the technique can be applied.

#### REFERENCES

1. E. D. Scott, and J. J. Rodden, "Performance of gravity gradient VCMG systems," Conference on Gravity Gradient Attitude Stabilization, (1968), sponsored by Air Force Systems Command Space and Missile Systems Organization and The Aerospace Corporation.
2. B. E. Tinling, and V. K. Merrick, "Exploitation of inertial coupling in passive gravity gradient stabilized satellites," *Journal of Spacecraft and Rockets*, Vol. 1, No. 4, pp. 381-387 (1964).
3. D. L. Blanchard, et al.: "Design, simulation and flight performance of the radio astronomy explorer - A satellite," Conference on Gravity Gradient Attitude Stabilization (1968), sponsored by Air Force Systems Command Space and Missile Systems Organization and The Aerospace Corporation.
4. G. Kanning, *The Influence of Thermal Distortion on the Performance of Gravity-Stabilized Satellites*, NASA TN D-5435 (1969).
5. F. C. Rushing, A. B. Simon, and C. I. Denton, "Torsionally Rigid and Thermally Stable Boom," *Proceedings of the Third Aerospace Mechanisms Symposium*, JPL 33-382 (1968).
6. R. D. Schalow, and V. W. Eveleigh, "Quasilinearization and parameter estimation accuracy," *Proceedings of the Hawaii International Conference on System Sciences* (1968).
7. G. L. Smith, *On the Theory and Methods of Statistical Inference*, NASA TR R-251 (1967).

TABLE I. CHARACTERISTICS OF ACTUAL AND ASSUMED SATELLITE



	Actual				Assumed			
Total mass, kg	223				223			
Moments of inertia, kg-m <sup>2</sup>								
Main body, relative to V frame								
I <sub>11</sub>	3005.0				3064.8			
I <sub>22</sub>	3774.0				3784.7			
I <sub>33</sub>	780.0				708.5			
I <sub>12</sub>	65.0				58.8			
I <sub>13</sub>	6.6				0			
I <sub>23</sub>	-5				0			
Damper, about hinge axis	122.3				122.3			
Boom systems								
Main booms								
Diameter, cm	a	b	c	d	a	b	c	d
Tip mass, kg	1.14	1.14	1.14	1.14	1.14	1.14	1.14	1.14
Length, m	.727	.727	.727	.727	.727	.727	.727	.727
Reflectivity	30.7	30.1	30.6	29.7	30.0	30.0	30.0	30.0
Minimum radius of curvature due to solar radiation, m	.88	.86	.90	.86	.92	.92	.92	.92
Angle from vertical reference, $\theta$ , deg	305	261	366	261	457	457	457	457
Angle from vertical reference, $\theta$ , deg	27.1	25.6	28.2	27.3	26.7	26.7	26.7	26.7
Damper booms								
Length, m	15.0				15.0			
Tip mass, kg	.178				.178			
Spring constant, Newton-m rad	-.000536				-.000536			
Damping constant, Newton-m rad/sec	-.119				-.119			
Bias, $\theta_{ds}$ , deg	5				6			
Center of mass of stabilized package relative to center of sphere, m								
$\Delta x_{body}$	.16				0			
$\Delta y_{body}$	0				0			
$\Delta z_{body}$	-.04				0			
Uncompensated magnetic dipole, Weber-m <sup>2</sup>								
$\Delta m_1$	-.131 $\times 10^{-5}$				0			
$\Delta m_2$	.066 $\times 10^{-5}$				0			
$\Delta m_3$	-.227 $\times 10^{-5}$				0			

SESSION IV

SPARS

Chairman:  
Dr. J. LeMay  
The Aerospace Corporation  
El Segundo, California

---

SPARS - A Completely Strapdown Concept for Precise Determination of Satellite Vehicle Attitude	281
SPARS Algorithms and Simulation Results	293
Development and Test of Advanced Strapdown Components for SPARS	319
Concepts and Mechanization for Evaluating SPARS in the Laboratory and in Orbit	343
SPARS: The System, Algorithms, and Test Results	361
Appendix	*
A Precision Strapdown Inertial Reference Unit - Hardware Mechanization and Test Report	*
Laboratory Checkout and Testing of an Advanced Stellar Inertial Attitude Reference System	371
* Classified; published in Volume II	*

## SPARS - A COMPLETELY STRAPDOWN CONCEPT FOR PRECISE DETERMINATION OF SATELLITE VEHICLE ATTITUDE<sup>1</sup>

William R. Davis  
Lockheed MSC  
Sunnyvale, California

and

Joseph A. Miller  
Honeywell Aero Division  
Minneapolis, Minnesota

### ABSTRACT

This paper describes the concept and development of a completely strapdown system for determination of satellite vehicle attitude to high precision. Known as SPARS for Space Precision Attitude Reference System, this system is the result of a continuing effort on the part of the Air Force to improve attitude determination accuracy. The system described has been developed by Lockheed and Honeywell under Air Force sponsorship over the last 2-1/2 years. The SPARS program is described in terms of mission and mechanization considerations, the basic concept, the critical design considerations and tradeoffs, the resulting mechanization, and test considerations and results in validating and evaluating the concept and specific mechanization. SPARS uses vehicle-fixed star sensors in a mode in which they mark the time of transit or epoch of a star as it crosses the sensor field of view. To provide essentially continuous attitude information from intermittent star sightings vehicle rate is integrated. Rate is determined by vehicle-mounted precision rate integrating gyros. Parametric tradeoff studies in conjunction with complete system simulation on a GP computer are described. Results of these studies are reported along with results of precision laboratory tests of a prototype SPARS hardware system which show that the SPARS performance requirements can be achieved.

### INTRODUCTION

Ever since man started throwing rocks to provide food and defense he has faced the problem of hitting a target. To hit a target, one must in some sense first point at it. In modern weapon systems many types of pointing are required and used. Typically, however, one can distinguish between two basic types of pointing. The first and most familiar is identified here as closed loop, in which one observes the target in real time. The second, identified as open loop, uses knowledge about the relative target position not derived from direct, real-time observation. This paper discusses the development and laboratory test of SPARS, a system for high-precision

satellite attitude determination in support of precision open-loop pointing requirements.

It is appropriate at this point to identify the acronym PEPSY for Precision Earth Pointing System and its relation to SPARS (see Fig. 1). Whereas SPARS is solely for determining vehicle attitude relative to inertial space, PEPSY is a more complex system which utilizes SPARS information along with vehicle ephemeris and target ephemeris to provide any combination of the following: vehicle attitude relative to local horizontal, pointing of a gimbaled sensor line of sight (LOS) at a specified target, open-loop control of the LOS direction to high accuracy if necessary, knowledge of

<sup>1</sup>This work was supported by the Space and Missile Systems Organization of the Air Force under contract numbers: F04701-68-C-0069 and F04701-68-C-0227, F04701-68 C-0150

LOS direction to an accuracy that is compatible with SPARS accuracy, target ephemeris accuracy, and for earth targets, satellite ephemeris accuracy. The major portion of this paper relates to SPARS only. See Ref. 1 for PEPSY design considerations.

### Mission Considerations

In modern systems, direct observation of a target can be quite difficult for reasons such as lack of target identification or tracking observables. Indeed, the identification of observables is often a specific mission objective. In such missions, open-loop pointing is usually required. Typical of missions of this type that could be accomplished best by observation of locations or targets on earth from satellite-based sensors if adequate point accuracy were available are: autonomous navigation, laser pointing, earth resources location, absolute position determination for ABM, and missile test range calibration. The desire to develop the basic technology for such missions has provided the major motivation for SPARS development.

High angular resolution is a common requirement of these missions, due mainly to the large satellite-to-target distance. This implies narrow field-of-view (FOV) sensors and thus a capability for precise pointing control in order to guarantee the target in the FOV. Even more, it implies a requirement for precise pointing knowledge in order to effectively utilize the high resolution. It is important here to distinguish between knowledge and control. For closed-loop pointing, knowledge and control are usually intimately connected. Thus, in OAO knowledge of telescope pointing relative to the star being tracked is of the order of the tracking accuracy, say 0.1 arc sec. This is typically ten times better than the knowledge of the location of the star relative to the rest of the fixed stars.

For open loop pointing, knowledge and control have an arbitrary interrelation. Typically though, one needs pointing control accuracy to some fraction between one-third and one-tenth of the FOV and pointing knowledge on the order of three to ten resolution elements. Since FOVs are of the order of 10 arc min and up, control to about 1 arc min could be adequate. However, the need for resolution to a few feet ranges from very desirable to mandatory, and since an arc sec is about 6 feet at 200 nm, very accurate pointing knowledge is required.

### Implementation Considerations

In order to provide open-loop pointing from a base to a target, it is necessary to specify the direction of base-to-target line of sight (LOS) relative to the base. For pointing knowledge to a high accuracy from an earth satellite base, the most practical method of specifying the LOS direction is to use a stellar-inertial frame as the reference. This is because only in this frame is there the possibility of knowing accurately both the satellite orientation and the desired LOS

direction (from knowledge of target and satellite positions) without target cooperation or tracking. Other possible frames, such as those tied to the earth's magnetic or gravitational fields or to the earth's figure (horizon sensors), suffer from uncertainties on the order of an arc-min and thus lack the required accuracy. Other possible reference or fix techniques have unacceptable deficiencies; e.g., landmark tracking is not all-weather, radar requires active emissions, etc.

For the past two decades the traditional, and in most cases best, way of obtaining very accurate continuous knowledge of the angular orientation of a moving vehicle has been to employ gyros and, where necessary, star trackers on a gimballed system in which one gimbal is fixed in inertial space. In applications such as airplane or missile ascent guidance where the vehicle motion can include significant angular acceleration, this was, and in some cases still is, the best method. Implicit in this technique is the requirement to measure to the desired accuracy the absolute instantaneous orientation of the vehicle relative to the inertially fixed gimbal. For high-accuracy systems, this measurement can be quite difficult and often is the source of significant system error and complexity.

In cases in which angular accelerations of the moving system are insignificant other methods are used. The earth's inertial orientation, for example, can be ascertained by the simple measurement of time (clock) after a single star (inertial) fix since the earth's angular velocity is known and its angular acceleration is insignificant.

For SPARS' technology to be usable in a wide variety of missions it was important that the basic concept not include interaction with or be dependent upon the vehicle control system. However, it was to be primarily for satellites that were earth oriented, i.e., having a non-zero inertial angular velocity.

The major considerations and concomitant gross system outline that emerge from the foregoing includes high precision -- hence, digital techniques for both measuring and computation; stellar reference -- hence stellar sensors; slowly rotating vehicles with not insignificant angular accelerations -- hence gyros; early availability -- hence state-of-the-art hardware at least for components. At this level of definition a major decision was between strapdown and gimballed star sensors. In support of the LMSC/HI decision to develop a strapdown concept are the following considerations: elimination of error sources from gimbal motion and readout; utilization of vehicle motion to provide star field scan; ability to use time as the basic measurement; no requirement to point, i.e., control, a vehicle-borne device in order to acquire attitude knowledge and hence no requirement for an on-board computer for SPARS-only information; increased reliability from simpler mechanization, minimum demand on vehicle mounting location due to

small fixed vehicle window requirement -- thus allowing the possibility of mounting the star sensor(s) adjacent to critical payload(s); and finally, minimum hardware development beyond existing components and techniques.

### THE SPARS CONCEPT

The LMSC/HI SPARS concept consists of two star sensors with a 3-gyro package operating in conjunction with a digital computer. The orbital geometry of the concept is shown in Fig. 1.

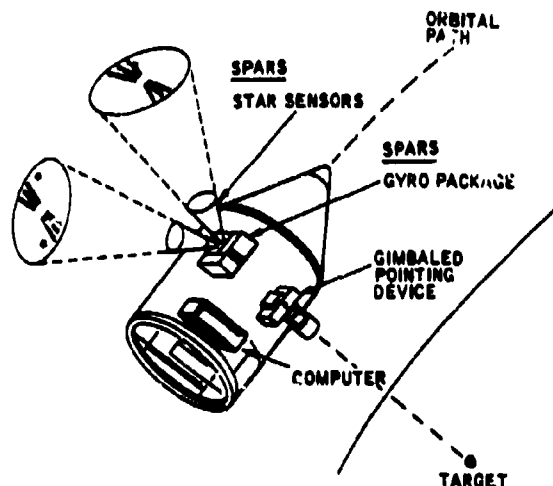


Figure 1. Precision Earth Pointing System Concept

The basic principle of operation of this system is that, in conjunction with the computer and a stored star catalog, information from the star sensors provides a primary (long-term) reference while the gyros provide a secondary (short-term) reference. The computer will process (pulse) information from each of the sensing sources to give continuous precision knowledge of vehicle inertial attitude. This information is available at the computer location.

As shown in Fig. 2, the gyros provide high bandwidth attitude data with unbounded errors (drift), whereas the star sensor provides low bandwidth data with bounded errors. The two types of data are combined and filtered so that they yield high bandwidth attitude knowledge with bounded errors.

SPARS uses vehicle-fixed star sensors in a mode in which they mark the time of transit or epoch of a star as it crosses the sensor FOV. To provide essentially continuous attitude information from intermittent star sightings vehicle rate is integrated. Rate is determined by vehicle-mounted precision rate integrating gyros. The intermittent star transits are used not only to give periodic attitude fixes but also to trim the

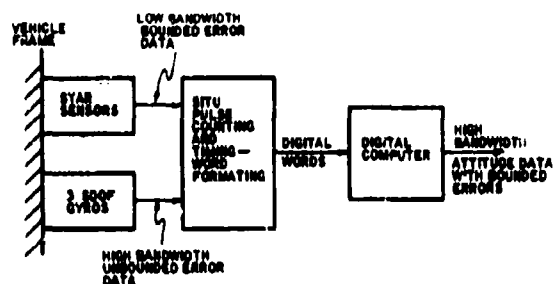


Figure 2. SPARS Component Block Diagram

gyro drifts and thus -- in a bootstrapping fashion -- increase the accuracy for the same interval between star sightings. This process is implemented with Kalman recursive filter techniques.

To make the system independent of specific computer I/O, star sensor and gyro outputs are processed by a special "interface and timing unit." As a result the computer requirements for SPARS computations are nominal and can be met by any modern aerospace machine, and because the sensors are all body mounted requiring no information about vehicle attitude to operate, the computer can be either on board or on the ground and the data processing can be either in real time or delayed.

The star sensors are conceptually simple instruments. They utilize concentric optics to focus star energy onto a detector at the focal surface of the optical system. The detector consists of narrow strips of photosensitive elements arranged in a spoke-like array. Specifically, doped cadmium sulfide deposited as a thin film on a curved substrate is used as the photosensitive element. The spokes are oriented so that vehicle pitch rotation causes the star image to traverse the slits in a nominally transverse direction. As the image transits a spoke, a pulse of current is generated. The time of occurrence of the pulse is the fundamental measurement used to determine attitude.

Three single-degree-of-freedom, gas bearing, pulse rebalance gyros are used for measuring vehicle rate. Pulses are summed in the "timing" unit and associated with star "transit pulses" for processing in the computer.

In the computer the vehicle attitude existing at the time of an actual star transit pulse is determined. This attitude is combined with knowledge of the transited star's position from a stored catalog of stars to establish a measure of attitude error. This measure is then used to make incremental corrections to the computed values of vehicle attitude and gyro drift.

Fig. 3 is a functional block diagram of SPARS.



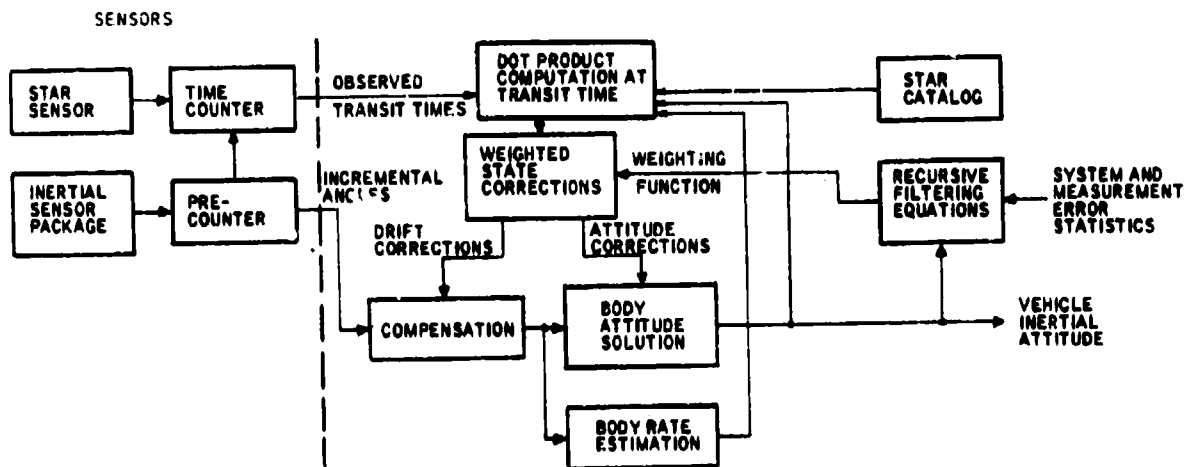


Figure 3. SPARS Functional Block Diagram

This mechanization is identified as "implicit" in that direct or explicit computation of attitude is not outputted in association with an external event such as a specific star sighting. However, since a very accurate estimate of the vehicle attitude state is always available, it is possible to relate the time of transit of any stored star to a measure of attitude error irrespective of actual vehicle motion.

For this reason, in SPARS only time must be measured in determining a vehicle's orientation in space. Fig. 4 shows how this time differential can be visualized. The projection of a detector slit on the star field at the actual transit time is shown with solid lines (LOS 1), and the projection at the computed transit time is shown with dashed lines (LOS 2). The angle (time) difference between these projections is used to correct the computed attitude and rate. As shown, the difference  $\Delta\theta$  appears predominantly as a pitch error. Roll and yaw errors

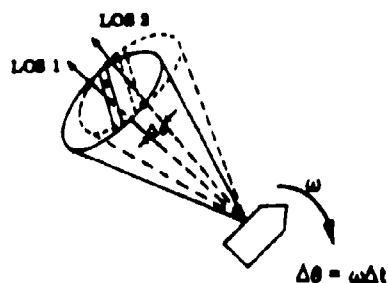


Figure 4. Time/Attitude Relationship in the Implicit System

would cause respectively either different stars to be transited or a sequence of two or more stars to be transited at still different times. With the implicit approach, the  $\Delta\theta$ 's of three or more successive transits are used to obtain a best-fit attitude estimate about all three axes.

Although a single detector slit can, in principle, provide 3-axis information, tradeoff studies have shown that higher system reliability, better performance, and shorter acquisition time, i.e., convergence, are realized by using two star sensors, each having six slits. A total failure of one star sensor will still permit excellent system performance.

Additional insight into system operation is provided through consideration of a typical sequence of events. At the time of a star transit on a detector strip the following events occur:

- 1) A high-resolution timer is started and continues until the computer samples the gyro output at the next sampling instant.
- 2) A computed vehicle attitude and rate about all three axes at the gyro sampling time is generated.
- 3) This computed attitude and rate, along with the elapsed time since the star transit (1), is used to generate a computed attitude at the time of transit.
- 4) The computed attitude at the star transit time is compared with star catalog information (in the computer) to determine whether or not a star transit should have occurred at about that attitude.

- 5) If a transit should not have occurred, this false data is rejected and no further calculations are performed until the next star transit.
- 6) If the computer acknowledges that a transit should have occurred at about the attitude that it did occur, then the system calculates system state corrections based upon a measure of attitude error computed at the time of transit.
- 7) Recursive filtering techniques utilize the body attitude solution and known system error statistics to generate a weighting function that minimizes system error.

### CRITICAL DESIGN CONSIDERATIONS AND TRADEOFFS

The major critical design consideration at the initiation of the SPARS program was the viability of the solid-state detector and the advantage it had, if any, over a photomultiplier tube (PMT). A limited amount of work had been done in this solid-state area on the STAFF program and it was largely due to the results obtained on this program that the solid-state detector was viewed optimistically.

During the course of first phase of the SPARS program, three potential star sensor suppliers conducted tests that indicated that either cadmium sulfide or cadmium selenide could be used successfully as the detector in the star sensor. One of these tests even included the detection of actual 4th magnitude stars with reasonably sized optics. Since the Air Force had expressed a desire for a solid-state device and since solid-state devices tend to have greater growth potential than do vacuum tubes, the decision was made to go solid state.

A second major design decision involved the choice between an electrostatic gyro (ESG) and the single-degree-of-freedom (SDOF) floated gyro. A trade study was performed on these two approaches which carried through a paper design to the point of determining computer requirements, physical characteristics, cost, and delivery. Surprisingly, neither of these systems displayed any significant advantage in any of the tradeoff areas. Since the SDOF gyro was available in the required configuration and the ESG required some ball pattern and readout development, it was decided to use the SDOF gyro in SPARS.

It was of interest in the initial study that the low drift rate characteristic of the ESG allowed some operational advantages in the acquisition area that were very attractive. This was true to such an extent that the ESG portion of the trade study was extended to include two gimbaled and one strapdown configurations. In

neither of these two additional cases was the resulting system more attractive than the SDOF gyro system, so the original recommendation was upheld.

While PMT versus solid-state detectors and ESG versus SDOF gyros were the pivotal design decisions in the SPARS development, numerous other tradeoffs were performed before the system was built and tested. In this, computer simulation was used to develop tradeoff information in the areas of star sensor look angle, star sensor separation, star sensor random noise, star transit interval, gyro random noise, star sensor slit configuration, attitude integration step size, attitude integration word length, and gyro pulse weight. These tradeoffs are treated in detail in Ref. 2. From this tradeoff information, it was apparent that the component performance dictated by system performance was reasonably attainable and that the system was relatively insensitive to small variations in component performance. One noteworthy result of the study was the nearly complete lack of sensitivity of system steady-state performance to the average interval between star crossings.<sup>2</sup> Thus, if steady-state performance were the only consideration in selecting star transit interval, the star sensor FOV and sensitivity requirements could have been greatly relaxed from those that are now specified.

The star transit interval requirement that finally resulted grew out of a requirement for acceptable acquisition time. Considerations such as worst case (i.e., star power) orbits, and acquisition convergence recycling led to the conclusion that approximately eight stars had to be detected by each star sensor in each orbit. With eight stars per orbit identified as a star sensor requirement, computer scans of the star catalog were run to establish the functional relationship between FOV and star magnitude. It was by this functional relationship between FOV and star magnitude, along with accuracy requirements, that the star sensor performance requirements were specified.

Four different star sensor configurations were considered during the course of the preliminary design study. These four configurations included various values of FOV, sensitivity and accuracy. No clear cut advantage for any of the configurations emerged from the design study. The decision to specify a sensor with a relatively narrow FOV was influenced by the following: the system analysis had been done assuming a narrow FOV; the dimmer stars associated with the narrow FOV telescope were expected to have better uniformity than brighter stars allowed by a wider FOV; and the off-axis accuracy of a narrow FOV sensor was believed to be inherently better than the off-axis accuracy over a wider FOV.

Some additional design decisions that have stood out in the program are: selection of pulse rebalance rather than analog rebalance gyros;

<sup>2</sup> The steady-state performance is, however, quite sensitive to the length of the longest interval between star sightings.

selection of ratio detection on the leading edge of the star sensor pulse rather than leading edge trailing edge averaging; and the use of recursive rather than batch data processing for acquisition.

Most practical experience with fractional arc sec measurement increments for gyro rebalance had been obtained using analog loops and voltage-to-frequency converters. Some systems were using pulse rebalance but their pulse weights were so large that it was difficult to correlate their capability with the required performance for SPARS. Special tests were conducted to uncover any small pulse nonlinearities or pulse-induced noise in the pulse rebalance system. Significantly no practical lower limit was found to the pulse rebalance pulse weight and nonindication of pulse-induced noise was found during these tests, hence the decision was made to use pulse rebalanced gyros in SPARS.

The star transit detector selection was similar in that the final approach selected was based upon empirical results. Wave shape and time delay data of star crossings was obtained in the laboratory with the final configuration detector. This test data indicated that the leading edge rise times of normalized star transit pulses were independent of star brightness. This data also showed that the decay times of the star transit pulses were so long and unpredictable that they were unusable for level switching. In light of these findings a height-independent trigger (HIT) circuit which operated on the leading edge of the star sensor pulse was incorporated into the star sensor electronics.

Initially it was thought that too many special-decision features were required for acquisition to be performed by the steady-state algorithm. A good deal of effort in the development of batch processor was expended with some success before the steady-state recursive approach was tried<sup>3</sup> and found to be superior.

The steady-state algorithm was modified to include among other things a provision for a variable tolerance on what constituted a "good" star transit and a provision for recycling the acquisition sequence if convergence did not occur. Simulation results demonstrated the acceptable performance of the recursive system and the revised computer programs gave evidence of the advantage of the recursive system from a computer requirement standpoint. Hence, further work on batch processing was dropped and the recursive approach to acquisition was adopted as a part of the baseline system.

#### SPARS MECHANIZATION

As previously indicated (Fig. 2) the major functional components of SPARS are: two strap-down star sensors, a three-axis strapdown gyro reference assembly, an interface and timing unit

(ITU) and a digital computer, see Ref. 3.

Transits of known stars on the star sensors provide precise attitude information of discrete times. The output of the star sensor is a single pulse at each star transit. The gyro assembly provides continuous three-axis attitude information in the form of a digital word for motion about each axis. The ITU provides short-term storage for the signals from the sensors and converts them from asynchronous to synchronous signals before passing them on to the computer. Finally, the computer determines the vehicle attitude by processing star sensor and gyro data by means of recursive filtering.

#### The Star Sensors

The two star sensors used in SPARS are physically identical. The design features a compact, high-resolution optical system in a strapped-down, no moving parts configuration. Fig. 5 shows the sensor's simplicity.

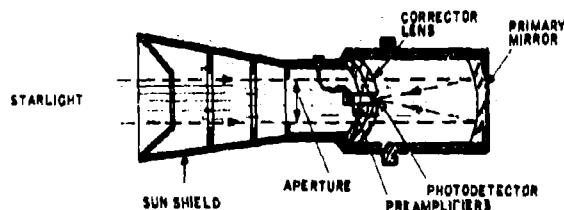


Figure 5. Star Sensor

#### Optical Design

To provide a good quality, bright circular star image over the entire FOV, SPARS utilizes a concentric optical system. Unlike conventional refractive systems which are large, heavy, and demand many elements to correct optical errors or aberrations, the concentric optical system is simple, small, and lightweight.

The major element of the concentric optical system is the primary mirror shown in Fig. 6.

Parallel rays of star light entering the aperture are focused on a spherical focal surface (detector location). Since all optical surfaces share a common center and every ray of light is on an axis, off-axis errors are normally eliminated. Spherical aberration, the only on-axis error, is minimized by employing a corrector lens. Because insertion of this refractive

<sup>3</sup>Suggested by Dr. J. L. LeMay.

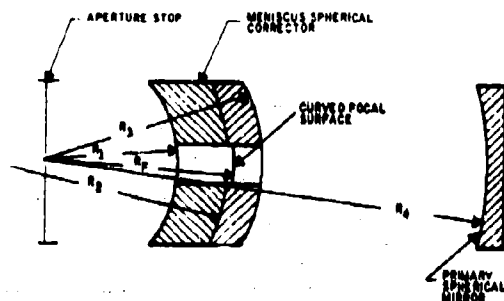


Figure 6. Concentric Optical System

corrector lens introduces chromatic errors, the mating surfaces of a dual element corrector lens are contoured for color correction.

The size of the star sensor is minimized by using a small aperture and short focal length. The system is diffraction limited. The sun shield reduces the risk of loss of the star field due to interference from bright objects such as the sun, moon, and earth. Damage to the star sensor from direct sunshine is avoided by a fast-response shutter.

#### Photosensitive Detector

The SPARS star sensor employs a solid-state cadmium sulfide (CdS) detector (Fig. 7). The detector is fabricated by depositing six narrow strips or slits of CdS on a curved glass substrate. The curved substrate is formed on the same center of curvature as the star sensor optics.

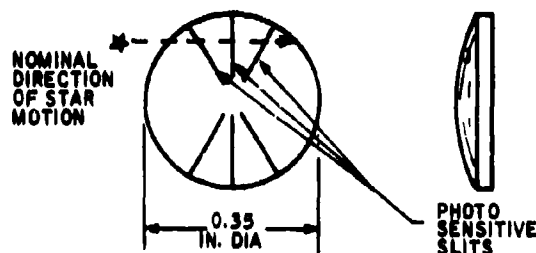


Figure 7. Solid-State Cadmium Sulfide Detector

Each slit is less than 1/1000 inch wide and just approximates the star image diameter. Cadmium sulfide is a photoconductive material which, with proper electrical as well as background light bias, changes its electrical resistance when illuminated by light in the 5000Å region.

#### Time of Transit Measurement

As a star image transits each slit, a pulse-type signal is generated. This signal rises to a peak as the image moves onto the slit and gradually decays as the image moves off of the slit. A threshold detector is tripped by the leading edge of the star signal and thereby generates a digital pulse to the timing unit. The threshold level is tied to the pulse height to compensate for star pulse leading edge variations caused by variations in detector response and/or star magnitude and color (Fig. 8).

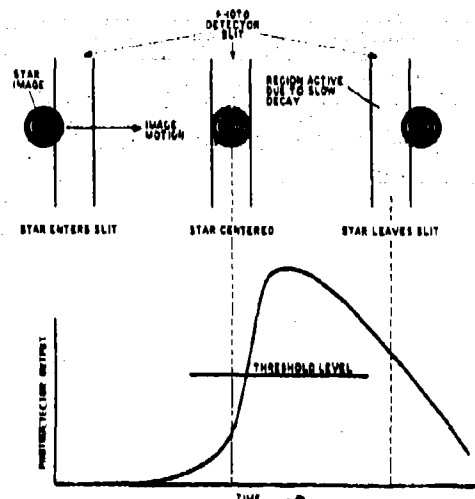


Figure 8. Time of Transit Measurement

Each detector slit is operated with a separate set of electronics using a matched, low-noise preamplifier mounted near the detector to minimize noise pickup. The preamp output is amplified and fed into an electronic filter (Fig. 9). The filter both delays the signal and processes it to enhance the signal-to-noise ratio. The signal is fed to a comparator with a variable threshold level controlled by a peak signal detector which compensates for star pulses of different

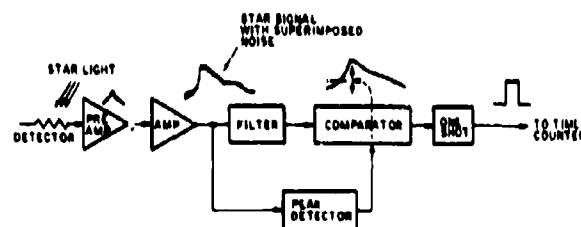


Figure 9. Time of Transit Detection Electronics

magnitude. Exceeding the threshold level triggers a "one-shot" which provides a logical "one" to the SITU which generates a word containing slit identification as well as time of transit.

#### Performance

The SPARS star sensor can detect stars down to 4th magnitude<sup>4</sup> in the visible spectrum. This means that the sensor can detect more than 450 stars distributed throughout the celestial sphere. In a star-poor worst-case orbit, a minimum of eight stars can be seen in one revolution. This is a sufficient number to maintain desired accuracy.

The SPARS star sensor has the ability to detect stellar targets of varying brightness and color in the presence of 1) random noise caused by background and star radiation, and 2) noise intrinsic to the detector itself. The sensor uses a threshold level set above the normal noise level and below the minimum signal level so that the tendency to either indicate false stars<sup>5</sup> or to miss stars is minimized. Design parameters including slit width, transit time, and electronic filtering have been optimized to essentially eliminate false star occurrence while maintaining a detection probability of 0.99. Error in determining transit time is minimized by providing adequate signal to noise for those stars which are accepted by the system.

#### The Gyros

SPARS uses three identical gyros that are mounted within a single package identified as the Inertial Reference Assembly (IRA). The SPARS IRA is identical to the Honeywell GG2200, a unit currently in production for Air Force Program 467. This IRA contains three Honeywell GG334A6 gas bearing gyros in pulse rebalance loops. The GG334A6 is a high-performance, single-degree-of-freedom floated gyro designed explicitly to meet the demanding performance requirements of advanced strapdown systems. Salient features of the unit are:

- Hydrodynamic, gas bearing spinmotor for maximum bearing life, reliability, and low gyro noise
- Precision, moving-coil, permanent-magnet torque generator with very low linearity error, high-scale-factor stability, and two torque windings to facilitate testing
- Pivot-jewel output axis bearing with microinch bearing clearances for improved output axis definition, and piezoelectric mounting for low friction

- High-viscosity, low pour point flotation fluid for improved g-insensitive drift stability with nonoperative cool-down exposures

The GG2200 IRA is 9 by 9 by 6.5 in. high, and weighs approximately 18 pounds. The base is aluminum honeycomb design, with the three gyros located close to the base mounting points for maximum rigidity.

Some of the significant construction features used to keep the size and weight of the IRA as small as possible are:

- Many circuits are mechanized on ceramic substrates with deposited resistors and conductors. Discrete microelectric components such as integrated circuits, semiconductors, and capacitors are soldered to the substrate.
- Multilayer printed circuit boards are used, especially where many interconnections are required between discrete components, integrated circuit flatpacks, and ceramic substrates.
- Flexible printed circuit tape is used for interconnecting circuit boards, gyros, and connectors. This tape consists of a flat layer of conductive material bonded between two sheets of flexible insulation.

The GG2200 IRA operates directly from the unregulated 29 vdc generating all required logic and excitations internally including:

- Pulse rebalance electronics for each gyro
- Crystal oscillator and countdown electronics
- D-C power supplies and EMI filters
- Signal generator excitation
- Dual voltage spinmotor supply
- Constant-current supply and precision reference voltage
- Temperature-control amplifiers for each gyro and for oven
- Telemetry signal-conditioning circuits

<sup>4</sup> A 4th magnitude star is just visible to an average observer on earth on a clear night.

<sup>5</sup> A "false star" is an indication of a star transit caused by 1) noise when no star is present, or 2) repeated triggering of the one-shot caused by noise superimposed on a pulse from a single valid star transit.

## The SPARS ITU

In order to reduce the demand on the computer I/O and software, the sensor signals are being fed to the computer. This processing is performed by the ITU. The ITU provides as its main function all of the input/output circuits necessary to perform real-time information transfer from the sensors to the computer. The functional relationship of the ITU is shown in Figure 10.

computational time are required to perform all the PEPSY computations.

## TEST CONSIDERATIONS AND RESULTS

From the beginning of the development of SPARS concepts and synthesis it was recognized that testing and evaluating SPARS would be a difficult task. The basic reason is that the desired laboratory performance is near the limit of measurement capability and of physical system

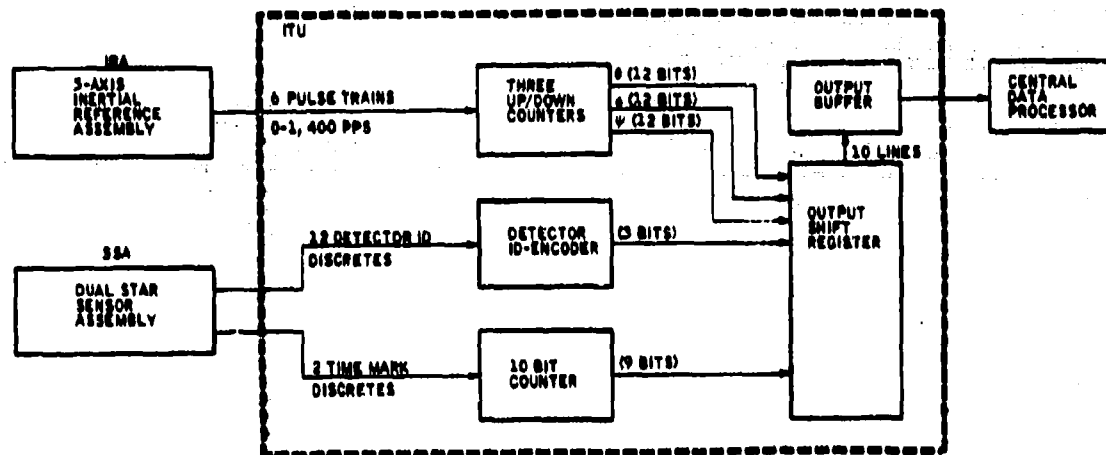


Figure 10. SPARS ITU Functional Block Diagram

The ITU consists of three 11-bit + sign up/down counters for accumulating gyro pulses, a 9-bit counter for storing star transit events, a 3-bit encoder for star sensor detector identification. In addition to this input circuitry the ITU contains a 6 x 12-bit shift register, with a 12-bit output buffer stage, a synchronizing clock and a power supply. A total of 525 gates and 162 J-K master slave-type flip flops are used in the ITU function.

## The SPARS Computer

It is planned to use the Univac 1824 as the major computing element in the system in the current tests. The 1824 is a general-purpose stored program aerospace computer with an order repertoire of 41 single-address instructions. To evaluate the capability of the 1824 for SPARS, all of the equations and algorithms required for PEPSY tests have been organized for this computer. The computer capacity required for their solution is summarized in Table 1.

As can be seen, the required operations are within the capability of the 1824. Specifically, these results show that only 61 percent of the available NDRO words, 76 percent of the available DRO words, and 81 percent of the available

Table 1. Computer Compatibility Comparison

Task/Module	84-Bit Words		Required Time/Cycle	Percentage of Computer Time Used
	DRO	NDRO		
Executive	30	600	0.5 ms/1 ms	20.0
SPARS				
Attitude Iner. Cos.	8	100	18 ms/100 ms	15.0
Attitude Filter	100	1000	100 ms/star transit	0.4
Special Logic	-	200		
Star Catalog	-	1000		
Target Pointing	30	400	2 ms/100 ms	3.0
Link...	40	500	4 ms/50 ms, 8 ms/100 ms	16.0
GPU Pointing	30	300	30 ms/100 ms	20.0
Self-Test	30	100	(During dead time only)	-
Data Processing	30	300		2.0
Program Constants		500		-
Total	390	3020		81.0
Univac 1824C	512	8192		100.0

Note:

\* NDRO = Nondestructive Readout Words  
NDRO = Nondestructive Readout Words  
Link signals processed every 50 ms

stabilities. The problem is two-fold in that testing in both laboratory and orbital environments are considered necessary. If not mandatory, prerequisites to any operational deployment of SPARS.

Considerations for in-orbit testing and evaluation of SPARS were important in the evolution of the requirement for PEPSY with its optical pointing device subsystem. That is to say, part of the motivation for developing a complete PEPSY was to provide in-orbit observable measurements that would allow the evaluation of SPARS.

Although in-orbit tests are generally conceded to present more problems than equivalent lab tests, for SPARS, the in-orbit environment has one very important characteristic not easily available in the lab and that is the accurately known absolute reference frame afforded by the fixed stars.

However, the simple economics and logical step-wise development of a complex system such as SPARS call for lab testing to precede in-orbit tests and in fact successful lab validation is probably a necessary prerequisite to justifying the expense of an orbital test.

As a first step in implementing this philosophy, lab tests on an engineering model of SPARS were performed in late 1968 and early 1969. The results of these tests on the LMBC/HI SPARS mechanization were very encouraging and supported previous analyses and simulations in the conclusion that the mechanization was capable of delivering the desired accuracy.

Two types of mutually supporting tests were performed. The first were component or subsystem tests in which the effects of varying several aspects of the environment were noted. The second was a system test in which the external environment was maintained nominally invariant and system parameters were varied.

#### Subsystem Tests

Subsystem testing on the gyro and timing unit was straight forward and will not be elaborated upon here (see Ref. 4). Major emphasis was on star sensor testing. Tests included operation on both real stars outside and artificial (simulated) stars in the lab. They covered static and dynamic response of the detectors over a range of star intensity and color and background illumination. Two areas of major concern, detector sensitivity and star epoch timing accuracy for different star intensities, were studied in some depth. Results are summarized here. Illustrated in Fig. 11 are real-star transits of Feb. 4, 1969, which show signal-to-noise ratios in excess of 20:1 with SPARS star transit on 69 Ursa Major (3m 44, A3) through moderately clear sky condition.

Figure 12 shows the variation in epoch timing (i. e., the point of 50 percent pulse rise) with star magnitude. This performance is adequate to provide star epoch transits of a frequency and accuracy sufficient to support SPARS.

#### System Tests

Systems testing of the SPARS presented an



Figure 11. Observed Representative Dim Star Transit Detection



DELAY - 16 MS  
STAR MAG - 1.1



DELAY - 21 MS  
STAR MAG - 2.2



DELAY - 21 MS  
STAR MAG - 3.3

Figure 12. Epoch Timing Variation with Star Magnitude (sweep speed = 50 ms/div.)

interesting challenge in that SPARS performance would be determined by measuring the orientation of a precision rate table, as it rotated at 240 deg/hr, by two different systems of comparable accuracy--namely the lab instrumentation and SPARS. From this, only the difference between the two measurements is available and neither measurement can be considered correct. Furthermore the "lab measurement system" was made up of several independent instruments in

contrast to the SPARS which is an integrated measuring system. This is significant in that it was recognized ahead of time that the most difficult aspect of establishing the performance of SPARS would probably be establishing a laboratory test concept and setup having sufficient accuracy to "see" the SPARS performance.

The system test program confirmed this prediction. The measured difference between the SPARS measurement and the "laboratory" measurement exhibited an exponential improvement in performance with increased test time. After correction of initial setup mistakes, etc., essentially all improvement came by gaining insight into the "fine structure" performance of the test facility. The most valuable tool in this process was SPARS itself.

Figure 13 shows the final results of measuring table rotation. The ordinate "observation error" is the difference between the SPARS measurement and the lab instrument measurement of table angle. The abscissa is table angle, which is scaled so that the ordinate values of attitude error for successive revolutions are shown at the same points. This plot suggests that a significant part of the error is systematic at table period; i.e., note that the roll error for revolution 3 lies nearly on top of the roll error for revolution 2. The RSS of the error in all three axes averaged over four revolutions in the final run was 2°. As an indication of the rate of improvement in test performance, the RSS total error dropped from about 7 to the final value of 2 in the course of about three iterations of the test process that consisted primarily of facility calibration improvement.

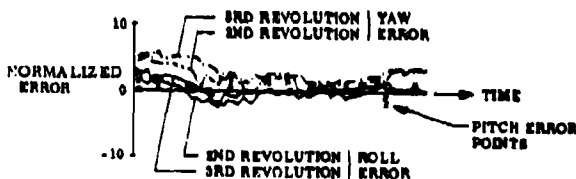


Figure 13. SPARS Observation Error; Real-Time System Test

Since there is no known error source in the SPARS itself that is systematic at table period, it is considered appropriate to ascertain the SPARS performance by removing from the observation error the systematic error at table period. Doing this gives a total random observation error of 1.1. Taking the probable lab random error from this leaves 1 as the probable SPARS error.

Thus, with actual hardware operating over a limited but representative set of "worst case" star interval conditions, the LMSC/HI SPARS concept was shown to have the capability of meeting the SPARS performance requirements.

## CONCLUSION

At the beginning of the SPARS program it was recognized that in order to achieve the SPARS objective of improving attitude reference system performance significantly it would be necessary to stretch technology a little. Small increment pulse rebalance strapdown gyros, strapdown solid-state star sensors, recursive filtering, real-time on line data processing, on-the-fly laboratory autocollimator measurement and stable laboratory stars all were elements in this need to stretch.

As a result of the program to date, a high level of confidence now exists both in the ability of the SPARS system to deliver its required performance in orbit and in the ability to test the system to this performance in the laboratory. One additional, somewhat subjective result of the program, has also become apparent. There seems to have developed among the personnel associated with the program a sense of satisfaction in knowing that in conducting SPARS, they have grown a little in their search to do things a better way.

## REFERENCES

1. W. R. Davis, et al., (U) Space Precision Attitude Reference System (SPARS) Phase 0 Final Report SAMSO-TR-68-217, April 1968 (Secret).
2. D. C. Paulson, D. B. Jackson, and C. D. Brown, (U) SPARS Algorithms and Simulation Results, Spacecraft Attitude Determination Symposium, October 2, 1969 (Secret).
3. R. T. Scott and J. E. Carroll, (U) Development and Test of Advanced Strapdown Components for SPARS, Spacecraft Attitude Determination Symposium, October 2, 1969 (Confidential).
4. V. Hvoshchinsky and F. Y. Hortuchi, Concepts and Mechanisation for Evaluating SPARS in the Laboratory and in Orbit, Spacecraft Attitude Determination Symposium, October 2, 1969.
5. W. R. Davis, et al., (U) Space Precision Attitude Reference System (SPARS) Phase IA Final Report SAMSO-TR-69-72, February 1969 (Secret).

<sup>6</sup> Non-dimensional units normalized to the SPARS performance requirement.



## SPARS ALGORITHMS AND SIMULATION RESULTS<sup>1</sup>

D. C. Paulson, D. B. Jackson, and C. D. Brown  
Aerospace Division  
Honeywell Inc.  
Minneapolis, Minnesota

### ABSTRACT

This paper describes data processing algorithms for the LMSC/HI Space Precision Attitude Reference System (SPARS), emphasizing the application of discrete Kalman filter theory to the processing of data from the strapdown gyros and passive star sensors. The descriptions are at a level of detail that reflects refinement in digital simulation and real time system test. A three degree-of-freedom digital simulation, which includes the SPARS equations along with a "truth model" and dynamic error sources, is described. Results of simulation runs are presented which show sensitivity of attitude reference performance to star sensor geometry, measurement errors and detectability, to gyro drift and to computational errors. These results show that errors from the dynamic error sources are well within the SPARS requirements. Results of a series of simulation runs to determine convergence of the attitude error from large initial values (acquisition) are presented. Star sensor design parameters are shown to have a significant effect on convergence time. The paper concludes with a summary of computational requirements, showing that the SPARS algorithm can be implemented in a typical modern aerospace computer.

### INTRODUCTION

The SPARS algorithms represent a new application of recursive filtering to strapdown sensor data for precise determination of satellite attitude. This paper presents a detailed description of these algorithms in the form they would be used in an orbiting vehicle with an on-board digital computer. An all-digital simulation, with which these algorithms have been analyzed and refined, is presented along with some simulation results. As described in more detail in Ref. 1, these results have been verified, using the SPARS algorithms in a slightly modified form, in a dynamic system laboratory test, which consisted of the real time determination of rate table attitude to high precision.

The coming of age of the high speed digital flight computer permits a transference of certain functions from the hardware to the software with

a consequent overall reduction in hardware complexity and improvement in system performance. In SPARS, the strapdown star sensors provide discretes, and the function of relating these to one another to bound the drift of the strapdown gyro data is performed in the computer. By providing near-instantaneous sensing of vehicle non-linear dynamics, the gyros create a reference trajectory about which attitude errors behave linearly, thus permitting use of linear recursive filtering without torque modeling. The recursive approach maintains a current and accurate attitude reference without the difficulties inherent in batch processing of large quantities of data.

The concept of applying recursive filtering to attitude determination was first proposed in the SPARS Phase O proposal in early 1967 (Ref. 2). In support of the proposal, a single degree-of-freedom simulation was performed. Simulation

<sup>1</sup>The conception of the algorithms and the generation of the simulation program was Honeywell-sponsored in early 1967. The simulation analysis effort was carried out under subcontract 24-16582 to Lockheed Missiles and Space Company.

was expanded to a complete three degree-of-freedom simulation (described herein) in the mid-1967 period prior to commencement of the Phase O SPARS contract in December, 1967. The majority of the simulation effort was carried out under the Phase O contract (Ref. 3).

Most of the algorithm details, including the portions considered to be original, were developed in the mid-1967 time frame. The exception was the extension of the recursive approach to acquisition<sup>2</sup>, an approach which was taken in Phase O after initial attempts to use a discrete batch processing approach had yielded poor results. Three noteworthy innovations devised for the SPARS application and incorporated into these algorithms are: 1) the particular use in the measurement calculation of the dot product between the star sensor detector slit normal and the star vector, 2) the use of the dot product variance, computed in the weighting function calculation, as a tolerance factor in the decision making process for star identification, and 3) the formulation of the noise term in the covariance matrix propagation using test-verified white noise drift.

These and the other SPARS algorithms, such as star catalog sorting, gyro rate calculation and integration, and derivations of the geometry matrix and transition matrix equations, are presented in a level of detail that is meant to convey the great depth to which algorithm development has progressed in the SPARS simulation and test program. The descriptions of the simulation program and simulation results are not presented in the same level of detail. The reader is referred to Ref. 3 for an in-depth treatment of these subjects.

### SENSOR CONCEPT

The SPARS uses two complementing forms of sensor data; gyro data to provide an essentially continuous attitude reference, and star sensor data to bound the long term gyro drift. Strapped down mechanizations of both types of sensors are used. A brief description of these sensors follows; more detailed descriptions are given in Refs. 1 and 4.

The inertial reference assembly (IRA), described in Ref. 4, uses three single degree-of-freedom rate integrating gyros mounted with their input axes forming a nominally orthogonal triad. A ternary pulse rebalance mode is used to maintain good scale factor stability and minimize random drift. The IRA outputs are three asynchronous pulse trains, each pulse representing a fixed increment of the integral of rate experienced by the vehicle about the respective gyro input axis. Each pulse train is summed in a separate precounter, the contents of which are periodically strobed into a digital computer for solution of attitude change over the sample period.

The relatively benign angular motion of the satellite enables this solution to be accomplished at a relatively low frequency without the usual concern for the "coning" considerations of strapdown attitude computations.

The two identical SPARS star sensors, also described in detail in Ref. 2, each utilizes medium field-of-view ( $< 10^\circ$ ) concentric optics to image a portion of the celestial sphere on a detector surface. The detector consists of a number of photosensitive elements, hereinafter denoted as slits, arranged in a spoke-like array to take advantage of the relative motion of the star field caused by the nominal pitch motion of the Earth-stabilized vehicle. Fig. 1 shows the arrangement of the star sensor viewing directions and slit orientations with respect to the vehicle. The values of  $\beta$  and  $\gamma$  can be varied over a wide range to accommodate vehicle mounting constraints without significantly affecting attitude reference performance.

The basic star sensor measurement, referred to as a transit, is the epoch at which the image of a star crosses one of the photo-sensitive slits. This generates a current pulse which starts a counter that is terminated at the next IRA precounter sampling time. The contents of the star sensor counter are strobed into the digital computer along with the IRA data. These data allow correction of the attitude state at the precise instant that the transit occurred.

The orientations of the star sensor slits are precisely measured in a preflight calibration. A single transit provides information of vehicle orientation with respect to the measured star. Coupled with the knowledge of star celestial coordinates, a transit provides partial information of vehicle inertial attitude. Multiple transits on different stars and on slits of varying angle with respect to vehicle motion provide the necessary data for complete attitude update.

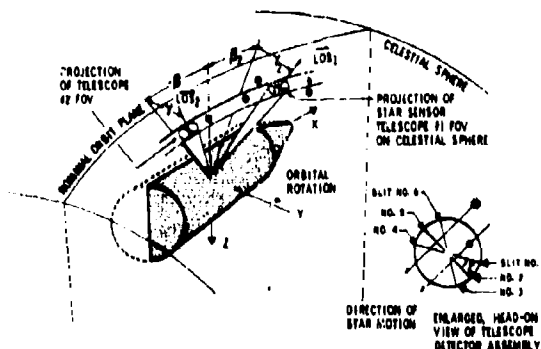


Fig. 1. Star Sensor-Vehicle Geometry

<sup>2</sup>Suggested by Dr. J. L. Lemay

## DATA PROCESSING CONCEPT

The SPARS data processing can be divided into two major categories: gyro data processing and star sensor data processing. These take place at different frequencies; the gyro data is processed at a constant frequency of several times per second, and the star sensor data is processed at irregular intervals as determined by star transits. Fig. 2 shows a block diagram with these functions further subdivided.

### Gyro Data Processing

After processing in the precounters, the IRA gyro data is input to the computer for rate derivation, gyro bias compensation, gyro misalignment correction, and attitude (direction cosine) solution. Gyro data processing blocks are those in the lower half of Fig. 2.

**Rate Derivation** -- Let the sum of the gyro pulses be denoted by  $\Delta\theta_i$  where  $i = x, y, z$ . These are measures of the integrals of rate about the respective gyro input axes over the sampling interval. A first order approximation for rate would yield  $\omega_{gi} = \Delta\theta_i/\Delta t$  and the so-called commutation error, which arises from the fact that angles are not vectors and thus do not commute.

The commutation error occurs only when there are simultaneous rates about two or more axes. The magnitude of a typical error term per sample is roughly given by the product of the accumulated angle integrals (in radians) about two input axes over a sampling interval. For nominal body rates and sampling intervals in the SPARS application, the commutation error will introduce an equivalent drift into the body attitude solution that is less than one tenth the random gyro drift. However, for worst case body rates, the drift becomes sufficiently large such that a correction is desirable.

A straightforward method of correction is provided by fitting a polynomial to successive values of a  $\Delta\theta_i$ , then differentiating that function to obtain rate at the end points. This approach has been taken, using a second order curve fit (Ref. 5). An equivalent result was obtained in Ref. 6. The expression resulting for derived gyro rate  $\omega_{gi}$  is (from Ref. 5):

$$\omega_{gi}(t_k) = [3\Delta\theta_i(t_k) - \Delta\theta_i(t_{k-1})] \frac{1}{2\Delta t} \quad (1)$$

where  $\Delta\theta_i(t_k)$  is the precounter sum over the last sampling interval,  $\Delta t$ , for the  $i$ th gyro ( $i = x, y$ , or  $z$ ) and  $\Delta\theta_i(t_{k-1})$  is the sum over the

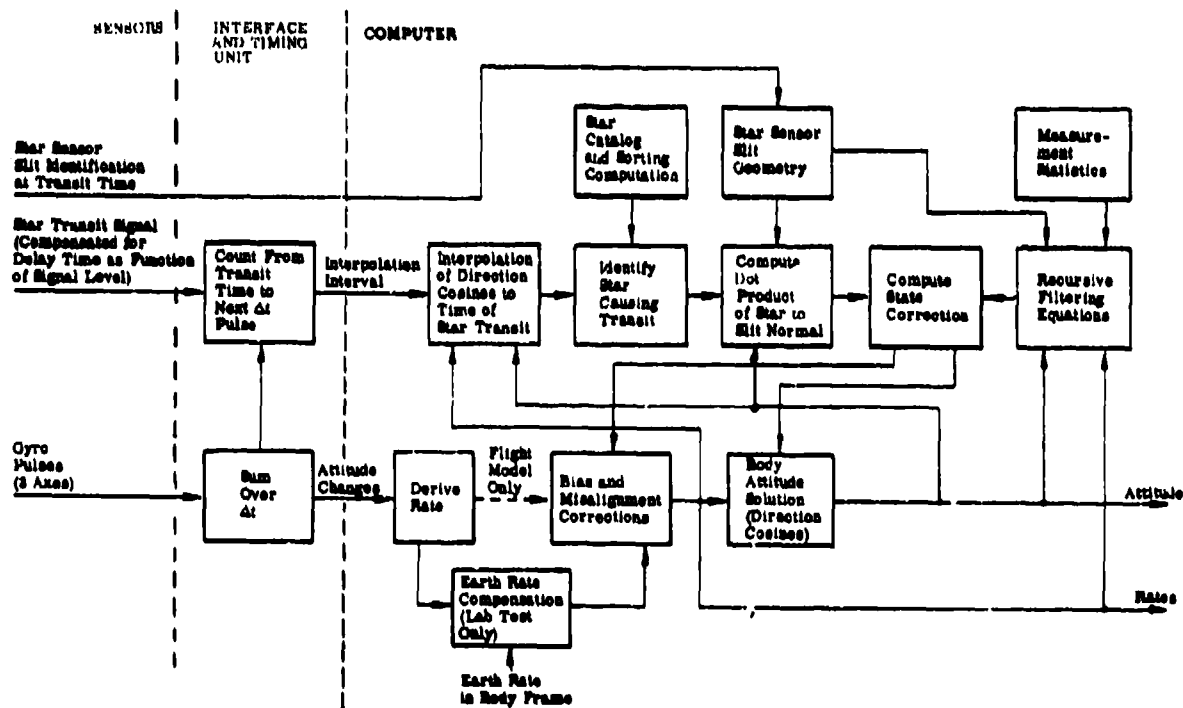


Fig. 2. Block Diagram of SPARS Computational Function

previous sampling interval for that same gyro. Equation (1) yields a second-order estimate of the gyro sensed rates at the end of the most recent sampling interval ( $t_k$ ).

Rates at the beginning of that interval are given by

$$\omega_{g_i}(t_{k-1}) = [\Delta\theta_i(t_k) + \Delta\theta_i(t_{k-1})] \frac{1}{2\Delta t} \quad (2)$$

Both  $\omega_{g_i}(t_k)$  and  $\omega_{g_i}(t_{k-1})$  are used in the body attitude solution described in a later paragraph. Only  $\omega_{g_i}(t_k)$  is used for the rate output.

**Gyro Non-orthogonality Correction** -- The actual alignments of the gyro input axes are not critical, but must be measured and compensated for accurately. The equation for the compensation is:

$$\bar{\omega}_o(t_k) = [T_{on}] \bar{\omega}_g(t_k) \quad (3)$$

and

$$\bar{\omega}_o(t_{k-1}) = [T_{on}] \bar{\omega}_g(t_{k-1})$$

where

$$\bar{\omega}_g(t) = \begin{bmatrix} \omega_{gx}(t) \\ \omega_{gy}(t) \\ \omega_{gz}(t) \end{bmatrix}$$

and

$[T_{on}]$  is a 3 x 3 matrix,

generally non-orthogonal, which is determined in a pre-flight calibration of the IRA. The resultant orthogonal rate vectors  $\bar{\omega}_o(t_k)$  and  $\bar{\omega}_o(t_{k-1})$  represent the measured rate components along the same three axes to which the star sensor photosensitive elements are referenced.

**Gyro Drift Compensation** -- Estimated vehicle rates,  $\bar{\omega}$ , are obtained by adding the gyro drift compensation vector,  $\bar{B}_g$ , to the orthogonal measured rates

$$\bar{\omega}(t_k) = \bar{\omega}_o(t_k) + \bar{B}_g \quad (4)$$

and

$$\bar{\omega}(t_{k-1}) = \bar{\omega}_o(t_{k-1}) + \bar{B}_g \quad (5)$$

which implies that the components of  $\bar{B}_g$  are correction terms for drift about the orthogonal body reference axes rather than the gyro input axes. Since these corrections are for constant drift, there is no need to apply the compensation about the gyro input axes. Furthermore, the elements of  $\bar{B}_g$  are updated periodically from star sights, which are all related to the orthogonal body reference axes. Use of gyro drift corrections in these same axes saves one extra coordinate transformation. The updating of  $\bar{B}_g$  is described in a later paragraph.

**Body Attitude Solution** -- There are many types of parameters which can be used to implement the numerical solutions of attitude from

gyro-measured rates. Among these are Euler angles, direction cosines and symmetrical Euler parameters (a form of quaternions). Euler angles are undesirable in that a numerical solution of equations using them involves time-consuming trigonometric functions. Direction cosines involve only multiplications and additions in the solution, but there are nine equations which must be solved. Symmetrical Euler parameters hold some advantages in that there are only four equations to be solved, again involving only multiplications and additions. However, since the attitude output of SPARS is to be used in coordinate transformations for Earth targeting, direction cosines will be necessary in any case. This would require a special transformation from the four-parameter set to direction cosines, taking extra computer storage as well as computation time. Therefore, direction cosines have been chosen for the SPARS body attitude solution.

The equations to be solved are:

$$\begin{aligned} \lambda_n(t_k) &= \lambda_n(t_{k-1}) + \int_{t_{k-1}}^{t_k} [\omega_z \mu_n - \omega_y \nu_n] dt \\ \mu_n(t_k) &= \mu_n(t_{k-1}) + \int_{t_{k-1}}^{t_k} [\omega_x \nu_n - \omega_z \lambda_n] dt \quad (6) \\ \nu_n(t_k) &= \nu_n(t_{k-1}) + \int_{t_{k-1}}^{t_k} [\omega_y \lambda_n - \omega_x \mu_n] dt \end{aligned}$$

where  $\lambda_n$ ,  $\mu_n$ ,  $\nu_n$  denote direction cosines between the body x, y, z axes, respectively, and the nth inertial axis ( $n = 1, 2, 3$ ). The times  $t_k$  and  $t_{k-1}$  denote present and last previous times at which the gyro precounters were sampled.

Equations (6) are solved numerically by a second order improved Euler integration scheme. The rates  $\omega(t_{k-1})$  and  $\omega(t_k)$  from Eqs. (4) and (5) represent the rates at the beginning and the end of the integration interval, and are substituted into Eq. (6) for the  $\omega_i$  ( $i = x, y, z$ ) as appropriate for the second order solution.

The body attitude solution is incremental in nature rather than absolute, and as such the gyro precounters must be sampled and processed without losing any data. This implies use of an interrupt in interfacing the gyro precounters with the computer.

The nine direction cosines of Eqs. (6) receive their initial conditions from and are updated periodically by the star sights, which bound the errors in attitude resulting from random gyro drift and other lesser error sources. Among these lesser error sources are the effects of computational roundoff and truncation as well as the commutativity effect mentioned earlier. The computational errors will cause the direction cosines (hereinafter denoted collectively as  $T_{BI}$ ) the 3 x 3 transformation from inertial to body

coordinates) to become non-orthogonal. This is corrected as part of the attitude updating process once per star sight, as described in a later paragraph. The overall effects of computational errors are described in a later portion of this paper.

### Star Sensor Data Processing

The processing of data from the star sensor is shown in the upper half of Fig. 2. Based on the input star sensor counter value, the attitude matrix is interpolated back to the star transit time, the star involved in the transit is identified, a dot product is computed using aberration corrected star catalog data, and the attitude and gyro bias states are corrected using a Kalman filter-generated weighting function.

#### Interpretation of Star Sensor Input Data --

As described earlier, a star sensor transit pulse starts a counter in the interface and timing unit which is terminated at the next gyro sampling instant. The contents of the counter, termed the interpolation interval, is input to the computer along with the gyro data. Also input to the computer at the same time is a coded word indicating which slit was involved in the transit. This latter information is not actually necessary during steady state operation when the attitude uncertainty is sufficiently small to permit slit identification in the software. However, information is necessary for the acquisition process from large initial attitude uncertainties, as will be explained later.

The interpolation interval is added to the star sensor time delay, which is predetermined from a star sensor calibration, and the sum is used to define the limits in Eqs. (6) for an integration of the attitude matrix backward from  $t_k$  to the time of transit. Note that this calculation is performed only when a transit has occurred within the last gyro sampling interval, which is seldom, relative to frequency of solutions of Eqs. (6).

#### Star Catalog and Sorting Computation --

Before the attitude matrix at transit time can be used to compute the star measurement, the star involved in the transit must be identified.

The on-board star catalog consists of the right ascension,  $\alpha_c$ , and declination,  $\delta_c$ , in fixed inertial coordinates, of all stars to be utilized in a given mission. It is conceivable that this catalog could include only a segment of the celestial sphere covering a "swath" equal to the sensor field of view plus allowances for limit cycle excursions and orbital precession. However, this implies prior knowledge of the orbit orientation in inertial space, which could be changed considerably due to launch delays.

Rather than require changes in the star catalog right up to the time of launch, it is considered desirable to pay the small penalty in computer storage necessary to store coordinates of all detectable stars in the celestial sphere.

For convenience in sorting, a special, temporary star catalog is periodically created in the computer from the inertial catalog described above. It is an orbit-oriented catalog, for which right ascension,  $\alpha^o$ , and declination,  $\delta^o$ , with respect to a nominal orbit plane, are computed for each star. The computation uses a transformation,  $T_{OI}$ , relating orbital to inertial coordinates. It is defined as

$$T_{OI} = \begin{bmatrix} -\cos i_o \sin \Omega_o & \cos i_o \cos \Omega_o & \sin i_o \\ -\sin i_o \sin \Omega_o & \sin i_o \cos \Omega_o & -\cos i_o \\ -\cos \Omega_o & -\sin \Omega_o & 0 \end{bmatrix} \quad (7)$$

where  $i_o$  and  $\Omega_o$  are the nominal orbit inclination and nodal longitude, respectively. The equations for  $\alpha^o$  and  $\delta^o$  are:

$$\alpha_o = \arctan(\mu_o^o / \lambda_o^o) \quad (8)$$

and

$$\delta_o = \arctan \frac{v_o^o}{\sqrt{1 - (v_o^o)^2}} \quad (9)$$

where

$$\begin{bmatrix} \lambda_o^o \\ \mu_o^o \\ v_o^o \end{bmatrix} = [T_{OI}] \begin{bmatrix} \cos \alpha_c \cos \delta_c \\ \sin \alpha_c \cos \delta_c \\ \sin \delta_c \end{bmatrix} \quad (10)$$

Only those stars which are within a certain range of declinations are put in the temporary catalog. The range of declinations is defined by the sensor field of view plus an allowance for limit cycle excursions. Those within the range form a "swath" of stars for which only the right ascension and an identification number (referring to the permanent inertial catalog) are stored. A schematic of a swath in a portion of the celestial sphere is shown in Fig. 3. Only one such swath is needed if the two star sensor telescopes are mounted on the same side of the vehicle at the same angle from the orbital plane. The swath must be updated periodically to account for orbital precession.

In addition to the above once per day sorting on declination, the number of candidate stars can be further reduced at the time of transit by sorting on right ascension. This is done by computing the right ascensions,  $\alpha_{s1}$ , and  $\alpha_{s2}$ , of both star sensor telescope optical axes in the orbit coordinate frame, then retaining for star identification, only those stars whose  $\alpha^o$  are within a range of one of these two values (see Fig. 3). The sensor right ascensions in the orbit frame are:

$$\alpha_{s1} = \arctan(v_{LOS1}^o / \mu_{LOS1}^o) \quad (11)$$

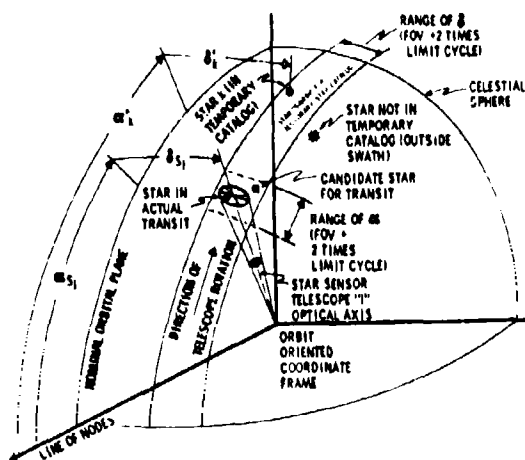


Fig. 3. Star-Telescope-Swath Geometry

$$\alpha_{s_2} = \arctan \left( \frac{\lambda^0 \text{LOS}_2}{\mu^0 \text{LOS}_2} \right) \quad (12)$$

where

$$\begin{bmatrix} \lambda^0 \text{LOS}_t \\ \mu^0 \text{LOS}_t \\ \nu^0 \text{LOS}_t \end{bmatrix} = [T_{OI}] [T_{BI}(t_m)]^T \text{LOS}_t^B \quad (\ell=1, 2) \quad (13)$$

and where  $\text{LOS}_1^B$  and  $\text{LOS}_2^B$  are the two vectors defining the star sensor telescope optical axes in the body reference frame; these are stored constants. The transformation,  $T_{BI}(t_m)$ , is the body attitude solution interpolated back to the time of measured transit.

Equations (11) and (12) are used, together with the temporary star catalog (stored in order of increasing  $\alpha^0$  to simplify sorting), to determine those stars which are within the candidate range for transit. Each such star is corrected for aberration and used in a final star identification.

**Aberration Correction** -- Correction for aberration of the apparent star positions must be made for both vehicle velocity around the Earth and Earth velocity around the Sun. The corrections are necessary because the effect of

these velocities causes shifts in apparent star position by several seconds of arc over an orbit and/or mission.

Only rough estimates of vehicle and Earth velocity are needed to make adequate aberration corrections. To obtain the components of Earth velocity around the Sun, the value of time,  $t$ , and initial Earth angle in the Ecliptic,  $\phi_E$ , (for  $t = 0$ ) are required. Earth velocity is then roughly

$$\vec{V}_E = V_{E_{avg}} \begin{bmatrix} \cos \left( \frac{2\pi}{8760} t + \phi_E \right) \\ (\cos i_E) \sin \left( \frac{2\pi}{8760} t + \phi_E \right) \\ (\sin i_E) \sin \left( \frac{2\pi}{8760} t + \phi_E \right) \end{bmatrix} \quad (14)$$

where  $V_{E_{avg}}$  is the average linear velocity of the Earth around the Sun,  $i_E$  is the inclination of the elliptic to the equator, and  $t$  is in hours.

The vehicle velocity,  $\vec{V}_s$ , may be provided from an external computation to SPARS, or it may be estimated from body attitude as follows:

$$\vec{V}_s = \begin{bmatrix} \vec{X}_B^T \end{bmatrix} \vec{V}_{s_{avg}} \quad (15)$$

where  $\vec{V}_{s_{avg}}$  is an average linear velocity of the vehicle around the Earth and  $\vec{X}_B^T$  is the transpose of the first row in the body attitude matrix,  $T_{BI}$ ; i.e.,  $\lambda_1$ ,  $\lambda_2$ , and  $\lambda_3$  from Eqs. (8). Equation (15) is valid when the vehicle is Earth-stabilized in a near-circular orbit.

The aberration correction for both the above velocities is a simple vector addition

$$\vec{S}_k^I = \frac{\vec{V}_E + \vec{V}_s}{c} + \begin{bmatrix} \cos \alpha_{ck} \cos \delta_{ck} \\ \sin \alpha_{ck} \cos \delta_{ck} \\ \sin \delta_{ck} \end{bmatrix} \quad (16)$$

where  $\vec{S}_k^I$  is the apparent position of the  $k^{\text{th}}$  star in the Cartesian inertial frame,  $c$  is the speed of light, and the terms in the brackets are the vector components of the  $k^{\text{th}}$  star in inertial coordinates as calculated from the stored right ascension  $\alpha_{ck}$  and declination  $\delta_{ck}$ . The result from Eq. (16) is not a unit vector; however, the deviation is so small (on the order of one part in  $10^8$ ) that normalization of  $\vec{S}_k^I$  is not necessary.

For each star that is identified as a transit candidate using the temporary, orbit oriented star catalog, the correction of Eq. (16) is made prior to final star identification. The identification number stored in the temporary catalog provides the means for referring back to the inertial  $\alpha_c$  and  $\delta_c$  for use in Eq. (16).

**Dot Product Computation and Star Identification** -- The parameter used in final

identification of the star involved in the transit is the value of the star sensor measurement; i.e., the dot product between the star vector and the star sensor detector slit normal.

For a transit to occur, a star vector must intersect one of the star sensor photodetector slits. As shown in Fig. 4, the photodetectors in either telescope consist of six slits across the field of view. It is assumed that each detector slit defines a single plane with the telescope optical axis. The  $j$ th slit plane is defined by a unit normal vector,  $\vec{I}_{Nj}$ . Deviations along any slit from the planar assumption represents one of the error sources in star measurements. Part of this error can be removed with appropriate calibration and software.<sup>3</sup>

When a star vector intersects a slit plane, the dot product of the star vector and the normal to that plane should be zero. That is,  $DOT = 0$  in

$$DOT = \vec{I}_{Nj} \cdot \vec{S}_k \quad (17)$$

for the correct star,  $k$ .

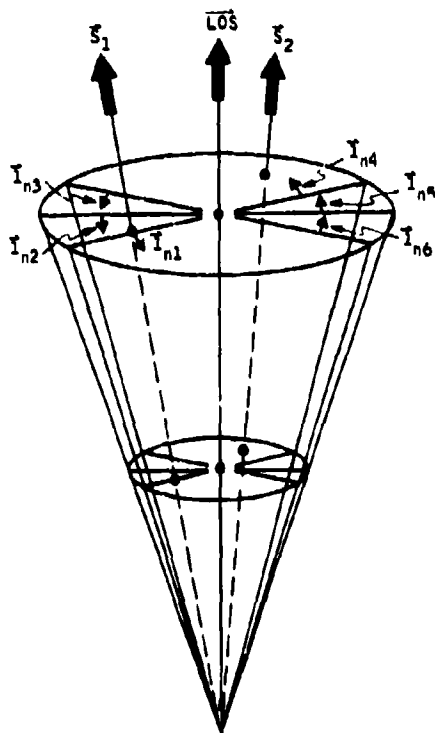


Fig. 4. Star-Telescope Geometry at Time of Transit

<sup>3</sup>Six slits are used in SPARS. A larger number of slits may be used with a correspondingly larger number of defining vectors.

The slit normal vector,  $\vec{I}_{Nj}$ , is fixed in body coordinates, whereas the star vector,  $\vec{S}_k$ , is fixed (except for aberration corrections) in inertial coordinates. In order to evaluate DOT, one of these vectors must be transformed into the frame of the other. The transformation involved is that resulting from the body attitude solution,  $T_{BI}$ . If we choose to resolve the star vector into body coordinates, Eq. (17) can be written as:

$$DOT = \vec{I}_{Nj}^B \cdot \left\{ \left[ T_{BI}(t_m) \right] \vec{S}_k^I \right\} \quad (18)$$

where the  $t_m$  indicates that the specially evaluated  $T_{BI}$  at the transit time is used in the solutions of Eq. 18.

The procedure for finding the star causing the transit is to evaluate DOT for each candidate, using the  $\vec{I}_{Nj}$  for the slit identified by the input identification word, and compare the result with a preset threshold or tolerance. The latter is a function of the system performance level, determined by the Kalman filtering calculations, and is described in a later paragraph. DOT for the correct star should be less than the tolerance; all other DOTs should be larger.

If more than one of the star candidates yield a  $|DOT|$  less than the tolerance (which is extremely unlikely during steady state operation when the tolerance level is very small), the measurement is declared invalid and no state corrections are made. Similarly, if none of the candidates yield a  $|DOT|$  less than the tolerance (as would be the case when a star that is not in the catalog has caused the transit), the measurement is disregarded. This technique eliminates the probability that uncatalogued stars, illuminated dust particles, or ambiguous transits can cause improper state corrections to be made. Furthermore, it enables exercise of choice in selecting the on-board star catalog, in that all detectable stars need not be catalogued. In regions of the sky where stars are more closely spaced, only selected stars would be catalogued, which reduces computer storage without sacrificing overall system performance.

When a single valid transit candidate has been identified, the value of DOT for that star is used for the state correction. Note that for a perfect star sensor measurement DOT represents the sine of the angle which is the projection of the system attitude error onto a plane parallel to the star vector and perpendicular to the slit plane. Since DOT is small at a transit calculation, a first order approximation can be made equating DOT to the value of the above error angle in radians. This is the quantity to be multiplied by the Kalman weighting vector for state correction.

**State Correction** -- The SPARS data processing concept makes use of linear recursive filtering theory to correct state. Since the basic SPARS equations of attitude are non-linear, they must be linearized to apply this theory. The

approach is valid if the system behaves linearly when perturbed about the non-linear solution, obtained numerically in the on-board computer. This is true in the SPARS case.

Although the non-linear solution of attitude utilizes direction cosines, it is undesirable to linearize these equations to define state. They are nine parameters, and are not independent. Instead, three independent Euler angles are used, along with the three gyro bias correction terms, as the variables from which linearized state is derived. The state,  $X$ , is defined as

$$\bar{X} = \begin{bmatrix} \delta \phi \\ \delta \theta \\ \delta \psi \\ \delta B_x \\ \delta B_y \\ \delta B_z \end{bmatrix} \quad (19)$$

where the top three elements are linearized Euler angles and the bottom three are linearized gyro bias corrections. The incremental correction to state is given by

$$\Delta \bar{X} = \bar{K} \cdot (\text{DOT}) \quad (20)$$

where  $\bar{K}$  is a six-element weighting vector, the generation of which is described in a later paragraph.

In order to apply this state correction after a star transit, the direction cosines of the body attitude solution must first be converted to Euler angles. The corrections of Eq. (20) are then added, the first three elements of  $\Delta \bar{X}$  to the Euler angles, and the last three to the gyro bias correction terms  $B_x$ ,  $B_y$ , and  $B_z$  [used in Eqs. (4) and (5)]. Although this conversion to and from Euler angles would seem to require extra computation time as well as storage relative to performing all computations with Euler angles, overall time is actually reduced because the high speed body attitude solution utilizes direction cosines, which are more efficient, as discussed in a previous paragraph. Furthermore, the procedure automatically orthogonalizes the direction cosine matrix, thus no special function is needed for this purpose.

The equations used to perform the transformations between direction cosines and Euler angles depend on the Euler angle sequence. To avoid singularities involved in computing Euler angles from direction cosines, the sequence is defined relative to the orbit-oriented coordinate frame. Use of a pitch-roll-yaw ( $\theta$ - $\phi$ - $\psi$ ) sequence then avoids the "gimbal lock" problem in that the roll and yaw angles are known to not exceed a few degrees.

The Euler angles for this sequence are related to the direction cosines by

$$T_{BI}(t) = \begin{bmatrix} \cos \phi \cos \theta & \sin \phi \cos \theta & -\sin \theta \sin \phi \cos \theta \\ \sin \phi \cos \theta & \cos \phi \cos \theta & -\sin \theta \cos \phi \cos \theta \\ \sin \theta & \cos \theta & \cos \theta \end{bmatrix} [T_{OI}] \quad (21)$$

where  $[T_{OI}]$  is the inertial-to-orbit transformation defined by Eq. (7) once per day. From this are defined the Euler angles

$$\begin{aligned} \phi &= \arctan \frac{-v_2^0}{\sqrt{1-(v_2^0)^2}} \\ \theta &= \arctan \left( v_1^0 / v_3^0 \right) \\ \psi &= \arctan \left( \lambda_2^0 / \mu_2^0 \right) \end{aligned} \quad (22)$$

where  $\lambda_2^0$ ,  $\mu_2^0$ ,  $v_1^0$ ,  $v_2^0$ , and  $v_3^0$  are elements of

$$[T_{BO}(t)] = [T_{BI}(t)] [T_{OI}]^T \quad (23)$$

The computational functions of star catalog sorting, aberration correction, and transit time prediction may take as long as one or two gyro precounter sampling intervals to complete. It is assumed that the linear correction to state can be made at that time rather than at the time of measurement with negligible error. The last solution of  $T_{BI}(t_k)$  is thus used in Eqs. (23) and (22) to compute Euler angles. After the corrections to state are applied by adding the elements of  $\Delta \bar{X}$  from Eq. (20) to the appropriate Euler angles and gyro bias compensation terms, the conversion back to direction cosines is made, using Eq. (21), to obtain the updated attitude at the same time,  $t_k$ . This becomes the new initial condition for the body attitude solution, Eq. (6).

**Weighting Function Generation** -- As described in the preceding section, the SPARS data processing concept is an application of linear recursive estimation theory. This theory is well known and documented in the literature; Ref. 7 gives an over-all view with pertinent comments that will be referenced herein.

The essence of linear estimation theory is the solution of a (six element) weighting vector,  $K$ , which provides a means for correcting state in real time that minimizes the expectation of error in a least squares sense. The weighting function is computed from a  $6 \times 6$  covariance matrix,  $P$ , which is a running estimate of system error statistics. As derived in Ref. 7, the computation is



$$\bar{K} = PH^T [HPH^T + R]^{-1} \quad (24)$$

where H is a geometry matrix of partial derivatives relating perturbations in state to perturbations in measurement, and R is the estimated measurement covariance matrix. For the SPARS case, the measurement is a scalar, hence R is the variance of the star sensor uncertainty in angular units. Eq. (24) is solved once per star transit and used in the state correction. The geometry matrix (a 1 x 6 row vector in this case), is derived in Appendix A to be:

$$H = H \begin{bmatrix} \bar{I}_{N_j}^B & T_{BI} & T_{OI} & \bar{S}_k^I \end{bmatrix} \quad (25)$$

The covariance matrix, P, in Eq. (24) is time variant. In the SPARS application, its computation can be discrete (see Ref. 7) since the star measurements occur relatively infrequently with respect to the high speed solution of state. In the discrete computation, the covariance matrix, P, is propagated from the time of one measurement to the next by means of a 6 x 6 transition matrix,  $\Phi(t_k; t_{k-1})$ , which is defined as that matrix which relates linearized state,  $\bar{x}$ , from one time,  $t_{k-1}$ , to the next,  $t_k$ , by

$$\bar{x}(t_k) = \Phi(t_k; t_{k-1}) \bar{x}(t_{k-1}) \quad (26)$$

The propagation equation is:

$$P(t_k) = \Phi(t_k; t_{k-1}) P(t_{k-1}) \Phi^T(t_k; t_{k-1}) + U(t_k) \quad (27)$$

where  $t_{k-1}$  and  $t_k$  are times of the previous and present star transits, respectively, and  $U(t_k)$  is a matrix representing the contributions to system errors, between measurements, of unmodeled or inaccurately modeled system dynamics, i.e., plant noise. Included in the latter are computational errors, and most importantly, random gyro drifts.

The transition matrix,  $\Phi(t_k; t_{k-1})$ , is obtained by numerical integration of the equation

$$\frac{d}{dt} \left[ \Phi(t; t_{k-1}) \right] = [F(t)] \left[ \Phi(t; t_{k-1}) \right] \quad (28)$$

Since [F] is a matrix of time varying coefficients from the body attitude solution, this integration must take place in parallel with the solution of Eq. (6). The matrix [F] is derived in Appendix B, and is as follows:

$$F(t) = \begin{bmatrix} 0 & 0 & -\dot{\phi} \sin \psi + q \cos \psi & \cos \psi & -\dot{\theta} \sin \psi & 0 \\ \dot{\phi} \sin \psi + q \cos \psi & 0 & \dot{\phi} \cos \psi - q \sin \psi & \sin \psi & \dot{\theta} \cos \psi & 0 \\ q \cos \psi - \dot{\phi} \sin \psi & 0 & 0 & 0 & 0 & 0 \\ 0 & 0 & 0 & 0 & 0 & 0 \\ 0 & 0 & 0 & 0 & 0 & 0 \\ 0 & 0 & 0 & 0 & 0 & 0 \end{bmatrix} \quad (29)$$

where  $p = \dot{\omega}_x$ ,  $q = \dot{\omega}_y$ ,  $r = \dot{\omega}_z$ , and  $\phi$ ,  $\theta$ ,  $\psi$  are the Euler angles relating body attitude to the orbital coordinate frame. The initial condition to Eq. (29) is  $\Phi(t_k; t_{k-1}) = I$  (unity matrix). A rectangular integration algorithm for solution of Eq. (28) is adequate, since precision is not critical. The elements  $\sin \psi$ ,  $\sin \phi$ ,  $\cos \psi$ , etc. in F(t) can be derived from the attitude matrix  $T_{BI}(t)$  [see Eq. (21)] by simple arithmetic operations without inverse trigonometric functions.

At the time of a valid transit, Eqs. (27), (25), and (24) are solved in that order. The weighting vector,  $\bar{K}$ , is used to apply a state correction according to Eq. (20). The additional equation

$$P = P - KHP \quad (30)$$

must also be solved to update the covariance matrix for error improvement resulting from the state correction. The result of this calculation is stored for propagation ahead by Eq. (27) at the time of the next transit.

#### Determination of the "Noise Matrix," U(t) --

The matrix U(t<sub>k</sub>) in Eq. (27) must be somewhat empirical inasmuch as it accounts for both known (statistically) and unknown plant noise. However, if the assumption is made that the unknown plant noise is small compared to the known, then an approximate form for U(t<sub>k</sub>) can be derived. In this case, random gyro drift is the dominant known plant noise. Assuming this to be a white noise process (evidence of this from test data is given in a later paragraph) the form of U is derived in Appendix C to be:

$$U(t_k) = \begin{bmatrix} v_1^2 \Delta t_T & 0 & 0 & 0 & 0 & 0 \\ 0 & v_2^2 \Delta t_T & 0 & 0 & 0 & 0 \\ 0 & 0 & v_3^2 \Delta t_T & 0 & 0 & 0 \\ 0 & 0 & 0 & 0 & 0 & 0 \\ 0 & 0 & 0 & 0 & 0 & 0 \\ 0 & 0 & 0 & 0 & 0 & 0 \end{bmatrix} \quad (31)$$

where  $v_1^2$ ,  $v_2^2$ ,  $v_3^2$  are the components of low frequency gyro drift power spectral density<sup>4</sup>, and  $\Delta t_T$  is the time since the last transit. This form is approximate in that the assumptions of constant pitch rate and zero roll and yaw rates are necessary to obtain a solution. The exact representation of the effect of white noise gyro drift could be handled by solving the linear symmetric matrix differential equation

$$\frac{d}{dt} [P(t)] = F(t) P(t) + P(t) F^T(t) + Q(t) \quad (32)$$

in place of Eqs. (27) and (28), where Q(t) is the expected covariance of the noise  $\bar{v}(t)$  in the standard equation

$$\frac{d}{dt} [\bar{x}(t)] = F(t) \bar{x}(t) + \bar{v}(t) \quad (33)$$

<sup>4</sup>  $v_1^2$ ,  $v_2^2$ , and  $v_3^2$  are in units of (drift)<sup>2</sup>/Hz.

That is,

$$E[\bar{v}(t) v^T(\tau)] = Q(t) \delta(t-\tau) \quad (34)$$

for white noise, where  $\delta$  is the Dirac delta function.

This approach is not taken in SPARS, primarily because the solution of Eq. (32) is slightly more complex than solving Eqs. (27) and (28), and the performance obtained with the latter is satisfactory.

Equation (31) must be augmented in practical application to account for the unknown plant noise (e.g., computational errors). Experience in the SPARS application has shown that use of the other three diagonal terms is sufficient. These are determined by empirical means. Constant and time dependent terms have been tried with approximately equivalent results.

## SIMULATION AND MODELING

The complexity and non-linearities of the SPARS problem necessitated the use of digital simulation techniques for performance studies. Interrelationship of error sources required the use of a single, comprehensive digital simulation. As shown in Fig. 5, the simulation consists of two main parts; a truth model, which simulates vehicle and sensor dynamics, and the SPARS algorithms. The latter are essentially those equations and logic discussed in the previous sections and need no further explanation. The remainder of this section describes the truth model, i.e. the left-hand side of Fig. 5, and the error processing techniques.

The major elements of the truth model are the star transit calculations, the attitude and limit cycle solutions, and the sensor error models.

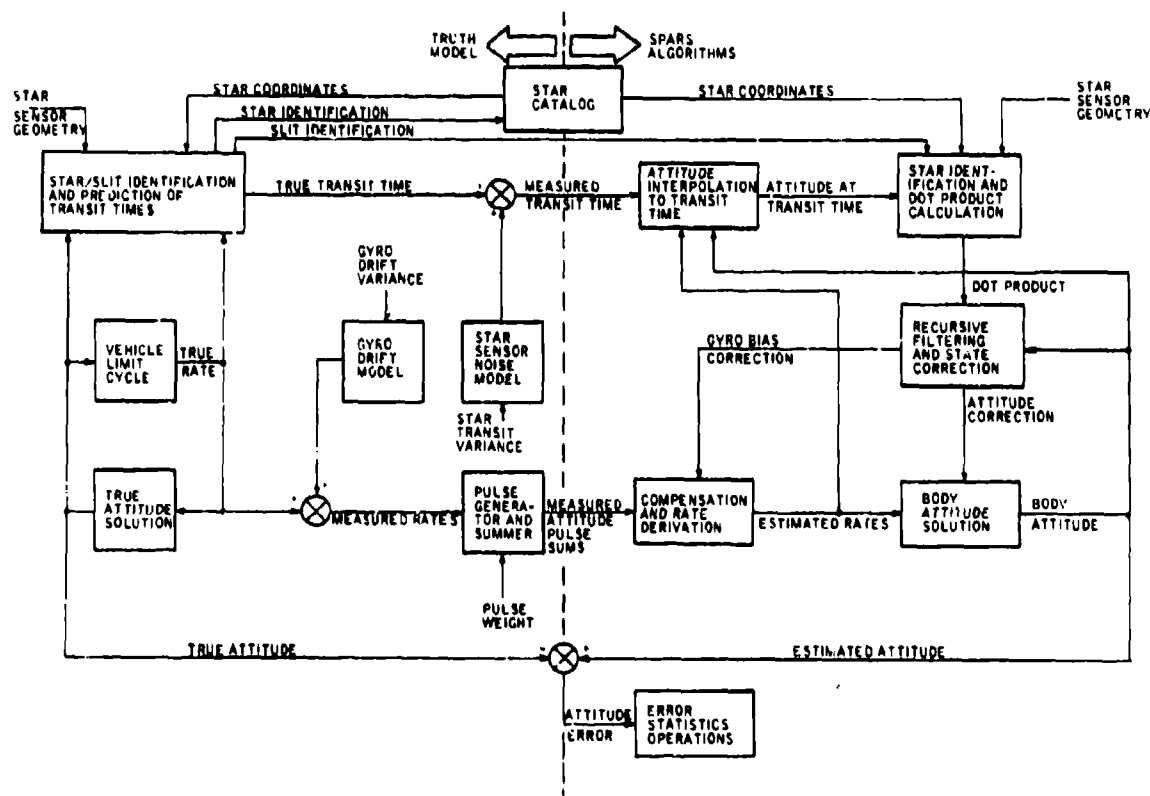


Fig. 5. Three-Degree-of-Freedom SPARS Simulation Block Diagram

## Star Transit Calculations

A star transit prediction table is maintained in the truth model for generation of true transit times. Each time one of the imaginary leading edges (which are a fixed angular distance ahead of the star sensors as shown in Fig. 6) passes a star, a linear prediction of transit time is computed, using true rates and attitudes, and entered into the table. When the predicted transit time is within 150 seconds of computed current time, the transit is re-predicted and the table is updated. This is repeated 15 seconds before estimated transit and for every  $\Delta t$  thereafter until the transit occurs or until the sensor passes by the star. Attitude is interpolated within the last  $\Delta t$  using a Newton-Raphson iteration on the dot product to define precisely the true transit time. The logic employing the 150 and 15 second ranges was developed to give accurate iteration near transit time yet minimize the number of time consuming iteration between transits.

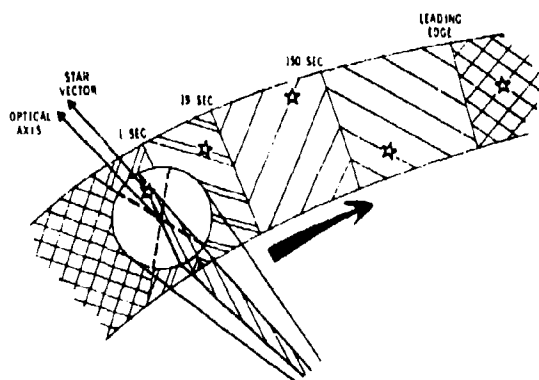


Fig. 6. 3 DOF Simulation Star Field Geometry

The above calculations are done for each star within transit range for each slit. At time of transit, the slit identification is tagged for use in algorithm calculations, and the star identification is tagged for informational print out only.

Whenever the rates change due to limit cycle control, the predictions are no longer accurate and the entire table of transit times are re-predicted. Note that the above logic applies only to the truth model; the SPARS algorithms do not predict transits before they occur, but respond only after a transit signal is received from one of the star sensors.

## Attitude and Limit Cycle Solution

The truth model implements a highly accurate attitude solution by using a fourth order Runge Kutta integration of true rate. This true

attitude is used for star transit generation, attitude error calculation, and true rate generation. A modified vehicle limit cycle model changes rate as though a reaction control jet fired whenever an attitude deadband limit is exceeded. Unlike a true vehicle attitude controller, the simulated jet firings continue until the limit cycle rate magnitude exceeds some minimum. Thus, a worst case vehicle rate is simulated.

## Sensor Error Models

The star sensor error model consists of fixed errors in the knowledge of star sensor geometry and detector slit orientations, simulating calibration uncertainties, and random errors to simulate variations in threshold transit time detection, non-planar slits, and noise in the star sensor processing electronics. This additive random noise has a normal distribution with a variance equal to that expected of the star sensors.

The gyro drift model simulates three components. They are: Constant bias drift, sinusoidal drift, and random drift.

In order to define an appropriate model, these components were measured using available computer sampling and data reduction schemes on test gyros. Less emphasis was placed on the first two components since SPARS corrects for the bias as part of the algorithm, and sinusoidal drifts typically occur only during gyro warmup or temperature transients. The latter are small in SPARS due to the active gyro temperature control. Considerable emphasis was given to the modeling of gyro random drift, however, because of its importance in performance evaluation. It is shown in Ref. 4 that the random drift of the SPARS gyros can very closely be represented by white noise over the frequency spectrum of interest. Thus, a model for white noise gyro drift was developed. The following are considerations of this development.

For times much longer than the random gyro drift correlation time (i.e., longer than the longest gyro drift autocorrelation function time constant, which is usually quite short), it is shown in Ref. 8 that:

$$E[\Delta \theta^2(t)] = 2\pi G_{xx}(0) t \quad (35)$$

where  $\Delta \theta(\cdot)$  is the attitude error due to gyro drift,  $G_{xx}(0)$  denotes power spectral density at zero frequency,  $t$  is time and  $E$  denotes expectation. This shows that the long period variance of the integral of exponentially correlated gyro drift is proportional to the product of the power spectral density at zero frequency and time. It is not possible to simulate this phenomena directly with white noise on a digital computer, due to the fact that a finite integration step size must be used. The method of introducing random rate error  $\Delta \omega_i$  in the SPARS simulation can be represented by the block diagram of Fig. 7.

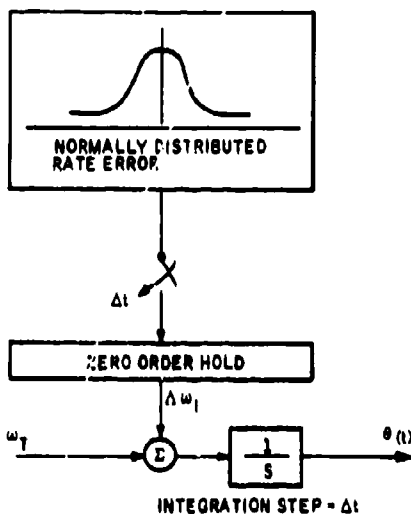


Fig. 7. Random Gyro Drift Simulation

The incremental attitude error incurred during any given period  $\Delta t$  is

$$\Delta \theta_i = \Delta \omega_i \Delta t \quad (36)$$

and, since the individual rate error samples are uncorrelated, the Central Limit Theorem can be invoked to give the error after a time  $t = n \Delta t$ :

$$\begin{aligned} \theta_i(t) &= \sum_{i=1}^n \Delta \theta_i \\ &= \Delta t \sum_{i=1}^n \Delta \omega_i \end{aligned} \quad (37)$$

which leads to the variance equation

$$E[\Delta \theta^2(t)] = n \Delta t^2 E(\Delta \omega^2) \quad (38)$$

Equations (35) and (38) lead to the following relation which must be satisfied by the digital simulation

$$[E(\Delta \omega^2)]^{1/2} = \left( \frac{2\pi G_{xx}(0)}{\Delta t} \right)^{1/2} \quad (39)$$

However, a gyro specification is not always written in terms of the zero-frequency power spectral density, but more often in terms of its integral to some frequency,  $\omega_c$ .

$$\int \text{PSD} = \int_{-\omega_c}^{\omega_c} G_{xx}(\omega) d\omega = 2\omega_c G_{xx}(0) \quad (40)$$

so

$$[E(\Delta \omega^2)]^{1/2} = \left( \frac{\pi \text{PSD}}{\Delta t |\omega_c|} \right)^{1/2} \quad (41)$$

or

$$[E(\Delta \omega^2)]^{1/2} = \left( \frac{\text{PSD}}{2\Delta t |f_c|} \right)^{1/2} \quad (42)$$

where  $f_c = \omega_c/2\pi$ . As an example, consider a one second truth model integration step size and  $|f_c| = 0.5$  Hz. These values yield the required standard deviation for the rate power spectral density:

$$[E(\Delta \omega^2)]^{1/2} = (\text{PSD})^{1/2} \quad (43)$$

Notice that if the integration step size were changed to 0.1 second, the rate power spectral density would have to be changed to

$$[E(\Delta \omega^2)]^{1/2} = \sqrt{10} (\text{PSD})^{1/2} \quad (44)$$

to yield the same simulation results. Equation (42) defines the required standard deviation input scaling of the gaussian random number generator used in the SPARS simulation for modeling gyro drift.

The simulated gyro drift is added to true rate to give measured rate. This is then quantized into an integral number of weighted pulses for input to the system and the remainder after quantization is added to measured rate in the next sampling interval.

#### Error Processing Technique

Attitude error is computed during the simulation run and stored on magnetic tape with many other system variables for display and input to the many analysis routines available. A running RMS of the attitude errors is also generated in the simulation to indicate one sigma (over time) performance.

This simulation was programmed using the Honeywell-developed COMRADE (COMputer-Aided-DEsign) system which operates on a hybrid computer. This is an extensive on-line executive system that provides the user with a man-machine communication link, enabling the engineer to control the computer through a repertoire of simple commands. These commands permit the user to control all of the input-output devices, run programs, adjust input data, and graph data on a display scope. Emphasis is placed on man-in-the-loop decision making at a modest sacrifice in computer utilization efficiency. The SPARS simulation has been incorporated within the framework of the COMRADE system to allow simple and rapid changes to system parameters, immediate display of results, and evaluation of results using them as inputs to many other statistical and spectral analysis programs. A list of input

parameters that can be varied in the simulation to investigate system performance is given in Table 1.

More than 45 standard analysis routines are available in the COMRADE program library. Several of these which have been particularly useful to the analysis of SPARS system errors and gyro drift data are described in Table 2.

Table 1. List of Simulation Input Parameters

Initial attitude error
Initial rate error
Limit cycle rate (three axes)
Limit cycle excursion angles (three axes)
Attitude jet thrust time and time constant
Star sensor random error
Gyro pulse weight
Gyro precounter sampling frequency
Fixed point attitude solution word length
Detectable star magnitude
Gyro fixed bias
Recursive filtering parameters
Star star transits and star catalog errors
Gyro random drift
Star sensor and detector geometry
Tolerance multiplication factor

Table 2. Useful COMRADE Library Programs

Name	Description
AUTOCOR	Computes mean, variance, intensity, linear trend, autocorrelation function, spectral density estimates, and spectral density estimates convolved with the Hamming spectral window on a set of data samples.
COURIER	Computes the Fourier line spectrum on a set of data samples using the Cooley and Tukey Fast Fourier Transform.
EPHINT	Prints a rapid, low resolution graphical copy of any x-y pair.
PROBDENS	Computes mean, intensity, variance, probability density function (PDF) and the PDF integral on a set of data samples.
SAMPLE	Generates a set of data samples by periodically sampling from one to five analog signals at a specified rate.

## ANALYSIS AND SIMULATION RESULTS

During the past two and a half years on the SPARS program, a large amount of analytical and computer simulation results have been compiled, in addition to the actual component and system testing efforts. This section will describe a few of the more interesting and unique analysis and simulation results.

### Single-axis Analytical Results

A single-axis analytical approach has been used on SPARS to gain initial insight into the

general error propagation characteristics of the strapdown mechanization, and to evaluate the effects of gross system parameter changes prior to detailed computer simulation. In essence, the steady state or quasi-steady state Riccati equation and related steady state stochastic equations can be manipulated to yield RMS dynamic attitude error values for updated attitude reference systems. These equations can also be manipulated to yield the required values of star sensor accuracy or star transit interval for a given level of system accuracy. This analysis is performed on a single-axis basis. Certain plausible multipliers can be introduced to obtain three-axis performance estimates.

The steady-state performance of a system with gyros can be bounded quite easily from above and below. The lower bound is obtained by assuming constant star transit intervals and an optimal linear filtering mechanization. The upper bound is obtained with a realistic star transit frequency distribution (zero-order Poisson) and a particular nonoptimal filtering solution; namely, an attitude gain of one. Let  $P$  be the attitude error variance. Then between star transits, the equation describing the buildup of the variance is

$$P_{n-} = P_{n-1+} + Q\Delta t_{AV} \quad (45)$$

where  $Q$  is the zero-frequency power spectral density of the gyro drift and  $\Delta t_{AV}$  is the time between transits. At a transit, the optimal attitude gain is

$$K_n = P_{n-} H^T [H P_{n-} H^T + R]^{-1} = \frac{P_{n-}}{P_{n-} + R} \quad (46)$$

where  $H=1$  for this single-axis system and  $R$  is the star sensor error variance. The attitude variance update is then described by

$$\begin{aligned} P_{n+} &= (1 - K_n H) P_{n-} \\ &= \left[ 1 - \frac{P_{n-}}{P_{n-} + R} \right] P_{n-} \\ &= \frac{P_{n-} R}{P_{n-} + R} \end{aligned} \quad (47)$$

Now, the crucial step is in recognizing that for steady-state operation and constant star transit intervals,

$$P_{n-1+} = P_{n+} \quad (48)$$

Thus, substituting Eq. (47) into Eq. (45) using (48),

$$P_{n-} = \frac{P_{n-} R}{P_{n-} + R} + Q\Delta t_{AV} \quad (49)$$

where the N have been dropped because they are now redundant. Eq. (49) is a quadratic equation in P-:

$$P_-^2 - P_- Q \Delta t_{AV} - R Q \Delta t_{AV} = 0 \quad (50)$$

Eq. (50) clearly has only one positive solution. The attitude error variance picture shown in Fig. 8 can now be drawn.

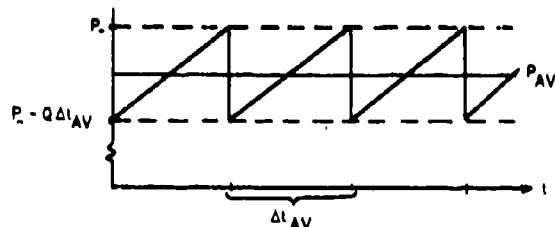


Fig. 8. Attitude Error Variance Behavior (Lower Bound)

The mean-square single-axis attitude error  $P_{AV}$  is given by

$$P_{AV} = P_- - \frac{Q \Delta t_{AV}}{2} \left( \frac{Q^2 \Delta t_{AV}^2}{4} + R Q \Delta t_{AV} \right)^{1/2} \quad (51)$$

This is the single-axis attitude error lower bound. It is optimistic because of the equal star transit assumption.

The upper bound is obtained by a quite different approach; by using the attitude gain = one mechanization, and assuming that the star transit interval spacing is Poisson distributed. (This is a pretty good assumption. Also note that the star transit interval correlation plays no role in this discussion). In this case, the attitude variance propagates after a transit like

$$P = R + Q t \quad (52)$$

Since the star transit intervals are zero-order Poisson distributed, the star transit interval probability density function is

$$P(\Delta t) = \frac{1}{\Delta t_{AV}} e^{-\frac{\Delta t}{\Delta t_{AV}}} \quad (53)$$

where  $\Delta t_{AV}$  is the same number as in the constant transit interval discussion. Now, the probability density function for being in the transit interval whose length is between  $t$  and  $t + \Delta t$  at any particular time is then given by the first-order Poisson distribution

$$P(\Delta t) = \frac{\Delta t}{(\Delta t_{AV})^2} e^{-\frac{\Delta t}{\Delta t_{AV}}} \quad (54)$$

During any particular transit interval, the average attitude variance is

$$P_{AV \text{ INT.}} = R + \frac{Q t}{2} \quad (55)$$

Therefore, integrating over all possible interval lengths

$$P_{AV} = \int_0^\infty \left( R + \frac{Q t}{2} \right) \frac{1}{(\Delta t_{AV})^2} e^{-t/\Delta t_{AV}} dt = \frac{1}{\Delta t_{AV}} \int_0^\infty \left( R + \frac{Q t}{2} \right) e^{-t/\Delta t_{AV}} dt = \frac{R}{\Delta t_{AV}} + \frac{Q}{2} \quad (56)$$

(Notice that if the transit interval spacing was uniform instead of Poisson, the average attitude variance would be  $R + Q \Delta t_{AV}/2$ . This is an important point, as it shows the effect of interval distribution.) This is the single-axis attitude error upper bound. It is a conservative estimate because of the nonoptimal filtering assumption. Therefore:

$$\left( \frac{Q^2 \Delta t_{AV}^2}{4} + R Q \Delta t_{AV} \right)^{1/4} \leq (P_{AV})^{1/2} \leq (R + Q \Delta t_{AV})^{1/2} \quad (57)$$

TRUE

Equations (51) and (56) are the equations of interest, as parametric curves can now be drawn for such things as star transit interval. One word of caution. For wide fields of view, more slits will tend to smooth out the interval irregularities and the attitude accuracy will approach the lower bound. However for small fields of view, this will not be true, since the interval distribution will remain Poisson no matter how many slits are added. (Of course,  $\Delta t_{AV}$  will go down though).

The above approach to parametric analysis is valid only for a single-axis system. However, to get a good idea of three axis performance, multiply the answers by 3, i.e.,  $\sqrt{3} \times \sqrt{3}$ . One of the  $\sqrt{3}$  factors comes from the fact that each of the single-axis errors will be about the same order of magnitude. Thus the vector sum would be  $\sqrt{3}$  times any single component. The other factor of  $\sqrt{3}$  comes from the fact that the average sensitivity (H) of attitude error in one axis to a given transit is not one, but a number like  $1/\sqrt{3}$ .

This approach to determining attitude reference performance and the parametric impact of transit interval and star sensor accuracy, yields a rapid inexpensive "ball-park" estimate which defines the limits of system performance. In problems where it is required to define a level of performance in a short time, such as in proposal exercises, it allows the investigator to remain in close contact with the essence of the problem, rather than becoming embroiled in completely unrelated problems involved with getting

a complex simulation modified and operational in a short time, and minimizes the possibility of error, since the answers are easily checked.

The method provided a guide in SPARS for selection of input parameters for the simulation which was more complex and expensive to run.

#### Star-Transit Interval Study

A comprehensive computer study of the star-transit interval characteristics of candidate SPARS strapdown star sensors has been conducted to identify parametric relationships and the extreme frequency variations possible. To establish limits on potential system errors between star sightings in the SPARS, which utilizes body-fixed star sensors on a rotating vehicle with (drifting) gyros for interpolation between sightings, it is important to know how the interval between star sightings may vary. To optimize sensor and system design, interval variation as a function of star magnitude, sensor FOV, sensor orientation, and orbit orientations must be known. A computer analysis on transit intervals was therefore conducted early in the Phase 0 study (Ref. 3).

The analysis was made for a satellite in a near-polar orbit, with a pitch motion of 240 deg/hr. Star data were obtained from the Smithsonian star catalog (Ref. 9). To gain insight into the effect of orbit orientation, six equally spaced line-of-node arguments were used. For each of these, runs were made for four limiting star magnitudes. Since the initial objective was to bound the problem and determine trends, a typical star sensor configuration was used, namely two sensors with single slits, both pointed 30 degrees off vertical to the same side of the orbit plane and at an angle of 60 degrees to each other in that plane. Runs (swaths) were made with the sensors pointing in turn to both sides of the orbit plane. Sensor FOV was varied from 2 to 10 degrees.

The analysis consisted of averaging the time interval between star-slit transits over one orbit for one set of parameters. The summary results of this analysis are given in Fig. 9. In Fig. 9 the lower and upper bounding lines represent the best and worst star swaths found, respectively. (The worst swath is not necessarily the same one for different FOV's or limiting magnitudes). The line in the center of each spread represents the mean time between transits for all swaths at that magnitude. The spread indicates the range of values resulting from the six different line-of-node orientations. If a larger number of swaths had been used, the mean points would fall more exactly on a straight, 45-deg line for small FOV's. That is, for a sufficiently large statistical sample, as the FOV is doubled, the average time between star transits is halved. These results show that for the baseline optical system the average time between star transits for all orbits is 210 sec. For the extreme orbits, this varies between 160 and 340 seconds.

#### Dynamic Attitude Error Results

The SPARS simulations have identified that the SPARS dynamic error requirement is easily satisfied with the proven performance of GG334A gyros and state-of-the-art star sensors. Single-degree-of-freedom simulation results and the more comprehensive three-degree-of-freedom simulation have shown that there are two primary contributors to the dynamic SPARS attitude error; gyro random drift variance, and star sensor error variance. It is possible - with modest system complexity - to minimize the effect of all other dynamic error sources, such as star transit interval (as shown in Fig. 11), computational roundoff and integration algorithm truncation, gyro pulse weight, fixed drift, and gyro misalignment. Static errors caused by such things as optical misalignments, shifts, and imperfect calibration were analyzed separately.

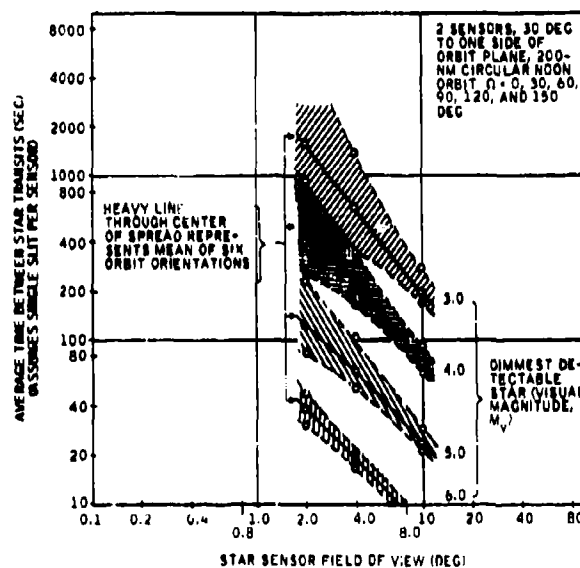


Fig. 9. Star Transit Intervals versus FOV

The effects of the two primary error sources on system performance are shown in Figs. 10 through 12. The normalized three-axis, 1σ attitude reference system dynamic error is shown as a function of the empirical noise parameter  $U$ , which is discussed in the SPARS data processing section of this document.  $U$  is related to the forward loop gain of the recursive filtering calculations during steady-state operation. The figures show that the optimum system accuracy is a very shallow function of  $U$  until a relatively large value is reached. This is in contrast to the results that were obtained early in the study when a random-walk gyro drift model was used. In that case, optimal system performance was quite sensitive to  $U$ . However, the

extensive gyro testing (Ref. 4) has shown conclusively that the random-process gyro model being used presently is the correct representation in the frequency range of interest.

The simulation results summarized in Figs. 10 to 12 were used to create design curves for the Phase O star sensor specifications.

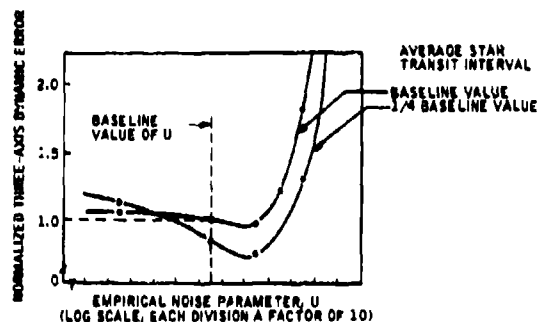


Fig. 10. Effect of Star Transit Interval

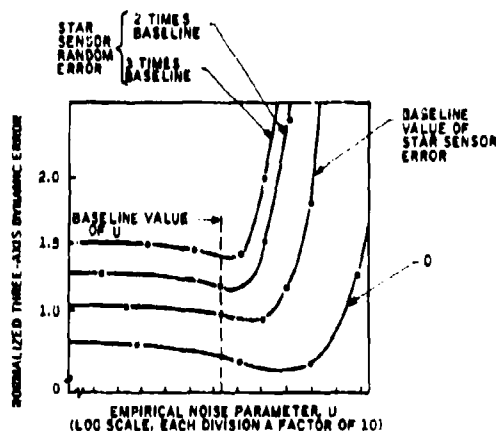


Fig. 11. Effect of Star Sensor Error

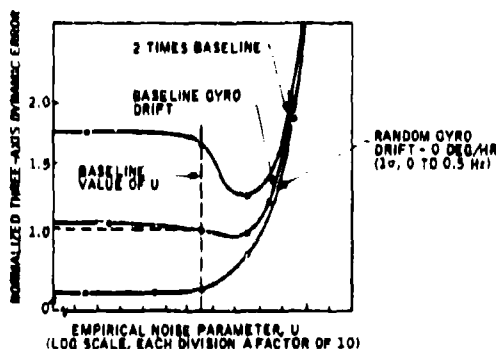


Fig. 11. Effect of Gyro Drift

The baseline system specified in Phase O had an ample margin of meeting the required one sigma accuracy. There were three main reasons for having this margin.

- (1) The  $1\sigma$  errors shown were computed over many orbits to be truly representative. The system performance statistics are somewhat variable from orbit to orbit due to fluctuations in the filtering equations and variations in the number of stars seen; the baseline mechanization provides sufficient margin to comply with the specified accuracy even for the "worst orbit" condition.
- (2) The primary intent of the  $1\sigma$  SPARS accuracy requirement is that the system error never exceed three times this value. This is true regardless of attitude error statistical distribution. In the case of SPARS, the attitude error statistics are "steeper" than Gaussian, and sufficient margin is provided to guarantee  $3\sigma$  performance.
- (3) Sufficient margin was also allowed for static errors, shifts, etc., which were specified as design-to parameters.

The following significant conclusions have been reached:

- (1) The system performance is not sensitive to any nonuniform distribution of stars.
- (2) The GG334 gyro proven performance is more than adequate for SPARS.
- (3) The risk involved, if any, due to the development status of the star sensor is minimized, because the star sensor error is attenuated in its effect on system error.

#### Star Sensor Geometry Results

The SPARS three-degree-of-freedom simulation results have shown that the attitude reference system error time history is relatively insensitive to the star sensor angular orientations and detector geometries over a broad range of values. Probably the most useful function of the SPARS three degree-of-freedom (3 DOF) simulation at Honeywell has been the determination of the effect of various changes in star sensor geometry and slit configuration. It would be extremely difficult to obtain reasonable estimates of these sensitivities analytically, since the parametric relationships involved are highly nonlinear and often not too intuitive. However, operating in an on-line mode with the SPARS 3 DOF simulation, observing the performance characteristics for various parametric combinations, and making corresponding changes resulted in a rapid determination of the effects of sensor geometry on



system performance. The significant conclusion of this study has been that star sensor geometry, other than the FOV, does not have a strong effect on system performance.

Telescope look-angle studies indicate that there is no apparent performance advantage to having the individual star telescopes cut different star swaths in the celestial sphere. With this being the case, having the telescopes oriented one behind the other eliminated 10 star simulators in the lab test and minimized the star catalog size. The studies further indicated that the out-of-orbit star swath angle and the angle between star telescopes have little effect on performance for a wide range of angles.

Because performance is not a constraint and because there is a severe sun shield penalty for look angles closer than 30 deg to the sun, the telescopes are oriented 60 deg apart. This separation ensures that at least one of the two sensors can see stars at all times without the telescopes having to be oriented closer than 60 deg to the horizon.

The salient results (normalized) of the star sensor slit studies are shown on Fig. 13 for the star sensor geometrical combinations considered. Both one and two sensor configurations were studied. The first two-sensor configuration shown has a single slit in each sensor. The slits are canted at 45 deg to the direction of motion in an attempt to gain attitude information about both axes parallel to the focal plane. The resulting error is seen to be relatively large. The addition of a second slit more than doubles the number of star transits and yields increased pitch axis sensitivity, cutting the attitude error in half. Also shown are the performance results of a number of two-sensor configurations with three slits per sensor. For the first one shown, it is seen that the slit angle has little effect on system performance. The reason for this is that increasing the angle increases the sensitivity to attitude errors about an axis parallel to the direction of motion, but counteracting this is the fact that fewer stars are seen by the canted slits. Several asymmetrical three-slit arrangements were also investigated, and very little change in system performance was observed.

One additional significant result of this study is that configurations with just one star sensor did not perform as badly as might be expected. This result has strong implications on system reliability considerations, since the failure of one of two star sensors would not be catastrophic and a modest performance degradation would be experienced. The reason one might expect a big error when using only one sensor is that the sensitivity of one sensor to attitude errors about its optical axis is quite low. Fortunately, this is compensated for by the fact that this axis keeps changing continually with respect to inertial space, so that three-axis inertial information is ultimately obtained.

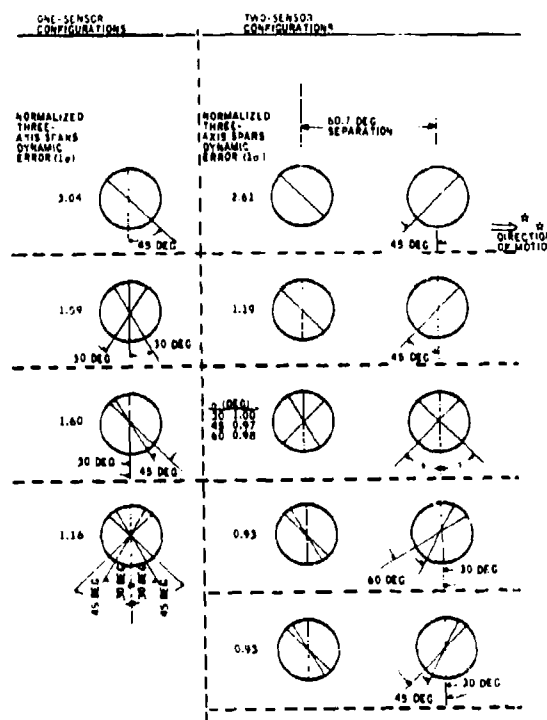


Fig. 13. Effect of Star Sensor Detector Geometry

#### Computational Error Study

Results obtained with the SPARS three-degree-of-freedom (3 DOF) simulation have demonstrated that the computational errors in attitude calculation are small with respect to other system error contributors when the 1824 computer is used, and that the design value of gyro pulse weight is an optimum value. There are three primary computational contributors to the SPARS attitude error: integration algorithm truncation, roundoff of the numerical values of critical parameters due to finite register length, and the quantization of attitude changes due to the digital rebalance electronics of the gyros. There is a tradeoff between roundoff errors and truncation errors for a given word length and integration algorithm. Longer integration step sizes result in a poorer approximation of the algorithm to the kinematics of the attitude relationships, whereas shorter step sizes result in more computer adds and multiplies per unit time, resulting in more rapid loss of accuracy in the least significant bits of the attitude variables.

The SPARS 3 DOF simulation was used to evaluate integration algorithms and computation step sizes. The first method investigated was a first-order (rectangular) method with a step size of 2.0 sec. The resulting computational drift rate was approximately 0.1 deg/hr. In an effort to reduce this drift to an acceptable value, a second-order Runge-Kutta/improved Euler algorithm was added, resulting in a reduction of the computational drift rate by three orders of magnitude. Operating within the framework of a typical system mechanization, it is important to know what effect this has on the attitude error statistics. Fig. 14a shows the effect of second-order integration step size on SPARS performance. The best performance occurs in the 1-sec range, with the error increasing somewhat sporadically for longer time, and also increasing in the 0.1-sec region as roundoff error starts to come into play. However, this study was done at 39-bit accuracy, and the optimum point will shift to the left for the baseline 48-bit integration in the UNIVAC 1824.

The effect of gyro pulse weight is shown in Fig. 14c. The dotted line is the result that is obtained when the standard deviation of the quantization uncertainty for each gyro ( $1/\sqrt{3}$  times the pulse weight) is root-sum-squared with the attitude error at a pulse weight of zero. The actual data are seen to roughly follow this expected trend, with some superimposed "beat frequency" effects resulting from the interplay between pulse weight size and forced limit cycle amplitudes that were used in the simulation to maintain worst-case rates and maximum jet firings. The baseline choice of pulse weight is substantiated by the data.

#### ACQUISITION STUDIES

Prior to steady-state operation, an acquisition phase is necessary to remove large attitude uncertainties and residual gyro biases. A crude initial vehicle attitude relative to inertial space may be obtained from the orbital ephemeris data and assumed vehicle earth-oriented control. The uncertainties in this computation are directly proportional to the vehicle control system limit cycle amplitude. These could be reduced if the error signals from the separate vehicle control system were used in the initial calculation. Although not necessary, this would reduce acquisition time.

The body attitude solution begins from the initial condition using gyro data and preflight drift compensation coefficients. Initial residual gyro drift uncertainty may be a relatively large constant bias. This is gradually reduced to the level of the random drift by the rate portion of the state corrections as they are made at accepted star transits.

Due to the large initial attitude uncertainty, special logic is required during acquisition. At a star transit, there may be more than one catalogued star within the attitude uncertainty of any given detector slit and more than one slit within the attitude uncertainty of the transiting star. It

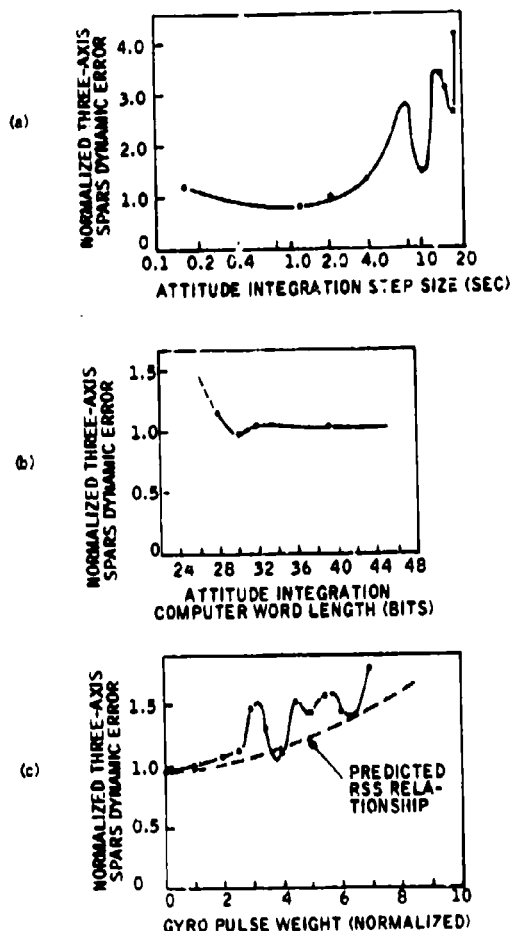


Fig. 14. Computational Effects

is clear from Fig. 15 that if only a single detectable star were within the field of view, there would still be an ambiguity as to which detector was involved in a transit. Thus, acquisition requires a scheme to identify both star and detector at each transit before a state correction can be computed. This is not necessary in steady-state since the attitude uncertainties are extremely small and a small measurement tolerance will sort out the proper slit as well as star. Thus, it is from acquisition that the requirement for a slit identification signal sent from the star sensors to the computer originates.

As mentioned above, there may be several stars at a transit time that are within the attitude uncertainty of the identified detector plane. The catalogued star which gives the smallest dot product (DOT from Eq. 18) is not necessarily the star causing the transit. Applying a state correction from a false star can cause rapid divergence of the attitude error, since this constitutes a

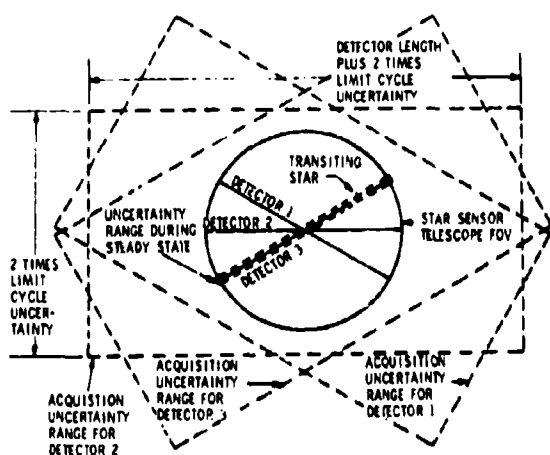


Fig. 15. Acquisition Uncertainty - Detector Not Known

non-linearity in violation of the basic algorithm assumptions. To avoid this, the values of DOT for all candidate stars are tested against a tolerance which represents the maximum expected value of DOT. If more than one star gives a magnitude of DOT within the tolerance, it can be inferred that the stars are spaced too closely for identification and the transit must be neglected. Similarly, if none of the DOT magnitudes are within the tolerance, the transit must be disregarded. The latter case may be due to transiting an uncatalogued star, an illuminated dust or propellant particle, or noise in the detector electronics; in all of these situations no state correction should be made.

The tolerance used in the candidate selection needs to be large at the start of acquisition because of the large attitude uncertainty. As the uncertainty is reduced, the tolerance should also be reduced to minimize the number of rejected transits due to ambiguities, thus increasing the percentage of accepted transits.

The most appropriate time-variant tolerance is

$$T = M \left[ HPH^T + R \right]^{1/2} \quad (58)$$

where the bracketed quantity is the variance of DOT, and is computed in Eq. 24. The factor, M is a constant multiplier. The quantity  $HPH^T$  is that portion of the variance in DOT due to attitude uncertainties, and R is that portion due to measurement uncertainties within the sensor itself. The multiplier, M, boosts up the tolerance to cover the full range of possible measurement values since  $[HPH^T + R]^{1/2}$  is a one-sigma uncertainty and thus is often smaller than the actual error.

Initially the values in the P matrix are large to represent initial condition uncertainties. These values diminish at each state correction, consistent with expected system error. When steady-state performance is reached the covariance matrix terms are small and T approaches the level of  $R^{1/2}$ , resulting in acceptance of nearly every valid transit. T will not tend to zero because of the constant variance R and the plant noise term added to prevent the terms in P from diminishing to zero.

An illustrative example of the dot product and tolerance convergence is shown in Fig. 16. The dot product and tolerance generally decrease at each state correction but the tolerance is always greater than the correct dot product at each valid transit.

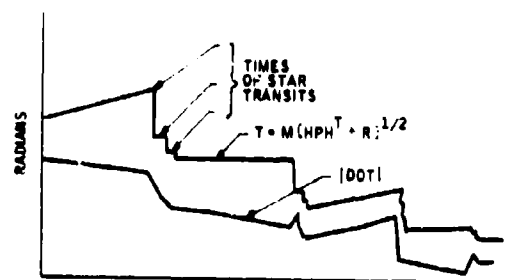


Fig. 16. Example of DOT Product and Tolerance Convergence

Despite the logic to guard against false transits, a small probability still exists that a transit can be incorrectly identified. This results when a transit from an uncatalogued star, dust particle, etc, occurs and a DOT from one and only one catalogued star is less than the tolerance at that time. The result is an incorrect state correction, which usually causes increased system error; yet the covariance matrix and hence the tolerance for accepting future transits decreases as if the correction were made on the correct star. Further transits may be rejected or falsely identified due to the correct star being outside the reduced acceptability tolerance. In most cases this causes the system error to increase rapidly as shown in Fig. 17, due to gyro bias compensation errors. In a few cases the attitude error is excessive but not diverging, and is characterized by continued rejection of future star transits. Fig. 18 is an example of this tolerance/dot product relationship. System error could remain outside the tolerance without diverging if a means were not provided for sensing and correcting the situation.

Two methods are used to test for excessive attitude error. The first is a comparison of system Euler angles to a crude attitude based on orbital ephemeris. If the difference for any one axis is greater than that expected from limit cycle and ephemeris uncertainties, the acquisition process is restarted. Should the attitude error

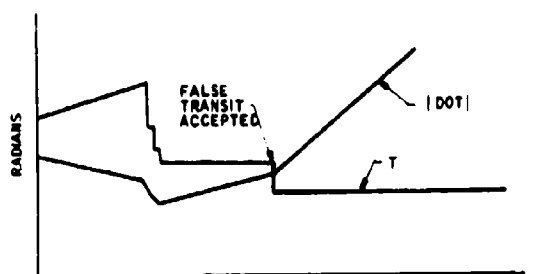


Fig. 17. Example of Attitude Divergence After Acceptance of False Transit

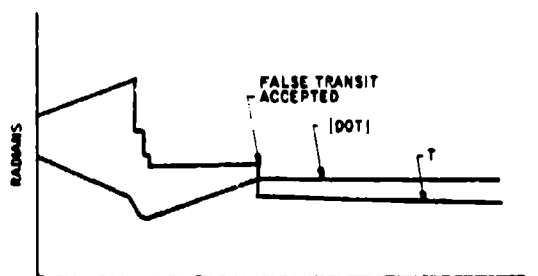


Fig. 18. Example of Excessive Attitude Error After Acceptance of False Transit

become large enough to cause rejection of transits on the basis of tolerance, but not sufficiently large as to cause restart by the above method, a second method is used. It is a test on the number of successive transits for which there are no DOT's from catalogued stars within the tolerances. A few such transits must be permitted to allow for uncatalogued stars and false transit signals. Rejected transits based on more than one DOT within the tolerance should not be included in the count to determine restart, since this often occurs in the early stages of convergence in a fairly dense portion of the sky. However, many zero candidate transits in succession indicate that the error estimates are lower than the actual errors and the acquisition process must be restarted.

The simulation program previously described was used to study convergence time sensitivities to initial conditions and system parameters. A plot of convergence time versus initial condition uncertainties is shown in Fig. 19. In general, the convergence time increases as the initial attitude errors increase. Sensitivity to changes in initial drift compensation errors was small except for the worst case 2-1/4 degree and 0.5 degree/hour error condition. (Convergence time with zero initial errors was not zero because the initially large covariance matrix causes early state corrections to be excessive). Convergence times can be further reduced when the initial uncertainties are reduced if a corresponding reduction is made in the initial covariance matrix.

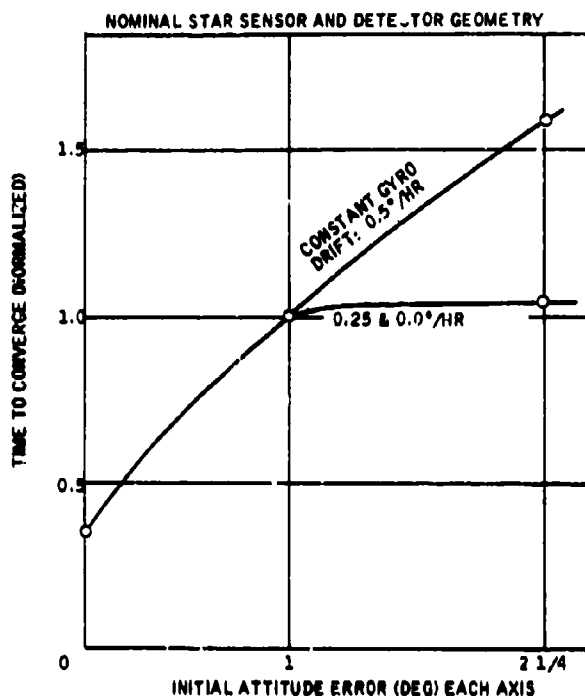


Fig. 19. Convergence versus Initial Condition Uncertainties

Simulation runs were made to investigate two aspects of the effect of star sensor detector sensitivity; 1) the effect of the number of detectable stars as established by detector sensitivity, and 2) the effect of a difference between the number of catalogued stars and the number of detectable stars.

One would expect that as the number of detectable stars increases, convergence time will decrease, simply because attitude measurements become more frequent. However, as the number of detectable stars is further increased, a point will be reached where convergence time begins to increase again due to rejections of multiple transit candidates within the tolerance. Results of simulation runs indicated that this latter effect was not a significant factor over the range of detector sensitivities being considered. In fact, the effect of the number of detectable stars was found to be much less important than the difference between the number of detectable and catalogued stars.

The effect of such a difference is shown in Fig. 20. These data were obtained by varying the number of detectable stars while holding fixed the number of catalogued stars. The results, as expected, indicate that the better the assessment of which stars the detector can "see", the faster the acquisition process.

Simulation data was also obtained to show sensitivity of convergence time to star sensor field of view (FOV). The results, shown in Fig. 21, indicate that a large FOV is desirable from

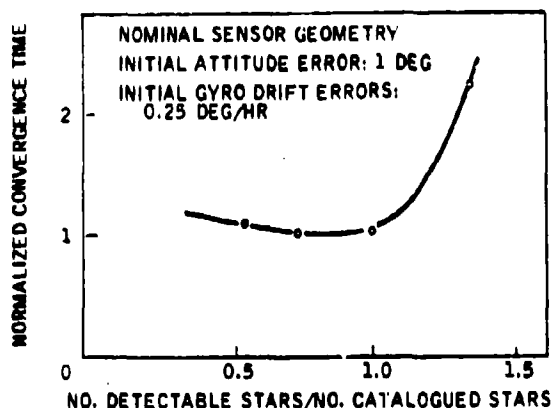


Fig. 20. Convergence Time versus Detector Sensitivity

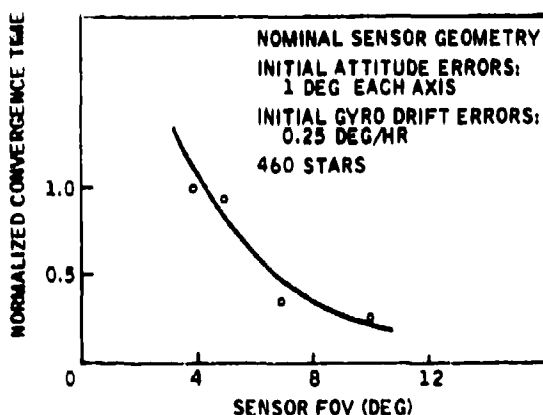


Fig. 21. Convergence Time versus Sensor FOV

an acquisition standpoint. However, this must be traded off against other considerations such as accuracy, the "window required in the spacecraft," and sun baffling, all of which pose problems at large fields of view.

#### CONCLUSION

The SPARS algorithms described herein have been proven in digital simulation and real time system test. During the tests performed in Phase IA, the algorithms were implemented on an SDS-9300 computer. Most of the algorithms were programmed in Fortran, with the exception of input/output interrupt servicing routines. Considerable knowledge was gained in handling the

problems of interrupts, which is a critical area in SPARS computations. That knowledge is currently being applied in Phase IB to program the SPARS algorithms for the UNIVAC 1824C flight computer. Laboratory tests will begin in early 1970 using the programmed 1824 with a complete SPARS prototype (Ref. 10). The SPARS algorithms are also being programmed for a Honeywell DDP-516 computer for real time solution in parallel with the 1824.

An estimate of the computational requirements for the 1824 computer is given in Table 3. This shows that the SPARS algorithms require less than half of the capacity of this computer from both a storage and speed standpoint. Thus, the SPARS can be implemented in a flight vehicle with a typical aerospace general purpose computer with plenty of space and time remaining for other computational functions (e.g., vehicle control, experiment pointing, etc.).

The simulation program described herein has been a powerful tool in analyzing SPARS performance and delimiting design parameters. The simulation results presented have shown that the SPARS dynamic errors are within the requirements of the SPARS program for state-of-the-art components. Needless to say, the simulation data, as well as test data, have proved the feasibility of the SPARS algorithms.

Table 3. SPARS Computational Requirements

Task Module	44 bit Words		Request Time/Cycle	Percentage of Computer Time Used
	DDP	SDS		
Acquisition	20	400	0.5 min/Sec	11.0
State Data Processing	80	150	15 min/100 Sec	11.0
Star Sensor Data Processing				
Star Catalog	---	1000		
Sorting	---	200	10 min/100 Sec	11.4
Identification	100	1000	40 min/100 Sec	11.4
Program Constants	---	300		
Totals	200	1050		22.0
UNIVAC 1824 C	512	8192		100.0

DDP = Digital Data Processor  
SDS = Scientific Data System

#### APPENDIX A

##### DERIVATION OF GEOMETRY MATRIX

The geometry matrix,  $H$ , is defined as the matrix of partial derivatives relating perturbations in state to perturbations in measurement. Thus:

$$\delta(\text{DOT}) = [H] \delta \bar{x} \quad (\text{A1})$$

where

$$H_i = \frac{\partial}{\partial x_i} (\text{DOT}) \quad (i = 1-6) \quad (\text{A2})$$

$$\text{and } \text{DOT} = \bar{I}_N^B \cdot \left\{ [T_{B_i}(t)] \bar{S}^I \right\} \quad (\text{A3})$$

which is the dot product of the unit normal vector to the detector slit plane,  $\bar{I}_N^B$ , in body coordinates and the unit vector to the star ray,  $\bar{S}^I$ , in the inertial coordinate frame transformed to body coordinates thru  $[T_{BI}]$ . The dot product represents the one dimensional angular error (small angle approximation) in the transformation matrix  $[T_{BI}]$  at the measured time of transit.

Evaluating (A2) yields

$$H_i = \frac{\partial}{\partial x_i} \left\{ \bar{I}_N^B \cdot [T_{BI}(t)] \bar{S}^I \right\} \\ = \bar{I}_N^B \cdot \left\{ \frac{\partial}{\partial x_i} [T_{BI}(t)] \bar{S}^I \right\} \quad (A4) \\ (i = 1-6)$$

Operation on text Eq. (21) yields the partial derivatives:

$$\frac{\partial}{\partial \phi} [T_{BI}] = [G_\phi] [T_{OI}] \quad (A5)$$

$$= \begin{bmatrix} \nu_1 \sin \psi & \nu_2 \sin \psi & \nu_3 \sin \psi \\ \mu_2 \sin \theta & \nu_2 \cos \psi & \mu_2 \cos \theta \\ \nu_2 \sin \theta & -\cos \phi & \nu_2 \cos \theta \end{bmatrix} [T_{OI}]$$

$$\frac{\partial}{\partial \theta} [T_{BI}] = [G_\theta] [T_{OI}] \quad (A6)$$

$$= \begin{bmatrix} \lambda_3 & 0 & -\lambda_1 \\ \mu_3 & 0 & -\mu_1 \\ \nu_3 & 0 & -\nu_1 \end{bmatrix} [T_{OI}]$$

$$\frac{\partial}{\partial \psi} [T_{BI}] = [G_\psi] [T_{OI}] \quad (A7)$$

$$= \begin{bmatrix} \mu_1 & \mu_2 & \mu_3 \\ -\lambda_1 & -\lambda_2 & -\lambda_3 \\ 0 & 0 & 0 \end{bmatrix} [T_{OI}]$$

$$\frac{\partial}{\partial B_x} [T_{BI}] = \frac{\partial}{\partial B_y} [T_{BI}] \\ = \frac{\partial}{\partial B_z} [T_{BI}] = 0 \quad (A8)$$

where  $\lambda_i$ ,  $\mu_i$ , and  $\nu_i$  are direction cosines between the body x, y, and z axes, respectively, and the  $i^{\text{th}}$  axis of the orbit oriented inertial coordinate frame ( $i = 1, 2, 3$ ), and  $\phi$ ,  $\theta$ , and  $\psi$  are the inertial Euler angles roll, pitch, and yaw, respectively.

The geometry matrix then becomes

$$H_i = \bar{I}_N^B \cdot \left\{ [G_i] [T_{OI}] \bar{S}^I \right\}, \quad i = \phi, \theta, \psi \\ [H] = [H_\phi \ H_\theta \ H_\psi \ 0 \ 0 \ 0] \quad (A9)$$

## APPENDIX B

### DERIVATION OF TRANSITION MATRIX

The linearized state vector elements have been defined as perturbations from the non linear solution values of three Euler angles and three body rates

$$\bar{x} = \begin{bmatrix} \phi \\ \theta \\ \psi \\ p \\ q \\ r \end{bmatrix} \quad (B1)$$

It is desired to define the fundamental matrix,  $[F]$ , in the solution of the linearized state propagation equation

$$\dot{\bar{x}} = [F] \bar{x} \quad (B2)$$

since that matrix is required for determination of the transition matrix,  $\Phi$ .

The Euler angles  $\phi$ ,  $\theta$ ,  $\psi$  relate the angular position of the body relative to an orbit oriented reference frame. Since the body rotates thru 2 radians in pitch and only very small angles in the other two axes, a pitch-roll-yaw sequence was chosen to avoid singularities.

To obtain the relation between Euler rates and body rates, consider the infinitesimal rotation  $\delta \bar{n}$  about some axis. This can be represented with components:

$$\delta \bar{n} = \delta \theta \bar{J} + \delta \phi \bar{I}' + \delta \psi \bar{K}'' \quad (B3)$$

where  $\bar{I}$ ,  $\bar{J}$ , and  $\bar{K}$  are an orthogonal right hand triad fixed in the orbital reference frame,

$\bar{I}'$ ,  $\bar{J}'$ , and  $\bar{K}'$  are a similar triad fixed in the body and the primes indicate convenient intermediate frames. The vectors  $\bar{J}$ ,  $\bar{I}'$ , and  $\bar{K}''$  can be represented in terms of  $\bar{I}$ ,  $\bar{J}$ , and  $\bar{K}$  as follows:

$$\bar{J} = \bar{J}' \cos \phi - \bar{K} \sin \phi \\ \bar{I}' = \bar{I} \cos \psi - \bar{J} \sin \psi \\ \bar{K}'' = \bar{K} \\ \bar{J}' = \bar{J} \cos \psi + \bar{I} \sin \psi \quad (B4)$$

Substituting these into Eq. (B3) gives

$$\begin{aligned}\delta \bar{n} &= \delta \theta (\bar{j} \cos \psi \cos \phi + \bar{i} \sin \psi \cos \phi - \bar{k} \sin \phi) \\ &+ \delta \phi (\bar{i} \cos \psi - \bar{j} \sin \psi) + \delta \psi \bar{k} \\ &= (\delta \theta \sin \psi \cos \phi + \delta \phi \cos \psi) \bar{i} \\ &+ (\delta \theta \cos \psi \cos \phi - \delta \phi \sin \psi) \bar{j} \\ &+ (-\delta \theta \sin \phi + \delta \psi) \bar{k}\end{aligned}\quad (B5)$$

Dividing both sides of Eq. (B5) by  $\delta t$  and taking the limit as  $\delta t$  goes to zero

$$\begin{aligned}\frac{d\bar{n}}{dt} &= (\dot{\theta} \sin \psi \cos \phi + \dot{\phi} \cos \psi) \bar{i} \\ &+ (\dot{\theta} \cos \psi \cos \phi - \dot{\phi} \sin \psi) \bar{j} \\ &+ (-\dot{\theta} \sin \phi + \dot{\psi}) \bar{k}\end{aligned}\quad (B6)$$

But the  $\bar{i}$ ,  $\bar{j}$ ,  $\bar{k}$  components of  $\frac{d\bar{n}}{dt}$  are just the body rates  $p$ ,  $q$ , and  $r$  respectively,

$$\begin{aligned}p &= \dot{\theta} \sin \psi \cos \phi + \dot{\phi} \cos \psi \\ q &= \dot{\theta} \cos \psi \cos \phi - \dot{\phi} \sin \psi \\ r &= -\dot{\theta} \sin \phi + \dot{\psi}\end{aligned}\quad (B7)$$

Finally solving Eq. (B7) the Euler rates are

$$\begin{aligned}\dot{\phi} &= p \cos \psi - q \sin \psi \\ \dot{\theta} &= (p \sin \psi + q \cos \psi) \frac{1}{\cos \phi} \\ \dot{\psi} &= r + \tan \phi (q \cos \psi + p \sin \psi)\end{aligned}\quad (B8)$$

Let

$$\begin{aligned}p &= p_m + B_x \\ q &= q_m + B_y \\ r &= r_m + B_z\end{aligned}\quad (B9)$$

where  $p_m$ ,  $q_m$ , and  $r_m$  are the measured rates and  $B_x$ ,  $B_y$ , and  $B_z$  are the compensation terms for constant gyro bias, which are determined initially in calibration but which are desired to be updated as part of the state vector.

Then upon linearization

$$\begin{aligned}\Delta p &= \Delta B_x \\ \Delta q &= \Delta B_y \\ \Delta r &= \Delta B_z\end{aligned}\quad (B10)$$

Expanding Eq. (B8) in a Taylor series evaluated at a reference which includes limit cycling and taking only first order terms

$$\begin{aligned}\Delta \dot{\phi} &= \frac{d}{dt} \Delta \phi = -p \sin \psi \cos \phi - q \cos \psi \cos \phi + \cos \psi \sin \phi - \sin \psi \Delta \phi \\ \Delta \dot{\theta} &= \frac{d}{dt} \Delta \theta = (p \sin \psi + q \cos \psi) \frac{\sin \phi}{\cos^2 \phi} \Delta \phi \\ &+ \frac{1}{\cos \phi} (p \cos \psi \sin \phi - q \sin \psi \sin \phi + \sin \psi \Delta p + \cos \psi \Delta q) \\ \Delta \dot{\psi} &= \frac{d}{dt} \Delta \psi = \sec^2 \phi (q \cos \psi + p \sin \psi) \Delta \phi \\ &+ \tan \phi (-q \sin \psi \cos \phi + p \cos \psi \cos \phi + \sin \psi \Delta p) \\ &+ \cos \psi \Delta q + \Delta r\end{aligned}\quad (B11)$$

The linearized state equation  $\dot{\bar{X}} = [F] \bar{X}$  in matrix form is then

$$\frac{d}{dt} \begin{bmatrix} \Delta \phi \\ \Delta \theta \\ \Delta \psi \\ \Delta p \\ \Delta q \\ \Delta r \end{bmatrix} = \begin{bmatrix} 0 & 0 & 0 & -(p \sin \psi + q \cos \psi) \frac{\sin \phi}{\cos^2 \phi} & -\sin \psi & \cos \psi \\ (p \sin \psi + q \cos \psi) \frac{\sin \phi}{\cos^2 \phi} & 0 & \frac{p \cos \psi \sin \phi - q \sin \psi \sin \phi}{\cos \phi} & 0 & 0 & 0 \\ \sec^2 \phi (q \cos \psi + p \sin \psi) & \tan \phi (-q \sin \psi \cos \phi + p \cos \psi \cos \phi + \sin \psi \Delta p) & \cos \psi & 0 & 0 & 0 \\ 0 & 0 & 0 & 0 & 0 & 0 \\ 0 & 0 & 0 & 0 & 0 & 0 \\ 0 & 0 & 0 & 0 & 0 & 0 \end{bmatrix} \begin{bmatrix} \Delta \phi \\ \Delta \theta \\ \Delta \psi \\ \Delta p \\ \Delta q \\ \Delta r \end{bmatrix}\quad (B12)$$

The solution of the transition matrix,  $[\Phi(t; t_0)]$ , makes use of this same matrix,  $[F]$ , and is well known to be

$$\frac{d}{dt} [\Phi(t; t_0)] = [F] [\Phi(t; t_0)] \quad (B13)$$

where  $[\Phi(t_0; t_0)] = I$ , the identity matrix, which is initialized at every star transit. By taking advantage of the many zero elements of  $[F]$  Eq. (B13) can be written

$$\begin{aligned}\dot{\Phi}_{1,j} &= F_{1,3} \Phi_{3,j} + F_{1,4} \Phi_{4,j} + F_{1,5} \Phi_{5,j} \\ \dot{\Phi}_{2,j} &= F_{2,1} \Phi_{1,j} + F_{2,3} \Phi_{3,j} + F_{2,4} \Phi_{4,j} \\ &+ F_{2,5} \Phi_{5,j} \\ \dot{\Phi}_{3,j} &= F_{3,1} \Phi_{1,j} + F_{3,3} \Phi_{3,j} + F_{3,4} \Phi_{4,j} \\ &+ F_{3,5} \Phi_{5,j} + \Phi_{6,j} \\ \dot{\Phi}_{4,j} &= \dot{\Phi}_{5,j} = \dot{\Phi}_{6,j} = 0 \\ j &= 1, 2, \dots, 6\end{aligned}\quad (B14)$$

## APPENDIX C

### DERIVATION OF THE "NOISE MATRIX," $U(t)$

The propagation of white plant noise in the discrete case of linear recursive filtering can be expressed in the following form

$$U(t) = \int_{t_k}^t \Phi(t, \tau) Q(\tau) \Phi^T(t, \tau) d\tau \quad (C1)$$

(for example, see Ref. 11). The matrix is the transition matrix given by Eq. (28) in the text, and  $Q(\tau)$  is the covariance expectation of the plant noise,

i.e.,

$$E[\bar{v}(t)\bar{v}(\tau)] = Q(t)\delta(t-\tau) \quad (C2)$$

where  $\bar{v}(t)$  is the plant noise vector in the canonical equation

$$\frac{d\bar{x}(t)}{dt} = F(t)\bar{x}(t) + \bar{v}(t) \quad (C3)$$

When random gyro drift is the only plant noise

$$\bar{v}(t) = \begin{bmatrix} v_1(t) \\ v_2(t) \\ v_3(t) \\ 0 \\ 0 \\ 0 \end{bmatrix} \quad (C4)$$

where  $v_1(t)$ ,  $v_2(t)$ , and  $v_3(t)$  are the expected random drift components along the orthogonal axes, and are assumed to be white noise over the spectrum of interest. Substituting this in Eq. (C2) yields

$$Q(t) = \begin{bmatrix} v_1^2 & 0 & 0 & 0 & 0 & 0 \\ 0 & v_2^2 & 0 & 0 & 0 & 0 \\ 0 & 0 & v_3^2 & 0 & 0 & 0 \\ 0 & 0 & 0 & 0 & 0 & 0 \\ 0 & 0 & 0 & 0 & 0 & 0 \\ 0 & 0 & 0 & 0 & 0 & 0 \end{bmatrix} \quad (C5)$$

In order to obtain a closed form solution for  $\Phi$  from

$$\dot{\Phi}(t, \tau) = [F(t)] \Phi(t, \tau) \quad (C6)$$

$F(t)$  must be describable by a continuous analytic function. If it is assumed that  $\psi = \phi = 0$  and  $q = \text{const.}$  in  $F(t)$  [Eq. 29 of the text], then  $\Phi(t, \tau)$  becomes

$$\Phi(t, \tau) = \begin{bmatrix} \cos qt & 0 & -\sin qt & \frac{1}{q} \sin qt & 0 & -\frac{1}{q}(1 - \cos qt) \\ 0 & 1 & 0 & 0 & t & 0 \\ \sin qt & 0 & \cos qt & \frac{1}{q}(1 - \cos qt) & 0 & \frac{1}{q}(\sin qt) \\ 0 & 0 & 0 & 1 & 0 & 0 \\ 0 & 0 & 0 & 0 & 1 & 0 \\ 0 & 0 & 0 & 0 & 0 & 1 \end{bmatrix} \quad (C7)$$

If it is further assumed that star transits occur frequently enough that  $\cos qt = 1$  and

$\sin qt = qt$ , then:

$$\Phi(t, \tau) = \begin{bmatrix} 1 & 0 & -qt & t & 0 & 0 \\ 0 & 1 & 0 & 0 & t & 0 \\ qt & 0 & 1 & 0 & 0 & t \\ 0 & 0 & 0 & 0 & 0 & 0 \\ 0 & 0 & 0 & 0 & 0 & 0 \\ 0 & 0 & 0 & 0 & 0 & 0 \end{bmatrix} \quad (C8)$$

Substitution of Eq. (C5) and (C8) into (C1) and integrating yields

$$U(t) = \begin{bmatrix} v_1^2 \Delta t_T & 0 & 0 & 0 & 0 & 0 \\ 0 & v_2^2 \Delta t_T & 0 & 0 & 0 & 0 \\ 0 & 0 & v_3^2 \Delta t_T & 0 & 0 & 0 \\ 0 & 0 & 0 & 0 & 0 & 0 \\ 0 & 0 & 0 & 0 & 0 & 0 \\ 0 & 0 & 0 & 0 & 0 & 0 \end{bmatrix} \quad (C9)$$

where  $\Delta t_T = t - t_k$  and the assumptions have been made that:

$$v_1^2 \gg (v_1^2 - v_3^2) qt$$

and

$$v_1^2 \gg v_1^2 q^2 t^2$$

## REFERENCES

1. W. R. Davis and J. A. Miller, "SPARS - A Completely Strapdown Concept for Precise Determination of Satellite Vehicle Attitude," Presented to the Spacecraft Attitude Determination Symposium, The Aerospace Corporation, September 30 to October 2, 1969.
2. "(U) Space Precision Attitude Reference System," Vol. I Technical Proposal, (Confidential), LMSC 699615, 15 May 1967.
3. W. R. Davis et al., "(U) Space Precision Attitude Reference System (SPARS) Phase O Final Report," Vols. I and II (SECRET), LMSC B098019, SAMSO - TR - 68 - 219, April 1968.
4. R. T. Scott and J. E. Carroll, "Development and Test of Advanced Strapdown Components for SPARS," Presented to the Spacecraft Attitude Determination Symposium The Aerospace Corporation, September 30 to October 2, 1969.
5. John J. Sullivan, "A Solution of the Critical Computational Problems Associated with Strapdown Navigation Systems," AIAA/JACC



Guidance and Control Conference, Seattle, Washington, August 15-17, 1966.

6. W. K. Clarkson, "Long Life Digital Attitude Control System - Estimate of Computational Requirements," Aerospace Report No. TR-1001 (2307)-13, Air Force Report No. SSD-TR-67-136, April, 1967.
7. Dr. Joseph L. LeMay, "Theory and Applications of Linear Estimation Theory," Instrument Society of America Preprint 3.2-1-65, October 4-7, 1965.
8. D. B. Jackson, "Applications of Nonlinear Estimation Theory to Spacecraft Attitude Determination Systems," Presented to the Spacecraft Attitude Determination Symposium, The Aerospace Corporation, September 30 to October 2, 1969.
9. Smithsonian Astrophysical Observatory Star Catalog, Smithsonian Institute, Washington, D.C., 1966.
10. V. Kvoschinsky and F. Y. Horiuchi, "Concepts and Mechanization for Evaluating PEPSY in the Laboratory and in Orbit," Presented to the Spacecraft Attitude Determination Symposium, The Aerospace Corporation, September 30 to October 2, 1969.
11. A. E. Bryson and Y. C. Ho, Applied Optimal Control (Blaisdell Publishing Co., Waltham, Mass., 1969) Appendix A4.

## DEVELOPMENT AND TEST OF ADVANCED STRAPDOWN COMPONENTS FOR SPARS<sup>1</sup>

R. T. Scott  
Space Flight Systems, Aerospace Division  
Honeywell Inc.  
Minneapolis, Minnesota

and

J. E. Carroll  
Edina Space and Defense Systems  
Control Data Corporation  
Minneapolis, Minnesota

### ABSTRACT

This paper describes the concepts and implementation of the design and development of the Honeywell SPARS components. The components described are a strapdown Inertial Reference Assembly (IRA), a strapdown Star Sensor Assembly (SSA), and a SPARS Interface and Timing Unit (SITU). Of these, the IRA is a flight qualified unit in production for another Air Force program, and as such the discussion in this paper consists of a description of the design and a presentation of test concepts and results pertinent to the SPARS application. The remaining components are undergoing development specifically for SPARS, and are presently in the second cycle of a development and test program leading to flight qualifiable hardware. The design, development and tests of the SPARS Phase IA engineering models of the SSA and SITU are also described. Included is a discussion for each device of the design, fabrication and test considerations of the current SPARS Phase IB program to develop prototypes of flightworthy models. Included in these discussions are descriptions of subassembly development tests which played an important part in final component design definition. Examples of this are the series of tests to develop solid state cadmium sulfide detectors for the SSA, and extensive testing of random drift characteristics of the gas bearing gyros in the IRA.

### I. INTRODUCTION

The SPARS components, consisting of an inertial reference assembly, star sensor, and interface unit, provide extremely high precision strapdown data for spacecraft attitude determination. These components are presently in a second-generation development program which will culminate in a SPARS laboratory system test in early 1970. These tests will be followed by a qualification and an orbiting satellite flight test program, scheduled for completion in the early 1970s.

This paper presents the design concepts for these components, and emphasizes those aspects relating to the critical design requirements of

SPARS. Test data is presented to illustrate the extreme precision attainable with state-of-the-art strapdown sensors. Supporting information relative to the SPARS program is provided in Ref. 1, in which the development history of SPARS is traced from the beginning of the Phase 0 conceptual definition in early 1967 through breadboard build and testing in Phase IA and into the current Phase IB prototype development. Also described in Ref. 1 are the tradeoffs performed to select the SPARS components and baseline design parameters, along with a functional description of how the components relate to each other to provide a precision inertial attitude reference. Reference 2 describes the details of processing the sensor data in

<sup>1</sup> This work was supported by the Space and Missile Systems Organization of the Air Force, the IRA under contract number F04701-68-C-0061 and the SSA and SITU under contract numbers F04701-68-C-0069, F04701-68-C-0227, and F04701-69-C-0150.

the computer, and Ref. 3 addresses the considerations for testing SPARS as a system both on the ground and in orbit.

In the early phases of the space program, strapdown inertial sensors were looked upon strictly as a means of implementing a simple reference and control system for short-term, relatively low accuracy applications. Strapdown gyros were used for missile and satellite booster guidance in the late 1950s and early 60s on such programs as Vanguard and Titan. Vibration and high angular rate environments limited then, and still do, the ability to remove drift errors in a strapdown system.

Applications of strapdown gyros to orbiting vehicles (e.g., Agena) and interplanetary space vehicle (e.g., Mariner), which began in the mid 1960s, took advantage of an environment in which isolation from vibration and high rates through gimbals is not required in order to achieve low drift rates. The development of improved gas bearing gyros and pulse torquing techniques has led to strapdown systems which approach the random drift performance of the most sophisticated gimballed systems.

The obvious advantage of strapdown is the elimination of the complex gimbal assemblies. An equally important advantage results when the gyros are to be used together with body-mounted, absolute attitude sensors. In such a case, strapdown gyros provide necessary relative attitude change information directly, whereas a gimballed platform does so through the gimbal readouts, involving an additional error source. This advantage was dramatically emphasized in the SPARS Phase 0 gyro tradeoffs between single degree-of-freedom strapdown and electrostatic gyro (ESG) concepts. The drift rate of the latter is so low that star sensors would have to be employed only for initial alignment with periodic alignment every month or two; yet the basic limitations in the readout of a reasonably sized ESG (analogous to gimbal readouts on a platform) were above SPARS error requirements. The higher random drifts of the single degree-of-freedom (SDOF) gyros ultimately selected for SPARS were less important, since the resultant drift in the attitude reference is bounded by the discrete star sensor measurements.

The concept of pulse torquing gyros was investigated in the mid 1950s. It was apparent then that a digital, rather than an analog output from strapdown gyros, offered advantages in scale factor stability and linearity, drift rate, and compatibility with the digital computer, which at that time was in its embryonic stage (Ref. 4). Studies were made at Honeywell for implementation of a strapdown attitude reference computation in a computer on the GAINS program by Anderson, et al. (Ref. 5). This work was extended to development of the SIGN class of guidance systems (Ref. 6) flown on the PRIME program. The present day version of this is the SIGN-III system, which uses the same basic gyros and pulse rebalance techniques as the SPARS

inertial reference assembly. The latter is the GG2200, a strapdown inertial reference assembly developed specifically for orbiting spacecraft on Air Force Program 467 (Ref. 7). It is currently in the final stages of flight qualification. The performance characteristics of this system and the timeliness of its development have, in large part, been responsible for the success of the LMSC-Honeywell SPARS program.

The development of a strapdown scanning-type star sensor (sometimes referred to as a Starmapper) represents an alternative to the gimballed star tracker as a sensor suitable for spacecraft attitude determination. The first article appeared in 1961 and considered both navigation and attitude determination from a spinning vehicle in interplanetary space (Ref. 8). Two articles in 1966 discussed an internal spinning roticle as a means of obtaining the star transits from an inertially stabilized vehicle (Ref. 9). An article in this conference presents the results of a Starmapper experiment aboard ATS-C (Ref. 10). The application of such an instrument to planetary surfaces to determine astronomic position or the motion parameters of the body is discussed in Ref. 11. Numerous other articles have been written on more restricted facets of Starmapper design. These four, however, illustrate well the developmental history.

Application of the scanning-type star sensor to SPARS was conceived during the Phase 0 proposal period (Ref. 12). This represented a departure from the applications described above in that the motion of the star images across the detector elements (caused in the SPARS case by vehicle Earth-oriented rotation in orbit) is considerably slower. This permitted use of solid-state detectors, which have a somewhat slower response time than photomultiplier-type sensors but offer significant advantages in terms of size, power, reliability, and cost. Consequently, development of the SPARS star sensor has been most notable in two areas: optical design and detector development.

## II. INERTIAL REFERENCE ASSEMBLY

The Inertial Reference Assembly (IRA) used in SPARS consists of three single-degree-of-freedom gyros mounted with input axes in a nominal orthogonal triad. The package shown in Fig. 1 and designated the GG2200 has been under development on Air Force Program 467 since late 1967. Each axis employs a closed-loop pulse rebalanced gyro. Digital data from each axis is provided on two output lines, one for each polarity of input motion. The pulses appearing on these lines have a one-to-one correspondence with gyro torquer rebalance pulses and, therefore, represent an incremental measurement of attitude.

The GG2200 consists of three functional groups: inertial sensing, loop closure, and supporting functions. A discussion of the design of each group follows. Figure 2 shows the IRA block diagram.

The GG334A gyro characteristics and environmental capability are shown in Table 1.

Table 1. GG334A Characteristics and Environmental Capability

Parameter	Value
Angular Momentum	$3 \times 10^8$ gm-cm <sup>2</sup> /sec
Output Axis Damping	$6 \times 10^8$ dyn-cm-sec
Gimbal Output Axis Inertia	286 gm-cm <sup>2</sup>
Characteristic Time	0.46 msec
Gimbal Freedom	±0.6 deg
Input Axis Freedom	±1.5 deg
Gyro Transfer Function	8.8 volts/radian
Operating Temperature	180° F
Size	
Diameter	3.32 inches
Length	4.7 inches
Weight	1.7 pounds
Spinmotor Power (55-volt start, 30 volt run)	4.8 watts
Torquer	
Scale Factor	1880 deg/hr/rad
Max Continuous Torquing Rate	100 deg/sec
Aux Torquer Scale Factor	80 deg/hr/rad
Signal Generator Sensitivity	84 volts/radian
Spinmotor Runup Time	80 seconds
Environmental Capability	
Storage Temperature	-40° F minimum
Temperature	300° F maximum
Random Vibration (30-2000 Hz)	88 g rms
Sine Vibration	
30-400 Hz	5 g zero to peak
400-800	10
800-1800	80
1800-2000	decreasing at 12 db/oct from 80 to 30
Shock	80 g peak, 8 msec
Acceleration	18 g's



Fig. 1. GG2200 Inertial Reference Assembly

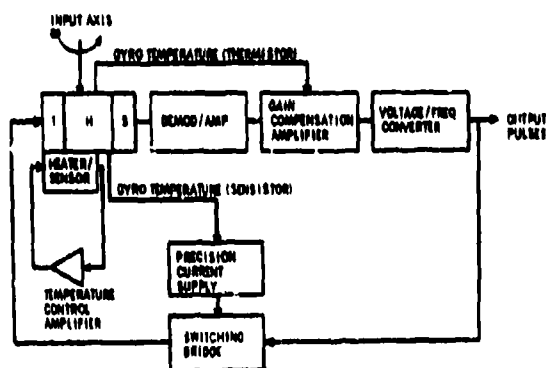


Figure 2. GG2200 IRA Simplified Single-Axis Block Diagram

#### A. Inertial Sensing

Inertial sensing is performed by three single-degree-of-freedom gyros. Angular motions about an IRA axis are sensed by the gyro associated with that axis which outputs an electrical signal proportional to the input. A cutaway view of the gyro, showing the primary mechanical features, is shown in Fig. 3. The gyro employs a gas bearing spinmotor which affords long life and low-noise performance. This facilitates a low threshold and the determination, with minimum uncertainty, of input axis rate. The design also employs a permanent magnet torquer for high torquing capability. Each gyro employs four temperature sensors, one for telemetry and three which function as references in temperature compensation or control circuits.

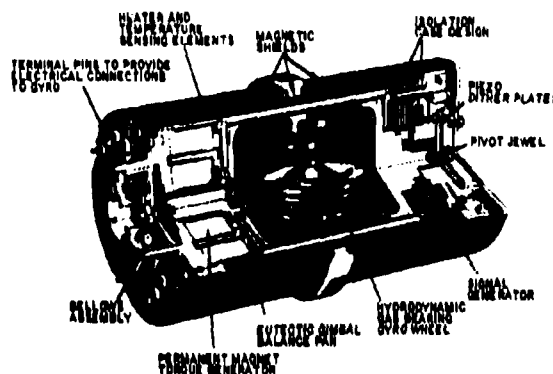


Fig. 3. GG334A Gas Bearing Gyro

## B. Loop Closure

Closed-loop operation is effected with pulse rebalancing; that is, discrete impulses of torque are applied (fed back) to the gyro precession axis. These impulses are a function of precession axis displacement, which is a function of input axis motion. The approach associated with generating these torque impulses is discussed in the following paragraphs.

1. Ternary Torquing -- The loop employs ternary torquing; that is, at each allocated specific time slot provided by the timing reference, either a positive pulse, a negative pulse, or "no pulse" is fed to the gyro precession axis torquer. Ternary torquing is used because it affords better performance than does binary torquing. In a binary torquing system, the loop can provide only a positive or negative pulse. The equivalent "no pulse" state with binary torquing is achieved by alternating positive and negative pulses into the gyro torquer. Considerations associated with these two different approaches are discussed below.

At low input rates a difference between the positive and negative pulse scale factors of the loop rebalance pulses will induce a gyro drift proportional to this difference and to the frequency of alternate pulse occurrence. The frequency of occurrence for binary torquing is equal to one-half the maximum rebalance frequency, about 5000 Hz. With ternary torquing this frequency is generally less than 10 Hz. The corresponding induced drifts are, therefore, in the ratio of 500:1.

Ternary torquing generally involves a limit cycle frequency that is two orders of magnitude less than that of a binary torquing system. The inherent rate determination capability with a ternary system is, therefore, superior to that of a binary system. This follows from examination of the distribution of net output pulse counts that would occur within a given sampling period; that is, the period that would be employed for the rate determination process. In general, a lower frequency limit cycle gives rise to less variance in the net pulse count distribution. This variance is a direct measure of the "noise" or uncertainty in the rate determination.

The loop decision process associated with generating a pulse consists of establishing a pulse rate which is approximately proportional to precession axis displacement. This pulse rate function is achieved with a voltage-to-frequency converter.

The loop employs interrupted constant-current type pulses. These pulses are nominally rectangular in terms of current magnitude and duration. They are formed by the switching bridge operating in conjunction with a precision current supply and the timing reference.

While there is virtually no restriction in the form of a rebalance pulse, only the rectangular and half sinusoids have common usage.

Rectangular pulses are preferred because of the simpler mechanization of the switching bridge and the constant-current supply.

2. Dynamic Range Extension -- In order to achieve a low rate uncertainty characteristic, a relatively low pulse size is employed. As a consequence, the pulse rate required at high input rate conditions would generally be excessive in terms of attendant inaccuracies and complexity. To obviate these difficulties, the loop employs a pulse weight change when the input rate reaches a prescribed range. The automatic increase in pulse weight is accompanied by a corresponding decrease in forward loop gain in order to maintain the loop dynamic characteristics. The increase in pulse weight is also accompanied with an output discrete that identifies the output pulses as either high or low in value.

## C. Supporting Functions

The supporting functions of the loop relate to power, temperature control and compensation, timing references, telemetry, and test. The most notable among these functions is the use of temperature compensation techniques to conserve power. In order to conserve power, the temperature of the sensors is allowed to vary over a limited range and the resulting effect on output scale factor and loop gain is compensated in the electronics.

Loop scale factor variation with temperature occurs primarily because of gyro torquer scale factor variation. This torquer variation is compensated by controlling the precision current supply value as a function of gyro temperature. This control is accomplished with a temperature sensor that is physically located upon the gyro and connected in the feedback loop of the current supply.

Loop gain variations with temperature occur because of the change of gyro damping with temperature. This effect is compensated with a forward loop amplifier whose gain is controlled as a function of gyro temperature. This control is achieved with a gyro temperature sensor that is connected in the feedback circuit around the amplifier. The variation of the gyro time constant with temperature is not compensated because its effects are negligible.

## D. Electronic Circuit Packaging

State-of-the-art packaging techniques are used for the IRA electronics. Most of the IRA circuits are packaged on printed wiring boards, both two-sided and multi-layer. Mounted on these boards are thick film assemblies, discrete components, and integrated circuits. The loop electronic assembly, shown in Fig. 4, is typical of the electronic circuit packaging. Each of three identical assemblies consists of a multilayer printed wiring board (six copper layers) on which are mounted the discrete components and thick-film assemblies needed to provide the required functions.

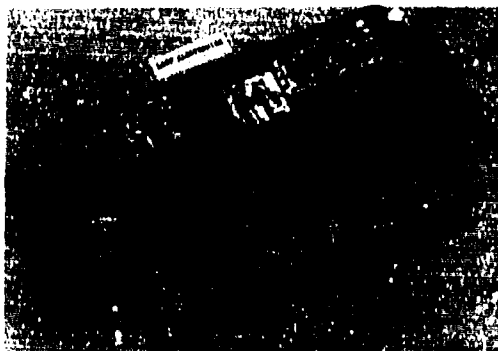


Fig. 4. Loop Electronics Assembly

#### E. GG2200 Performance

The performance requirements of the GG2200, the SPARS requirements, and the acceptance test data taken on the Phase IA IRA are shown in Table 2. Of the drift parameters, only random drift is important, since g-insensitive (fixed) drift is corrected by star sensor data in the SPARS optimal filtering calculations, and g-sensitive drift is negligible in the orbital environment. Rate range of the GG2200 is more than adequate since the SPARS gyros see orbital rate or less. Scale factor linearity is important over the particular range of rates seen by the gyros, since variations in rate cause an apparent equivalent random drift in the measured rate output. Frequency response is not critical in SPARS because of the low frequency of input rate changes.

Table 2. IRA Performance Requirements and Phase IA IRA Acceptance Test Data

Parameter	GG2200 Requirement	SPARS Requirement	Phase IA IRA Acceptance Data		
			Roll	Yaw	Yaw
G-Insensitive Drift (deg/hr)	1	not critical	0.87	1.24	1.28
G-Sensitive Drift (deg/hr/g)	1	not critical	0.98	1.98	1.48
Random Drift (units <sup>2</sup> )	10	1	0.38	0.38	0.38
Scale Factor Linearity					
Full Range, (%)	0.1	not critical			
Limited Range, (%)	0.1	0.01	0.008	0.01	0.008
Frequency Response, (db at 10 Hz)	-3 min	not critical	-1.84	-1.78	-1.88

\*Normalized to SPARS gyro random drift requirement.

Since scale factor linearity and random drift are the significant parameters affecting SPARS performance, tests were conducted to specifically evaluate them for SPARS. Tests were also conducted to determine runup to runup and long-term (months) drift stability. The

latter information is indicative of initial condition uncertainties in drift rate for the SPARS acquisition process.

1. Scale Factor Linearity Tests -- The torquer linearity error was computed by the method of least squares from analog torquing data on a GG334A gyro. The results are presented in Fig. 5, and show linearity errors below 0.01 percent to rates exceeding one rad/sec.

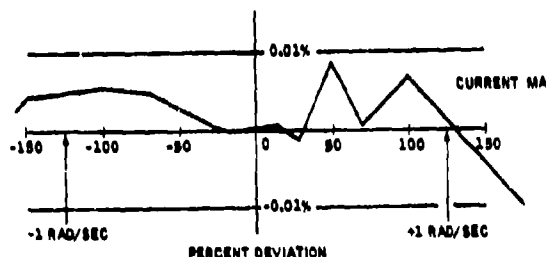


Figure 5. GG334A Torque Linearity (Analog Data)

Torquing linearity tests have also been performed using pulse rebalance electronics. The results are presented in Fig. 6 and again show linearity errors below 0.01 percent to rates exceeding 40 deg/sec.

2. Random Gyro Drift Tests -- Extensive random gyro drift tests were conducted on the GG334A gyro during the Phase 0 program. In these tests, the gyro is operated in a closed analog loop, and the output signal is fed to a precision voltage-to-frequency converter. This rate signal is integrated with resettable up-down counters, which can be sampled and reset

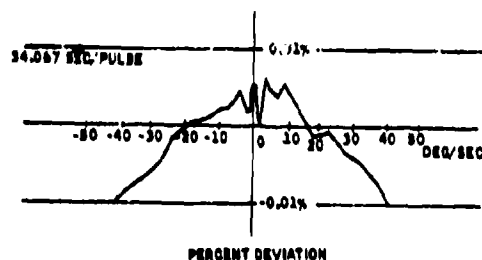


Figure 6. GG334A Torque Linearity (Pulse Rebalance Data)

at any frequency of interest. The data was subsequently analyzed on a digital computer. The details of these tests and the results are described in Appendix B.

### 3. Runup-to-Runup and Long-Term

**Drift Tests --** The stability of the GG-334A gyro drift rate has been determined as a function of spinmotor runup-to-runup. Figure 7A is a histogram of drift rate shifts with the input axis vertical (IAV) for 16 gyros.

Histograms showing the 0°F cooldown drift rate stability of 24 GG334A gyros are shown in Figs. 7B, 7C, and 7D. The values in the histograms are the RMS of the change in drift rate between successive cooldowns for each gyro.

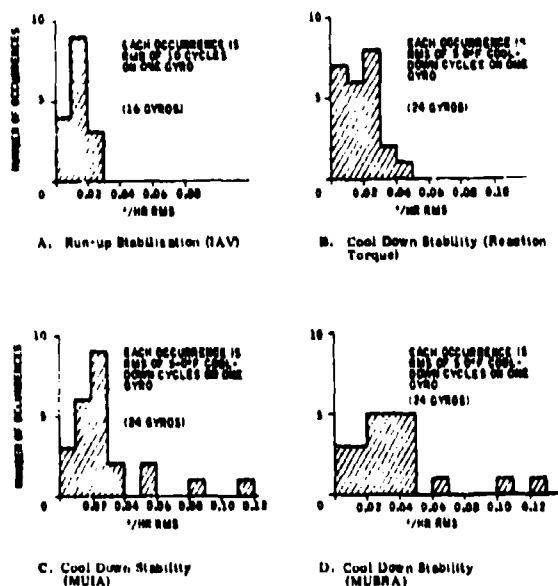


Figure 7. Error Torque Stability

The long-term drift rate stability measured on GG334A gyros is shown in Figs. 8 and 9. During the time period noted the gyros were subjected to 0°F cooldowns, long-term continuous operation, and various torquing tests.

### F. SPARS IRA Gyro Input Axis Calibration

One of the necessary calibrations for SPARS operation is the determination of the IRA gyro input axis orientations with respect to the same set of reference surfaces to which the star sensors and ultimately the optical alignment link or optical pointing device are aligned. These reference surfaces are three sides of an optical cube.

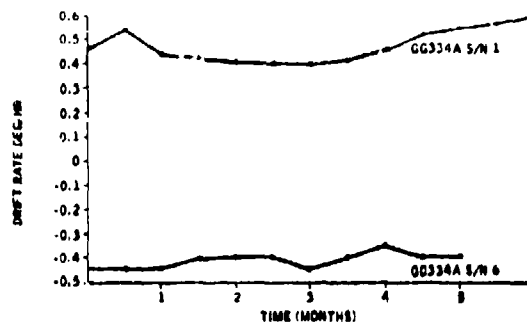


Figure 8. GG334A G-Sensitive Torque Stability

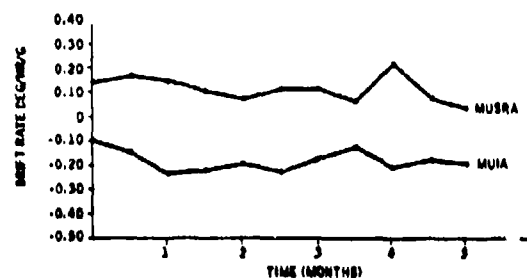


Figure 9. GG334A G-Sensitive Torque Stability

The output of the IRA alignment process is a  $3 \times 3$  transformation matrix which is used to transform the three rates, derived from the accumulated pulse sums from the three IRA gyros, into an orthogonal coordinate reference frame. This orthogonal coordinate reference frame would ideally be coincident with the normals to the optical cube. If these cube surfaces are not normal to each other to the desired degree of accuracy, then the reference frame is formed by selecting three vectors as follows: 1) the normal to one particular cube face; 2) a vector that is 90 degrees from that normal and in the plane of that normal and the normal to a second reference surface; and 3) the orthonormal. This was the case in the Phase 1A system, since the surfaces on the optical cube were not aligned as accurately as they could be measured. The reference frame and the gyro input axes are shown in Fig. 10.

The accuracy requirement for determination of gyro input axes derives from the equivalent drift associated with integration of attitude

using rate about the wrong axes -- that is, a cross coupling error. It must be realized that cross coupling arising from body rates that are essentially constant over many star sensor measurements, such as is the orbital pitch rate, will create an equivalent bias drift that will be compensated for in the recursive filtering state correction. Therefore, the rates which are important in specifying gyro alignment accuracies are actually changes in rate which occur within short time periods. For the flight system, vehicle limit cycle rate changes are the dominant error source. The SPARS flight model specification value of gyro input axes calibration accuracy is based on a maximum allowable equivalent drift change of 10 percent of the specified gyro random drift level for typical limit cycle rate changes.

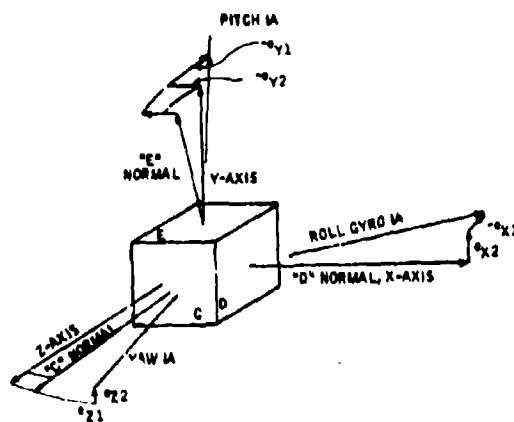


Fig. 10. Gyro and Cube Coordinate Frames

### 1. Gyro Input Axis Alignment Measurement Procedure

-- The procedure requires that a fixture be built to hold the SPARS base, mounting the IRA package and the optical cube such that each of the three gyro input axes can, in turn, be oriented along the vertical. The fixture is then mounted on a precision single-axis rate table whose spin axis is nominally aligned to vertical. The rate table must have a precision constant-speed drive, excellent low wobble characteristics, and accommodate the weight of the IRA and mounting fixture. Rotation of the package on the table results in a saturated output rate from the gyro whose input axis (IA) is parallel to the table spin axis, and low rates from the other two gyros. The angle output from either of the two gyros with IAs perpendicular to the table spin axis is proportional to the deviation from 90 degrees of the angle between that gyro's IA and the table spin axis. By rotating the table through precisely 360 degrees at a constant rate, the effect of earth's rate is canceled out.

The misalignment angles of the two gyros are directly obtained from the angle sums; then the process is repeated twice more with the other two IRA axes parallel to the table spin axis. A total of six misalignment angles are obtained, which completely describe the misalignments of the three gyro IAs, with respect to the table spin axis.

In each of the three SPARS base orientations on the rate table, the deviation of two optical cube surfaces from the turntable spin axis must be measured. Then the six desired alignment errors, namely the angle between the gyro IA and the optical cube normals, can be calculated. The measurement of the gyro input axis relative to the optical cube normals is performed in two parts: measurement of the mirror normals relative to the turntable spin axis; and measurement of the gyro input axis relative to the turntable spin axis.

With these two pieces of data, the desired alignment errors of the gyro input axis relative to the mirror normals can be calculated. The first of these measurements is made with a theodolite, using the local vertical as an intermediate transfer medium between several table and theodolite positions. The gyro-to-spin-axis measurements are performed by rotating the table at a high speed and counting pulses from the two gyros whose input axes are nominally normal to the table spin axis.

2. Transformation Matrix -- Once the gyro input axes have been located relative to the cube face normals, it is possible to transform rates about the gyro input axes into rates about the orthogonal reference axes. The nonorthogonality of the optical cube is measured before the cube is mounted on the SPARS base. The transformation matrix is the inverse of a small-angle matrix which is calculated from the input axis alignment data and cube geometry data.

The orthogonal reference axes have been defined as follows:

X axis -- normal to cube face "D"

Z axis -- 90 degrees from the X axis in the plane defined by normals to cube faces "D" and "C" and in the approximate direction of the "C" face normal.

Y axis -- normal to the plane of X and Z. (Right hand system in X, Y, Z.)

Figure 10 demonstrates relative positions of the reference axes, cube face normals, and gyro input axes. From this figure it is relatively easy to resolve the three input axes into X, Y, and Z coordinates thus relating rates about the reference axes to rates about the gyro input axes. This relationship is shown in Eq. (1).

$$\vec{W}_g = [T_{no}] \vec{W}_r \quad (1)$$



where:

$\vec{W}_g$  is the rate vector about the gyro input axes

$\vec{W}_r$  is the rate vector in the reference frame, and

$[T_{no}]$  is the inverse of the transformation matrix used in Ref. 2 to transform gyro data into the reference frame.

The transformation matrix,  $T_{no}$ , is computed from the misalignment angles shown in Fig. 10 as:

$$[T_{no}] = \begin{bmatrix} 1 - 1/2(\epsilon_{x1}^2 + \epsilon_{x2}^2) & \epsilon_{x2} & \epsilon_{x1} \\ \epsilon_{y2} & 1 - 1/2(\epsilon_{y1}^2 + \epsilon_{y2}^2) & \epsilon_{y1} \\ \epsilon_{z1} & \epsilon_{z2} & 1 - 1/2(\epsilon_{z1}^2 + \epsilon_{z2}^2) \end{bmatrix} \quad (2)$$

The small angle approximation introduces less than 0.2 arc second error for angles less than one degree.

#### G. Phase IA IRA

The Phase IA IRA was a modified breadboard version of the GG2200 IRA. The breadboard IRA electronics are shown in Fig. 11. This type of construction allowed rapid assembly and test. The separate gyro package was physically the same size as the GG2200, shown in Fig. 1.

The Phase IA IRA does not have dual rate range, provision for accepting an external timing reference, or dual voltage spinmotor operation. In all other respects, it is functionally the same as the GG2200.

### III. STAR SENSOR

The developmental history of the SPARS star sensor is principally one of solid-state photodetectors - or rather of their application to star sensors.

The development of the star sensor itself represents an alternative to the star tracker as a sensor suitable for spacecraft attitude determination. The first article (Ref. 8) appeared in 1961 and considered both navigation and attitude determination from a spinning vehicle in interplanetary space. A pair of articles (Ref. 9) in 1966 discussed an internal spinning reticle as a means of obtaining the star transits from an inertially stabilized vehicle. An article in this conference (Ref. 10) presents the results of a star sensor experiment aboard ATS-III. The application of such an instrument to planetary



Fig. 11. Phase IA IRA Electronics

surfaces to determine astronomic position or the motion parameters of the body is discussed in (Ref. 11). Numerous other articles have been written on more restricted facets of star sensor design. These four, however, illustrate well the developmental history.

In the following paragraphs we will first of all describe the SPARS star sensor in its current design. Using this as a reference point, we will then chronicle its development since 1967.

#### A. Phase IB Star Sensor

The operation of the two star sensors in the SPARS system has already been described. Figure 12 shows some details of the lens elements, photodetector, and electronics. Each is described separately below.

1. Choice of Optical System -- The optical system shown in Fig. 12 is of the type called "corrected rear concentric". That is, except for the aspheric corrector plate at the aperture and the meniscus interface, all radii of curvature (including that of the focal surface) are concentric with the aperture. Such a design is inherently free of coma, astigmatism, and distortion in addition to possessing a theoretical 180 deg. FOV. The meniscus interface is used for color correction and is not concentric with other surfaces. The aspheric surface provides almost perfect correction at the design wavelength but is, of course, also not concentric. These latter two surfaces thus reduce the usable FOV as well as introducing slight amounts of the other aberrations.

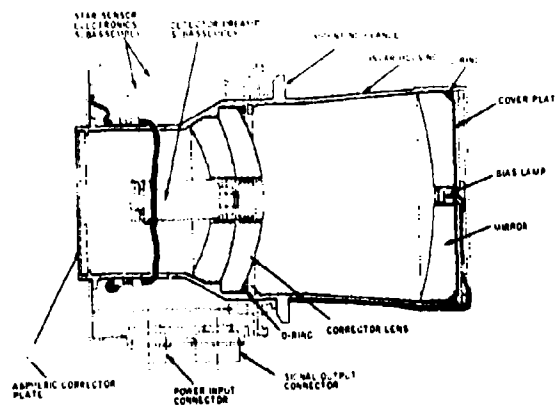


Figure 12. Phase IB SPARS Star Sensor

The performance of this optical system is shown in Fig. 13 for both on-axis images and for two degrees off-axis (four-degree FOV). It can be seen that there is almost identical performance throughout the field which is a very important criterion in star sensors. All of the star sensor optics were manufactured by E & W Optics Inc., of Minneapolis, Minn.

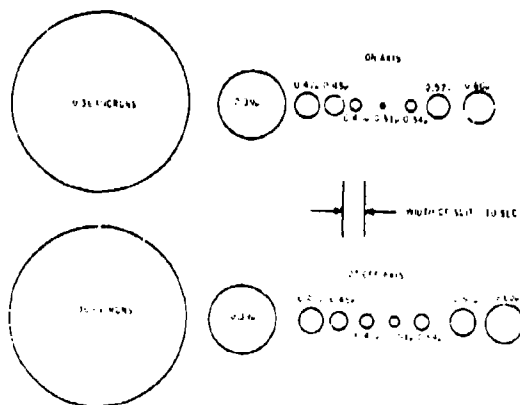


Figure 13. Star Sensor Optical System Performance

The invention of the concentric system was the simultaneous but unrelated work of Bouwers (Ref. 13) and Maksuto (Ref. 14). The design steps involved in these systems is outlined in (Ref. 15) of the present conference.

Unlike most optical designs, the allowable tolerances on radius thicknesses, and separations are very small. Generally only 0.003 in. is permitted while for some dimensions (the radius of the meniscus entrance face and the total meniscus thickness), no more than 0.001 in. deviation

from the design can be permitted. Element centering should also be within 0.001 in. in order that focus be maintained at the field edge.

A further consideration when such tolerances are applicable is operation over a temperature range. It has been found that the back focal length (the axial distance from the mirror to the focal surface) changes slightly with temperature. Since the detector sensitivity was determined empirically to be the major limiting parameter of the system, the fastest realizable optics system was designed to operate with it. Because of the low  $f/\text{number}$  ( $f/1.14$ ), the focal surface must remain within microinches of its "best" focus. To achieve this, the expansion of the Invar housing is counteracted by that of the meniscus in which the focal surface is mounted by appropriately locating the lands for the optical elements.

As one would expect, thermal gradients are of serious concern. A temperature difference from one side of the housing to the other of only  $30^\circ\text{F}$  will cause the mirror to tilt relative to the meniscus and, therefore, cause a pointing error relative to the mounting flange that is significant relative to the SPARS accuracy requirement. To prevent such gradients from occurring, a combination of high conductance coatings, insulation, and reflective paints is employed. Care will have to be exercised that such a gradient does not enter via the mounting flange. Finally, heat sources within the star sensor electronics must be adequately analyzed to make sure gradients are minimized and those that remain are symmetrical.

**2. Detector** -- The detector for the Phase IB SPARS star sensor has been developed by Allen-Bradley Corporation of Milwaukee, Wisconsin and is composed of thin-film cadmium sulfide (CdS) deposited on a four-inch radius of curvature disk and overlaid with an electrode/slit pattern. The configuration and construction techniques are outlined in Fig. 14. The employment of stretched wires of very small diameter (0.0003 in.) for the electrical mask has proven to be a good technique for solving the problems of substrate curvature and high length-to-width ratio (433). Photographic or other schemes have not been tried, but it is doubtful they could provide the necessary resolution under these conditions. The definition of slit edge is of paramount importance for accuracy. The stretched wire technique creates extremely smooth edges (roughness less than 10 to 20  $\mu$ inches) with occasional "chips" of 100  $\mu$  inches or so caused probably by tiny dust particles which remain on the wire despite elaborate cleaning.

Exactly how the (circular) star image interacts with the CdS material as it crosses the slit is very difficult to analyze. Two characteristics are clear, however, as illustrated in the photographs of Fig. 15:

- (1) The output pulse from the detector contains a fast (60 m sec) leading edge followed by a slower decay (relaxation

of the material after light passage).

- (2) Considerable variation in response occurs along the slit [Fig. 15 (b)] caused by the star image passing over crystals or combinations of crystals having varying sensitivities.

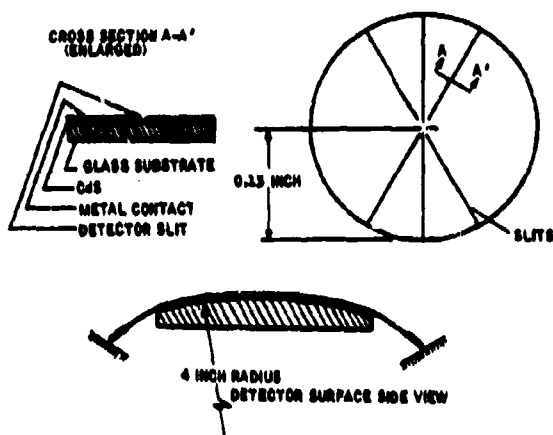


Figure 14. Thin Film CdS Photodetector

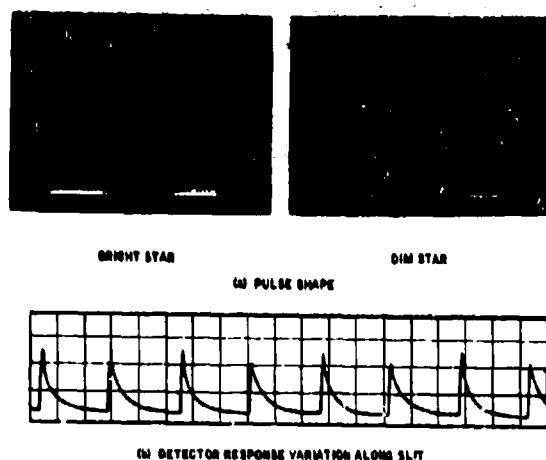


Figure 15. CdS Photodetector Star Transit Outputs

A number of articles have been published on thin-film CdS. The best are perhaps those of Refs. 16, 17 and 18. None, however, treats the situation as it exists in the SPARS star sensor: a small spot of light moving normal to a long strip of active area. Only a small portion (approximately 1/400) of the strip or slit takes part in the signal, whereas the entire slit contributes to the noise. Furthermore, the slit passage is much faster than the normal time

constants of the material itself. For example, it typically requires 300 msec for the signal to rise to 83 percent of its ultimate height when excited by a one-foot-candle step function of light and operated with an optimum value of background light. A star image is past the slit in 80 msec for a vertical slit and 70 msec for those canted at 30 degrees. Nevertheless, sufficient star detection signal is obtained from this fraction of peak value as will be discussed in the next section.

A considerable amount of study and testing remains to be done on the detector. These include tests for the effect of star intensity and color on rise time, and the effects of temperature and humidity environment.

3. **Electronics** -- As shown in Fig. 12, the SPARS star sensor electronics consists of two portions: (a) the preamplifiers, mounted immediately behind the detector; and (b) the main amplifiers, detection and control circuitry, and power distribution all wrapped around the outside of the sensor fore-housing.

There are six slits and six identical sets of electronics from preamp through level detection. Each channel operates as shown in Fig. 16 (only the concepts are shown; many details are omitted). Detection is on the leading edge and occurs at a fixed fraction of the pulse peak. Leading edge detection avoids problems caused by pulse asymmetry (Ref. 15), and detection at a constant fraction (e.g., half) of the peak takes care of variation due to detector response as well as star magnitude.

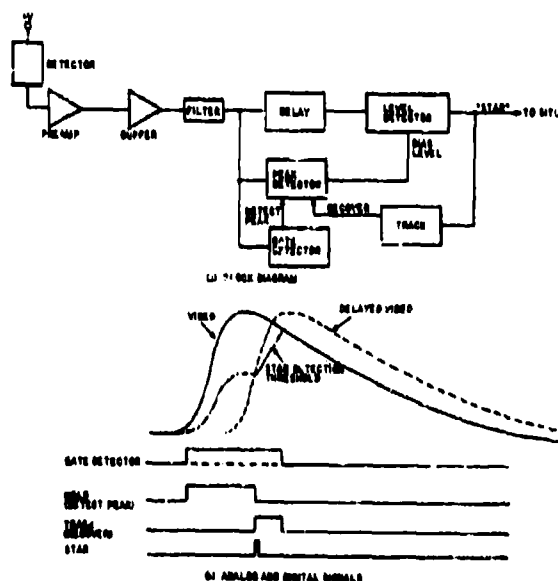


Figure 16. Star Sensor Phase 1B Electronics

Fractional peak or "adaptive" detection is achieved by sending the pulse through two channels; one which delays the pulse, the other which stores the peak of the pulse. A fixed fraction of this peak value is then applied as a bias level to the detection circuit. The delayed pulse, when it reaches the level detector, is thus detected (i.e., causes a logic level output to be sent to the SITU) at a fixed value of its peak.

Pulses which are below a minimum signal-to-noise (S/N) ratio are not processed at all, thereby minimizing false transits from stars dimmer than the limiting detectable magnitude. Pulses which saturate the system also do not cause an output to the SITU because this state is detected and blocks such output as well as discharging capacitors so as to arrive as quickly as possible back in the operating range. Changes in the average detector dark current (due principally to the sun) are eliminated by a baseline follower circuit which allows the average light level to increase by a factor of ten over that normally supplied by the background light in the sensor itself.

4. Alternate Detector Approaches -- Besides the thin-film CdS photodetector discussed above, two alternate solid-state schemes are being investigated for SPARS:

- A thin film, single crystal volume effect CdS
- A photodiode,

The first is being pursued by the Marquardt Corporation, Van Nuys, California, and is shown in Fig. 17. The unique feature here is that the substrate is a single crystal of sapphire and the transparent electrode and CdS layers are epitaxially grown as a single crystal. This should produce inherent uniformity of response along the slit. In addition, since the electrodes are on either side of the CdS, the conduction is through the material rather than across its surface as in the baseline approach currently in use. This should produce more efficient use of incoming light since electrons released by each photon quickly reach the electrodes.

The principal disadvantage lies in the particular geometry employed. The transparent electrode, being on the substrate side of the CdS, forces the light to traverse the substrate. It is currently impractical to make the electrode itself only 0.0003 inch wide; thus, the defining slit must be on the other side of the substrate. This makes the light passing through the slit fan out considerably (about equal to the distance travelled at f/1), thereby applying much lower foot-candle ratings to the detector than would have been the case had the light been focussed directly on the detector. For example, a one foot candle focussed spot fans out through 10 mils of substrate to a spot which is 10 mils in diameter (up by a factor of 80 from 0.0002 inch). The light level at the detector is thus down by a factor of  $(80)^2$  to  $4 \times 10^{-4}$  foot candles.

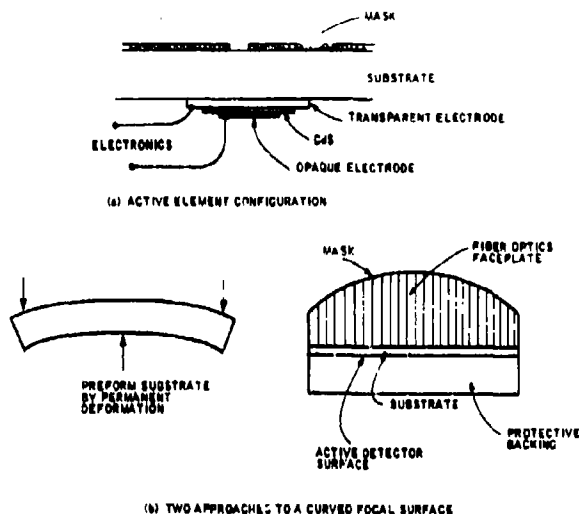


Figure 17. Volume Effect CdS Fabrication

The second alternate approach to a SPARS photodetector-photodiodes is being pursued by Electro Nuclear Labs, Menlo Park, California. The approach used is illustrated in Fig. 18. A flat silicon disk has 0.004 inch wide active regions diffused in the desired radial pattern. Not shown in Fig. 18 is a fiber-optic faceplate flat on one side (which contacts the silicone) and curved on the other side. The defining slit mask is deposited on thin curved face. (This is one of the alternates shown in Fig. 17 b.) Star image light is then conducted by the fibers to the active silicone regions.

Very special photodiode characteristics are required for this application, the most demanding of which is that the NEP in the bandwidth of interest (below seven Hertz) must be in the  $10^{-13}$  to  $10^{-14}$  watt region in order to detect the signal (about  $10^{-12}$  watt) with adequate S/N ratio. Such a low NEP at low frequencies demands that the  $1/f$  noise component have a break frequency below 100 Hertz.

## B. Development of the SPARS Star Sensor

1. Phase 0 -- Star sensor studies at the beginning of Phase 0 were in the categories of system studies, and capability and availability of detectors. In the system study area, questions of slit geometry, number of slits, field of view, and number of sensors were addressed.

On the hardware side, the search for a suitable photodetector rapidly converged on both CdS thin film and photodiodes as the only promising devices.

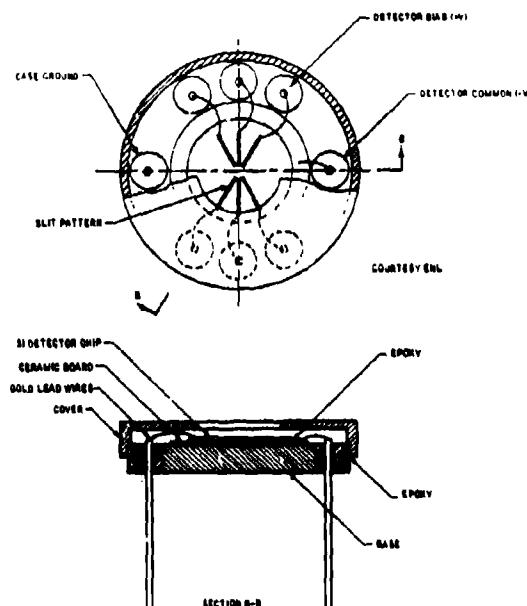


Figure 18. Multi-Element Photodiode

As the program progressed, it became clear that suitable credibility could be established only by showing some experimental results. Acting on this belief, a rather large, 10 degree FOV, concentric optical system was constructed (Fig. 19) and measurements made on both thin-film CdS (produced in CDC's Research Division) and on a Hewlett Packard photodiode with fibre optics leading from the slit to the detector, Fig. 20.

The test results are summarized in Fig. 21. This data was sufficient for the moment to show that a solid-state star sensor was feasible. In addition, arguments could be made that a half-sized sensor would work about equally well - with either CdS or the photodiode. Improvements in each detector were, of course, anticipated.

3. **Phase 1A** -- During the nine months of Phase 1A (June, 1968, to March, 1969), three star sensors were built (two used in the SPARS breadboard at Honeywell and one retained at CDC for detector testing); outside suppliers were introduced for the photodetectors (notably Allen-Bradley); a laboratory test fixture was developed for inside testing; and the peak-storage circuit was developed to circumvent detector response variation. Because all else depended on it, the detector development will first be discussed.

a. **Detector** -- At the very end of Phase 0, it was felt that cadmium selenide (CdSe) should provide a better detector than CdS. This was because of its faster response and broader spectral region. Work thus proceeded in this direction

as Phase 1A opened. Results soon indicated, however, that stability was a very great problem, and it did not appear that the cause of the instability could be isolated without greatly improving laboratory conditions.

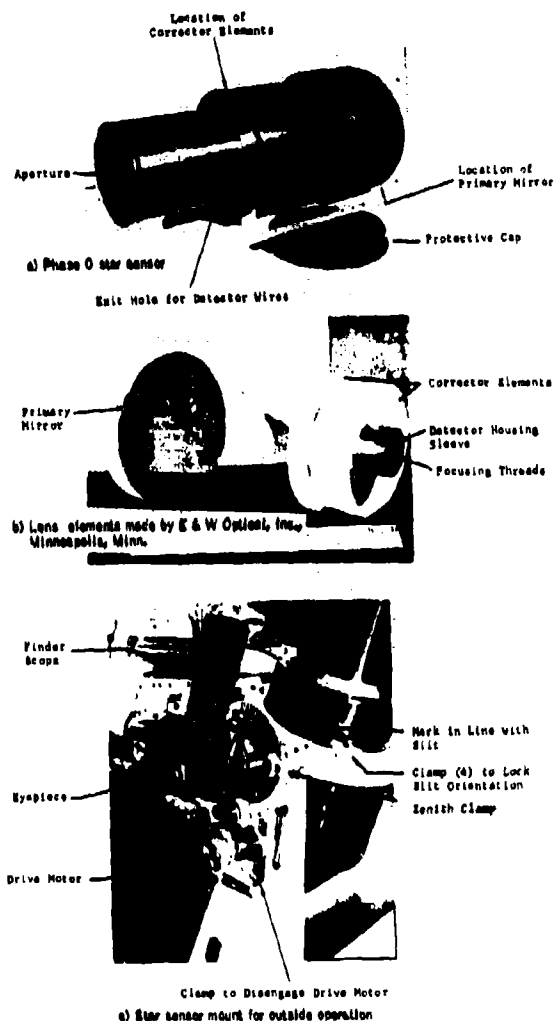


Figure 19. Phase 0 Equipment Photos

In light of this situation, it was decided to attempt to obtain detectors from existing leading detector manufacturers. Numerous suggestions and names were gathered from the AF, LMSC, HI, and CDC detector people, as well as from available literature. Investigations, letters, visits, and the writing of specifications became a major effort during August, 1968. The end result was that Allen-Bradley was selected in

the CdS area and United Detector Technology in the photodiode area.<sup>2</sup>

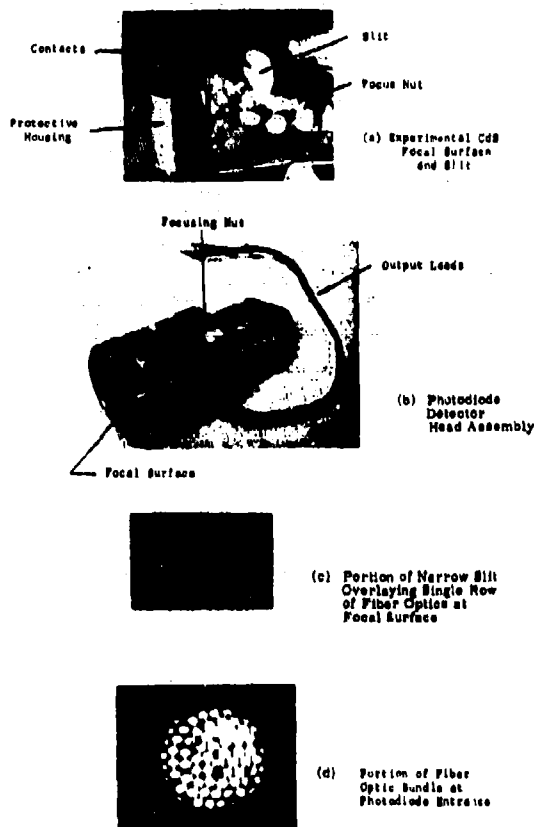


Figure 20. Detector Photos

Altogether, in the remainder of Phase 1A, 32 detectors were received from Allen-Bradley during the course of a development which included doping changes, impedance variations, endless discussions as to how, exactly, the detector was to function, similar discussions as to correspondence between CDCs and A-Bs testing procedures, variations in slit width, variations in response time; and many other menaces which are all part of a rapidly developing sub-technology. One can summarize by saying that

<sup>2</sup>UDT tried to produce narrow photodiodes on a curved substrate. A few were received but were unable to detect the low light levels present in the star sensor. Thus, no further mention is made of this effort.

the original detectors received were responsive even to bright stars over only about five percent of the slit lengths and even this five percent was scattered along the slit. By early 1968, however, advances had been made to where 70 percent of the slit was adequately responding to a fourth magnitude star when operating in a star sensor with a three-inch aperture.

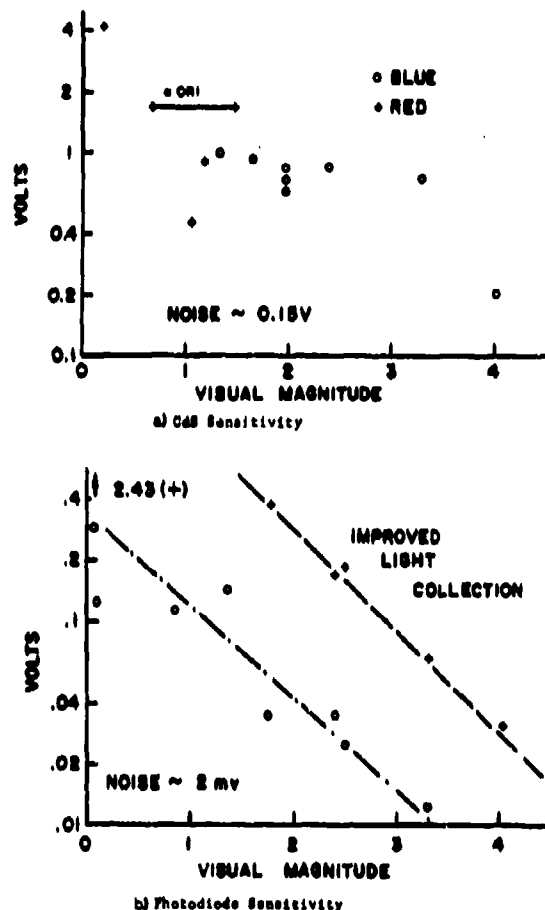


Figure 21. Phase O Results

b. Star Sensors -- Figure 22 shows a photo of the Phase 1A star sensor, three of which were constructed during 1968. These were an approximately half-scale version of the Phase 0 experimental sensor except that enough glass was included for a 3 in. aperture (the design was for 2.25 in.), and the FOV was 4 degrees as finally decided upon from computer simulations at Honeywell and other considerations such as sun shielding. The focal length was 4 inches

making the optics  $f/1.78$  with the aperture stop on and about  $f/1.3$  with it removed.

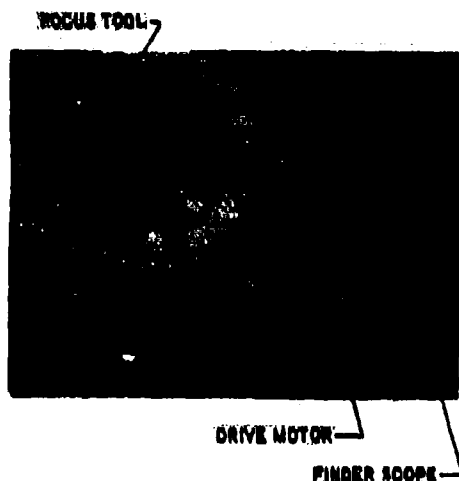


Fig. 22. Phase IA Star Sensor

Each optical system was slightly different, responding to changes that were occurring in the detector. In the early states, when it was believed that CdS would be the ultimate detector, the design wavelength was set near 6200 Angstroms and Schott glasses BaK1 and LF1 were used in the meniscus.<sup>8</sup> This we called Serial No. 1. By the time Serial No. 2 was well along, the switch back to CdS had been made. This was too late to affect the meniscus, but a change in the mirror produced acceptable color response for CdS. Serial No. 3 was then designed for CdS but still used the original glasses. In addition, an aspheric aperture plate design was first attempted with Serial No. 3.

c. Laboratory Test Fixture -- Because outside testing is highly variable at best, one of the principal tasks in Phase IA was to develop a test bed in the laboratory for star sensor exercising and detector evaluation. Figure 23 is a photo of the resulting laboratory test bed developed in Phase IA. As can be seen from the photo, the rear of the star sensor is in the foreground in a yoke which can be tilted by the micrometer head attached to the frame. The device at the far end of the fixture is a star sky simulator. This existing star simulator was modified to produce stars from  $0^m$  to  $6.4^m$  in steps of about  $1.1^m$ .

Just in front of the star sensor is a Herchel wedge assembly. In effect, this moves the stars back and forth across the (vertical) slit detector in the star sensor. The micrometer is used to position the region of transit along the slit. Alternately, the micrometer can be slowly driven

so that each transit occurs at a slightly different position along the slit. (This is how the trace of Fig. 15 b was made.)

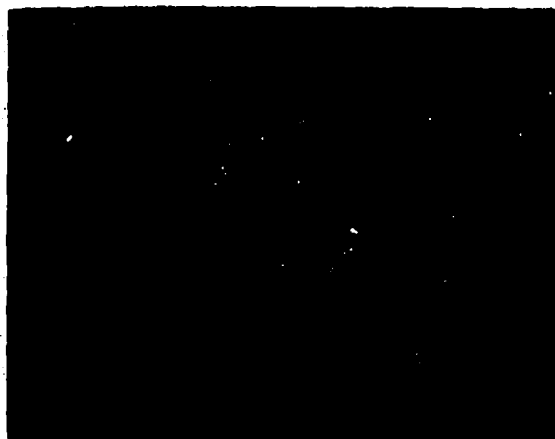


Fig. 23. Star Sensor Test Bed

Besides determining the S/N ratio (in a statistical sense) along the slit, the test fixture can also evaluate accuracy. The angle encoder can be used to indicate wedge position (and thus star angle) at the instant of a "star" output (one-shot) pulse from the electronics. The scatter about of the mean position, the dependence on star magnitude, and the curvative of the slit, can all be measured with this fixture.

d. Development of Adaptive Electronic Detection Scheme -- Towards the end of 1968, two conclusions became evident relative to achieving the desired sensor accuracy:

- (1) The output pulse from CdS was definitely unsymmetric and thus detection on both slopes of the star transit pulse would produce large errors.
- (2) Leading-edge-only detection with a fixed (or even a series of fixed) bias level would also lead to large errors because the time of transit signal rise to any particular absolute value depended upon maximum pulse height.

The sensitivity to pulse height would be a serious enough problem if it were only a function of star intensity. However, it would always be possible to calibrate this and let the computer correct the measured time appropriately. What makes this calibration impossible in practice is the variability of response along the slit, since

<sup>8</sup> The design steps and various rationale are illustrated in Ref. 15 of this conference.

no gradual function of slit uniformity would be applicable. Errors in the many tens of arc seconds were being created.

To overcome this, the peak-storage (or adaptive) scheme shown back in Fig. 16 was developed. The rationale for this came from noticing that the leading edges of all the pulses (regardless of ultimate height) differed only by a scale factor. Thus, if detection were to occur always at a fixed percentage of the pulse peak, then it would also occur when the star image bore a fixed relation to the slit (slightly past it).

Some of the results obtained during the final Phase IA demonstration to the Air Force in February, 1969 are shown in Fig. 24. Each scope trace uses a different star magnitude and is triggered by the angle encoder on the test fixture. Thus, position along the sweep correlates with the image position on the star sensor focal surface. One can see that the 50 percent point on each pulse is within one or two arc seconds of the others.

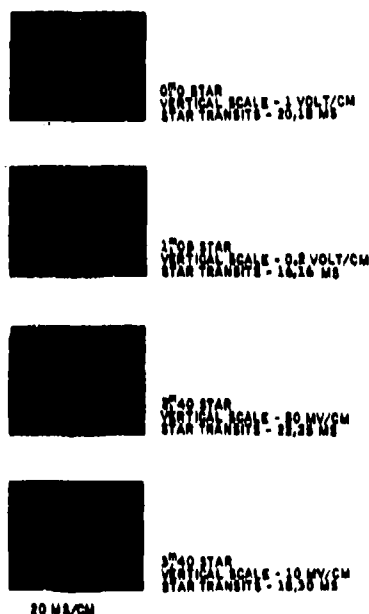


Fig. 24. Phase IA Demonstration of 50% Bias Level

The method chosen to achieve this fixed percentage or adaptive detection is to delay the pulse in one channel while measuring its peak and setting the trigger level in a second channel. The accuracy of this scheme, as demonstrated at the end of Phase IA, is shown in Fig. 25.

• Outside Testing -- At the end of Phase IA (early 1969) extensive testing was conducted against real stars from the roof of Building 1C at the CDC headquarters complex in Minneapolis.

The scope photos in Fig. 26 show some typical results. Besides verifying overall sensor performance against real stars (and through an atmosphere), these tests substantiated the tests performed under more controlled laboratory conditions.

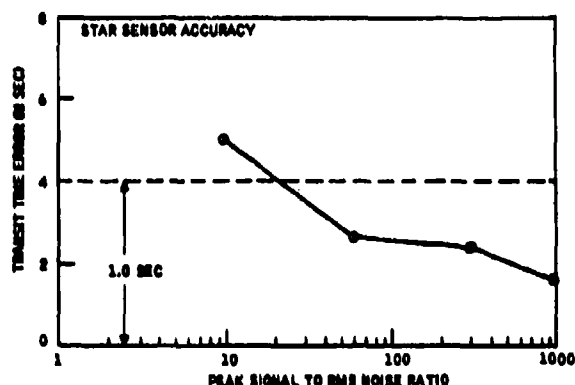


Figure 25. Phase IA Star Sensor Accuracy Demonstration

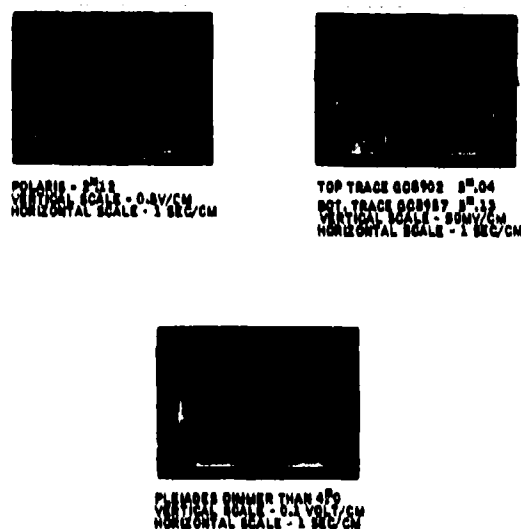


Figure 26. Representative Real Star Transits

Some interesting insight into the thermal stability of the sensor was also obtained by these outside tests. Since focus was established in the lab at room temperature, and temperatures outside to  $-15^{\circ}\text{F}$  did not noticeably affect image quality, it was concluded that the sensor was relatively insensitive to ambient temperature changes.



#### IV. SPARS INTERFACE AND TIMING UNIT (SITU)

The data transfer from the SPARS gyro assembly and star sensors to the computer presents a highly sensitive interface area within the system, because the unique operational characteristics of each one of these system components make them inherently incompatible with each other. The output from the gyro assembly is in the form of three pulse trains in which the repetition rate of the pulses is directly proportional to the sensed rate in each one of the gyros. The star sensors generate event-oriented output pulses, where each pulse signifies a star-image transit across one particular detector. The outputs from the gyro assembly and from the star sensor assemblies are, therefore, asynchronous with respect to each other and to any basic computer clocking cycle and present a severe strain on the capabilities of any input/output unit.

For an operation such as SPARS with its extreme accuracy requirements, it is nearly impossible to transfer the gyro and star sensor data directly into the computer without introducing degeneration of data quality. When in addition it is required to relate these data to laboratory reference points, the SITU becomes a necessity.

The main purpose of the SITU is, thus, to desensitize this critical interface by providing any auxiliary functions that are needed to allow the usage of a general purpose computer (GPC) for the SPARS computations. In this capability the SITU can, therefore, be described as a special extension to the GPC input/output unit. In particular, this must include the establishing of the time-interrelationship of the gyro star sensor and laboratory reference system output data and the conversion of these data into a GPC input/output compatible format. To accomplish this task, the following major functions were incorporated in the SITU:

- The capability to precount both the positive and negative asynchronous rate gyro pulses for each of the three gyro axes over continuously consecutive precise time intervals,
- The capability to register, and resolve with respect to time, the occurrences of star image transits across each individual detector of the two star sensor assemblies,
- The capability to register, and resolve with respect to time the occurrence of a rate table reference marker, for the Phase IA system only.
- The formatting of these data into binary coded data words.
- The temporary storage of these data words to accommodate a smooth computer controlled data transfer into the GPC.

- The capability to communicate with that GPC at a 100 millisecond cycle rate.

The principal functional blocks of the SITU mechanization are shown in Fig. 27. The Phase IA breadboard SITU is shown in Fig. 28.

A high-precision oscillator provides the necessary timing references and is used as the master clock in the system.

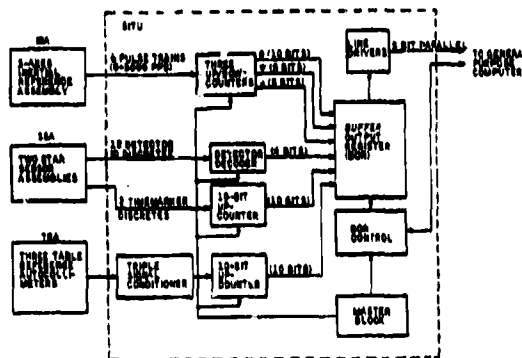


**Figure 27. Functional Block Diagram of Phase 1A SITU**

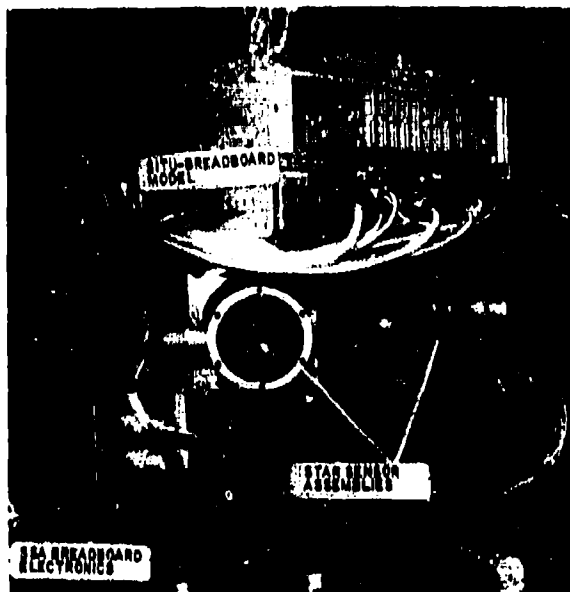


**Fig. 28. Phase IA SITU and SSA**

The asynchronous gyro pulse trains are accumulated in conventional up/down counters over 100 millisecond periods and at the end of each period the contents of these three counters are strobed in parallel into their own specific data word slots of a ten 5-bit word buffer output register (BOR). After the strobing action the counters are reset to zero for the next 100 millisecond cycle. During the interval of shifting gyro counts into the BOR and the counter reset action, all the input circuits to the counters are inhibited from receiving gyro pulses. Any gyro pulses generated during this interval are automatically routed to individual holding registers from where they are strobed into the counters after the inhibit is lifted.

The star transit timer, the associated star detector decoder and the reference marker timer are equipped with similar holding registers at their inputs, so that the complete SPARS system is capable of running independent of computer cycle constraints.

The time referencing of the star transit and rate table position reference markers is accomplished with the use of ripple-up counters where the discrete pulse generated by the sensors at the time of the event is used to gate in a 10 KHz clock for the remainder of the 100 millisecond time interval in which the event occurred. The individual star detector identification pulses are coded in a hexadecimal coder. The contents of these time counters and the detector coder are also strobed into their individual slots in the BOR so that at the end of each 100 millisecond period all the significant information about that period is stored in the correct binary format and word sequence and ready to be input into the computer.

A fixed delay after the BOR is filled, the SITU sends a priority interrupt to the computer to indicate that it is ready to be interrogated. The data shift out operation from that point on is under control of the computer, but must be completed before the end of the next 100-millisecond cycle to prevent loss of valid data.

In the Phase IB SITU the basic functions from the Phase IA unit were preserved, but were modified to present a closer approach to a flight worthy configuration, Fig. 28. The gyro up/down counters were all made to have equal capacity and the star transit time count and detector identification information are no longer formatted as separate words but multiplexed into a single data word. The basic clock frequency is increased from 100 KHz to 2MHz to allow faster strobe and reset operation, and an internal DC to DC power converter was added to allow operation from an unregulated 28 Vdc supply.

For simultaneous operational capability with a flight computer and a GPC, a more complex BOR control and a dual buffered output were added.

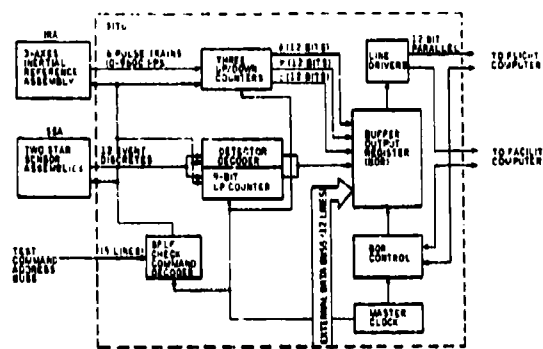


Figure 28. Functional Block Diagram of Phase IB SITU

The BOR format was changed to a five 12-bit word configuration and has a parallel word entry capability to accommodate a shift through capability for facility information and data from other flight systems to the computer complex via one common output bus.

A step-by-step, remotely addressable, self-check system was incorporated for pre-system run verification purposes and failure isolation in case of a system breakdown. This self-check system can be automatically activated by the facility computer or manually by the operator at the control station.

#### APPENDIX A DERIVATION OF IRA MISALIGNMENT EQUATION AND ERROR ANALYSIS

The actual input rate along the IA of one of the gyros being aligned is given by

$$W_{IA} = (W_T + W_E \sin L) \sin \epsilon + W_E \cos L \cos \epsilon \cos \theta \quad (A1)$$

where:

$W_{IA}$  is the gyro input axis rate

$W_T$  is the turntable rate

$W_E$  is earth's rate

$L$  is the latitude of the test site

$\epsilon$  is the error angle between the gyro IA and the table spin axis, and

$\theta$  is the angle between the gyro IA and north

This equation assumes that the table spin axis is aligned with the local vertical, or that  $L$  is the angle between the table spin axis and the earth's spin axis. Rotation of the table through 360 degrees at a constant rate is presented by the following integration of Eq. (A1):

$$\int_0^{2\pi} W_{IA} d\theta = \int_0^{2\pi} \left[ (W_T + W_E \sin L) \sin \epsilon + W_E \cos L \cos \epsilon \cos \theta \right] d\theta \quad (A2)$$

$$W_T \int_0^T W_{IA} d\theta \frac{dt}{d\theta} = 2\pi (W_T + W_E \sin L) \sin \epsilon \quad (A3)$$

where  $W_T = d\theta/dt$ , and  $T$  is the time for one

revolution,  $T = 2\pi/W_T$ . The integral  $\int_0^T W_{IA} dt$

is by definition the angular equivalent of the accumulated pulses from the gyro being measured.

This equivalent gyro input angle will be denoted by  $P_{WN}$ , where  $P_W$  is the gyro pulse weight in radians per pulse, and  $N$  is the accumulated pulse count. Solving for the misalignment, we have

$$\sin \epsilon = \frac{P_{WN}}{2\pi \left( 1 + \frac{W_E}{W_T} \sin L \right)} \quad (A4)$$

For misalignment angles of a degree or less, the small-angle approximation

$$\epsilon = \frac{P_{WN}}{2\pi \left( 1 + \frac{W_E}{W_T} \sin L \right)} \quad (A5)$$

can be used, where the approximation error is less than 0.2 arc second.

#### Alignment Errors

A number of uncertainties will result in the data obtained from the above alignment procedure. These are listed in Table A1. The total uncertainty is well within the SPARS requirement.

Table A-1. Summary of Uncertainties in IRA Input Axis Calibration

Error Source	Maximum Error, Normalized*	
	Per C	Per Axis
Gyro Pulse Weight Uncertainty	0.120	0.167
Gyro Drift	0.013	0.020
IRA Pulse Count Quantization	0.002	0.003
Table Encoder Quantization	0.007	0.013
Table Bearing Wobble	0.333	0.467
Table Speed Variations	0.007	0.013
Mirror to Spin Axis Measurement	0.200	0.200
Small Angle Approximations	0.067	0.093
Total one- $\sigma$ Measurement Uncertainty		0.533

\*Normalized to SPARS gyro input axis calibration accuracy requirement.

#### APPENDIX B SPARS INERTIAL REFERENCE ASSEMBLY RANDOM DRIFT TESTS

Gyros of the floated, air bearing, pulse rebalanced rate integrating type with extremely low, stable drift rates are the candidates for the SPARS attitude reference system. The Honeywell GG334A is this type of gyro. One of the major problems in determining system attitude accuracy is the accurate modeling of floated, pulse-rebalanced gyro drift characteristics. Constant gyro drift is unimportant in this application because it gets calibrated out completely in the SPARS recursive filtering equations. High-frequency gyro drift, on the other hand, has such a low amplitude that it does not integrate to an appreciable angle. The drift that affects system accuracy the most is in the 0.0001 to 0.1 Hz range. Accurate power spectral density information on gyro drift in this region is somewhat difficult to isolate and obtain. Long sampling times and a significant amount of data are involved. This appendix describes the results of GG334A gyro drift testing, statistical analysis, and modeling.

Two primary methods were used by Honeywell to gather gyro drift data during the SPARS GG334A drift testing program. The first method is to feed the gyro d-c rate output to precision voltage-to-frequency converters. This rate proportional a-c signal is then integrated with resettable up-down counters. The counters can be sampled and reset to zero at any frequency of interest, and the sampled counts are then punched on paper tape or sent directly to

the SDS 9300 computer, with six-decimal digit accuracy. This method is used to investigate the drift spectral characteristics out to half the sampling frequency, using the approximation that the rate error is constant over any one sample period. This test setup proved to be extremely accurate, but unfortunately has the characteristic of exhibiting frequency folding effects in the sampled data; i. e., drift at frequencies greater than the sampling frequency appears in the lower frequency part of the sampled spectrum.

To eliminate any frequency folding effects, a second method of gathering data was employed. Here, the rate output is amplified with a high-gain, low-noise buffer amplifier right at the test setup to minimize noise pickup and transmission losses. The amplified signal is then fed to a low-pass, seventh-order filter whose cutoff frequency can be varied between 2.0 and 25 Hz. The voltage output from the filter can be read with an RMS reading meter, for comparison with the standard deviation of the rate output computed in the computer facility from the time history. This amplified and filtered signal is then routed to the A/D converters in the hybrid computer facility via coaxial cable. The sample and hold amplifiers are interrogated and reset by the computer at any frequency of interest. The filter cutoff frequency in the gyro lab is always adjusted so that it is half the sampling frequency, to eliminate "folding" completely. This gives a true picture of the drift power out to half the sampling frequency. The signal flow through this test setup is shown in Fig. B1.

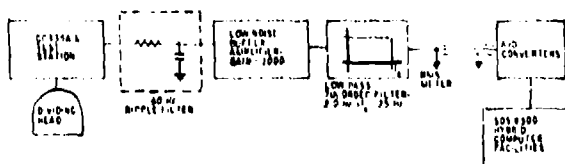


Figure B1. Gyro Drift Test Configuration

Once the gyro drift sample time history has been obtained, the autocorrelation function and the power spectral density (PSD) are computed. The mean is given by:

$$\bar{x} = \frac{1}{N} \sum_{j=1}^N x_j \quad (B1)$$

where  $N = 5000$ .

Once the mean has been computed, a new sequence of sample values is defined

$$y_j = x_j - \bar{x} \quad (B2)$$

Next, the intensity of  $x$  is computed

$$E[(y - \bar{x})^2] = E(x^2) = \frac{1}{N} \sum_{j=1}^N (y_j - \bar{x})^2 \quad (B3)$$

This intensity is, of course, a measure of the total average power.

The autocorrelation function of the  $y$  process is estimated by

$$R(\tau) = \frac{1}{N-k} \sum_{j=1}^{N-k} y_j y_{j+k} \quad (B4)$$

where  $k = 0, 1, 2, \dots, m$ ;  $\tau = kT$ ; and  $T$  is the sample period. Here,  $m$  is the specified number of lags (maximum allowed is 2000).

The variance of  $x$ , a measure of the average power associated with the a-c component, is given by  $R(0)$  since

$$R(0) = E(y^2) = E[(x - \bar{x})^2] \quad (B5)$$

An estimate of the power spectrum, sometimes referred to as the power spectral density, is obtained from the Fourier spectrum of this truncated autocorrelation function. Since  $R(\tau)$  is an even function,

$$S_e(f) = \int_{-\infty}^{\infty} R(\tau) e^{-2\pi i f \tau} d\tau = 2 \int_0^{\infty} R(\tau) \cos(2\pi f \tau) d\tau \quad (B6)$$

computed at intervals of  $f_s/2m$  over the range  $0 \leq f \leq f_s/2$ , where  $f_s$  is the sampling frequency.

A weighted average of adjacent values of  $S_e(f)$  is obtained corresponding to a convolution with a spectral window; in particular, the Hamming window.

$$S\left[\frac{nf_s}{2m}\right] = 0.23 S_e\left[\frac{(n-1)f_s}{2m}\right] + 0.54 S_e\left[\frac{nf_s}{2m}\right] + 0.23 S_e\left[\frac{(n+1)f_s}{2m}\right] \quad (B7)$$

for  $n = 1, 2, \dots, m-1$ , and

$$S(0) = 0.48 S_e\left[\frac{f_s}{2m}\right] + 0.54 S_e(0) S\left[\frac{f_s}{2}\right] = 0.48 S_e\left[\frac{(m-1)f_s}{2m}\right] + 0.54 S_e\left[\frac{f_s}{2}\right] \quad (B8)$$

The resolution is actually  $f/m$  even though the spectrum is computed every  $f/2m$  cps. Finally, the area under the curve  $S(f)$  is computed,  $0 \leq f \leq f/2$ , and multiplied by a factor of 2 to obtain a comparison between  $R(O)$  as computed earlier, and as computed from the power spectrum estimated.

An alternate method of calculating the PSD is also available, and gives results which agree very well with the lagged products approach outlined above. This computation involves evaluating the coefficients of the complex Fourier series of a periodic process,  $y(t)$ , which is identical to the process  $x(t)$  over some finite interval,  $0 \leq t \leq T_0$ . These coefficients have the form

$$C_k = \frac{1}{NT} \sum_{n=0}^{N-1} x(nT) e^{-j2\pi kn \frac{T}{NT}} \cdot T,$$

$$k = 0, 1, 2, \dots, N-1 \quad (B9)$$

A computational algorithm due to Cooley and Tukey<sup>4</sup> called the Fast Fourier Transform was used, which reduces the computational requirements for evaluating these Fourier coefficients enormously.

A number of samples were taken for different gyro loop bandwidths, since the sensitivity of low-frequency gyro drift to loop bandwidth might have an important bearing on this design parameter. Drift data was taken at 20 ms and 0.25 sec, yielding spectral and statistical data out to 25 and 2.0 Hz, respectively. Fig. B2

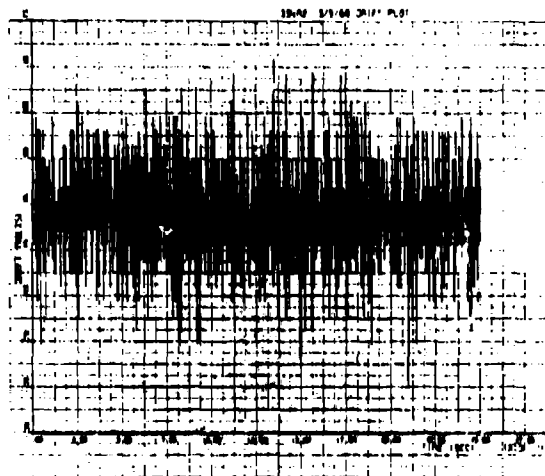


Figure B2. Gyro Drift Below 2 Hz - 0.1 Hz Loop Bandwidth

shows a typical set of data that was taken: 250 seconds (out of 1250) sampled at 0.25 sec with a 0.1 Hz loop bandwidth. The scale factor for these tests was 2.7 volts/deg/hr.

The statistical and spectral results are shown for a 0.1 Hz loop bandwidth gyro in Figs. B3 to B5. Fig. B3 shows that the drift autocorrelation time constant is well below 0.1 seconds. The power spectral density peaks in the 7 Hz range. The probability density functions (actually histograms) for the 20 ms and 0.25 sec sampling rates are also shown in Fig. B3. The numerical values of the standard deviations for all this data are given in Table B1.

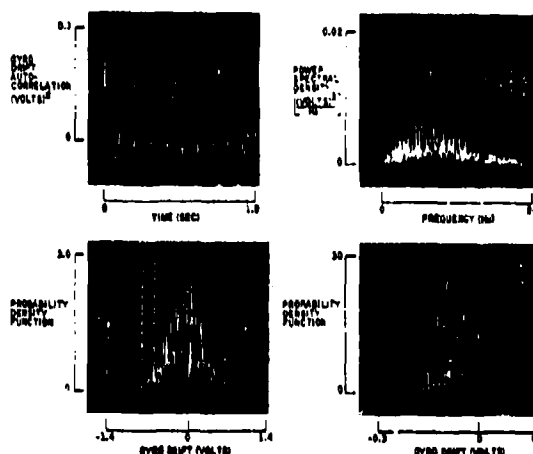


Figure B3. Autocorrelation Function, PSD, and Statistics - 0.1 Hz Loop Bandwidth

Table B1. Gyro Drift Test Summary

Drift	Gyro No.	Run Duration (sec)	Sampling Interval (sec)	Loop Bandwidth (Hz)	1-σ Drift Below 1 Hz	1-σ Drift Below 0.1 Hz
0-1-67	A	4000	10.0	0.1	0.005	-
0-2-67	A	1070	1.0	0.1	1.315	-
10-25-67	B	6670	1.4	0.1	0.021	-
10-25-67	C2	6660	1.4	0.1	0.045	-
0-1-68	-	6660	1.4	0.1	1.31	-
0-0-68	C4	17000	0.5	0.1	0.700	-
0-0-68	C6	Splinterer CS	1.07	-	0.000	-
0-0-68	C4	Loop Open (Servo Shorted)	1.07	-	0.00	-
0-0-68	2000	100	20 ms	0.1	1.10	0.003
0-0-68	2000	1000	0.15	0.1	2.15	0.003
0-0-68	2000	100	20 ms	1.0	10.4	0.070
0-0-68	2000	1000	0.25	1.0	5.00	0.070
0-0-68	2000	100	20 ms	10.0	63.7	0.011
0-0-68	2000	1000	0.25	10.0	3.41	0.011

<sup>a</sup>Normalized to SPARS 0 - 0.5 Hz random drift requirement

<sup>4</sup>IEEE Transactions on Audio and Electroacoustics, Vol. AU-15, No. 2, (June 1967).

The upper left photograph in Fig. B4 shows in more detail the spectrum out to 2.0 Hz, which was obtained with the slower 0.25 sec sampling and a 2.0 Hz filter cutoff frequency. To demonstrate that no folding from higher frequencies is present in this data, the spectrum derived from the higher sampling rate of 20 ms is overlaid as a series of dots on this picture, showing very close correlation. The envelope of the Fourier line spectrum, obtained with the Fast Fourier Transform, exhibits a shape nearly identical to the PSD. The photograph on the right shows an expanded picture of the PSD out to 0.1 Hz. This data is quite flat and well-behaved, devoid of spikes or discontinuities.

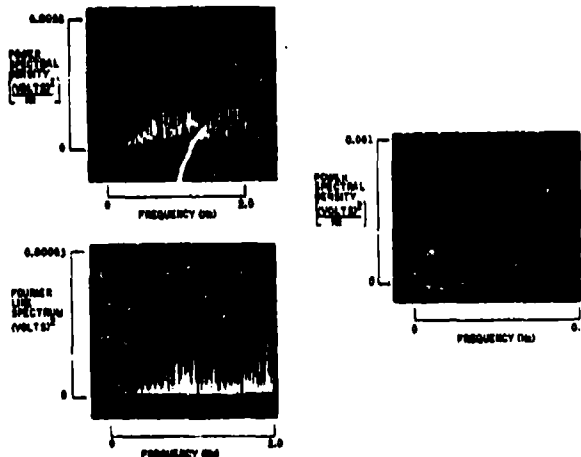


Figure B4. PSD Detail - 0.1 Hz Loop Bandwidth

The net result of all this is the plot of gyro drift power (the integral of the PSD) versus frequency. This data for the 0.1 Hz loop bandwidth gyro is shown in Fig. B5. The complete picture out to 25 Hz is shown on the left. The discontinuity at 19.1 Hz is due to a large spike in the PSD due to the natural resonance and motion of the test pad at this frequency. That part of the integral, therefore, is not attributable to gyro drift but to actual measured angular motion at that frequency. The flattening of the integral at 25 Hz indicates that nearly all of the drift power is included below this frequency.

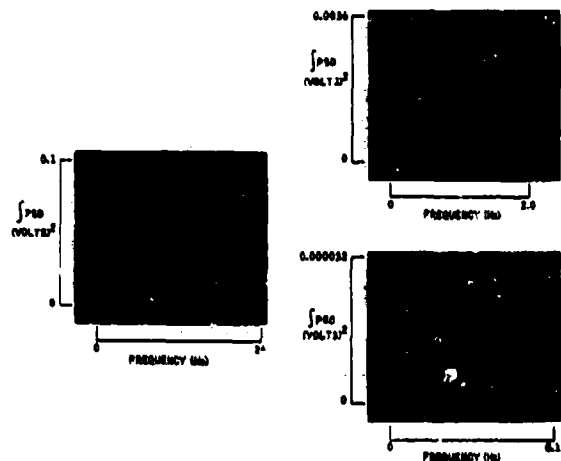


Figure Bb. Gyro Drift Power - 0.1 Hz Loop Bandwidth

An expansion of the data in the 0 to 2 Hz range is shown with the 0.25 sec sampled data, and the 25 Hz data is overlaid as a dotted line, again showing excellent correlation and a lack of frequency folding. A further expansion in the 0 to 0.1 Hz range is also shown.

Figures D6 through B11 show corresponding sets of data for 1.0 and 10.0 Hz loop bandwidth, respectively. The main change in the data is that the drift standard deviation grows larger with increasing loop bandwidth as the power spectral density grows in the 1-25 Hz range. The question of importance, though, is how loop bandwidth affects gyro drift performance in the low frequency region. The upper photograph in Fig. B12 shows, from top to bottom, the power out to 2 Hz for 10, 1, and 0.1 Hz loop bandwidth gyro loops, respectively. There is considerable difference at 2 Hz, but the lower picture shows that in the region 0 to 0.5 Hz, the PSD integrals are practically coincident. Therefore, the conclusion has been reached that the loop bandwidth can be selected using criteria other than system performance.

It is also apparent from Fig. B12 that the PSD integral is very linear out to 0.25 Hz, which means that the PSD is essentially flat, or "white" out to this frequency. Based on these results, it appears that the most realistic mathematical representation for floated gyros of the GG334A class in the low frequency range is a random process whose variance is matched to the actual gyro drift variance at the sample frequency. This is a result that has far-reaching implications in the design of bounded (e.g., celestial/inertial) attitude reference systems. In unbounded, strapped-down attitude reference systems, the critical gyro parameter is the

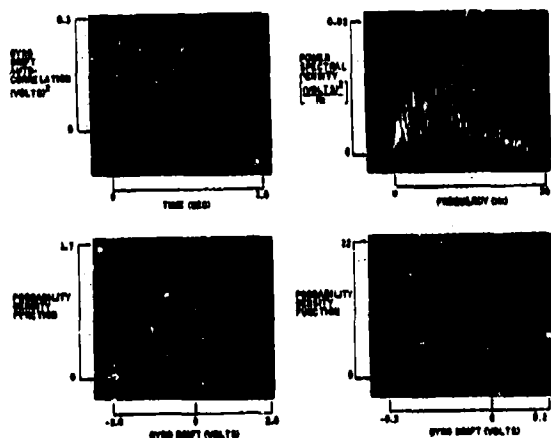


Figure B6. Autocorrelation Function, PSD, and Statistics - 1.0 Hz Loop Bandwidth

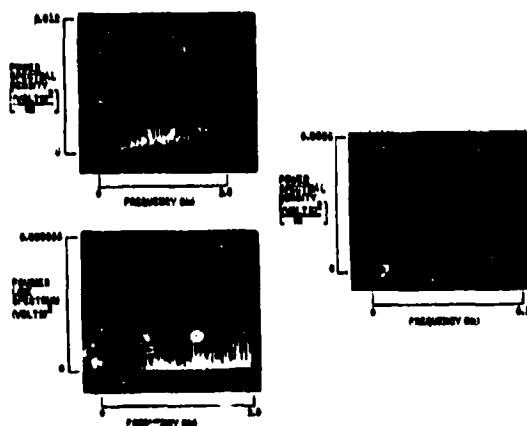


Figure B7. PSD Detail - 1.0 Hz Loop Bandwidth

absolute, long-term drift rate stability, since there is no capability for calibration while operating. This long-term stability may very well look like a random walk or damped random walk process.

In the design of bounded systems, this very long-term stability assumes secondary importance and the critical item becomes the shorter-term drift. However, it takes more than a specification of the amplitude of the short-term drift to determine the effect on system performance (angular errors versus time). Of equal importance are the spectral characteristics of

this short-term drift. Table B1 summarizes the gyro drift test program that was conducted in support of the Phase 0 SPARS program. The last six items in this table summarize the tests covered by Figs. B2 through B12.

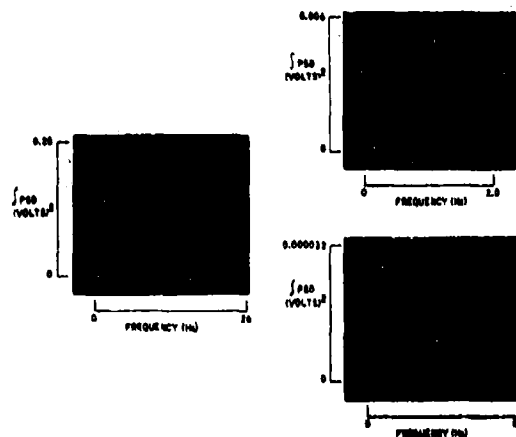


Figure B8. Gyro Drift Power - 1.0 Hz Loop Bandwidth

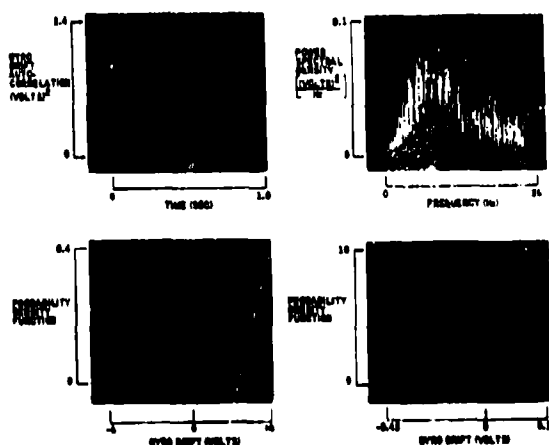


Figure B9. Autocorrelation Function, PSD, and Statistics - 10 Hz Loop Bandwidth

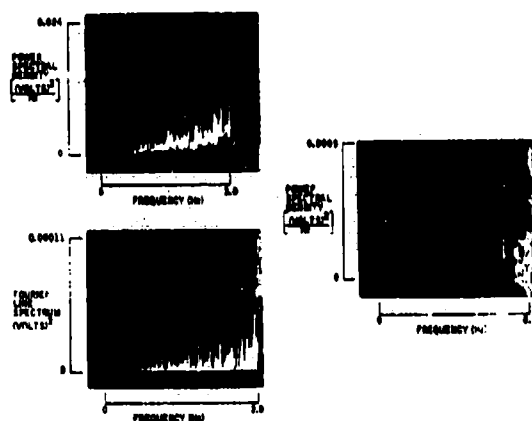


Figure B10. PSD Detail - 10 Hz Loop Bandwidth

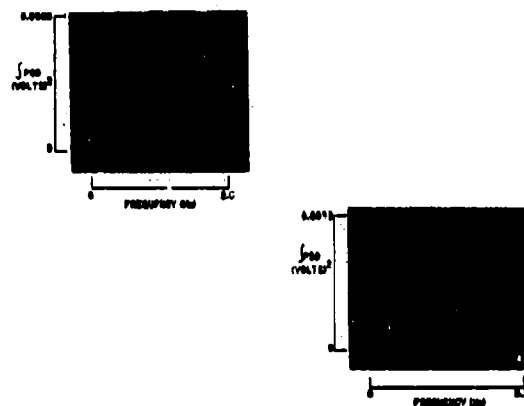


Figure B12. Comparison of Gyro Drift Power at Different Loop Bandwidths

#### REFERENCES

1. W.R. Davis and J.A. Miller, "SPARS - A Completely Strapdown Concept for Precise Determination of Satellite Vehicle Attitude," presented to the Spacecraft Attitude Determination Symposium, The Aerospace Corporation, September 30 to October 2, 1969.
2. D.C. Paulson, D.B. Jackson, and C.D. Brown, "SPARS Algorithms and Simulation Results," presented to the Symposium on Spacecraft Attitude Determination co-sponsored by AFSC, SAMSO, and The Aerospace Corp., El Segundo, California, September 30, October 1-2, 1969.
3. V. Hvoschinsky and F. Horiuchi, "Concepts and Mechanization for Evaluating PEPSY in the Laboratory and in Orbit," presented to the Spacecraft Attitude Determination Symposium, The Aerospace Corporation, September 30 to October 2, 1969.
4. R.O. Maze et al., (U) Study and Development of Pulse Torquing for Inertial Gyroscopes (CONFIDENTIAL) - A Technical Proposal, Minneapolis Honeywell Aero Document R-ED 6020, 28 January 1957.
5. J.E. Anderson et al., (U) The Gimballess Analytic Inertial Navigation System (GAINS) (CONFIDENTIAL), Minneapolis Honeywell Aero Document R-ED-6029, August 1, 1957.
6. J.W. Minor, Low Cost Strapdown Inertial Systems, presented to AIAA/ION Guidance and Control Conference, Minneapolis, Minnesota, August 16-18, 1965.

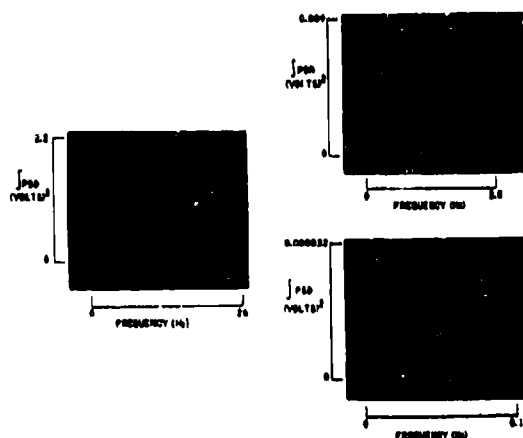


Figure B11. Gyro Drift Power - 10 Hz Loop Bandwidth



7. Inertial Reference Assembly (Honeywell Part No. GG 2200 AC), Utility Technical Manual, Honeywell Document 20973-UTM2, prepared under contract F04701-68-C-0061, 1 August 1969.
8. R.L. Lillestrand and J.E. Carroll, "Self Contained System for Interplanetary Navigation," American Astronautical Society, San Francisco, August 1961.
9. R.L. Lillestrand, et al., "Celestial Successor to Inertial Guidance," Electronics, March 21, 1966. Also, "Automatic Celestial Guidance, Part 2: New Challenge to Designers' Ingenuity," Electronics, April 9, 1966.
10. A. LaBonne, et al., "The SCNS Attitude Determination Experiment on ATS-III," presented at the Spacecraft Attitude Determination Symposium, The Aerospace Corporation, El Segundo, September 30, October 1-2, 1969.
11. J.E. Carroll, "An Automatic Instrument for the Determination of Astronomic Position," Surveying and Mapping, to be published.
12. (U) Space Precision Attitude Reference System, Vol. I Technical Proposal, (CONFIDENTIAL), LMSC 699615, 15 May 1967.
13. A. Bouwers, Achievements in Optics, Elsevier, 1950.
14. D.D. Maksutov, "New Catadioptric Meniscus System," J. Opt. Soc. Amer., Vol. 34, No. 5, p. 270, May 1944.
15. J.E. Carroll, "Sub-Arc Second Star Sensors, Design and Fabrication," presented at the Spacecraft Attitude Determination Symposium, The Aerospace Corporation, El Segundo, September 30, October 1-2, 1969.
16. Richard H. Bube, Photoconductivity of Solids, John Wiley & Sons, Inc., New York, 1960.
17. K.W. Boer, et al., "Properties of Recrystallized Evaporated CdS Layers," Solid State Physics, Vol. 16, p. 697, 1966.
18. Physics and Chemistry of II-VI Compounds, edited by M. Aven and J.S. Prener, North-Holland Publishing Company, Amsterdam, 1967, especially Chapter 13 and 14.

## CONCEPTS AND MECHANIZATION FOR EVALUATING SPARS IN THE LABORATORY AND IN ORBIT<sup>1</sup>

Vladimir Hvoschinsky and Fred Y. Horiuchi  
Lockheed Missiles & Space Company  
Sunnyvale, California

### ABSTRACT

This paper describes the concepts and mechanization for evaluating the Space Precision Attitude Reference System (SPARS) as part of a Precision Earth Pointing System (PEPSY). Pertinent information is included concerning test installations, critical specifications, and error budget. These concepts have been developed by Lockheed and Honeywell under Air Force sponsorship over the last 2-1/3 years in an effort to improve the techniques of attitude determination and precision pointing from the spacecraft to a terrestrial target. The PEPSY hardware system presently is being designed and built. Within the next year, complete end-to-end PEPSY performance will be evaluated in test laboratories at Lockheed and at Holloman Air Force Base.

The orbital experiment with the PEPSY, known as PEPEX, is proposed as a followup phase of the present hardware development and evaluation program. The proposed concepts and mechanization for performing such an experiment are presented.

### INTRODUCTION

The intent of this paper is to present highlights of concepts and ideas for evaluating an extremely accurate precision earth pointing system (PEPSY) in a laboratory environment and in an operational satellite environment. The authors would like to share with the readers basic difficulties and possible solutions to the problems generated by such a task. It is desired to present philosophically practical concepts exposing mostly the "happenings," and de-emphasizing mathematical proofs and specialized statistical computations. Such an approach is appropriate since during this session several papers will be presented dealing with specifics of algorithms, design, and testing for different PEPSY subsystems and outlining the basic system concept and mission applications. (See Refs. 1, 2, 3, 4)

In order to familiarize the reader with this system, and to help him with the acronyms a synopsis of PEPSY is presented in the first section. Following the synopsis, the next three sections will treat the evolution of the basic test concepts, the mechanization of the laboratory test, and the proposed approach to the orbital experiment.

### EVOLUTION OF PEPSY

Recognition of potential operational use for the extremely accurate attitude knowledge supplied by SPARS was sufficient to motivate developing that technology. However, it was soon clear that to gain acceptance for operational deployment of such a system it would be necessary to prove its performance in a near-operational situation. The realization that the only way one could accomplish an in-orbit check on the accuracy of satellite attitude determination suggested making SPARS an element of a precision pointing system (PEPSY). This in effect closed the loop by using the attitude knowledge of SPARS in such a way that any deficiency would be reflected as a (major) deficiency in system performance. Since one of the major operational uses proposed for SPARS was as a component of a precision pointing system, it was, therefore, appropriate to synthesize a precision pointing experiment to test SPARS. As this concept evolved, it became evident that the mechanization of a precision pointing experiment, particularly at an earth target, was a worthwhile objective in its own right. Thus, in spite of the fact that an experiment to point at stars for attitude information only could have fewer error sources and thus allow potentially narrower bounds on

<sup>1</sup>This report was prepared under Air Force Contract F04701-69-C-0150 on 20 September 1969.

establishing SPARS performance, the more complex concept of pointing at an earth target was retained as the primary PEPSY test objective.

Ideally, one would specify that the test equipment (the pointing device) have an accuracy an order of magnitude better than the item to be evaluated (SPARS). It seemed unlikely that this could be achieved at a reasonable cost in this case. Thus, for the purpose of evaluating SPARS, the PEPSY experiment as conceived presents the problem of separating the errors due to SPARS from those due to the pointing device and the rest of PEPSY.

Thus concepts for PEPSY testing with the objective of SPARS evaluation had an impact on the synthesis of PEPSY itself. The result is the system described in the following sections.

### ELEMENTS OF PEPSY

The Precision Earth-Pointing System shown conceptually in Fig. 1 consists of a combination of four major subsystems described briefly below.

#### SPARS

The Space Precision Attitude Reference System consists of three orthogonally placed rate integrating gyros and two star sensors mounted together in a strap-down configuration. The gyro package provides continuous three-axis wide-band attitude information, while time transits of known stars on the star sensors provide a precise attitude up-date at discrete times. This subsystem, together with a computer, provides extremely accurate real time satellite attitude knowledge in an inertial reference frame.

#### OPD

The Optical Pointing Device consists of two main elements. One is a telescope-sensor and the other is a two-axis gimbal assembly. Two 720-pole 7-in. read-in Inductosyns mounted on the pitch and roll gimbals and used in conjunction with a high-gain closed-loop servo point the telescope along a commanded line of sight. Telescope aiming is based upon information received from SPARS, OAL, and the ephemerides of the ground target and spacecraft. Any misalignment between the satellite-target line of sight (LOS) and the OPD LOS is sensed by the telescope-sensor. The OPD is capable of being commanded in both open-loop and closed-loop modes.

#### OAL

The Optical Alignment Link consists of optical transmitter and receiver assemblies which dynamically monitor relative angular displacements between the SPARS and OPD packages. Displacements detected by OAL are fed to the computer for the generation of pointing commands to the OPD.

#### Airborne Computer

The UNIVAC 1824C selected for the airborne computer is a high-performance, general-purpose, binary machine which can store up to 12,288 18-bit instruction words in its nondestructive readout memory

and operates upon data contained in 512 24-bit words of destructive readout memory. Prime functions of the computer in the PEPSY application are:

- Perform attitude state computations (SPARS)
- Generate pointing commands for OPD
- Store star catalog, calibration data, constants, and initial conditions.

In support of the above, a space-ground telemetry link sends information to, and receives information from, the on-board computer and/or sensors. This information includes orbital parameters established by ground tracking and errors in pointing commands.

### THE LABORATORY TEST CONCEPT

In its entirety, the PEPSY system advances the state-of-the-art in these fields:

- Accurate determination of satellite attitude in real time or post flight (SPARS)
- On-orbit accurate evaluation and calibration of SPARS
- Accurate LOS pointing and knowledge in pointing of a sensor from a vehicle to a ground target in open or closed-loop modes (OPD)
- Ephemeris updating techniques (OPD)
- Extremely accurate, dynamic, three-axis angular alignment measuring device (OAL)

The concept is good, but how can its performance be established? What accuracies are to be expected and allocated to individual subsystems? How should the test of such a system be mechanized and what is the error budget?

Clearly, accuracy is the name of the game. The accuracy requirements of the SPARS subsystem dictate the performance accuracy of the other subsystems which are to be used for its evaluation as well as the maximum permissible error contribution of the test installation and instrumentation. To gain insight into the feasibility of synthesizing a practical PEPSY, relative error budgets were generated. These were based on a trade-off between desired performance for SPARS evaluation and the difficulty (cost) of the achieving a precision OPD. Two configurations, remote and integral (corresponding to the relative mounting locations of the OPD and SPARS) were considered. The budgets for these configurations are shown in Figs. 2 and 3.

The economics and step-by-step process for developing a sophisticated system such as PEPSY call for laboratory testing to precede in-orbit tests. Indeed, successful laboratory validation is undoubtedly a necessary prerequisite to justifying an orbital test. Although in-orbit tests are usually more difficult than corresponding laboratory tests, for PEPSY the in-orbit environment has at least one advantage not available in the laboratory, but important to precision evaluation, and that is the accurately known absolute reference frame created by the fixed stars. This brings up the

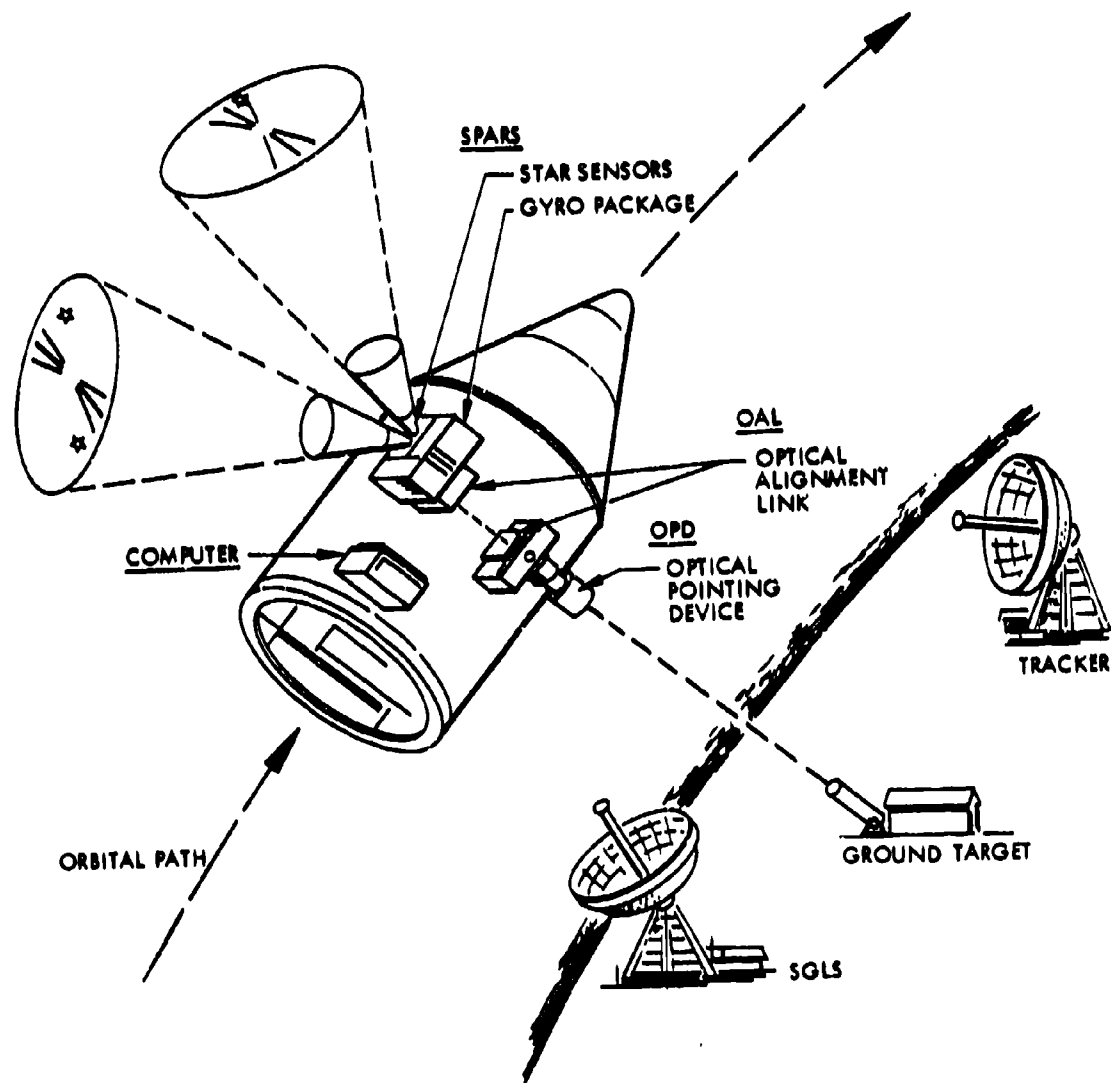


Fig. 1 Precision Earth Pointing Concept

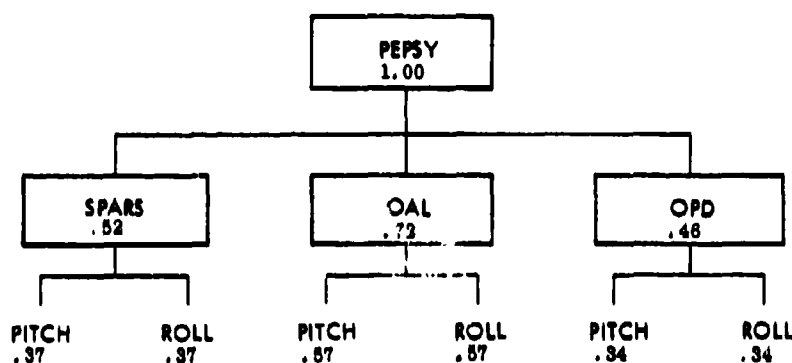


Fig. 2 Fractional Error for Main Subsystems of PEPsy in Remote Configuration

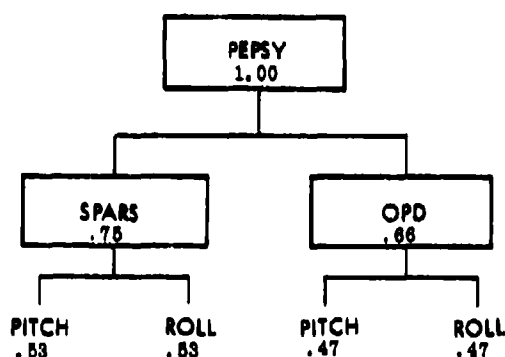


Fig. 3 Fractional Error for Main Subsystems in Integral Configuration

question of the approach to be taken in the laboratory. Should one simulate whatever takes place in orbit and thus compound the errors, or should one simplify the laboratory mechanization in order to decrease the error sources at the expense of the faithfulness of simulation?

The latter approach has been selected. Only essential dynamic and geometrical conditions will be simulated in order to establish as accurately as possible the hardware performance in the laboratory.

Figure 1 shows a satellite moving around the earth and rotating (pitching) to maintain a nominally constant attitude relative to the local vertical. In this attitude, the OPD is pointed toward the ground target and maintains the required LOS during the experiment pass. The target with known earth coordinates is pointing at the known satellite position and continues to point at it throughout the pass. The OPD is commanded to point at the target on the basis of satellite attitude determined by SPARS, satellite ephemeris computed in the computer, ground target coordinates, and OAL corrections.

To show the correspondence between the laboratory and orbital test geometry, Fig. 4, along with the pointing Eqs. (1) and (2), are presented.

Line of sight vector to ground target in OPD frame

$$\mathbf{L}^O = \mathbf{T}_{S20} \mathbf{T}_{I2S} \mathbf{L}^I \quad (1)$$

Line of sight vector to ground target in inertial frame

$$\mathbf{L}^I = \mathbf{T}_{E2I} \mathbf{R}_T^E - \mathbf{R}_S^I \quad (2)$$

where:

$\mathbf{R}_S^I$  = satellite ephemeris in the initial frame

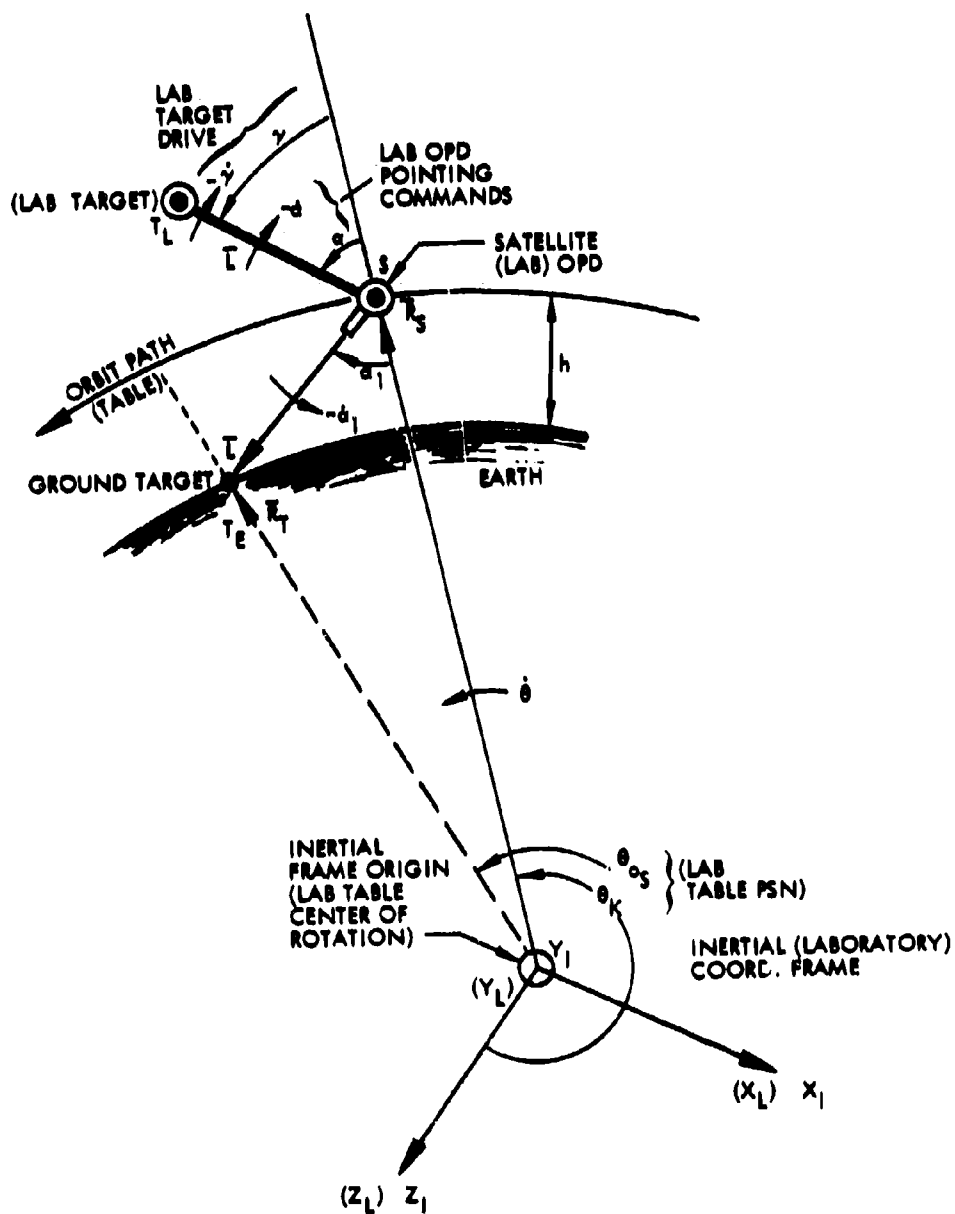


Fig. 4 Laboratory and Orbital Geometry

$\bar{R}_T^E$  = Earth Target coordinates

$T_{E2I}$  = transformation from earth to inertial frame

For the laboratory end-to-end testing of PEPsy hardware, the following essential elements related to orbital conditions are included:

- Pointing line of sight vector from OPD to the ground target
- Pointing vector maximum line of sight rate for the lowest orbit
- Star distribution in angle and brightness factors representing nominal and worst case orbits
- Pitching and limit cycle motion of the satellite

The elements encountered in orbit and contributing to the system error while testing in orbit but not necessary for hardware evaluation in the laboratory are:

- Ephemeris  $\bar{R}_p$  (Eq. 2) computation obtained by integrating the equations of satellite motion or ephemeris update from the ground station
- Earth target coordinates  $\bar{R}_T$  and earth-to-inertial transformation  $T_{E2I}$

The elements present only the earth laboratory environment whose error contribution must be minimized and/or identified are:

- Star field instability due to the thermal and mechanical stresses in the star simulators and their mountings
- Earth rotation which is sensed by gyros
- Wobble in the rate table used to simulate orbital rate
- Vibration and drifts of seismic mass on which PEPsy is to be mounted
- Gravity which is not present in orbital testing but must be accounted for during laboratory testing and preflight calibration of the system (OPD)

One important deviation from orbital geometry was made for the laboratory test. From Fig. 4, it can be seen that "ground target" will be mounted with SPARS and OPD on a rate table simulating orbital rate. This, of course, is not what will happen during the orbital experiment. Why should one do it in the laboratory? A simplification can be made in the laboratory setup and still achieve a meaningful end-to-end evaluation of PEPsy. The only important requirement is to simulate the pointing LOS vector  $\bar{L}$  from OPD to the target. Thus, the target in the laboratory  $T_p$  will rotate around point S, in line with the intersection of

the OPD gimbal axis and will describe the angle  $\gamma$  which is identical to the angle  $\alpha$  which OPD LOS vector goes through during the orbital overpass. This simplification requires only one precision rate table and decreases the number of error sources.

### LABORATORY TEST FACILITY

The SPARS subsystem will be tested at Honeywell Minneapolis and then shipped to LMSC Sunnyvale for integration with the Optical Pointing Device and other major PEPsy subsystems. At LMSC complete System Acceptance Test (SAT) will be performed. Final systems evaluation will take place at Holloman Air Force Base upon completion of SAT.

In order to perform the SAT, three adjacent areas totaling 2500 sq ft are planned. (See Figs. 5, 6, and 8).

- A clean room for the PEPsy test setup
- An area for PEPsy control consoles, instrumentation and control functions
- An air-flow bench area for assembly and maintenance of PEPsy components and subsystems

### Clean Room

The clean room is being built to approximate Federal Standard 209 for a 100,000 class installation. Foreign particle size will not exceed 10 microns and air lock passages and positive air pressure displacement will be incorporated. This room will house a seismic mass, upon which is located the Goerz Precision Rate Table with the PEPsy test specimen. It will be light tight and painted a special color to reduce unwanted light reflections. A diffused air conditioning system will minimize air currents and thermal gradients in the vicinity of the test setup.

The following environmental conditions will be maintained:

Temperature  $72^\circ\text{F} \pm 2^\circ\text{F}$

Humidity  $40\% \pm 10\% \text{ RH}$

A special overhead cable handling system will be installed for completing the electrical connections between the "PEPSY" setup on the rate table and equipment in the control room area. A servoed cable drum may be used to follow the table rotation (plus and minus 2.5 turns), thereby unloading the cable torque from the rate table.

A seismic mass 16-ft long  $\times$  15-ft wide  $\times$  2-ft thick will be made from reinforced Class E-1 concrete and installed 6 months prior to the test on a pneumatic suspension system. Three main functions of this mass are:

- Maintain stability in azimuth and tilt to within 0.5 arc-seconds per day
- Maintain the relative motion between the test equipment to less than 0.5 seconds of arc

- Provide isolation from external vibrations by a pneumatic support system having attenuation characteristics with a slope corresponding to a second order system with a resonance at 3 Hz.

A modified Goertz Model 500 air-bearing rate table will be installed on the seismic mass and used to provide a rotational motion to the entire PEPSY specimen. It will supply accurate (pitch) position readout during pretest calibrations and test. The table will be operated primarily in the rate mode using the synchronous drive system and will have a readout position accuracy of less than 0.4 arc seconds RMS, and a resolution of 0.36 arc. The nominal angular velocity during the test will be 4 degrees per minute. Peak-to-peak table wobble of the unmodified model was measured to be less than 0.6 sec of arc.

Also mounted on the seismic mass are eight to fourteen star simulators placed in a random pattern around the rotary table to simulate a "statistically nominal" star field. Star simulators are 5 inches in diame-

ter and 36 inches long. In the simulator, light from a tungsten filament bulb is passed through two filters, focused on a pinhole, and collimated by an achromatic objective. By inserting different neutral density filters, stars from +1.0 to +6.0 visual magnitude can be simulated. Insertion of color correction filters permits stars of the A0, G5, M5 spectral classes to be simulated. Star image size is smaller than 5 arc seconds while uniformity is better than  $\pm 0.2$  magnitudes.

Figure 7 shows star distribution for the selected orbit. Stars A and B are used for the calibration of the OPD axis and yaw misalignment. Each simulator will be mounted on a pier and enclosed by a protective cage to prevent accidental contact and misalignment. The pier-simulator spatial stability will be better than 1 arc second for a 12-hour period. The star field will be calibrated before and after each run by the OPD and the rate table. A provision in the star simulator mount will be made to allow adjustment of the elevation angle by  $\pm 2$  degrees from the nominal "orbit plane."

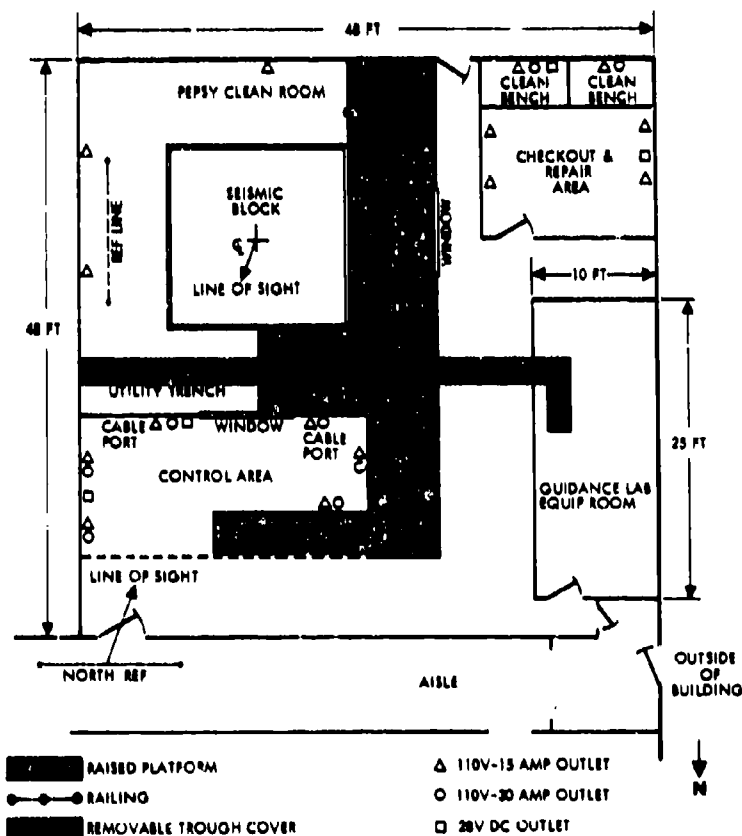


Fig. 6 Test Facility Floor Plan



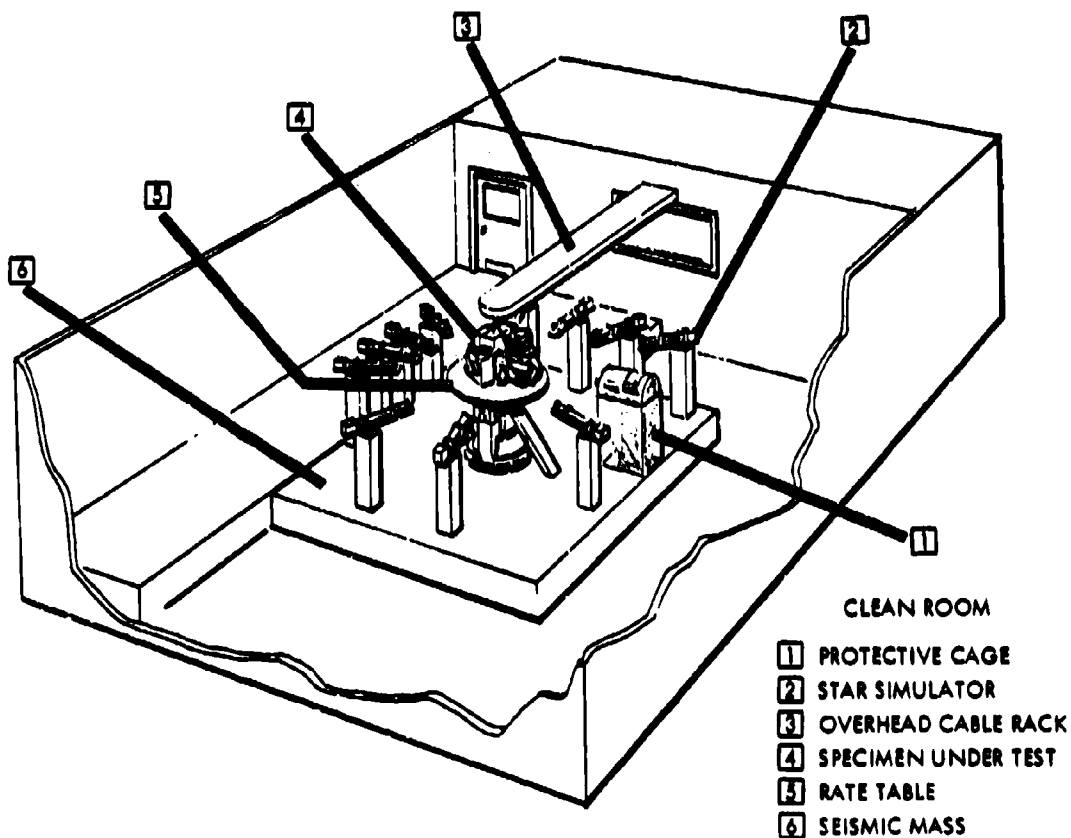


Fig. 6 PEPHY Test Facility Perspective, LMSC, Sunnyvale

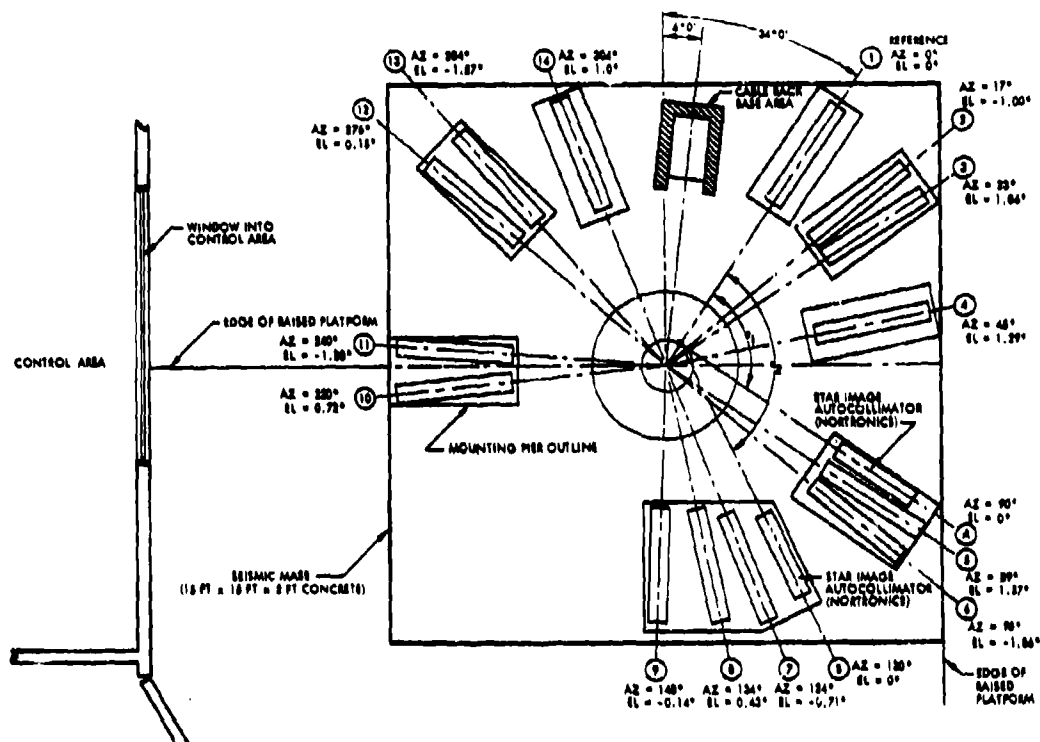


Fig. 7 Distribution of Star Simulators

#### PEPSY Control Area

The PEPSY control area, shown in Fig. 8, will be located immediately adjacent to the clean room and will house the consoles and racks of equipment associated with:

- Power and controls for PEPSY operation
- Power and controls for the Goerz Rate Table
- AGE for the Univac 1824C computer
- Test data acquisition and quick-look displays
- Supplementary computer support for target commands, calibration, SPARS checkout, and data formatting

#### Laboratory Test (SAT LABEX) Mechanization

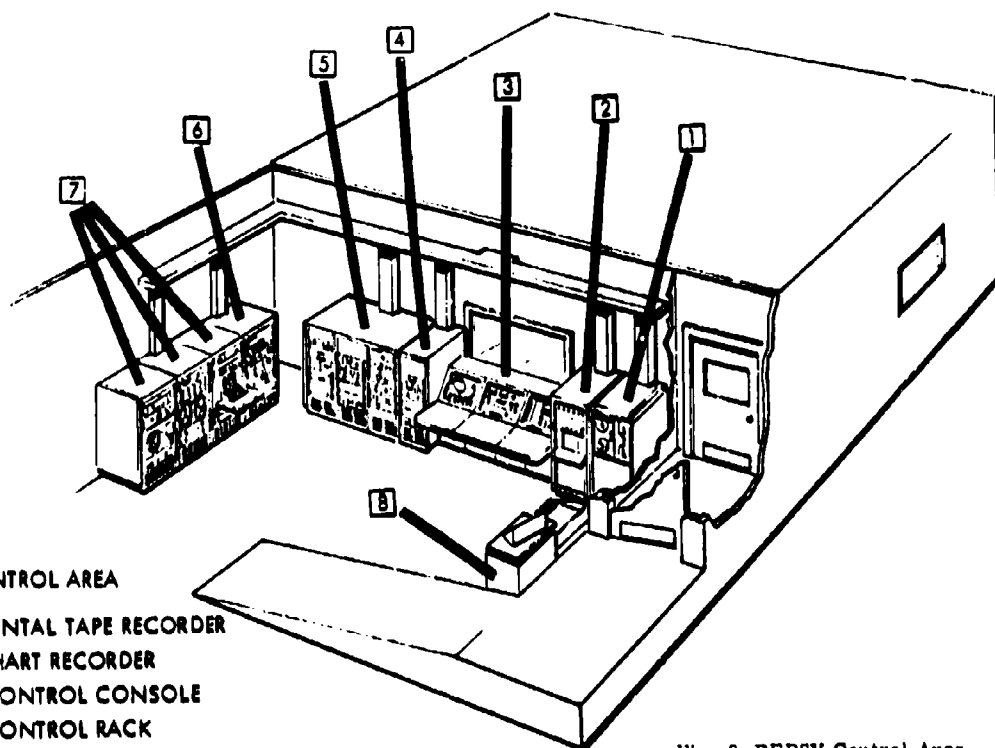
The following typical mission operating optical and dynamic conditions will be simulated:

- Nominal orbital rate
- Random swath of "stars" varying in color, magnitude, azimuth, and elevation

- Dynamic structural flexures occurring between SPARS and OPD when mounted in the "remote" configuration
- A cooperative "ground target" with known coordinates
- Pointing of OPD toward "ground target"
- Limit cycle motion of a satellite

The PEPSY test spoolmen, consisting of SPARS, the OPD, the OAL, Airborne Computer, and Interface and Timing Unit, will be assembled on the precision rate table as shown in Fig. 9. The Goerz table will simulate orbital motion by turning at a rate of four degrees per minute, causing the SPARS star sensor to sweep by the stars.

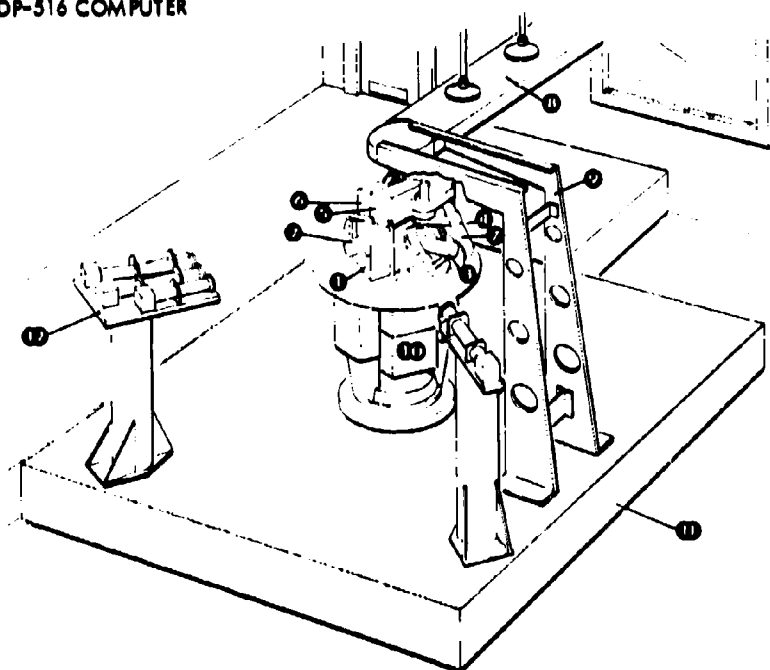
Prior to the actual test, all equipment will be allowed to stabilize in a state of readiness for several hours. No personnel will be permitted in the clean room and final calibration will be performed automatically. This procedure will not only save time but will also decrease the long-term drift of the test equipment due to temperature change.



#### CONTROL AREA

- 1 INCREMENTAL TAPE RECORDER
- 2 STRIP CHART RECORDER
- 3 PEPsy CONTROL CONSOLE
- 4 PEPsy CONTROL RACK
- 5 GOERTZ TABLE CONTROLS (3 BAYS)
- 6 ULTRA CONSOLE (OPD)
- 7 1824 C AGE (3 BAYS)
- 8 DDP-516 COMPUTER

Fig. 8 PEPsy Control Area



- 1 SPARE
- 2 SPARE STAR SENSOR
- 3 OPTICAL POINTING DEVICE
- 4 OAL OBSCURED BY OPD
- 5 AIRBORNE COMPUTER
- 6 INTERFACE AND TIMING UNIT
- 7 OPTICAL TARGET
- 8 OVERHEAD CABLE TRAY
- 9 CABLE SERVO SUPPORT RACK
- 10 PRECISION RATE TABLE
- 11 SEISMIC MASS
- 12 TYPICAL STAR INSTALLATION  
(SEE FIG. 7 FOR DETAILS OF  
STAR DISTRIBUTION)

Fig. 9 PEPsy Test Setup

Most interesting automatic calibrations are:

- SPARS "autocal" procedure determines the orientation in laboratory coordinates of the twelve-star sensor detector slit normal vectors.
- STAR distribution is determined with the OPD in elevation and with the OPD plus rate table position readout in azimuth.
- Calibration of OPD outer gimbal axis and yaw misalignment with the two additional Star Simulators "A" and "B" shown in Fig. 7.

All calibration data is computed and stored in the "airborne" computer as well as in a laboratory computer.

All data to be recorded will be fed first to the laboratory computer for conditioning. For quick-look analysis the lab computer will calculate the Euler angles at each star transit and subtract it from the rate table position. This information will provide a real time indication of the difference between the SPARS and the rate table readouts.

The ground target simulator consists of a Cassegrainian optical collimating source with an image size of 3 arc seconds and a single gimbal structure with an Inductosyn readout accurate to 1.5 arc sec and repeatable to 0.2 arc seconds. The target axis of rotation will be vertical and will pass through the intersection of the OPD axes.

Motion of the target will be programmed by the lab computer. It will be completely independent of the PEPSY system and will be similar to the line-of-sight-motion  $\alpha_1$  in the orbital case (see Fig. 4).

$$\gamma = \tan^{-1} \left[ \frac{\sin(\theta_{oj} - \theta_K)}{1 - \frac{h}{R_E} - \cos(\theta_{oj} - \theta_K)} \right] \quad (4)$$

$$\frac{h}{R_E} = \text{orbital constant}$$

$$\theta_{oj} - \theta_K = \text{rate table position read out}$$

$$\dot{\gamma}_{\max} = 120 \text{ degrees per minute for } 100\text{-nm orbit}$$

$$\gamma = \text{range } \pm 60^\circ$$

The OPD will be commanded by the "airborne" computer to point at and follow the ground target at a line-of-sight rate typical of that encountered in orbit. The pointing vector in OPD coordinate is given by Eq. (5) below.

$$\bar{L}^O = T_{S2O}^T T_{L2S}^T T_{TAB2L}^T T_{TA2TAB}^T \bar{L}_{TA}^{TA} \quad (5)$$

$$\bar{L}_{TA}^{TA} = \begin{bmatrix} S_n \gamma \\ 0 \\ C_n \gamma \end{bmatrix} \quad (6)$$

$\bar{L}_{TA}^{TA}$  = a vector from the OPD gimbal point to the target in target coordinates.

$T_{j2K}$  = transformation matrices from j to k coordinate frame.

O = OPD;

S = SPARS

L = laboratory

TAB = table

TA = ground target

It can be seen from Eqs. (4), (5), and (6) that OPD is pointed at a known target ( $\bar{L}_{TA}^{TA}$ ) by using a SPARS generated direction cosine matrix ( $T_{L2S}$ ), and the OAL data  $T_{S2O}$ .

A special mechanism will be used to introduce dynamic disturbances between the bases of SPARS and OPD thereby simulating vehicle flexure. At this point, it is interesting to observe the similarity between LOS pointing vector equations written for orbital and laboratory cases in the OPD frame. One is Eq. (1) previously indicated and second is Eq. (5) written in slightly different form to underline the similarity.

#### Orbit

$$\bar{L}^O = T_{S2O} T_{L2S} \bar{L}^L \quad (1)$$

#### Laboratory

$$\bar{L}^O = T_{S2O} T_{L2S} \bar{L}^L \quad (5)$$

Two-axis operation of the OPD will be accomplished by mounting the OPD pitch axis 30 degrees from vertical and maintaining the target in the horizontal plane. The OPD can operate in the open-loop or closed-loop modes. The airborne computer generates outer and inner gimbal pointing commands by converting the pointing vector  $\bar{L}^O$  (Eq. 5)

$$\bar{L}^O = \begin{bmatrix} L_x^O \\ L_y^O \\ L_z^O \end{bmatrix} \quad (7)$$

Open loop:

$$\alpha = \tan^{-1} \frac{L_x^O}{L_z^O} \quad (8)$$

$$\beta = \tan^{-1} \frac{L_y^O}{\sqrt{1 - L_y^{O2}}} \quad (8)$$

Closed loop:

$$\alpha = \tan^{-1} \frac{-L_z^0}{L_x^0} - \frac{\Delta X}{\cos \beta} \quad (10)$$

$$\beta = \tan^{-1} \frac{-L_y^0}{\sqrt{1 - L_y^0}} + \Delta Y \quad (11)$$

Where  $\Delta X$  and  $\Delta Y$  are the OPD telescope outputs fed back to the "airborne" computer. In the closed-loop mode, the measured OPD-target error is used to track the target.

In order to obtain a larger sample of mutually independent data points, the OPD and target will be exercised several times per table revolution, a situation corresponding to passing over several ground targets per orbit. This is a technique for minimizing the time for data accumulation. The STAR distribution pattern in azimuth will be changed from orbit to orbit to minimize systematic errors in table periodicity experienced in earlier testing. Data accumulated during the test will be processed statistically to ascertain SPARS and PEPsy performance accuracy.

The major error sources for the PEPsy test are grouped in Fig. 10 according to whether they are attributable to the system or the laboratory.

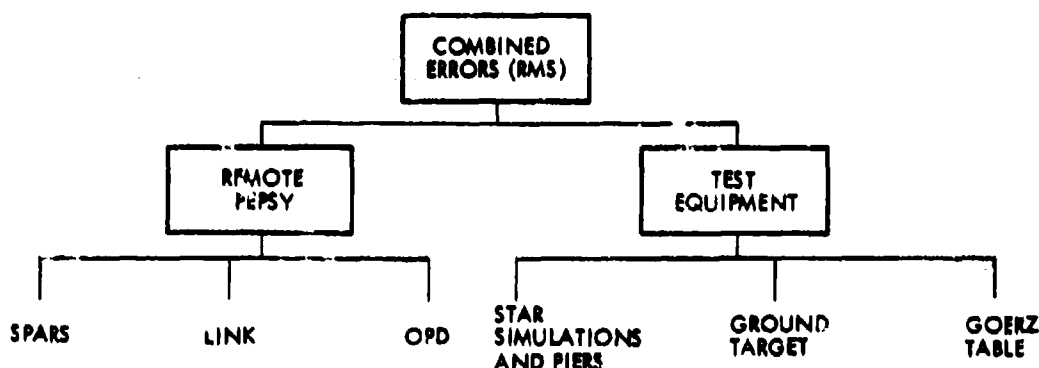


Fig. 10 Combined System Error Budget

End-to-end PEPsy performance can be summarized by specifying the three quantities defined below:

- **Pointing Error.** The angular deviation of the OPD Telescope-Sensor (T-S) optical axis from the line of sight to the target. The pointing error is indicated directly by the T-S output. Typically this must be kept smaller than the T-S field of view.
- **Pointing Knowledge.** The ability to compute the line of sight to the target from post-test data analysis. The pointing knowledge is derived from knowledge of the pointing error, the OPD servo error (inductosyn signal), and the commanded OPD gimbal angle.
- **Error in Pointing Knowledge.** The angular deviation of the computed line of sight to the target from the actual line of sight to the target. The actual line of sight to the target is derived from a combination of the commanded target angle and the target servo error. It is assumed that the error in pointing knowledge obtained during a large number of tests will be normally distributed.

#### ORBITAL TEST (PEPEX) MECHANIZATION

The orbital evaluation of the SPARS, integrated with an optical pointing device, will be implemented in the Precision Earth-Pointing Experiment (PEPEX). The primary objective of the PEPEX is to obtain the necessary quality and quantity of those measurements from which statistically meaningful data on the SPARS performance may be derived in a post-flight analysis. The experiment requires five major elements: The PEPsy mounted on a satellite; a cooperative ground laser target; a satellite ground communication link; a multi-station satellite tracking network; and auxiliary tracking systems.

#### Approach to the Experiment

For PEPEX, the SPARS/OPD combination will be mounted on an attitude-controlled satellite which is nominally oriented in the local horizontal plane as it traverses its orbital path about the earth. The resulting pitching motion of the satellite with respect to inertial space provides the motion enabling the SPARS star sensors to sweep the celestial sphere and encounter the star transits with which it will establish the orientation of the inertial coordinate frame.

Typically, the PEPEX will be conducted in the following manner: After the satellite is injected into orbit and sufficient time is allowed for vehicle outgassing to be completed, accurate orbit determination will begin using tracking data from the Air Force Satellite Control Facility (SCF) System. After the last tracking pass prior to PEPEX operation, the best orbit fit is made by the SCF and an ephemeris is generated and extrapolated through the experiment pass. A state vector from this ephemeris is transmitted to the satellite to be used as a set of initial conditions from which the flight computer would generate an ephemeris through the target pass. The flight computer, utilizing this on-board ephemeris, vehicle attitude data from SPARS, vehicle flexure data from the OAL, and the stored-target location, will then determine the commands required to point the OPD Telescope-Sensor (T-S) at the cooperative ground target and to maintain that target in the T-S field of view (FOV).

The ground target will be a high-intensity light source generated by a continuous-wave gas laser. This laser operating in the TEM<sub>00</sub> mode provides an output beam with a Gaussian cross-sectional intensity function. The beam divergence is established in such a way that for the 2-sigma poorest beam-pointing accuracy and a 2-sigma worst satellite-position prediction, the beam will illuminate the PEPEX satellite at one-half the maximum laser output power.

The baseline candidate for the laser is a stabilized 8-w argon ion unit. This laser features a lightweight head (80 lb) and a compact power supply (250 lb). At the 5145 Å line, chosen for its similarity to starlight, the laser has a guaranteed power output of 2.5 w after 1 year of continuous operation.

For a laser beam divergence of  $\pm 550$  arc sec at the half-power points, and an atmospheric transmission computed at a look angle of 30 deg up from the horizon, the laser power density is several orders of magnitude greater than that from a second-magnitude star. For example, at a 700-nm range, laser power density is  $5 \times 10^{-8}$  w/m<sup>2</sup>, whereas the power density from a typical second-magnitude star is  $5 \times 10^{-10}$  w/m<sup>2</sup>. Since the telescope-sensor of the OPD is designed to "see" a second-magnitude star, this design allows "seeing" the laser under less favorable conditions than assumed above. Daylight detection of the laser against a sunlit earth is possible because of the monochromatic nature of the laser and the narrow instantaneous field of view of the telescope-sensor. A spectral filter, a few angstroms wide at 5145 Å, eliminates most of the reflected solar spectrum. For the no-cloud atmospheric conditions specified, the signal-to-noise ratio when observing the laser against the sunlit earth is greater than 20 to 1.

To enable the T-S to receive the laser signal, the highly directional laser beam must be precisely pointed such that the satellite is illuminated throughout the pass over the target station. These pointing commands will be generated open-loop in ground computers utilizing the best current satellite ephemeris. Open-loop beam pointing demands a very accurate gimbal-alignment and drive system. This accuracy minimizes compounding of errors already present as a function of beam divergence and satellite position uncertainty.

Present beam divergence will accommodate the two-sigma, worst-case ephemeris errors and allow a reasonable beam-pointing accuracy. In spite of this, open-loop pointing is preferable to closed-loop because neither an onboard retro-reflector nor a ground receiver unit with its supporting equipment is necessary. Beam pointing will be accomplished in open-loop by driving a two-axis gimballed mirror that deflects the light beam emanating from a laser transmitter fixed to a stationary base. Considering the required accuracy, pointing a small mirror is simpler than pointing the whole laser.

During the experiment pass, precision satellite tracking data will be gathered by means of a ballistic camera located with the laser target (at Edwards AFB), and/or a complex of four geodetic SECOR ground stations (Fig. 11). These data will provide the high-precision satellite ephemeris necessary in the post-flight analysis to determine the portion of the target-image error contributed by inaccuracies in the real time onboard ephemeris.

The ballistic camera, with a pre-pass fixed setting, has the desirable feature of providing a direct orientation measurement of the OPD LOS in inertial space. It will photograph the vehicle in earth orbit against a star reference background. The vehicle will be equipped with a flashing Xenon light for locating purposes. However, this approach is limited in data-gathering opportunity to a short segment of each night overpass and is subject to data loss due to cloud cover. The magnitude of celestial segment observed is dependent upon the field of view (FOV) of the camera.

The veracity of any experimental result increases with the quantity of the experimental data injected into the analysis. For this reason, the SECOR complex would offer an advantage since additional experimental data could be gathered on any flight. The system will track a transponder-equipped satellite over the full span (elevation angles greater than 15 deg) of any day or night overpass without regard to the extent of cloud cover over any or all stations. An additional advantage of SECOR is its capability to provide a real-time ephemeris update. An update is required for open-loop OPD pointing to be accomplished without a loss of the target from the OPD field of view. The possible magnitude of the errors in the SCF extrapolated ephemeris would not preclude target acquisition due to the wide T-S acquisition FOV but could cause the target to drift out of a high-accuracy narrow T-S steady-state FOV. Since loss of target cannot be compensated post flight, an improved ephemeris must be provided to the on-board computer.

A drawback to the SECOR system is that the satellite ephemeris is determined relative to the earth-fixed reference of the SECOR ground complex. The transformation to an inertial reference produces errors due to the uncertainty in the precise location of the ground complex. This error can be removed by adjusting the ephemeris to incorporate the direct inertial orientation measurement of the relative vehicle position vector acquired by the ballistic camera.

The Space-Ground Link System (SGLS) station at Vandenberg AFB will serve as the real-time telemetry, command, and experiment direction link between the

ground control center and the vehicle. All PEPEX telemetry data will be transmitted to ground stations via the SGLS on a real-time basis during PEPEX operation or tape recorded for later readout. These data include the time variation of the target image error and all inputs and outputs to the on-board computer which are necessary for the post-flight evaluation of PEPSY performance.

After an experiment pass is completed, a new ephemeris is generated in the ground computer center and extrapolated to the next experiment pass. At the conclusion of the flight, all accumulated telemetry and tracking data will be utilized in the post-flight analysis to establish the accuracy of pointing knowledge achieved by PEPSY.

#### Contributors to Pointing Error

Open-loop pointing commands to the OPD are generated in the flight computer utilizing data from the SPARS and OAL subsystems, stored information concerning geodetic location of the ground target, and the satellite ephemeris as determined onboard in real time. The pitch ( $\alpha$ ) and roll ( $\beta$ ) commands to the inner and outer gimbals respectively were defined in Eqs. (8) and (9) in terms of components of the relative position vector between the satellite and the ground target which was defined in Eqs. (1) and (2).

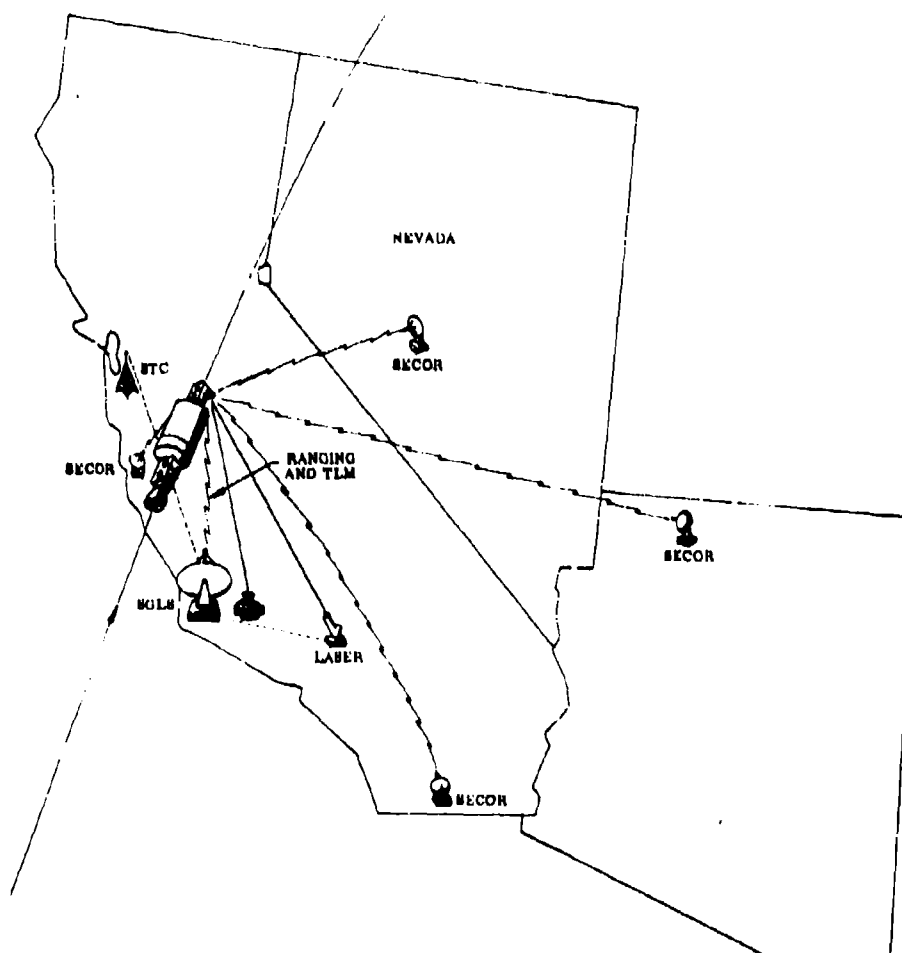


Fig. 11 Precision Tracking in PEPSY Evaluation Accomplished With Operational Systems

The accuracy of the pointing commands must be such that the target remains within the narrow (high accuracy) field of view of the OPD telescope-sensor throughout the experiment pass. The extent to which the pointing accuracy is achieved will be determined by the accuracy with which the onboard systems can determine T2S, TS2O, compute the pointing commands, and execute them. The T2S would be updated once a day to reduce precession and mutation errors. The elements not wholly within the control of the system hardware are the accuracy of the target location and the satellite ephemeris. Target location error is dependent upon geodetic survey accuracies and can be in excess of 100 feet. The satellite ephemeris carried or computed on board would be the most significant contributor to an experiment pointing error. The necessary ephemeris accuracy is a function of orbit altitude and the nominal offset angles from the local vertical.

#### On-Board Ephemeris Computation

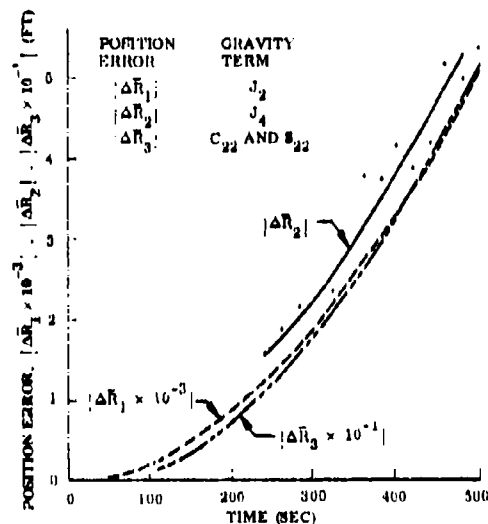
The onboard ephemeris is computed over a given time interval using initial-conditions input received from the ground. Two error sources come into play. The error in the initial conditions and the error in the computed ephemeris. The former is a function of the ground tracking network, the tracking coverage, the atmospheric and gravitational model errors, and the extent to which the fitted ephemeris must be extrapolated forward from the last tracking pass. The latter is a function of the method of computation. This can be accomplished by the closed form or numerical integration of the equations of motion. The selected method and degree of complexity of the equations of motion to be used was chosen on the basis of position accuracy, computation time, and computer capacity requirements for the range of orbit altitudes and overpass time spans of interest. The time history of position accuracies for a 200-nm orbit utilizing the numerical integration of simplified equations of motion was examined. See Fig. 12. It was found that at the end of a 5-minute overpass the retention of only the  $J_2$  zonal harmonic of the gravitational potential (Eq. 12) will result in a position 20 feet from that determined when utilizing the  $J_2$  and  $J_4$  zonals as well as the tesseral harmonics,  $C_{22}$  and  $S_{22}$ , representing the ellipticity of the equator. Air drag was found to make a smaller contribution to the position error than those attributed to the tesseral harmonics and was thus dropped from the equations of motion. This difference is more pronounced for higher orbit altitudes.

#### Ephemeris Determination With Ground Tracking Network

The uncertainty in the on-board ephemeris, however, can never be less than that of the initial conditions transmitted to the flight computer from the ground. These initial conditions are derived from the best real-time prediction of the satellite ephemeris by a ground computer center fitting the orbital equations of motion to observed data from a network of widely dispersed tracking stations. This real-time ephemeris is updated with each succeeding pass of tracking data. The best fit just prior to an experiment pass will be extrapolated forward to a point just preceding predicted target acquisition. These initial conditions are then transmitted to the satellite. The accuracy of this prediction is dependent upon the characteristics of the

tracking network being used, the quality, quantity, and distribution of the tracking data, and the accuracy of the mathematical gravitational and atmospheric density models.

The tracking data errors consist of random errors and data biases peculiar to the equipment of the tracking network being used. In addition, the tracking station locations and station times can also be in error. The tracking network to be used consists of the AFSCF SGLS stations and the Satellite Test Center (STC) computer facility in Sunnyvale. Errors in the gravitational model include the inaccuracies in the zonal and tesseral coefficients and the earth's gravitational constant. The atmospheric density model errors of interest during the fitting and extrapolation intervals are those due to the uncertainties in the contribution of actual geomagnetic activity to the short period density fluctuations. These



$$\frac{dx}{dt} = \dot{x}$$

$$\frac{dy}{dt} = \dot{y}$$

$$\frac{dz}{dt} = \dot{z}$$

$$\frac{dx}{dt} = -\frac{\mu}{R^3} \left[ 1 - J_2 \left( \frac{R_{eq}}{R} \right)^2 \frac{3}{2} \left( \frac{x^2}{R^2} - 1 \right) \right] \quad (12)$$

$$\frac{dy}{dt} = -\frac{\mu}{R^3} \left[ 1 - J_2 \left( \frac{R_{eq}}{R} \right)^2 \frac{3}{2} \left( \frac{y^2}{R^2} - 1 \right) \right]$$

$$\frac{dz}{dt} = -\frac{\mu}{R^3} \left[ 1 - J_2 \left( \frac{R_{eq}}{R} \right)^2 \frac{3}{2} \left( \frac{z^2}{R^2} - 1 \right) \right]$$

Where:  $x, y, z$  = inertial position components

$\mu$  = gravitational constant

$J_2 = -1084.7 \times 10^{-6}$  = zonal harmonic

$R = \sqrt{x^2 + y^2 + z^2}$

Fig. 12 The Integration of the Equations of Motion Omitting all but the  $J_2$  zonal harmonic term of the Gravitational Potential Results in Approximately a 20-Ft Position Error After a 5-Min Integration Period



uncertainties are functions of the assumed variations in the half-day averages of the geomagnetic index  $K_p$ . Representative density variations are used simulating minimum, moderate, and intense levels of geomagnetic heating based on observed  $K_p$  data correlated with observed density fluctuations.

A comprehensive analysis of the accuracy of ephemeris determination and extrapolation can be made only when the specifics of the available tracking network are known. However, for insight into the problem, the accuracies obtained utilizing the AFSCF network for a hypothetical 200-nm altitude orbit were examined. These results represent the maximum in-track position uncertainties assuming the availability of 11 passes of radar data over an interval of 16 hours. These data were processed in a weighted least-squares fit of all data at a rate of one point every 15 sec and extrapolated forward for a maximum of 5 revolutions. The fitting parameters consist of the six-orbit elements and the vehicle ballistic parameter.

Although for the case of maximum  $K_p$  activity position uncertainties in the initial portion of the fitting interval were on the order of several miles, the fit for the 200-nm circular orbit converged after 8 hours of data to a constant in-track position uncertainty. This situation continues until the cessation of tracking. Extrapolation of the fitted orbital elements results in the predicted maximum RSS in-track position uncertainties growing by a factor of four after five revolutions. The state of the art of ephemeris determination has progressed to the point where the errors in the extrapolation of an orbital fit for five revolutions under the worst conditions will not impose excessive requirements on minimizing the divergence of the target laser beam to ensure acquisition of the target. The air drag uncertainties are the dominant error source. For low  $K_p$  activity periods, the station location and gravity model uncertainties are the major error sources for the extrapolation. Random data errors and data biases have small effects compared to other sources. Therefore, the use of more accurate tracking data at the SCLS station locations will not noticeably affect the accuracy of the predicted ephemeris. Improvements in the air drag model, ground station survey, and gravity model are necessary to significantly reduce the ephemeris prediction error. The domination of the extrapolation by the air drag model errors in high magnetic heating periods leads to increasing ephemeris uncertainties at lower PEPEX orbit altitudes. This occurs due to the higher densities at the lower altitudes.

#### Real-Time Ephemeris Update

The wide FOV incorporated in the OPD/T-S and the narrow width of the ground laser beam have been specified so that errors in the extrapolation of the predicted satellite ephemeris under worst atmospheric conditions and the lowest anticipated orbit altitudes will not preclude the acquisition of the target by the T-S. However, the gathering of acceptable test data requires that the target be maintained in the high-accuracy narrow FOV of the T-S. While a large initial pointing angle error can be removed by a compensating gimbal bias, the causal large ephemeris error will soon move the target image out of the narrow FOV. In order to

preclude this possibility, a gross ephemeris correction will be determined in the ground computers by performing a least squares fit on the T-S detector data over a short time span assuming that the total pointing error is due to satellite in-track position error. Fitting only to a correction in the in-track position permits the rapid calculation and transmittal of the correction to the flight computer. The ephemeris correction also might be accomplished utilizing the SECOR data.

#### Post-Flight Analysis

The OPD pointing angle error data recorded and telemetered to the ground station during the flight will be processed in the post-flight analysis to establish the uncertainty in PEPSY pointing knowledge. The evaluation will be performed by an error-separation method utilizing a least squares fitting technique. The basic premise in this method is that pointing angle errors occurring due to errors in the vehicle and PEPSY state vectors propagate in time in distinctive ways. In contrast the satellite ephemeris errors are assumed to remain constant over the short duration of any experiment pass. This approach requires that the time variation of the error parameters be accurately modeled. Error models for all of the system error sources will be determined from previous test and calibration data taken during the experiment. The parameters of the error models then become the fitting parameters in the least squares fitting equation:

$$\Delta L = \left[ Q^T W^{-1} Q + \Sigma_0^{-1} \right]^{-1} (Q^T W^{-1} \Delta q) \quad (13)$$

where  $\Delta L$  is the differential correction to the vector of fitting parameters,  $Q$  is the matrix of partial derivatives of the T-S detector data to the fitting parameters,  $W^{-1}$  is the data weighting matrix,  $\Sigma_0^{-1}$  is a preloaded covariance matrix and  $q$  is the vector of residuals of the observed detector data with respect to the computed data based on the current best estimate of the fitting parameters. The time history of  $Q$  is determined analytically based on the nominal trajectory for the experiment pass.

The fitting parameters are varied in order to yield a least squares fit of the total modeled pointing error to the actual error as determined from the telemetered data. The PEPSY errors are then determined as being the values of the PEPSY parameters which gave the best fit, i.e., the smallest residuals over the pass of data being analyzed. The uncertainty in the knowledge of these PEPSY parameters, and thus the SPARS performance, will be dependent upon the quality and quantity of test data, the validity of the error models, and the accuracy with which the fitting is accomplished.

A UNIVAC 1108 program simulating the post-flight error separation method has been developed, coded, and partially checked out. The program requires the input of radar tracking data, two axis T-S detector data, nominal OPD pitch and roll gimbal angle histories, a best estimate of the orbital initial conditions, and error model parameters. The program has been checked out with noise-free simulated AFSCF range

data. OPD detector data generated by the input of six components of satellite position, velocity errors and a set of SPARS pitch bias and drift-rate errors. The accuracy with which these eight parameters were fitted is presented in Fig. 13. The errors in the fitted parameters are the values obtained after nine iterations using the least squares method. As can be seen from the table of the RMS detector and range data residuals,

the fit has converged after seven iterations.

Further work in checking out the fitting of the remaining error parameters, the determination of the effects of noise on the data and the extent of the correlation between parameters will be conducted in the next phase of the program.

	Parameter		Input Error	Fit Correction*	Error in Fit*
	True	Fit*			
$X_I$	-19149535 ft	-19149535	-500 ft	-500.16959 ft	.16959 ft
$Y_I$	-3468659.9 ft	-3468658.9	-500 ft	-499.00596 ft	-.99404 ft
$Z_I$	10476490.1 ft	10476490	-500 ft	-499.97058 ft	-.02942 ft
$\dot{X}_I$	12091.4321 fps	12091.433	0 fps	$.16898 \times 10^{-2}$ fps	-.0016898 fps
$\dot{Y}_I$	128.577193 fps	128.56730	0 fps	$-.98930 \times 10^{-2}$ fps	.0098930 fps
$\dot{Z}_I$	22168.2427 fps	22168.242	0 fps	$-.30770 \times 10^{-3}$ fps	.0003077 fps
$\theta$	0 rad	$.1912 \times 10^{-8}$	$-.5 \times 10^{-5}$ rad	$-.4998 \times 10^{-5}$ rad	$-.0002 \times 10^{-5}$ rad
$\dot{\theta}$	0 rad/sec	$-.2716 \times 10^{-10}$	$-1 \times 10^{-5}$ rad/sec	$-1.0003 \times 10^{-5}$ rps	$.0003 \times 10^{-5}$ rps
No. of Iterations	RMS Data Residuals				
	$X_T$ , arc-sec	$Y_T$ , arc-sec	Range, ft		
5	$.887506 \times 10^{-2}$	$.218703 \times 10^{-2}$	$.44641 \times 10^{-3}$		
7	$.23614 \times 10^{-3}$	$.26320 \times 10^{-3}$	$.11310 \times 10^{-3}$		
9*	$.10950 \times 10^{-3}$	$.23696 \times 10^{-3}$	$.3298 \times 10^{-4}$		

\*Values given are after the 9th iteration

Fig. 13 Error Separation

#### REFERENCES

1. W. R. Davis, et al., (U) Space Precision Attitude Reference System (SPARS) Phase O Final Report, SAMSO-TR-68-217, Secret (Apr 1968).
2. U. C. Paulson, D. B. Jackson, and C. D. Brown, (U) SPARS Algorithms and Simulation Results, Spacecraft Attitude Determination Symposium (Oct 1969).
3. R. T. Scott and J. E. Carroll, (U) Development and Test of Advanced Strapdown Components for SPARS, Spacecraft Attitude Determination Symposium (Oct 1969).
4. W. R. Davis and J. A. Miller, SPARS - A Completely Strapdown Concept for Precise Determination of Satellite Vehicle Attitude (Sep 1968).
5. W. R. Davis, et al., (U) Space Precision Attitude Reference System (SPARS) Phase IA Final Report, SAMSO-TR-69-72, Secret (Feb 1969).

# SPARS: THE SYSTEM, ALGORITHMS, AND TEST RESULTS<sup>1</sup>

N. F. Toda, J. L. Heiss, and F. H. Schlee  
IBM Federal Systems Division  
Owego, New York

## ABSTRACT

SPARS - A Space Precision Attitude Reference System, has three major subsystems: an Inertial Reference Unit, a Star Sensor Assembly, and a Digital Computer Subsystem. The IRU consists of three strapdown gyros employing pulse torque servo amplifiers for rebalancing. The star sensor assembly is a two-axis pitch within roll gimbaled telescope. The computer subsystem issues pointing commands to the telescope and processes measurement data from the star sensor assembly and the inertial reference unit to obtain an "optimal" estimate of spacecraft attitude. This paper describes the IBM system configuration and the performance achieved during laboratory testing.

## I. INTRODUCTION

SPARS, a Space Precision Attitude Reference System, consists of: an Inertial Reference Unit, a Star Sensor Assembly, and a Digital Computer Subsystem. The Inertial Reference Unit (IRU) effectively serves as the attitude memory between star sightings. It consists of three strapdown gyros employing pulse torque servo amplifiers for re-balancing. The Star Sensor Assembly (SSA) is a two-axis, pitch within roll gimbaled telescope. Digital readout is provided by incremental gimbal encoders and silicon digital detectors. The latter measures the position of the star image within the field of view of the telescope. The computer subsystem issues pointing commands to the telescope and processes measurement data from the SSA and IRU to obtain an "optimal" estimate of spacecraft attitude.

To demonstrate the accuracy of SPARS for a spacecraft that is controlled to be nominally aligned to the local vertical, an extensive laboratory development program was undertaken to provide a very accurate test bed for the SPARS equipment. The principal laboratory subsystems were a precision rate table and star simulators. The IRU and the SSA were mounted on the rate table which provided both a velocity environment and an independent measurement of attitude.

Quaternions or Euler four parameters were employed to represent attitude rather than direction cosines or Euler angles. The attitude integration algorithm is particularly simple in this representation. The Kalman filter was employed to process the star sensor data into "optimal" estimates of spacecraft attitude.

This paper describes the IBM SPARS configuration and the performance achieved during laboratory testing. Some qualitative data are included in the main text; quantitative test results and conclusions appear in the classified (SECRET) appendix to this paper. Laboratory test equipment and procedures are discussed by Schlee and Nielsen in Reference (1). A description of the IRU used is given by Baum and Sheldon in Reference (2).

## II. SPARS CONFIGURATION

The IBM SPARS configuration consists of: a strapdown Inertial Reference Unit (IRU), a gimbaled Star Sensor Assembly (SSA), and an onboard computer which utilizes a software package employing Kalman filtering techniques.

The IRU is ideally suited for orbital applications where relatively low angular rates are experienced. The gimbaled star sensor supplements the inertial

<sup>1</sup>Work described in this paper was performed under Contract F04701-68-C-0325.

packages by providing regular and frequent attitude updates via celestial "fixes." High resolution of the star position is realized by utilizing a gimbaled telescope with a small Field of View (FOV).

The IRU consists of three integrating gyroscopes operated in a forced limit cycle rebalance loop. The output of the gyroscopes is in the form of pulse counts which are proportional to the integral of the body angular rates.

The SSA features gray-coded silicon coordinate readout devices combined with a pitch within roll gimbal design. The purpose of the silicon coordinate readout device, which is subsequently referred to as a digital readout, is to measure the X and Y coordinates of the star image within the telescope FOV. This provides a measurement of the star line of sight relative to the telescope axis; orientation of the telescope relative to the SPARS base plate is provided by the pitch and roll gimbal encoders. The X and Y coordinate measurements and the pitch and roll gimbal angle measurements were combined by the SPARS software into pitch and roll angles which defined the star line of sight orientation relative to the SPARS base plate. It is these angles which were input to the Kalman filter.

The SSA was designed to operate in a non-nulling mode, i.e., the gimbal drive servos were not driven so that the star image lies in the center of the telescope FOV. Instead, the telescope was driven so that the star image remains within the FOV and has no relative motion. Motion of the star image across the digital detector would smear the star image and would result in X and Y coordinate readout errors.

The non-nulling approach was selected to permit use of a rate servo rather than a position servo, thereby minimizing the gimbal servo design and improving star image detection. Since the star image remains motionless on the sensitive digital detector grid, the image signal-to-noise ratio can be increased by lengthening the image exposure time.

The SSA developed, fabricated, and demonstrated during the SPARS Phase 1A effort is physically made up of two components: the gimbaled telescope and the electronics cabinet. Figure 1 shows the SSA. The functional breakdown of these two components is illustrated in Figure 2.

### III. DIGITAL DETECTOR AND TELESCOPE

The digital detectors are silicon photovoltaic sensors employing a gray coded binary pattern which produces a direct digital readout of a line image that impinges on the pattern. The line image is generated by the optics which include cylindrical elements. Pre-amplification electronics for digital detector outputs are contained in the telescope assembly. Be-

cause the detailed description of the optical prescription, the digital detectors, and their associated signal processing circuits are of a proprietary nature, they are not included in this paper. The overall telescope FOV, which is defined by the optical prescription and the digital detector cell dimension, is 600 arc seconds. An additional element exists between the cylindrical lens and the detector cell to provide star signal modulation.

The overall gimbal assembly employs a cantilever design rather than the conventional gimbal design. Figure 1 shows the case of the roll gimbal serving as the mounting fixture to the spacecraft. The pitch gimbal assembly is mounted on the roll gimbal shaft and the telescope assembly is mounted on the pitch gimbal shaft. Gimbals were free to rotate through at least 90 degrees.

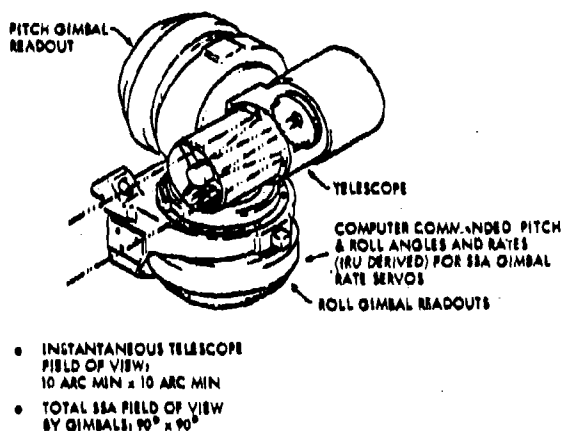


Fig. 1. SSA

Beginning with warmup and star sensor energization and self-test, an operational sequence consisting of star search and acquisition is performed. SPARS is designed to determine precisely the attitude of a vehicle whose attitude is already known to an accuracy of  $\pm 2\frac{1}{4}$  degrees per axis. Thus the initial star acquisition problem for the SPARS consists of searching for a star within a cone having a half angle of  $2\frac{1}{4}$  degrees. Because the probability of the first three stars falling within the  $10 \times 10$  arc minute field-of-view of the star sensor is very low, a search mode is implemented for acquisition. Following the first three star fixes, knowledge of the attitude is improved to the point that subsequent star sensor pointing commands will assure that the star falls within the telescope FOV. Subsequent star fixes at 30 second intervals then are processed with the on-board filter to improve the attitude estimate, to calibrate the IRU gyros, and to estimate star sensor misalignments. Operational utilization of SPARS requires only a single instantaneous snapshot of a star once every 30

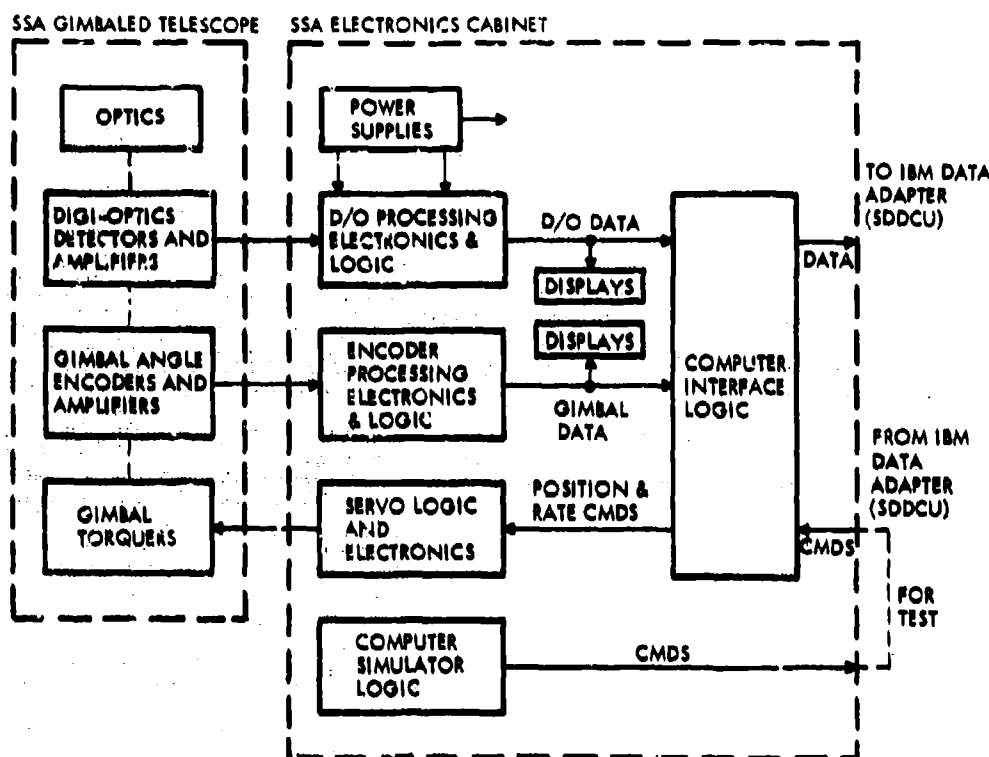


Fig. 2. SSA Functional Diagram

seconds. The attitude during the interval between these fixes is remembered by the IRU gyros, which will have been calibrated by the SPARS software. The IRU data is sampled every 123 milliseconds to provide a relatively continuous estimate of spacecraft attitude.

#### IV. SPARS LABORATORY OPERATING CONCEPT

The Phase IA laboratory implementation of the SPARS hardware and software required some modifications from the orbital case in order to accommodate the earthbound laboratory environment (e.g., the influence of earth's rate on the IRU gyros) and the absence of the search function in the SSA feasibility model. The laboratory operation therefore was constrained to initial attitude errors of less than  $\pm 5$  arc minutes as dictated by the SSA telescope FOV. The arrangement of the star simulator in the IBM SPARS Laboratory was such that only one quarter of an orbit could be traversed with a regularity of star sightings. However, this approximately 20 minute test duration was sufficient to demonstrate optimal filter convergence and steady-state behavior. Full orbit operation in the laboratory also was performed with attitude maintenance during the additional

3/4 orbit travel wholly dependent on the calibrated gyro performance.

#### V. ATTITUDE REPRESENTATION

There are many sets of dependent variables which can be employed to represent the attitude of the spacecraft. The most common are Euler angles, the direction cosine matrix, and quaternions.\* The kinematic equations describing the attitude may be written as

$$\frac{dp}{dt} = f(p, w)$$

where  $p$  denotes the variables which represent spacecraft attitude and  $w$  denotes the vehicle angular velocity. Euler angles have the advantage that only three parameters are required, and the disadvantage that the vector function  $f(p, w)$  is a transcendental function of  $p$ . The direction cosine matrix and quaternion representation require nine and four parameters respectively, but have the advantage that  $f$  is a linear function of  $p$ .

SPARS employs quaternions to represent the orientation of the body relative to an inertial frame.

\*Quaternions are sometimes called Euler four parameter or Cayley-Klein parameters. The four parameter representation was first derived by Euler before Hamilton developed quaternions.

The reasons for employing quaternions (see References 3 and 4) are:

- $f(p, w)$  is linear in  $p$
- quaternions utilize only four parameters to specify attitude in contrast to nine when direction cosines are used
- the time history of spacecraft attitude is given by the integration of a vector differential equation instead of a matrix differential equation resulting in fewer computations per integration step
- "renormalization" of the quaternions is much more simply accomplished than the corresponding operation for direction cosines. The significance of the renormalization operation will be explained subsequently when the numerical integration of the attitude differential equation is discussed.

An aid to understanding quaternions can be derived from Euler's theorem which states that any sequence of rotations utilized to bring two orthogonal reference frames into coincidence is equivalent to a single rotation about some fixed axis. Let  $\mu(t)$  be the angle of rotation and let  $\alpha(t)$ ,  $\beta(t)$  and  $\gamma(t)$  be the direction cosines defining the fixed axis.

The quaternion elements  $q_i(t)$ ,  $i = 1, 2, 3$ , 4 are

$$\begin{aligned} q_1(t) &= \cos \alpha(t) \sin (\mu(t)/2) \\ q_2(t) &= \cos \beta(t) \sin (\mu(t)/2) \\ q_3(t) &= \cos \gamma(t) \sin (\mu(t)/2) \\ q_4(t) &= \cos (\mu(t)/2) \end{aligned}$$

The quaternion representation of the kinematic equations becomes

$$\frac{dq}{dt} = \frac{1}{2} \Omega q \quad (2)$$

where  $\Omega$  is the skew symmetric matrix

$$\Omega = \begin{bmatrix} 0 & w_3 & -w_2 & w_1 \\ -w_3 & 0 & w_1 & w_2 \\ w_2 & -w_1 & 0 & w_3 \\ -w_1 & -w_2 & -w_3 & 0 \end{bmatrix} \quad (3)$$

and  $w_i$  denotes the spacecraft angular velocity in body coordinates.

The solution of (2) is approximately

$$q(t) = \exp \left[ G(t) \right] q(t_k) \quad (4)$$

where

$$G(t) = \Omega(t_k)(t-t_k) \quad (4)$$

This formulation was an appropriate one to be employed in SPARS since angular increments rather than rates are the outputs of the gyros. The elements of  $G(t)$  are  $w_i(t-t_k)$ , which is the angular change about the  $i$ th body axis during the time interval  $(t_k, t)$  assuming that rates are constant during this interval. For the SPARS application, rates are almost constant except during short attitude control thrusting intervals.

A hierarchy of integration algorithms can be developed by replacing the exponential by its power-series expansion. Such a hierarchy has been constructed by Wilcox (4). In the SPARS application, algorithms of higher than second order generally did not exhibit the accuracy predicted by theoretical analysis. This is because the gyro outputs are quantized and therefore available only to limited accuracy. The accuracy of the second order algorithm can be improved by replacing it by a "modified second order" algorithm as suggested by Wilcox (loc cit). This modified second order algorithm can be expressed by the equation:

$$q(t) = \left[ 1 \left( 1 - \frac{c(t)}{12} \right) + \frac{G(t)}{2} \right] q(t_k) \quad (5)$$

where

$$c(t) = \sum_{i=1}^3 \left[ \int_{t_k}^t w_i(\tau) d\tau \right]^2$$

and  $I$  is the identity matrix. In the development of (5), use has been made of the relation:

$$G(t)^2 = -c(t)I$$

The quaternion produced by the integration algorithm (5) will gradually depart from normality in the sense that the scalar

$$\sum_{i=1}^4 q_i^2(t) \quad (6)$$

will differ from unity as the integration proceeds. This effect can be compensated by periodic renormalization, i.e., by dividing the elements of the quaternion produced by (6) by the scalar (6). By utilizing the properties of quaternion norms it is easy to show that no accuracy is lost by normalization at every  $N$ th step rather than at every step. Therefore the normalization need be undertaken only when attitude information is needed for calculation external to the attitude integration.

The simplicity of the normalization correction for quaternion integration is quite in contrast to the corresponding procedure for direction cosines. Integration of the differential equations for the direction cosine representation of attitude requires not only a periodic renormalization of the rows (or columns) of the direction cosine matrix, but a re-orthogonalization of the rows (or columns).

## VI. FILTER FORMULATION

The actual orientation of the SPARS attitude reference frame differed from the estimate of its orientation produced by the computer because of errors in the initial estimate of attitude and because of drifts in the gyros. The objective of the Kalman filter was to estimate, by a sequence of sightings on selected stars, the attitude error and the bias components of the gyro drift rates producing these errors. Estimation began with initialization of the filter to the current best estimate of the body attitude reference frame and gyro drift biases. This estimate of attitude was propagated to the time of the first star sighting by the integration of the quaternion. At the time of the first star sighting, the estimates of the pitch and roll angles of the line of sight to the star (computed on the basis of the computer's estimate of attitude) were compared with the measured pitch and roll angles. The differences were multiplied by the Kalman filter weighting matrix to produce corrections to the estimates of attitude and gyro drift biases. Utilizing the new estimates of attitude, the attitude quaternion was re-initialized, the gyro outputs were compensated by the new estimates of gyro biases, and the attitude differential equations integrated to the time of the next star sighting where the update procedure followed at the first star sighting was repeated. This procedure continued as long as star sightings were taken.

The usual formulation of a linear filter problem requires a linearization of (2) about the best current estimate of the state. Straightforward application of this technique would result in at least seven state variables: four representing deviations in the elements of the quaternion and three for the gyro drift biases. The filter so designed would have to incorporate a constraint on state variables since the quaternion must have unit norm.

To reduce the dimension of the state vector to six elements and to remove the constraint on the state vector, the very small attitude error was represented by three (infinitesimal) angular rotations  $\psi_1, \psi_2, \psi_3$  about the three body axes.

Let  $\hat{w}_c = (\hat{w}_1, \hat{w}_2, \hat{w}_3)^T$  and  $w_c = (w_1, w_2, w_3)^T$  denote the angular velocities of the computed and true body frames respectively. The circled subscript denotes the frame in which the components are evaluated. The angular velocity of the computed frame in

components along the true axes is

$$\hat{w}_c = w_c + \dot{\psi} \cdot \begin{bmatrix} 1 & -\psi_3 & \psi_2 \\ \psi_3 & 1 & -\psi_1 \\ -\psi_2 & \psi_1 & 1 \end{bmatrix} \begin{bmatrix} \hat{w}_1 \\ \hat{w}_2 \\ \hat{w}_3 \end{bmatrix} \quad (6)$$

Rearrange terms to obtain

$$\begin{bmatrix} \dot{\psi}_1 \\ \dot{\psi}_2 \\ \dot{\psi}_3 \end{bmatrix} \begin{bmatrix} 0 & \hat{w}_3 & -\hat{w}_2 \\ -\hat{w}_3 & 0 & \hat{w}_1 \\ \hat{w}_2 & -\hat{w}_1 & 0 \end{bmatrix} \begin{bmatrix} \psi_1 \\ \psi_2 \\ \psi_3 \end{bmatrix} = \begin{bmatrix} \hat{w}_1 - w_1 \\ \hat{w}_2 - w_2 \\ \hat{w}_3 - w_3 \end{bmatrix}$$

Although the gyros are physically mounted along the true body axes, they sense a combination of true rate  $w$  plus drift  $b$  and noise  $\eta$ ; the computer assigns the sensor outputs in the computed body frame: i. e.,

$$\hat{w}_c = w_c + b_c + \eta_c$$

Assuming gyro drift is constant and their input axes are perfectly aligned to the true body axes we obtain the system equation

$$\frac{d}{dt} \begin{bmatrix} \psi \\ \delta b \end{bmatrix} = \begin{bmatrix} \Omega^* & I \\ 0 & 0 \end{bmatrix} \begin{bmatrix} \psi \\ \delta b \end{bmatrix} + \begin{bmatrix} \eta \\ 0 \end{bmatrix} \quad (7)$$

where  $\Omega^*$  denotes the upper (3x3) submatrix of  $\Omega$  and  $\eta$  denotes gyro or process noise. Additional state variables could be added to include other dynamical biases and instrument biases. (See Section 7.)

The measurements are the roll  $\phi$  and pitch  $\theta$  angles of the line of sight to a star. These pseudo-measurements are the roll and pitch obtained by combining gimbal angle encoder and digital detector readings into equivalent roll and pitch angles of the LOS. The observation errors are related to the state variables by

$$\begin{bmatrix} \delta\phi \\ \delta\theta \end{bmatrix} = \begin{bmatrix} H_1 & 0 \end{bmatrix} \begin{bmatrix} \psi \\ \delta b \end{bmatrix} + v = H \begin{bmatrix} \psi \\ \delta b \end{bmatrix} + v \quad (8)$$

where  $v$  represents the SSA instrument noise. Under suitable conditions on the statistics of the state variables at the initial time, the process noise  $\eta$  and the instrument noise  $v$  we have formulated a canonical linear filter problem in equations (7) and (8). In this formulation, the gyro readings are not considered to be measurements in the usual filter sense since they do not appear in (8). If the dynamical equations of motion describing spacecraft attitude were employed to predict attitude, then gyroscope outputs could be employed as additional "filter" measurements.

## VII. FILTER IMPLEMENTATION

The organization of the SPARS on-board software,

including the attitude filter, is shown in Figure 3. The filter gain matrix computations were based on:

$$W_i = P_i(-) H_i^T [H_i P_i(-) H_i^T + R]^{-1}$$

$$P_i(+) = (I - W_i H_i) P_i(-) (I - W_i H_i)^T + W_i R W_i^T$$

$$P_{i+1}(-) = \Phi(t_{i+1}, t_i) P_i(+) \Phi^T(t_{i+1}, t_i) + Q_i$$

$P(-)$  is the covariance of the state vector immediately before the  $i$ th observation,  $P_i(+)$  is the covariance immediately after the  $i$ th observation.  $H_i$  is the gradient of the  $i$ th pitch and roll observation relative to the filter states,  $R$  is the covariance of the measurement noise,  $Q_i$  is the covariance of the noise accumulated in the interval  $(t_i, t_{i+1})$  due to random gyro noise. Finally,  $\Phi(t_i, t_{i+1})$  is the transition matrix for the state vector.

The Kalman filter estimates a differential correction to the state, i.e.,

$$\begin{bmatrix} \psi(t_i) \\ \delta b(t_i) \end{bmatrix} = W \begin{bmatrix} \tilde{\phi}_i - \hat{\phi}_i \\ \tilde{\theta}_i - \hat{\theta}_i \end{bmatrix}$$

where the tilde denotes measured values and the hat denotes estimates. The estimate  $\psi(t_i)$  is transformed into an update of the quaternion by the formula

$$q(t_i^+) = q(t_i^-) - \frac{1}{2} S(t_i) q(t_i^-)$$

where  $S(t)$  is a skew symmetric matrix having same form as  $\Omega$  with  $w_j$  replaced by  $\psi_j(t_i)$ . It is easily

shown that if  $q(t^-)$  has a unit norm then  $q(t^+)$  also has unit norm. The gyro drift bias is updated by

$$b(b_i^+) = b(b_i^-) + \delta b(t_i).$$

The formula selected for the update of the filter covariance at star observation time differs from the customary formula which is

$$P(t_i^+) = P(t_i^-) - W_i H_i P(t_i^-) = (I - W_i H_i) P(t_i^-)$$

The selected formulation which can be found in many references, e.g., in the text by Bryson and Ho (3) was chosen for implementation in the filter since it is less sensitive to roundoff errors.

### VIII. ERROR MODEL

Errors in the measurements were characterized either as a zero mean independent random sequence or a zero mean random variable. The random sequences combine to form the measurement and process noise errors which were represented in the filter equations by the covariance matrices  $R$  and  $Q$  respectively. Biases were modeled as random variables. Certain bias errors can be included in the filter state. This is discussed further in Section VI of Reference (1).

Bias errors were associated with alignment calibration. SSA alignment errors occurred in the measured (calibrated) alignment of: (1) the pitch and roll gimbal axes ( $\gamma_{RX}, \gamma_{RZ}, \gamma_{PX}, \gamma_{PY}$ ) and (2) telescope (optic) axis with respect to the gimbal axes ( $\gamma_{OY}, \gamma_{OZ}$ );  $\gamma$  denotes the angular orientation. The first subscript refers to either the roll, pitch or optic axis and the second subscript the axis of rotation.

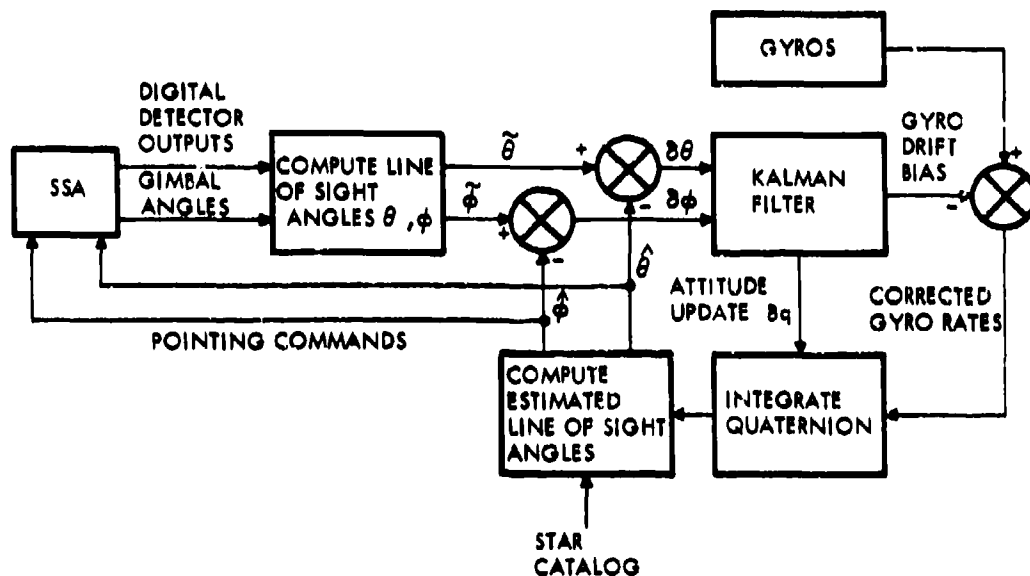


Fig. 3. On-Board Software



The errors consist of: (1) bias error in the instrument alignment and calibration; (2) cyclic error in the modeling of repeatable bearing motion; (3) random error in the form of non-repeatable bearing motion; and (4) thermal and gravity induced bending. SSA thermal bending errors were negligibly small in the controlled laboratory environment. Gravity induced bending in the laboratory was assumed to be negligible except for the roll gimbal. However, test results indicate that this may have been a poor assumption (Reference 1). The X, Y, and Z gyro input axes were not perfectly aligned with the coordinates defined by the IRU optical cube. However, uncertainty in these alignments had negligible effect on SPARS performance.

The noise-like random sequence errors are associated with read-out and fabrication errors. The readout errors include resolution (quantization) and fabrication of the readout devices, the gimbal encoders and the digital detectors. Resolution limitations impose uniformly distributed errors with maxima equal to one-half the magnitude of the least significant bit readout. Fabrication errors arise from imprecision in manufacture and the resultant inaccuracies of extrapolation techniques. Fabrication errors are for the most part repeatable at each readout position. However, the likelihood of a particular readout position recurring with significant frequency during a test run was sufficiently small to allow modeling of fabrication error as a random phenomenon.

The digital detector error model includes: resolution (quantization) and fabrication, servo-induced image motion, and thermal and gravity induced bending of the telescope. Over the long term, the detector quantization error appears to be uniformly distributed with standard deviation of  $QD/\sqrt{12}$ , where  $QD$  is the resolution of the detector, while the normal error due to fabrication has magnitude of  $\sigma_{FO}$ . An additional readout-type error source is imposed on the digital detector by servo-induced image motion across the digital detectors. This image motion results from servo rate following error and high frequency rate oscillation (jitter). The servo errors cause a smear of the star image on the detectors, reducing the signal-to-noise ratio and resulting in a readout of the mean image position. The gimbal encoders are modeled by quantizing the gimbal angle plus fabrication noise. One-half of an encoder bit ( $EW/2$ ) is added (subtracted) to the gimbal encoder reading for positive (negative) gimbal rates to reduce quantization errors. After compensation, the encoder causes errors which over the long term resemble a uniformly-distributed source with a maximum value of  $EW/2$  combined with a normally-distributed source of magnitude  $\sigma_{FE}$  caused by fabrication errors.

Gyro quantization causes a readout error. The IRU is an angle measuring device with readout con-

sisting of a series of pulses each representing an angular rotation about the input axis. The readout error can have a maximum value of one Pulse Weight (PW) and was assumed to be uniformly distributed between 0 and 1 PW.

In addition to readout errors, the gyro outputs are in error due to gyro drift and angular noise in the gyro. Gyro drift was characterized as bias and was included in the filter state; angular gyro noise appears in the filter equations as process noise. Because a statistical description of gyro noise error did not exist, the IRU vendor was requested to perform a series of tests on an experimental version of the SPARS IRU. The data obtained from these tests were used to establish an empirical gyro noise model as described below.

Single channel gyro pulse counts (incremental angles) were accumulated over an interval of time and the total number of pulse counts recorded. This was done for one millisecond and thirty second time intervals. Analysis of the collected data indicates that each gyro channel presents data containing a one sigma error of less than one rebalance pulse. Examination of the data revealed a high correlation between millisecond samples and showed that a second harmonic of reduced magnitude is also present. The correlation function implied a harmonic component with a frequency of approximately 250 Hz. Thus the gyro noise (angle error) was modeled as a sum of a sinusoid and a white gaussian sequence.

The process noise covariance matrix  $Q$  then becomes

$$Q = C^2 \begin{bmatrix} I & 0 \\ 0 & 0 \end{bmatrix}$$

where  $I$  is a  $(3 \times 3)$  identity matrix and  $C$  is the standard deviation of gyro noise.

Small ad hoc terms also were added to each of the six diagonal elements of  $Q$  primarily to increase the elements of  $W$  relating to gyro drift bias updates.

## IX. TEST RESULTS

Static and dynamic laboratory tests are described in Reference (1). Qualitative test results are described in this section and quantitative results in the classified (Secret) appendix to this report.

### A. Convergence/Divergence

The SPARS attitude filter should quickly reduce large initial attitude errors, i.e., demonstrate initial convergence. Additionally, once the error in the attitude estimate converges, it should not exhibit a secular growth as more and more observations are processed by the filter. This section discusses initial convergence and long-term divergence of the

filter. Since there was a comparatively long period between receipt of the IRU and receipt of the SSA, initial convergence and long-term divergence were briefly studied by employing real IRU data and simulated SSA data.

An attitude control system was assumed which slaves the spacecraft to a local vertical/orbit plane coordinate system to within  $\pm 2\frac{1}{4}$  degrees.

Figure 4 shows the convergence of the attitude estimate within about five minutes in the face of initial attitude errors of  $2\frac{1}{4}$  degrees per axis. The first few points are off scale. The dots and asterisks denote respectively the attitude history just before and just after a filter correction.

Long-term divergence of the filter was not fully examined. There were no known significant, unmodeled, dynamical biases, a major cause of filter divergence [6]. It had been demonstrated in the SPARS Phase 0 effort that, if the gyros exhibited a drift component characterized by a random walk process, the filter would diverge if the algorithm assumed the gyro process noise was white. Static gyro test data did not reveal a random walk process. The filter was, however, designed to account for a small random walk component. The filter also employed small ad hoc terms in addition to modeling and random walk to keep the gyro drift components of the filter gain open. Figure 5 shows no apparent tendency of the filter to diverge for 6,300 seconds of operation.

#### B. Extended State Filter

The detailed analysis of SPARS and laboratory errors indicated the desirability of adding more state variables to the filter to reduce the effect of both system and the laboratory errors on measured attitude.

The major unmodeled errors were six SSA and star simulator alignment uncertainties. Provision was made in the test plan to estimate these biases in the SSA dynamic calibration test [1].\* Theoretically these biases are observable. However, simulations showed them to be poorly observable in the comparatively short (twenty-minute) test.

Early testing of the SPARS filter employing six state variables, three representing attitude errors and three representing gyro drift biases, indicated that the unmodeled biases caused attitude errors that were slightly larger than would be predicted by the filter's estimate of the error covariance matrix. This behavior was attributed, at least in part, to the unmodeled alignment biases. Furthermore, it was felt that in orbital flight, calibration or estimation of SSA biases might be required. Therefore, a twelve-state variable SPARS filter was also designed for the laboratory testing.

An analysis showed that only ten of the twelve state variables or linear combinations of the state variable were estimable. The twelve state filter was shown by simulation and error analysis to give modest improvement in attitude over the normal twenty minute laboratory test.

Direct comparison of the six and twelve state filters was made for one test. Actual SSA, gyro and rate table data were recorded from a SPARS dynamic test employing a six state filter. The recorded sensor data was then employed to drive a simulation of the twelve state filter. The mean attitude error over the last fifteen minutes of testing showed an improvement of 33 percent. Using the twelve state filter, a 24 percent improvement in 67 percent point\*\* was noted. Error analyses predicted a more significant improvement for longer tests.

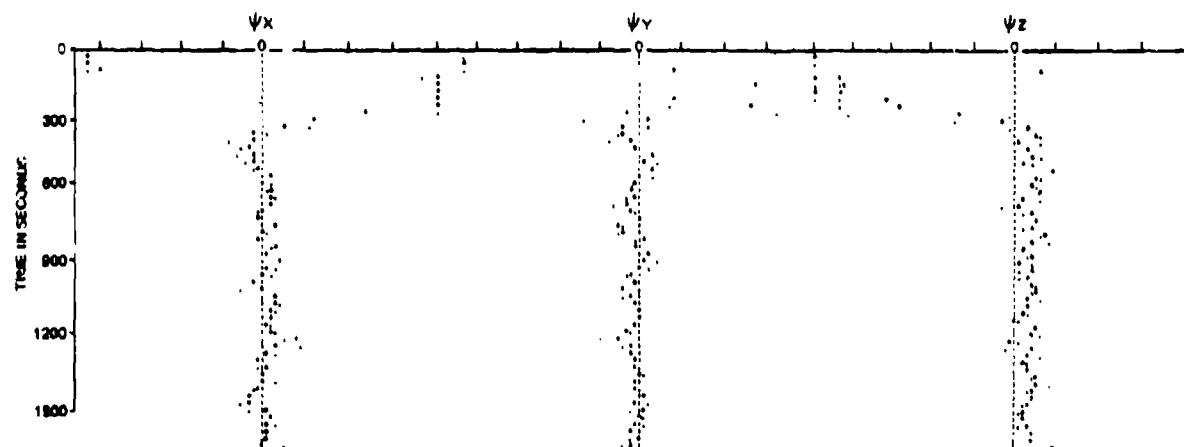


Fig. 4. Convergence from  $2\frac{1}{4}$  Degrees Initial Error

\*A test employing only rate table and SSA data, i.e., no gyro data.

\*\*By definition 67 percent of the measured attitude errors have magnitudes smaller than the 67 percent point.

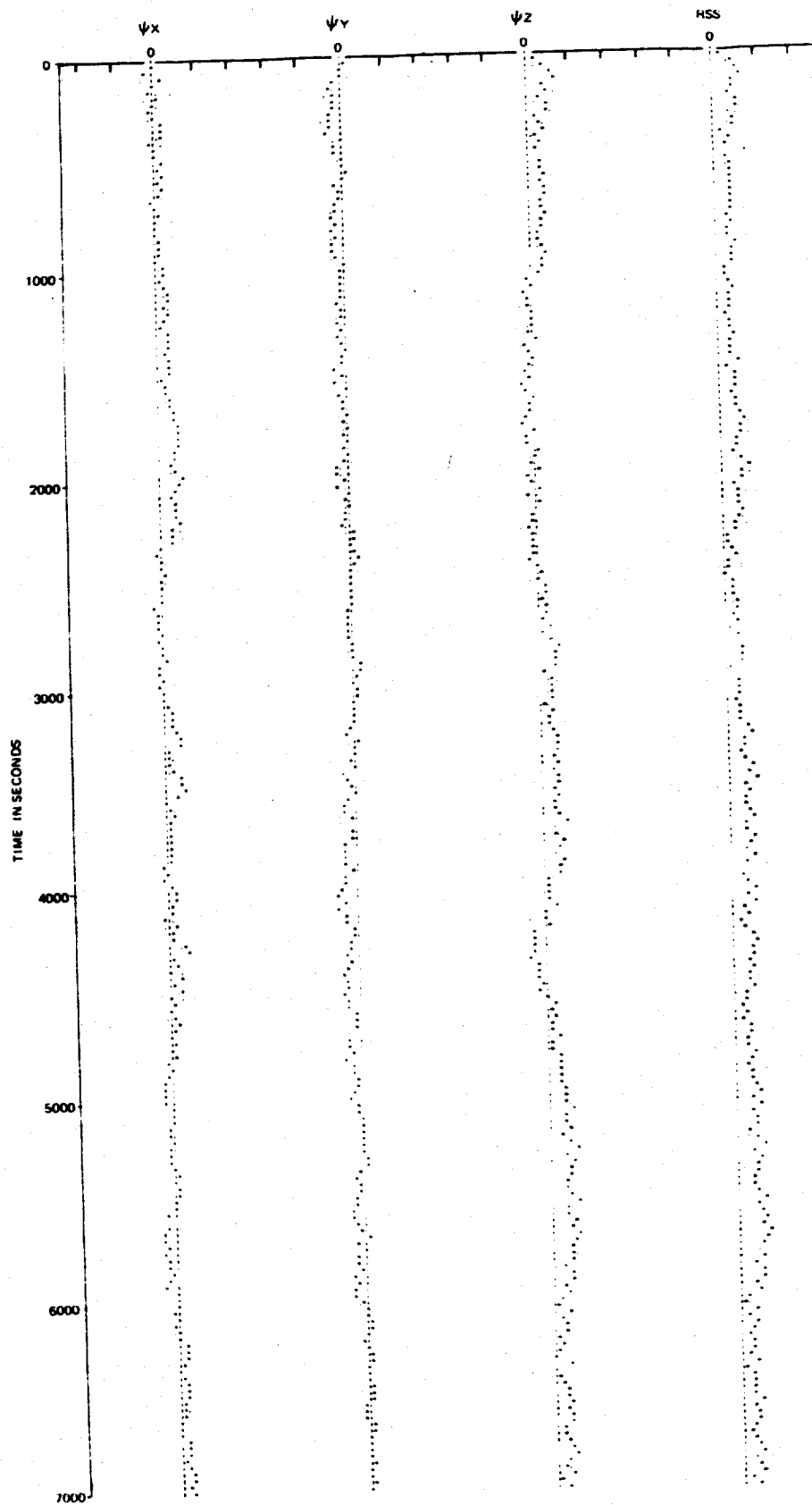


Fig. 5. Long Term Stability of Attitude Accuracy

For orbital applications, no more than 11 state variables would be employed. Due to the unobservability of two state variables the filter could be designed for nine state variables without degrading attitude accuracy.

#### X. CONCLUSIONS

This paper has described the configuration, algorithms and qualitative test results of a precision attitude reference system. Quantitative results are given in the classified (Secret) appendix to this paper.

The outstanding feature of the IBM SPARS design is the use of a gimbale star sensor. The pointing freedom provided by a gimbale star sensor results in a small star catalog consisting only of the brightest and best located stars. With pointing freedom, a star is almost always available and sighting schedules can be adjusted to be as frequent as required to optimize system performance. Furthermore, the gimbale design can use a small telescopic FOV in order to achieve high resolution with moderate size optics.

The gimbale star sensor's ability to point to a star at any desired time is particularly significant during the initial acquisition phase when frequent sightings are desired to estimate attitude and drift rate parameters. Such multiple sightings could be used together with a suboptimal filter which is less sensitive to convergence difficulties than the Kalman filter. One possible technique is the deterministic filter.

#### REFERENCES

- [1] Schloe, F. H., Neilson, G., "Laboratory Checkout and Testing of an Advanced Stellar Inertial Attitude Reference System," Spacecraft Attitude Determination Symposium, Aerospace Corp., El Segundo, Calif., Sept. 30 to Oct. 2, 1969.
- [2] Baum, R., Sheldon, D., "A Precision Strap-down Inertial Reference Unit -- Hardware Mechanization and Test Report," Spacecraft Attitude Determination Symposium, Aerospace Corp., El Segundo Calif., Sept. 30 to Oct. 2, 1969.
- [3] Robinson, A. C., "On the Use of Quaternions in Simulation of Rigid-Body Motion," Wright Air Development Center, USAF, Wright-Patterson AFB, Ohio, Dec. 1968.
- [4] Wilcox, J. C., "A New Algorithm for Strapped-Down Inertial Navigation," IEEE Transactions on Aerospace and Electronic Systems, Vol AES-3, No. 5, Sept. 1967.
- [5] Bryson, A. E., and Ho, Y. C., "Applied Optimal Control," Blaisdell Publishing Company, pp. 364, 1969.
- [6] Schlee, F. H., Standish, C. J., Toda, N. F., "Divergence in the Kalman Filter," ALAA Journal, Vol. 5, No. 6, June 1967.

(U) LABORATORY CHECKOUT AND TESTING OF AN  
ADVANCED STELLAR INERTIAL ATTITUDE REFERENCE SYSTEM

F. H. Schlee and G. Neilson  
IBM Federal Systems Division  
Owego, New York

ABSTRACT

An advanced state-of-the-art stellar inertial attitude reference system has undergone laboratory testing by the IBM Federal Systems Division for the Space Precision Attitude Reference System (SPARS) program. Discussed in this paper are the test laboratory configuration and the test sequence. The system tested consisted of a gimballed star tracker, a three-gyro strapped-down inertial reference unit, and associated data processing.

A hierarchy of tests was performed upon the system and laboratory devices taken individually and also in combination. This sequence of tests was designed to isolate component and interface problems at the earliest possible time. Tests proceeded from simple functional checkouts to increasingly complex tests which exercised more and more of the complete SPARS/LABORATORY system and which more closely resembled the final SPARS system test.

A short time schedule coupled with a sequential delivery of hardware required a flexible test philosophy in which special purpose tests were configured as subclasses of the final SPARS system test.

This paper also discusses the laboratory instrumentation for calibration and alignment and its related monitoring activities. Laboratory facilities developed for these tests demonstrated short time stabilities of one and one-half arc seconds and long time alignment stabilities of approximately ten arc seconds.\*

1. INTRODUCTION

The IBM SPARS Laboratory was specifically designed to test the attitude reference system of the SPARS. This system consisted of a gimballed star sensor and strapped down inertial reference unit mounted to a common base plate. The SPARS system was designed to estimate the inertial attitude of a satellite in an earth orbit. The satellite was to contain an independent attitude reference and control system maintaining the satellite in a rough local vertical orientation. The purpose of the SPARS system was to refine the knowledge of alignment beyond the initial two and one half degree alignment accuracy provided by the spacecraft attitude control system.

The laboratory test of the SPARS was designed to prove the system concept. A prototype star sensor assembly and inertial reference unit were mounted to

a common baseplate and tested in a benign environment. The baseplate was mounted on a rate table which rotated past a set of fixed star simulators at a rotational rate characteristic of a low earth orbit. Superimposed on this orbit rate was a limit cycle simulating the effects of the vehicle attitude control system.

The star simulators were placed at fixed orientations relative to the rate table, and the SPARS star sensor assembly was made to slew from star to star following a realistic star pointing schedule. Vibrational and thermal disturbances were minimized; no stray light effects characteristic of sun, moon, or earth corona were simulated.

The test was designed to show the accuracy of the system under steady state conditions, that is, the

\* Design characteristics of the SPARS software, the Star Sensor, and the Inertial Reference Unit (IRU) and test data are given by N. F. Toda, et al., Reference (1).

accuracy that could be achieved once the initial attitude error had been reduced to a level near the steady state operating condition. Thus, the testing did not include search and acquisition of stars.

The principal items of laboratory equipment were a rate table and a set of four star simulators. The purpose of the rate table was twofold: first, to rotate the SPARS at orbital rate past the set of fixed star simulators, and second, to provide a measure of the angle through which the SPARS had been rotated. This angular read-out of the rate table was used to generate a laboratory measurement of the SPARS attitude, which is the measured direction cosine matrix relating a coordinate frame fixed to the SPARS baseplate to a laboratory fixed coordinate frame. These two coordinate frames were referred to as body and laboratory axes, respectively. The measured attitude was then compared with the attitude as computed by the SPARS system. The difference between these two attitudes was the measured SPARS attitude error. This measured attitude error contained both laboratory errors and SPARS errors. That is, the laboratory misalignment and rate table readout errors contributed to the measurement of the SPARS errors. The effects of constant and slowly varying misalignments were minimized by periodic calibrations of the laboratory instrumentation. However, short term instabilities and noise-like errors did affect the tests. These effects were additive and caused the test data presented in the appendix to Reference (1) to be a pessimistic measure of SPARS performance.

The SPARS attitude reference system measured the inertial rate of the baseplate using an Inertial Reference Unit (IRU) containing three orthogonally mounted gyroscopes. The system also measured the orientation of the star line of sight relative to the baseplate using a Star Sensor Assembly (SSA). The basic principle used to estimate attitude was to compare the star line of sight measured by the SSA with an estimated line of sight. The latter was based upon a known orientation of the star line of sight and the current estimate of system attitude. Residual differences between the observed line of sight and the computed line of sight were input to a filter which corrected attitude and attitude rate parameters so as to better fit these line of sight differences. This process relied on tracking a known star, i.e., a star whose line of sight orientation was known in some suitable reference frame.

Errors in the calibration of the star simulator orientation caused errors in the SPARS attitude and for a single star sighting had the same effect upon system performance as an error in the rate table orientation. Rate table readout error had an additive effect upon system accuracy. Thus, the prime goal of the laboratory configuration was to provide a stable and accurately measurable orientation of the star simulators relative to the rate table. A stable and uniform rate table rotation readout was needed so that the

motion of the SPARS relative to the star simulators could be accurately modeled and accurately measured.

The inertial reference unit measurement of attitude rate served the function of an attitude memory and enabled the SPARS to combine many line of sight measurements into an accurate measurement of system attitude and attitude rate.

The rate table and star simulators were mounted upon a reinforced concrete pier isolated from ground vibration by pneumatic (air pad) supports. Numerous optical devices were used to monitor alignment of the entire laboratory setup.

Data processing was performed by a remotely located IBM 7094 computer which executed the SPARS attitude estimation and sensor pointing functions. In an operational case these estimation and star sensor pointing functions would be performed by an on-board computer. Test consoles for the inertial reference unit and star sensor components and also data adapters were located in the laboratory chamber proper. Two IBM 7094 computers were available; either one could be used to control the laboratory test. Except for turn-on of equipment, these dynamic tests were entirely under the control of the digital computer. Data processing was performed in real time and recorded on tape. Offline processing of this tape generated printouts and plots of system and component performance.

## II. TEST DESIGN

Four types of tests were performed to verify that the star sensor assembly, the inertial reference unit, and laboratory test equipment performance met design specifications:

- Laboratory test equipment certification
- IRU functional, static, and dynamic tests
- Star sensor functional, static, and dynamic tests
- Integrated SPARS test

Details of laboratory equipment, alignment, and testing are given in Section III. Sections IV through VI describe the IRU and SSA tests and the final SPARS system test. Dynamic tests are further divided into open loop and closed loop tests. Closed loop implies that a Kalman filter was used to process line-of-sight residuals into improved estimates of attitude and bias parameters. Open loop implies that no filter was used. The purpose of the open loop tests was to ascertain the effectiveness of previous calibration procedures. Open loop tests were better for this purpose than closed loop tests because the action of a

Kalman filter continuously correcting attitude and bias parameters masked the effects of misalignments or gyro drift biases or other random system fluctuations.

Two types of closed loop dynamic tests were planned for both the SSA and the IRU:

- Dynamic Calibration
- Dynamic Sensitivity

The Dynamic Calibration tests were designed primarily to calibrate a single component, either IRU or SSA, in a dynamic environment which matched the subsequent SPARS test. These tests had the secondary goal of debugging the real time interfaces between the subsystem and the real time test control program. Dynamic Sensitivity tests were designed to show the sensitivity of the SPARS performance to the errors of one subsystem. The SSA Dynamic Sensitivity test used a real SSA mounted on the moving rate table but used simulated IRU data. The IRU Dynamic Sensitivity test used real IRU data but simulated SSA data. In both cases, the simulated data was computed from rate table angle and angular rate data.

Dynamic tests were scheduled to be performed for the IRU first and the SSA second in the following order:

1. Closed loop dynamic calibration
2. Open loop
3. Closed loop dynamic sensitivity

This sequential approach was motivated by the subsystem delivery schedule and the short time available between delivery and the demonstration of the full SPARS system test. By employing simulated SSA data in the IRU dynamic tests, it was possible to debug real time computer programs and test procedures. The SSA dynamic tests permitted greater error isolation by not using data from the IRU. In addition to studying the effects of gyro noise models, the IRU Dynamic Sensitivity test was designed to give an indication of anticipated system performance well before delivery of the SSA.

The SSA Dynamic Calibration test was also designed to calibrate a group of SSA and laboratory calibration parameters. This end-to-end calibration under dynamic conditions was considered vital for the success of the full SPARS test because preliminary error analyses indicated that laboratory calibrations and alignments could contribute significant error to the SPARS test performance.

All of these tests were not actually performed in the IBM-SPARS effort for reasons discussed in sections IV and V. They are included here for their possible application to other related test programs.

### III. LABORATORY CONFIGURATION

The SPARS laboratory, shown in Figure 1, was situated in a 30 by 30 foot single-floored building separated from the main engineering buildings by about 10 feet and located about 75 feet from the computer complex. The SPARS equipment was surrounded by the optical test equipment mounted on concrete and steel structures referenced to the common pier. Associated electronics and a data adapter were mounted separate from the pier on a raised floor. Prior to erection of the equipment in the room, the entire wall and ceiling area was covered with an insulated dry wall finished with a low reflectivity black paint.

A dropped ceiling with perforated panels served as a pressurized distribution plenum providing a laminar down flow from the ceiling to the return grills located at floor level along the walls. Equipment cooling was accomplished through insulated ducts providing closed loops independent from the room air system. However, despite all the precautions taken to assure a minimum of air currents in the room, individual shrouding was required for most of the alignment optical paths.

#### A. Stable Pier

Since the task involved high precision optical alignments and measurements, the SPARS experiment was conducted on an isolated pier measuring 21 feet long, 12 feet wide, and 2 feet thick. The pier was a welded steel structure encased in concrete and floated on 10 pneumatic isolation mounts supported directly by the reinforced concrete floor poured on the shale rock stratum. The pier attitude was servo controlled from three sensors measuring pier attitude in relation to the floor at three strategic points under the pier. An indication of the sensitivity of the pier suspension system was demonstrated by a firm finger pressure impulse on the pier causing a momentary change in attitude of up to one minute of arc followed by 1 cycle per second oscillations gradually decreasing in amplitude.

Adjustments on the pneumatic servo valves permitted releveling of the pier to compensate for attitude changes caused by shifting or addition of equipment weight on the pier. A catwalk, straddling the pier, permitted access to the pier-mounted equipment without introducing attitude transients.

#### B. Pier Monitoring

The SPARS test was conducted less than four months after the concrete pier was poured and pier aging effects were expected. Moreover, since the ability of the isolation system to maintain and return to a constant attitude also was an unknown parameter, two pier monitoring systems were implemented. One system was a long-term manual system consisting of

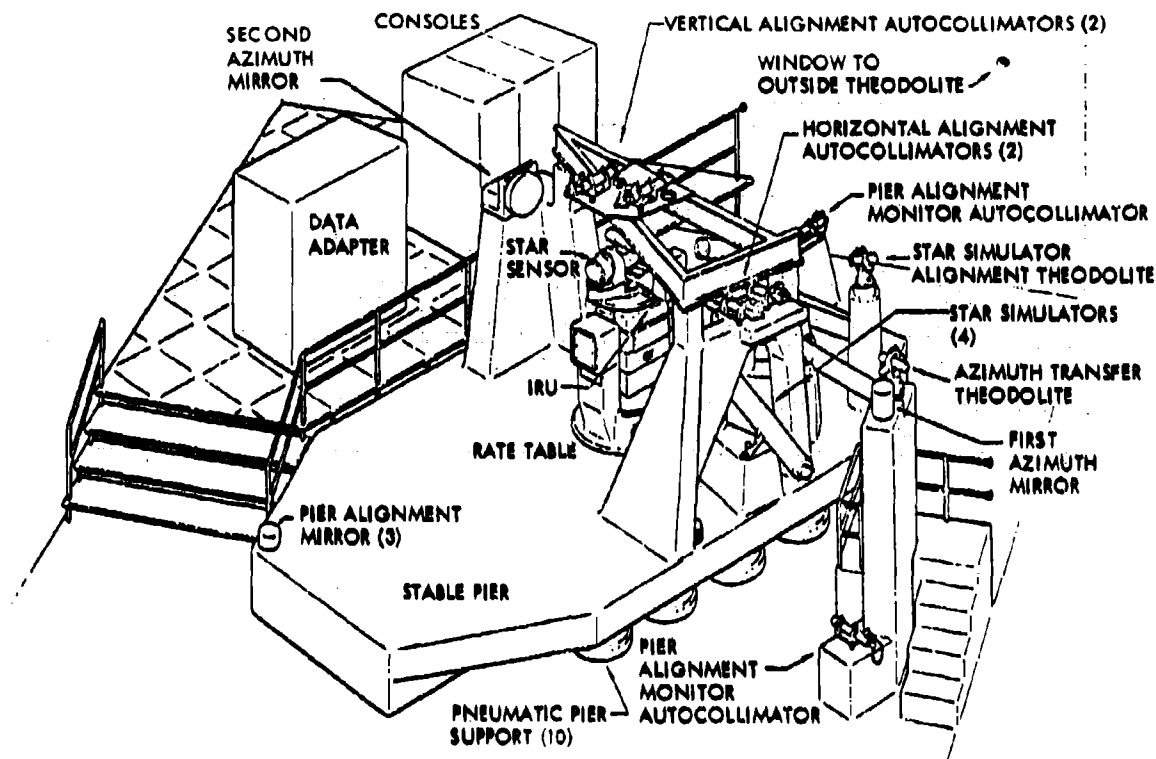


Fig. 1. SPARS Test Set Up

two auto collimators mounted on individual concrete pillars poured directly on the shale sub-base. The collimators were mounted horizontally at right angles to each other and in line with three mirrors mounted permanently to the pier. Two of the mirrors were at opposite ends in the long direction of the pier and, through a split collimator field, they provided pier azimuth as well as pier tilt and bending about the short axis. The third mirror mounted at the middle of the front long side provided tilt about the long axis plus redundant azimuth information. Pier bending as well as a gradual tilting of the pier in the order of five arc seconds per three weeks was experienced. The mean azimuth orientation changed back and forth a few arc seconds. No provisions were made for monitoring the auto collimators; their individual pillars and mountings were assumed to be fixed references. The standard deviation for the collimator readings was .16 arc second.

The second monitoring system was short term but automatic, consisting of a two axis automatic autocollimator receiving reflected light from a mercury pool mounted adjacent to one of the manual auto collimators. A fixture forming an integral part of the isolated pier positioned the automatic auto collimator one inch above the mercury surface, and the instantaneous two-axis attitude information was continuously recorded during the experiments. A random motion of  $\pm 1.5$  arc seconds represented the daily attitude motion of the iso-

lated pier. However, IRU calibration tests, which were sensitive to high frequency instability of the pier, indicated that pier motion during the test was considerably less than 1.5 arc seconds.

### C. North Reference

Proper compensation of the IRU output required a knowledge of its orientation in relation to north. This was obtained in two steps. The first step involved transferring north information from Polaris to a 18-inch diameter mirror called the second azimuth mirror mounted on a concrete pedestal grouted to the pier. A transfer mirror, called the first azimuth mirror, was used to establish the reference between polaris and the room, and for the subsequent transfer from the room to the pier.

For Polaris observations, a theodolite was mounted on a concrete pillar outside the lab and an external reference mark two miles away facilitated observations as prescribed in the manual of Geodetic Astronomy, special publications Number 237.

The theodolite station was protected from weather and ambient light by a small shelter. An asbestos pipe shrouded the optical path from the shelter into the first azimuth mirror. Airflow and consequent image jitter was reduced by a pellicle mounted at the inside end of the pipe.



The second step involved transferring the north reference from the second azimuth mirror to the IRU alignment cube. This was accomplished by an autocollimator mounted on a concrete structure and positioned perpendicularly to the second azimuth mirror and in line with the cube. The autocollimator was aligned and calibrated with the rate table turned to a position permitting a clear line of sight to the 16 inch mirror. A parallel path was provided by a second autocollimator used in a similar manner for establishing the orientation of the SSA alignment cube in relation to North.

Sightings on Polaris were made on three different evenings with a total of 32 sightings resulting in a standard deviation of the North angle in relation to the first azimuth mirror of  $\sigma = 2.24$  arc seconds. Transferring of the North angle from the first azimuth mirror to the second azimuth mirror was performed shortly after the equipment was assembled and a total of 12 transfer checks were made. The standard deviation for azimuth transfers was  $\sigma = .66$  arc second.

A reading from the rate table, after it had been adjusted to provide parallelism between the IRU cube and second azimuth mirror, represented the north reference angle, and the IRU collimator reading established the relative azimuth angle between the two cubes. The standard deviation of the measurements from the second azimuth mirror to the cubes including the rate table setting was  $\sigma = .28$  arc second.

#### D. Rate Table

The IRU and SSA were rotated at controlled rates about the local vertical by an air-bearing rate table whose adjustable base was grouted to the isolated pier. A stress-relieved precision-machined casting, mounted directly to the rate table top, served as the mounting base for the IRU and SSA. Pins and sloped surfaces were used for registration and the units were mounted in a fixed manner to form an integral part of the rate table top. Information on their relative position was obtained from the optical alignment cubes as described earlier. Rate table air-bearing performance depended on a balanced load achieved by careful counterbalancing. Vertical alignment was monitored with an automatic autocollimator mounted to the overhead structure above the rate table axis. See Figure 1. This autocollimator was zero calibrated against a mercury pool which was positioned during the calibration mode on a three point adjustable mirror mounted on a fixture above the SPARS equipment. Proper adjustment of three variables: rate table vertical adjustment, counterweights, and the adjustable mirror resulted in a maximum total runout from the local vertical of one arc second. A firm finger pressure at the edge of the table introduced a transient in the order of one arc second. This deflection was minimized by special handling of the cables connecting the SPARS and the data adapter. Use of springs would have further re-

duced disturbance torques upon the rate table. Rate table angle readouts were calibrated by mounting a high accuracy angle divider on the table and counter-rotating the divider to the same angular values as were commanded to the rate table. An autocollimator null sensor was used to determine the return to zero comparison of rate table and angle divider readouts. This was done in one-degree increments. Rate error was measured by two methods. One method utilized the rate table electronics and compared time intervals between one degree readout pulses when driving at a constant rate. The other method utilized the measured angular errors between successive one-degree increments and divided this by the average time for the given rate.

The results of the tests were:

- Maximum peak-to-peak azimuth error =  $+0.55$  arc sec,  $-0.65$  arc sec
- Worst case rate error = 0.02 percent

The rate table was driven at a nominal 16 earth rates. Vehicle limit cycle effects were included by switching from 15 to 17 earth rates thereby simulating a  $\pm 15$  arc second per second limit cycle.

#### E. Star Simulators

A simulated star field was produced by four star simulators aligned in relation to the local vertical and north. In order to minimize motion on the cables leading to the rate table mounted units, distribution was kept within a horizontal sector of  $110^\circ$ . The tracking time for each star was optimized by placing the stars at  $120^\circ$  down from the vertical. The Star Simulator had a 5.5 inch, diffraction limited refractive objective. The spectral bandwidth was fixed, ranging from  $.82\mu$  to  $1.0\mu$  and peaking at  $.85\mu$ . The objective was achromatized for 5893, 8521, and 10140A. A constant current DC power supply energizer, a ribbon filament lamp, and a condenser relay lens superimposed the ribbon image on a .0007 inch diameter pinhole. The angular subtense was 2.5 arc seconds and counter rotating neutral wedges facilitated adjustment of the simulated stars to calibrated star magnitudes.

Concrete pedestals grouted to the pier served as the fixed base for the stars and threaded studs permitted alignment in azimuth and elevation. Critical alignment of the stars was not required, however knowledge of their final position was important and was obtained by multiple surveys using the theodolite mounted on the rate table. Because of isolation pier effects, the theodolite bubble readings were ignored and zero position was established by autocollimation off the second azimuth mirror. The theodolite was read in direct as well as plunged positions and the rate table was rotated in  $90^\circ$  intervals while the theodolite

was counter rotated. Multiple readings were made at three different times. Each time the standard deviation for star azimuth in relation to azimuth mirror number one and elevation angle in relation to rate table axis was 1.5 arc seconds. However, mean star position readings taken six weeks apart indicated that stars had shifted randomly on the order of 10 arc seconds. SSA Dynamic Calibration data indicated shifts on the order of 4 arc seconds in a one-week period. These shifts were attributed to a combination of pier warping, star simulator alignment instability, and possibly internal instability of the star simulator.

#### IV. TEST PLAN

This section discusses the test plan outlined in Figure 2. Functional tests were primarily checks of system operability while static tests were used to calibrate certain aspects of subsystem performance. The SSA and IRU dynamic tests had the same purpose as the static tests, but were more like the SPARS test in their operational environment since they exercised the IRU or the SSA at operational rates and angles and processed data using filters which were similar to the SPARS attitude filter. The dynamic tests aided in validating the SPARS filter software particularly in the checkout of sensor data handling techniques and system interfaces.

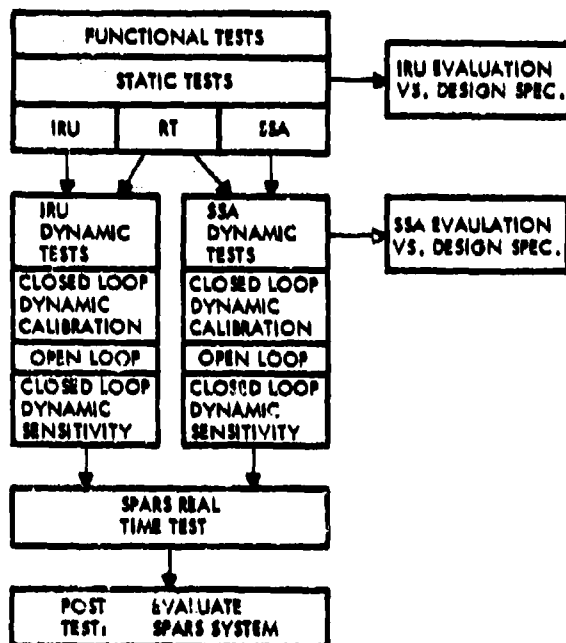


Fig. 2. Test Sequence

The goal of the SPARS laboratory tests was to demonstrate the attitude estimation accuracy of the SPARS which included both hardware (gyros and star sensor) and software (the SPARS algorithm). Attitude accuracy had been interpreted to mean a statistical meas-

ure of the difference between attitude as measured by the SPARS generated quaternion and attitude as measured by the laboratory instrumentation. The precise criteria used in this evaluation are discussed in Section VIII.

#### A. Functional Tests

The functional tests were only intended to be a receiving and inspection test on the SSA and IRU. These abbreviated tests were performed upon receipt from the vendor's facility and were designed to exercise all subsystem elements.

#### B. SSA Functional Tests

The functional tests were required to check that the SSA Gimbal Telescope Assembly, SSA digital detector, and the SSA Electronics Cabinet were operational. These tests were performed upon receipt of the SSA and its associated test equipment. The tests were performed manually to evaluate the operational readiness of the SSA and not to check against precise specifications. After these items proved to be operational, the SSA was integrated with the data adaptor and again functionally exercised, this time under computer control, using the diagnostic programs.

#### C. IRU Functional Tests

The purpose of these tests were: to validate the IRU, and IRU console status; to calibrate the gyro scale factor; and to determine scale factor linearity. The tests were performed upon initial integration in the SPARS laboratory and as a diagnostic checkout. The tests required the IRU console, test cable, standard laboratory equipment and a high accuracy angle indicator to allow positioning of the IRU in the vertical plane. After a visual inspection, the power-up sequence was checked and signal characteristics verified to and from the unit. A calibration of the gyro followed with data being recorded for conditions of: (1) X-axis up, (2) X-axis down, (3) Y-axis up, (4) Y-axis down and (5) Z-axis up.

Rotation rates from three degrees per second up to five times earth rate were used in the determination of gyro scale factor and linearity. These tests were performed manually and the data was reduced using an algorithm supplied by the IRU vendor. After the IRU proved to be functional and the results obtained were comparable to those of the vendor, the unit was integrated with the data adaptor and functionally exercised under computer control using diagnostic programs.

#### V. STATIC AND CALIBRATION TESTS

The SSA static tests and IRU calibration tests were intended to check the performance and accuracy of each device while it was mounted on the rate table in

## VI. DYNAMIC TESTS

The dynamic tests were intended to evaluate the performance and accuracy of the SSA and IRU separately and in combination (SPARS). These tests were intended to provide confidence in the performance evaluation of the respective units as viewed from a system level.

### A. IRU Dynamic Tests

The IRU Dynamic Calibration test organization is sketched in Figure 3. In this case, the IRU was mounted on a rotating rate table and gyro pulse counts were processed into estimates of the three axis system attitude and the three gyro drift biases. The purpose of this test was to generate gyro drift bias estimates in a dynamic environment. Note that in dynamic tests, rate table speed errors caused the same effect as the vertical gyro drift bias and could only be distinguished using an independent source of data such as the static gyro calibration.

The IRU Open Loop test was simply a Dynamic Calibration test without the filter. Such a test is a better indication of gyro drift stability than the Dynamic Calibration test in which the Kalman filter is continuously adjusting attitude and drift rate compensation parameters.

The IRU Dynamic Sensitivity test was similar to the Dynamic Calibration test; the same filter was used; however, the treatment of rate table data was different. Instead of simply comparing gyro derived attitude with rate table derived attitude, as is done in calibration, the sensitivity test used rate table data to simulate the noisy outputs of the star sensor. These simulated star sensor outputs were then processed in the same way as real star sensor data would have been processed in a full SPARS test. The IRU Dynamic Sensitivity test was, in effect, a SPARS test with a simulated star sensor.

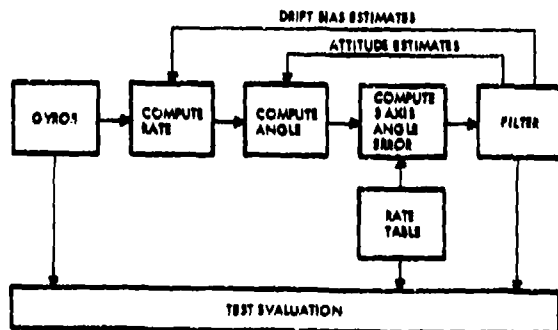


Fig. 3. IRU Dynamic Calibration Test

### B. SSA Dynamic Test

The SSA Dynamic Calibration test provided an

SSA and laboratory calibration carried out under a realistic dynamic environment. That is, the rate table was turning and the SSA was following a realistic star sighting schedule. Figure 4 shows the top level organization of the SSA Dynamic Calibration test. Rate Table data updated by filter corrections was used to generate SSA pointing commands. The Kalman filter updated a group of laboratory alignment errors and SSA alignment errors. The purpose in estimating these errors was to calibrate the SSA and the laboratory in order to reduce the effect of such errors upon the SPARS test.

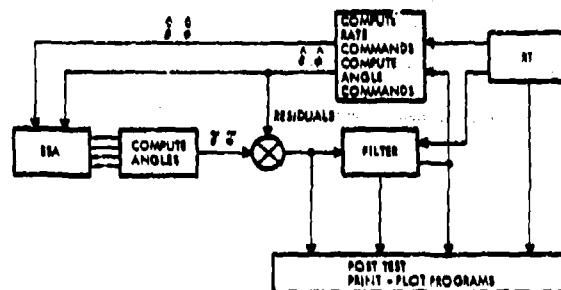


Fig. 4. SSA Dynamic Calibration

Analysis of the SSA Calibration test indicated that the following nine parameters were observable or estimatable from a single star sighting:

1.  $\psi X$  - X component of attitude error
2.  $\psi Y$  - Y component of attitude error
3.  $\psi Z$  - Z component of attitude error
4.  $\gamma BY + \gamma PY$  - Y component of base plate to rate table misalignment plus Y component of SSA pitch axis misalignment.
5.  $\gamma BX + \gamma RX$  - X component of baseplate to rate table misalignment plus X component of SSA roll axis misalignment.
6.  $\gamma PX$  - X component of SSA pitch axis misalignment
7.  $\gamma OY$  - Y component of SSA optic axis misalignment
8.  $\gamma OZ$  - Z component of SSA optic axis misalignment star
9.  $\delta v$  - Simulator azimuth difference.

The ninth parameter was the difference in azimuth between the two star simulators which were currently being tracked. Star schedules used in this test involved alternating between stars one and three during the first

the SPARS laboratory. However, due to the compressed SSA test schedule, the SSA Gimbal and Servo tests were deleted and the associated computer programs were not generated. Instead, the diagnostic program was used with an increased number of star sightings and longer run time to generate SSA static test data.

#### A. SSA Static Tests

The basic SSA static tests consisted of:

- Gimbal Test
- Servo Test
- Mapping Test

#### B. SSA Gimbal Test

This test was designed to ascertain gimbaling integration and accuracy. The SSA was to be mounted on the rate table at a precisely known position. With gimbal rate command at zero, the proper gimbal position command would be sent to the SSA to drive the telescope to the target star simulator. After the SSA had indicated star presence, the gimbal and digital detector readouts were to be read. Several passes would be made and the mean value of pitch and roll gimbal angles for each star would be computed. The LOS to each star simulator would be determined by the mean values of pitch and roll and then compared to the known orientation of each star simulator. The star separation determined from SSA measurement would be compared to the known separation. This procedure would be repeated for several precisely known rate table positions.

#### C. SSA Servo Test

The purpose of this test was to determine the capability and accuracy of the SSA servo in response to a fixed rate command. This test also required the SSA to be mounted on a stationary rate table. The SSA would be driven to some arbitrary position near its gimbal limits via a computer gimbal angle position command with the gimbal rate commands at zero. When the SSA was settled into the command position, the computer would issue a gimbal rate command. After allowing a period for the SSA servo to accelerate to the command rate, a sequence of gimbal position readings would be taken and time tagged. From this data, the actual servo rate would be determined and compared to the commanded rate.

#### D. SSA Mapping Test

A so-called mapping test was performed to determine whether there were any areas in the gray-coded digital devices which were of degraded accuracy. These tests were performed by initially aligning the

star sensor upon a star simulator so that a zero digital reading was measured. One gimbal at a time was then moved by small angular increments. At each increment both gimbal angle and digital outputs were recorded. These recorded values were then compared; differences in the digital reading and the gimbal angle increment were ascribed to errors in the gray-coded digital device. This test was performed for both the pitch and the roll axes.

#### E. IRU Calibration Tests

The purpose of the IRU tests was to give confidence and a data base for the IRU and SPARS dynamic test software and procedures. A stationary rate table allowed integration, checkout, and debugging of the SPARS/IRU software and hardware interface in an environment which minimized the number of error sources and equipment synchronization problems.

This test also was used to isolate and evaluate the effect of IRU and test equipment error sources on the SPARS filter performance. These include:

- Gyro bias errors
- Gyro Moding (high frequency noise)
- Filter Convergence from error in initial attitude angle and rate
- Pier motion

In this test the IRU was mounted on a stationary rate table positioned to one of the four cardinal positions or to the initial starting position for the SPARS test. IRU outputs were then compared with the static rate table position to determine attitude error. Drift rate was determined from attitude error and time measurements. The drift rate measured by this test was the drift rate of the gyro plus a small error due to software and integration errors.

Data for this test was stored on magnetic tape and processed off line (non-real time) by a Data Analysis Program. The IRU static test utilized the IRU Dynamic Calibration Program initialized for a static case. Data exchange occurred through the data adapter under control of the IBM 7094 computer and was stored on tape. The IRU Data Analysis Program then processed the data off-line allowing a common set of data to be processed by various gyro and filter models. The Data Analysis Program computed the estimates of gyro drift rate by comparing the attitude rate of change as determined by the Kalman filter with the attitude rate of change estimates found from rate table data. An average of RMS drift rate errors was computed for each of the gyro channels.

half of the test and alternating between stars two and four during the second half of the test. Updates in these nine parameters were used to update 11 parameters as follows:

$$(\gamma_{BY})_{i+1} = (\gamma_{BY})_i + 1/2 \delta (\gamma_{BY} + \gamma_{PY})$$

$$(\gamma_{PY})_{i+1} = (\gamma_{PY})_i + 1/2 \delta (\gamma_{BY} + \gamma_{PY})$$

$$(\gamma_{BX})_{i+1} = (\gamma_{BX})_i + 1/2 \delta (\gamma_{BX} + \gamma_{RX})$$

$$(\gamma_{RX})_{i+1} = (\gamma_{RX})_i + 1/2 \delta (\gamma_{BX} + \gamma_{RX})$$

$$(\gamma_{PX})_{i+1} = (\gamma_{PX})_i + \delta \gamma_{PX}$$

$$(\gamma_{OY})_{i+1} = (\gamma_{OY})_i + \delta \gamma_{OY}$$

$$(\gamma_{OZ})_{i+1} = (\gamma_{OZ})_i + \delta \gamma_{OZ}$$

$$(\nu_j)_{i+1} = (\nu_j)_i + \delta \nu_j \quad (i \text{ is the number of observations})$$

$$j = 1, 2, 3, 4$$

where

$$\begin{aligned} \delta \nu_1 &= + \delta \nu & \text{When star simulator 1} \\ & & \text{provides the update} \\ & & \text{data.} \\ \delta \nu_3 &= - \delta \nu \end{aligned}$$

and

$$\begin{aligned} \delta \nu_1 &= - \delta \nu & \text{When the update is de-} \\ & & \text{rived from tracking star} \\ & & \text{simulator 3.} \\ \delta \nu_3 &= + \delta \nu \end{aligned}$$

$$\begin{aligned} \delta \nu_2 &= + \delta \nu & \text{When star simulator 2} \\ & & \text{provides the update} \\ & & \text{data.} \\ \delta \nu_4 &= - \delta \nu \end{aligned}$$

$$\begin{aligned} \delta \nu_2 &= - \delta \nu & \text{When star simulator 4} \\ & & \text{provides the update} \\ & & \text{data.} \\ \delta \nu_4 &= + \delta \nu \end{aligned}$$

The updated estimates of attitude  $\psi_X$ ,  $\psi_Y$ ,  $\psi_Z$  also were used to correct star simulator position. These attitude estimates were derived from a sequence of star sightings in which rate table misalignments were indistinguishable from a rotation of the star pairs, i.e., a rotation of stars one and three for the first half of the test and a rotation of stars two and four for the second half of the test. It was decided to apply the information contained in the estimates of  $\psi_X$ ,  $\psi_Y$ ,  $\psi_Z$  to correcting the estimated star simulator azimuth and elevation angles. These corrections were, as suggested above, effectively a rotation of the star pairs. With the addition of four star simulator elevation angles, the total number of parameters calibrated in the SSA Dynamic Calibration became 15.

The Open Loop SSA test differed from the Dynamic Calibration SSA test by virtue of not using a filter. It

did, however, use the best estimates of bias errors generated in preceding SSA Dynamic Calibration. Note that both the Closed Loop Dynamic Calibration and the Open Loop SSA tests used rate table data to compute an essentially error-free attitude and attitude rate. The pitch and roll line of sight residuals were then due only to SSA misalignments, SSA random fluctuations, and star simulator misalignments. (Rate table misalignments were indistinguishable from star simulator misalignments; rate table read out errors were small). A Kalman filter acted upon observed pitch and roll residuals and attempted to adjust the set of state variables so as to minimize the observed residuals. To evaluate the SSA itself, the filter was deactivated and uncompensated pitch and roll residuals were analyzed. This was the SSA Open Loop test. It was performed after a series of SSA Dynamic Calibration tests in order to minimize the effect of all observable bias errors.

The Closed Loop Dynamic Sensitivity SSA test was similar to the Dynamic Calibration in that the rate table data updated by a Kalman filter was used to point the SSA. However, the filter in this case was the regular SPARS filter rather than the special purpose SSA Dynamic Calibration filter which was specifically designed to calibrate laboratory and SSA bias errors. Another difference is that rate table data was first processed to simulate noisy gyro pulse count data so that the regular SPARS gyro processing software could be used. With these conditions, the SSA Dynamic sensitivity test was nothing more than a SPARS test with a simulated gyro. The purpose was partially validation of the SPARS software and partially evaluation of SSA hardware in a realistic SPARS type environment.

The SPARS dynamic test mentioned above was similar to the SSA and the IRU Dynamic Sensitivity tests. The fundamental difference was that all real sensors were used in the SPARS test. In this test, rate table data had the primary function of test evaluation. The SPARS dynamic test was the culmination of all the preceding tests and was the prime means of demonstrating system concept feasibility.

## VII. COMPUTER PROGRAM STRUCTURE

A real time digital computer program was required not only to implement the SPARS attitude filter but also to manage the collection and recording of test data. This was particularly true because of the precise time tagging requirements which resulted from the SPARS test performance goals. Every gyro pulse-count, every SSA angle reading, and every rate table output pulse had to be precisely time tagged to maintain attitude computation accuracy.

The SSA required pointing commands in real time and therefore required a real time test control program. The only real time program required for IRU dynamic tests was a data collecting and recording pro-

gram. To achieve the simplest possible IRU dynamic test, the IRU Dynamic calibration and Open Loop tests were designed as a non-real time program which read a tape-recording of the actual rate table and gyro test outputs. There were only two real-time test programs:

- SSA-SPARS Test Program
- Data Collection Program

These programs were used to perform tests as outlined in Figure 5. The post test PRINT program performed tabular and plot formatting and some data processing functions. The diagnostic programs checked the data flow to and from the SPARS hardware, the data adapter and the computer. Diagnostic programs were written for the rate table, IRU, and SSA.

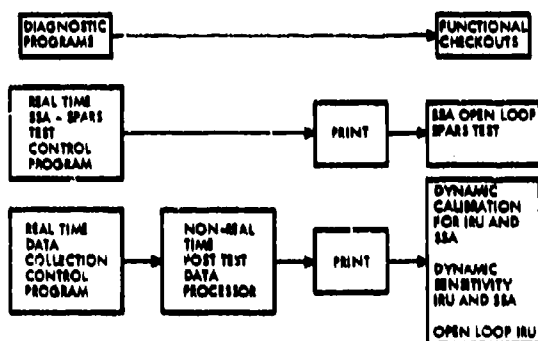


Fig. 5. Test Control Program Structure

The first step in development of the real time laboratory program was writing the real-time control program. This executive program was married to a previously generated equation simulation program which included simulated IRU, SSA, and Rate Table to produce a program that would operate in real time. As hardware became available, the simulated equipment was replaced by real hardware. Output formats of the real-time programs presented significant data in tabular and/or graphic display. These output formats gave time histories of the attitude errors, gyro drift bias estimates, pitch and roll residuals, etc., as well as performance summaries of each test run similar to that produced in the post test evaluation program. The primary output even for real time tests was generated by the post test PRINT program.

## VIII. EVALUATION OF ATTITUDE ERRORS

Attitude error was defined as the difference between SPARS attitude measured by the laboratory instrumentation and SPARS attitude as estimated by the SPARS system. Attitude in turn had been defined as

the orientation of a body-mounted coordinate frame relative to a laboratory-fixed coordinate frame. Rotation of the rate table rotated the body frame relative to the laboratory frame.

Attitude as measured by the laboratory instrumentation was the direction cosine matrix DCLAB. Attitude measured by the SPARS system was the direction cosine matrix DCSPR. Each of these direction cosine matrices mapped a vector from the laboratory to the body frame:

$$V_B = DCLAB \cdot V_L$$

where  $V_B$  is a vector in the body frame and  $V_L$  is the same vector in the laboratory frame. A similar relationship holds for DCSPR.

The matrix DCLAB is given by

$$DCLAB = \begin{bmatrix} CA & SA & 0 \\ -SA & CA & 0 \\ 0 & 0 & 1 \end{bmatrix} \begin{bmatrix} 1 & 0 & -\gamma_{AY} \\ 0 & 1 & -\gamma_{AX} \\ \gamma_{AY} & \gamma_{AX} & 1 \end{bmatrix}$$

Where CA and SA are the cosine and sine of the rate table rotation angle respectively and  $\gamma_{AX}$  and  $\gamma_{AY}$  are the X and Y components of the small angular tilt of the rate table axis with respect to the Z or vertical axis of the laboratory frame.

The matrix DCSPR is given by:

$$DCSPR = \begin{bmatrix} (q_1^2 - q_2^2 - q_3^2 + q_4^2) & 2(q_1 q_2 + q_3 q_4) & 2(q_1 q_3 - q_2 q_4) \\ 2(q_1 q_2 - q_3 q_4) & (-q_1^2 + q_2^2 - q_3^2 + q_4^2) & 2(q_2 q_3 + q_1 q_4) \\ 2(q_1 q_3 + q_2 q_4) & 2(q_2 q_3 - q_1 q_4) & (-q_1^2 - q_2^2 + q_3^2 + q_4^2) \end{bmatrix}$$

where  $q_1, q_2, q_3$ , and  $q_4$  are the components of the attitude quaternion generated by the SPARS system. The difference between the two direction cosine matrices is given by the product  $DCLAB \cdot DCSPR^T$  where T denotes the transpose. If both matrices are perfect (have no errors) then the above product results in an identity matrix. However, if there are small errors in either or both of the direction cosine matrices, the product results in:

$$DCLAB \cdot DCSPR^T = \begin{bmatrix} 1 & -\psi_Z & +\psi_Y \\ +\psi_Z & 1 & -\psi_X \\ -\psi_Y & +\psi_X & 1 \end{bmatrix}$$

where  $\psi_X$ ,  $\psi_Y$ ,  $\psi_Z$  are the X, Y, and Z components of the attitude error. \* Plots of these component errors are shown at the end of this paper and in the appendix to Toda (IBID).

Also used to evaluate the attitude error are the sample statistics:

- Mean =  $\frac{1}{N} \sum_{i=1}^N \psi(i)$

Where  $\psi(i)$  is a component attitude error at the  $i$ th star sighting

- Standard Deviation =

$$\left( \frac{1}{N-1} \sum_{i=1}^N (\psi(i))^2 - (\text{Mean})^2 \right)^{1/2}$$

- 67 percent point

The 67 percent point is the error level which exceeds 67 percent of the component attitude errors in a given test. These three statistics were applied to the X, Y, and Z component attitude errors and also to a so-called RSS error measure:

$$\text{RSS}(i) = \left( (\psi_X(i))^2 + (\psi_Y(i))^2 + (\psi_Z(i))^2 \right)^{1/2}$$

The  $\text{RSS}(i)$  term is the magnitude of the attitude error at the  $i$ th star sighting. The mean of the  $\text{RSS}(i)$  terms is perhaps the most meaningful single error measure used; this term gives the average magnitude of the attitude error in a given test.

Also used in the early stages of testing was a ratio criterion given by:

$$\frac{1}{M} \sum_{i=1}^M \frac{\text{RSS}(i)}{\text{RMS}(i)}$$

Where  $\text{RMS}(i)$  is the square root of the estimation error covariance matrix immediately after the  $i$ th update. The integer  $M$  is the number of updates occurring in the two minutes immediately preceding the  $i$ th update. The ratio criterion was computed at two minute intervals and plotted for the duration of a given test. This parameter gave an indication of the actual error performance relative to the anticipated error performance as expressed by the error covariance

matrix. Large ratio criteria are symptomatic of either incorrect error models leading to an incorrect covariance matrix or of improper system operation.

## IX. TEST RESULTS

The major system test error contributors were rate table readout error and star simulator line of sight instability. Rate table readout uncertainty was on the order of .2 arc second one sigma and had the same effect as an additive white noise in the Z (vertical) gyro. This effect increased the apparent noise in the Z gyro by .02 arc second per second using 30 second sampling intervals. Rate table rate errors were insignificant. Likewise, there was no perceptible instability of the rate table axis orientation.

Star simulator lines of sight did exhibit instability: shifts over a forty day interval on the order of 10 arc seconds were detected. Shifts of 4 arc seconds were noted during a one week period. It was not possible to determine whether these shifts were due to instability of the star simulator itself or were caused by warping of the concrete pier, and star simulator pedestal. Long term pier orientation in azimuth and in level axes was greater than five arc seconds but had no significant effect upon the accuracy of gyro compensation for earthrate.

As discussed earlier, calibration procedures minimized the effects of slowly varying misalignments, but high frequency noise-like laboratory error sources caused the test results to be a pessimistic measure of SPARS performance. Some quantitative evaluation of this effect is given by Toda (IBID).

The Dynamic Calibration of the Star Sensor failed to achieve satisfactory results: the Kalman filter did not generate bias parameters corrections which reduced line of sight residuals to the required levels. Subsequent Open Loop SSA tests showed large residuals indicating incorrect calibration parameters. This difficulty was at first attributed to large errors in the initial estimates of the parameters being calibrated. It is known that a Kalman filter can fail to converge (see Reference 3) under such circumstances. To avoid this difficulty, it was decided to perform the Dynamic Calibration test using an iterative least squares algorithm. The subsequent failure of this procedure was ascribed to an incorrect error model. Review of the vendor calibration procedures indicated that so called "gravity droop" terms were not correctly utilized in the Dynamic Calibration test error model. These gravity droop terms were meant to compensate for the bending and twisting of the star sensor mounting caused by

\*This definition of attitude error corresponds to the drift error described by Koenke in Reference (2). In this paper, Koenke also defines a scale error and a skew error which are related to the fact that DCSPR may not be orthonormal when the attitude integrations are performed in a direction cosine matrix format. In the present case, attitude computations are performed in a quaternion format which includes periodic normalization of the quaternion. Given that the quaternion is a unit vector, the matrix DCSPR must be orthonormal virtually to the limit of word length accuracy. Thus, scale and skew errors are small and were not evaluated in the SPARS test.

gravity torques. The effective torque varies with telescope orientation, which in this case is roll angle. Thus the gravity droop terms were modeled as misalignments which varied as a function of roll angle,  $\phi$ :

$$\begin{aligned}\psi_{PY} = & \psi_{PY_1} + \psi_{PY_2} \sin \phi \\ & + \psi_{PY_3} \cos \phi \\ & + \psi_{PY_4} \sin 2\phi \\ & + \psi_{PY_5} \cos 2\phi\end{aligned}$$

Where  $\psi_{PY}$  is the Y component of the small angle which expresses the pitch axis misalignment. A similar expression was used for  $\psi_{PX}$ , the X component of misalignment of the pitch axis. At zero roll angle, the SSA pitch axis is parallel to the Z or vertical axis. The initial incorrect error model applied gravity droop terms to  $\gamma_{RX}$  and  $\gamma_{RZ}$ , misalignments of the roll axis. Furthermore, droop terms were initially predicted to be on the order of 10 to 15 arc seconds. During calibration it became apparent that droop effects were an order of magnitude larger.

The droop coefficients were derived by curve fitting to calibration data which were generated by the vendor. Because of the large magnitude of these coefficients, several are on the order of 100 to 200 arc seconds, even small errors in the droop model can have serious effects upon dynamic test performance.

Time did not permit derivation of a satisfactory bending model. Instead, acceptable Open Loop SSA performance was achieved by using compensation terms which were in turn derived from an unsatisfactory Open Loop test. The procedure used was as follows: an Open Loop test was performed and pitch and roll residuals were recorded for each star sighting. These residuals were then used to compensate the next Open Loop test which was run using the same star sighting schedule and the same rate table rate and starting angle. The previously recorded residuals were then used to compensate the current observations. At each star sighting, the previously recorded pitch residual was subtracted from the current pitch residual. And similarly, the previously recorded roll residual was subtracted from the current roll residual. This procedure was repeated to reduce the effects of random noise-like errors. Residuals from the second Open Loop test were multiplied by a less than unity gain and added to the previously recorded compensation term. Between three and four iterations were required to achieve a stable set of compensation terms.

The resulting table of compensation terms was uniquely tailored to the run conditions under which they were derived, i.e., they were appropriate to a particular star schedule and rate table schedule. However, this procedure was found to give good results in

the face of small, 100 arc second, initial attitude errors and with limit cycles of  $\pm 15$  arc seconds per second.

The table of compensation terms represented a temporary measure which, given sufficient time and calibration data, would have been replaced by an analytical solution of the bias calibration modeling and estimation problem. Such an analytical solution had the clear advantage of not being limited to any particular star or rate table schedule.

Quantitative results of the SSA Open Loop and SPARS tests are given in the classified Appendix to Reference (1) using both the table of compensation terms, referred to as empirical calibration, and the bias compensation terms derived from least squares estimation. The latter is referred to as analytic compensation. Figure 6 shows a typical time history of SSA pitch residuals generated from a Dynamic Calibration test using empirical compensations. The residual amplitude scale has been removed in order to avoid classification.

Figure 7 shows gyro rate data from an Open Loop Dynamic Test.

A typical SPARS test result is shown in Figure 8. This figure contains the time history of the RSS attitude error. As discussed in Section VIII, the RSS attitude is a measure of the total three axis attitude error. Angle error scales have been removed to avoid classification. Quantitative data are given by Toda in Reference 1.

## X. CONCLUSIONS

This paper has described the philosophy and implementation of a laboratory test program designed specifically for evaluation of the SPARS attitude reference system. In addition to functional and static tests, a sequence of dynamic tests was used to evaluate the system components. Difficulties encountered in the Dynamic Calibration of the SSA were never fully resolved due to test time limitations. However, alternate calibration procedures allowed successful demonstration of concept feasibility, and system accuracy.

The Dynamic Sensitivity SSA test was not conducted. The long period between delivery of the IRU and delivery of the SSA resulted in a high degree of confidence in the IRU performance prior to SSA delivery. Given this confidence, it was deemed unnecessary to perform SPARS-like tests with simulated IRU data, so real IRU data was used instead. The Open Loop IRU test was dropped midway through the test sequence in favor of a special output format in the post test PRINT program. This format was designed to monitor the open loop drift stability of each gyro.



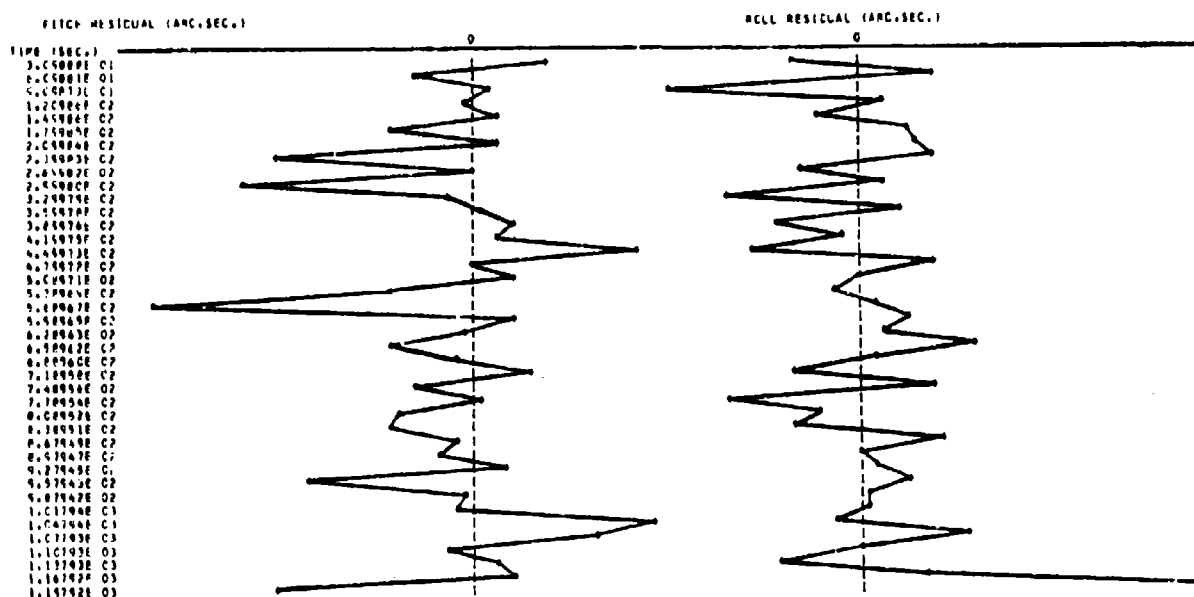


Fig. 6. Typical SSA Dynamic Calibration Test

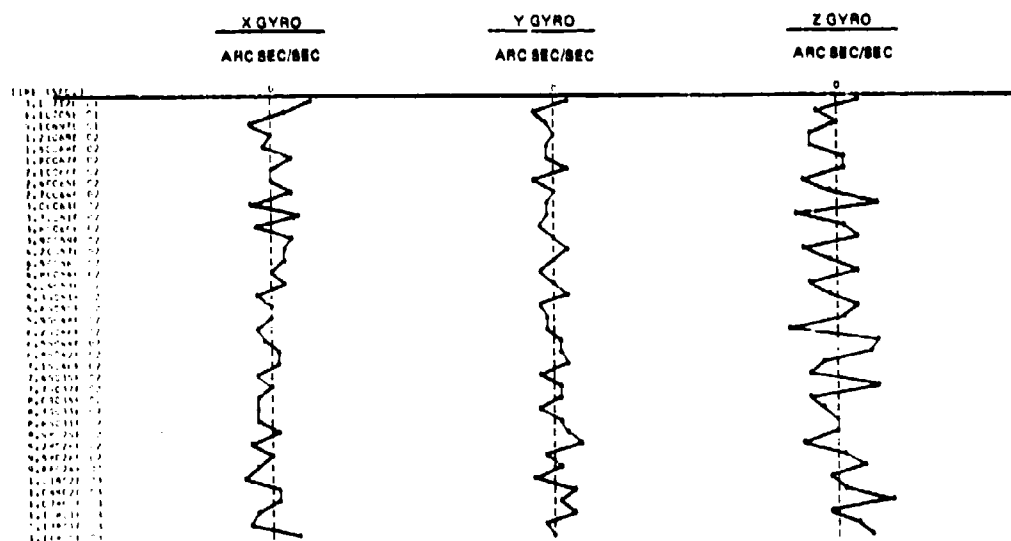


Fig. 7. Open Loop Gyro Test

BODY FRAME RSS (ARC.SEC.)

TIME (SEC.)

3.09980E 01  
 6.09973E 01  
 9.09965E 01  
 1.20996E 02  
 1.40995E 02  
 1.70994E 02  
 2.00993E 02  
 2.30992E 02  
 2.60991E 02  
 2.90990E 02  
 3.20988E 02  
 3.50987E 02  
 3.80985E 02  
 4.10984E 02  
 4.40983E 02  
 4.70981E 02  
 5.00980E 02  
 5.30978E 02  
 5.60976E 02  
 5.90974E 02  
 6.20973E 02  
 6.50971E 02  
 6.80969E 02  
 7.10967E 02  
 7.40965E 02  
 7.70963E 02  
 8.00962E 02  
 8.30960E 02  
 8.60958E 02  
 8.90956E 02  
 9.20954E 02  
 9.50953E 02  
 9.80951E 02  
 1.01749E 03  
 1.04759E 03  
 1.07794E 03  
 1.10794E 03  
 1.13793E 03  
 1.16793E 03  
 1.19793E 03

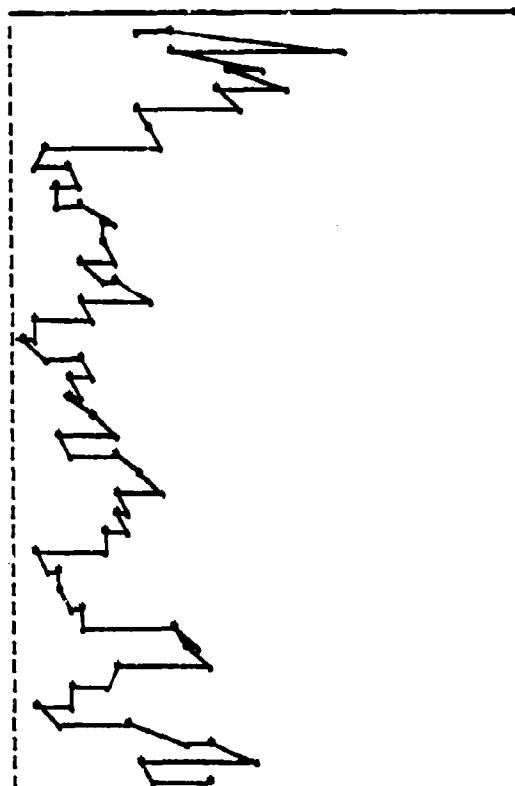


Fig. 8. Typical SPARS Test Result

#### REFERENCES

1. Norman F. Toda, Gerald L. Heles, and Frank H. Schlee, "SPARS: The System, Algorithms, and Test Results," Spacecraft Attitude Determination Symposium, Aerospace Corp., El Segundo, Calif., Sept. 30 to Oct. 2, 1969.
2. E. J. Koenke, "Attitude Computation for Strapdown Navigation Systems," Oct 1969, Guidance and Control Research Directorate NASA Electronics Research Center, Cambridge, Mass.
3. Norman F. Toda, Frank H. Schlee, and Paul Obsharsky, "The Region of Kalman Filter Convergence for Several Autonomous Navigation Modes," AIAA Journal, April 1969.

SESSION V

ATTITUDE DETERMINATION SYSTEMS II

Chairman:  
Prof. R. C. K. Lee  
University of California at Irvine  
Irvine, California

---

Space-Based Surveillance	*
Gyrostatt Precision Attitude Determination and Control	387
High-Accuracy Real-Time Attitude and Line-of-Sight Determination for a U.S. Satellite	*
Attitude Determination Performance Potential for a Yaw-Spin Satellite	
Part One: Formulation of the Estimation Equations	397
Part Two: Performance of the Attitude Estimator	*
Attitude Determination Schemes for a Variety of Spacecraft Configurations	*
* Classified; published in Volume II	*

## GYROSTAT PRECISION ATTITUDE DETERMINATION AND CONTROL\*

John J. Ribarich  
Hughes Aircraft Company  
Los Angeles, California

### ABSTRACT

A dual-spin (Gyrostet) vehicle attitude determination and control system concept that has the potential to attain 1.0 arcsec pointing accuracy is presented. Star sensor and bearing technology improvements, micro-g accelerometer, active rotor balancing, and onboard data processing are the key control system elements. Preliminary analysis and simulation data support the feasibility of attaining the performance goal.

### INTRODUCTION

Space missions being planned for the near future will involve sophisticated payloads such as lasers and surveillance cameras that must have their primary functional axis determined and controlled to within 1 arcsec (30' or less. Progress toward this precision performance goal is presently being achieved through the Orbiting Astronomical Observatory Program (Ref. 1) hardware technology improvements and experimental efforts, and a variety of system studies (Refs. 2 and 3). This paper presents the results to date of a Hughes Aircraft Company study that is considering the use of a dual-spinning vehicle (Gyrostet system) as a bus for precision performance payloads. The general design guidelines and considerations are given first, followed by a state-of-the-art Gyrostet system performance and limitation discussion, precision Gyrostet system design and performance, hardware implications, and tentative conclusions and comments.

### DESIGN GUIDELINES/CONSIDERATIONS

A set of design guidelines has been formulated based on Hughes studies to generate meaningful, practical results for a series of specific concepts. Therefore, the information presented will be applicable to many particular systems conceived during the 1970's.

A Gyrostet configuration with a platform-mounted precision payload is placed in a synchronous stationary earth orbit with the general requirement to maintain payload pointing accuracy to within 1.0 arcsec. The spacecraft is placed on station using present techniques with an attitude uncertainty of 100 to 200 arcsec (Ref. 4). Although the orbit determination uncertainty contribution to the total pointing

error has not been thoroughly investigated, Ref. 5 indicates that accuracy comparable to the 1.0 arcsec goal can be achieved. The stationkeeping and periodic spacecraft attitude corrections required to compensate for orbital drifts, solar and gravity gradient torques, and other environmental factors are assumed to be determined and applied independent of the control concepts presented in this paper and compatible with mission requirements. References 4 and 5 discuss recent approaches to this problem.

The payload sensor must be pointed from one nominal direction to another (slew) at various times during the mission. Once a nominal pointing direction has been attained, 1.0 arcsec pointing uncertainty must be achieved and maintained within and for a reasonable period of time. In general, the shorter the slewing and transition times, the better the payload duty cycle. The payload motion will be provided by the normal Gyrostet platform azimuth freedom and a payload elevation gimbal system attached to the platform.

The payload sensor nominal direction varies continuously to correct for orbital motions. It is assumed that these slowly varying rates can be programmed in an open-loop manner with periodic updating and that precision control will not be degraded. Similar open-loop computations of spacecraft orbital parameters will be performed to allow for a common reference system for the target and spacecraft.

An inertial reference system is postulated to enable the spacecraft to perform accurate pointing computations using star measurements. In addition, celestial references satisfy the desire to design a system which can be as independent of ground cooperation (i.e., autonomous) as practical.

\* Company-sponsored precision pointing studies.

Although the prime function of the Gyrostat platform is to support and control the payload sensor, other items may be mounted on the platform. The most likely candidate is a steerable communications antenna. Such systems are assumed to have independent control mechanisms and will not interfere with the precision pointing performance.

The desire to generate an autonomous design leads to the inclusion of onboard computers into the control loop. Computer technology advances applied to such applications appear promising not only in terms of an autonomous control loop but with respect to a complete autonomous design which, in cooperation with the ground, can adapt to many unexpected events. The use of an onboard computer, as in the case for all components of the control loop, must also be evaluated with reference to reliability (3 to 5 years), testability, weight, power, size, schedules, and costs.

#### BASELINE GYROSTAT

A state-of-the-art Gyrostat system will be discussed to indicate present design technology and performance limitations from which a precision concept is developed. This baseline is extracted from Hughes experience with the TACSAT, Intelsat IV, and various Company efforts. Figure 1 illustrates the baseline with a simplified payload sensor and key control subsystem hardware items which must be improved or added. Table 1 summarizes the performance of the significant contributors to the total pointing budget. The errors are shown as rotations normal to and about (azimuth) the nominal spin-axis direction. Although the actual payload sensor errors depend on its attitude with respect to the spacecraft, the total res errors shown bound the sensor errors.

The rotor unbalance of 30 arcsec is due to the present preflight balancing equipment and techniques utilized. The effect is to produce a coning motion of the spacecraft geometrical axis

about the nominal desired spin direction at the spacecraft spin frequency (wobble).

The bearing runout phenomenon, which is a deformation of the despin coupling mechanism producing an elliptical rather than a circular bearing race, manifests itself as a 10-arcsec wobble. This limitation is set by present machining technology.

The residual nutation of 50 arcsec is a result of the reaction torque acting on the spacecraft during platform azimuth slewing. This figure has been used as an upper bound rather than a 3-arcsec figure associated with steady-state conditions. This limit is determined by present spacecraft mass properties and despin control system design.

The platform jitter of 40 arcsec is the only significant contributor to azimuth motions. This error is a function primarily of present-day star sensor accuracy, platform rotor instrumentation, despin motor torque variations, and digital control quantization.

The total stability errors are 59 and 40 arcsec, 3 $\sigma$ . These totals do not include misalignment of the payload sensor reference axis with respect to the common spacecraft, control system, and measurement system axis. Such alignment errors are the largest contributors to the overall pointing accuracy budget.

The alignment of various spacecraft items is referenced to the Gyrostat platform-rotor coupling, the BAPTA (bearing and power transfer assembly). The items of concern include the rotor-mounted star sensors, which experience initial laboratory installation and g-field misalignments, boost phase deflections and varying in-orbit deflections due to thermal gradients; BAPTA spin-despin mechanical deformations; and BAPTA azimuth uncertainties between spinning-despun sections due to electro-mechanical instrumentation misalignment. The total error for each coordinate for this class of errors is 100 arcsec.

Misalignment of the payload sensor coordinates with respect to the common BAPTA reference is caused by similar initial laboratory misalignments, g-field, and boost deflections. Also, thermal deformations are significant error sources, and this includes those within the payload itself. Another contributor is the uncertainty in the elevation gimbal system, which includes bearing runout, repeatability encoding, and other factors which revolve about present technology status of the particular design. The total payload misalignment error along each coordinate is 100 arcsec. The 3 $\sigma$  totals of all the errors shown in Table 1 are 154 and 147 arcsec, which are interpreted as reasonable state-of-the-art pointing accuracy limits.

It should be recognized that the performance values given are representative only. Many of the error sources could be reduced if the sys-

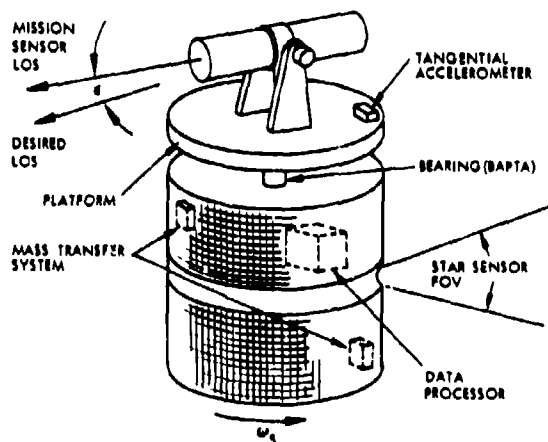


Figure 1. Precision Gyrostat

TABLE 1. BASELINE ERROR BUDGET

Error Source	$\pm \theta$ , arcsec	Azimuth, arcsec	Limiting Factors
Rotor static/dynamic unbalance (wobble)	30	—	Balancing equipment and techniques
Bearing runout (wobble)	10	≈0	Machining limitations on bearing
Residual nutation	50 transient, 3 steady-state	—	1) Control system design 2) Lack of key sensors
Platform jitter	0	40	1) Star sensor, 10 arcsec 2) Torque variation 3) Digitizing 4) Lack of key sensors
3σ res total	59	40	
Alignment with respect to BAPTA reference	100	100	1) Alignment equipment and techniques 2) G-field calibration 3) Thermal gradient protection 4) BAPTA design 5) MIP design
1) Star sensor			
a) Lab equipment, 10 arcsec			
b) Boost			
c) Thermal			
2) BAPTA spin with respect to despin			
3) MIP			
Mission sensor	100	100	1) Alignment equipment and techniques 2) G-field calibration 3) Thermal gradient protection
1) Lab equipment, 10 arcsec			
2) G-field			
3) Boost			
4) Structure			
5) Resolver			
3σ res total	154	147	

tem required such a design. The major alignment error sources are highly dependent on the spacecraft and payload sensor structural and thermal characteristics and are subject to much speculation. It is not clear if there is any definite correlation between total alignment errors and structural size, but studies of a few specific cases indicate that large configurations present large uncertainties. If large payload sensors are involved, their basic pointing limitations

should be investigated early in the program to ensure that the remainder of the spacecraft system is not overdesigned, especially in regard to pointing accuracy.

#### PRECISION GYROSTAT

A Gyrostat control subsystem has been conceived which significantly reduces the uncertainties previously discussed. Figure 2 depicts

the control subsystem data flow from the sensors to the onboard data processor to the final controllers. The components shown in Figure 2, along with those shown in Figure 1 which were not discussed previously, will be explained in this section.

A micro-g accelerometer is mounted on the Gyrostat platform to measure inertial accelerations in a tangential direction and plane normal to the spin axis. This orientation allows three major components of acceleration to be monitored: 1) that due to wobble produced by rotor unbalance and BAPTA bearing runout, 2) induced nutations resulting from platform motions and outside disturbances, and 3) tangential accelerations resulting from platform torquing via the despinn control motor. The accelerometer signal is operated on by the data processor to remove the three acceleration components and estimate the wobble, nutation, and despinn torque. The wobble information is used to drive a mass transfer device which balances the rotor, thereby reducing the initial rotor unbalance and effective rotor unbalance due to bearing runout.

The nutation data are used by the despinn control motor to null the spacecraft nutation. Present Gyrostat system designs control nutation via the despinn motor but do not derive nutation data from accelerometer measurements. Instead, relative platform-rotor positional data are the source data, master index pulse (MIP).

The platform tangential acceleration resulting from despinn motor torquing allows torque jitter to be sensed immediately and damped by the control loop. Present designs are limited in control accuracy by the jitter.

The rotor-mounted star sensor provides data which allow inertial attitude determination and control to be accomplished. The accelerometer cannot provide such data. The star data are used by the data processor to generate reference pointing directions for the platform azimuth control and payload sensor loops. Also involved in these computations are ground-generated orbital and coordinate system data, target pointing data, and payload sensor elevation position (resolver/encoder) data.

Since the control system concept presented to this point has not accounted for the primary accuracy uncertainty due to deformations between the payload sensor primary axis and the spacecraft reference system, an additional feature must be included. It is assumed the payload sensor has star sensing capabilities and can be used periodically to view various stars and thereby allow the system to be calibrated. The deviations between the actual star positions and estimated positions as seen by the payload sensor allow for the misalignment between the star reference frames to be determined and taken into account. The effectiveness of the calibration procedure depends on mission constraints, spacecraft particulars, and payload design. If, for example, the system cannot be calibrated often enough because of main mission pointing duty cycle requirements, structural deformations caused by thermal gradients may result in excessive pointing uncertainties. In general, a design concept based on the approach presented should provide the on-orbit flexibility to allow the vehicle characteristics to be evaluated during the initial mission phases and then provide for modification of the mission operations and spacecraft design parameters.

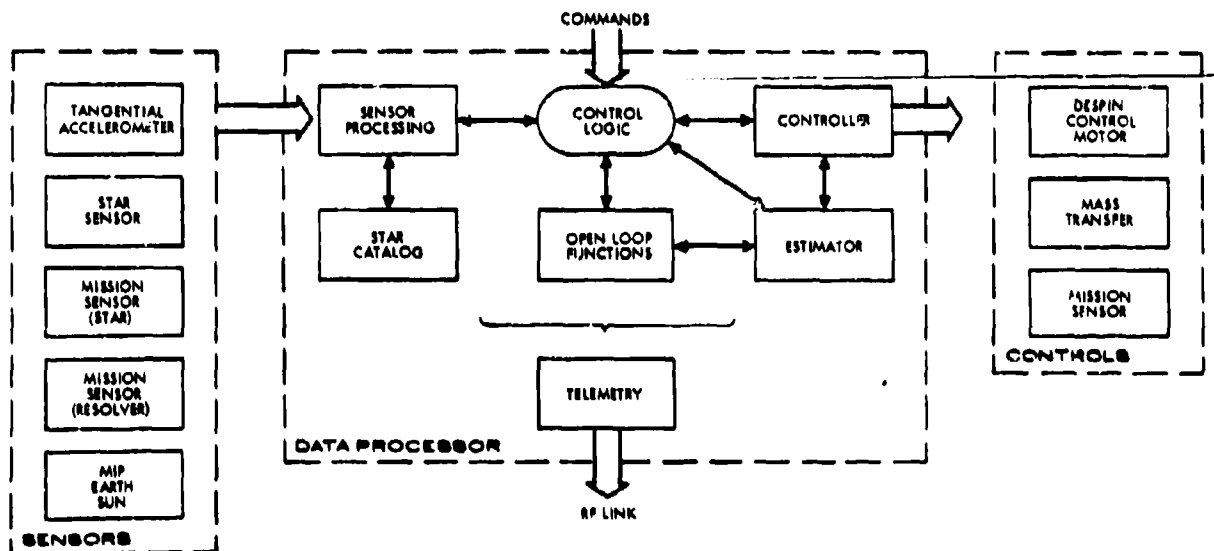


Figure 2. Precision Gyrostat Control System

In addition to the items discussed, Figure 2 indicates that the sensor complement includes earth and sun sensors which function in a conventional manner prior to the initiation of a precision pointing phase. Also, the control subsystem must have provisions for accepting ground commands and providing telemetry data.

The evaluation of the precision pointing performance and the feasibility of implementing the control subsystem is being accomplished by means of a variety of approaches. Table 2 is an error budget for the precision Gyrostat performance using the same format as Table 1. The values presented were obtained primarily from the application of conventional deterministic and stochastic servo loop analysis to the anticipated attainable hardware performance during the next few years.

Rotor unbalance, 0.1 arcsec, is dependent on the estimation accuracy and mass transfer device performance limits. The mass transfer device, based on a fluid transfer design being developed at Hughes, is judged to be the limiting factor.

Bearing runout, 0.1 arcsec, is based on the assumption that the significant bearing runout error occurs at the spin frequency and manifests itself as an "effective" rotor wobble. This assumption is supported by past tests and studies plus current in-depth BAPTA studies. Tests are presently being conducted on BAPTA units which should provide better understanding of this error source. Therefore, within the correctness of this assumption, the uncertainty is limited, as in rotor unbalance, to the performance of the mass transfer system.

Attainment of 0.1 arcsec residual nutation requires a significant platform product of inertia to allow effective despun control system damping of nutation. This requirement presents no significant problem in general; but, if a particular design cannot provide this feature, other types of active nutation control can be invoked.

Platform jitter, 1.0 to 2.0 arcsec, is a result of incorporating accelerometer feedback to directly damp random torques, and upgrading star sensor measurement uncertainties to within 1 arcsec or less. The confidence in obtaining this performance is based on recent vendor discussions of flight proven micro-g accelerometers (Ref. 6) and star sensors and Hughes hardware developments of similar items. A reduction in the Gyrostat rotor spin speed further improves the star sensor measurement accuracy. The performance also requires digital control electronic improvements (finer quantization) which could be considered state-of-the-art and therefore not requiring major advancements. The resultant 3 $\sigma$  stability error is 0.18 arcsec and 1.0 to 2.0 arcsec for the two coordinates defined previously.

As discussed previously, the remaining error sources are dependent on the particular system design and may limit pointing accuracy unless special techniques are employed. The 1.0 arcsec values listed assume that the payload sensor can measure star directions periodically, and these data are used to calibrate the system. For example, if the star measurements were noise free, measurements would be required every 10 minutes, assuming that the alignment error was due to a thermal gradient deformation with a nominal rate of 60 arcsec/hour estimated to within 10 percent. Since measurements are not perfect, the calibration interval would be less than 10 minutes. Also, two or more stars with acceptable angular separations would probably be required. The significance of such a calibration procedure is strongly dependent on the payload sensor primary mission constraints.

Aside from thermal gradient and star measurement errors, there are errors such as payload elevation gimbal bearing performance uncertainties, payload structural bending and elevation angle measurement errors. These errors are especially significant for large payload sensors.

Another important problem arises if the payload cannot sense stars. One approach is to autocollimate between the rotor-mounted star sensor and payload sensor, but this presents difficult, if not impossible, mechanization problems because of the platform-rotor relative motion. Mounting of star sensors on the platform or, even more desirable, attaching star sensors directly to the payload sensor, may be the solution. This also leads to the possibility of eliminating the rotor-mounted star sensor if the data rates and accuracy of the platform instrumentation are adequate.

The final values listed in Table 2 are the total payload sensor pointing accuracy values of 1.0 and 1.4 to 2.2 arcsec (3 $\sigma$ ).

To obtain a high degree of confidence in predicted system performance prior to total system preflight testing and actual inflight results, it is generally agreed that as detailed a computer simulation as practical should be developed. The simulation will allow the best hardware data and their complex interaction to be studied and evaluated. Toward this goal, a simulation is being developed which presently utilizes a linearized stochastic model of the Gyrostat and its control system (see Appendix for details). Presently, simulation results are giving added confidence to the precision pointing control system concept presented being able to achieve the performance indicated in Table 2. The system is assumed to begin operation at the completion of a somewhat coarse acquisition mode, and estimate and control payload sensor/spacecraft attitude through to a final regulation phase. All significant parameters are estimated



TABLE 2. PRECISION GYROSTAT ERROR BUDGET

Error Source	$\pm$ H, arcsec	Azimuth, arcsec	Supporting Factors
Rotor static/dynamic unbalance (wobble)	0.1	—	1) Estimate wobble a) Studies b) Simulations 2) Mass transfer a) Fluid system b) Mechanical devices
Bearing runout (wobble)	0.1	0	1) Hardware advances 2) Estimate wobble 3) Tests/studies 4) Mass transfer
Residual nutation	0.1	$\approx 0$	1) Estimate nutation a) Studies b) Simulations 2) Despin control/platform product of inertia 3) Active nutation control
Platform jitter	—	1.0 to 2.0	1) Accelerometer feedback 2) Star sensor, 1.0 arcsec 3) Finer digital quantization 4) Studies/simulations
3 $\sigma$ rse total	0.18	1.0 to 2.0	
Alignment with respect to BAPTA reference	<1.0	<1.0	1) Star data every 10 minutes, <10 seconds accuracy, 60 sec/hr thermal deflection $\approx$ 10 percent 2) Position mission sensor 3) Thermal protection: blankets, heaters, heat pipes, and mounting 4) Upgrade alignment equipment and techniques 5) G-field compensation
1) Star sensor			
a) Lab equipment, 10 arcsec			
b) G-field			
c) Boost			
d) Thermal			
2) BAPTA spin with respect to despin			
3) MIP			
Mission sensor			
1) Lab equipment, 10 arcsec			
2) G-field			
3) Boost			
4) Thermal			
5) Structure			
6) Resolver			
3 $\sigma$ rse total	1.0	1.4 to 2.2	

and all controls exercised continuously in an acceptable manner.

Figures 3 and 4 are plots of the actual and estimated spacecraft inertial transverse attitude and platform azimuth, respectively. The transverse attitude bias results from model errors which will be eliminated. The system shows convergence to within a few arcseconds in approximately 40 seconds.

Figure 5 is a plot of the angular rate associated with the single transverse axis attitude history given in Figure 3. Figure 6 is a plot of the unbalance in a single plane of the rotor.

Figure 7 shows the basic accelerometer output signal with wobble, nutation, and process

and measurement noise components. The accelerometer signal includes the three components previously discussed plus random process and measurement noise.

It is anticipated that in actual operation the controls would be exercised in steps: first, estimate and damp the nutation; then, estimate the wobble and balance the system; and then, operate the nutation and azimuth control loop. This approach may result in the use of a time invariant estimator and controller, which simplifies data processing. Also, the estimation might only use accelerometer data prior to controlling platform azimuth.

Although the simulation results give added confidence to obtaining the desired precision performance, much remains to be done in the simulation area. Effort is presently under way to derive a complete detailed Gyrostat simulation (includes nonlinearities) with a practical estimator and controller mechanization. In addition, a star data processing algorithm, a detailed mission profile, and environmental disturbances will be incorporated.

#### HARDWARE CONSIDERATIONS

Although the analysis aspects of the precision Gyrostat concept are given major emphasis in this paper, they should not overshadow the formidable hardware technological aspects involved in precision pointing in the 1-second region. The following is a series of summary

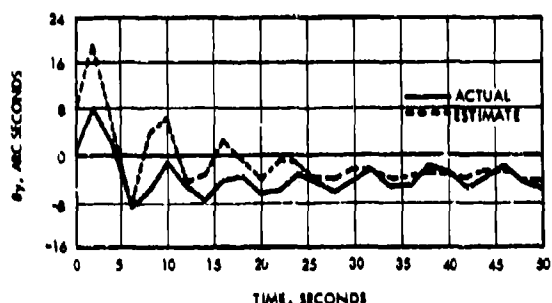


Figure 3. Transverse Attitude Response

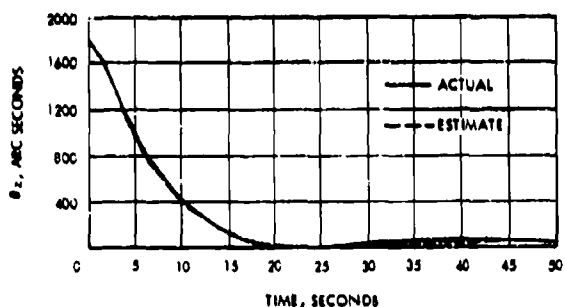


Figure 4. Platform Azimuth Response

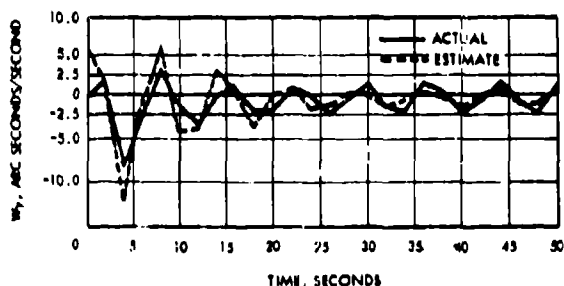


Figure 5. Transverse Rate

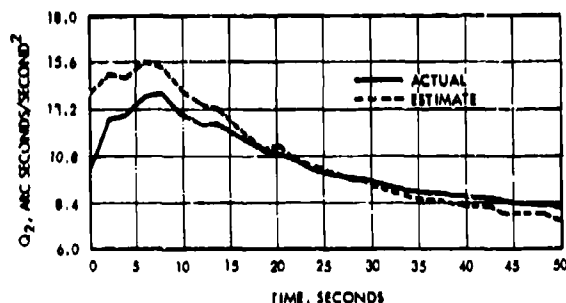


Figure 6. Rotor Unbalance

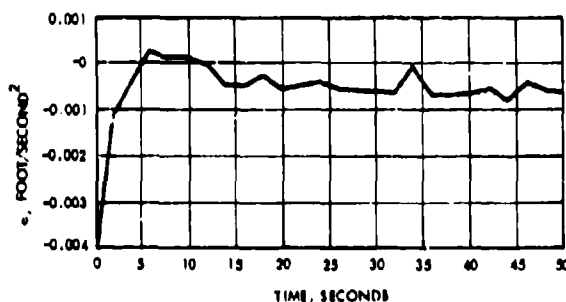


Figure 7. Accelerometer Signal

comments for each of the key hardware items of concern to the precision Gyrostat system design.

#### Micro-g Accelerometer

The platform-mounted accelerometer must be sensitive to a range of  $10^{-3}$  to  $10^{-7}$  g and provide a digital output. A micro-g accelerometer satisfying these gross requirements has been flown during the past few years (Ref. 6). Its measurement accuracy, weight, power, size, and costs all satisfy tentative requirements. Its reliability for a 3 to 5 year mission looks good but has yet to be demonstrated.

#### Bearing and Power Transfer Assembly (BAPTA)

Advanced techniques are required to provide a deepin bearing joint that will result in motion errors (wobble and noise) of the despun platform less than 1.0 arcsec in magnitude. Hughes is currently developing a deepin bearing assembly which analysis indicates will result in motion errors no greater than 10.0 arcsec. Recent analysis revealed that motion errors could be reduced to approximately 3.0 arcsec using techniques similar to those employed in the referenced bearing assembly, but with a bearing spacing of 20 inches.

#### Data Processor

It is estimated that the star data processing estimator, controller, open-loop orbital and coordinate computations, and other control system functions can be performed by an onboard general-purpose computer having 8,000 to 10,000 words of memory (24 bits/word). The flight-proven Univac 1824 appears to satisfy these and control loop rate computational requirements (Ref. 7). The weight, power, size, etc., are reasonable for incorporation into an onboard system.

#### Star Sensors

A slit-type star sensor has been developed at Hughes for use on the Gyrostat system. It is estimated that a measurement accuracy of a few arcseconds can be achieved through design improvements and rotor spin speed reductions (20 rpm). Discussions with Control Data Corporation personnel also support these conclusions.

#### SUMMARY/CONCLUSIONS

- The mechanization of a Gyrostat attitude determination and control system to achieve 1.0 arcsec pointing accuracy appears very promising. The design depends on bearing and star sensor technology improvements, platform-mounted micro-g accelerometer, active rotor balancing, and onboard data processing.
- The orbit determination aspect of precision pointing presents no critical prob-

lems, but the same is not true of payload sensor calibration. The calibration procedure is highly dependent on mission and spacecraft design and will probably require an investigation phase early in the mission. In general, payload sensor limitations should be thoroughly understood before the control system design phase.

- Use of a payload sensor with star sensing capability reduces the calibration problem and could simplify the Gyrostat control system (no rotor-mounted star sensor).
- Precision pointing designs will require many advances in technology and a detailed investigation of those effects that formerly have been considered as contributing insignificant effects on pointing accuracy. Also, complete system simulation based on hardware test data and practical control system design are recommended.

#### ACKNOWLEDGMENT

The study results presented in this paper were provided by the efforts of many Company personnel. Special thanks are given to L.H. Grasshoff, Dr. T. Fong, Dr. C.P. Liu, T.M. Isaacs, and J. Yocum, who encouraged and assisted in the study efforts.

#### REFERENCES

1. N.A. Cundersen, "Princeton Experiment Package for OAO-C," Journal of Spacecraft and Rockets, April 1968.
2. W.B. Chubb and D.N. Schultz, "Attitude Control and Precision Pointing of Apollo Telescope Mount," AIAA Journal of Spacecraft and Rockets, August 1968, p. 896.
3. A.J. Iorillo, "Hughes Gyrostat System," Proceedings of the Symposium on Attitude Stabilization and Control of Dual-Spin Spacecraft, 1 - 2 August 1967, Aerospace Corporation, El Segundo, California, TR-0158 (3307-01)-16, November 1967.
4. W.H. Sierer and J. Del Riego, "TACSAT Attitude Determination," Spacecraft Attitude Determination Symposium, Aerospace Corporation, El Segundo, California, 30 September, 1 - 2 October 1969.
5. A. Braga - Ila, "Preliminary Report on the Orbital Operation of the Automatic Station-Keeping System of LES-6," AIAA Guidance, Control and Flight Mechanics Conference, Princeton University, August 1969.

6. E.H. Metzger and M.A. Meldrum, "Miniature Electrostatic Acceleration (MESA)," Textron's Bell Aerosystem Company paper, 1967; also "Electrostatic Accelerometer Scores Firsts in Agena Flight," Aerospace Technology, 28 August 1967.
7. Univac 1824 Computer Technical Description, Univac Federal System Division, St. Paul, Minnesota.
8. A.E. Bryson, Jr., and Y.C. Ho, Applied Optimal Control, Blaisdell Publishing Co., Waltham, Mass., 1969.

#### APPENDIX

A digital computer simulation of a precision Gyrostat system being developed at Hughes Aircraft Company is described in this appendix.

#### Gyrostat Equations of Motion

The linearized equations of motion for a Gyrostat in inertial coordinates are:

$$\begin{bmatrix} I_{t1} & -I_{45} & -I_{46} \\ -I_{45} & I_{t2} & -I_{56} \\ -I_{46} & -I_{56} & I_6 \end{bmatrix} \begin{Bmatrix} \dot{\psi}_x \\ \dot{\psi}_y \\ \dot{\psi}_z \end{Bmatrix} =$$

$$\begin{bmatrix} 0 & I_3 \Omega & 0 \\ -I_3 \Omega & 0 & 0 \\ 0 & 0 & 0 \end{bmatrix} \begin{Bmatrix} \omega_x \\ \omega_y \\ \omega_z \end{Bmatrix} +$$

$$\begin{Bmatrix} Q_1 \cos \Omega t + Q_2 \sin \Omega t \\ Q_1 \sin \Omega t - Q_2 \cos \Omega t \\ T_m + T_b + w(t) \end{Bmatrix} \quad (1)$$

where

$I_6, I_{45}, I_{56}, I_{46}$  = spin inertia and cross products of inertia of the despun platform about spacecraft cg

$I_{t1}, I_{t2}$  = transverse moments of inertia of the entire spacecraft about the spacecraft cg

$I_3$  = spin axis moment of inertia of rotor

$\Omega$  = spin rate of rotor

$Q_1, Q_2$  = unbalance parameters of the rotor which includes effective bearing wobble

$T_m$  = control torque about bearing axis

$T_b + w(t)$  = friction torque of bearing: ( $T_b$  = unknown mean value and  $w(t)$  = randomly varying torque noise - assumed white)

In order to completely describe vehicle motion, the following equations are necessary:

$$\dot{\theta}_i = \omega_i \quad (i = x, y, z) \quad (2)$$

$$\dot{Q}_i = u_i \quad (i = 1, 2) \quad (3)$$

$$\dot{T}_b = 0 \quad (4)$$

where  $u_i$  are the rates of mass transfer in an active balancing control system on the rotor. Equations (1) through (4), in general state space are (using Ref. 8 notation):

$$\dot{x} = Fx + Gu + \Gamma w \quad (5)$$

where

$$x = \begin{bmatrix} \theta_x \\ \theta_y \\ \theta_z \\ \psi_x \\ \psi_y \\ \psi_z \\ Q_1 \\ Q_2 \\ T_b \end{bmatrix} \quad u = \begin{bmatrix} u_1 \\ u_2 \\ T_m \end{bmatrix}$$

$w$  = friction torque noise effecting  $\dot{\theta}_{x, y, z}$   
 $F, G, \bar{I}$  = matrices derived from Eqs. (1) through (4)

#### Measurement Function

The rotor-mounted star sensor and platform-mounted accelerometer outputs are linear combinations of the system state plus additive measurement noise formulated as:

$$z = Hx + v \quad (6)$$

where

$$z = \begin{bmatrix} \theta_x \\ \theta_y \\ \theta_z \\ a_t \end{bmatrix} \quad v = \begin{bmatrix} v_x \\ v_y \\ v_z \\ v_a \end{bmatrix}$$

$$a_t = r_y \dot{\omega}_x' - r_x \dot{\omega}_y' + r_z \dot{\omega}_z'$$

$\dot{\omega}_{x, y, z}' = \dot{\omega}_{x, y, z}$  with  $u$  and  $w$  components removed

$r_{x, y, z}$  = inertial components of accelerometer position

$v_{x, y, z}$  = noise components associated with  $\theta_{x, y, z}$  and  $a_t$

It is assumed that  $\theta_{x, y, z}$  are available once each spin period as the output from a star data processing algorithm and that the accelerometer data are continuous. This obtained from this information and a substitution of Eq. (5) into the acceleration expression. It should be noted the acceleration expression does not presently include spacecraft cg misalignment with respect to the spin axis. Analysis has shown this term can be incorporated in a linear sense.

#### Estimator/Controller (Ref. 8)

A Kalman filter has been mechanized for the estimator. A continuous representation is used with proper provisions for sampled data. The controller is based on the use of a quadratic performance index. This mechanization is suited to the time-varying characteristics of the system.

# ATTITUDE DETERMINATION PERFORMANCE POTENTIAL FOR A YAW-SPIN SATELLITE

## PART ONE: FORMULATION OF THE ESTIMATION EQUATIONS

J. E. Lesinski  
Electronics Division  
The Aerospace Corporation  
El Segundo, California 90245

### ABSTRACT

A computational algorithm is developed for precisely estimating the attitude of an orbiting spacecraft from data provided by a body-fixed star telescope. The algorithm is designed for application to a particular satellite configuration -- namely, a spinning satellite that has its spin axis nearly aligned with the local vertical and that has an internally mounted reaction wheel which approximately cancels its spin component of angular momentum.

The paper is divided into two parts. Part One presents a development of the attitude estimation equations. Particular attention is given to the selection of an efficient set of coordinate systems to define the problem. The philosophy underlying the algorithm development represents an attempt to obtain a potential for high attitude estimation accuracy by providing the estimator with accurate models of the problem. The attitude estimation algorithm is based upon the Kalman filtering technique developed for linear systems, but uses nonlinear state prediction equations and a nonlinear measurement model. The dynamic characteristics of the particular satellite configuration are exploited in the development of an approximate closed-form solution for the satellite motion which is utilized for the filter state prediction equations.

Part Two, a classified supplement, presents numerical results assessing the attitude estimation performance potential. These results were obtained from a digital computer simulation that contains a detailed simulation of the actual spacecraft motion as influenced by the operation of the attitude control system and external torques, a simulation of the star sensor measurement process, and a simulation of the attitude determination algorithm.

### I. INTRODUCTION

This paper treats the implementation of an algorithm to provide continuous "realtime" estimates of the attitude of a particular satellite from measurement data provided by a star telescope fixed to the satellite body. Star sensor measurement data are transmitted in realtime via a telemetry link to be processed in a ground-based computational facility.

The spacecraft configuration of interest is shown in Fig. 1. This vehicle spins about its yaw axis at a nominal rate of 6 rpm. A constant speed, internally mounted reaction wheel is pro-

vided to approximately cancel the spin axis component of the total angular momentum so that the spin axis can be precessed at orbital rate and maintained in close alignment with the local vertical. The satellite is designed for operation at synchronous altitude.

An active attitude control system (ACS) employing gas jets is utilized for spin axis pointing control and for trim of the residual angular momentum. Attitude pointing error signals are obtained from a single horizon sensor which continuously scans over an angular region of space that contains the earth edge. Periodical "sampling" of the horizon sensor four times per

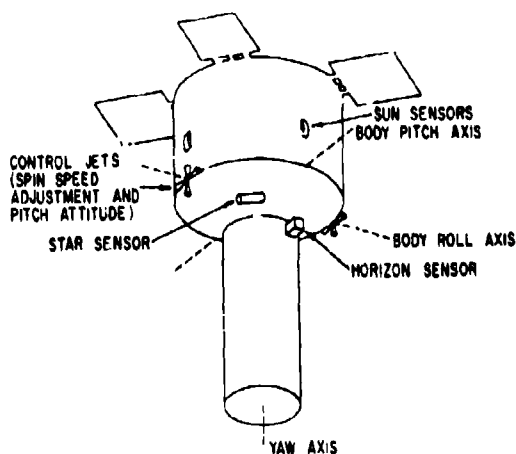


Fig. 1. Spacecraft Configuration

spin cycle yields two-axis pointing error information. A sun sensor provides a timing pulse which is used to synchronize the horizon sensor sampling times and the control jet firing times. Figure 2 illustrates the operation of the horizon sensor. The time  $t_0$  represents the synchronization pulse produced by the sun sensor. The figure illustrates the location of the horizon sensor scan regions at the four sampling times  $t_1$  through  $t_4$ . The pitch control jet firing times

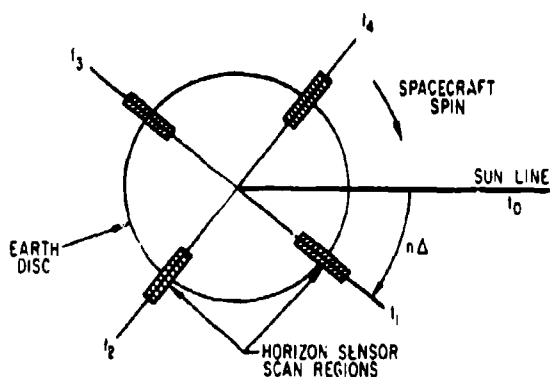


Fig. 2. Horizon Sensor Operation

are also synchronized with the horizon sensor sampling times to provide de-commutation of the control torque in space. The spin jets, which are used to adjust the satellite spin rate so as to null the spin axis component of angular momentum, are activated infrequently--about once per week.

The details of the attitude control logic are not immediately relevant to the attitude estima-

tion problem, and thus are omitted from the discussion herein. The operation of the attitude control system does, however, represent a major effect to be considered in the implementation of the attitude estimator. In order that the computational algorithm can make some provision for the effects of ACS operations, the following data are telemetered to the computational facility:

1. Control jet valve driver input pulses (jet on and off times)
2. Reaction wheel tachometer pulses (reaction wheel speed information)

A body-fixed star sensor provides the basic measurement data for attitude estimation. The star sensor optical system may be represented schematically as shown in Fig. 3. The star sensor consists of a lens system, which produces a star image on the focal plane; a reticle containing three slits oriented as shown in the figure; and a photomultiplier tube and associated electronics, which detect the time at which a star image falls in the center of one of the slits. Photomultiplier outputs are sampled at a high rate and telemetered to the ground. A preprocessor on the ground

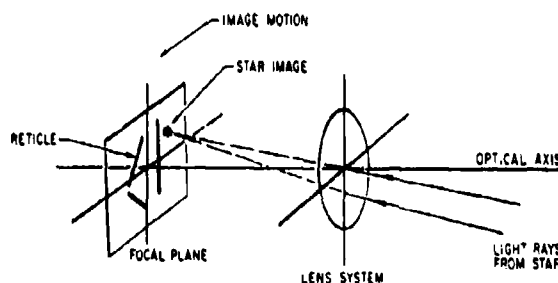


Fig. 3. Star Sensor Schematic

operates on the raw telemetry data to compute the time at which a star image crosses one of the star sensor slits. This "measured" star crossing time is sent to the estimation algorithm to be used to update the current attitude estimates. For purposes herein, the details of the preprocessor signal processing are ignored, and it is assumed that these measured star crossing times define the star sensor measurement output. Because of optical system limitations, background noise, electronic errors, and telemetry limitations, this measured crossing time differs from the true time at which a star image actually crossed the slit. This error is assumed to be characterized by a zero-mean Gaussian random sequence, uncorrelated from measurement to measurement. Typically, the standard deviation of the star sensor measurement error is around 5 arc sec (expressed as the angular azimuth uncertainty in the star location at the measured detection time).

The star telescope is mounted so that its optical axis is approximately normal to the vehicle spin axis and the vertical slit shown in Fig. 3 is approximately parallel to the spin axis. In this manner, the field of view of the "vertical" slit scans a great circle band in the celestial sphere as a result of the satellite spin (see Fig. 4). In this way, stars are sensed as their images cross the slit pattern in the telescope focal plane. The vertical slit instantaneous field of view is 3 deg.

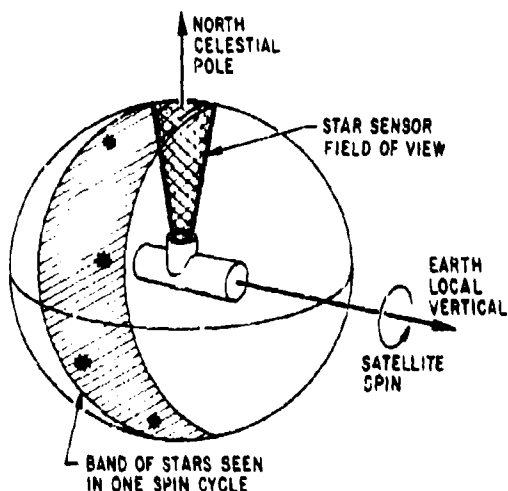


Fig. 4. Star Sensor Scan Geometry

## II. CONFIGURATION OF ATTITUDE ESTIMATOR

In general, spacecraft attitude estimation can be defined as:

The estimation of the angular orientation relative to some reference basis of a meaningful coordinate frame which is embedded in the satellite body.

The word "estimation" is used because the desired information must be extracted from noisy sensor data. A meaningful coordinate frame refers to some coordinate frame attached to the spacecraft which is useful to the problem at hand. In general, several possible choices exist for this coordinate frame, which defines the basis for definition of satellite attitude, and its proper selection is important to attitude estimation performance. This aspect of the problem is emphasized in the next section, which discusses the implementation of the estimation equations.

In the present section, the general mathematical structure of the attitude estimation problem is examined, and a particular filter configuration is postulated.

Let  $x(t)$  denote an  $n$ -vector that defines the state of the system under consideration. The

vector  $x$  is comprised of the set of variables and parameters sufficient to describe the spacecraft attitude motion and measurement processes. The evolution of the state over an arbitrary time interval from  $t_N$  to  $t$  is assumed to be governed by an equation of the form

$$\dot{x}(t) = f[x(t_N), t, t_N] + \Gamma(t, t_N)v(t_N) \quad (1)$$

where  $v(t_N)$  denotes a vector-valued random sequence which represents unknown disturbances to the state; the function  $f(\cdot)$  is a vector-valued function defining the trajectory of the state vector in time. The scalar measurement process denoted  $z(t_N)$  can be represented as a function of the state with additive measurement noise  $u(t_N)$  in the following form:

$$z(t_N) = h[x(t_N)] + u(t_N) \quad (2)$$

It is assumed that the measurement noise is a zero-mean, white noise sequence with known variance. Equations (1) and (2) constitute a description of the "real world" system motion and measurement process, respectively. The functions  $f(\cdot)$  and  $h(\cdot)$  define the "predictable" portion of the system motion and measurement.

Simply stated, the estimation problem is to find some method of forming an estimate of the state, which is in some sense close to the actual state, given a sequence of measurements  $z(t_N)$ . In particular, we are searching for an operator that transforms the observation sequence to an estimate of the state. The exact solution to the optimal estimation problem with nonlinear dynamics and/or measurements is not known. However, the optimal estimation problem for linear systems has been solved, and many different techniques of forming an approximate solution to the nonlinear problem have been proposed in the literature.

The estimation algorithm presented here is developed heuristically on the basis that the problem can be considered "nearly" linear. It is therefore postulated that the filter configuration that is optimal if the problem were exactly linear is a reasonable (but not necessarily best) choice for the actual problem at hand. Furthermore, the filter is structured so that the nonlinearities that must be ignored are higher-order terms in the state estimation error. If the filter design is at all reasonable, the estimation error will tend to become smaller with increasing filter time and thus increase the validity of the linear approximations.

The basic philosophy in developing the estimation algorithm is first to assume a particular filter configuration and then to find the set of filter gains that are approximately the optimal gains for the assumed configuration. In particular, it is assumed that the estimation algorithm consists of the following basic structure:



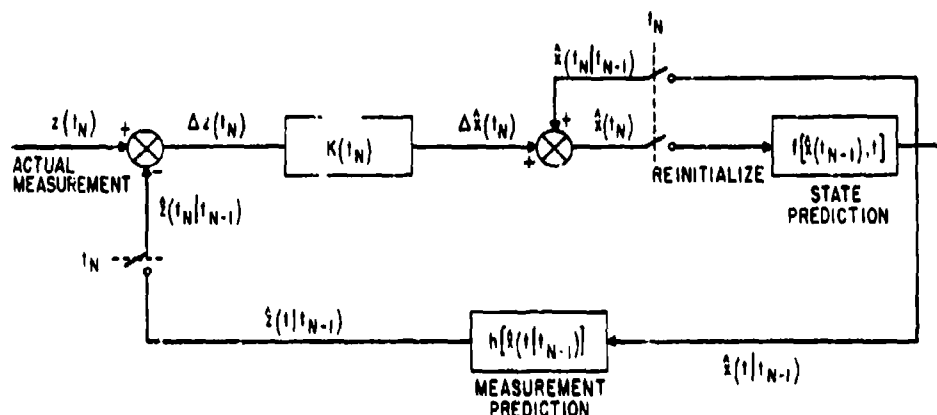


Fig. 5. General Configuration of Attitude Estimator

State prediction<sup>1</sup>:  $t_{N-1} \leq t < t_N$

$$\hat{x}(t|t_{N-1}) = f[\hat{x}(t_{N-1}), t, t_{N-1}] \quad (3)$$

Measurement prediction:

$$\hat{z}(t_N|t_{N-1}) = h[\hat{x}(t_N|t_{N-1})] \quad (4)$$

Filtered state estimates<sup>2</sup>:

$$\hat{x}(t_N) = \hat{x}(t_N|t_{N-1}) + K(t_N)[z(t_N) - \hat{z}(t_N|t_{N-1})] \quad (5)$$

Equation (3) is used to predict the state between measurements given the value  $\hat{x}(t_{N-1})$ , which is the filtered state estimate at the last measurement time. The measurement prediction is based on the predicted state. When a measurement becomes available, the filtered state estimate is formed by the addition of a correction term to the predicted state, as seen in Eq. (5). The correction term consists of the difference between the actual measurement and the predicted measurement multiplied by a gain matrix  $K(t_N)$ . Figure 5 shows the mechanization of the attitude estimation equation in block diagram form.

The filter gain equations used here are the Kalman equations developed for the case of linear system dynamics and a linear discrete measurement process (Ref. 1). The steps leading up to the application of these results to the present nonlinear problem will now be examined to clarify the approximation involved. Let the following notational conveniences be introduced:

<sup>1</sup>The notation  $\hat{x}(t|t_{N-1})$  denotes the estimate of the vector  $x$  at time  $t$  given measurements up to time  $t_{N-1}$ .

<sup>2</sup>The filtered state estimate  $\hat{x}(t_N)$  is understood to denote  $\hat{x}(t_N|t_N)$ .

a. Prediction error:

$$\tilde{x}(t|t_{N-1}) = x(t) - \hat{x}(t|t_{N-1}) \quad (6)$$

b. Filtering error:

$$\tilde{x}(t_N) = x(t_N) - \hat{x}(t_N) \quad (7)$$

The system dynamic equations as defined by Eq. (1) are expanded in a Taylor series about the point  $\hat{x}(t_{N-1})$ , the most recent filtered state estimate, to give the following result:

$$\begin{aligned} x(t) = & f[\hat{x}(t_{N-1}), t, t_{N-1}] + \theta(t, t_{N-1})\tilde{x}(t_{N-1}) \\ & + \Gamma(t, t_{N-1})v(t_{N-1}) \\ & + \text{higher-order terms in } \tilde{x}(t_{N-1}) \end{aligned} \quad (8)$$

where  $\theta(t, t_{N-1})$  denotes the  $n \times n$  partial derivative matrix of the vector function  $f = (f_1, f_2, \dots, f_n)^T$  with respect to the state; that is,

$$\theta_{ij}(t, t_{N-1}) = \frac{\partial f_i[x(t_{N-1}), t, t_{N-1}]}{\partial x_j} \bigg|_{x=\hat{x}(t_{N-1})} \quad (9)$$

Similarly, Eq. (2), the measurement equation, can be expanded in a Taylor series about the point  $\hat{x}(t_N|t_{N-1})$  to produce the following result.

$$\begin{aligned} z(t_N) = & h[\hat{x}(t_N|t_{N-1})] + H(t_N)\tilde{x}(t_N|t_{N-1}) + u(t_N) \\ & + \text{higher-order terms in the prediction error} \end{aligned} \quad (10)$$

The matrix  $H(t_N)$  is a  $1 \times n$  matrix defining the partial derivatives of the measurement function  $h(\cdot)$  with respect to the state; that is,

$$H_{1,j}(t_N) = \left. \frac{\partial h[x(t_N)]}{\partial x_j} \right|_{x=\hat{x}(t_N|t_{N-1})} \quad (11)$$

Now, neglecting the higher-order terms in Eqs. (8) and (11) and using the results of Eqs. (3)-(5) yields the following linear approximation for the propagation of the prediction error and filtering error from one measurement time to the next:

Prediction error:

$$\tilde{x}(t_N|t_{N-1}) = \theta(t_N|t_{N-1})\tilde{x}(t_{N-1}) + \Gamma(t_N, t_{N-1})v(t_{N-1}) \quad (12)$$

Filtering error:

$$\tilde{x}(t_N) = \tilde{x}(t_N|t_{N-1}) + K(t_N)[H(t_N)\tilde{x}(t_N|t_{N-1}) + u(t_N)] \quad (13)$$

If a) the dynamic equations and measurement equations are linear in the state variables, b) the random sequences  $v(t_N)$  and  $u(t_N)$  are white, Gaussian, zero mean with covariances  $Q$  and  $R$ , respectively, and c) the initial guess of the state vector is such that  $\tilde{x}(t_0)$  is zero mean and Gaussian, then Eqs. (12) and (13) are exact and the prediction error and filtering error are zero-mean, Gaussian, random sequences with covariances  $M(t_N)$  and  $P(t_N)$ , respectively, which are found from Eqs. (12) and (13), as follows:

$$M(t_N) = \theta(t_N, t_{N-1})P(t_{N-1})\theta^T(t_N, t_{N-1}) + \Gamma(t_N, t_{N-1})Q\Gamma^T(t_N, t_{N-1}) \quad (14)$$

$$P(t_N) = [I - K(t_N)H(t_N)]M(t_N)[I - K(t_N)H(t_N)]^T + K(t_N)RK^T(t_N) \quad (15)$$

with  $P(t_0) = E[\tilde{x}(t_0)\tilde{x}(t_0)^T]$ . Reference 1 shows that the optimal gain matrix that minimizes the variance of the filtering error is given by

$$K(t_N) = M(t_N)H^T(t_N)[H(t_N)M(t_N)H^T(t_N) + R]^{-1} \quad (16)$$

Thus, if assumptions a)-c) hold true, then Eqs. (14)-(16) form a coupled set of matrix equations

which define the gain matrix sequence to produce a minimum variance estimate of the state.

In the nonlinear problem here, none of these assumptions is strictly valid; nevertheless, Eqs. (14)-(16) are used to compute the filter gain matrix. Equations (9) and (11) are used to compute the  $\theta$  and  $H$  matrices. Note that these matrices are updated at each measurement time to reflect evaluation of the partial derivatives at the most recent state estimate. For the nonlinear problem, the matrices  $M$  and  $P$  lose their significance as covariance matrices and the gain matrix is no longer optimal. The one justification for use of these equations in the present nonlinear problem is that fairly accurate initial estimates of the system state are available. This fact tends to give some degree of validity to Eqs. (12) and (13) as representing the propagation of the actual filtering error, as the neglected terms are higher-order terms in the state estimation error multiplied by second-order and higher partial derivatives of the measurement function and dynamic equations. Under these conditions, one might expect Eqs. (14) and (15) to approximate the actual covariance matrices and Eq. (16) to work rather well as a gain matrix for the filter. In the attitude estimation problem here, initial estimates of attitude are accurate to within 1 deg, owing to the operation of the attitude control system. The higher-order terms dropped from Eqs. (12) and (13) are several orders of magnitude smaller than the linear terms.

### III. IMPLEMENTATION OF ATTITUDE ESTIMATOR

The details of implementing the attitude estimation equations for the problem at hand will now be examined. Then, the coordinate systems that serve to define the problem are introduced, and the star sensor measurement functions are obtained. Next, particular attention is given to the selection of a specific coordinate frame that serves to define satellite attitude, and to the development of an approximate closed-form solution for the satellite motion. Finally, the specific configuration of the attitude estimator is presented.

#### A. Coordinate Systems

An inertial frame (I-frame), earth-centered and nonrotating in celestial space, is the fundamental basis from which all orientations are referenced. The unit vectors  $\bar{x}_I$ ,  $\bar{y}_I$ ,  $\bar{z}_I$  are the orthonormal basis vectors for this frame which are oriented as follows:

$\bar{x}_I$  points toward the first point of Aries

$\bar{z}_I$  points toward the north celestial pole

$\bar{y}_I$  completes orthogonal right-hand set

An intermediate attitude reference frame (R-frame) is introduced as a convenience to aid in defining attitude. The R-frame is an earth-oriented reference frame that forms the basis

from which satellite attitude angles are measured and is defined as follows:

Origin: satellite mass center

Unit vectors:  $\bar{x}_R, \bar{y}_R, \bar{z}_R$

$\bar{z}_R$  points along line from satellite mass center to the earth's geocenter

$\bar{x}_R$  points along the positive projection of the satellite velocity vector on the plane normal to  $\bar{z}_R$

$\bar{y}_R$  is normal to the instantaneous orbit plane completing an orthogonal right-hand set

The body-reference frame (B-frame) is a coordinate system embedded in the satellite mass system, which forms the basis to which the attitude angles are measured. The specific orientation of this coordinate system with respect to the satellite is defined in a subsequent paragraph. The B-frame is here defined in the following general terms:

Origin: satellite mass center

Unit vectors:  $\bar{x}_B, \bar{y}_B, \bar{z}_B$

$\bar{z}_B$  defines the satellite yaw axis, positive toward the end of the satellite which is earth-pointed

$\bar{y}_B$  denotes satellite pitch axis

$\bar{x}_B$  denotes satellite roll axis

Three star sensor coordinate systems  $SS_1, SS_2, SS_3$  define the star sensor measurement geometry. The orientation of these coordinate systems in the vehicle is determined by the orientation of the reticle and the star sensor optical center. These coordinate systems are defined in

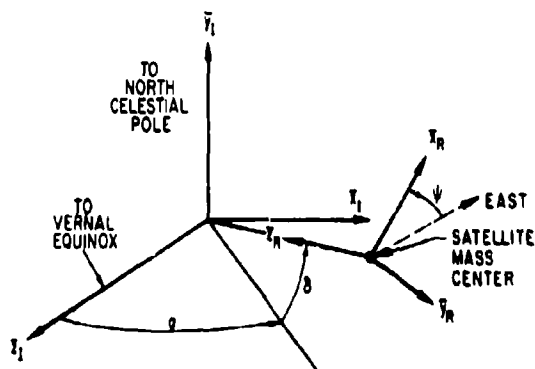


Fig. 6. Definition of Attitude Reference Frame Orientation

a subsequent paragraph discussing the star sensor measurement functions.

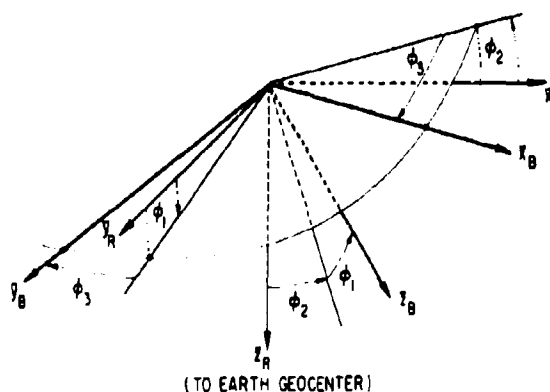
The orientation of the R-frame with respect to the I-frame is determined by the satellite ephemeris and is illustrated in Fig. 6.

Satellite attitude is defined in terms of three Euler angles  $\phi_1, \phi_2, \phi_3$ , which respectively define the roll, pitch, and yaw attitude of the B-frame with respect to the R-frame. The rotation sequence in going from the R-frame to the B-frame is, first, pitch  $\phi_2$  about  $\bar{y}_R$ ; next, roll  $\phi_1$  about the new  $\bar{x}$  axis; finally, yaw  $\phi_3$  about the new  $\bar{z}$  axis as illustrated in Fig. 7. The body attitude is then defined by the transformation

$$\begin{pmatrix} \bar{x}_B \\ \bar{y}_B \\ \bar{z}_B \end{pmatrix} = [\phi] \begin{pmatrix} \bar{x}_R \\ \bar{y}_R \\ \bar{z}_R \end{pmatrix} \quad (17)$$

where

$$[\phi] = [\phi_3]_z [\phi_1]_x [\phi_2]_y \quad (18)$$



$$\begin{pmatrix} \bar{x}_B \\ \bar{y}_B \\ \bar{z}_B \end{pmatrix} = [\phi_3]_z [\phi_1]_x [\phi_2]_y \begin{pmatrix} \bar{x}_R \\ \bar{y}_R \\ \bar{z}_R \end{pmatrix}$$

Fig. 7. Definition of Satellite Attitude Angles

The subscript notation on rotation matrices will be used throughout to denote the three fundamental rotation matrices:

$$[a]_x = \begin{bmatrix} 1 & 0 & 0 \\ 0 & \cos a & \sin a \\ 0 & -\sin a & \cos a \end{bmatrix}$$

$$[a]_y = \begin{bmatrix} \cos \alpha & 0 & -\sin \alpha \\ 0 & 1 & 0 \\ \sin \alpha & 0 & \cos \alpha \end{bmatrix}$$

$$[a]_z = \begin{bmatrix} \cos \alpha & \sin \alpha & 0 \\ -\sin \alpha & \cos \alpha & 0 \\ 0 & 0 & 1 \end{bmatrix}$$

#### B. Star Sensor Measurement Process

In the case of an ideal star sensor, the measured star crossing time can be considered to be that time when a unit vector to a star lies in a particular plane fixed to the star sensor. For the reticle configuration illustrated in Fig. 3 we can define three star planes to be the conditions for generation of a star crossing time signal for each of the three slits. Each of these "star planes" is the plane formed by the system optical center and the center line of the corresponding reticle slit. Figure 8 illustrates this star sensor geometry. Note that the three star planes intersect at a common point: the system optical center. This point will be used to define the origin of our star sensor coordinate systems. Three star sensor coordinate frames, each having the  $\bar{y}$  unit vector pointing perpendicular to one of the star planes, are introduced as follows:

##### SS-1 Coordinate System

$\bar{x}_{SS1}$  lies in Star Plane No. 1 pointing outward along the projection of the line of intersection of Star Planes 2 and 3 on the plane

$\bar{y}_{SS1}$  is normal to Star Plane No. 1

$\bar{z}_{SS1}$  lies in Star Plane No. 1 completing right-hand set

##### SS-2 Coordinate System

$\bar{x}_{SS2}$  points along the intersection of Star Planes 2 and 3

$\bar{y}_{SS2}$  is normal to Star Plane No. 2

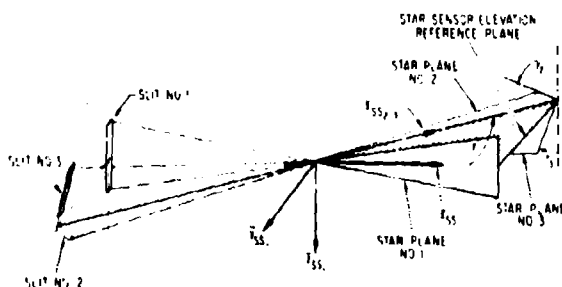


Fig. 8. Star Sensor Optical Geometry

##### SS-3 Coordinate System

$\bar{x}_{SS3}$  is identical to  $\bar{x}_{SS2}$

$\bar{y}_{SS3}$  is normal to Star Plane No. 3

The angles  $\gamma_1, \gamma_2, \gamma_3$  illustrated in Fig. 8 define the orientation of the three star planes. The orientation of the SS-2 and SS-3 coordinate frames relative to the SS-1 frame can be expressed in terms of these angles as follows:

$$\begin{pmatrix} \bar{x}_{SS2} \\ \bar{y}_{SS2} \\ \bar{z}_{SS2} \end{pmatrix} = [\Gamma_2] \begin{pmatrix} \bar{x}_{SS1} \\ \bar{y}_{SS1} \\ \bar{z}_{SS1} \end{pmatrix} \quad (19)$$

$$\begin{pmatrix} \bar{x}_{SS3} \\ \bar{y}_{SS3} \\ \bar{z}_{SS3} \end{pmatrix} = [\Gamma_3] \begin{pmatrix} \bar{x}_{SS1} \\ \bar{y}_{SS1} \\ \bar{z}_{SS1} \end{pmatrix} \quad (20)$$

where

$$[\Gamma_2] = [\gamma_2]_x [-\gamma_1]_z \quad (21)$$

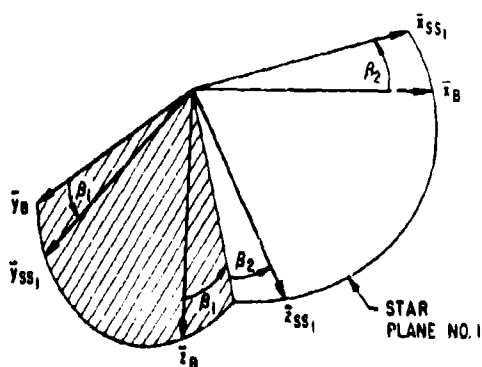
$$[\Gamma_3] = [-\gamma_3]_x [-\gamma_1]_z \quad (22)$$

The orientation of the SS-1 frame with respect to the B-frame is defined by two angles  $\beta_1$  and  $\beta_2$  as illustrated in Fig. 9. Note that we have removed some of the generality in the definition of the B-frame and have restricted  $\bar{x}_B$  to lie in Star Plane No. 1. The angle  $\beta_1$  designates the angular "twist" of the star sensor about  $\bar{x}_B$ , and  $\beta_2$  indicates the "elevation" of the star sensor relative to the  $\bar{x}_B$ - $\bar{y}_B$  plane. From the figure, the orientation of the SS-1 frame is expressed as follows:

$$\begin{pmatrix} \bar{x}_{SS1} \\ \bar{y}_{SS1} \\ \bar{z}_{SS1} \end{pmatrix} = [\theta] \begin{pmatrix} \bar{x}_B \\ \bar{y}_B \\ \bar{z}_B \end{pmatrix} \quad (23)$$

where

$$[\theta] = [\beta_2]_y [\beta_1]_x \quad (24)$$



$$\begin{pmatrix} \vec{x}_{ss1} \\ \vec{y}_{ss1} \\ \vec{z}_{ss1} \end{pmatrix} = [\beta_2]_y [\beta_1]_x \begin{pmatrix} \vec{x}_B \\ \vec{y}_B \\ \vec{z}_B \end{pmatrix}$$

Fig. 9. Orientation of Star Sensor Frame Relative to Body Frame

In the case of an ideal star sensor, the measured star crossing time produced by a star image crossing a given slit is simply the time at which the dot product of the unit star vector with the particular star plane normal ( $\vec{y}_{ss1}$ ) vanishes. Because of optical aberrations, background noise, and random errors in the generation of the star detection time, it is not possible to assign a unique location to the star vector in the body at its time of detection. The set of all possible star vectors at the detection time for a particular slit forms an ensemble of random vectors in the satellite. For this case, the concept of the "star plane" is still useful if the star plane is considered as that plane forming the best mean square fit over the field of view to this random ensemble of star vectors. In this situation, the measured star crossing time  $t_N$  produced by Star  $j$  crossing Slit  $i$  is defined implicitly by

$$\vec{S}_j \cdot \vec{y}_{ss1}(t_N) + e_j = 0 \quad (25)$$

where  $\vec{S}_j$  = unit vector to Star  $j$ , and the error  $e_j$  represents the random error in the detection process and geometrically represents a small displacement of the star vector normal to the star plane. For purposes herein, this error shall be considered to be a zero-mean, Gaussian, random variable.

The attitude estimator requires that the measurement process be represented as a function of the state variables in a form given by Eq. (2). Should the measurement variable  $z$  be defined as being the star crossing time, some difficulties can arise because of the implicit nature of Eq. (25) in generating a value for the predicted time. A different approach is used here that avoids the necessity of computing an explicit

value for the predicted star crossing time. The approach is to define the measurement  $z$  as being identical to the dot product in Eq. (20); that is, we define the measurement  $z(t_N)$  as

$$z_i(t_N) = \vec{S}_j \cdot \vec{y}_{ss1}(t_N) + e(t_N) = 0 \quad (26)$$

where again  $t_N$  designates the measured star detection time for Slit  $i$ . The measurement function  $h(\cdot)$  is then defined as

$$h_i[x(t_N)] = \vec{S}_j \cdot \vec{y}_{ss1}(t_N) \quad (27)$$

where the subscript  $i$  designates the measurement function for Slit  $i$ . The quantity  $e(t_N)$  in Eq. (26) corresponds to the measurement noise  $u(t_N)$  in Eq. (2). In view of these definitions, the predicted value of the measurement is calculated as

$$\hat{z}_i(t_N) = \vec{S}_j \cdot \hat{\vec{y}}_{ss1}(t_N) \quad (28)$$

where  $\hat{\vec{y}}_{ss1}$  denotes the estimated unit normal vector corresponding to Slit  $i$ . The measurement residual  $z$  is simply

$$\tilde{z}_i = z_i(t_N) - \hat{z}_i(t_N) = -\vec{S}_j \cdot \hat{\vec{y}}_{ss1}(t_N) \quad (29)$$

That is, the measurement residual is formed merely by means of computing the dot product in Eq. (29) and sampling it at the measured star crossing time. This can be done because the actual measurement  $z_i(t_N)$  was explicitly defined as being identically zero. This procedure is computationally more efficient than explicitly computing time residuals, and produces the same information for the filter.

The measurement functions for the three slits can be expressed in terms of the attitude angles  $\phi_1, \phi_2, \phi_3$  and star sensor alignment angles  $\beta_1, \beta_2$  by use of Eqs. (17)-(24) to express the dot products to give the following results:

$$h_1 = \vec{S}_j \cdot \vec{y}_{ss1} = [0 \quad 1 \quad 0][\beta][\phi](S_j)_R \quad (30)$$

$$h_2 = \vec{S}_j \cdot \vec{y}_{ss2} = [0 \quad 1 \quad 0][\Gamma_2][\beta][\phi](S_j)_R \quad (31)$$

$$h_3 = \vec{S}_j \cdot \vec{y}_{ss3} = [0 \quad 1 \quad 0][\Gamma_3][\beta][\phi](S_j)_R \quad (32)$$

The quantity  $(S_j)_R$  is a column matrix composed of the components of the star vector  $\vec{S}_j$  in the R-frame; that is,

$$(S_j)_R = \begin{pmatrix} S_j \cdot \bar{x}_R \\ S_j \cdot \bar{y}_R \\ S_j \cdot \bar{z}_R \end{pmatrix} \quad (33)$$

### C. Selection of a Body-Reference Frame

The B-frame up to this point has been considered to be an arbitrary coordinate frame embedded in the satellite body. From the standpoint of the attitude determination problem, the selection of a specific B-frame coordinate system is an important consideration.

The primary consideration for selection of a B-frame should be the accuracy to which its attitude can be determined. Mathematically, this question is one of the degree of "observability" of the attitude of the coordinate frame, given the particular set of attitude measurements. Not all coordinate frames are equally observable. Speaking heuristically, the degree of observability of a particular coordinate frame is associated with the extent that its attitude displacements affect the measurements. In order for a particular frame to be observable, it is thus necessary that its attitude directly affects the measurement process or indirectly affects it by changing the dynamic motion of the attitude sensor.

From an operational standpoint, there often exists a well-defined coordinate frame whose attitude we would like to obtain, namely, a coordinate frame fixed to some mission sensor whose pointing direction in space is of primary interest. This coordinate frame would be the most desirable choice for a B-frame, but unfortunately, such a frame is in general not observable. This is true because changes in alignment of the mission sensor relative to the satellite will have no effect upon the star sensor measurements or upon the vehicle motion. In order to determine the pointing direction of the mission sensor, one can rely on prelaunch measurements defining the alignment relative to some other frame (B-frame) whose attitude is observable from the star sensor measurements.

In cases where extremely accurate determination of the mission sensor pointing direction is required, prelaunch alignments may not provide sufficient accuracy because of errors incurred during boost and during the varying orbital thermal environment. In these cases, on-orbit calibration of the mission sensor alignment relative to the B-frame must be provided. This is often done by using the mission sensor to sight objects with known locations, and using the information together with the estimates of the attitude of the B-frame to update the knowledge of mission sensor alignment relative to the B-frame. Obviously, the accuracy of this "boresight" procedure is related to the accuracy of the knowledge of the attitude of the B frame.

Thus, from an operational standpoint, even though the attitude of our B-frame is not of itself of primary interest, it is essential to choose a B-frame whose attitude can be most accurately determined. An additional consideration in the selection of the B-frame is the stability of its alignment relative to the mission sensor, in cases where an on-orbit boresight of the mission sensor is not performed.

At first glance, the most obvious choice for the B-frame would appear to be the star sensor frame (SS-frame). However, this turns out to be an undesirable choice for two reasons: First, the stability of the star sensor alignment relative to the mission sensor is poor. The nature of the effect of the thermal environment on the structure is such that it causes large "twisting" deflections of the star sensor about its optical axis relative to the mission sensor. Second, even in the absence of these alignment variations, the observability of the attitude of the star sensor coordinate frame is poor. This fact is a result of the narrow field of view of the star sensor ( $\pm 1.5$  deg) which makes it difficult to estimate the angle of rotation about the sensor optical axis.

In view of these difficulties, it becomes desirable to examine the vehicle dynamic characteristics in an attempt to select an alternate coordinate system whose attitude has some particular significance in terms of the motion of the star sensor in space. It will be shown that a zero-momentum satellite must spin about a particular axis fixed in its body. This "spin axis" is selected to define the Z axis of the B-frame.

Let the following notation be introduced:

- $\bar{I}$  = the dyadic defining the moment of inertia of the total satellite mass system with respect to its mass center
- $\bar{\omega}$  = angular velocity of the B-frame relative to inertial space
- $\bar{H}$  = total system angular momentum relative to its mass center
- $\bar{h}$  = "relative angular momentum"<sup>3</sup> or the contribution to the total angular momentum  $\bar{H}$  which is generated by elements of mass moving relative to the B-frame
- $\bar{z}_w$  = unit vector pointing along the reaction wheel bearing axis
- $C_w$  = reaction wheel moment of inertia about its bearing axis
- $\omega_R$  = reaction wheel angular velocity relative to the satellite

<sup>3</sup>See Ref. 2 for a general development of the concept of "relative angular momentum."

It is shown in Ref. 2 that the total angular momentum for a satellite of arbitrary configuration can be expressed in the following form:

$$\vec{H} = \vec{I} \cdot \vec{\omega} + \vec{h} \quad (34)$$

Let  $(H)$ ,  $(\omega)$ ,  $(h)$  denote the  $3 \times 1$  component matrices of the vectors  $\vec{H}$ ,  $\vec{\omega}$ ,  $\vec{h}$  expressed in an arbitrary coordinate frame (A-frame) embedded in the satellite body, and let  $[I]$  denote the  $3 \times 3$  component matrix of the dyadic  $\vec{I}$  expressed in this A-frame. The matrix form of Eq. (34) is as follows:

$$(H) = [I](\omega) + (h) \quad (35)$$

The angular velocity can be expressed in terms of  $(H)$  and  $(h)$  by inversion of Eq. (35) to yield

$$(\omega) = [I]^{-1}(H) - [I]^{-1}(h) \quad (36)$$

Let us further define

$$(\delta\omega) = [I]^{-1}(H) \quad (37)$$

$$(\omega^*) = -[I]^{-1}(h) \quad (38)$$

so that we can express the total angular velocity as follows:

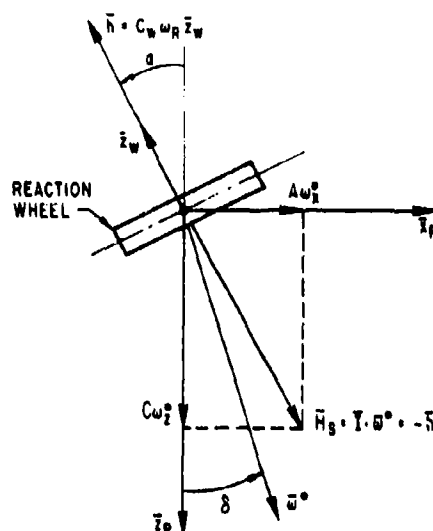
$$(\omega) = (\delta\omega) + (\omega^*) \quad (39)$$

Equations (37) and (38) each define components of a vector in the arbitrary A-frame. Equation (39) states that the body angular velocity can be considered as the vector sum of two components -- one component being the contribution of the total system angular momentum  $\vec{H}$ , and the other being the contribution of the relative angular momentum generated by moving parts.

If the satellite structure can be considered to be rigid, the relative angular momentum results solely from the motion of the reaction wheel relative to the satellite body. If the wheel has mass symmetry about its bearing axis, the relative angular momentum vector is given as

$$\vec{h} = C_w \omega_R \vec{e}_w \quad (40)$$

For the case of the vehicle configuration of interest, the total angular momentum is a small fraction of the wheel momentum owing to the satellite outer structure spinning in space opposite to the internal spinning reaction wheel. Attitude control thrusters are used to "trim" the



$\vec{z}_p$ : "YAW" PRINCIPAL AXIS OF TOTAL MOMENT OF INERTIA DYADIC  
 $\vec{z}_R$ : "ROLL" PRINCIPAL AXIS OF TOTAL MOMENT OF INERTIA DYADIC  
 A, B, C = ROLL, PITCH, YAW PRINCIPAL MOMENTS OF INERTIA  
 COMPONENTS OF SPIN VECTOR IN PRINCIPAL AXES:

$$\begin{aligned} \omega_R^* &= \frac{C_w \omega_R}{A} \sin \alpha & \omega_p^* &= \frac{C_w \omega_R}{C} \cos \alpha \\ \omega_Y^* &= 0 & \tan \delta &= \frac{\omega_R^*}{\omega_p^*} = \frac{C}{A} \tan \alpha \end{aligned}$$

Fig. 10. Illustration of Spin Vector Orientation

total angular momentum as required to maintain the "residual" angular momentum less than 0.2% of the wheel momentum; that is,

$$|\vec{h}| < 0.002 |\vec{H}| \quad (41)$$

Because of this fact, we find

$$|\delta\vec{\omega}| \ll |\vec{\omega}^*| \quad (42)$$

and the total angular velocity vector approximately coincides with the vector  $\vec{\omega}^*$ .

The vector  $\vec{\omega}^*$  is a body-fixed vector whose components were defined by Eq. (38), and thus has particular significance in terms of the motion of our satellite. This vector, which will be designated the "spin vector," represents the body angular velocity vector necessary to produce zero-total angular momentum. Figure 10 illustrates the orientation of the spin vector for the case where the reaction wheel bearing axis is misaligned with respect to the vehicle yaw principal axis. In the idealized case of a vehicle with a rigid structure and balanced reaction wheel spinning about an axis fixed in the structure, one finds:

1. Orientation of the spin vector in the vehicle is fixed by virtue of Eq. (38)
2. The magnitude of the spin vector is directly proportional to the wheel relative speed  $\omega_R$ .
3. If the spacecraft total angular momentum remains identically zero, the satellite motion consists of a pure spin about the vector  $\bar{\omega}^*$  which is fixed both in space and in the satellite body.

Thus, for the case of identically zero-total angular momentum, the motion of the star sensor is a pure spin about the vector  $\bar{\omega}^*$ , which is located approximately 90 deg from the star sensor optical axis. The orientation of the spin vector in space is of fundamental importance in determining what the star sensor sees. For this reason, the  $\bar{z}$  axis of the B-frame was chosen to lie along the spin vector. The  $\bar{x}$  axis of the B-frame was previously defined to lie in the star sensor vertical slit plane. This coordinate frame represents the only alternate to the star sensor frame which is observable from the star sensor measurements if total angular momentum is identically zero. This is true because in this case, the orientation of the vector  $\bar{\omega}^*$  relative to the star sensor and relative to celestial space is the only thing affecting the star sensor measurement process. The attitudes of the vehicle principal axes or the wheel bearing axis are both unobservable in the zero-momentum case because, for any orientation of the principal axes, there exists a corresponding reaction wheel orientation that leaves the orientation of the spin vector invariant with respect to the star sensor.

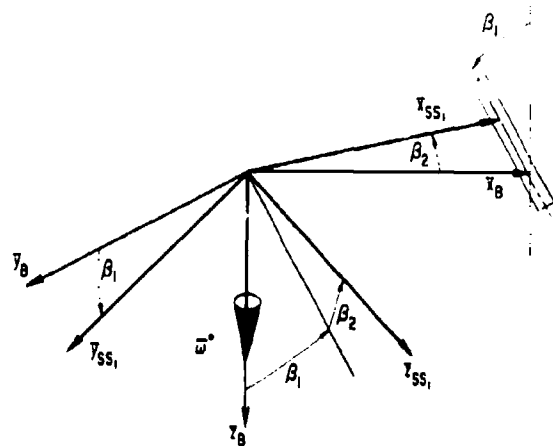
If the total angular momentum is nonzero, the spin vector still remains fixed in the body, but no longer remains fixed in space. The next section of the paper presents an approximate solution for the attitude motion of the B-frame.

It is desirable to restrict the B-frame to be fixed relative to the satellite structure. Lack of mass symmetry of the reaction wheel results in the vector  $\bar{h}$  "coning" in the vehicle at wheel speed, resulting in a coning in the spin vector relative to the structure. These effects are extremely small, but for purposes of generality any difficulties can be circumvented by defining the B-frame in terms of the average orientation of the spin vector over one wheel spin cycle.

The vehicle B-frame which defines the basis for definition of vehicle attitude is thus defined in terms of the unit vectors  $\bar{x}_B$ ,  $\bar{y}_B$ ,  $\bar{z}_B$  which are defined as follows:

- $\bar{x}_B$  lies in star sensor vertical slit plane
- $\bar{z}_B = \bar{\omega}^* / |\bar{\omega}^*|$
- $\bar{y}_B$  completes an orthogonal right-hand set

Figure 11 illustrates the orientation of our B-frame relative to the SS-1 star sensor frame.



$$\begin{pmatrix} x_{SS1} \\ y_{SS1} \\ z_{SS1} \end{pmatrix} = [\beta_2]_y [\beta_1]_x \begin{pmatrix} x_B \\ y_B \\ z_B \end{pmatrix}$$

Fig. 11. Definition of Body Reference Frame

#### D. Development of an Approximate Solution to the Vehicle Motion

The attitude of the B-frame with respect to the R-frame was defined in terms of the three angles  $\phi_1$ ,  $\phi_2$ ,  $\phi_3$ . The vehicle kinematic equations for the rotation convention defined by Eq. (18) were derived in Ref. 3, which gave the following result:

$$\begin{pmatrix} \dot{\phi}_1 \\ \dot{\phi}_2 \\ \dot{\phi}_3 \end{pmatrix} = \begin{pmatrix} 0 \\ \omega_0 \\ 0 \end{pmatrix} + \begin{bmatrix} \cos \phi_3 & -\sin \phi_3 & 0 \\ \sin \phi_3 / \cos \phi_1 & \cos \phi_3 / \cos \phi_1 & 0 \\ \sin \phi_3 \tan \phi_1 & \cos \phi_3 \tan \phi_1 & 1 \end{bmatrix} \begin{pmatrix} \omega_1 \\ \omega_2 \\ \omega_3 \end{pmatrix} \quad (43)$$

where  $\omega_1$ ,  $\omega_2$ ,  $\omega_3$  represent components of the angular velocity of the B-frame expressed in the B-frame, and  $\omega_0$  is the magnitude of the angular velocity of the R-frame (orbital rate). Equation (39) is used to expand the angular velocity vector. As a consequence of the definition of the B-frame the spin vector may be expressed as

$$\bar{\omega}^* = 0 \cdot \bar{x}_B + 0 \cdot \bar{y}_B + |\bar{\omega}^*| \bar{z}_B \quad (44)$$



The magnitude of the spin vector is proportional to the reaction wheel rate of rotation with respect to the spacecraft  $\omega_R$  and may be expressed as

$$|\omega^*| = K\omega_R \quad (45)$$

The constant of proportionality can be shown to be given by

$$K = \frac{C_W}{C} \left[ \left( \frac{C}{A} \right)^2 \sin^2 \alpha_2 + \left( \frac{C}{B} \right)^2 \sin^2 \alpha_1 \cos^2 \alpha_2 + \cos^2 \alpha_1 \cos^2 \alpha_2 \right]^{1/2} \quad (46)$$

where A, B, C are the spacecraft principal total moments of inertia;  $\alpha_1$  and  $\alpha_2$  are angles defining the orientation of the wheel bearing axis with respect to the spacecraft yaw principal axis  $\bar{x}_P$ ; and  $C_W$  is the wheel spin moment of inertia. Now, letting  $\delta\omega_{B1}$ ,  $\delta\omega_{B2}$ ,  $\delta\omega_{B3}$  denote the B-frame components of the vector  $\delta\bar{\omega}$  as defined by Eq. (37), and substituting the expanded angular velocity vector into Eq. (43), we obtain

$$\begin{pmatrix} \dot{\phi}_1 \\ \dot{\phi}_2 \\ \dot{\phi}_3 \end{pmatrix} = \begin{pmatrix} 0 \\ \omega_0 \\ K\omega_R \end{pmatrix} + \begin{bmatrix} \cos \phi_3 & -\sin \phi_3 & 0 \\ \sin \phi_3 / \cos \phi_1 & \cos \phi_3 / \cos \phi_1 & 0 \\ \sin \phi_3 \tan \phi_1 & \cos \phi_3 \tan \phi_1 & 1 \end{bmatrix} \begin{pmatrix} \delta\omega_{B1} \\ \delta\omega_{B2} \\ \delta\omega_{B3} \end{pmatrix} \quad (47)$$

Since  $\delta\omega_{B1}$ ,  $\delta\omega_{B2}$ ,  $\delta\omega_{B3}$  are each zero when the spacecraft total angular momentum is zero, Eq. (47) has a rather simple solution for this case, namely,

$$\left. \begin{aligned} \phi_1(t) &= \phi_1(t_0) \\ \phi_2(t) &= \phi_2(t_0) + \omega_0(t - t_0) \\ \phi_3(t) &= \phi_3(t_0) + K[a(t) - a(t_0)] \end{aligned} \right\} \quad (48)$$

where

$$a(t) - a(t_0) = \int_{t_0}^t \omega_R(\tau) d\tau \quad (49)$$

is the total angular excursion of the reaction wheel relative to the spacecraft in the interval  $(t_0, t)$ .

The effect of finite total angular momentum produces a contribution to the motion which adds to Eq. (48). An approximation to this contribution is now developed.

The key to obtaining an approximate solution to Eq. (47) is to express the vector  $\delta\bar{\omega}$  in terms of the components of the total angular momentum vector expressed in the attitude reference frame. Since the components of angular momentum in the B-frame are given in terms of the components in the R-frame by the equation

$$\begin{pmatrix} H_{B1} \\ H_{B2} \\ H_{B3} \end{pmatrix} = [\phi_3]_z [\phi_1]_x [\phi_2]_y \begin{pmatrix} H_{R1} \\ H_{R2} \\ H_{R3} \end{pmatrix} \quad (50)$$

and using Eq. (50) to express Eq. (37) in the B-frame, we can write

$$\begin{pmatrix} \delta\omega_{B1} \\ \delta\omega_{B2} \\ \delta\omega_{B3} \end{pmatrix} = [I_B]^{-1} [\phi_3]_z [\phi_1]_x [\phi_2]_y \begin{pmatrix} H_{R1} \\ H_{R2} \\ H_{R3} \end{pmatrix} \quad (51)$$

where  $[I_B]$  is the B-frame component matrix of the dyadic I. Note that for the vehicle of interest, the angles  $\phi_1$  and  $\phi_2$  will be kept small by the action of the attitude control system. If Eq. (51) is substituted into Eq. (47), and small angle approximations are made for  $\phi_1$  and  $\phi_2$ , the following result is obtained:

$$\begin{pmatrix} \dot{\phi}_1 \\ \dot{\phi}_2 \\ \dot{\phi}_3 \end{pmatrix} = \begin{bmatrix} 1 & 0 & 0 \\ 0 & 1 & 0 \\ 0 & \phi_1 & 1 \end{bmatrix} [\phi_3]_z^T [I_B]^{-1} [\phi_3]_z \times \begin{bmatrix} 1 & 0 & -\phi_2 \\ 0 & 1 & \phi_1 \\ \phi_2 & -\phi_1 & 1 \end{bmatrix} \begin{pmatrix} H_{R1} \\ H_{R2} \\ H_{R3} \end{pmatrix} + \begin{pmatrix} 0 \\ \omega_0 \\ K\omega_R \end{pmatrix} \quad (52)$$

In the absence of external torques, the total angular momentum vector is fixed in inertial space. For circular orbits, the attitude reference frame rotates at a constant rate  $\omega_0$ . For these conditions, the components of the total angular momentum vector expressed in the attitude reference frame are given by the following closed-form equation:

$$\begin{pmatrix} H_{R_1}(t) \\ H_{R_2}(t) \\ H_{R_3}(t) \end{pmatrix} = \begin{bmatrix} \cos \omega_0(t - t_0) & 0 & \sin \omega_0(t - t_0) \\ 0 & 1 & 0 \\ -\sin \omega_0(t - t_0) & 0 & \cos \omega_0(t - t_0) \end{bmatrix} \times \begin{pmatrix} H_{R_1}(t_0) \\ H_{R_2}(t_0) \\ H_{R_3}(t_0) \end{pmatrix} \quad (53)$$

where  $\omega_0$  is the angular velocity of the R-frame (orbital rate).

Equation (53) constitutes a first integral for the problem. The availability of the exact solution is the reason for selecting angular momentum in the R-frame as one portion of the state vector.

One additional step is required in the formulation of equations for solution: the simplification of the form of the moment of inertia matrix. The total moment of inertia tensor expressed in terms of its principal axes is in general given by

$$\bar{I} = \begin{pmatrix} \bar{x}_P \\ \bar{y}_P \\ \bar{z}_P \end{pmatrix}^T \begin{bmatrix} A & 0 & 0 \\ 0 & B & 0 \\ 0 & 0 & C \end{bmatrix} \begin{pmatrix} \bar{x}_P \\ \bar{y}_P \\ \bar{z}_P \end{pmatrix} \quad (54)$$

Let the orientation of the principal axes with respect to the B-frame be given by the following transformation:

$$\begin{pmatrix} \bar{x}_P \\ \bar{y}_P \\ \bar{z}_P \end{pmatrix} = [\epsilon_2]_y [\epsilon_1]_x [\epsilon_3]_z \begin{pmatrix} \bar{x}_B \\ \bar{y}_B \\ \bar{z}_B \end{pmatrix} \quad (55)$$

The angles  $\epsilon_1$  and  $\epsilon_2$ , which are the angles between  $\bar{x}_P$  and  $\bar{x}_B$ , are small for the vehicle of interest. The moment of inertia matrix in the B-frame is then given by

$$[I_B] = [\epsilon_3]_z^T [\epsilon_1]_x^T [\epsilon_2]_y^T \begin{bmatrix} A & & \\ & B & \\ & & C \end{bmatrix} \times [\epsilon_2]_y [\epsilon_1]_x [\epsilon_3]_z \quad (56)$$

The vehicle of interest is very nearly symmetric about the yaw principal axis such that  $A = B$ . This fact can be used to simplify the form of the moment of inertia matrix still further. Let the following quantities be defined:

$$A' \equiv 2AB/(A + B) \quad (57)$$

and

$$\nu \equiv (A - B)/(A + B) \quad (58)$$

In Ref. 3 a Taylor series expansion of the moment of inertia matrix inverse in terms of  $\epsilon_1$ ,  $\epsilon_2$ , and  $\nu$  was made and the first-order terms were substituted in Eq. (52). By so doing, we found that these terms gave a periodic contribution to the attitude motion, which under worst-case conditions had an amplitude of less than 0.5 arc sec. An appreciable simplification results if these terms are assumed to be zero and the "zeroth"-order approximation for the matrix inverse is used, which is given by

$$[I_B]^{-1} = \begin{bmatrix} 1/A' & 0 & 0 \\ 0 & 1/A' & 0 \\ 0 & 0 & 1/C \end{bmatrix} \quad (59)$$

Substituting Eq. (59) into Eq. (52), expanding, and neglecting second-order terms in  $\phi_1$  and  $\phi_2$ , we obtain the result

$$\begin{pmatrix} \dot{\phi}_1 \\ \dot{\phi}_2 \\ \dot{\phi}_3 \end{pmatrix} = \begin{bmatrix} 0 & -\frac{C}{A'} y_3 & 0 \\ \frac{C}{A'} y_3 & 0 & 0 \\ \left(\frac{A'}{C} - 1\right) y_2 & \frac{A'}{C} y_1 & 0 \end{bmatrix} \begin{pmatrix} \phi_1 \\ \phi_2 \\ \phi_3 \end{pmatrix} + \begin{pmatrix} y_1 \\ y_2 + \omega_0 \\ y_3 + K\omega_R \end{pmatrix} \quad (60)$$

where

$$\begin{pmatrix} y_1 \\ y_2 \\ y_3 \end{pmatrix} = \begin{pmatrix} H_{R_1}(t)/A' \\ H_{R_2}/A' \\ H_{R_3}(t)/C \end{pmatrix} \quad (61)$$

Equation (60) is a linear time varying equation of the form

$$\dot{\phi} = F(t)\phi + u(t)$$

The coefficients of the matrix  $F(t)$  are functions of the "y" variables which vary slowly in time. In the absence of external torques, an exact solution for the variation in the y variables is available from Eq. (53). A closed-form solution to Eq. (60) can be obtained if the coefficients of the  $F$  matrix are treated as being stepwise constant over finite segments of time. It has been found that this can be done over lengths of time as long as several hundred seconds without compromising accuracy. We obtained results, which are valid over one of these time intervals, by solving the constant coefficient differential equations; they are given as follows:

$$\begin{pmatrix} \phi_1(t) \\ \phi_2(t) \\ \phi_3(t) \end{pmatrix} = \begin{bmatrix} \theta^N(t - t_N) \end{bmatrix} \begin{pmatrix} \phi_1(t_N) \\ \phi_2(t_N) \\ \phi_3(t_N) \end{pmatrix} + \begin{pmatrix} U_1(t, t_N) \\ U_2(t, t_N) \\ U_3(t, t_N) \end{pmatrix} \quad (62)$$

$$\left. \begin{aligned} y_1(t) &= y_1(t_N) \cos \omega_0 \Delta t + y_3(t_N) \frac{C}{A'} \sin \omega_0 \Delta t \\ y_2(t) &= y_2(t_N) \\ y_3(t) &= y_1(t_N) \frac{A'}{C} \sin \omega_0 \Delta t + y_3(t_N) \cos \omega_0 \Delta t \end{aligned} \right\} \quad (63)$$

where

$$\theta^N(t - t_N) = \begin{bmatrix} \cos a_N(t - t_N) & -\sin a_N(t - t_N) & 0 \\ \sin a_N(t - t_N) & \cos a_N(t - t_N) & 0 \\ \theta_{31} & \theta_{32} & 1 \end{bmatrix} \quad (64)$$

$$\theta_{31} = \frac{1}{a_N} \{ b_N \sin a_N(t - t_N) - c_N [\cos a_N(t - t_N) - 1] \} \quad (65)$$

$$\theta_{32} = \frac{1}{a_N} \{ b_N [\cos a_N(t - t_N) - 1] + c_N \sin a_N(t - t_N) \} \quad (66)$$

$$a_N = (C/A')y_3(t_N) \quad (67)$$

$$b_N = (1 - A'/C)y_2(t_N) \quad (68)$$

$$c_N = (A'/C)y_1(t_N) \quad (69)$$

$$U_1 = \Delta t y_1 - \frac{\Delta t^2}{2} a_N y_2 - \frac{\Delta t^3}{6} y_1 (a_N^2 + \omega_0^2) \quad (70)$$

$$U_2 = \Delta t (y_2 + \omega_0) + \frac{\Delta t^2}{2} a_N y_1 - \frac{\Delta t^3}{6} a_N^2 y_2 \quad (71)$$

$$U_3 = K[a(t) - a(t_N)] + \Delta t y_3 + \frac{\Delta t^2}{2} y_1 y_2 + \frac{\Delta t^3}{6} y_3 [y_1^2 + (1 - \frac{C}{A'})y_2^2 - \omega_0^2] \quad (72)$$

In Eqs. (70)-(72),  $\Delta t$  denotes  $(t - t_N)$  and the  $y_i$  represent  $y_i(t_N)$ . The functions  $U_1$ ,  $U_2$ ,  $U_3$  are actually obtained as low-frequency trigonometry functions, but were expanded in a Taylor series in time and truncated after the cubic terms to give the results in Eqs. (70)-(72). This was done to simplify the results. The use of three terms in the series expansion is adequate if the time step  $\Delta t$  is no greater than a few hundred seconds.

The method of including the effects of control jet firings in the dynamic model is outlined as follows. It is assumed that jet pulse duration is small, so that the control torque is assumed to be applied impulsively. The basic idea is to make a step change in the three components of the angular momentum vector in the attitude reference frame at the time of occurrence of the jet pulse.

The following information is required from the attitude control subsystem:

$t_F$  denotes time of occurrence of the torque pulse

$P_W$  is equivalent rectangular pulsewidth

$(M_B)$  denotes components of control torque in the B-frame

Given this information, we can calculate the components of angular momentum in the B-frame as

$$(\Delta H_B(t_F)) = (M_B)P_W$$

The three attitude angles can be evaluated at time  $t_F$ , and  $\Delta H_B$  can be resolved into the attitude reference frame to produce the following correction to the state:

$$\begin{pmatrix} \Delta y_1(t_F) \\ \Delta y_2(t_F) \\ \Delta y_3(t_F) \end{pmatrix} = \begin{bmatrix} 1/A' & 0 & 0 \\ 0 & 1/A' & 0 \\ 0 & 0 & 1/C \end{bmatrix} \times [\phi_2(t_F)]_y^T [\phi_1(t_F)]_x^T [\phi_3(t_F)]_z^T \times \begin{pmatrix} M_{B_1} \\ M_{B_2} \\ M_{B_3} \end{pmatrix} P_W \quad (73)$$

The corrections to  $y_1$ ,  $y_2$ ,  $y_3$  are then added to the previous values, and the solution equations are updated with the corrected  $y$  values. The solution is then reinitialized at time  $t_F$ , and the correction process is complete.

The primary external disturbance torque for the vehicle of interest is the torque resulting from solar pressure. All other disturbance torques are expected to be less than 1% of the worst-case solar torque. The minor disturbance torques do not require modeling in the prediction equations as the attitude estimator is able to handle their effects by treating these torques as being a hypothetical time sequence of random disturbances. If maximum performance of the attitude estimator is to be attained, it is desirable to provide the prediction equations with a model of the major solar torque effect. This enables the estimator to form a continuous estimate of the appropriate torque parameters and to remove the associated uncertainty from the vehicle motion model.

A solar torque model is developed by assuming that the vehicle can be considered to have geometric symmetry about the  $\bar{x}_B$  axis. Under these conditions, the solar torque acts normal to the plane formed by the  $\bar{x}_B$  axis and the unit vector  $\bar{\sigma}$  pointing from the satellite to the sun, and thus may be expressed as  $\bar{T} = K_s \bar{x}_B \times \bar{\sigma}$ . The parameter  $K_s$  is a function of the satellite geometry, surface reflectivities, sun angle, etc., and thus varies as a function of satellite location in orbit. The eleventh-state variable to be estimated is defined to be equal to this parameter divided by the moment of inertia parameter  $A'$ ; that is,  $x_{11} = K_s/A'$ . The estimator models this variable as a random walk and in practice is able to track continuously its actual value.

One obtains the necessary corrections to the state prediction equations by expressing the solar torque vector in the attitude reference frame,

and then performing an approximate integration by assuming this vector to be constant over one measurement interval. The resulting corrections to the attitude angles and angular momentum parameters are given in Eq. (74):

$$\left. \begin{aligned} \Delta \phi_1(t) &= -(\sigma_{yR} + \phi_1 \sigma_{zR})(t - t_N)^2 x_{11}/2 \\ \Delta \phi_2(t) &= (\sigma_{xR} - \phi_2 \sigma_{zR})(t - t_N)^2 x_{11}/2 \\ \Delta \phi_3(t) &= (A'/C)(\phi_2 \sigma_{yR} + \phi_1 \sigma_{xR})(t - t_N)^2 x_{11}/2 \\ \Delta y_1(t) &= -(\sigma_{yR} + \phi_1 \sigma_{zR})(t - t_N) x_{11} \\ \Delta y_2(t) &= (\sigma_{xR} - \phi_2 \sigma_{zR})(t - t_N) x_{11} \\ \Delta y_3(t) &= (A'/C)(\phi_2 \sigma_{yR} + \phi_1 \sigma_{xR})(t - t_N) x_{11} \end{aligned} \right\} \quad (74)$$

where  $(\sigma_{xR} \sigma_{yR} \sigma_{zR})^T$  are components in the R-frame of a unit vector pointing from the satellite to the sun.

The solution as given by Eqs. (62)-(72) will produce accurate results over long periods of time if Eqs. (62) and (63) are reinitialized every few hundred seconds. Comparison of the solution results against digital simulation of the exact satellite dynamics and attitude control system with zero solar torque have verified that an accuracy of a few arc seconds can be maintained for up to 1 hr. This accuracy is dependent upon the ACS keeping the spin axis within 0.3 deg of the local vertical.

#### E. Summary of Estimation Equations

The general structure of the attitude estimator was defined by Eqs. (3)-(5). Equations (30)-(32) define the measurement prediction equations. The dynamic model as given by Eqs. (62)-(74) define the state prediction equations for the estimator.

The set of variables to be estimated should include all unknown variables that contain enough uncertainty to exert a detectable influence upon the attitude motion process or measurement process. In order that a given variable can be estimated, its time history must in some sense be predictable. A number of effects such as fuel slosh and structural vibration do influence the attitude motion to a measurable extent, but are essentially unpredictable. Variables associated with these effects will not be estimated. In addition, a number of other variables have uncertainties small enough to exert a negligible influence on the attitude motion or measurements. The set of variables that fall in this category will be treated as deterministic parameters. The set of state variables to be estimated are defined in Table 1.

Table 1. Definition of State Variables

State Variable	Symbol	Comment
$x_1$	$\phi_1$	Roll angle between B-frame and R-frame
$x_2$	$\phi_2$	Pitch angle between B-frame and R-frame
$x_3$	$\phi_3$	Yaw angle between B-frame and R-frame
$x_4$	$H_1/A'$	These variables have units of angular rate; $H_1, H_2, H_3$ are components of total angular momentum of satellite in R-frame
$x_5$	$H_2/A' + \omega_0$	
$x_6$	$H_3/C$	
$x_7$	$K$	Ratio of magnitude of spin vector to wheel angular speed, i.e., $\omega^*/\omega_R$
$x_8$	$\beta_1$	Star sensor twist misalignment angle between B-frame and SS-1 frame
$x_9$	$\beta_2$	Star sensor elevation misalignment angle between B-frame and SS-1 frame
$x_{10}$	$\dot{\beta}_1$	Rate of change of $\beta_1$
$x_{11}$	$x_{11}$	Proportional to magnitude of solar torque angular acceleration
$x_{12}$	$ M_B /A'$	Magnitude of control jet angular acceleration

The state variables of primary interest are  $\phi_1, \phi_2, \phi_3$ , which are angles that define the attitude of the B-frame with respect to the R-frame. The B-frame is the basic satellite body reference frame. The particular body reference frame chosen to define the basis for attitude determination is the "spin axis" reference frame, which was explicitly defined in Section III. C. The variables  $x_4, x_5, x_6$  are required to define the motion of the attitude angles. The parameter  $K$  is required in order to account for the effect of yaw moment of inertia uncertainty and its variation upon the yaw motion. The angles  $\beta_1$  and  $\beta_2$ , which define the orientation of the star sensor relative to the B-frame, are required in the measurement prediction equations. It was also found desirable to estimate the rate of change  $\dot{\beta}_1$ .

The variable  $x_{11}$  is the unknown solar torque parameter entering the dynamic model in Eqs. (74). The variable  $x_{12}$  is introduced to account for the limited a priori knowledge of the magnitude of the attitude control thruster torque level. The ability to estimate the variable is

dependent on the control torque having some degree of repeatability from firing to firing. This variable can be estimated if appropriate modifications are made to the filter covariance matrix at the jet firing times. These modifications, which will not be given here, are in Appendix G of Ref. 3. The estimates of this variable enter the state prediction equations via Eq. (73). The direction of control torque vector in the B-frame is assumed to be known from a priori data to within 1 deg. Errors in control torque direction are accommodated by appropriate increments being made to the filter covariance matrix at the jet firing time.

The state prediction equations for the first through sixth state variables are defined by Eqs. (62) and (63). The variables  $x_7, x_9, x_{10}, x_{11}, x_{12}$  are predicted to be constant between measurements, and

$$x_8(t) = x_8(t_N) + (t - t_N)x_{10}(t_N)$$

In practice, a "Q" term is added to the filter covariance matrix at each measurement time to simulate a hypothetical random disturbance to  $x_7, x_9, x_{10}, x_{11}$  to compensate for modeling errors and enable the filter to "track" these variables when they vary slowly with time.

The estimate of  $x_{12}$  represents the estimate of the control torque at the most recent jet firing time. In this case, the appropriate increments to the filter covariance matrix are made only at the jet firing times to account for the random variation in torque from firing to firing.

In addition to the set of state variables, a number of other variables and parameters are required to be known for a complete definition of the problem. These variables are treated as deterministic quantities and are listed in Table 2.

The reaction wheel angle of rotation  $\alpha(t)$  is actually determined by filtering of tachometer pulse data. This angle so obtained is treated as a known quantity. The orbital angular rate, satellite right ascension, declination, and heading angle are obtained from ephemeris data. The jet firing time  $t_C$  and jet pulsewidth are assumed to be available from telemetry.

The final filter configuration for the problem at hand is summarized in block diagram in Fig. 12. Note that the measurement residual is formed by transformation of the known components of the star vector in the attitude reference frame (R-frame) to the "estimated" star sensor coordinate frame using the estimated values of  $\phi_1, \phi_2, \phi_3, \beta_1, \beta_2$  in the coordinate transformation. The measurement residual is then computed by the process of sampling the  $-y$  component of the vector for the appropriate slit. Note that the slit producing the star pulse, as well as the particular star, must be identified. In practice, after an initial lock-on process, the attitude estimates are sufficiently accurate to guarantee successful identification.

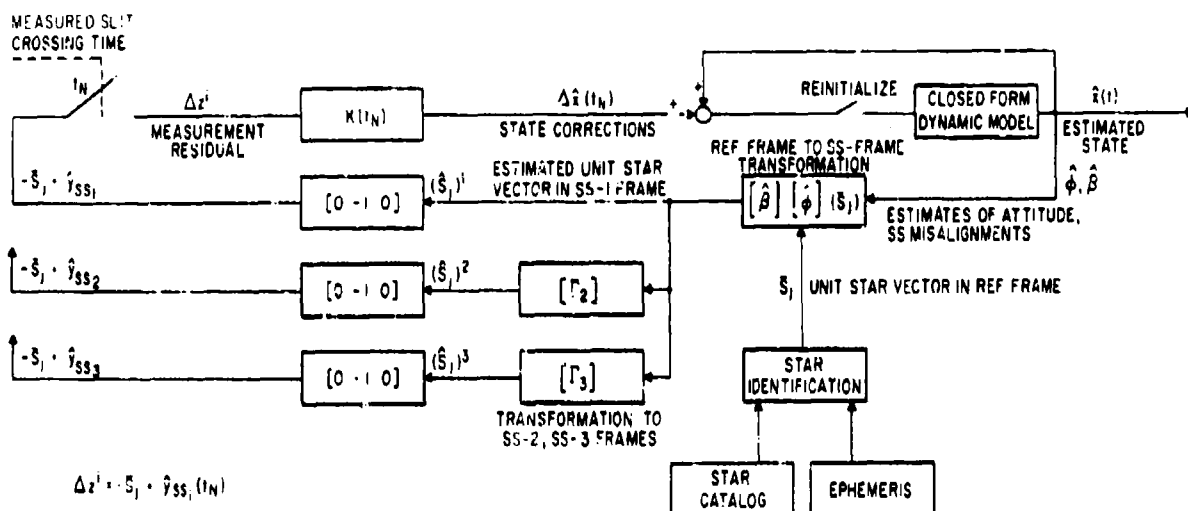


Fig. 12. Filter Configuration

Table 2. Deterministic Parameters

Variable	Comment
$A^1/C = 2AB/C(A+B)$	Moment of inertia parameter
$P_W$	Control jet pulsewidth
$t_C$	Time of initiation of control torque pulse
$\alpha(t)$	Reaction wheel angle of rotation
$\alpha_s, \beta_s, \omega$	Satellite right ascension, declination, and heading angle
$\gamma_1, \gamma_2, \gamma_3$	Star sensor slit angles
$\omega_0$	Magnitude of orbital angular rate

#### REFERENCES

1. R. E. Kalman, "A New Approach to Linear Filtering and Prediction Problems," *J. Basic Eng.*, Trans. ASME 82, 35 (1960).
2. Robert Roberson, Preliminary Report on the Foundations of Attitude Determination from a Spinning Gyrostat, Aerojet-General Corp., Report SEMR 71-20 (6 Aug. 1968).
3. J. E. Lesinski, Precise Attitude Estimation for an Orbiting Spacecraft, Aerospace Corp., Report TOR-0066(5129-01)-1 (July 1969).

SESSION VI

PANEL DISCUSSION

Chairman:  
Mr. Dennis F. Meronek  
The Aerospace Corporation  
El Segundo, California

---

Panel Discussion 417

Transcription \*

Biographies 419

\*Classified; published in Volume II \*

## PANEL DISCUSSION

---

The panel was chaired by Mr. Dennis F. Meronek of The Aerospace Corporation. It comprised Major William Hartung of the Air Force (SAMSO) and the chairmen of the five previous sessions: Professor Harold Sorenson, Mr. Robert Lillestrand, Dr. James D. Gilchrist, Dr. Joseph LeMay, and Professor R. C. K. Lee.

The discussion began with each chairman summarizing his session, and Major Hartung examining possible future missions requiring high-accuracy attitude determination. A transcription from the tape recordings of the entire discussion is published in Volume II (classified) of these proceedings.

Brief biographies of the chairmen, speakers, and other coauthors follow, if they were available at the time of printing.



## BIOGRAPHIES

### The Aerospace Corporation Representatives

The Aerospace Corporation, El Segundo, California, which cosponsored the symposium, was represented by the following cochairmen and speakers. Each is a member of the Control and Sensor Systems Subdivision, Electronics Division, Engineering Science Operations. Dr. Henriksen and Mr. Lesinski, together with Captain D. Evans, USAF (SAMSO), cochaired the symposium.

J. D. Gilchrist, chairman of Session III, was born in Winnipeg, Canada. He received his BS and MS at the University of Manitoba in 1959 and 1961, respectively, and his PhD in electrical engineering at the University of Minnesota in 1965. From 1964 to 1968 he worked at Honeywell, Inc., on various projects, including trajectory optimization, optimal guidance schemes, spacecraft attitude control systems, and attitude determination. At Aerospace he has been involved in attitude determination and sensor line-of-sight determination problems. Dr. Gilchrist also presented a paper during Session V of the symposium.

L. J. Henriksen, a cochairman of the symposium, received his AB from Harvard and his SM from MIT. He has been a teaching fellow at Harvard, and a research assistant at both Harvard and MIT. At Harvard, he obtained his PhD in control and estimation theory. While in graduate school, he was associated with the Dynamics Research Corporation in Stoneham, Massachusetts. There he applied estimation theory to the analysis of the Ship's Inertial Navigation System (SINS) for the Navy's Polaris submarine program. Since joining The Aerospace Corporation in 1967 he has been involved in spacecraft attitude and line-of-sight determination problems. Dr. Henriksen has published papers on correlated measurement noise and nonlinear estimation.

Joseph L. LeMay, chairman of Session IV, hails from Michigan. He earned his electrical engineering BS at the University of Detroit in 1957 and his MS at the California Institute of Technology in 1959. From 1955 to 1959 he was a research engineer with General Motors Corporation, and from 1959 to 1962, a teaching fellow at the University of Michigan, where he received his PhD in instrumentation engineering. He has been with The Aerospace Corporation since that time, first as a section manager and now as a program director. Dr. LeMay lectures on modern control theory at UCLA, is the author of numerous publications on control and navigation systems theory, and is a member of AIAA and IEEE.

J. E. Lesinski, a cochairman of the symposium, is a native of Michigan. He received his BS in aeronautical engineering from the University of Michigan as well as his MS in instrumentation engineering in 1962, and has been with The Aerospace Corporation since that time. His areas of specialization are guidance control, estimation applications, and the sensitivity analysis of optimal filters. Most recently he has been involved in a study of the implementation of optimal estimators for satellite attitude determination. Mr. Lesinski also presented a paper in Session V of the symposium.

D. F. Meronek, chairman of Session VI, is a Wisconsinite. He obtained his BS and MS in electrical engineering at the University of Wisconsin, the latter in 1958. He has been at The Aerospace Corporation since 1962, where he is head of the control systems department, which is involved in the design and analysis of terminal guidance and spacecraft and reentry vehicle control systems, and in attitude determination schemes.

### SAMSO Representatives

The Space and Missile Systems Organization, Air Force Systems Command, Los Angeles Air Force Station, Los Angeles, California, a cosponsor of the symposium, was represented by the following chairman and speaker.

David J. Evans, Captain, USAF, a cochairman of the symposium, is a native of Pennsylvania, where he received a BS in engineering physics at Lehigh University in Bethlehem in 1966. He graduated from the Air Force Institute of Technology in 1968 with an MS in space physics engineering. Since that time, he has been assigned to the Deputate for Technology, Exploratory Development Branch, Space and Missile Systems Organization in Los Angeles.

William E. Hartung, Major, USAF, received a BS in chemistry from the University of Santa Clara in 1954. His BS and MS in aeronautical and astronautical engineering came from the University of Illinois in 1963 and 1964, respectively, whence he was directly assigned to Headquarters, Space Systems Division. There he participated in the management of preliminary design studies for the Special Defense Program. After flying C-130s in the Philippines in support of South Vietnam, he was assigned to his present post at the Space and Missile Systems Organization. His mission analysis work last year was on the Surveillance of Objects in Space in the 1970s (SOS-70); currently, it is on the missile and space defense of the United States. Major Hartung presented a paper in Session V.

#### Other Representatives

Other session chairmen, speakers, and authors of symposium papers are listed below alphabetically under the name of the organization each represents.

#### **AEROJET-GENERAL CORPORATION**

R. A. Lucas was born in Illinois. He received his BS in mathematics, with honors, from California State Polytechnic College in Pomona in 1966. Since that time, Mr. Lucas has been with the Aerojet-General Corporation in Azusa, California, working on attitude determination and simulation. He and his coauthor presented their paper in Session V of the symposium. He volunteers that he has two brilliant, beautiful children and is nice to cats, birds, and secretaries.

#### **BARNES ENGINEERING COMPANY**

Robert W. Astheimer, chairman of Session II of the symposium, received a BS in mechanical engineering in 1944 and an MS in physics in 1949 at Stevens Institute of Technology. As an engineering trainee with the American District Telegraph Company, he developed automatic fire detection systems and components. From 1944 to 1946, he served in the Army Signal Corps on mobile radio equipment; then until 1951 he was a physics instructor at Stevens where he did research on refractive index measurements and self-diffusion of metals, and electron microscope studies of metallic structure. At the Naval Ordnance Laboratory from 1951 to 1953 he investigated underwater explosion phenomena and developed atomic and hydrogen bomb blast measurement instruments. When he joined Barnes Engineering Company, Stamford, Connecticut, in 1953, he was concerned with infrared missile tracking, imaging units, and radiometers and spectrometers; portable and mobile IR pointing and scanning; satellite stabilization sensors, weather reconnaissance, and new thermal detectors. Later he became technical director, responsible for the administration and technical direction of engineering, research, and development activities. He is now Vice President and General Manager of the Defense and Space Contracts Division. Mr. Astheimer is a fellow of the Optical Society of America, and contributes extensively to technical publications.

#### **CONSULTANT**

Robert E. Roberson received his BS in physics, his MS in mathematics, and a PhD in mechanics, all from Washington University in St. Louis by 1951. After 17 years of experience in government laboratories and industry, he became a consultant to industry in 1960 in aerospace vehicle dynamics and control. In addition, in 1964 Dr. Roberson became a professor of engineering at the University of California, Los Angeles, and has been with the University of California, San Diego, as professor of aerospace engineering since 1967. Dr. Roberson presented the first paper of the symposium.

#### **CONTROL DATA CORPORATION**

Joseph E. Carroll, a native of Wisconsin, attended St. Mary's College and then the University of Minnesota, where in 1963 he received an MS in physics. He joined Control Data Corporation, Minneapolis, Minnesota, in 1961, and has been active in the design, analysis, fabrication, and testing of spacecraft navigation and attitude detection systems and their application to ground-based astronomical surveys. He is now technical director of the SPARS star sensor development. The author of numerous technical papers and holder of four patents, Mr. Carroll is a member of the Institute of Navigation, the Arctic Institute of North America, and the American Congress on Surveying and Mapping. He authored the paper he presented in the symposium's Session II, and coauthored a paper given in Session IV.

Charles B. Grosch, a Chicagoan, obtained his BS in education and MS in mathematics from Iowa State University in 1955. He did graduate work in mathematics there and later at the University of Minnesota. He was in the mechanical division of General Mills from 1956 through 1962, and then did army duty for six months. Later that year, Mr. Grosch joined Control Data Corporation in Minneapolis, where he has been involved in the problems of applied mathematics directed primarily toward attitude determination and celestial mechanics. Mr. Grosch is coauthor of a paper presented in Session III.

Anton E. LaBonte is a coauthor of the paper he presented in Session III of the symposium. A native of Minneapolis, he received his BS, MSEE, and PhD (in electrical engineering and mathematics) from the University of Minnesota. While there, he did electrical engineering undergraduate teaching and research in the micromagnetic characterization of ferromagnetic thin films. Upon receiving his PhD in 1966, he joined the Control Data Corporation, Minneapolis, where his work has been in star mapper attitude determination, its data reduction and evaluation, and systems engineering for scanning instrumentation and software for the analysis of photographic star plates.

Robert L. Lillestrand, chairman of Session II, served from 1945 to 1946 in the U.S. Navy. At the University of Minnesota he achieved his BA and MA in physics in 1949 and 1951, respectively. He then went to General Mills, Inc., where, until 1960, he was concerned with self-contained optical systems for space navigation based on star aberration only; precise IR search and track systems; error analysis of the ICBM impact prediction system; the design of the aberrascope; the monopulse radar antenna pedestal for IRBM guidance and the precision automatic leveling platform. In 1960 Mr. Lillestrand joined Control Data Corporation in Minneapolis where he has been, successively, director of aerospace research, staff consultant to the research division, and currently director of electro-optics research. He holds five patents in the space navigation and detection field (including the stellar aberrascope), and has five pending. His papers have appeared in numerous journals such as Electronics, ARS Journal, and the IEEE Transactions on Aerospace and Navigational Electronics. He has presented papers at numerous symposia, and is a member of the American Physical Society, American Optical Society, American Astronautical Society, AIAA, and the Arctic Institute of North America. Mr. Lillestrand has made two expeditions to the North Pole and two to northern Greenland; in the latter, in spring 1969, he discovered the new northernmost point of land in the world.

Bruce D. Vannelli was born in St. Paul and received a BS in 1959 and an MS in 1963, both in mathematics and from the University of Minnesota. He was with the Mitre Corporation in Boston in 1961 working on display programs for high-altitude air traffic control. The following year, Mr. Vannelli went to Control Data Corporation, Minneapolis, as a programmer analyst on projects such as computer programs for attitude determination devices, stellar pattern recognition, and satellite navigation using an ejected probe. Mr. Vannelli coauthored a paper given in Session III.

#### HONEYWELL, INC.

Gerald R. Arneson received both his BS and MS in electrical engineering from the University of Minnesota, the latter in 1968. Since 1967 he has been involved in simulation problems in the computer sciences section at Honeywell, Inc., Aerospace Division, Minneapolis. These have included a hybrid simulation of a VTOL aircraft to evaluate wind gust disturbance, digital simulation of an attitude reference using laser gyros, and a real-time data processing algorithm for SPARS. Mr. Arneson recently has been developing and implementing hybrid software for the Honeywell SDS 9300 and Sigma V hybrid computation facilities. In addition to these computers, he has worked with the CDC 1604-6600, and the Honeywell H-21 and H-1800. Mr. Arneson is a coauthor of the paper he presented in Session III.

Craig D. Brown is coauthor of a paper given in Session IV of the symposium. Having received his BSEE and MSEE at Purdue University by 1966, he joined Honeywell, Inc., Aerospace Division, as a principal development engineer. In this capacity, he has made analysis tradeoff studies using the SPARS 3DOF computer simulation and was responsible for application of the SPARS algorithm to real-time software in Phase IA. Previous to his work on SPARS, Mr. Brown had worked on the verification of a 13-foot air bearing test table and on an acceptance test program for a space vehicle motion simulator for NASA's Manned Spacecraft Center.

David B. Jackson received a BS in electrical engineering from the University of Minnesota in 1961, and did a year of graduate study there in automatic control and digital computers. From 1962 to 1965 he was with the Lockheed-California Company on a number of NASA and Air Force studies. Recently, he represented Honeywell at the NASA Electronics Research Center at Cambridge, Massachusetts, where he worked on the application of stochastic estimation to the mechanization of strapdown attitude reference systems for spacecraft, and where he prepared the paper he gave in Session I of the symposium. Previously, Mr. Jackson was involved in the three-degree-of-freedom computer program and simulation study in SPARS Phase 0 and in the Apollo Block II display coupler studies. He is presently with the Aerospace Division of Honeywell, Inc., in Minneapolis.

Jerome C. Kollodge\* is a coauthor of a paper in Session II. He is with Honeywell, Inc., Radiation Center, Lexington, Massachusetts.

D. Alexander Koso,\* coauthor of the paper he presented during Session II of the symposium, is with Honeywell, Inc., Radiation Center, Lexington, Massachusetts.

\* Biographical information not available.

Joseph A. Miller is coauthor of the paper he presented in Session IV of the symposium. He received both his BS and MS in electrical engineering from MIT in 1953 and then joined Honeywell, Inc., Aerospace Division, where he is the SPARS project leader. He has supervised the concept and system requirements on the Block I Apollo SCS for four years, from concept definition to hardware verification. Mr. Miller has also been involved in its entry and Delta V operation and closed-loop system tests, as well as directing the selection study of the attitude reference system for both Blocks I and II.

Gerald D. Nelson earned both his BS and MS at the University of Minnesota, in 1960 and 1968, respectively. Since 1963 he has been employed by the Aerospace Division of Honeywell, Inc., as an analyst in the computer sciences section. Mr. Nelson has been responsible for the design and implementation of digital computer programs for a multisensor reconnaissance model, an Apollo tolerance analysis program, and a general-purpose program for the analysis of linear systems, known as VALUE. His work has made him familiar with the IBM 7090-7094, the CDC 3600 and 6400-6600, and the Honeywell H-1800 computers. Mr. Nelson coauthored a paper given in Session III.

David C. Paulson received his BS and MSME at the University of Minnesota, the latter in 1960. From then until 1966 he was with the United Aircraft Corporation involved in conceptual design studies of missile, satellite, and space vehicle navigation and precision stellar-inertial attitude reference and pointing systems. Since 1966, he has been a staff engineer at Honeywell, Inc., Aerospace Division, where he is currently responsible for the Phase IB SPARS concept development, analysis, and testing. During Phases 0 and IA, he was work director for the system analysis, and responsible for the conceptual application of recursive filtering in the SPARS design. Mr. Paulson holds a patent for an autonomous orbital navigation mechanization, and is the coauthor of the paper he presented in Session IV.

David K. Scharmack, whose paper was presented in Session I, received his BSE and MS from the University of Michigan, and worked for the Kuhlman Electric Company from 1957 to 1960. He is in the St. Paul Systems and Research Division at Honeywell, Inc., which he joined in 1960, and is preparing for a PhD in control sciences at the University of Minnesota. His work has been largely in the field of digital computers, with his major research effort resulting in the "predictor method," a powerful tool for determining optimal trajectories as functions of parameters. He has worked in the diverse areas of optical correlation and attitude determination, the latter being concerned with the orbital scanner. In addition to writing journal papers, Mr. Scharmack is the author of a chapter in Volume V of Advances in Control Systems: Theory and Practice, and has lectured on trajectory optimization in the UCLA short-course series.

Robert T. Scott earned his BSEE from Catholic University in 1950, and his MSEE from Purdue University in 1952. He has been with the Honeywell, Inc., Aerospace Division since that time, and is currently the work director on SPARS Phase IB component design and development. This was preceded by his efforts on the inertial reference assembly hardware requirements in Phase 0, and in the IRA building and testing in Phase IA. Prior to SPARS, he was involved in the rate gyro package for the MOL and in guidance amplifiers for Gemini. Mr. Scott has specialized in inertial grade gyros, including the development and test of a rate gyro package for Sprint, and is the holder of two patents concerned with gyro temperature control. Mr. Scott coauthored the paper he gave in Session IV of the symposium.

N. W. Tidwell is a principal systems analyst at Honeywell, Inc., Aerospace Division, Minneapolis. He is also working toward his MS in electrical engineering at the University of Minnesota, having received his BS in engineering physics at the University of Illinois in 1962. He is currently engaged in the mathematical modeling of spacecraft perturbation torques and in a system parametric analysis to determine spacecraft parameter sensitivity to the accuracy of attitude determination of a celestial map-per. Other areas of his experience relate to the orbital scanner spacecraft; horizon definition measurement program; F104 aircraft computer; the Electrically Suspended Gyro Monitor (ESGM), for which he developed optical alignment techniques; and the Advanced Orbiting Solar Observatory (AOSO), including sensor and solar simulation design and scheduling and testing on the six-foot air bearing table. Mr. Tidwell presented a paper in Session I of the symposium.

#### HUGHES AIRCRAFT COMPANY

Joseph Del Riego, currently in charge of the TACSAT attitude determination and control and station-keeping at Hughes Aircraft Company in Los Angeles, received his BS in mathematics at Pennsylvania State University in 1962. In the guidance and controls department at Hughes, Mr. Del Riego is involved in the design and analysis of trajectory and orbit shaping and on-orbit control of spin-stabilized spacecraft. He has participated in the real-time launch and orbit phases of the Intelsat II, ATS, and the TACSAT. Mr. Del Riego coauthored a paper in Session III.

John J. Ribarich earned his BS in electrical engineering at the University of Minnesota. Mr. Ribarich presented a paper in Session V of the symposium. He is with the Hughes Aircraft Company in Los Angeles, where he is section head in the guidance and control department. At present, he is involved in precision pointing studies.

Warren H. Sierer is a staff engineer in the Space Systems Division of the Hughes Aircraft Company, Los Angeles. He went to work there in 1964, having received both his BS and MS in space physics at UCLA. Working in the area of attitude sensing and determination, he was a member of the team specializing in this and in-orbit control during launch of ten spacecraft for NASA, Comsat Corporation, and the Air Force. For the TACSAT, he developed the in-orbit control computer system and was chief of orbital maneuvers during initial launch operations. Mr. Sierer coauthored the paper he gave in Session III.

#### IBM CORPORATION

J. L. Heiss,\* coauthor of a paper presented in Session IV, is with the Federal Systems Division of IBM, Westlake, California.

W. C. Martin was awarded a BS in mathematics at Fresno State College in 1957 and an MS in engineering at UCLA in 1968. He has worked extensively in the field of computer and control applications at the U.S. Naval Ordnance Test Station, the Ford Motor Company, and The Aerospace Corporation. Together with his coauthor, he presented a paper in Session V of the symposium.

Gunnar Nielsen, coauthor of a paper presented during Session IV, received his BME at the OMT in Denmark in 1948. Joining IBM in 1951, he became a member of the medical engineering department of the physics laboratory and was assigned to heart, lungs, and artificial limbs. This led to work on periscopes and precision optical and mechanical projection and measuring systems. Included were the map-match projection system, the photographic system for the AN/ASQ-38 (B-52) bombing navigation system, and the bombing navigation map-match system for the XB-70 aircraft. At present he is an advisory engineer in the physical simulation department at IBM in Owego, New York, supporting the design and integration of opto-mechanical simulation equipment.

Frank H. Schlee graduated from Brooklyn Polytechnic Institute with a BS in aeronautical engineering in 1956. At the University of Michigan, he received an MS in 1959 and a PhD in 1963, both in instrumentation engineering, a subject he also taught part time. He then joined IBM in the Federal Systems Division, Owego, New York, where he went to work on mission analysis for the standardized space guidance system. He then became involved in Gauss-Markov optimal estimation in autonomous spacecraft navigation, the MOL, the Gemini navigation experiment, navigation systems for lifting reentry vehicles, and the test design and evaluation of SPARS. At present, Dr. Schlee is working on the design of the A7 navigation and weapon delivery system. He coauthored two papers in Session IV, one of which he also presented.

N. F. Toda was an instructor in the department of engineering mechanics at Cornell University from 1950 to 1957. It was there that he earned his BME in 1950 and MME in 1953. After leaving Cornell, he went to the Sperry Gyroscope Company where, until 1964, he was engaged in the development of floated gyros and the navigation and guidance of space vehicles. He then joined IBM in the Federal Systems Division at Westlake, California, where he is manager of the systems analysis department. At IBM, Mr. Toda has been involved in autonomous navigation, guidance of space vehicles, and the Defense Support Program attitude determination. He was also manager of the guidance analysis department for SPARS. His paper was given in Session IV.

#### LOCKHEED MISSILES AND SPACE COMPANY

William R. Davis, coauthor of a paper presented in Session IV, received his BS in electrical engineering and MS in physics from the California Institute of Technology. The latter was in 1947 after a stint at the U.S. Naval Academy in the USNR Officer Training. In 1966, he received his PhD in electrical engineering. From 1947 until 1956, he worked at several companies in the development of stable platforms, celestial navigation equipment, angle transducers, and high-speed commutators. He then joined Lockheed Missiles and Space Company at Sunnyvale, California, where he is project leader in navigation, guidance, and control, directing the SPARS program. While at Lockheed, Dr. Davis has been involved in guidance and control, satellite drag makeup experiments, advanced technical planning, and advanced satellite and missile system synthesis-guidance and control. He also directed the initial synthesis and development of the Agena ascent guidance and orbit attitude control systems.

Fred Y. Horiuchi received a BS and MS in aeronautical engineering from the University of Illinois, the latter degree in 1958. After working in the Missile and Space Division of Douglas Aircraft Company, he joined Lockheed Missiles and Space Company, Sunnyvale, California, in 1960, where he is a research specialist in the guidance and flight mechanics department. Being responsible for the design of the precision earth-pointing experiment of the SPARS program, Mr. Horiuchi is concerned primarily with the accurate determination of satellite orbits and drag lifetimes, and with atmospheric density analyses and satellite rendezvous studies. Mr. Horiuchi coauthored a paper presented in Session IV.

\*Biographical information not available.

Vladimir Hvoshinsky received a Diploma Engineers degree from EPUL in Switzerland in 1954 and an MSEE from the California Institute of Technology in 1960. He designed wideband instrumentation for Dynasoar at Ampex Corporation, and did research and development on electronic systems and servo controls at Leach Corporation, Magnetic Research Corporation, Allen Bradley, and Brown-Bovery, Ltd., in Switzerland. In 1963 he joined Lockheed Missiles and Space Company and was project leader for the microwave radiometer terminal guidance and low-cost inertial guidance projects, including flight and sled test experiments. He designed high-precision servos for the laser pointing communication system for the special LOCAT satellite. Currently, Mr. Hvoshinsky directs the tests and experiment definition for PEPSY laboratory evaluation. He coauthored a paper which he presented in Session IV of the symposium.

Michael G. Lyons is a senior research engineer at the Lockheed Missiles and Space Company, Sunnyvale, California. He received his BA in engineering physics at Cornell University in 1965 and his MA in electrical engineering at Stanford University in 1966. At Lockheed, Mr. Lyons' work includes the design and analysis of spacecraft attitude control, and estimation techniques for attitude determination. He coauthored the paper he gave during Session III.

E. D. Scott,\* coauthor of a paper presented in Session III, is with Lockheed Missiles and Space Company, Sunnyvale, California

#### MARQUETTE UNIVERSITY

E. C. Foudriat, author of the second paper of the symposium, graduated from the University of Illinois in 1950 and went to Ohio State University where he earned both MS and PhD degrees by 1966. He has worked for the Battelle Memorial Institute, North American Aviation, Inc., and NASA at Langley Research Center from 1957 through 1967. Dr. Foudriat then joined Marquette University, Milwaukee, Wisconsin, as an associate professor of electrical engineering.

#### MASSACHUSETTS INSTITUTE OF TECHNOLOGY

Juri Valge,\* with MIT's Instrumentation Laboratory, Cambridge, Massachusetts, coauthored a paper given in Session II of the symposium.

#### NATIONAL AERONAUTICS AND SPACE ADMINISTRATION

Howard J. Curfman, Jr., a native of Norfolk, Virginia, graduated from the Virginia Polytechnic Institute in 1945 with a BS in aeronautical engineering. In January 1946 he went with NASA at the Langley Research Center, Hampton, Virginia, where he is assistant head of the aerospace mechanics branch of the applied materials and physics division. His research has been in automatic stabilization and control of freely flying models of both aircraft and missiles. Mr. Curfman was manager of Project Scanner, is the author of 17 technical reports, and coauthored a paper presented in Session II of the symposium.

Paul B. Davenport received his BA and MA in mathematics at the University of Delaware, the latter degree in 1958. From then until 1962 he was with the computing facility of the Westinghouse Defense Center as a numerical analyst specializing in space applications. He then went to NASA's Goddard Space Flight Center, Greenbelt, Maryland, where he is head of the mathematical and operations analysis section. Mr. Davenport's work has been mainly the mathematical modeling for the ground control of the Orbiting Astronomical Observatory (OAO). His paper was given in Session III of the symposium.

Richard desJardins received his BA in physics and his MA in mathematics from The Catholic University of America. He is a mathematics instructor there, at the same time working for NASA at the Goddard Space Flight Center in Greenbelt, Maryland. For NASA, Mr. desJardins performs mathematical and operations analysis for control of the Orbiting Astronomical Observatory (OAO). He presented his paper in Session II of the symposium.

John A. Dodgen, born in South Carolina, graduated from its Clemson College with a BME degree in 1947. Since that time he has been employed at NASA's Langley Research Center, Hampton, Virginia, where he is head of the navigational instrumentation development section of the flight instrumentation division. His work in the areas of flight instrumentation and guidance and control has involved him in the research aircraft flown at the Flight Research Center in California. Mr. Dodgen supervised the early X-15 horizon definition flight experiment, was experimenter on the Project Scanner rocket, and participated in the early manned lunar mission studies. He is a coauthor of the paper he presented in Session II.

\*Biographical information not available.

Daniel Sheldon\* is a coauthor in Session IV. He is employed at Hamilton Standard Division, United Aircraft Corporation, Farmington, Connecticut.

Robert J. Slabinski, born in Pennsylvania, achieved his BS at the University of Hartford in 1964 and his MS at the University of Connecticut in 1967, both in electrical engineering, where he is at present pursuing a PhD in the same field. From 1960 through 1964, he worked at the Royal McBee Corporation in the analysis and design of small high-speed mechanisms. At United Aircraft Corporation's Hamilton Standard System Center in Farmington since 1964, Mr. Slabinski has been active in sensor loop design and the dynamic performance analysis of strapdown inertial systems. The paper that he coauthored was given in Session IV of the symposium.

#### UNIVERSITY OF CALIFORNIA

R. C. K. Lee is an associate professor of aerospace engineering at the University of California, Irvine, in Irvine, California. He received his BS, MS, and ScD degrees from MIT in aeronautics and astronautics. The next 12 years he spent first at Honeywell, Inc., and then at The Aerospace Corporation working in the areas of space guidance and control, airborne vehicles, estimation theory, and adaptive control systems. He holds several patents in these fields. Dr. Lee was chairman of Session V of the symposium.

Harold W. Sorenson, the chairman of Session I, received his BS at Iowa State University in 1957 and his MS and PhD from the University of California, Los Angeles, in 1963 and 1966, respectively. During 1957 to 1962, he was a senior research engineer in the flight performance and guidance analysis group at General Dynamics/Astronautics. From 1963 to 1966, he was head of space systems in the Electronics Division of General Motors Corporation. The following year, he was a guest scientist at the Institut für Steuer-und-Regeltechnik, DVL, Oberpfaffenhofen in West Germany. Upon his return, Dr. Sorenson became an assistant professor in the system dynamics and control section of the department of the aerospace and mechanical engineering sciences at the University of California, San Diego, in La Jolla, California.

---

\*Biographical information not available.

Mark Gorstein has been working for NASA at the Electronics Research Center in Cambridge, Massachusetts, since 1966. He received his BSEE at the City College of New York in 1958 and his MSAE from MIT in 1965, where he continues to work for his PhD in aeronautical engineering. From 1958 to 1960, Mr. Gorstein was employed at General Precision Laboratory on the circuit design for Doppler navigation systems. He then transferred to the Kollman Instrument Company, first as a staff engineer in various star-tracking systems, and then as a resident at the MIT Instrumentation Laboratory. There he was responsible for the design and development of the Apollo horizon and star trackers, and sextant. At NASA, he is in applied research in electro-optical guidance systems in computer and guidance technology. His two pending patents include one for the quantasyn, an improved ultraviolet detector. In September 1968, Mr. Gorstein presented a paper at the EASCON conference, and, in Session II of the present symposium, he gave a paper which he coauthored.

James Nelson Hallock is coauthor of a paper given in Session II. After receiving his BS in physics at MIT in 1963, he became a staff physicist there from 1964 to 1966. He was in the Apollo optics group, and also participated in the Gemini GT-7 and GT-10 experiments to measure landmark contrast. He has been with NASA since 1966 as a member of the computer and guidance technology branch at the Electronics Research Center at MIT. There he obtained his MS in physics this year, and has completed his course work. Mr. Hallock has written numerous internal MIT and NASA reports, published in the American Journal of Physics, presented papers, and holds two patents. He belongs to the Optical Society of America, the American Physical Society, the American Association for the Advancement of Science, and Sigma Xi.

Dwayne E. Hinton was born in Louisiana and received his BS in physics from Kentucky Wesleyan College in 1962. He has done graduate work at both the College of William and Mary and George Washington University. Since February 1964 he has been with NASA at the Langley Research Center, Hampton, Virginia, in the navigation and guidance research branch. Mr. Hinton is primarily engaged in the attitude determination of spin-stabilized vehicles and experimental measurements in the IR of blackbody cavity emittance. He is coauthor of the paper he presented to begin Session III of the symposium.

Vernon K. Merrick,\* a coauthor of a paper in Session III, is with NASA's Ames Research Center in Moffett Field, California.

Bruce Tinling received his BS in mechanical engineering from the University of Texas in 1945 and his MS in engineering mechanics from Stanford University in 1947. Since that time he has been employed at NASA's Ames Research Center, Moffett Field, California. Starting in 1962, he has specialized in the passive attitude control of satellites. Mr. Tinling and Vernon Merrick are the inventors of the passive gravity stabilization system used on the ATS, DODGE, and RAE satellites, and coauthors of the paper Mr. Tinling presented in Session III.

Thomas M. Walsh, coauthor of a paper presented in Session III, is a native of Pennsylvania. He received his BSEE from Ohio University in 1953 and his MSE from the University of Akron in 1962. He served in the U.S. Army from 1953 to 1955 at the Engineers Research and Development Laboratory, Virginia. Subsequently, he worked for the Westinghouse Electric and Goodyear Aerospace Corporations and the Martin Company, primarily in the area of fire control systems. In 1962 he joined NASA at the Langley Research Center, Hampton, Virginia, in the fields of guidance and control and stellar reference systems, and the stability of various reentry spacecraft. At the University of Virginia's extension division at Langley, Mr. Walsh has taught graduate control courses.

TRW, INC.

J. P. O'Malley attended the University of California, Berkeley, where he received his AB in physics in 1957. He was employed at North American Aviation's Space and Information Systems Division from that time to 1963, when he joined the TRW Systems Group in Redondo Beach, California. Mr. O'Malley is a section head in the systems design department there. He presented a paper in Session I.

#### UNITED AIRCRAFT CORPORATION

Robert A. Baum was born in Pennsylvania, and received a BS in physics from the Pennsylvania State University in 1962. From the Rensselaer Polytechnical Institute in Hartford, Connecticut, he obtained an MS in engineering science in 1965. He had already joined the United Aircraft Corporation's Hamilton Standard System Center in Farmington, Connecticut, in 1962, where he became active in the development, test, and analysis of strapdown inertial systems. At present Mr. Baum is a section engineer in the systems analysis group of the guidance and control department. He presented the paper that he coauthored for the symposium in Session IV.

\* Biographical information not available.



SYMPOSIUM ATTENDEES

---

SYMPOSIUM ATTENDEES

The Aerospace Corporation Attendees

R. M. Allman  
Ralph Austin  
Barbara Ayotte  
Gus Bartos  
Ray Berg  
P. G. Blandin  
John A. Bond  
A. F. Brigante  
Bruce Campbell  
Fred Campbell  
Val Chobotov  
R. G. Clabaugh  
T. Coffey  
P. R. Dahl  
W. K. Davis  
Vincent De Marco  
Marshall Earle  
I. Egashira  
D. D. Elliott  
R. V. Erilano  
H. L. Ferger  
N. Fiamenco  
K. F. Fishback  
I. A. Jetting  
J. D. Gilchrist  
L. J. Ginsberg  
A. Gutman  
K. E. Hagen  
Roy Hammerand  
L. J. Henriksen  
G. I. Iwanaga

M. W. Jensen  
Paul Jorgensen  
D. L. Kleinbub  
G. F. Kuncir  
R. C. LaFrance  
W. C. Lawrence  
A. Lazarus  
E. A. Lee  
R. C. K. Lee  
J. LeMay  
Carl Lenander  
Charles Leontis  
J. E. Lesinski  
R. Levinson  
C. S. Lorens  
R. K. Luke  
L. E. Lundquist  
A. S. Mager  
S. Marcus  
R. A. Marutt  
George Masters  
R. K. McClean  
H. E. McDonnell  
N. Menden  
A. W. Merrill  
Dennis Meronek  
F. Morse  
E. Nowacki  
R. Olander  
Frank O'Leary  
Ray Papich

C. L. Patterson  
K. C. Paulson  
L. D. Roberts  
W. J. Russell  
A. J. Schiewe  
M. Schlessinger  
Bernard L. Shanks  
P. Sheldon  
D. A. Shermerhorn  
R. J. Skrinska  
P. L. Smith

W. G. Smith  
H. Sokoloff  
R. L. Stewart  
M. Sturm  
T. C. Taylor  
R. M. Terasaki  
L. H. Wald  
M. T. Weiss  
R. W. Wheeler  
D. E. Whelan

SAMSO Attendees

G. E. Aichinger  
SMBA

James E. Albert  
SMTGS

Lt. Col. K. R. Burns  
SMTGS

Lt. Rodney Byler  
SMT

Capt. L. A. Deem  
SMUB

Lt. D. E. Eagles  
SMAAS

Capt. David Evans  
SMTAE

Maj. W. Glushko  
SMTGS

Capt. T. E. Goodwin  
SMT

Maj. W. Hartung  
SCL-6

Capt. E. L. Heinz  
SMAASD

Maj. F. J. Hellings  
SMTGS

Joseph Hess  
SMT/CRZ  
(AF Cambridge Research Lab.)

Maj. B. F. Johnson  
SMGS

Capt. James T. Jones  
SMTGS

Capt. George Lippincott  
SMTGS

Lt. J. K. Lyons  
SMTGS

Lt. Cmdr. T. J. Maguire  
NSbA-50

Lt. V. Munn  
SMFT

Col. D. W. Pearsall  
SMF

Lt. Col. D. D. Ryder  
SMGS

Lt. L. F. Sendlin  
SMTGS

Lt. Martin Stoehr  
SMAAS

Lt. Col. P. L. Suttler, Jr.  
SMAO-2

Lt. James C. Traeger  
SMTGS

Maj. H. R. Witsig  
SMUB

Capt. Roger Yepp  
SMAAS

Other Attendees

Krishin P. Abichandani  
Aerojet-General Corp.  
1100 W. Hollyvale St.  
Azusa, Calif. 91702

Gerald J. Adams  
Hughes Aircraft Co.  
Space Systems Div.  
Box 92919  
Los Angeles, Calif. 90009

Donald F. Adamski  
North American Rockwell  
12214 S. Lakewood Blvd.  
Downey, Calif. 90241

William Adler  
Kollsman Motrumment Corp.  
575 Underhill Blvd.  
Syosset, N. Y. 11791

Joseph B. Alario  
Aerojet-General Corp.  
1100 W. Hollyvale St.  
Azusa, Calif. 91702

Davinder K. Anand  
The Johns Hopkins University  
Applied Physics Laboratory  
8621 Georgia Ave.  
Silver Spring, Md. 20910

Gerald R. Arneson  
Honeywell, Inc.  
Aerospace Div.  
2600 Ridgeway Rd.  
Minneapolis, Minn. 55413

Robert W. Astheimer  
Barnes Engineering Co.  
30 Commerce Rd.  
Stamford, Conn. 06904

Jerry C. Bates  
Honeywell, Inc.  
Aerospace Div.  
2600 Ridgeway Rd.  
Minneapolis, Minn. 55413

Robert A. Baum  
Hamilton Standard Div.  
United Aircraft Corp.  
Bradley International Airport  
Windsor Locks, Conn. 06096

Leo Beltracchi  
Avco Systems Div.  
201 Lowell St.  
Wilmington, Mass. 01887

Thomas R. Bierma  
TRW Systems Group  
One Space Park  
Redondo Beach, Calif. 90278

Bernard H. Billik  
Hughes Aircraft Co.  
Space Systems Div.  
Box 92426  
Los Angeles, Calif. 90009

Craig D. Brown  
Honeywell, Inc.  
Aerospace Div.  
2600 Ridgeway Rd.  
Minneapolis, Minn. 55413

Herbert O. Buolteman  
Lockheed Missiles and Space Co.  
Box 504  
Sunnyvale, Calif. 94088

James W. Burns  
Lockheed Missiles and Space Co.  
Box 504  
Sunnyvale, Calif. 94088

Joseph E. Carroll  
Control Data Corp.  
7200 France Ave. South  
Minneapolis, Minn. 55435

James W. Chapman  
Control Data Corp.  
3101 E. 80th St.  
Minneapolis, Minn. 55420

Daniel J. Chiarappa  
General Dynamics Convair  
Box 1128  
San Diego, Calif. 92112

Thomas F. Clancy  
IBM Corp.  
Federal Systems Div.  
Box 780  
Westlake Village, Calif. 91360

Richard L. Cleavinger  
Ball Brothers Research Corp.  
Box 1062  
Boulder, Colo. 80303

Kenneth C. Coon  
Control Data Corp.  
7200 France Ave. South  
Minneapolis, Minn. 55435

Millard C. Crocker, II  
American Science & Engineering, Inc.  
11 Carleton St.  
Cambridge, Mass. 02142

Paul B. Davenport  
NASA  
Goddard Space Flight Ctr.  
Spacecraft Control Prog.  
Branch (Code 542)  
Greenbelt, Md. 20771

John E. Davis  
Aerojet-General Corp.  
9100 E. Flair Dr.  
El Monte, Calif. 91734

Thomas D. Davis  
Lockheed Missiles and Space Co.  
Box 504  
Sunnyvale, Calif. 94088

William R. Davis  
Lockheed Missiles and Space Co.  
Box 504  
Sunnyvale, Calif. 94088

Joseph Del Riego\*  
Hughes Aircraft Co.  
Space Systems Div.  
Box 90919  
Los Angeles, Calif. 90009

Richard L. desJardins  
NASA  
Goddard Space Flight Ctr.  
Spacecraft Control Prog.  
Branch (Code 542)  
Greenbelt, Md. 20771

James C. Devolitos  
IBM Corp.  
Federal Systems Div.  
Box 780  
Westlake Village, Calif. 91360

John A. Dodgen  
NASA  
Langley Research Ctr.  
Hampton, Va. 23365

J. C. Donald\*  
ADCOL

Hugh J. Dougherty  
Lockheed Missiles and Space Co.  
Box 504  
Sunnyvale, Calif. 94088

R. Edwards\*  
TRW Systems Group  
One Space Park  
Redondo Beach, Calif. 90278

Harold Elliott\*  
Quantic Industries, Inc.  
999 Commercial St.  
San Carlos, Calif. 94070

H. Epstein  
Hughes Aircraft Co.  
Research and Development Div.  
Centinela and Teale  
Culver City, Calif. 90230

Erik M. Eriksen, Jr.  
Grumman Aerospace Corp.  
Bethpage, N.Y. 11714

Dean C. Ewalt  
IBM Corp.  
Federal Systems Div.  
Box 780  
Westlake Village, Calif. 91360

Robert L. Farrenkopf  
TRW Systems Group  
One Space Park  
Redondo Beach, Calif. 90278

Seymour C. Ferdman  
Hughes Aircraft Co.  
Research and Development Div.  
Centinela and Teale  
Culver City, Calif. 90230

Arthur Fishman\*  
Barnes Engineering Co.  
2500 So. LaCienega Blvd.  
Los Angeles, Calif. 90034

J. Flannery\*  
TRW Systems Group  
One Space Park  
Redondo Beach, Calif. 90278

Franklin W. Floyd  
Massachusetts Institute of  
Technology  
Lincoln Laboratory  
Box 73  
Lexington, Mass. 02173

Herbert S. Fong  
Hughes Aircraft Co.  
Research and Development Div.  
Centinela and Teale  
Culver City, Calif. 90230

Edwin C. Foudriat  
Dept. of Electrical Engineering  
School of Engineering  
Marquette University  
1515 W. Wisconsin Ave.  
Milwaukee, Wisc. 53233

Glen H. Fountain  
The Johns Hopkins University  
Applied Physics Laboratory  
8621 Georgia Ave.  
Silver Spring, Md. 20910

Allan M. Frew  
TRW Systems Group  
One Space Park  
Redondo Beach, Calif. 90278

Robert Frimtsis  
Hughes Aircraft Co.  
Space Systems Div.  
Box 92426  
Los Angeles, Calif. 90009

Theodore B. Garber  
RAND Corp.  
1700 Main St.  
Santa Monica, Calif. 90406

\*Unclassified sessions only.

Darrell L. Giesekeing  
McDonnell Douglas Astronautics  
Co.  
3000 Ocean Park Blvd.  
Santa Monica, Calif. 90406

Ronald W. Gillett  
Hughes Aircraft Co.  
Space Systems Div.  
Box 92919  
Los Angeles, Calif. 90009

Richard H. Goodlin\*  
TRW Systems Group  
One Space Park  
Redondo Beach, Calif. 90278

Edward Gordon  
Aerojet-General Corp.  
1100 W. Hollyvale St.  
Azusa, Calif. 91702

G. D. Gordon\*  
Communications Satellite Corp.  
COMSAT Laboratories  
Box 115  
Clarkeburg, Md. 20734

Mark Gorstein  
NASA  
Electronics Research Ctr.  
565 Technology Square  
Cambridge, Mass. 02139

Richard J. Gran  
Grumann Aerospace Corp.  
Bethpage, N.Y. 11714

Eugene F. Grant  
Hughes Aircraft Co.  
Space Systems Div.  
Box 92919  
Los Angeles, Calif. 90009

Carlton R. Gray  
Massachusetts Institute of  
Technology  
68 Albany St.  
Cambridge, Mass. 02139

Jon Green\*  
Hughes Aircraft Co.  
Space Systems Div.  
Box 92919  
Los Angeles, Calif. 90009

Charles B. Grosch  
Control Data Corp.  
7200 France Ave. South  
Minneapolis, Minn. 55435

Morgan A. Gunet, Jr.  
Quantic Industries, Inc.  
999 Commercial St.  
San Carlos, Calif. 94070

Helen E. Gustafson  
Quantic Industries, Inc.  
999 Commercial St.  
San Carlos, Calif. 94070

Richard L. Gutshall  
Ball Brothers Research Corp.  
Box 1062  
Boulder, Colo. 80303

Frederick W. Hager  
NASA  
Goddard Space Flight Ctr.  
Code 723  
Greenbelt, Md. 20771

Edward P. Harris, III  
Hughes Aircraft Co.  
Space Systems Div.  
Box 92919  
Los Angeles, Calif. 90009

Marcellus W. Haupt  
Hughes Aircraft Co.  
Space Systems Div.  
Box 90910  
Los Angeles, Calif. 90009

Jerald L. Heiss  
IBM Corp.  
Federal Systems Div.  
Route 17C  
Owego, N.Y. 13827

Richard L. Held  
TRW Systems Group  
One Space Park  
Redondo Beach, Calif. 90278

Walter H. Hiekel  
TRW Systems Group  
One Space Park  
Redondo Beach, Calif. 90278

James A. Hill  
North American Rockwell  
12214 S. Lakewood Blvd.  
Downey, Calif. 90241

Dwayne E. Hinton  
NASA  
Langley Research Ctr.  
Hampton, Va. 23365

Fred Y. Horiuchi  
Lockhead Missiles and Space Co.  
Box 504  
Sunnyvale, Calif. 94088

Harold K. Hultner  
General Dynamics Convair  
5001 Kearny Villa Rd.  
San Diego, Calif. 92112

William F. Hummell, Jr.  
Hughes Aircraft Co.  
Space Systems Div.  
Box 92919  
Los Angeles, Calif. 90009

\*Unclassified sessions only.

Vladimir Hvoshinsky  
Lockheed Missiles and Space Co.  
Box 504  
Sunnyvale, Calif. 94088

Sam S. Impiombato  
Perkin-Elmer Corp.  
9800 So. Sepulveda Blvd., Suite 214  
Los Angeles, Calif. 90045

John Irick  
Lockheed Missiles and Space Co.  
Box 504  
Sunnyvale, Calif. 94088

David B. Jackson  
Honeywell, Inc.  
Aerospace Div.  
2600 Ridgeway Rd.  
Minneapolis, Minn. 55413

Jack R. Jennings  
TRW Systems Group  
One Space Park  
Redondo Beach, Calif. 90278

William Jerkovsky  
TRW Systems Group  
One Space Park  
Redondo Beach, Calif. 90278

Jules I. Kanter  
NASA Headquarters (REG)  
Washington, D. C. 20546

John E. Keigler  
RCA, Astro-Electronics Div.  
Box 800  
Princeton, N. J. 08540

George Kerster  
Hughes Aircraft Co.  
Space Systems Div.  
Box 92919  
Los Angeles, Calif. 90009

Gary H. Kindorf  
Hughes Aircraft Co.  
Research and Development Div.  
Centinela and Teale  
Culver City, Calif. 90230

Kenneth A. Klementis  
IBM Corp.  
Federal Systems Div.  
Box 780  
Westlake Village, Calif. 91360

Bernard Klestadt  
Hughes Aircraft Co.  
Space Systems Div.  
Box 92919  
Los Angeles, Calif. 90009

Sheldon A. Knight  
Quantic Industries, Inc.  
999 Commercial St.  
San Carlos, Calif. 94070

William Kokot  
Perkin-Elmer Corp.  
50 Danbury Rd.  
So. Wilton, Conn. 06897

Ralph W. Kordes  
Hughes Aircraft Co.  
Space Systems Div.  
Box 92919  
Los Angeles, Calif. 90009

Willi Kortum<sup>u</sup>  
Dept of Applied Mechanics  
School of Engineering  
Stanford University  
Stanford, Calif. 94305

Dusan A. Koso  
Honeywell, Inc.  
2 Forbes Rd.  
Lexington, Mass. 02173

Walter H. Kroy  
McDonnell Douglas Astronautics  
Co.  
3000 Ocean Park Blvd.  
Santa Monica, Calif. 90406

Anton E. LaBonte  
Control Data Corp.  
7200 France Ave. South  
Minneapolis, Minn. 55435

Andrew Larsen, Jr.  
TRW Systems Group  
One Space Park  
Redondo Beach, Calif. 90278

Frederick Lebowitz  
Hughes Aircraft Co.  
Research and Development Div.  
Centinela and Teale  
Culver City, Calif. 90230

Robert E. Lee  
Hughes Aircraft Co.  
Research and Development Div.  
Centinela and Teale  
Culver City, Calif. 90230

Igor P. Leliakov  
Lockheed Missiles and Space Co.  
Box 504  
Sunnyvale, Calif. 94088

Peter Likens<sup>u</sup>  
University of California at  
Los Angeles  
Los Angeles, Calif. 90024

Robert L. Lillestrand  
Control Data Corp.  
8100 34th Ave. So.  
Minneapolis, Minn. 55440

Robert A. Lucas  
Aerojet-General Corp.  
1100 W. Hollyvale St.  
Azusa, Calif. 91702

<sup>u</sup>Unclassified sessions only.

Peter P. Lundquist  
Honeywell, Inc.  
Aerospace Div.  
2600 Ridgeway Rd.  
Minneapolis, Minn. 55413

Frans E. Lusch  
Quantic Industries, Inc.  
999 Commercial St.  
San Carlos, Calif. 94070

Michael G. Lyons  
Lockheed Missiles and Space Co.  
Box 504  
Sunnyvale, Calif. 94088

Donald E. Maas  
Martin Marietta Corp.  
Box 179  
Denver, Colo. 80201

Victor Marsalia  
Hughes Aircraft Co.  
Space Systems Div.  
Box 92426  
Los Angeles, Calif. 90009

Robert H. Marsh  
Hughes Aircraft Co.  
Space Systems Div.  
Box 92919  
Los Angeles, Calif. 90009

William C. Martin  
IBM Corp.  
Federal Systems Div.  
Box 780  
Westlake Village, Calif. 91360

Kevin J. McAloon  
TRW Systems Group  
One Space Park  
Redondo Beach, Calif. 90278

Patrick D. McCarroll  
TRW Systems Group  
One Space Park  
Redondo Beach, Calif. 90278

Robert J. McElvain  
Hughes Aircraft Co.  
Space Systems Div.  
Box 92919  
Los Angeles, Calif. 90009

Vernon K. Merrick  
NASA  
Ames Research Ctr.  
Moffett Field, Calif. 94035

Joseph A. Miller  
Honeywell, Inc.  
Aerospace Div.  
2600 Ridgeway Rd.  
Minneapolis, Minn. 55413

Rollin B. Mitchell  
IBM Corp.  
Federal Systems Div.  
Box 922  
Azusa, Calif. 91702

Charles S. Morris  
The Johns Hopkins University  
Applied Physics Laboratory  
8621 Georgia Ave.  
Silver Spring, Md. 20910

Richard E. Mortensen  
Aerojet-General Corp.  
1100 W. Hollyvale St.  
Azusa, Calif. 91702

Caswell B. Neal<sup>\*</sup>  
Hughes Aircraft Co.  
Space Systems Div.  
Box 92919  
Los Angeles, Calif. 90009

Dennis P. Nell  
Hughes Aircraft Co.  
Space Systems Div.  
Box 92919  
Los Angeles, Calif. 90009

Gerald D. Nelson  
Honeywell, Inc.  
Aerospace Div.  
2600 Ridgeway Rd.  
Minneapolis, Minn. 55413

Murray J. Neufeld  
Hughes Aircraft Co.  
Space Systems Div.  
Box 92919  
Los Angeles, Calif. 90009

Vance D. Norum  
Aerojet-General Corp.  
1100 W. Hollyvale St.  
Azusa, Calif. 91702

John E. Notti, Jr.  
North American Rockwell  
12214 S. Lakewood Blvd.  
Downey, Calif. 90241

Gerald S. Nurre  
NASA  
Marshall Space Flight Ctr.  
Huntsville, Ala. 35812

James P. O'Donnell  
Hughes Aircraft Co.  
Space Systems Div.  
Box 90919  
Los Angeles, Calif. 90009

Ezra G. Ogletree  
Massachusetts Institute of  
Technology  
Instrumentation Laboratory  
68 Albany St.  
Cambridge, Mass. 02139

<sup>\*</sup>Unclassified sessions only.



Ronald V. Ogren  
TRW Systems Group  
One Space Park  
Redondo Beach, Calif. 90273

Frank T. Ohgi  
McDonnell Douglas Astronautics  
Co.  
5301 Bolsa Ave.  
Huntington Beach, Calif. 92647

Joseph P. O'Malley  
TRW Systems Group  
One Space Park  
Redondo Beach, Calif. 90278

James R. Owens  
Communications Satellite Corp.  
COMSAT Laboratories  
Box 115  
Clarksburg, Md. 20734

David C. Paulson  
Honeywell, Inc.  
Aerospace Div.  
2600 Ridgeway Rd.  
Minneapolis, Minn. 55413

Harold Perkel  
RCA, Astro-Electronics Div.  
Box 800  
Princeton, N.J. 08540

R. P. Pieper\*  
TRW Systems Group  
One Space Park  
Redondo Beach, Calif. 90278

William F. Polich  
Aerojet-General Corp.  
1100 W. Hollyvale St.  
Azusa, Calif. 91702

Keith G. Powers  
Aerojet-General Corp.  
1100 W. Hollyvale St.  
Azusa, Calif. 91702

Ralph Pringle, Jr.  
Bell Telephone Laboratories  
Whippany Road  
Whippany, N. J. 07981

Robert M. Reid  
Lockhead Missiles and Space Co.  
Box 504  
Sunnyvale, Calif. 94088

Robert G. Rennie  
Grumman Aerospace Corp.  
Bethpage, N.Y. 11714

Arthur L. Reynolds\*  
Hughes Aircraft Co.  
Space Systems Div.  
Box 92919  
Los Angeles, Calif. 90009

John J. Ribarich  
Hughes Aircraft Co.  
Space Systems Div.  
Box 90919  
Los Angeles, Calif. 90009

Robert E. Roberson  
Aerojet-General Corp.  
1100 W. Hollyvale St.  
Azusa, Calif. 91702

John J. Rodden  
Lockhead Missiles and Space Co.  
Box 504  
Sunnyvale, Calif. 94088

Roger L. Rollins  
Philco-Ford Corp.  
Space & Reentry Systems Div.  
3825 Fabian Way  
Palo Alto, Calif. 94303

Richard K. Ronald  
Quantic Industries, Inc.  
999 Commercial St.  
San Carlos, Calif. 94070

Paul Rupert\*  
North American Rockwell  
Space and Info. Syst. Div.  
12214 Lakewood Blvd.  
Downey, Calif. 90241

William F. Sarles, Jr.  
Massachusetts Institute of  
Technology  
Lincoln Laboratory  
Box 73  
Lexington, Mass. 02173

Stephen E. Savas  
Aerojet-General Corp.  
1100 W. Hollyvale St.  
Azusa, Calif. 91702

Earl G. Schaller  
IBM Corp.  
Federal Systems Div.  
Box 780  
Westlake Village, Calif. 91360

Roger T. Schappell  
Martin Marietta Corp.  
Box 179  
Denver, Colo. 80201

David K. Scharmack  
Honeywell, Inc.  
Systems and Research Ctr.  
2345 Walnut St.  
St. Paul, Minn. 55113

Frank H. Schlee  
IBM Corp.  
Federal Systems Div.  
Route 17C  
Owego, N.Y. 13827

\*Unclassified sessions only.

Eldon D. Scott  
Lockheed Missiles and Space Co.  
Box 504  
Sunnyvale, Calif. 94088

Robert T. Scott  
Honeywell, Inc.  
Aerospace Div.  
2600 Ridgeway Rd.  
Minneapolis, Minn. 55413

James Sebben\*  
TRW Systems Group  
One Space Park  
Redondo Beach, Calif. 90278

Richard L. Seibert  
Hughes Aircraft Co.  
Research and Development Div.  
Cantinsela and Teale  
Culver City, Calif. 90230

Robert G. Seibert  
McDonnell Douglas Astronautics  
Co.  
3000 Ocean Park Blvd.  
Santa Monica, Calif. 90406

Lt. Kenneth D. Senne  
Frank J. Seiler Research  
Laboratory (OAR)  
USAF Academy, Colo. 80840

Warren H. Sierer  
Hughes Aircraft Co.  
Research and Development Div.  
Cantinsela and Teale  
Culver City, Calif. 90230

Kurt W. Simon  
TRW Systems Group  
One Space Park  
Redondo Beach, Calif. 90278

John O. Simpson  
Ball Brothers Research Corp.  
Box 1062  
Boulder, Colo. 80303

Bernard Sklar  
Air Force Weapons Laboratory  
Kirtland AFB, N. Mex.

Richard T. Skramstad  
Hughes Aircraft Co.  
Research and Development Div.  
Cantinsela and Teale  
Culver City, Calif. 90230

William A. Snyder  
Hughes Aircraft Co.  
Space Systems Div.  
Box 92919  
Los Angeles, Calif. 90009

Derle M. Solheim  
Hughes Aircraft Co.  
Research and Development Div.  
Cantinsela and Teale  
Culver City, Calif. 90230

David Sonnabend  
Ball Brothers Research Corp.  
Box 1062  
Boulder, Colo. 80303

Harold W. Sorenson  
Aerojet-General Corp.  
1100 W. Hollyvale St.  
Azusa, Calif. 91702

Tom M. Spencer  
Ball Brothers Research Corp.  
Box 1062  
Boulder, Colo. 80303

Fred W. Stang\*  
Barnes Engineering Co.  
2500 So. LaCienega Blvd.  
Los Angeles, Calif. 90034

Glenn T. Stebbins  
Hamilton Standard Div.  
United Aircraft Corp.  
8929 So. Sepulveda Blvd.  
Los Angeles, Calif. 90045

Gunter Stein\*  
Ball Brothers Research Corp.  
Box 1062  
Boulder, Colo. 80303

Walter W. Stevens  
Perkin-Elmer Corp.  
9800 So. Sepulveda Blvd., Suite 214  
Los Angeles, Calif. 90045

Lincoln Teng\*  
Optimal Data  
6218 Madison Pike  
Huntsville, Ala. 35806

Joe Thompson\*  
System Development Corp.  
2500 Colorado Ave.  
Santa Monica, Calif. 90406

Norris W. Tidwell  
Honeywell, Inc.  
Aerospace Div.  
2600 Ridgeway Rd.  
Minneapolis, Minn. 55413

Bruce E. Tinning  
NASA  
Ames Research Ctr.  
Moffett Field, Calif. 94035

Norman F. Toda  
IBM Corp.  
Federal Systems Div.  
Route 17C  
Owego, N. Y. 13827

\*Unclassified sessions only.

Nornian R. Trudeau  
Massachusetts Institute of  
Technology  
Lincoln Laboratory  
Box 73  
Lexington, Mass. 02173

Maj. Alvin R. Turner  
Hq. USAF Systems Command  
(SCTTI)  
Andrews AFB, Md. 20331

Richard S. Utter  
Hughes Aircraft Co.  
Space Systems Div.  
Box 90919  
Los Angeles, Calif. 90009

Juri Valge  
Massachusetts Institute of  
Technology  
Instrumentation Laboratory  
68 Albany St.  
Cambridge, Mass. 02139

Bruce D. Vannelli  
Control Data Corp.  
7200 France Ave. South  
Minneapolis, Minn. 55435

Lyman B. Van Vliet, Jr.  
Hughes Aircraft Co.  
Research and Development Div.  
Cantinsela and Teale  
Culver City, Calif. 90230

Robert H. VanVooren  
TRW Systems Group  
One Space Park  
Redondo Beach, Calif. 90278

Charles F. Vondra  
Honeywell, Inc.  
Aerospace and Defense Group  
650 No. Sepulveda Blvd.  
El Segundo, Calif. 90245

James W. Watson  
TRW Systems Group  
One Space Park  
Redondo Beach, Calif. 90278

C. Robert Welti  
Lockheed Missiles and Space Co.  
Box 504  
Sunnyvale, Calif. 94088

Phillip C. Wheeler  
TRW Systems Group  
One Space Park  
Redondo Beach, Calif. 90278

Eddy W. White  
Hughes Aircraft Co.  
Space Systems Div.  
Box 90919  
Los Angeles, Calif. 90009

Franklin R. Wiemann  
Honeywell, Inc.  
Aerospace and Defense Group  
650 No. Sepulveda Blvd.  
El Segundo, Calif. 90045

John S. Williams  
TRW Systems Group  
One Space Park  
Redondo Beach, Calif. 90278

Paul Wong  
Hughes Aircraft Co.  
Space Systems Div.  
Box 92426  
Los Angeles, Calif. 90009

John F. Yocum, Jr.  
Hughes Aircraft Co.  
Space Systems Div.  
Box 92919  
Los Angeles, Calif. 90009

Paul R. Yoder, Jr.  
Perkin-Elmer Corp.  
50 Danbury Rd.  
So. Wilton, Conn. 06897

Richard T. Yoshida  
Martin Marietta Corp.  
Box 179  
Denver, Colo. 80201

Terry Yuen  
System Development Corp.  
2500 Colorado Ave.  
Santa Monica, Calif. 90406

Terry S. Zaccane  
Philco-Ford Corp.  
Space and Reentry Systems Div.  
3825 Fabian Way  
Palo Alto, Calif. 94303

Walter S. Zukowsky  
Perkin-Elmer Corp.  
50 Danbury Rd.  
So. Wilton, Conn. 06897

\*Unclassified sessions only.

UNCLASSIFIED

Security Classification

DOCUMENT CONTROL DATA - R&D		
(Security classification of title, body of abstract and indexing annotation must be entered when the overall report is classified)		
1. ORIGINATING ACTIVITY (Corporate author) The Aerospace Corporation El Segundo, California		2a. REPORT SECURITY CLASSIFICATION Unclassified
		2b. GROUP
3. REPORT TITLE PROCEEDINGS OF THE SYMPOSIUM ON SPACECRAFT ATTITUDE DETERMINATION, SEPTEMBER 30, OCTOBER 1-2, 1969; VOLUME I: UNCLASSIFIED PAPERS		
4. DESCRIPTIVE NOTES (Type of report and inclusive dates)		
5. AUTHOR(S) (Last name, first name, initial) Symposium Chairmen: Evans, D., Captain, USAF, Henrikson, L. J., and Lesinski, J. E.		
6. REPORT DATE 69 OCT 31	7a. TOTAL NO. OF PAGES 425	7b. NO. OF REFS 224
8a. CONTRACT OR GRANT NO. F04701-69-C-0066	8b. ORIGINATOR'S REPORT NUMBER(S) TR-0066(5306)-12, Vol. I	
9. PROJECT NO.	9b. OTHER REPORT NO(S) (Any other numbers that may be assigned this report) SAMSO-TR-69-417, Vol. I	
10. AVAILABILITY/LIMITATION NOTICES This document has been approved for public release and sale; its distribution is unlimited.		
11. SUPPLEMENTARY NOTES		12. SPONSORING MILITARY ACTIVITY Space and Missile Systems Organization Air Force Systems Command Los Angeles, California
13. ABSTRACT These proceedings contain reproductions of the unclassified papers presented at the Symposium on Spacecraft Attitude Determination, held at The Aerospace Corporation on September 30 and October 1-2, 1969. Classified papers appear in Volume II. The symposium consisted of six sessions. A brief summary of the material in each of these sessions follows. Session I (Unclassified), Attitude Estimation Concepts, is devoted to papers surveying the general theory, modeling, and estimation algorithm concepts of use in estimating spacecraft attitude. Session II (Unclassified), Attitude Sensors and Sensing Techniques, presents papers examining the current state of the art and future potential of some of the sensing techniques used in attitude determination. Session III (Unclassified), Attitude Determination Systems I, comprises papers regarding attitude determination operational and design experience for several different satellite systems. Session IV (Secret), SPARS, contains papers that discuss the hardware, algorithms, and system test results. Session V (Secret), Attitude Determination Systems II, concerns papers on United States attitude determination requirements and classified applications. Session VI (Secret) is the Panel Discussion. An edited transcription of the panel discussion and audience participation appears in Volume II of these proceedings. (over)		

KEY WORDS

Attitude Estimation  
Attitude Sensors  
Optimal Filtering Applications  
Nonlinear Filtering Applications  
Satellite Disturbance Torques  
Least Squares Estimation Applications  
Quantized Data Filtering  
Star Trackers  
Star Mappers  
Solar Sensors  
Infrared Horizon Definition  
Infrared Horizon Sensors  
Satellite Dynamic Modeling  
Strapdown Inertial Reference Systems  
Testing of Inertial Components  
Attitude Determination Systems  
Attitude Determination Accuracy  
Strapdown Algorithms  
Gravity-Gradient Satellites  
Orbiting Gyrostats  
Estimation Theory  
Spin-Stabilized Satellites

Project Scanner  
ATS, Applications Technology  
Satellite  
TACSAT, Tactical Communications  
Satellite  
OAO, Orbiting Astronomical  
Observatory

Abstract (Continued)

Also included in the present volume are biographical sketches of the chairmen and speakers, and a list of the symposium attendees.